frontiers | Research Topics

Attainment of SDGs through the advancement in solar PV systems

Edited by
Praveen Kumar Balachandran, Sudhakar Babu Thanikanti, Bamidele Victor Ayodele, Murat Fahrioglu and Nnamdi Nwulu

Published in
Frontiers in Energy Research

ISSN 1664-8714
ISBN 978-2-8325-5162-2
DOI 10.3389/978-2-8325-5162-2

About Frontiers

Frontiers is more than just an open access publisher of scholarly articles: it is a pioneering approach to the world of academia, radically improving the way scholarly research is managed. The grand vision of Frontiers is a world where all people have an equal opportunity to seek, share and generate knowledge. Frontiers provides immediate and permanent online open access to all its publications, but this alone is not enough to realize our grand goals.

Frontiers journal series

The Frontiers journal series is a multi-tier and interdisciplinary set of open-access, online journals, promising a paradigm shift from the current review, selection and dissemination processes in academic publishing. All Frontiers journals are driven by researchers for researchers; therefore, they constitute a service to the scholarly community. At the same time, the *Frontiers journal series* operates on a revolutionary invention, the tiered publishing system, initially addressing specific communities of scholars, and gradually climbing up to broader public understanding, thus serving the interests of the lay society, too.

Dedication to quality

Each Frontiers article is a landmark of the highest quality, thanks to genuinely collaborative interactions between authors and review editors, who include some of the world's best academicians. Research must be certified by peers before entering a stream of knowledge that may eventually reach the public - and shape society; therefore, Frontiers only applies the most rigorous and unbiased reviews. Frontiers revolutionizes research publishing by freely delivering the most outstanding research, evaluated with no bias from both the academic and social point of view. By applying the most advanced information technologies, Frontiers is catapulting scholarly publishing into a new generation.

What are Frontiers Research Topics?

Frontiers Research Topics are very popular trademarks of the *Frontiers journals series*: they are collections of at least ten articles, all centered on a particular subject. With their unique mix of varied contributions from Original Research to Review Articles, Frontiers Research Topics unify the most influential researchers, the latest key findings and historical advances in a hot research area.

Find out more on how to host your own Frontiers Research Topic or contribute to one as an author by contacting the Frontiers editorial office: frontiersin.org/about/contact

Attainment of SDGs through the advancement in solar PV systems

Topic editors

Praveen Kumar Balachandran — Vardhaman College of Engineering, India
Sudhakar Babu Thanikanti — Chaitanya Bharathi Institute of Technology, India
Bamidele Victor Ayodele — University of Technology Petronas, Malaysia
Murat Fahrioglu — Middle East Technical University Northern Cyprus Campus, Cyprus
Nnamdi Nwulu — University of Johannesburg, South Africa

Citation

Balachandran, P. K., Thanikanti, S. B., Ayodele, B. V., Fahrioglu, M., Nwulu, N., eds. (2024). *Attainment of SDGs through the advancement in solar PV systems*. Lausanne: Frontiers Media SA. doi: 10.3389/978-2-8325-5162-2

Table of contents

frontiers | Frontiers in Energy Research

TYPE Editorial
PUBLISHED 02 July 2024
DOI 10.3389/fenrg.2024.1451373

OPEN ACCESS

EDITED AND REVIEWED BY
Michael Folsom Toney,
University of Colorado Boulder, United States

*CORRESPONDENCE
Praveen Kumar Balachandran,
praveenbala038@gmail.com
Sudhakar Babu Thanikanti,
sudhakarbabu66@gmail.com
Bamidele Victor Ayodele,
bamidele.ayodele@utp.edu.my,
ayodelebv@gmail.com
Murat Fahrioglu,
fmurat@metu.edu.tr
Nnamdi Nwulu,
nnwulu@uj.ac.za

RECEIVED 19 June 2024
ACCEPTED 20 June 2024
PUBLISHED 02 July 2024

CITATION
Balachandran PK, Thanikanti SB, Ayodele BV, Fahrioglu M and Nwulu N (2024), Editorial: Attainment of SDGs through the advancement in solar PV systems.
Front. Energy Res. 12:1451373.
doi: 10.3389/fenrg.2024.1451373

Editorial: Attainment of SDGs through the advancement in solar PV systems

Praveen Kumar Balachandran[1]*, Sudhakar Babu Thanikanti[2]*, Bamidele Victor Ayodele[3,4]*, Murat Fahrioglu[5]* and Nnamdi Nwulu[6]*

[1]Department of Electrical and Electronics Engineering, Vardhaman College of Engineering, Hyderabad, India, [2]Department of Electrical and Electronics Engineering, Chaitanya Bharati Institute of Technology, Hyderabad, India, [3]Chemical Engineering Department, Universiti Teknologi PETRONAS, Perak, Malaysia, [4]Center of Carbon Capture, Utilization and Storage (CCCUS), Institute of Sustainable Energy, Universiti Teknologi PETRONAS, Perak, Malaysia, [5]Department of Electrical and Electronic Engineering, Middle East Technical University – Northern Cyprus Campus, Guzelyurt, Türkiye, [6]Centre for Cyber Physical Food, Energy and Water Systems, University of Johannesburg, Johannesburg, South Africa

KEYWORDS

sustainable development goals, solar photovoltaic, clean electricity, energy efficiency, solar mini-grid

Editorial on the Research Topic
Attainment of SDGs through the advancement in solar PV systems

As we approach 2030, it is imperative to confront the significant disparities that are impacting our wellbeing, standard of living, and global economies. The development of renewable energy systems, particularly solar photovoltaic (PV) systems, can directly and indirectly contribute to the achievement of many of the UN's Sustainable Development Goals (SDGs). Solar PV systems are often regarded as highly efficient means of generating clean electricity, making them crucial for achieving these objectives. A multitude of researchers worldwide are presently concentrating on enhancing efficiency, minimizing expenses, recycling, reconfiguring, and innovating materials for solar PV systems. By employing sustainable energy systems for various purposes such as electricity production, farming, and electric vehicle charging, we may actively contribute to the successful attainment of the SDGs. Nevertheless, it is crucial to evaluate and emphasize the degree of achievement of SDGs in current research on solar PV systems.

The Research Topic "*Attainment of SDGs through the advancement in solar PV systems*" promotes research focused on achieving any of the 17 Sustainable Development Goals (SDGs) through the advancement of solar photovoltaic (PV) systems. Several authors have delved into the Research Topic by considering the progress in the efficient production and application of solar PV power systems; utilizing solar PV systems for everyday requirements such as electric vehicle (EV) charging; analyzes the achievement of SDGs through the use of renewable energy systems; progress in the modeling and optimization of solar systems via the application of innovative techniques and procedures to improve energy output.

Karna et al. provides a performance assessment of two solar mini-grid systems, namely, Thabang Solar Mini-Grid (TSMG) and Sugarkhal Solar Mini-Grid (SSMG), in Nepal. The study uses secondary data from 2021–2023 and PVsyst software 7.4 to measure the peak levels of irradiance in April for both systems. The study explores the process of energy generation by solar PV modules, emphasizing that it is closely correlated with the intensity

of irradiance levels. The authors reported that an increased irradiance leads to greater energy production, however elevated temperatures were reported to decreased production as a result of their negative effect on the efficiency of solar cells. Several variables were also reported to impact energy production, including temperature, shade, dust buildup, and the capability of system components. It was concluded that efficient placement and consistent upkeep of solar panels are essential for optimum energy production.

Srilakshmi et al. examines the integration of a unified power quality conditioner (5L-UPQC) with wind, solar, and battery storage systems as a solution to power quality problems. The study presents a suggested approach that utilizes an Artificial Neural Network-based Controller trained with the Levenberg–Marquardt algorithm. This ANNC generates reference signals for converters, hence removing the requirement for conventional transformations. The study assessed the system's performance in different scenarios, showcasing its efficacy in reducing current harmonics, enhancing power factor, and eliminating fluctuations in grid voltage. It proposes that the same approach can be applied to multilevel UPQC systems with fewer switches to achieve even greater improvements.

Aljafari et al. explores a new PV array layout inspired by the Renzoku puzzle pattern. The proposed layout aims to tackle the problem of power loss in PV systems that are only partially shaded. The PV array was suggested as a solution to address the limitations of prior configurations in terms of power generation and mismatch losses. The suggested arrangement was verified using a simulation of a 9 × 9 PV array in MATLAB/Simulink® and its subsequent construction in hardware. The study presents results and characteristic curves that demonstrated the efficacy of the layout under different amounts of partial shade.

Qin et al. presents a technique for monitoring the rapid frequency response of solar power stations in order to maintain the stability of the power grid. The system incorporates a sensor data gathering module and a data analysis module to accurately evaluate response rates. The study suggested method's anti-disturbance performance was validated using a frequency step disturbance test conducted at a power station in China.

Srilakshmi et al. describes an efficient architecture for a power system that combines solar, wind, battery, and electric vehicle technologies with a Unified Power Quality Conditioner. The study employs an advanced most valuable player algorithm to choose active filter and PID Controller settings for the purpose of regulating power flow and enhancing power quality. The findings demonstrate that the ANFIS-based power flow management, along with the optimal design of UPQC, effectively tackles the difficulties related to power quality (PQ) and achieves efficient power sharing.

In a similar study by Srilakshmi et al., a concept for a reduced switch converter, which aims to decrease costs and enhance reliability by utilizing a reduced number of switches was presented. The study introduces an innovative method of combining Static Harmonic and Reactive Power Filter with renewable energy sources. It showcases enhanced power quality and consistent power supply across different operating situations. The study examined four test scenarios in both grid and standalone situations, assessing the performance of the optimized controller in comparison to current approaches such as sliding mode control and classic fuzzy logic control.

Pushkarna et al. introduces a compensation approach that utilizes Unified electricity Quality Conditioner to establish a connection between wind farms and electricity networks that have low strength. The study discusses the difficulties of incorporating wind farms equipped with Squirrel Cage Induction Generators into vulnerable power networks, which can have negative impacts on Power Quality and stability. The study emphasizes the utilization of CUPS, specifically UPQC, to enhance voltage regulation and minimize variations at the Point of Common Coupling. The results indicate that the suggested compensatory approach improves power quality and stability in wind farms.

Luo et al. conducted a comparison of the environmental effects of solar photovoltaic power generation and coal power in Ningxia, China, employing life cycle assessment and ecological footprint analysis. The GHG emission rate of solar photovoltaic power generation was substantially lower in comparison to coal power. The solar photovoltaic power generation has an excess of ecological resources, whereas coal power displays an increasing shortage of ecological resources. The report proposes a transition towards sustainable energy sources, such as solar photovoltaic power generation, in order to match with China's objectives of achieving carbon neutrality.

Fekik et al. presented a battery management system that incorporates three separate modes: charging, direct, and discharging. These modes provide intelligent control over crucial circumstances. The simulation findings highlight the resilience of the suggested system across various conditions, showcasing its efficacy in regulating power distribution according to battery charge levels, even in situations with inadequate solar power. The study makes a significant contribution to the advancement of knowledge in PV/battery systems and provides a realistic and sustainable solution for improving energy generation, distribution, and storage.

Smida et al. proposed a novel metaheuristic maximum power point tracking called the Crow Search Algorithm (CSA) to ameliorate the tracking performance of a grid connected shaded PV system. The CSA is a nature inspired method based on the intelligent behaviors of crows in its search process for hidden food sources. This novel method succeeds to mitigate the adverse impacts of partial shading on the performance of PV systems by accurately tracking the GMPP. Based on the small-signal dynamic model, the stability of the proposed system is analyzed. Simulation results for three different levels of partial shading, including zero, weak, and severe shading, demonstrate the better performance of the suggested CSA compared to fuzzy logic controller (FLC) and Inc-Cond techniques.

Kumar et al. demonstrated the enhancement of power quality in a grid-connected PV system using a hybrid energy storage system. The proposed technique enhances the consistency of photovoltaic power generation, stabilizes the direct current voltage, and eliminates the harmonic distortions caused by non-linear loads on the power source. The two primary roles of the Shunt Active Power Filter functioning as a reactive power buffer mitigate variations and minimize distortions caused by current harmonics. This enables the direct transfer of active electricity into the electrical grid by harnessing sustainable solar PV energy. The effectiveness of

the projected compensation system may be observed by the sinusoidal current and reactive power compensation. The system's minimal overall harmonic distortion demonstrates the effectiveness of the configuration.

Baskaran et al. suggested the use of four high-step-up DC-DC converters to convert low-voltage sources, such as solar photovoltaic, fuel cells, and battery banks. Their performances were assessed based on their capacity to achieve optimal capability and maintain high dependability. Out of the four suggested designs, the bootstrap converter was chosen due to its capacity to minimize losses and eliminate unnecessary parameters. The suggested converter operates the inverter-driven switching reluctance motor (SRM) assembly using a directly coupled approach, therefore eliminating the requirement for battery banks and contributing to cost reduction.

The interest in the Research Topic "Attainment of SDGs through the Advancement in Solar PV systems" is evidenced by the subject set's cumulative view count, which at the time of writing this editorial had reached 7,815. There had also been 1,010 downloads of the different articles.

Author contributions

PB: Conceptualization, Visualization, Writing–review and editing. ST: Conceptualization, Visualization, Writing–review and editing. BA: Conceptualization, Writing–original draft. MF: Conceptualization, Visualization, Writing–review and editing. NN: Conceptualization, Visualization, Writing–review and editing.

Funding

The author(s) declare that no financial support was received for the research, authorship, and/or publication of this article.

Conflict of interest

The authors declare that the research was conducted in the absence of any commercial or financial relationships that could be construed as a potential conflict of interest.

Publisher's note

frontiers | Frontiers in Energy Research

TYPE Original Research
PUBLISHED 16 January 2024
DOI 10.3389/fenrg.2023.1321945

OPEN ACCESS

EDITED BY
Praveen Kumar Balachandran,
Vardhaman College of Engineering, India

REVIEWED BY
Sadhan Mahapatra,
Tezpur University, India
Koganti Srilakshmi,
Sreenidhi Institute of Science and Technology, India

*CORRESPONDENCE
Ajay Kumar Jha,
akjha@ioe.edu.np

RECEIVED 15 October 2023
ACCEPTED 28 November 2023
PUBLISHED 16 January 2024

CITATION
Karna SL, Jha AK, Yadav K and Kumar Mallik J (2024), Performance evaluation of solar PV mini grid system in Nepal: a case study Thabang and Sugarkhal.
Front. Energy Res. 11:1321945.
doi: 10.3389/fenrg.2023.1321945

Performance evaluation of solar PV mini grid system in Nepal: a case study Thabang and Sugarkhal

Sanjay Lal Karna[1,2], Ajay Kumar Jha[3]*, Kishori Yadav[4,5] and Jiwan Kumar Mallik[6]

[1]Central Department of Physics, Tribhuvan University, Kirtipur, Nepal, [2]Department of Physics, Tri-Chandra Multiple Campus, Tribhuvan University, Kathmandu, Nepal, [3]Department of Mechanical and Aerospace Engineering, Institute of Engineering, Tribhuvan University, Pulchowk Campus, Lalitpur, Nepal, [4]Department of Physics, Patan Multiple Campus, Tribhuvan University, Lalitpur, Nepal, [5]Innovative Ghar Nepal, Lalitpur, Nepal, [6]Renewable Energy for Rural Livelihood, Lalitpur, Nepal

This article investigates the performance metrics of two solar mini-grid systems, Thabang Solar Mini-Grid (TSMG) and Sugarkhal Solar Mini-Grid (SSMG), based on secondary live data, collected from Renewable Energy for Rural Livelihood (RERL) and PVsyst software 7.4 spanning the years 2021–2023. Notably, the highest irradiance levels were recorded in April for both TSMG and SSMG. TSMG exhibited an energy generation of 83.206 MWh/year in 2021 and 112.140 MWh/year in 2022, with a peak sun hour (PSH) of 5.5 h. Conversely, SSMG energy generated 64.14 MWh/year in 2021 and 68.79 MWh/year in 2022, with a PSH of 5.7 h. The capture loss of SSGM recorded 0.239 kWh/day to 3.322 kWh/day in 2021 and 0.082 kWh/day to 2.086 kWh/day in 2022. Also, the capture loss of TSGM recorded 1.573 kWh/day to 5.011 kWh/day in 2021 and 0.470 kWh/day to 4.261 kWh/day in 2023. The efficiency of SSMG is consistently higher efficiency compared to TSMG. The capture factor of SSMG increased from 9.76% in 2021 to 10.47% in 2022, while of TSMG 6.33% in 2021 to 8.53% in 2023. The findings provide valuable insights into the comparative performance of these solar mini-grid systems, contributing to the optimization and improvement of solar energy generation in diverse environmental conditions.

KEYWORDS

TSMG, SSMG, PVsyst software 7.4, energy generation, capture loss, capture factor

1 Introduction

Global interest is growing regarding the localization of renewable energy resources (RER) using solar mini grids (SMG). Social issues, financial, ecological, and technological advantages all come with SMG use. They reduce blackouts, deliver electricity in remote areas, and improve energy efficiency. However, due to increased demand, it has become harder to combine microgrids (MGs) and systems for managing energy while retaining robustness and effectiveness. Investigating renewable energy resources and building MGs with efficient and long-lasting power storage systems and demand-side control require sustainable techniques (Shafiullah et al., 2022). Solar panels are used in photovoltaic (PV) systems, which can range in size from tiny rooftop installations to massive utility-scale power plants. A basic PV system that connects to the grid is shown in Figure 1. Global energy consumption has grown significantly over the past three decades, increasing from 6131 TWh in 1973 to 23816 TWh in 2014, and it is anticipated that this increase will enable new technology and hence enhance quality of life. According to Guichi et al., by 2040, 56% of the global energy supply would

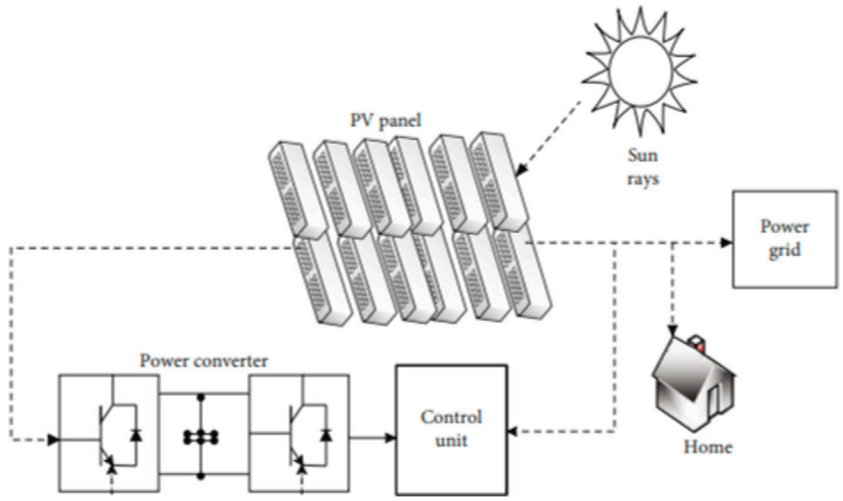

FIGURE 1
Grid-Connection PV module's configuration (Srimathi et al., 2022).

have been used (Guichi et al., 2018). Environmentally responsible and renewable sources of energy, such as solar energy, were one potential power source to replace non-renewable energy sources.

Solar energy has been popularly adopted as an off-grid electrification solution in many developing countries around the world, with varying degrees of success. It has been a successful solution in South Asia (Palit and Chaurey, 2011), in Tanzania and Mozambique (Ahlborg and Hammar, 2014), and in South Africa. It has also been found an affordable solution for rural electrification in Sub-Saharan Africa (Baurzhan and Jenkins, 2016). A review of global rural electrification policies across the world; found that off-grid renewable energy-based electrification is the best answer where grid extension is not feasible. An effective electrification strategy is one where the on-grid and off-grid electrification plans are complementary and avoid duplication of resources (Aziz and Chowdhury, 2020).

Currently, 69% of the nation's energy needs are met by biomass, which includes firewood and agricultural waste. Hydropower and small-scale renewable energy sources including PV, biogas, and micro-hydro that are purchased from India produce 25% of the remaining energy. Nepal is the nation that is most at risk from the effects of climate change. The Ministry of Energy and Water Resources (2023) aims to increase annual household electricity use between 267 and 700 kWh in 5 years and 1,500 kWh in 10 years. According to Kafle et al. (2023), Nepal experiences approximately 300 days of sunshine annually, resulting in an average daily amount of six and a half hours of sunlight and 4.7 kWh/m^2/day of insolation. Given the available resources and local knowledge, Nepal's existing MGs are not sufficiently built for the region (Shrestha et al., 2020).

Regarding Nepal specifically, over 55 MW of electricity have been generated through micro-hydropower and solar energy, supplying 3.6 million households, or 18% of the population, with access to electricity. Since the establishment of the Alternative Energy Promotion Center (AEPC) in 1996, Nepal has experienced a rapid acceleration in the growth of mini- and micro-hydropower, solar PV, and wind generating. The establishment of an off-grid SMG system and aggressive grid extension have both contributed to the electrification of rural areas of Nepal. In Nepal, 95.5% of families have some form of access to electricity, including grid or SMG power, solar home power, solar lights, rechargeable batteries, etc. Only 67% of people in the nation have access to power, according to the same survey (ESMAP, 2017). As an illustration, the loading factor and utilization factor for Baglung SMG in western Nepal have been determined to be 23% and 26%, respectively (Shrestha et al., 2020). Even though Nepal has a huge amount of potential for producing electricity from various renewable energy sources, 4.5% of its population still lacks access to electricity. This is a result of the country's hilly terrain. In terms of a management system for the long-term success of plants, Nepalese MGs have a significant failure rate. Rural areas still have trouble accessing dependable and consistent electricity because of these various concerns (SE4ALL, 2020).

1.1 Electricity scenarios in Nepal

Modern energy, comprising electricity, petroleum, and renewable, constitutes approximately 20% of Nepal's total energy consumption, a figure steadily on the rise. Among these modern energy sources, petrol holds the largest share at around 65%, while electricity accounts for approximately 15%, and the remaining 20% is attributed to other sources like coal. Nepal faces a rising demand for electricity, particularly in remote areas, where access is limited. Despite the availability of various renewable energy sources for lighting and cooking, achieving sustainable development goal number 7, which emphasizes universal access to affordable, reliable, and modern energy, remains a challenge. In alignment with global sustainability efforts, Nepal, during COP26, committed to achieving net-zero emissions by 2045 and increasing the share of clean energy to 15% while expanding forest cover to 45% by 2030. As of now, the country's total installed power plant

TABLE 1 SMG completed project reported by AEPC.

S.N.	Name of mini grid	District	Total installed capacity (kW)	Year of completion
1	Dhaubadi SWMG	Nawalparasi	12	2010
2	Bhorleni SWMG	Makawanpur	25	2013
3	Tatopani SWMG	Jumla	26	2014
4	Kamalbazaar SWMG	Achham	31	2015
5	Harrekanda-Taranga SWMG	Surkhet	8	2015
6	Chisapani SWMG	Sindhuli	35	2016
7	Parakatne SWMG	Bajhang	22	2016
8	Mityal SWMG	Palpa	25	2017
9	Narakot SWMG	Jumla	80	2017
10	Saptami SWMG	Panchthar	70	2018
11	Pamakham SWMG	Bhojpur	50	2020*
12	Dubung SMG	Tanahu	18	2015
13	Harkapur SMG	Okhaldhunga	31	2016
14	Chysmitar SMG	Khotang	17	2016
15	Kaduwa SMG	Khotang	21	2016
16	Ramitekhola SMG	Morang	30	2017
17	Olane SMG	Panchthar	25	2017
18	Rithachaupata SMG-1	Darchula	21	2018
19	Rithachaupata SMG-2	Darchula	13	2018
20	Gutu SMG	Surkhet	100	2018
21	Sugarkhal SMG	Kailali	75	2018
22	Malladehi SMG	Baitadi	30	2019
23	Hilepani SMG	Okhaldhunga	50	2019
24	Thabang SMG	Rolpa	150	2020
25	Susta SMG	Nawalparasi	100	2020
26	Dhading SMG	Dhading	4	2016
27	Kabilasi DC Solar Mini Grid	Sarlahi	6	2018
28	Naya Basti Solar Mini Grid	Morang	5	2019
29	Birpur Solar Mini Grid	Morang	8	2019
30	Avadhpur Solar Mini Grid	Parsa	5	2019
	Total kW		1,093	

*Represent work is not completed yet.

capacity stands at 2,265 MW, with 74 MW designated for off-grid use and 2,191 MW connected to the grid. The grid-connected facilities consist of 49.76 MW solar, 53.4 MW thermal, 6 MW biomass, and the majority, 2082 MW, from hydroelectric sources. An additional 74 MW of off-grid isolated generation capacity, developed by the AEPC, contributes to the overall installed capacity (Nepal Energy Outlook, 2022). The projected demand for electricity is expected to surge from an estimated 10,138 gigawatt-hours (GWh) in 2019–2020 to 31,196 GWh in 2029–2030, as per the National Planning Commission's 2018 projections. The complete SMG in the context of Nepal is shown in Table 1 reported by AEPC and the ongoing SMG under construction is shown in Table 2 reported by RERL.

PV systems offer an efficient and environmentally beneficial energy source, among its numerous benefits. According to

TABLE 2 Ongoing SMG project reported by RERL.

S.N.	Project detail	Project capacity (kW)
1	Construction of 50 kWp Solar Mini-grid System at Psheyphoksundo Rural Municipality, Ward No-4, Dungadhar, Namdopauwa, Namdosibu and Namdochu, Dolpa District, Karnali Province, Nepal	50
2	Construction of 55 kWp Solar Mini-grid System at Tajakot Rural Municipality, Ward No-5, Chihitole and Madana, Dolpa District, Karnali Province, Nepal	55
3	Construction of 70 kWp Solar Mini-grid System at Tajakot Rural Municipality, Ward No-4, Maila, sirupataHumla District, Karnali Province, Nepal	70
4	Construction of 120 kWp Solar Mini-grid System at Mahabu Rural Municipality, Ward No. 3, Jaganath, Dailekh District, Karnali Province, Nepal	120
5	Construction of 55 kWp Solar Mini-grid System at Chankheli Rural Municipality, Ward No-4, Lower Pali and Upper Pali, Humla District, Karnali Province, Nepal	55
6	Construction of 100 kWp Solar Minigrid System at Tilagufa Municipality, Ward no-4 Rachuli, Kalikot District, Karnali Province, Nepal	100
7	Construction of 17 kWp Solar Mini-grid System at Thawang Rural Municipality, Ward no-1, Chittiwang, Rolpa, Lumbini Province, Nepal	17
8	Construction of 50 kWp Solar Mini-grid System Guthichaur Rural Municipality Ward No-2, Murli of Jumla District, Karnali Province, Nepal	50
9	Construction of 50 kWp Solar Mini-grid System Tila Rural Municipality Ward No-6, Tila of Jumla District, Karnali Province, Nepal	50
10	Construction of 60 kWp Solar Mini-grid System Soru Rural Municipality Ward No-6, Sorukot of Mugu District, Karnali Province, Nepal	60
11	Construction of 75 kWp Solar Mini-grid System Raskot Municipality Ward No-9, Phukot of Kalikot District, Karnali Province, Nepal	75
12	Construction of 170 kWp Solar Mini-grid System Barekot Rural Municipality Ward No-5, Limsa, Tolkhan of Jajarkot District, Karnali Province, Nepal	170

research, Nepal has serious policy problems that have a negative impact on the growth of PV systems like poor technological standards, inadequate knowledge, absence of information transmission, etc. Low power factors, high voltage levels, and reduced losses are all benefits of the PV system. The nation's power utility does not provide electricity to about 22% of the population of Nepal, forcing them to find other means of electrification. This is because of the cost, performance, and reliability of rural electrification, non-technologically or economically feasible. So, the MG technology is one of the promising methods. The goal of this work is to evaluate the performance of the two TSMG and SSMG systems in Nepal, which have been constantly providing services to the community in the current environment. The performance metric help to understand the different problem which is helpful to other SMG.

1.2 Research gap

The performance and viability of off-SMG systems in the remote hilly regions of Sugarkhal and Thabang, particularly in Nepal are one of the biggest concerns of this study because no such research has been conducted in the context of Nepal for SSGM and TSMG systems. The research is about global interest in renewable energy resources, SMGs, and the challenges associated with integrating renewable energy into existing systems, because of the geographical structure of the research area and SMG system. The existing literature highlights the success of solar energy in various regions, including South Asia and Sub-Saharan Africa, but there is a dearth of information regarding the practical application and outcomes of off-SMGs in the unique context of remote hilly Sugarkhal and Thabang as well as in Nepal. Sugarkhal and Thabang encounter difficulties in conventional power infrastructure development due to challenging terrains, lack of transport infrastructure, and limited alternative energy sources, there is a need for a comprehensive study that evaluates the effectiveness, sustainability, and community impact of off-SMG systems in these specific locations. The areas have populations of 15,000 and 20,000, respectively according to the census of 2011, and exploring how SMGs can address their energy needs while considering factors such as population density, environmental sustainability, and economic viability would contribute valuable insights to the existing literature. The analysis of the performance metrics of TSMG and SSGMG systems is crucial for understanding their success and identifying potential areas for improvement. By focusing on these specific remote locations in the hilly region of Nepal. This research can provide actionable recommendations for other regions with similar characteristics, contributing to the broader goal of sustainable and effective off-grid electrification in remote hilly areas. The research parameters of the two systems are to comprehensively study PR, capture loss, system loss, irradiance, energy generation, capture factors, and system efficiency for TSMG and SSMG.

1.3 Novelty of the study

The novelty of this work is to explore the off-SMG systems located in remote hilly regions of Sugarkhal and Thabang. The research area faces different difficulties like encountering obstacles in conventional power infrastructure development due to challenging terrain, lack of transport infrastructure, and limited alternative energy sources. The establishment of SMGs offers a decentralized and adaptable energy solution tailored to the specific needs of these communities. The study of performance metrics of SSGM and TSGM help to evaluate the performance of the system and suggest the possibilities of improvement of the system which help us to preserve energy and make the system more effective in different aspect like cost, energy efficiency, loss of the system, performance ratio, capture factors, etc. This study also helped the improvement of other SMG systems located in different parts of remote Nepal. In remote regions, where there is a lack of road infrastructure and a national grid such a system is more beneficial. Because embracing clean and renewable solar energy aligns with environmental sustainability goals crucial for preserving the ecologically sensitive environment near SMG. The long-term cost-effectiveness of solar systems, coupled with the potential for job creation and community empowerment, renders this solution economically viable and socially beneficial. Additionally, the swift deployment of SMG systems enhances resilience to natural disasters, while ongoing technological innovations contribute to continuous improvements in solar technology.

2 Methods and materials

2.1 Research area

This research considered two research sites of SMG Nepal, Thabang and Sugarkhal, more detail in Figure 2. TSMG has been operated since 2021 with a 150 kWp installation capacity in the Thabang Rural Municipality of the Rolpa District of Nepal. The ground-mounted TSMG PV system is located at latitude 28.4954° North and longitude 82.7140° East. The tilt angle of the system's PV panels is 33°. SSMG has been operated since 2021 with a 75 kWp installation capacity in the Mohanyal Rural Municipality, Kailali District by AEPC. The ground-mounted SSMG PV system is located at latitude 28.7822°N and longitude 81.2358°E. The tilt angle of the PV panels is 29°.

2.2 Specification of the system module

The specifications of SSMG and TSMG systems with different specifications of major components are listed in Table 3. This helps to design and configuration of the system and also provide detail of the established system.

2.3 Sketch of PV module of SSGM and TSMG

The framework of SSGM and TSMG is shown in Figure 3 and a description of the major components is shown in Table 3.

2.4 Sun path

Along with an increasing need for electrification and worries about climate change, the use of renewable energy has started to rise. The best solar energy conversion takes place during insolation at an average maximum irradiation time, or PSH. PSH is a parameter that expresses the relationship between the maximum daily sun radiation exposure and the standard solar radiation intensity of 1 kW/m^2 (Megantoro et al., 2022). The University of Oregon's Solar Radiation Monitoring Laboratory's web resources were used to obtain the PSH of Thabang and Sugarkhal and found PSH for SSMG is 5.73 and TSMG is 5.49.

2.5 Tilt angle

The tilt angle refers to the inclination of photovoltaic modules from the horizontal plane in a fixed (non-tracking)

FIGURE 2
Google Earth image of **(A)** TSMG and **(B)** SSMG.

TABLE 3 Detail configuration and specification of SMG.

	Configuration detail	SSMG	TSMG	Unit
Solar Arry Size	Sun hour available at the site	4.5	4.5	h
	Select solar PV Module Size and rated power	430.00	315	Wp
	Derating factor	95%	95%	%
	Coloumbic efficiency	95%	9%	%
	Total required array output current per day	1018.45	33433.6	A
	Rated current of the proposed solar module	10.60	8.48	A
	Number of solar modules Required	192	504	No.
Battery Sizing	Select Battery Voltage	48	48	Volt
	Total amp-hours required per day	4583	21639.01	Ah/day
	Selected desired autonomy day	1.5	2	day
	AH Capacity of Selected Battery	2,000	1,500 Ah	Ah
	Depth of Discharge (DOD) of the battery	75%	80%	%
	Efficiency of Battery Bank	90%	90%	%
	Required capacity of Battery Bank	10184.44	295,553	Ah
	Total number of batteries required	120	264	No.
Voltage of Selected Solar PV Module (Volt)		48	24	Volt
Inverter	Efficiency of Inverter	95	95	%
	DC voltage of inverter (Volt)	48	48	
	DC/AC Inverter, 25 kW	3	7	No.
Distribution System		1 phase (1.5 km)	3 Phse (1.16 km) and 1 Phase (1.73 km)	km

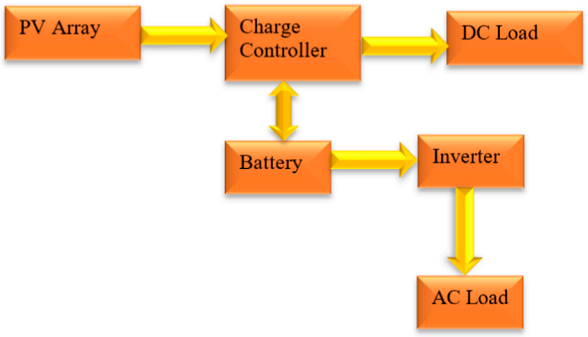

FIGURE 3
Configuration of SSMG and TSGM.

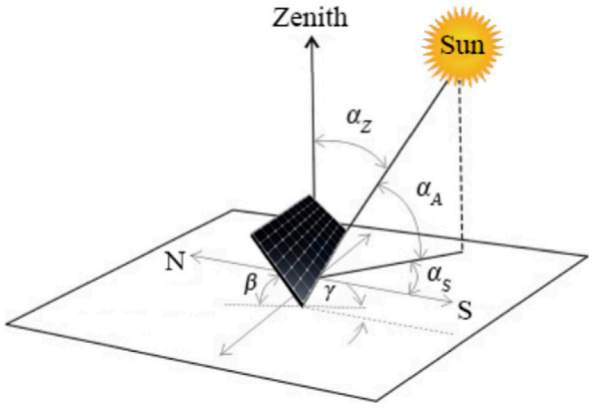

FIGURE 4
Simple Sketch of tilt angle, solar azimuth angle, and the azimuth orientation.

mounting system. It is commonly advised to install photovoltaic systems with a tilt angle matching the latitude of the site (Mondol et al., 2007). Figure 4, presents the concept and measurement of the tilt angle (Božiková et al., 2021).

The azimuth angle signifies the orientation of PV modules in relation to the South, where −90° represents East, 0° is South, and +90° indicates West (Božiková et al., 2021). In Figure 4, the solar altitude angle (α_A) is the angle between the horizontal plane and the line pointing to the Sun ($0^\circ \leq \alpha_A \leq 90^\circ$). The zenith angle ($\alpha_Z$), which complements this angle, is defined by the vertical plane and the line to the Sun, representing the angle of incidence of beam radiation on a horizontal surface. The parameters β is the tilt angle, and γ is the

azimuth angle, jointly determining the azimuthal orientation of the solar module.

2.6 Data collection

The global horizontal irradiance at all sky conditions is taken using PVsyst software 7.4 because the global horizontal irradiance is not uniformly available for the research site. The total energy generation of the TSMG and SSGM PV system is collected from RERL, Nepal on 3rd March 2023.

2.7 PV module technologies

There are four systems that makeup PV cell technologies; they are mono-crystalline (m-Si), poly-crystalline (p-Si), thin film, and hybrid systems. Table 4 below lists the specifications of the polycrystalline employed for our station under consideration.

2.8 PV module connections

To extract solar energy, there are four systems that make up PV cell technologies mono-crystalline (m-Si), poly-crystalline (p-Si), thin film, and hybrid systems. However, for this research, authors considered poly-crystalline because it is a dominant module in the context of Nepal. In addition, due to their great precision and performance under consistent solar insolation. The cell connections between the PV cells create a module or an array in order to maximize the current and voltage flowing. Cells coupled in series or parallel produce higher output voltage and cell current, respectively. There are 504–476 PV modules (Sunceco) in the TSMG plant with series and parallel arrangement with the tilt angle of 33°. Also, there are 192–238 PV modules in the SSMG plant with series and parallel with the tilt angle of 29° of 315 Wp(poly-crystalline) with an efficiency of 16.23%.

TABLE 4 Technical specification (Sunceco, 2023).

Parameter	Poly-crystalline
Solar cell type	Poly-crystalline 156 mm × 156 mm
Weight	23.20 kg
Dimensions	1,956 mm × 992 mm × 50 mm
Maximum Power (P_{max})	315 Wp
Voltage at P_{max} (V_{mp})	37.46 V
Current at P_{max} (I_{mp})	8.41 A
Open-Circuit Voltage (V_{oc})	44.82 V
Short-Circuit Current (I_{sc})	9.371 A
Maximum System Voltage (V_{DC})	1,000 V (IEC), 600 V (UL)
Cell Efficiency	18.34%
Module Efficiency	16.23%
Number of By-pass Diodes	6
Temperature Coefficient of P_{max}	−0.45%/°C
Temperature Coefficient of V_{oc}	−0.34%/°C
Temperature Coefficient of I_{sc}	−0.05%/°C
Nominal Operating Cell Temperature	47°C ± 2°C
Operating Temperature	−40°C–85°C

2.9 PV system

The performance of a grid-connected PV system is calculated based on a number of factors, including the PV system's energy production, PV yields (Y_a for array yield, Y_f for final yield, and Y_r for reference yield), performance ratio (PR), capacity factor (C_F), energy efficiency, and system losses. The PV indicators of performance can provide information on a PV system's efficiency in terms of how much energy it generates over time and how much solar radiation it absorbs. The total amount of direct current (DC) electricity delivered is multiplied by the nominal power of the PV system to determine the array yield (Y_a), which is expressed in kWh/kWp (Al-Najjar et al., 2022).

$$Y_a = \frac{E_{DC}}{P_{pv,rated}} = \tau_r \times \left(\sum_{day} P_A\right) \Big/ P_{pv,rated} \tag{1}$$

where $P_{pv,\text{rated}}$, is the nominal output of the PV system (kWp) and E_{DC} is the hourly total DC energy supplied by the PV system (kWh). The PV array's actual power output during the τ_r monitoring interval is represented by $\sum_{day} P_A$. The total electricity delivered by the PV system over the course of a given period divided by the nominal generating capacity of the installed PV system is known as the final yield of the PV plant (Y_f), which is expressed in kWh/kWp. It specifies the number of hours the PV system must operate at nominal power $P_{pv,rated}$ each day in order to match its monitoring contribution to the net daily load (Al-Najjar et al., 2022).

$$Y_f = \frac{E_{AC}}{P_{pv,rated}} = \tau_r \times \frac{\left(\sum_{day} P_A\right)}{P_{pv,rated}} = Y_a \times \eta_{pv,system} \tag{2}$$

The PV system's efficiency is $\eta_{pv,sys}$. The reference yield (Y_r), which is expressed in kWh/kWp, is derived by comparing the measured reference irradiation ($G_{I,ref}$) of the PV system to the global solar irradiation of the desired location. One kW/m^2 is the value of $G_{I,ref}$ under standard test conditions (STC). The PSH occurs every year. The reference yield is the total quantity of theoretical energy present at a specific location for a specific amount of time. It represents the exact energy that was observed.

$$Y_r = \tau_r \times \frac{\left(\sum_{day} G_I\right)}{G_{I,ref}} \tag{3}$$

The PR is the proportion of actual output as compared to anticipated output for a particular reporting period. It serves as a gauge for the overall impact on the rated output of the PV system. It shows the overall impact of output losses on the plant's rated array caused by environmental factors like temperature and irradiation along with system element inefficiencies like the inverter, cabling, connections, or failure, etc. (Kavuma et al., 2022).

$$\text{Performance Ratio (PR)} = \frac{Y_f}{Y_r} \quad (4)$$

The PV array losses (LC) create the array's capture losses (L_c), whereas the PV losses (L_s) are brought on by the inverter's DC-AC conversion.

$$L_C = Y_r - Y_a \quad (5)$$

$$L_S = Y_a - Y_f \quad (6)$$

The efficiency of the PV system, which consists of PV arrays and inverters, can be calculated as the ratio of the AC energy produced to the average daily radiation quantities $H_{I,d}$. Using the actual irradiation in the array's plane, these are determined (Kavuma et al., 2022).

$$\eta_{pv,system} = \frac{E_{AC}}{H_{I,d}} \times 100\% \quad (7)$$

The PV plant's efficiency is represented by its capacity factor (CF). It is the ratio of actual power produced to theoretical power; for instance, the capacity factor for a year is equal to real (average) power produced (kWh/year) divided by nominal power produced (kW) × 8,760 h/year. It is advised to use the AC voltage values while computing CF (Odeh, 2018).

$$CF = \frac{P_{avg}}{P_{pv,rated}} = \frac{\text{net annual energy (kWhAC/yr)}}{\text{system capacity (kWp)} \times 8760\text{hr/yr}} \quad (8)$$

Since the performance of a PV system in a laboratory environment differs from the performance of a PV system in actual open-air conditions, performance evaluation of PV systems in actual outside situations is crucial.

2.10 Solar irradiance in Nepal

The average daily irradiation for the horizontal surface in Nepal varies from about 4.5 kWh/m^2 in December to around 7.2 kWh/m^2 in May and more detail in Figure 5, in accordance with NASA's Surface Meteorology and sun Energy dataset. In the month of May average irradiance per month is highest while in month of December it is lowest.

2.11 Performance ratio, capture loss and system loss of SSGM and TSMG

The solar irradiance values mentioned in Table 5 show the amount of solar energy available at SSGM station for different months of 2021 and 2022. The monthly solar irradiance data was collected using PVsyst software 7.4 because ground-based data of solar irradiance is not available in considered location. The solar irradiance recorded at SSGM station is high during April 2021 and 2022 is 6.708 kWh/day and 6.098 kWh/day, respectively. In contrast, the minimum solar irradiance is also recorded during the months of December 2021 and January 2022 is 2.94 kWh/day and 2.646 kWh/day, respectively. The solar irradiance has a significant impact on the performance of a solar PV system. Higher solar irradiance values result in more electricity generation, whereas lower values result in less generation. Therefore, it is essential to consider the regional solar irradiance when designing and implementing solar mini grid PV systems. For instance, in regions with higher solar irradiance values, solar PV systems can be designed to produce more electricity and meet the higher demand during peak months, while in regions with lower solar irradiance values, solar PV systems may need to be supplemented with additional storage capacity or other energy sources to meet the demand during low solar irradiance months. It is also observed that the capture loss is higher in the months of April 2021 and 2022 is 3.322 kWh/day and 2.986 kWh/day, respectively. This higher capture loss may be due to a combination of factors, such as higher temperatures, shading from nearby buildings or vegetation, or soiling on the surface of the PV panels. The higher temperatures

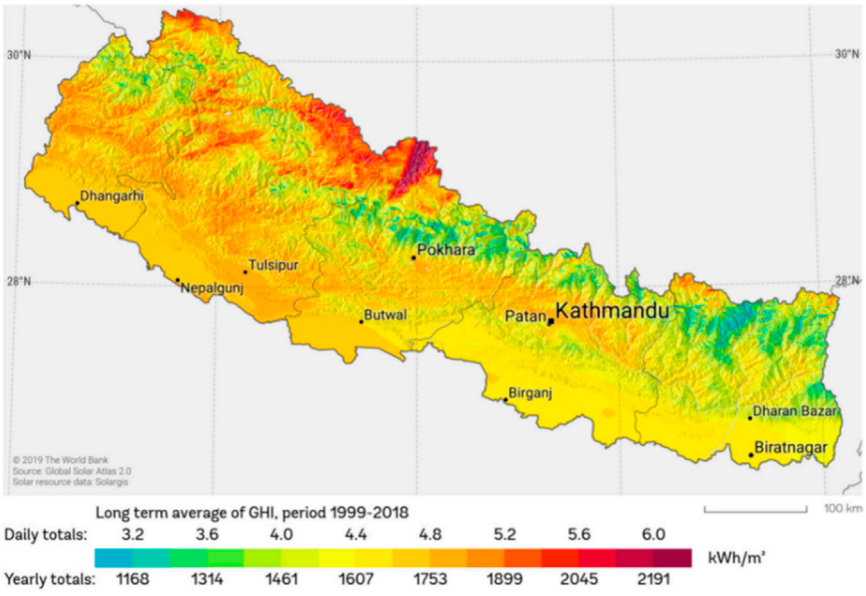

FIGURE 5
Solar irradiance above Nepal (Global Solar Atlas, 2023).

TABLE 5 Performance ratio, capture loss and system loss of SSGM.

Month	2021				2022			
	Irradiance (kWh/day)	L_C (kWh/day)	L_s (kWh/day)	PR	Irradiance (kWh/day)	L_C (kWh/day)	L_s (kWh/day)	PR
January	3.158	0.822	0.543	0.569	2.646	0.082	0.591	0.756
February	4.425	2.129	0.529	0.412	3.945	1.369	0.594	0.530
March	5.718	3.278	0.563	0.332	5.812	2.986	0.652	0.375
April	6.708	3.322	0.781	0.391	6.098	2.822	0.986	0.463
May	5.230	1.444	0.873	0.586	6.27	1.911	1.005	0.547
June	4.573	0.845	0.853	0.642	6.418	2.325	0.944	0.488
July	4.377	0.239	0.955	0.723	4.859	1.235	0.836	0.648
August	3.889	0.449	0.793	0.686	4.888	0.798	0.943	0.655
September	4.481	0.725	0.866	0.654	4.229	1.205	0.697	0.647
October	4.227	1.255	0.685	0.546	4.186	1.959	0.533	0.402
November	3.751	1.327	0.559	0.509	4.293	1.704	0.597	0.465
December	2.94	0.464	0.571	0.651	3.758	0.935	0.651	0.584

TABLE 6 Performance ratio, capture loss and system loss of TSMG.

Month	2021				2022			
	Irradiance (kWh/day)	L_C (kWh/day)	L_s (kWh/day)	PR	Irradiance (kWh/day)	L_C (kWh/day)	L_s (kWh/day)	PR
January	3.989	2.688	0.300	0.254	3.209	0.470	0.631	0.682
February	4.641	3.421	0.332	0.231	4.185	0.598	0.583	0.665
March	5.789	4.191	0.368	0.216	5.970	3.228	0.617	0.350
April	6.681	5.011	0.385	0.200	6.041	4.261	0.619	0.297
May	4.857	3.065	0.413	0.322	5.490	NA	NA	NA
June	4.200	1.757	0.563	0.528	5.608	2.956	0.582	0.372
July	4.165	1.836	0.537	0.449	4.093	2.734	0.583	0.402
August	3.566	1.573	0.459	0.461	4.542	2.424	0.548	0.399
September	4.164	2.035	0.491	0.416	3.988	1.367	0.547	0.490
October	4.357	2.478	0.433	0.364	4.075	2.045	0.452	0.534
November	4.158	2.785	0.453	0.318	4.483	1.592	0.668	0.499
December	NA	NA	NA	NA	4.102	0.569	0.813	0.662

TABLE 7 Performance ratio, capture loss and system loss of TSMG and SSMG.

Month	Thabang 2023				Sugarkhal 2023			
	Irradiance (kWh/day)	L_C (kWh/day)	L_s (kWh/day)	PR	Irradiance (kWh/day)	L_C (kWh/day)	L_s (kWh/day)	PR
January	3.958	0.995	0.683	0.590	3.453	0.936	0.595	0.565
February	5.282	1.422	0.890	0.565	4.950	2.280	0.616	0.420
March	5.257	2.166	0.713	0.456	5.668	2.951	0.627	0.373

can cause the PV panels to operate less efficiently, leading to a higher capture loss. On the other hand, the minimum capture loss is observed in the months of July 2021 and January 2022 is 0.239 kWh/day and 0.082 kWh/day, respectively. These lower capture loss values may be due to favorable weather conditions, such as clear skies and low humidity, which result in better performance and efficiency of the PV panels.

System loss in a PV system is due wiring, inverter inefficiencies, and other losses in the system. It is observed that the system loss is higher in the months of July 2021 and August 2022 with 0.955 kWh/day and 0.943 kWh/day, respectively. This higher system loss could be due to several factors such as aging of the system, inefficiencies in the inverter or wiring, or faulty components in the system. On the other hand, the minimum system loss is observed in the months of February 2021 and January 2022 with 0.529 kWh/day and 0.591 kWh/day, respectively. The performance ratio is observed higher in the months of July 2021 and January 2022 with 0.723 and 0.756, respectively. This higher PR could be due to favorable weather conditions, good maintenance, and efficient operation of the system. On the other hand, the minimum PR is observed in the months of March 2021 and March 2022, with values of 0.332 and 0.375, respectively. This lower PR could be due to unfavorable weather conditions, reduced system efficiency, and maintenance issues. A higher PR indicates that the system is performing efficiently and producing more energy, while a lower PR indicates that the system is not operating efficiently and may require maintenance or upgrades. Therefore, regular monitoring, maintenance, and upgrading of the system can help to improve the PR and optimize the performance of the PV system. In Nepal for consider SMG station, the higher PR observed in July 2021 and January 2022 can be attributed to the favorable weather conditions during these months. Nepal experiences a warm and dry climate during the summer months, which can enhance the performance of PV systems. However, during the winter months, the weather conditions can be challenging, with low temperatures and reduced sunlight, which can affect the performance of the PV systems. Therefore, proper system design and maintenance are crucial to ensuring the optimal performance of PV systems in Nepal.

The solar irradiance at TSGM station shows high values in April months of 2021 and 2022, with a minimum value in January of both years, more detail in Table 6. The capture loss is highest in April of both years, while the minimum is in August of 2021 and January of 2022. The system loss is highest in June of 2021 and December of 2022, while the minimum is in February of 2021 and October of 2022. The performance ratio is highest in June of 2021 and January of 2022, while the minimum is in April of 2021 and 2022. Also Table 7 shows the performance ratio, capture and system loss of TSGM and SSMG of 2023. These results suggest that the solar mini grid PV system in TSGM station has high solar irradiance values during the summer months, but experiences higher capture and system losses during the same time period. The performance ratio is also affected, indicating a need for optimization of the system to improve efficiency.

3 Results and discussion

3.1 Average solar irradiance and energy generation of Thabang solar mini grid

Figure 6, represent the daily solar irradiance with temperature and the energy generated by TSMG station and solar average irradiance variation with months, with standard error bar. The generation of energy per day is 419.5 kWh/day to 445.5 kWh/day when irradiance 5 kWh/m^2/day to 5.2 kWh/m^2/day with narrow temperature 7°C–10°C. The generation of energy in 2021 by TSMG is 83.206 MWh/year and 112.140 MWh/year in 2022. According to RERL report 2021/2022 the sunshine day is 311 days. Therefore, the energy generated per day is 0.268 MWh/day in 2021 and 0.361 MWh/day in 2022 with PHS 5.49. This suggests that the energy generation from solar PV modules is directly proportional to the irradiance level, as a higher irradiance level results in a higher energy generation. Additionally, the energy generation is also influenced by temperature, with higher temperatures resulting in lower energy generation. This is because solar cells have a maximum efficiency at a specific temperature and irradiance level, and changing as these factors change, the efficiency of the cells. This results in a change in the amount of electrical energy that can be generated by the cells. Additionally, changes in temperature can affect the electrical resistance of the cells and the electrical output of the system, further influencing the energy generation.

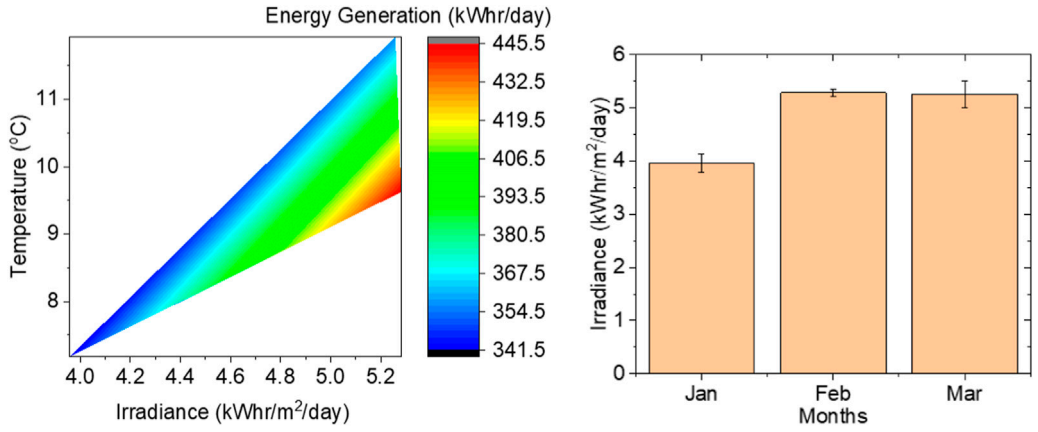

FIGURE 6
Energy generation in 2023 Thabang.

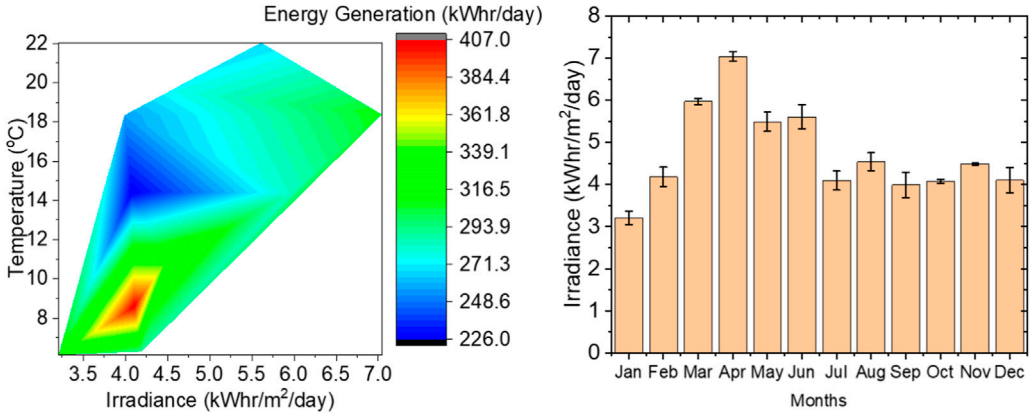

FIGURE 7
Energy generation in 2022 Thabang.

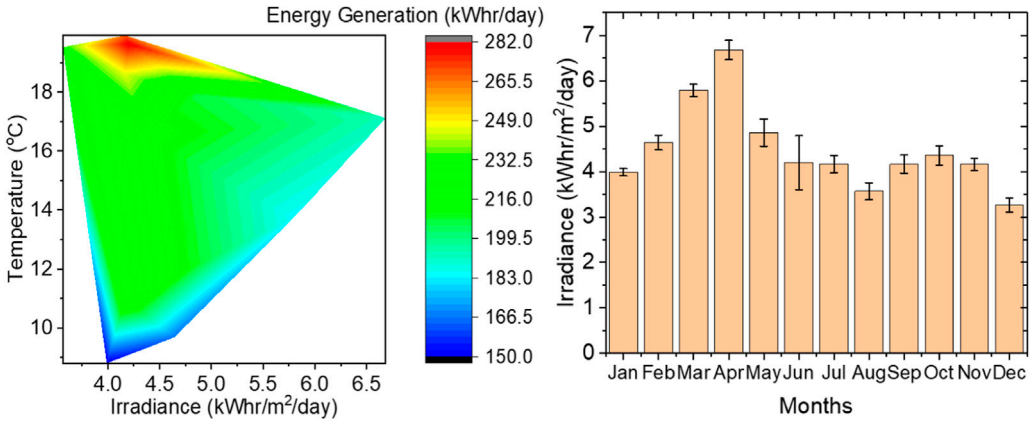

FIGURE 8
Energy generation at TSMG in 2021.

Figure 7, represent the energy generated by TSMG is high in between irradiance 3.75 to 4.27 kWh/m^2/day and at temperature 7°C to 10°C. Also, the variation of irradiance with month, the irradiance of solar is found higher in April. Even during months with high irradiance, shading from trees or buildings or the accumulation of dust on the solar panels can reduce the energy generation of a solar mini-grid. For example, the capacity of the system's components, such as the solar panels, inverter, and battery, may not be sufficient to handle the high irradiance levels during certain months. Additionally, if the solar panels are not positioned and angled optimally, they may not be able to capture the maximum amount of sunlight, reducing energy generation. Regular maintenance of the solar mini-grid system is essential for optimal energy generation. If the system is not maintained correctly, it can reduce the efficiency of the components and reduce the energy generation. The energy demand from the users connected to the solar mini-grid may vary throughout the year. During months with high irradiance, if the energy demand is low, the energy generation of the system may not reach its maximum capacity.

Figure 8, represent the energy generated by solar min grid is higher when irradiance is 4 kWh/m^2/day to 4.5 kWh/m^2/day at temperature 18.75°C–20°C. Also, the variation average irradiance with the months of 2021, the variation shows the irradiance is high in April month. The energy generation recorded up to 282.0 kWh/day maximum which is less than 2022 and 2023. This may be due to environmental factors such as shading, temperature, dust accumulation, cloud and other weather parameters.

3.2 Average solar irradiance and energy generation of Sugarkhal solar mini grid

Figure 9, represent the energy generated by solar min grid is higher when irradiance is 4.5 kWh/m^2/day to 5 kWh/m^2/day at temperature 22.0°C–24°C. Also, the variation average irradiance with the months of 2021, the variation shows the irradiance is high in April month. In 2021 SSMG generated maximum energy up to 239.0 kW/h/day and maximum irradiance 6.7 kWh/m^2/day in April month. The high energy generated by SSMG is lower than 2022 with very narrow region of irradiance. The energy generated by SSMG in 2021 is 64.14 MWh/year and 68.79 MWh/year in 2022.

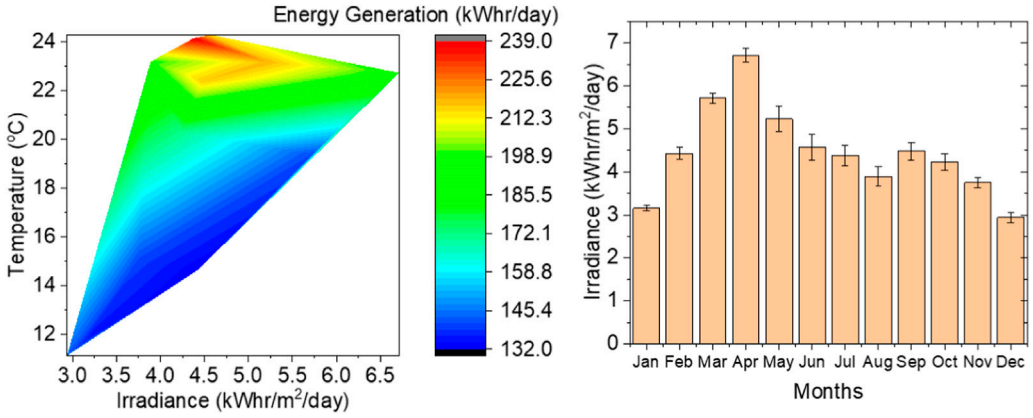

FIGURE 9
Energy generation in 2021 Sugarkhal.

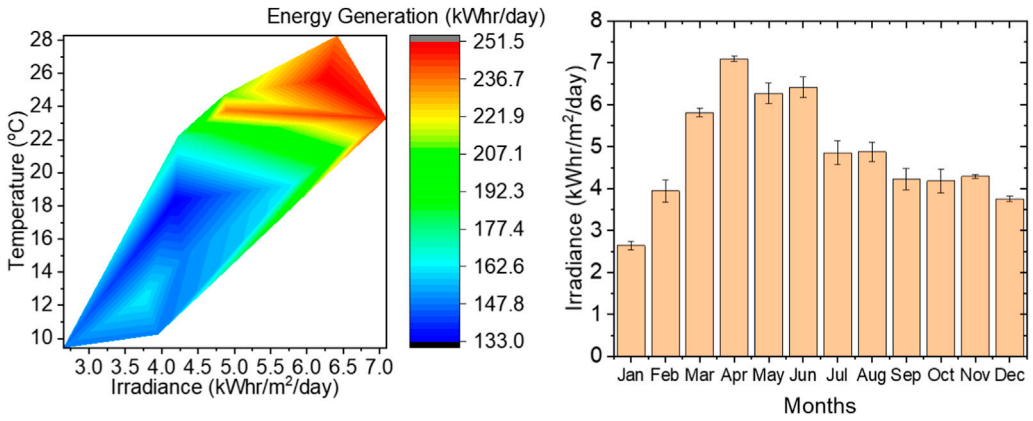

FIGURE 10
Energy generation in 2022 Sugarkhal.

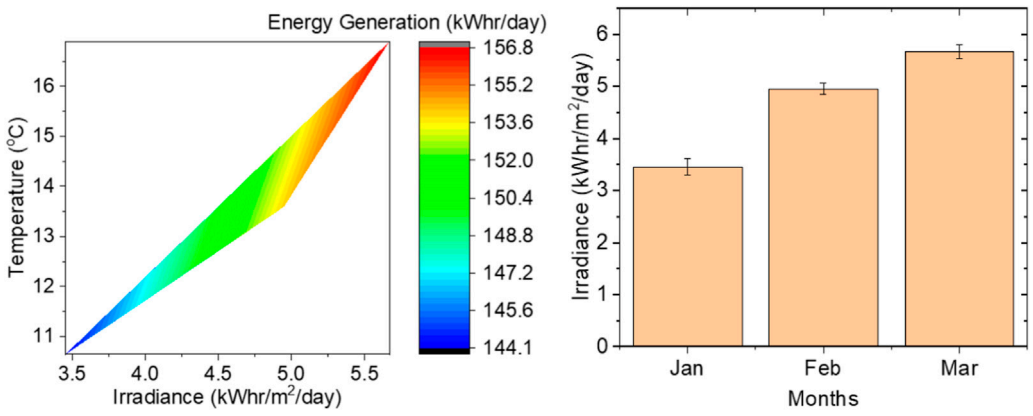

FIGURE 11
Energy generation in 2023 Sugarkhal.

According to RERL report 2021/2022 the sunshine day is 311 days therefore the energy generated per day is 0.206 MWh/day in 2021 and 0.221 MWh/day in 2022 with PHS 5.73.

Figure 10, represent the energy generated by solar min grid is higher when irradiance is 4.5 kWh/m^2/day to 7 kWh/m^2/day at temperature 21.5°C–28°C. Also, the variation average irradiance with the months of 2022, the variation shows the irradiance is high in April month. In addition, the irradiance is highly observed than 2021, in general. This causes the variation of wider range of energy generation of SSMG in 2022. In 2022 SSMG generated maximum energy up to 251.5 kW/h/day and maximum irradiance 6.9 kWh/m^2/day in April month. The energy generated by SSMG in 2022 is higher than 2021 with wider region of irradiance.

Figure 11, represent the energy generated by solar min grid is higher when irradiance is 4.75 kWh/m^2/day to 5.5 kWh/m^2/day at temperature 13.5°C–17.4°C. Also, the variation average irradiance with the months of 2023 (till the date), the variation shows the irradiance is high in March month. The variation of irradiance causes the variation of wider range of energy generation of SSMG. In 2022 SSMG generated maximum energy up to 156.8 kW/h/day and maximum irradiance 5.5 kWh/m^2/day in April month.

3.3 Performance ratio of Sugarkhal solar mini grid

Tiwari et al. reported performance ratio have been found to vary from 0.34 to 70 (Tiwari et al., 2017). Wassie and Ahlgren (2023) reported the performance ratio 0.47. Compared to this, the performance ratio of SSGM system falls within the low range. The impact of temperature, humidity, shadow, inclination angle of sun and dust are the most visible factors in December, where the SSMG experienced a PR drop of nearly 9% despite the high level of solar irradiation in the month. However, it is also important to note that a low PR value for an off-grid PV plant does not necessarily mean that the system is experiencing technical difficulties. Instead, it can be caused by a poor match between the SSMG system's installed capacity and electricity demand.

The PR of SSMG observed monthly shows PR ranges from 0.33 (33%) to 0.75 (75%). The PR is maximum recorded in January 2022 till date of research and lower in March 2023. Figure 12 visualized the performance ratio SSMG 2021–2023. A low PR value indicates that the system is not performing at its maximum potential and hence may not be meeting the energy demands of the users. System design plays a critical role in the performance of a SMG system. Sizing the system components appropriately is essential to ensure that enough energy is generated and stored to meet the demand. If the system is undersized, it may not be able to generate enough energy, resulting in a lower PR. Additionally, the choice of system components, such as solar panels, batteries, and inverters, can also affect performance. Choosing high-quality components can help to ensure that the system operates efficiently and maintains a high PR. Installation of a SMG system is also critical to its performance. Correct installation, including proper wiring, grounding, and orientation and tilt angles of solar panels, can help to maximize efficiency and energy output. Additionally, the proper placement of components, such as charge controllers and inverters, can also affect performance. Maintenance is essential to maintaining the performance of a solar mini-grid system. Regular cleaning of solar panels, inspection and replacement of damaged components, and proper charging and discharging of batteries are all critical to ensuring that the system operates efficiently and maintains a high PR. Environmental factors, such as temperature, humidity, and shading, can also affect the performance of a solar mini-grid system. High temperatures can reduce the efficiency of solar panels, while shading from trees, buildings, or other obstructions can reduce the amount of sunlight reaching the panels, resulting in a lower PR. Finally, technical issues, such as faults in inverters, charge controllers, or other system components, can also cause a decrease in system performance. Regular monitoring and analysis of system performance can help to identify and address these issues, ensuring that the system operates efficiently and maintains a high PR.

Higher temperatures can reduce the efficiency of the solar panels, leading to a lower PR. Additionally, during the spring and summer

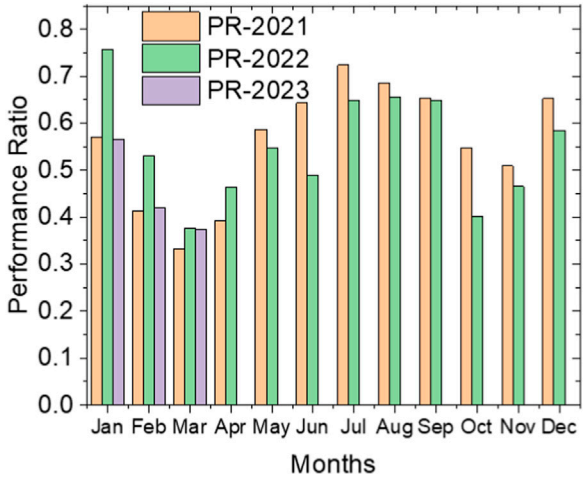

FIGURE 12
Performance ratio of SSMG.

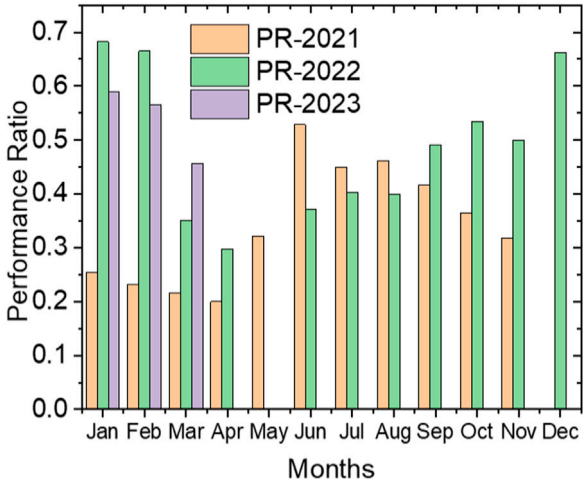

FIGURE 13
Performance ratio of TSMG.

months, there may be more cloud cover and occasional rain showers, which can further reduce the amount of sunlight reaching the solar panels and reduce energy output. It is worth noting that the exact pattern of monthly PR variation can depend on a variety of factors, including the location of the SMG system, local weather patterns, and the design and configuration of the system itself. Therefore, it is important to monitor the performance of the system regularly and make adjustments as necessary to ensure optimal energy output and PR over time.

3.4 Performance of Thabang solar mini grid

The PR of TSMG is shown in Figure 13 and shows that is ranges from 0.20 (20%) to 0.69 (69%), 2021–2023. The PR is maximum recorded in January 2022 till date of research and lower in March 2023. Figure 13 visualized the PR SSMG since established.

The results of the efficiency analyses showed that this PV power plant performs poorly with an average PR of 47.92%. A PV power system is typically considered to have high performance when its PR vale is above 70% (Kumar and Sudhakar, 2015). However, it is also important to note that a low PR value for an off-grid PV plant does not necessarily mean that the system is experiencing technical difficulties. Instead, it can be caused by a poor match between the MG system's installed capacity and electricity demand.

3.5 Capture loss

Capture loss in SMG systems refers to the amount of energy that is not captured or harnessed by the system due to various factors such as inefficiencies in the components, shading, weather conditions, and so on. The capture loss is measured in kWh/day (kilowatt-hours per day). Based on the given information, the capture loss of two types of solar mini grid systems (SSGM and TSGM) has been recorded for the years 2021, 2022, and 2023. For SSGM, the capture loss in 2021 ranged from 0.239 kWh/day to 3.322 kWh/day, in 2022 it ranged from 0.082 kWh/day to 2.086 kWh/day, and in 2023 it ranged from 0.935 kWh/day to 2.951 kWh/day. For TSGM, the capture loss in 2021 ranged from 1.573 kWh/day to 5.011 kWh/day, in 2022 it ranged from 0.470 kWh/day to 4.261 kWh/day, and in 2023 it ranged from 0.995 kWh/day to 2.166 kWh/day. It is important to note that capture loss is a normal occurrence in SMG systems, and the goal is to minimize it as much as possible. By regularly monitoring and optimizing the system's components and operation, it is possible to reduce capture loss and improve overall system efficiency.

3.6 System loss

System loss in a SMG refers to the amount of energy that is lost within the system due to various factors such as resistance in wires and cables, inefficiencies in components like inverters and batteries, and other electrical losses. The system loss is measured in kWh/day. Based on the given information, the system loss of two types of solar mini grid systems (SSGM and TSGM) has been recorded for the years 2021, 2022, and 2023. For SSGM, the system loss in 2021 ranged from 0.543 kWh/day to 0.955 kWh/day, in 2022 it ranged from 0.533 kWh/day to 1.005 kWh/day, and in 2023 it ranged from 0.595 kWh/day to 0.627 kWh/day. For TSGM, the system loss in 2021 ranged from 0.300 kWh/day to 0.563 kWh/day, in 2022 it ranged from 0.453 kWh/day to 0.813 kWh/day, and in 2023 it ranged from 0.683 kWh/day to 0.890 kWh/day. It is important to minimize system loss as it reduces the amount of energy that can be used by the consumers. By regularly maintaining and monitoring the SMG systems, it is possible to reduce system loss and improve the overall efficiency of the system. As noted by Hartvigsson et al. (2021) the viability and operational behavior of distributed MGs heavily depends on the interactions and feedback between endogenous factors (e.g., between electricity demand and supply) rather than exogenous factors. As such, the low PR value of PV system might be due more to the limited battery capacity limiting the amount of solar energy the system can capture and deliver. The disparity in module efficiency is related to the large PV array capture losses (L_c = 2.75 kWh/kWp/day). System and distribution losses (L_s = 0.40 kWh/kWp/day) accounted for the remaining 13% (Wassie and Ahlgren, 2023).

3.7 Capture factor

The CF of a SMG system refers to the ratio of the total energy produced by the solar panels to the amount of energy that is actually captured or harnessed by the system. It is expressed as a percentage and represents the efficiency of the system in capturing solar energy. Based on the given information, the capture factor of two types of solar mini grid systems (SSMG and TSGM) has been recorded for the years 2021, 2022, and 2023. For TSGM, the capture factor in 2021 was 6.33%, and in 2023 it was 8.53%. For SSGM, the capture factor was 9.76% in 2021 and 10.47% in 2022. A high capture factor indicates that the SMG system is efficiently capturing and utilizing the available solar energy. Factors such as proper maintenance, monitoring, and optimization of system components can help improve the capture factor of the SMG system. It is important to note that the capture factor can vary depending on various factors such as weather conditions, shading, and the efficiency of the components used in the system. Regular monitoring and optimization of the SMG system can help ensure that the capture factor remains high and the system operates at optimal efficiency.

3.8 Efficiency of system

The solar PV efficiency is typically measured by the amount of energy produced by the system relative to the amount of sunlight it receives. In this case, we have two different solar PV systems, one with a global irradiance of TSMG and the other with a global irradiance of SSMG (data sources: Global Solar Atlas, 2023). The solar PV system with TSMG had an efficiency of 10.40% in 2021 and 14.05% in 2022, while the system with SSMG had an efficiency of 15.02% in 2021 and 16.11% in 2022. Comparing these results with other solar PV systems requires additional information about the irradiance and energy generated by those systems. However, based on the provided information, we can see that the solar PV system with SSMG has a higher efficiency than the system with TSMG. This is likely due to the higher global irradiance of SSMG, which allows the system to produce more energy relative to the amount of

sunlight it receives. It is important to note that solar PV efficiency can vary widely depending on factors such as weather conditions, system design, and maintenance. Therefore, it is crucial to perform regular monitoring and maintenance to ensure optimal system performance.

3.9 Possibilities for improve the performance of grid system

The current trend is to integrate renewable energy sources like solar and wind into the grid for efficiency and demand improvement. However, this integration, along with power electronic devices and non-linear loads, poses power quality issues. To address this, researchers are developing new controllers and techniques, such as the Unified Power Quality Conditioner (UPQC) associated with solar power and battery storage, optimized through Boost and Buck Boost converters (Srilakshmi et al., 2022a). Additionally, for superior UPQC performance in unbalanced/distorted voltage conditions, a fuzzy logic controller and synchronization methods like self-tuning filter and unit vector generation are proposed (Srilakshmi et al., 2022b). Furthermore, the integration of renewable sources into local distribution systems and the non-linear behavior of advanced power electronics impact power quality. Approaches like the firefly algorithm-trained ANN controller for the shunt active filter and proportional-integral controller for the series active filter of UPQC, integrated with solar energy systems and battery storage via boost and buck boost converters, show excellent performance in reducing voltage fluctuations and total harmonic distortion, thereby improving power factor (Ramadevi et al., 2023). These approaches highlight the importance of advanced control methods for enhancing the performance of solar grid systems.

4 Conclusion

In conclusion, the analysis of energy generation data from the TSMG and SSMG solar mini-grid plants reveals distinct performance characteristics. TSMG exhibits optimal energy generation in the irradiance range of 4 kWh/m^2/day–4.5 kWh/m^2/day at temperatures between 18.75°C and 20°C, while SSMG performs better with irradiance levels between 4.75 kWh/m^2/day and 5.5 kWh/m^2/day and temperatures ranging from 13.5°C to 17.4°C. The performance ratios for both plants fall within a range of 20%–75%. Capture losses for SSMG and TSMG vary, with SSMG experiencing losses between 0.082 and 3.322 kWh/day and TSMG ranging from 0.470 to 5.011 kWh/day. Notably, SSMG demonstrates higher efficiency and capture factor compared to TSMG.

Data availability statement

The raw data supporting the conclusion of this article will be made available by the authors, without undue reservation.

Author contributions

SK: Formal Analysis, Writing–original draft. AJ: Supervision, Writing–review and editing. KY: Conceptualization, Validation, Writing–review and editing. JK: Writing–review and editing, Formal Analysis, Investigation.

Funding

The authors declare that no financial support was received for the research, authorship, and/or publication of this article.

Acknowledgments

The authors would like to express their sincere gratitude to all the faculties members of Central department of physics, Department of Mechanical and Aerospace Engineering, IOE, Pulchowk Campus, Department of physics of Tri-Chandra Multiple Campus and Patan Multiple Campus, Tribhuvan University, Renewable Energy for Rural Livelihood, Innovative Ghar Nepal, and Robotics Academy of Nepal for their valuable support and guidance throughout this research work. Their contributions and insights have been immensely helpful in shaping this article.

Conflict of interest

The authors declare that the research was conducted in the absence of any commercial or financial relationships that could be construed as a potential conflict of interest.

Publisher's note

References

Ahlborg, H., and Hammar, L. (2014). Drivers and barriers to rural electrification in Tanzania and Mozambique – grid-extension, off-grid, and renewable energy technologies. *Renew. Energy* 61, 117–124. doi:10.1016/j.renene.2012.09.057

Al-Najjar, H., Pfeifer, C., Al Afif, R., and El-Khozondar, H. J. (2022). Performance evaluation of a hybrid grid-connected photovoltaic biogas-generator power system. *Energies* 15 (9), 3151. doi:10.3390/en15093151

Aziz, S., and Chowdhury, S. A. (2020). Performance evaluation of solar mini-grids in Bangladesh: a two-stage Data Envelopment Analysis. *Clean. Environ. Syst.* 2 (1), 100003. doi:10.1016/j.cesys.2020.100003

Baurzhan, S., and Jenkins, G. P. (2016). Off-grid solar PV: is it an affordable or appropriate solution for rural electrification in Sub-Saharan African countries? *Renew. Sustain. Energy Rev.* 60, 1405–1418. doi:10.1016/j.rser.2016.03.016

Božiková, M., Bilcík, M., Madola, V., Szabóová, T., Kubík, L. ', Lendelová, J., et al. (2021). The effect of azimuth and tilt angle changes on the energy balance of photovoltaic system installed in the southern Slovakia region. *Appl. Sci.* 11 (19), 8998. doi:10.3390/app11198998

Energy Sector Management Assistance Program (ESMAP) (2017). *Multi-tier framework for measuring energy access household survey (MTF)*. Nepal: World Bank. Avaliable at: https://www.esmap.org/sites/default/files/esmap-npl-mtf-2017_final_2018-04-05.pdf.

Global Solar Atlas (2023). Globalsolaratlas. Avaliable at: https://globalsolaratlas.info/map (Accessed October 10, 2023).

Guichi, A., Talha, A., Berkouk, E. M., and Mekhilef, S. (2018). Energy management and performance evaluation of grid connected PV-battery hybrid system with inherent control scheme. *Sustain. Cities Soc.* 41, 490–504. doi:10.1016/j.scs.2018.05.026

Hartvigsson, E., Ehnberg, J., Ahlgren, E. O., and Molander, S. (2021). Linking household and productive use of electricity with mini-grid dimensioning and operation. *Energy Sustain. Dev.* 60, 82–89. doi:10.1016/j.esd.2020.12.004

Kafle, U., Anderson, T., and Lohani, S. P. (2023). The potential for rooftop photovoltaic systems in Nepal. *Energies* 16 (2), 747. doi:10.3390/en16020747

Kavuma, C., Sandoval, D., and Khan Jean de Dieu, H. (2022). Analysis of solar photovoltaic for grid integration viability in Uganda. *Energy Sci. Eng.* 10, 694–706. doi:10.1002/ese3.1078

Kumar, B. S., and Sudhakar, K. (2015). Performance evaluation of 10 MW grid connected solar photovoltaic power plant in India. *Energy Rep.* 1, 184–192. doi:10.1016/j.egyr.2015.10.001

Megantoro, P., Syahbani, M. A., Sukmawan, I. H., Perkasa, S. D., and Vigneshwaran, P. (2022). Effect of peak sun hour on energy productivity of solar photovoltaic power system. *Bull. Electr. Eng. Inf.* 11 (5), 2442–2449. doi:10.11591/eei.v11i5.3962

Mondol, J. D., Yohanis, Y. G., and Norton, B. (2007). The impact of array inclination and orientation on the performance of a grid-connected photovoltaic system. *Renew. Energy* 32, 118–140. doi:10.1016/j.renene.2006.05.006

Nepal Energy Outlook (2022). Kathmandu university, Institute of engineering, Nepal energy foundation, and niti foundation. Avaliable at: https://energizenepal.ku.edu.np/wp-content/uploads/2022/08/NEO-2022-Final.pdf.

Odeh, S. (2018). Analysis of the performance indicators of the PV power system. *J. Power Energy Eng.* 6, 59–75. doi:10.4236/jpee.2018.66005

Palit, D., and Chaurey, A. (2011). Off-grid rural electrification experiences from South Asia: status and best practices. *Energy Sustain. Dev.* 15 (3), 266–276. doi:10.1016/j.esd.2011.07.004

Ramadevi, A., Srilakshmi, K., Balachandran, P. K., Colak, I., Dhanamjayulu, C., and Khan, B. (2023). Optimal design and performance investigation of artificial neural network controller for solar- and battery-connected unified power quality conditioner. *Int. J. Energy Res.* 2023, 1–22. doi:10.1155/2023/3355124

SE4ALL (2020). *Sustainable energy for all (SE4ALL) database from the SE4ALL global tracking framework*. Washington, DC, USA: The World Bank.

Shafiullah, M., Refat, A. M., Haque, M. E., Chowdhury, D. M. H., Hossain, M. S., Alharbi, A. G., et al. (2022). Review of recent developments in microgrid energy management strategies. *Sustainability* 14 (22), 14794. doi:10.3390/su142214794

Shrestha, A., Rajbhandari, Y., Khadka, N., Bista, A., Marahatta, A., Dahal, R., et al. (2020a). Status of micro/mini-grid systems in a himalayan nation: a comprehensive review. *IEEE Access* 8, 120983–120998. doi:10.1109/access.2020.3006912

Shrestha, P., Shrestha, A., Shrestha, N. T., Papadakis, A., and Maskey, R. K. (2020b). Assessment on scaling-up of mini-grid initiative: case study of minigrid in rural Nepal. *Int. J. Precis. Eng. Manufacturing-Green Technol.* 7 (2), 391–405. doi:10.1007/s40684-019-00115-2

Srilakshmi, K., Srinivas, N., Balachandran, P. K., Reddy, J. G. P., Gaddameedhi, S., Valluri, N., et al. (2022a). Design of soccer league optimization based hybrid controller for solar-battery integrated UPQC. *IEEE Access* 10, 107116–107136. doi:10.1109/ACCESS.2022.3211504

Srilakshmi, K., Sujatha, C. N., Balachandran, P. K., Mihet-Popa, L., and Kumar, N. U. (2022b). Optimal design of an artificial intelligence controller for solar-battery integrated UPQC in three phase distribution networks. *Sustainability* 14, 13992. doi:10.3390/su142113992

Srimathi, R., Meenakshi, J., Vijayabhasker, R., and Belay, S. S. (2022). Performance evaluation and estimation of energy measures of grid-connected PV module. *Int. J. Photoenergy* 2022, 1–13. doi:10.1155/2022/7228470

Sunceco (2023). SEP300/320 solar electric propulsion system. Avaliable at: http://sunceco.com/wp-content/uploads/2017/01/SEP300-320.pdf.

Tiwari, B. R., Bhattarai, N., and Jha, A. K. (2017). Performance analysis of a 100 kWp grid connected solar photovoltaic power plant in kharipati, bhaktapur, Nepal. *Proc. IOE Graduate Conf.* 5, 629–636.

The Ministry of Energy and Water Resources (2023). Energy Synopsis Report 2023. FY 2078/79, Nepal. Available at: http://wecs.gov.np/source/Energy%20Synopsis%20Report%2C%202023.pdf.

Wassie, Y. T., and Ahlgren, E. O. (2023). Performance and reliability analysis of an off-grid PV mini-grid system in rural tropical Africa: a case study in southern Ethiopia. *Dev. Eng.* 8, 100106. doi:10.1016/j.deveng.2022.100106

frontiers | Frontiers in Energy Research

TYPE Original Research
PUBLISHED 18 January 2024
DOI 10.3389/fenrg.2023.1342085

OPEN ACCESS

EDITED BY
Kumaran Kadirgama,
Universiti Malaysia Pahang, Malaysia

REVIEWED BY
Nima Khosravi,
Other, Iran
Mohamed Salem,
University of Science Malaysia (USM), Malaysia

*CORRESPONDENCE
Shitharth Selvarajan,
s.selvarajan@leedsbeckett.ac.uk

RECEIVED 21 November 2023
ACCEPTED 31 December 2023
PUBLISHED 18 January 2024

CITATION
Srilakshmi K, Gaddameedhi S, Borra SR, Balachandran PK, Reddy GP, Palanivelu A and Selvarajan S (2024), Optimal design of solar/wind/battery and EV fed UPQC for power quality and power flow management using enhanced most valuable player algorithm. *Front. Energy Res.* 11:1342085. doi: 10.3389/fenrg.2023.1342085

Optimal design of solar/wind/battery and EV fed UPQC for power quality and power flow management using enhanced most valuable player algorithm

Koganti Srilakshmi[1], Sravanthy Gaddameedhi[1], Subba Reddy Borra[2], Praveen Kumar Balachandran[3], Ganesh Prasad Reddy[4], Aravindhababu Palanivelu[5] and Shitharth Selvarajan[6]*

[1]Department of Electrical and Electronics Engineering, Sreenidhi Institute of Science and Technology, Hyderabad, India, [2]Department of Information Technology, Malla Reddy Engineering College for Women, Hyderabad, India, [3]Department of Electrical and Electronics Engineering, Vardhaman College of Engineering, Hyderabad, India, [4]Department of Electrical and Electronics Engineering, A.M Reddy Memeorial College of Engineering, Guntur, AP, India, [5]Department of Electrical Engineering, Annamalai University, Chidambaram, TN, India, [6]Cyber Security and Digital Forensics, School of Built Environment, Engineering and Computing, Leeds Beckett University, Leeds, United Kingdom

The behavior and performance of distribution systems have been significantly impacted by the presence of solar and wind based renewable energy sources (RES) and battery energy storage systems (BESS) based electric vehicle (EV) charging stations. This work designs the Unified Power Quality Conditioner (UPQC) through optimal selection of the active filter and PID Controller (PIDC) parameters using the enhanced most valuable player algorithm (EMVPA). The prime objective is to effectively address the power quality (PQ) challenges such as voltage distortions and total harmonic distortions (THD) of a distribution system integrated with UPQC, solar, wind, BESS and EV (U-SWBEV). The study also aims to manage the power flow between the RES, grid, EV, BESS, and consumer loads by artificial neuro-fuzzy interface system (ANFIS). Besides, this integration helps to have a reliable supply of electricity, efficient utilization of generated power, and effective fulfillment of the demand. The proposed scheme results in a THD of 4.5%, 2.26%, 4.09% and 3.98% for selected four distinct case studies with power factor to almost unity with an appropriate power sharing. Therefore, the study and results indicate that the ANFIS based power flow management with optimal design of UPQC addresses the PQ challenges and achieves the appropriate and effective sharing of power.

KEYWORDS

power flow management, artificial neuro-fuzzy interface system, enhanced most valuable player algorithm, total harmonic distortion, power quality

1 Introduction

The integration of RES into the distribution network has gained more attention in the past few decades for lessening the burden on VSC's and reducing the necessity of higher device ratings. A novel solar-integrated UPQC configuration has been developed to effectively address the PQ problems. The various difficulties in exploiting renewable energy sources (RES) and various approaches for overcoming these difficulties have been discussed in (Madurai Elavarasan et al., 2020a; Madurai Elavarasan et al., 2020b; Elavarasan, 2020). Due to the intrinsic unpredictability of solar PV (SPV) systems, the grid is subjected to harmonic distortions, thereby affecting grid voltages and currents. FACTS devices have thus been used to reduce total harmonic distortions (THD) besides handling voltage stability-related issues and enhancing PQ of the grid (Shafiullah et al., 2018; Ashok Kumar and Indragandhi, 2020; Mohamed, 2020).

The benefits in view of enhancing PQ of UPQC in grid-connected SPV systems were investigated (Paramanik et al., 2019). A thorough analysis was focused on the features, charging methods, and benefits of electric vehicles (EVs) (Kong and Karagiannidis, 2016; Chellaswamy and Ramesh, 2017; Nunes and Brito, 2017). The UPQC was exhibited to be superior than those of DSTATCOM and DVR in terms of multitasking abilities, and employed with intended goals of raising power factor (PF), decreasing THD, boosting profiles of voltage, and boosting PQ of the system (Amirullah et al., 2020). The FLC was applied for integration of battery energy storage systems (BESS) with EVs for realizing better PQ, increased overall reliability of the grid with RES (Vivas et al., 2020).

The firefly optimization method, which simulates predator-prey dynamics, was employed to optimize the design of shunt active power filters for reducing the THD and enhancing the PF (Mahaboob et al., 2019). A PI-controller fine-tuning for SHAPF was devised using an Ant Colony Algorithm to minimize THD across various load combinations (Sakthivel et al., 2015). A novel control system incorporating both fuzzy logic and back-propagation was introduced for optimizing THD and enhancing PF in the context of a 5-level UPQC (Nagireddy et al., 2018). Nevertheless, in the micro-grid associated distribution system, PQ issues were resolved by employing UPQC to handle current and voltage imperfections. An adaptive network-based fuzzy inference system was introduced to enhance system efficiency and utilization (Renduchintala et al., 2021). A hybrid control technique that combines the Improved Bat Algorithm and Moth Flame Algorithm optimization was created to tackle PQ concerns within a micro-grid system, to minimize the error function related to power fluctuations. Furthermore, the operational costs of RESs were reduced by optimally tuning the K_p and K_i parameters (Rajesh et al., 2021).

Furthermore, a novel hybrid approach through integration of Enhanced Efficient Global Optimization with ANN techniques was introduced for shunt active power filter (SHAPF). This approach was designed to diminish current signal distortions and enhance the quality of power delivery in the distribution network (Ganesan and Srinath, 2019). Moreover, an examination of the power flow analysis of the UPQC was conducted on a three-phase distribution system under different operating conditions, focusing on the impedance matching technique (Zhao et al., 2021). A method utilizing self-tuning filters was devised for UPQC in conjunction with renewable energy sources to tackle PQ concerns (Mansoor et al., 2020). Concurrently, an implementation of ANN was applied to the Solar PV-powered UPQC to mitigate grid current THD during voltage variations such as sag and swell. Additionally, the effectiveness of this approach was assessed through a comparison with the State Repetitive Control and reactive power theory methods across diverse load scenarios (Okwako et al., 2022). However, to minimize system THD, a unique modified UPQC has been developed with multiple goals and variables that be optimized by employing the BHO and PSO approaches to change the PIC variables (Khosravi et al., 2023). In addition, a proposal was made to link AC/DC microgrid to the grid using power-compensating techniques to reduce the amplitudes of harmonics. This involves optimizing the coefficients of gain in certain filter compensation devices. The optimized coefficients were associated with a PIC including the cost functions incorporated the controller's error, current harmonics, and voltage harmonics (Khosravi et al., 2021).

The optimization of the gain coefficients for the MAPF and PFCK controllers was carried out hierarchically using the Harris hawk optimization, ABC, grasshopper optimization algorithm, and DE. This optimization was applied to the three control loops, which include voltage and current harmonics, as well as the system controller error. The goal was to reduce the range of these harmonics to within acceptable limits (Khosravi et al., 2022). A novel THD compensation scheme was developed for a hybrid micro-grid, employing a filter compensation device. The primary objective of this system is to mitigate the magnitude of the voltage and current harmonics (Khosravi Nima et al., 2021).

An extensive investigation was conducted to offer valuable insights into the influence of FACTS deployment on the integration of energy from renewable sources and the reduction of carbon emissions. The study examines the impact of many factors on sustainable energy entry, including system loading patterns, the placement of renewable power, and the placement of FACTS (Omid Mirzapour et al., 2023). Subsequently, a technique for reducing a lumped parameter thermal model was proposed, utilizing sensitivity analysis. This method aims to streamline the thermal model while still preserving the appropriate level of accuracy. The results demonstrated minimal discrepancy between the simplified thermal model approximation and the entire model, as evidenced by the low error (Mirzapour et al., 2018). The ANFIS model was created based on 390 metrics founded in literature (Seyed Alizadeh et al., 2021). However, vehicles powered by fossil fuels have been identified as the primary contributor to air pollution in urban areas, despite the advantages of electric automobiles in large cities. Additionally, they pose technical difficulties for electric electrical distribution systems (Pazouki and Olamaei, 2019). Besides, a mathematical model for efficiently scheduling and organizing the energy points in smart homes was designed to consider the demand of the smart home energy hub and classifies it into distinct types of loads. In

TABLE 1 Literature survey.

Ref	PQ problems					Power flow management	Loads			EV	Optimization
[No]	Control	THD	DC link stabilization	Swell & sag	Voltage harmonics		Active power	Rectifier bridge	Unbalanced		Algorithm
Amirullah et al. (2020)	Fuzzy	*	*	*		*	*				
Vivas et al. (2020)	Fuzzy					*	*				
Mahaboob et al. (2019)	PI	*	*					*	*		*
Sakthivel et al. (2015)	PI	*						*	*		*
Nagireddy et al. (2018)	Neuro-Fuzzy	*		*				*			
Renduchintala et al. (2021)	Neuro-Fuzzy	*		*				*			
Rajesh et al. (2021)	PI	*	*					*			
Ganesan and Srinath (2019)	Fractional order PID	*						*	*		*
Zhao et al. (2021)	PI	*									
Mansoor et al. (2020)	Neural Network	*	*	*	*			*	*		
Okwako et al. (2022)	Neural Network	*	*	*				*	*		
U-WBEV	**EMVPA-PIDC**	*	*	*	*	*	*	*	*	*	*

10.3389/fenrg.2023.1342085

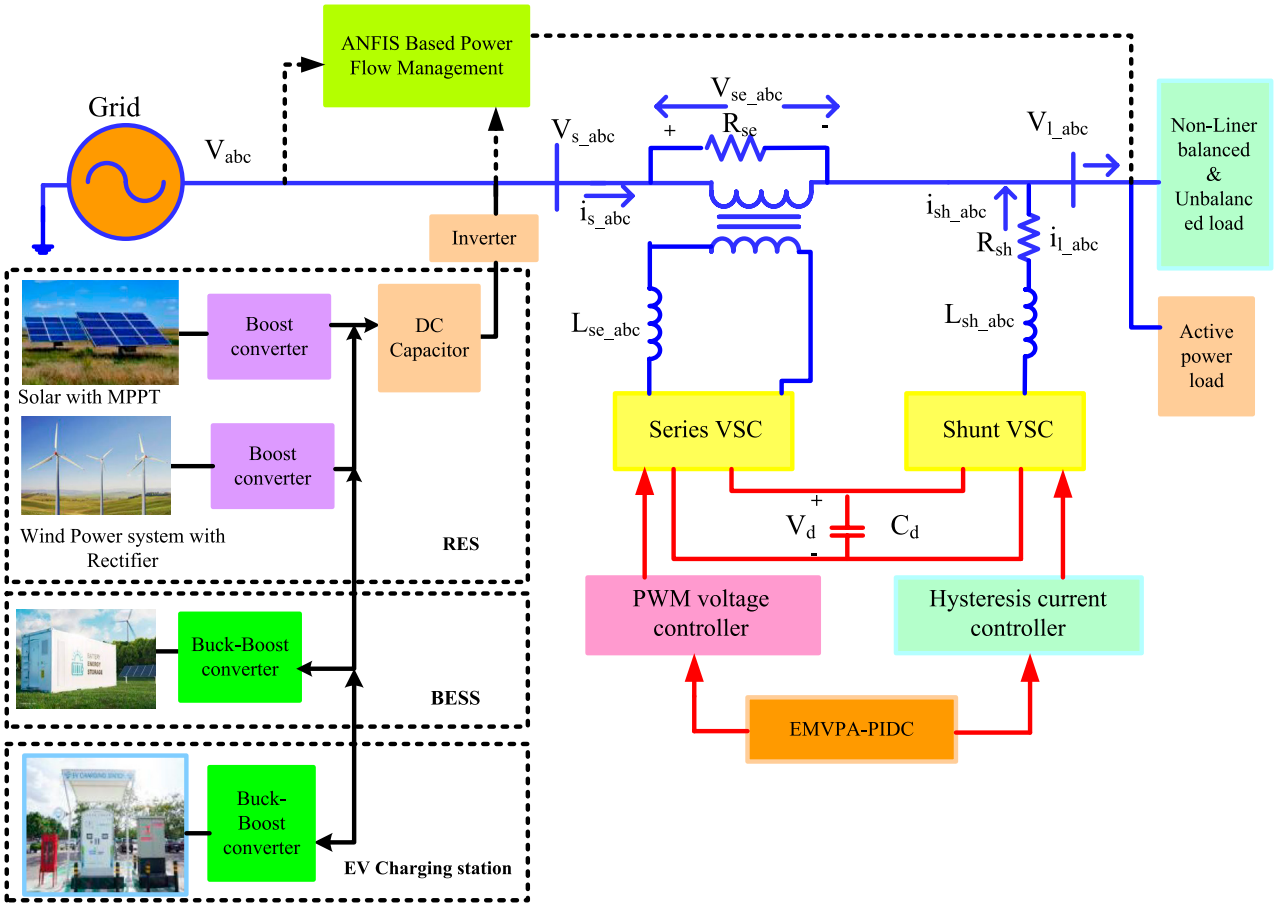

FIGURE 1
Structure of U-SWBEV.

TABLE 2 PV, wind, BESS and EV ratings.

Device	Configuration	Values
PV single panel (Sun power SPR-215-WHT-U)	PV cells connected in parallel, series	45, 10
	Rated Power	228.735 W
	SOC	8.18A
	OCV	37.1 V
	Under $P_{max}V_{PV}$&I_{PV}	29.9V/7.65A
Li-ion battery	Fully charge voltage	326.6 V
	Rated Q	400 A h
	COV	225 V
	NOV	300 V
	SOCB	95%
Wind Turbine	Nominal turbine P_{mop}	30 kW
	Maximum Θ_p	45deg
	Base V_W	15 m/s
	Maximum rate of change of Θ_p	25deg./second

TABLE 3 Lower and upper bonds for decision variables.

Decision variable	K_p	K_i	K_d	R_{se}	R_{sh}	L_{se}	L_{sh}
Lower	0.0001	0.0001	0.001	0	0	0.01	0.01
Upper	100	100	100	10	0.5	10	10

TABLE 4 Grid and load values chosen.

Source grid	V_S: 415V; f: 50 Hz
DC link capacitor	V_{dc}: 470V; C_{dc}: 100 μF
Loads	1. Rectifier bridge load R = 60; L = 0.15e-3
	2. Active power load: P_{L1} = 6 kW
	3. Rectifier bridge load R = 30; L = 20e-3
	4. Unbalanced load R1 = 10, R2 = 40, R3 = 70; L1 = 0.05 e−3, L2 = 0.1e-3, L3 = 0.15e-3
	5. Active and reactive power load R = 4kW; L = 1000Vars

TABLE 5 Test cases.

Condition	Case1	Case2	Case3	Case4
Fixed solar irradiation	*		*	
Varying solar irradiation		*		*
15 m/s wind velocity	*			*
11 m/s wind velocity		*	*	
Disturbance	*			
Swell		*		
Sag				*
Flicker			*	
Load 1	*		*	*
Load 2			*	*
Load 3		*		
Load 4			*	
Load 5	*	*		

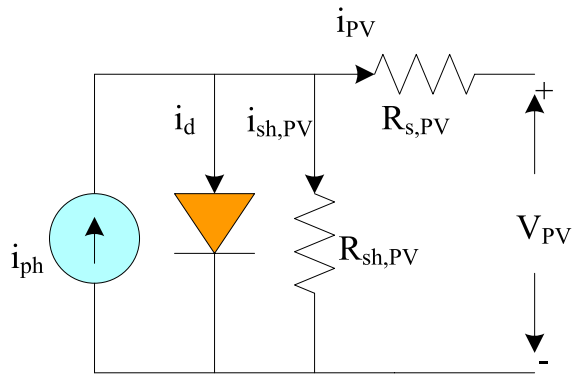

FIGURE 2
Single diode PV cell model.

addition, it encompasses the requirements for heating, cooling, and water, as stated in reference (Pazouki and Haghifam, 2021).

The development of the most valuable player algorithm involved the removal of undesirable and offensive players in order to avoid inefficient strategies and achieve rapid convergence. Subsequently, a new solution approach incorporating the improved most valuable player algorithm is proposed for addressing the optimal power flow problem. (Srilakshmia et al., 2020). On the other hand, optimized AI based techniques were adapted to renewable energy sources associated UPQC address PQ issues (Srilakshmi et al., 2022a; Srilakshmi et al., 2022b; Srilakshmi et al., 2023a; Srilakshmi et al., 2023b; Ramadevi et al., 2023).

As listed in Table 1, it is evident from the existing literature that the most recent research articles have predominantly concentrated on the application of UPQC in conjunction with RES, such as SPV and WSS. These studies have explored distinct control methods to enhance PQ by including BESS. However, there has been neglected the power flow management by the incorporation of EVs into these systems along with the optimal selection of controller and filter parameters of UPQC using metaheauristic algorithms.

It is worth noting that, particularly during periods of peak demand on the grid, excessive demand for power can be effectively managed using both BESS and EVs. This dual approach not only improves PQ but also facilitates power flow management concurrently. The key contributions of this study are outlined as follows:

- Development of an ANFIS-based hybrid control system to manage the power flow among the EVs, BESS, WES, RES and the grid.
- Optimal tuning of gain parameters of PIDC for shunt converter in addition to the selection of shunt and series filter parameters of UPQC by using EMVPA.
- Lowering the THD in the source side current and load terminal voltage, and mitigating grid voltage-related

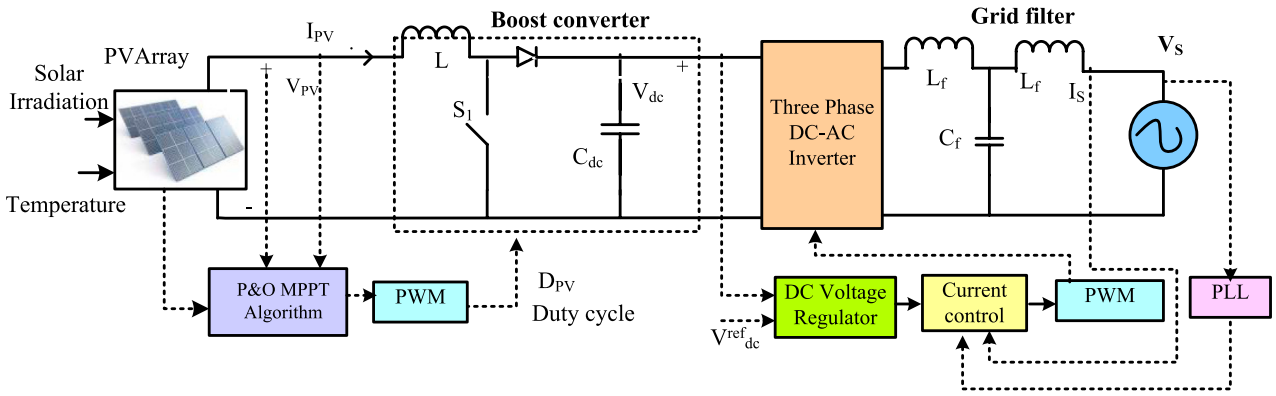

FIGURE 3
Solar with a boost converter and inverter control.

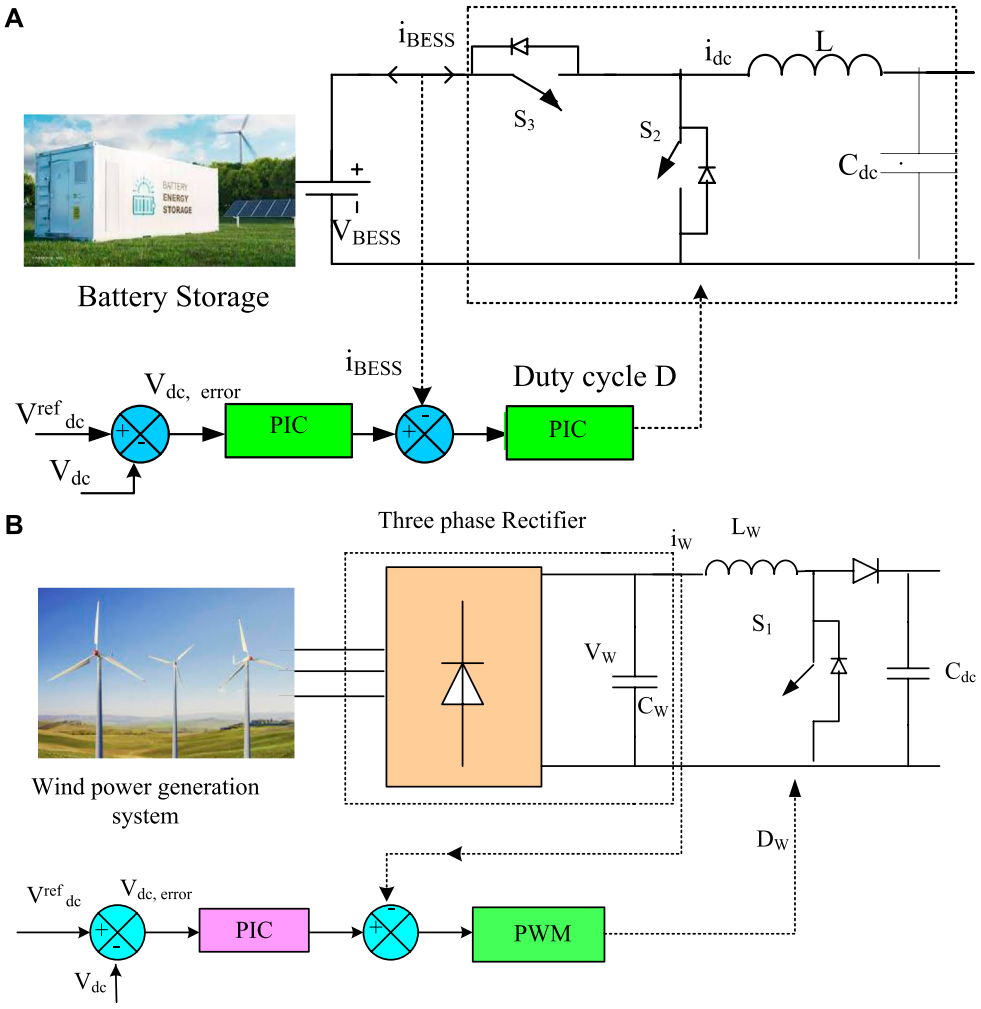

FIGURE 4
Battery and Wind control systems.

problems such as disturbances, swells, sags, and so on, through U-SWBEV.

- The incorporation of RES, EVs, and BESS into the UPQC serves to alleviate the strain on VSC, provides support for meeting load requirements, and ensures the steady maintenance of the stable voltage across DC link, even amidst variations in irradiation, wind velocity and load.

Furthermore, the proposed system was evaluated across four test scenarios involving varying loads, wind velocity and

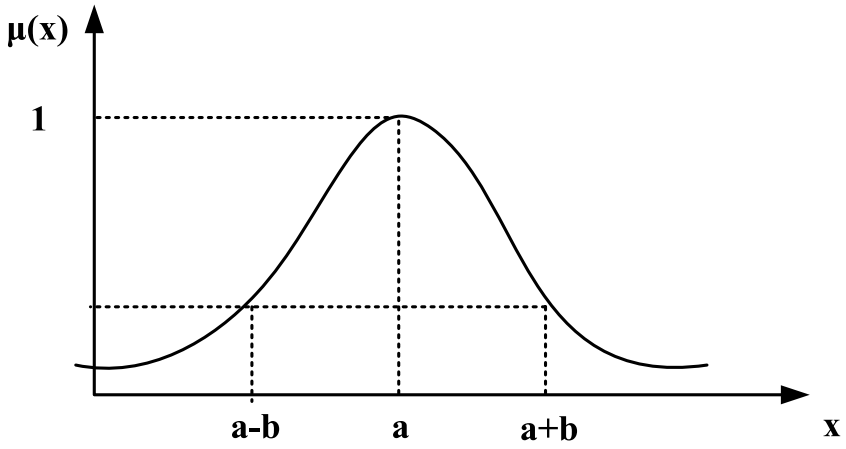

FIGURE 5
Gaussian MSF.

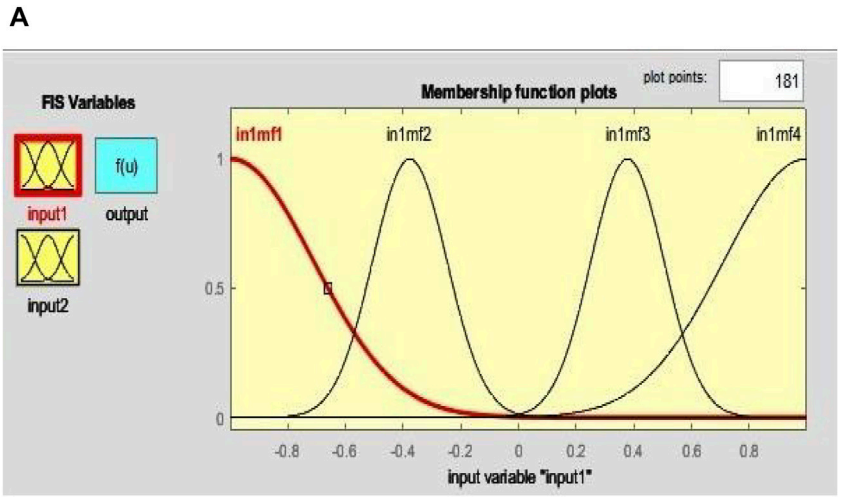

MSF of input-1

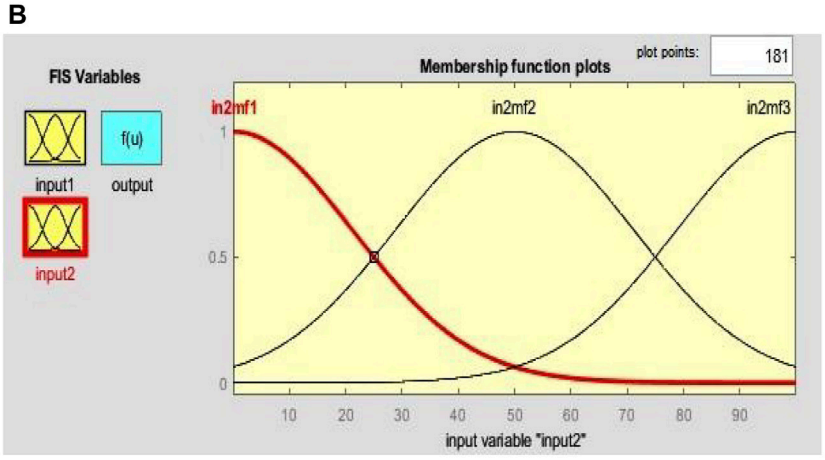

MSF of input-2

FIGURE 6
MSF for power management.

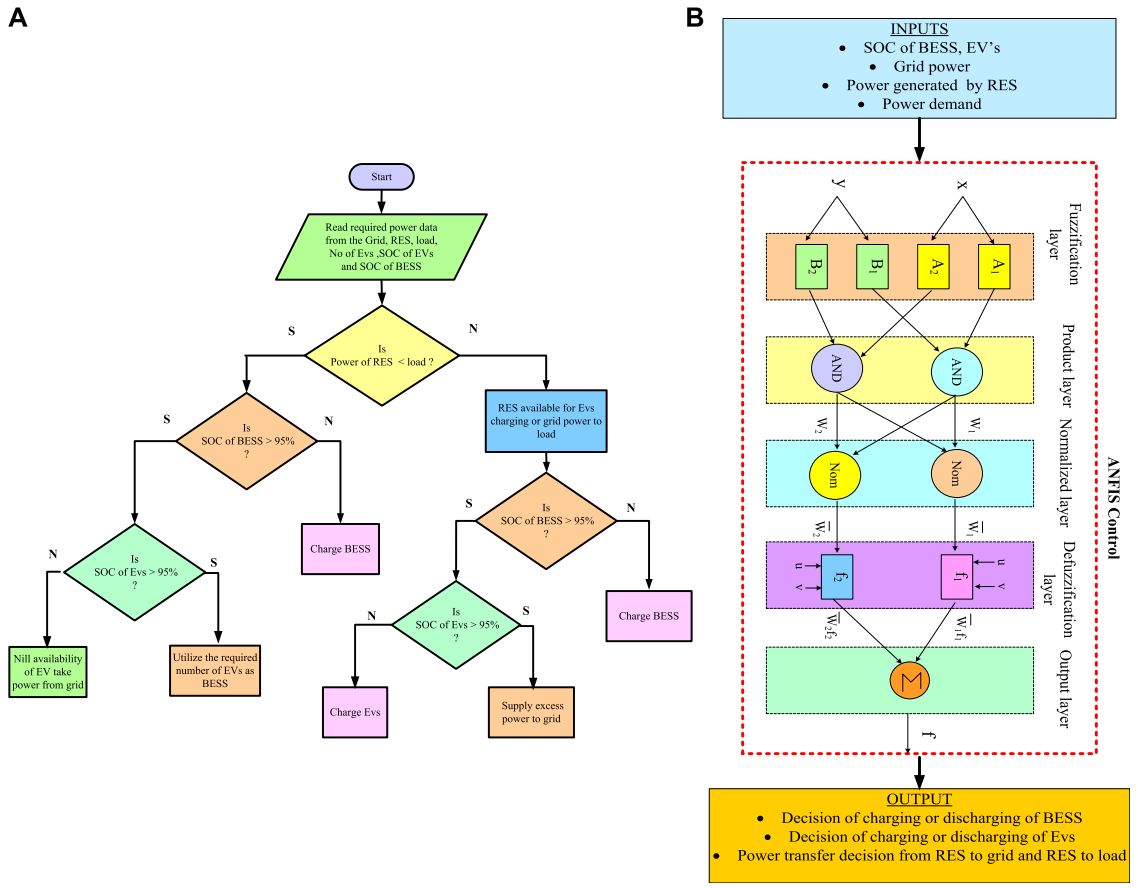

FIGURE 7
Power management.

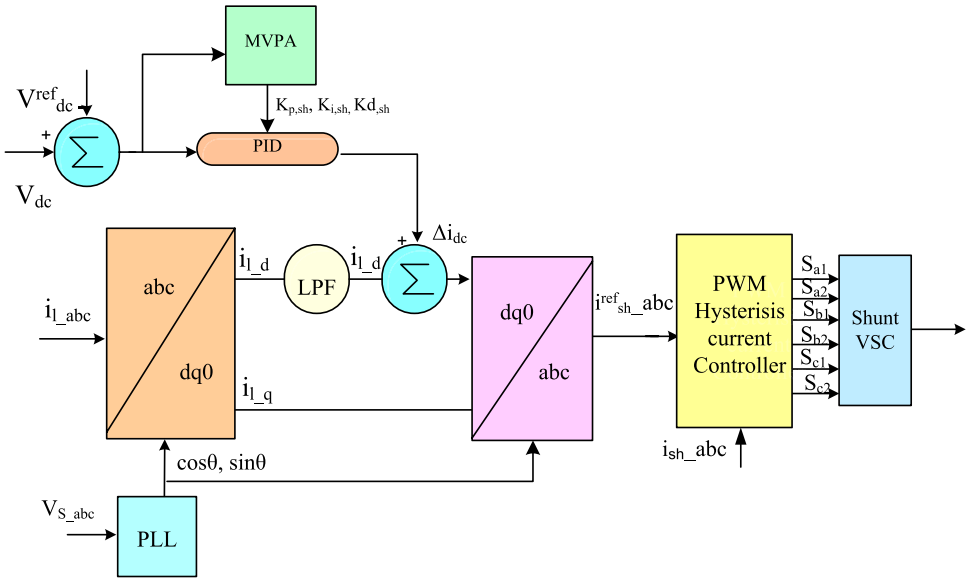

FIGURE 8
Shunt controller converter system.

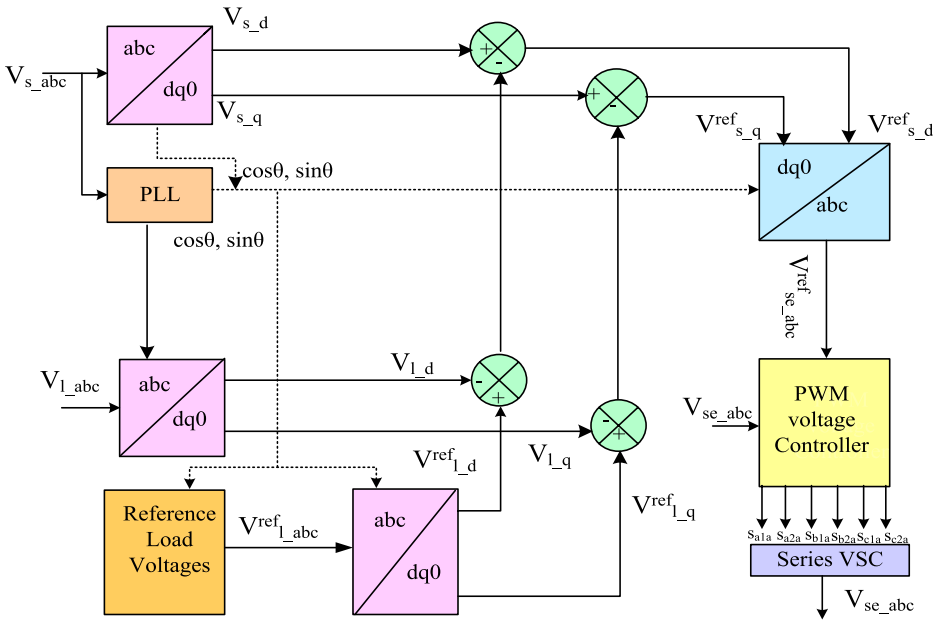

FIGURE 9
Series controller converter system.

irradiation circumstances. This assessment demonstrated its outstanding achievement in minimizing THD in current waveforms and reducing voltage waveform fluctuations. The system's performance was assessed through comparisons with the GA, PSO and ACO techniques.

The paper's organization is as follows: Section II delves into the modeling of U-SWBEV, while Section III provides the application of the techniques utilized in this study, focusing on the ANFIS and EMVPA. Section IV presents the results along with accompanying discussions. Lastly, Section V summarizes the conclusions drawn from the proposed work and provides the potential directions for future research in this field.

2 Proposed U-SWBEV

The suggested system's schematic arrangement is depicted in Figure 1. WES, SPV, BESS, and EV grid connection allows for parallel power flow management and PQ control. The series filter's main job is to take care of grid-side voltage-related problems. This is accomplished by supplying the necessary V_{se}, which is supplied via the interfacing transformer together with the appropriate choice of L_{se}. The shunt filter is linked to the grid through L_{sh} in a similar way. The SHAPF's job is to lower the harmonics in the current by adding compensating currents and preserving a steady DLCV. The primary benefit of external renewable source support lies in the reduction of the necessary converter ratings and the alleviation of converter stress. The parameters chosen for SPV, WES, BESS, and EVs can be found in Table 2. The power flow is determined using Eq. 1.

$$P_{PV} \pm P_{BESS} + P_w \pm P_{EV} + P_{Grid} = P_L \quad (1)$$

2.1 SPV structure

SPV technology harnesses sunlight to generate electricity, with its effectiveness contingent upon the configuration of PV modules interconnected in both series and parallel. PV modules are organized in a series arrangement to form what is known as a string, these strings are further linked in parallel to attain the required voltage and current levels. Each PV cell within a module is represented by a single-diode equivalent circuit, as illustrated in Figure 2. The control system of the SPV system with the boost converter is shown in Figure 3.

Thei_{ph} is obtained by Eq. 2, and PV module reverse saturation current i_{rs} is given by Eq. 3

$$i_{ph} = [i_{SC} + K_i(T - 298)]^* G/1000 \quad (2)$$

$$i_{rs} = i_{SC}/[\exp(qV_{oc}/N_s \eta k T) - 1] \quad (3)$$

The module saturation current depends on cell temperature, which is given by Eq. 4 and the output current of the module is given by Eq. 5

$$i_{mo} = i_{rs}[T/T_n]^3 \exp\left[q^* E_g/\eta k(1/T - 1/T_n)\right] \quad (4)$$

$$i_{PV} = N_p{}^* i_{ph} - N_p{}^* i_{mo}{}^* \left[\exp\left(V_{pv}/N_s + i_{PV}{}^*(R_{s,PV})/\eta V_t\right) - 1\right] - i_{sh,PV} \quad (5)$$

The P_{PV} is evaluated by Eq. 6.

$$P_{PV} = V_{PV} \times i_{PV} \quad (6)$$

2.2 BESS

The BESS plays a vital role in power management, ensuring the fulfillment of load demands. Batteries, cells are arranged in either series and or parallel, are employed to achieve the

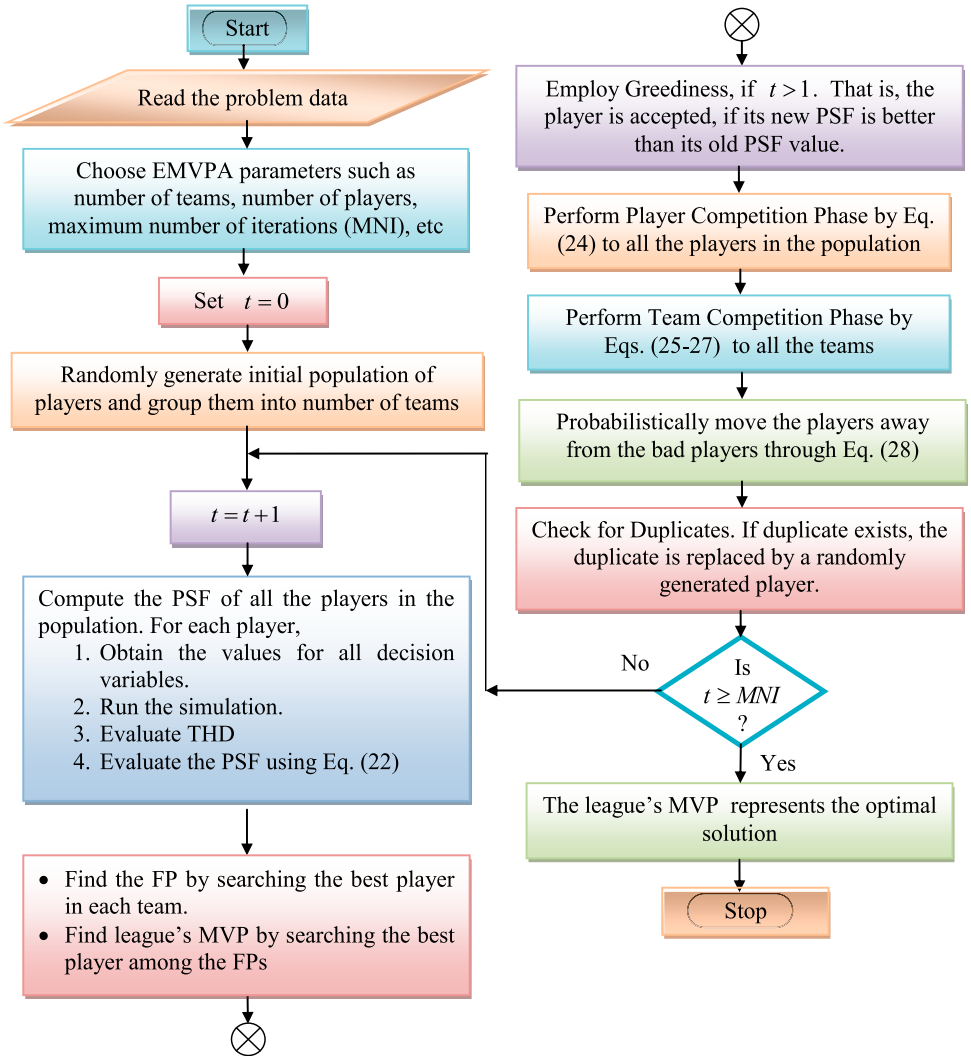

FIGURE 10
Flow of the filter parameters selection using EMVPA.

necessary current and voltage levels. The battery control system with a Buck-boost converter is illustrated in Figure 4A. The BESS also contributes to stabilizing the DLCV. The voltage and current requirements determine the specific arrangement of cells in the battery. For this research, a Li-ion battery has been chosen from the Simulink library. The *SOC* is represented in Eqs 7, 8.

$$SOC = 95\left(1 + \int i_{BSS}\, dtQ\right) \tag{7}$$

$$SOC_{\min} \leq SOC \leq SOC_{\max} \tag{8}$$

2.3 Wind system

By rectifying, the AC voltage generated by the WES is transformed into DC voltage, which is then raised with the aid of a boost converter that boosts the voltage. In this study, a permanent magnet synchronous machine is taken into consideration because of its dependability, affordability, ease of management, and superior performance. In Figure 4B, the WES controller is displayed. The power produced by WES can be found in Eqs 9–13.

$$R_{st} = \omega R_b / V_w \tag{9}$$

$$P_{mop} = 0.5\rho\pi R^{2_b} C_{pc} V^3 \omega \tag{10}$$

$$P_{mop} = \omega\, T_{mop} \tag{11}$$

$$C_p = \left(0.44 - 0.0167\theta_p\right) \sin \frac{3.14\,(N_r - 2)}{13 - 0.3\theta_p} \tag{12}$$

$$-0.0018\,(N_r - 2) = \theta_p \tag{13}$$

3 ANFIS power flow management

The ANFIS controller utilizes the RES power generation forecasting system and load forecasting system to manage the

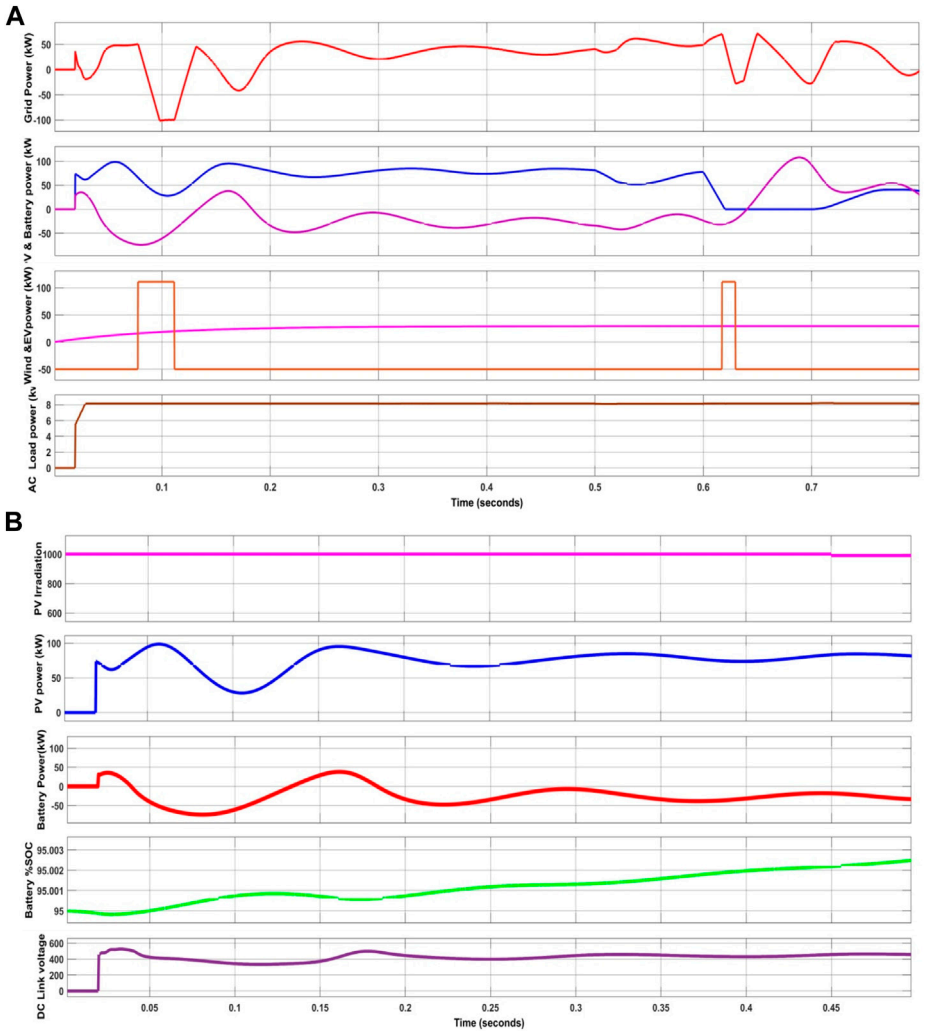

FIGURE 11
(Continued).

power exchange between EVs and the grid. It facilitates the transfer of power either from EVs to the grid or *vice versa*. This research offers insights into enhancing PQ in addition to power flow management in the grid system through the integration of EVs with UPQC. This highlights the primary objective of implementing ANFIS power flow management, which is to regulate the utilization of EVs as portable, temporary BESS. Consequently, when the stored energy is not needed, it can also be employed for transportation.

The ANFIS controller adapts the characteristics of an ANNC and an FLC. The inputs provided to the ANFIS are primarily calibrated based on the MSF to generate optimal results, as demonstrated in Figure 5. The ANFIS comprises of five layers, with the first layer being the Fuzzification layer, where the outputs consist of MSF as defined in Eq. 14.

$$\begin{aligned} &\mu_{Ai}(x), i = 1, 2. \\ &\mu_{Bj}(y), j = 1, 2. \end{aligned} \tag{14}$$

Here, $\mu_{Ai}\ \mu_{Bj}$ represents the outputs derived from the MSF in the first layer. The Gaussian MSF is represented in Eq. 15.

$$\mu(x) = e^{-\left(\frac{x-a}{b}\right)^2} \tag{15}$$

Moreover, in the second layer (where fuzzy rule weighting is performed), the AND logic is utilized to compute the firing capability w_i by considering the MSF generated in the first layer, the output of which is determined using Eq. 16.

$$w_k = \mu_{Ai}(x)^* \mu_{Bj}(y) i, j = 1, 2. \tag{16}$$

In the third layer, values received from the preceding layer undergo normalization. Each node in this layer achieves normalization by calculating the kth rule's truth value to the total summation of firing strengths, as described in Eq. 17.

$$\overline{w_k} = \frac{w_k}{w_1 + w_2} k = 1, 2. \tag{17}$$

The ANNC's ability to self-adapt is executed through the application of the inference variables (p_k, q_k, r_k) in the fourth layer, which produces an output as defined in Eq. 18.

$$\overline{w_i} f_i = \overline{w_i}\left(p_k u + q_k v + r_k\right) \tag{18}$$

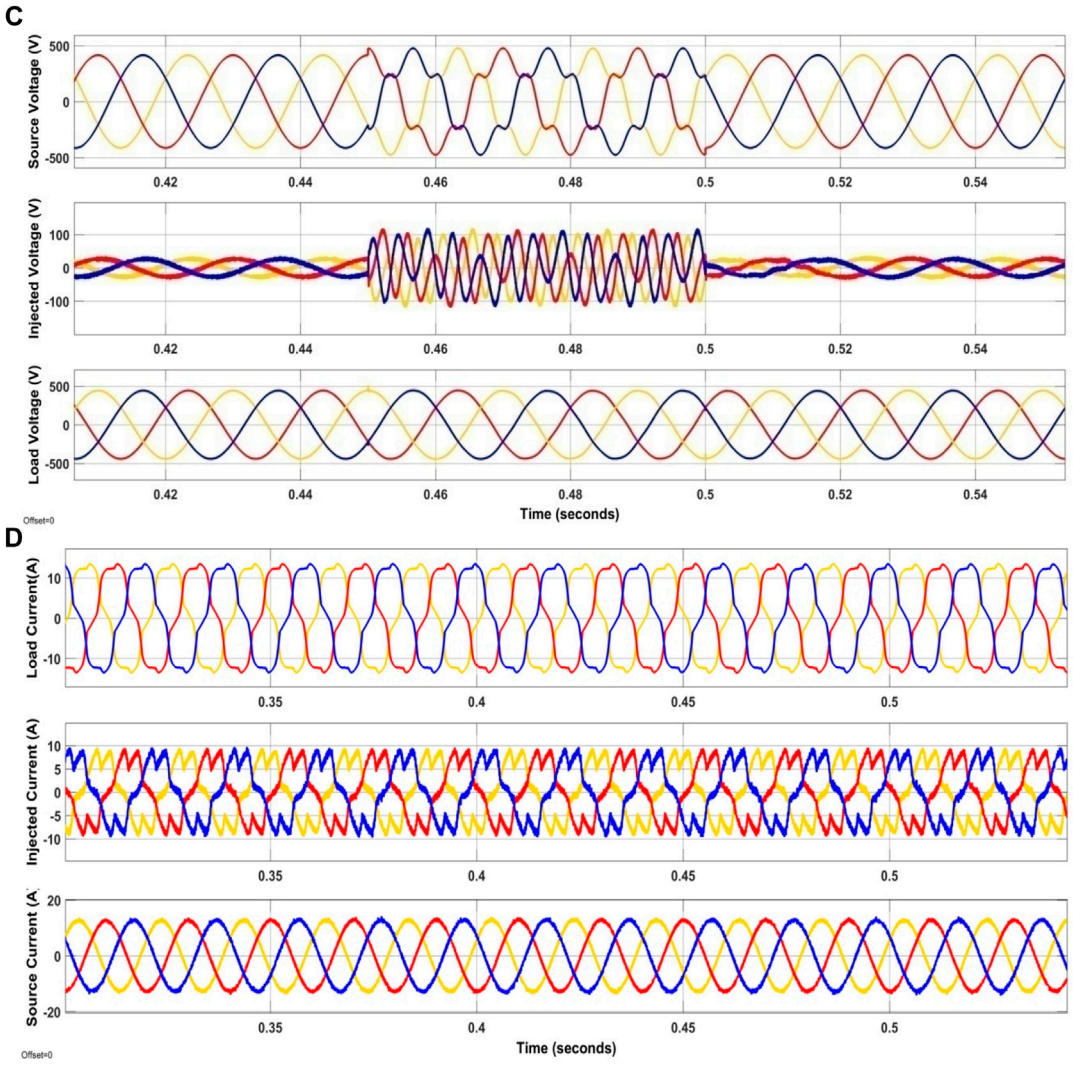

FIGURE 11
(Continued). Waveforms of the developed method for case1.

Finally, in the fifth layer, the inputs are aggregated to yield the ultimate desired output of the ANFIS, as indicated in Eq. 19. Figure 6 illustrates the configuration of the suggested ANFIS, and the Membership Function (MSF) for input 1 and input 2.

$$f = \sum_i \overline{w_i} f_i \tag{19}$$

In this work, the effective management of power flow is handled by ANFIS. Power flow occurs between the various entities, including the grid, RESs, BESS, and charging stations and load by ANFIS regulator. However, this plays a pivotal role in making decisions about EV charging. When EVs are not in use, they can be stationed at charging stations.

These EVs can also function as BESS during high load periods, which results in a reduction of the grid's peak load hour. The contribution of EVs and their SOCOB play a significant role in determining the amount of power they can provide to the grid. The operational process of the proposed power flow is explained through the flowchart presented in Figure 7A. The developed ANFIS-based power management system is visually depicted in Figure 7B.

4 Shunt and series controllers of UPQC

The shunt SVC to mitigate harmonics in the supply current and regulate the DLCV employs the dq0-abc transformation and its inverse with the optimally tuned PIDC using EMVPA. The PLL provides frequency and phasor information from the supply voltage to transfer the current at load terminals into dq0 components. The PIDC continually compares the actual DC voltage with a set reference voltage to provide stable DC voltage, making necessary current adjustments to correct any deviations. The *d*th component of the load current is integrated into the PIDC control. Gate signals are generated using a Hysteresis controller, as depicted in Figure 8.

After converting from the abc-dq0 domain and then converting back to the abc domain, the terminal voltage is compared to a predetermined reference voltage. This comparison process then

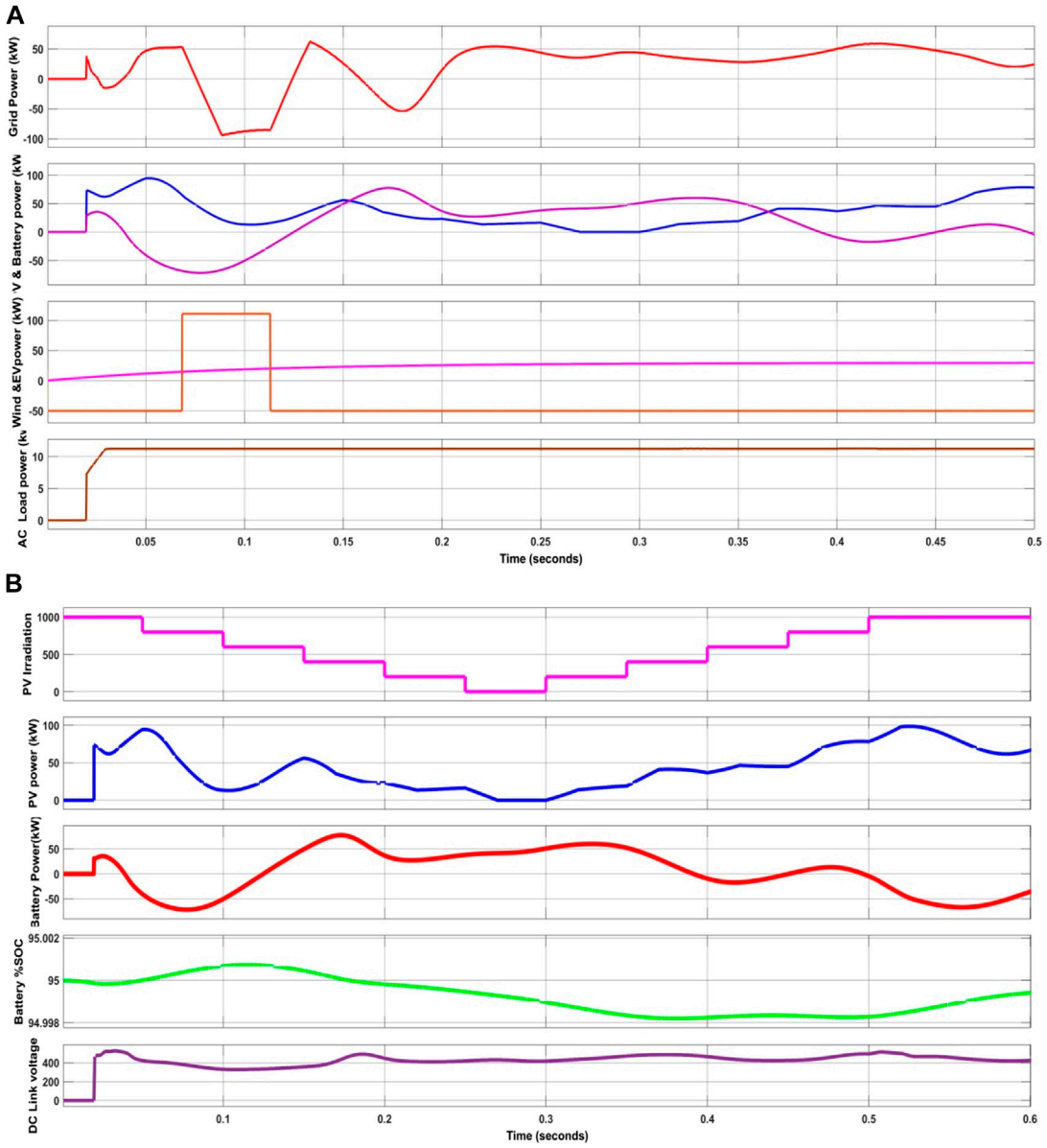

FIGURE 12
(Continued).

leads to the production of the essential gate current pulses for the series converter, as depicted in Figure 9. These current signals serve as the trigger pulses for the execution of PWM within the series converter.

4.1 EMVPA for optimal selection of PID controller gain values and filter parameters

The method proposed, known as EMVPA, encompasses the following key steps: (i) the creation of players (PLs), (ii) the establishment of a PSF, and (iii) the implementation of an "Avoidance of Bad PLs" approach to enhance the resilience of the existing EMVPA.

4.1.1 Players representation

The EMVPA is an algorithm rooted in swarm intelligence, drawing inspiration from sports games. In such games, a collective of PLs competes in multiple teams with the aim of achieving the championship title. Each PL within these teams plays individually with the ultimate objective of earning the MVP award. The set of PLs $\{P_1, P_2, \cdots, P_{nP}\}$ is initially distributed randomly to create multiple teams $\{\aleph_1, \aleph_2, \cdots, \aleph_{nT}\}$. The success of each PL within every team relies on their unique abilities and is measured using score. The player designated as *i*th, possessing a range of skills, is mathematically denoted as a variable in the problem.

$$P_i = [skill_{i,1}, skill_{i,2}, \cdots, skill_{i,ns}] \tag{20}$$

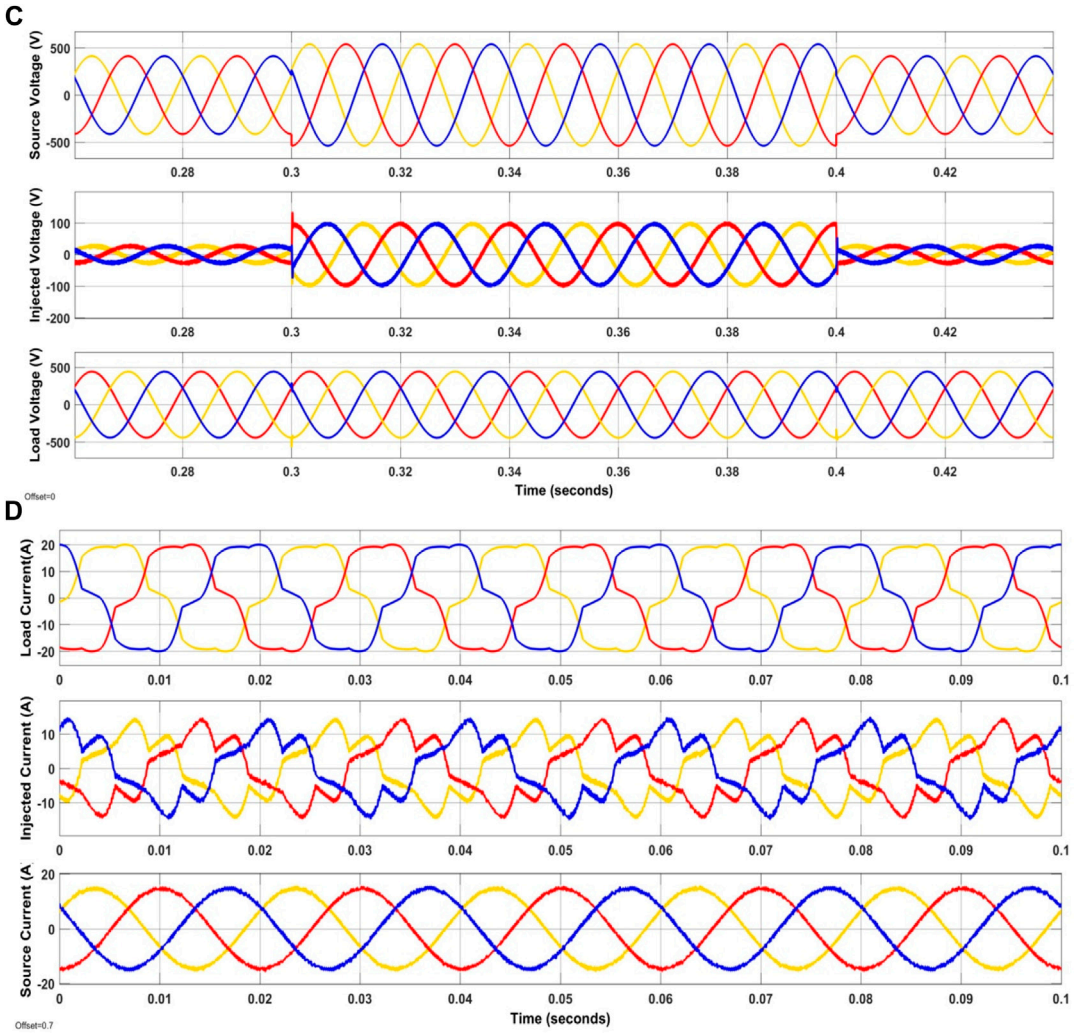

FIGURE 12
(Continued). Waveforms of the developed method for case2.

Each PL, with their unique skill set within the team, is symbolized to represent the gain values of the PIDC for the shunt controller, as well as the shunt and series filter parameters as control variables as defined in Eq. 21.

$$P_i = \left[K_p, K_i, K_d, R_{se}, R_{sh}, L_{se}, L_{sh}\right] \tag{21}$$

4.1.2 Performance score function

In most swarm-intelligence-based evolutionary algorithms, the performance of offspring is typically assessed using a FF. Since the EMVPA takes inspiration from sporting games where the victor is determined by their scores, the FF is referred to as the PSF. It is constructed from the objective of the problem selected while satisfying the constraint defined in Eq. 22, as follows:

$$\text{Maximize } PSF = \frac{1}{1 + THD} \tag{22}$$

Where, THD is evaluated by Eq. 23.

$$THD = \frac{\sqrt{(I^2{}_2 + I^2{}_3 + ...I^2{}_n)}}{I_1} \tag{23}$$

4.1.3 Competition among the players

Every PL within a team strives to boost their skills by engaging with their team's FP and the league's MVP with the goal of ascending to the role of their team's FP. The progression in skill enhancement during each iteration can be represented as follows:

$$\aleph_i = \aleph_i + rand \times (FP_i - \aleph_i) + C \times rand \times (MVP - \aleph_i) \tag{24}$$

Where, the constant C can be chosen as any integer value depending on the nature of the algorithm chosen for optimization.

4.1.4 Competition among the teams

Here, $\aleph_i$ team engages in a competition against a arbitrarily chosen opposing $\aleph_j (i \neq j)$ team. The probability of $\aleph_i$ team defeating team $\aleph_j$ is assessed as follows:

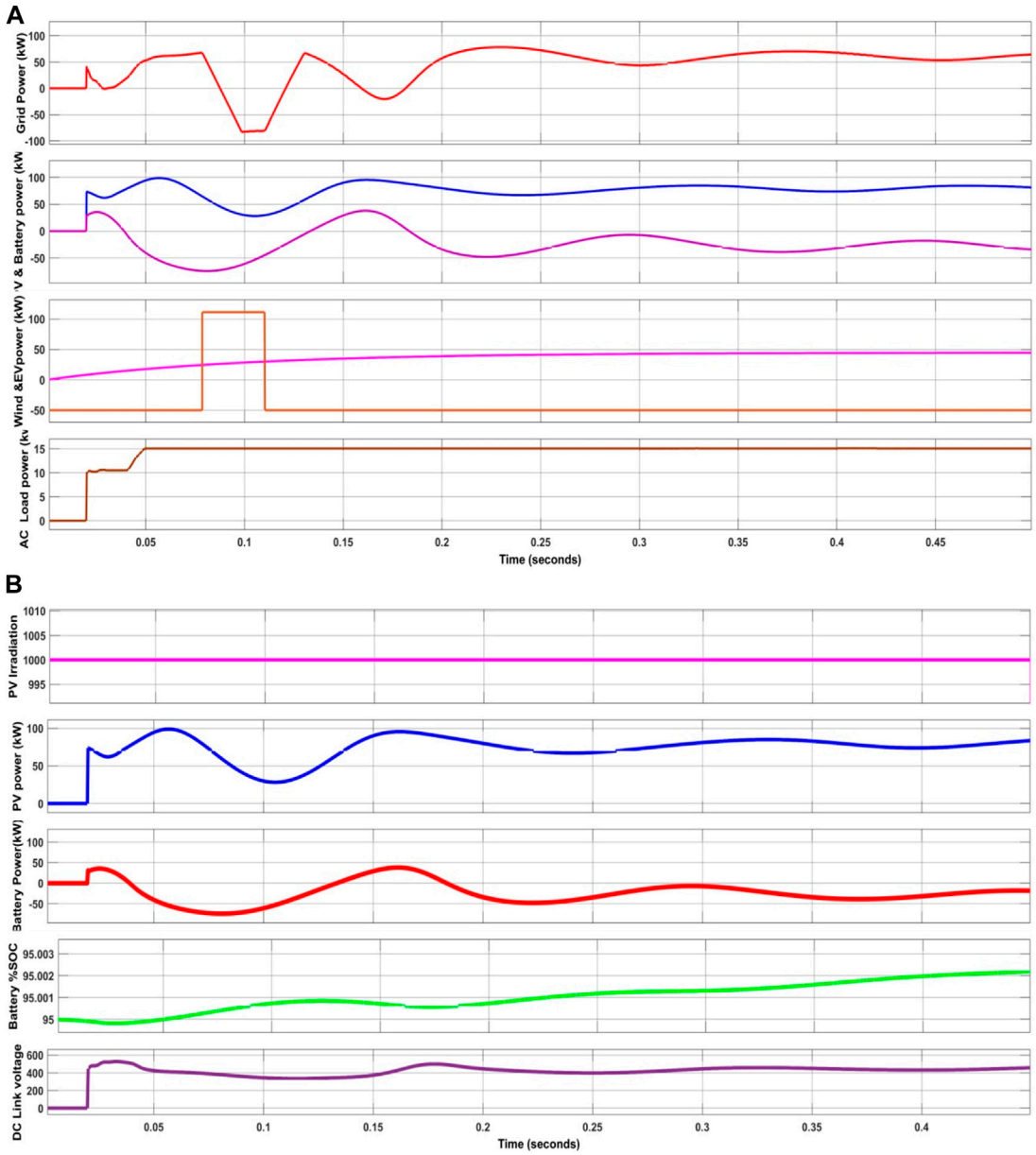

FIGURE 13
(Continued).

$$prob\left\{\aleph_i \text{ beats } \aleph_j\right\} = 1 - \left[\frac{\mathrm{PSF}(\aleph_i)^k}{\mathrm{PSF}(\aleph_i)^k + \mathrm{PSF}\left(\aleph_j\right)^k}\right] \quad (25)$$

Here, "k" denotes the winning probability and is set to 1, while $PSF(\aleph_i)$ represents the PSF of the selected PL in team $\aleph_i$. When team- $\aleph_i$ emerges as the victor in the game, the skills of the PLs in $\aleph_i$ undergo improvement as follows:

$$\aleph_i = \aleph_i + rand \times \left(\aleph_i - FP_j\right) \quad (26)$$

Otherwise, the skills of the PLs in $\aleph_i$ are improved as follows:

$$\aleph_i = \aleph_i + rand \times \left(FP_j - \aleph_i\right) \quad (27)$$

4.1.5 Escaping from bad players

The optimization process of the EMVPA can be further improved by considering the avoidance of suboptimal traps, particularly by identifying and mitigating the influence of underperforming players on the team. In sports physical contact between PLs can lead to injuries can result in PLs having to retire from the sport.

Even though various strategies were implemented to reduce injuries like helmet, pads, *etc.* Nevertheless, PLs in team sports tend to naturally avoid confrontations with aggressive or reckless PLs, maintaining distance to avoid contact-related injuries. This tendency of escaping problematic PLs can be adapted into the MVPA, with the aim of steering clear of

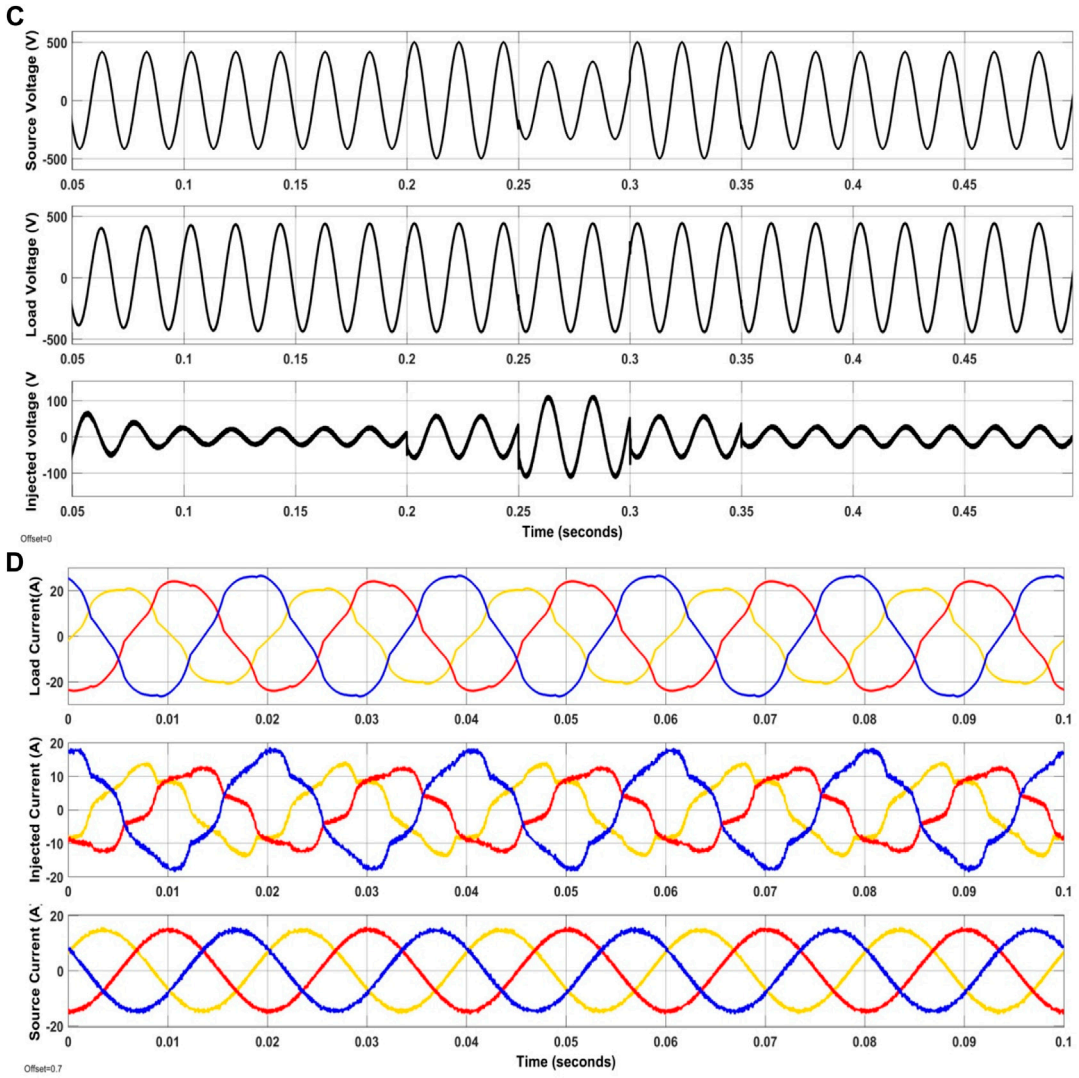

FIGURE 13
(Continued). Waveforms of the developed method for case3.

suboptimal outcomes by increasing the γ between each player and those deemed as subpar. This escaping mechanism can be implemented as follows:

$$\begin{aligned} P_i &\leftarrow P_i + \alpha.e^{-\gamma}, \quad if\ \gamma > 0 \\ P_i &\leftarrow P_i - \alpha.e^{+\gamma}, \quad if\ \gamma < 0 \end{aligned} \tag{28}$$

The described mechanism empowers PLs to steer clear of suboptimal solution points within the search space, bolstering their exploration capabilities and assisting the team in reaching the globally optimal solution.

4.1.6 Greediness

Following the sequence of PLs competitions, team competitions, and the avoidance of underperforming PLs by all team members, a greedy approach is applied to the PLs. This means that a new PL is accepted into the team only if their PSF is superior to the PSF value of the existing PL before the competition.

4.1.7 Solution process

An initial population of players, $\{P_1, P_2, \cdots, P_{nP}\}$, is generated by assigning random values within their respective bounds. These PLs are then randomly organized into multiple teams $\{\aleph_1, \aleph_2, \cdots, \aleph_{nT}\}$. The values of each PL, which represent the control variables for the PQ issue, are established as follows: parameters of PIDC, resistance and inductance values of filters. Subsequently, the PSF value for each player is computed after running simulink. This process is carried out for all PLs across all teams. Within each team, the player with the highest PSF value is recognized as the FP. Among all the FPs, the PL with the highest PSF value is bestowed with the title of the league's MVP. The PL and team competition

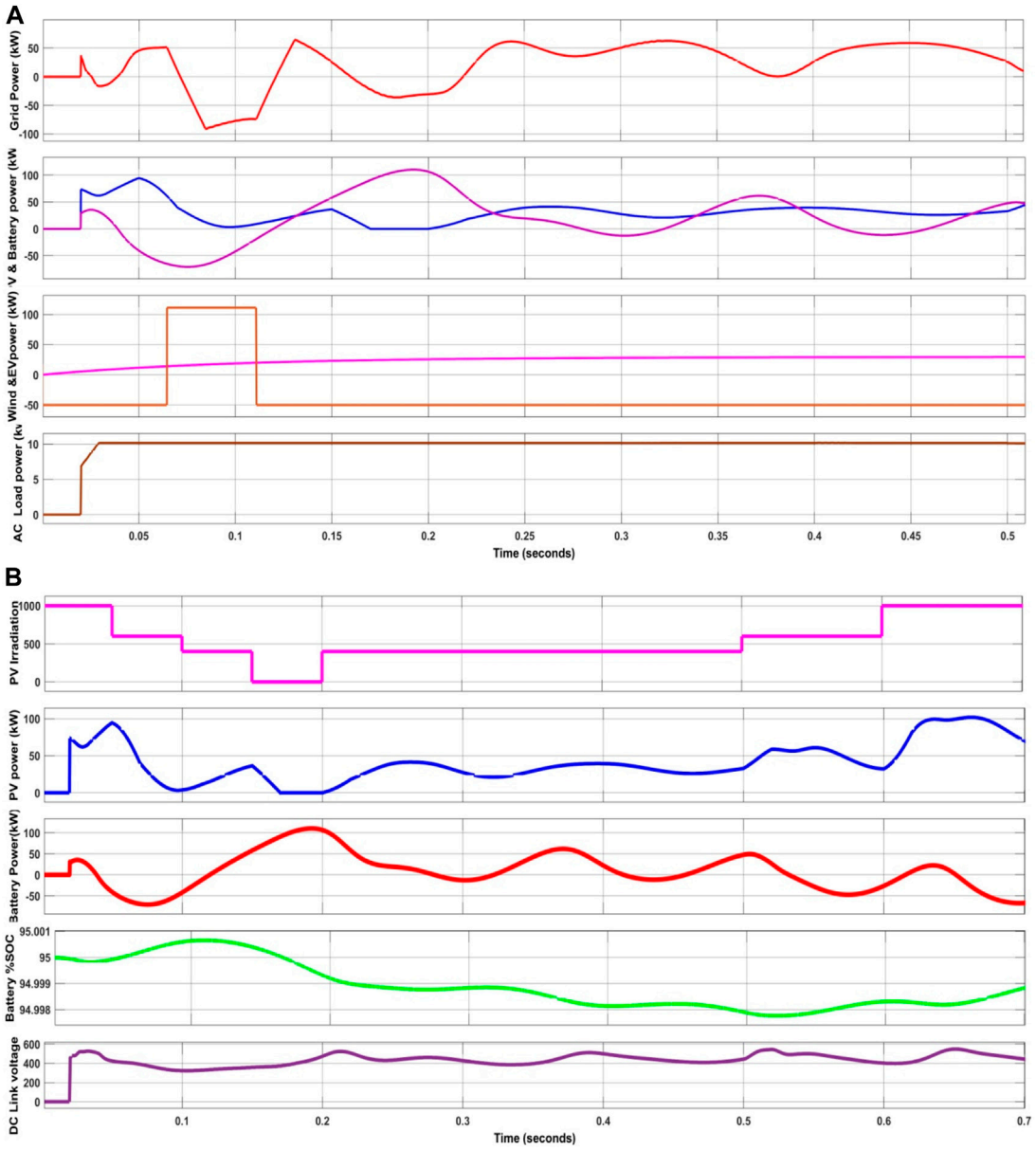

FIGURE 14
(Continued).

phases are initiated, following Eqs 24–27. The performances of the PLs are improved by mathematically distancing themselves from PLs that are considered "bad", as explained in Eq. 28.

The entire process, consisting of (i) computing PSF values, (ii) identifying FPs and the MVP, (iii) conducting PL competitions, team competitions, and avoiding bad PLs, constitutes a single iteration. The iterative cycle is repeated for a predetermined number of iterations, and the MVP at the point of convergence is identified as the global optima. Notably, the inclusion of a new player is contingent on their PSF value surpassing their previous PSF value. Moreover, the algorithm is designed to prevent ties, ensuring that in cases where two players attain an identical PSF value, a single player is chosen as the winner through a probabilistic selection process. However, the EMVPA was selected due to its advantages like fast convergence with lesser number of iterations with lower computational time for each iteration. Besides, the algorithm is having its own limitations like complexity due to which it is not preferable to solve multi objective engineering problems. In this work, the max number of iteration for termination is selected as 100 with 40 number of player in 4 teams (Srilakshmia et al., 2020). Figure 10 gives the visual representation of the proposed method's flowchart.

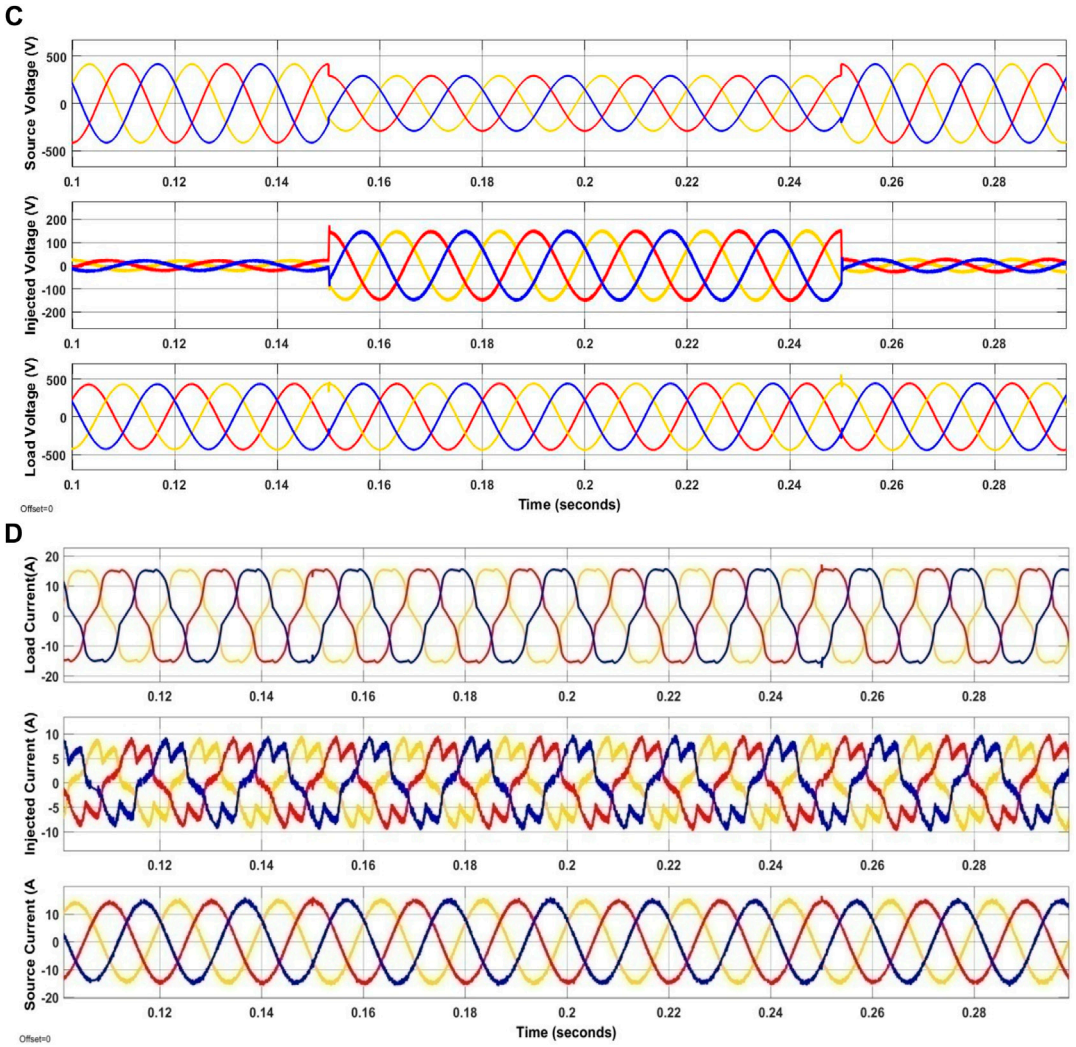

FIGURE 14
(Continued). Waveforms of the developed method for case4.

5 Results and discussions

The U-SWBEV integrated with ANFIS was developed and implemented using Simulink/Matlab 2022b. The simulation of the proposed system is visualized in Figure 16. The chosen system, as well as the selected parameters for the UPQC and the loads, is presented in Table 3 and Table 4. This study encompasses three distinct case studies given in Table 5, that involve various combinations of voltage-related problems such as sag, disturbance, and swell, along with scenarios that include fluctuating irradiation, wind velocity and a consistent temperature of 25°C. These case studies are employed to demonstrate the effectiveness of the developed ANFIS integrated with U-SWBEV. The primary objective of this work revolves around intelligent power flow management with a focus on effectively addressing PQ issues. This objective is achieved through the utilization of the ANFIS based power management and the UPQC for enhancing PQ.

As seen in Figure 11A for case 1, the suggested ANFIS is successfully handling EVSs in accordance with their SOCs. At this point, the grid draws power at 0.1 s while wind and PV provide their outputs. But in this scenario, BESS charge and EVs discharge (vehicle to the grid), delivering the required amount of power demand. Similarly, the grid provides power at 0.4 s when EVs are charging and PV, wind, and BESS provide their outputs. Here, RES provides power to the load in conjunction with the grid (grid to the vehicle). Furthermore, the constant irradiation and output power from the SPV system with a battery SOC of 95% are shown in Figure 11B in order to maintain stable DLCV. Next, Figure 11C shows how effectively the U-SWBEV series filter eliminates disturbances generated between 0.45 and 0.5 s by injecting the necessary voltage while aiming to keep the terminal voltage constant. Furthermore, as a result of the nonlinear load (the combination of loads 1 and 5), which causes the load current to be extremely polluted, the SHAPF provides the distortion free current to the supply by

TABLE 6 % THD comparison.

Case	Controller/Ref [ ]	%THD					
		Source current			Load voltage		
		Phase-a	Phase-b	Phase-c	Phase-a	Phase-b	Phase-c
1	PM with GA	4.98	5.01	4.68	1.48	1.43	1.39
	PM with PSO	4.78	4.98	4.77	1.46	1.37	1.30
	PM with ACO	4.57	4.65	4.73	1.34	1.32	1.35
	PM with EMVPA	**4.50**	**4.46**	**4.57**	**1.34**	**1.31**	**1.36**
2	PM with GA	3.98	3.77	3.56	1.47	1.41	1.39
	PM with PSO	3.91	3.68	3.87	1.35	1.31	1.39
	PM with ACO	3.82	3.47	3.51	1.47	1.33	1.34
	PM with EMVPA	**2.26**	**2.56**	**2.67**	**1.33**	**1.42**	**1.37**
	ANFIS Renduchintala et al. (2021)	2.43	--	--	--	--	--
	FLC Renduchintala et al. (2021)	6.13	--	--	--	--	--
	PIC Renduchintala et al. (2021)	14.74	--	--	--	--	--
	BF tuned PIC Sakthivel et al. (2015)	3.71	--	--	--	--	--
	ACO tuned PIC Sakthivel et al. (2015)	3.72	--	--	--	--	--
	PIC Sakthivel et al. (2015)	3.88	--	--	--	--	--
	PSO Mahaboob et al. (2019)	2.09	--	--	--	--	--
	HSO Mahaboob et al. (2019)	2.41	--	--	--	--	--
	ZN Mahaboob et al. (2019)	7.57	--	--	--	--	--
	ICM Mahaboob et al. (2019)	4.2	--	--	--	--	--
3	PM with GA	4.36	4.23	4.41	1.31	1.36	1.39
	PM with PSO	4.26	4.31	4.29	1.37	1.29	1.37
	PM with ACO	4.11	4.31	4.24	1.34	1.31	1.32
	PM with EMVPA	**4.09**	**4.13**	**4.32**	**1.27**	**1.21**	**1.26**
4	PM with GA	3.99	4.21	4.36	1.35	1.35	1.38
	PM with PSO	4.01	3.99	3.78	1.31	1.33	1.42
	PM with ACO	4.22	4.02	3.99	1.31	1.30	1.35
	PM with EMVPA	**3.98**	**3.99**	**4.21**	**1.30**	**1.32**	**1.34**

[a]Note: PM, is proposed method with ANFIS, power flow management.
Bold values indicate to highlight the proposed method.

injecting the necessary amount of current, as shown in Figure 11D which in turn reduces THD to 4.50% and enhances PF to almost unity.

In case 2, it is noted that the suggested method continues to function well in spite of variations in load and irradiation. Here, the grid draws power at 0.1 s from Figure 12A, with RES giving their output powers but at lower levels. To supply the necessary quantity of power to the load, EVs are made to be in the discharging condition in this instance while the BESS is in the charging state. The variable irradiation taken into account in this case during the load change from case 1 to case 2 is depicted in Figure 12B. Additionally, as shown in Figure 12C, the U-SWBEV series filter effectively reduces swell from 0.3 to 0.4 s by injecting the necessary compensatory voltage while keeping the terminal voltage constant. Besides, because load 3 and load 5 are nonlinear, the load current is heavily contaminated. To mitigate this, a shunt filter injects the necessary current as shown in Figure 12D and reduces THD to 2.26% and to almost unity.

In this case-3, a constant solar irradiation level is chosen while the load varies. Specifically, at 0.025 s, load 1 and 2 is added, and at 0.03 s, load 4 is included. The performance of the

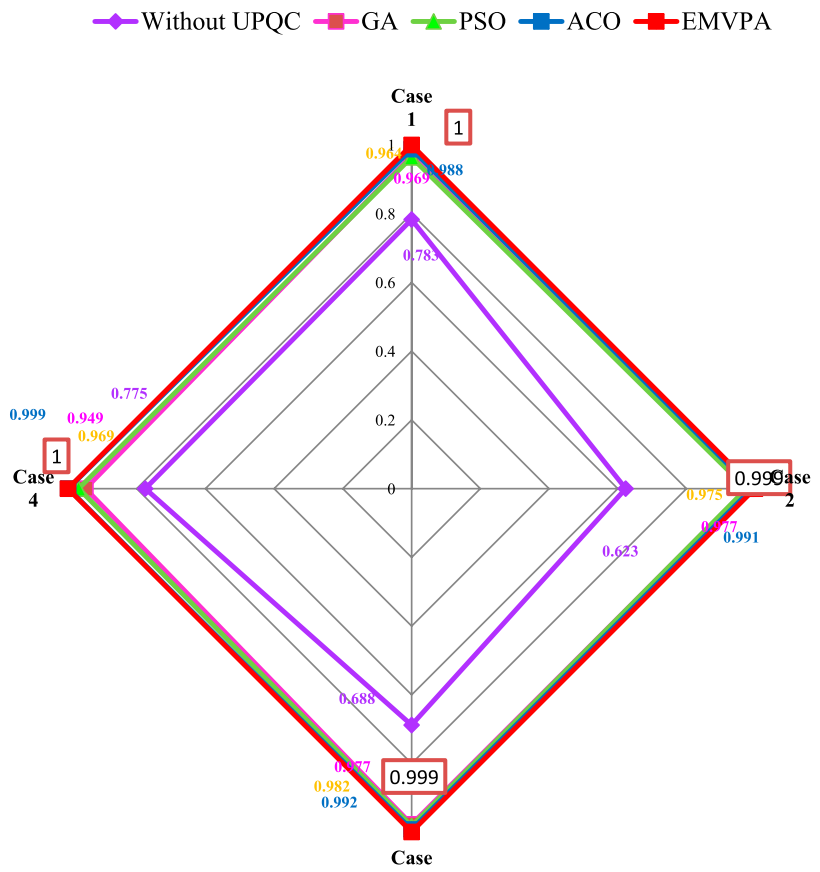

FIGURE 15
Comparison of PF.

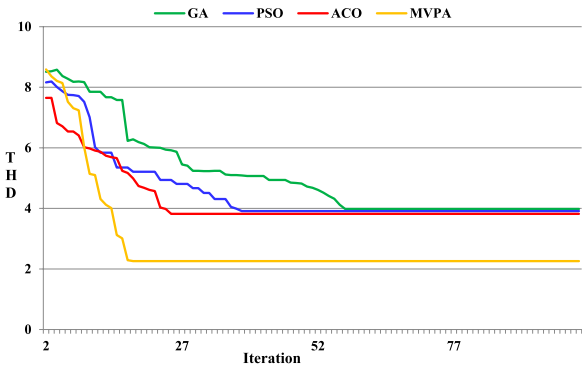

FIGURE 16
Comparison of convergence characteristics for case-1.

proposed method is seen in Figure 13A, which exhibits that the grid is under neutral state around 0.3 s. During this time, the RES supplies power to the load, while the BESS and EVSs are in the process of charging. Figure 13B displays the chosen constant solar irradiation alongside the power output and DLCV balancing. In this study, the voltage flicker situation is examined from 0.2 to 0.25 s which is efficiently mitigated by the UPQC. Additionally, the loads (in the combination of loads 1, 2 and 4), which leads to the unbalances and imperfections in the load current, the U-SWBEV handles effectively and provides sinusoidal source current with lower THD of 4.09% and enhances power factor to 0.999, as illustrated in Figures 13C, D.

In case 4, the variable solar irradiation is selected with load 1 at 0.025 s and load 2 at 0.03 s respectively. The performance of the proposed method can be seen in Figure 14A, where at 0.2 s, the grid is consuming power while the solar output is zero. The wind system, in conjunction with the BESS, supplies the necessary power to the load when EVSs are in the process of charging. Figure 14B illustrates the correlation between solar irradiation, PV power, BESS power, state of charge, and DLCV balancing. However, this study focused on the voltage sag condition occurring between 0.15 and 0.25 s. The compensation for this condition was efficiently achieved by the U-SWBEV, as illustrated in Figure 14C. In addition, the shunt filter effectively compensates for the polluted load current as depicted in Figure 14D, generated by rectified bridged non linear load and active power load which reduces THD to 3.98% which is much lesser that other methods listed in Table 6. Besides, it also boosts up the power factor to almost unity.

TABLE 7 Comparison of design parameters.

Case	Method	K_p	K_i	K_d	R_{se}	R_{sh}	L_{se}	L_{sh}
1	GA	44.631	63.741	1.124	1.362	0.165	8.365	8.997
	BBO	2.417	10.365	0.599	4.321	0.245	4.321	0.125
	ACO	3.124	44.981	1.899	6.347	0.199	3.740	0.124
	EMVPA	2.417	7.998	15.365	1.960	0.165	1.124	0.010
2	GA	64.998	71.369	54.325	2.365	0.124	5.982	9.998
	PSO	2.147	49.324	4.368	1.998	0.478	1.981	5.112
	ACO	4.001	47.369	1.336	6.347	0.398	3.447	3.987
	PIC Sakthivel et al. (2015)	0.507	10.3	--	--	--	--	--
	ACO tuned PIC Sakthivel et al. (2015)	0.912	247.93	--	--	--	--	--
	BF tuned PIC Sakthivel et al. (2015)	0.843	288.5	--	--	--	--	--
	PSO Mahaboob et al. (2019)	2.1345	10.2581	--	--	--	--	--
	HSO Mahaboob et al. (2019)	3.7151	45.4126	--	--	--	--	--
	ZN Mahaboob et al. (2019)	0.019	0.00042	--	--	--	--	--
	ICM Mahaboob et al. (2019)	0.0455	0.064	--	--	--	--	--
	ABC Rajesh et al. (2021)	8.2270	0.0020	--	--	--	--	--
	GSA Rajesh et al. (2021)	9.6325	2.3020	--	--	--	--	--
	FA Rajesh et al. (2021)	9.2545	1.6580	--	--	--	--	--
	MFOA Rajesh et al. (2021)	8.8554	1.8569	--	--	--	--	--
	EMVPA	6.124	5.369	4.998	8.561	0.435	2.365	5.325
3	GA	45.321	29.347	3.897	8.997	0.112	1.771	4.654
	PSO	1.945	81.369	7.698	7.658	0.214	5.334	5.974
	ACO	2.124	77.324	9.471	6.338	0.198	4.698	8.012
	EMVPA	3.987	0.100	5.487	9.412	0.401	1.974	9.778
4	GA	47.965	45.213	45.369	8.554	0.012	3.447	6.163
	PSO	10.981	0.112	81.654	7.211	0.201	2.001	7.549
	ACO	2.101	51.369	71.365	6.873	0.214	1.980	8.916
	EMVPA	19.981	19.336	43.541	1.557	0.272	5.145	4.749

The THDs of the suggested technique in all case studies is displayed in Table 6. The results demonstrate that the suggested method has significantly lower THD compared to other strategies, including those found in existing literature, and it also meets the standards set by the IEEE. In addition, the suggested system PF has value that is very close to unity, which is demonstrated in Figure 15, when compared to other approaches. Furthermore, it has been demonstrated as shown in Figure 16 that the proposed U-SWBEV with EMVPA achieves convergence to a reduced THD of 2.26% within 18 iterations. In comparison, GA, PSO, and ACO require 57, 38, and 25 iterations respectively to achieve convergence. Besides, the obtained designed parameter values of U-SWBEV were listed in Table 7.

Figure 17 depicts the FFT analysis of the source current for all cases in the proposed system. The proposed EMVPA technique is applicable for the best selection of shunt and series filters parameters optimally to reduce the burden on converters in addition to the elimination of imperfections in the current and voltage waveforms due to harmonics. Besides, the complexity of the proposed system can be justified by the optimal selection of filter parameters in addition to the controller parameters in association with AI control techniques for the better optimal solution.

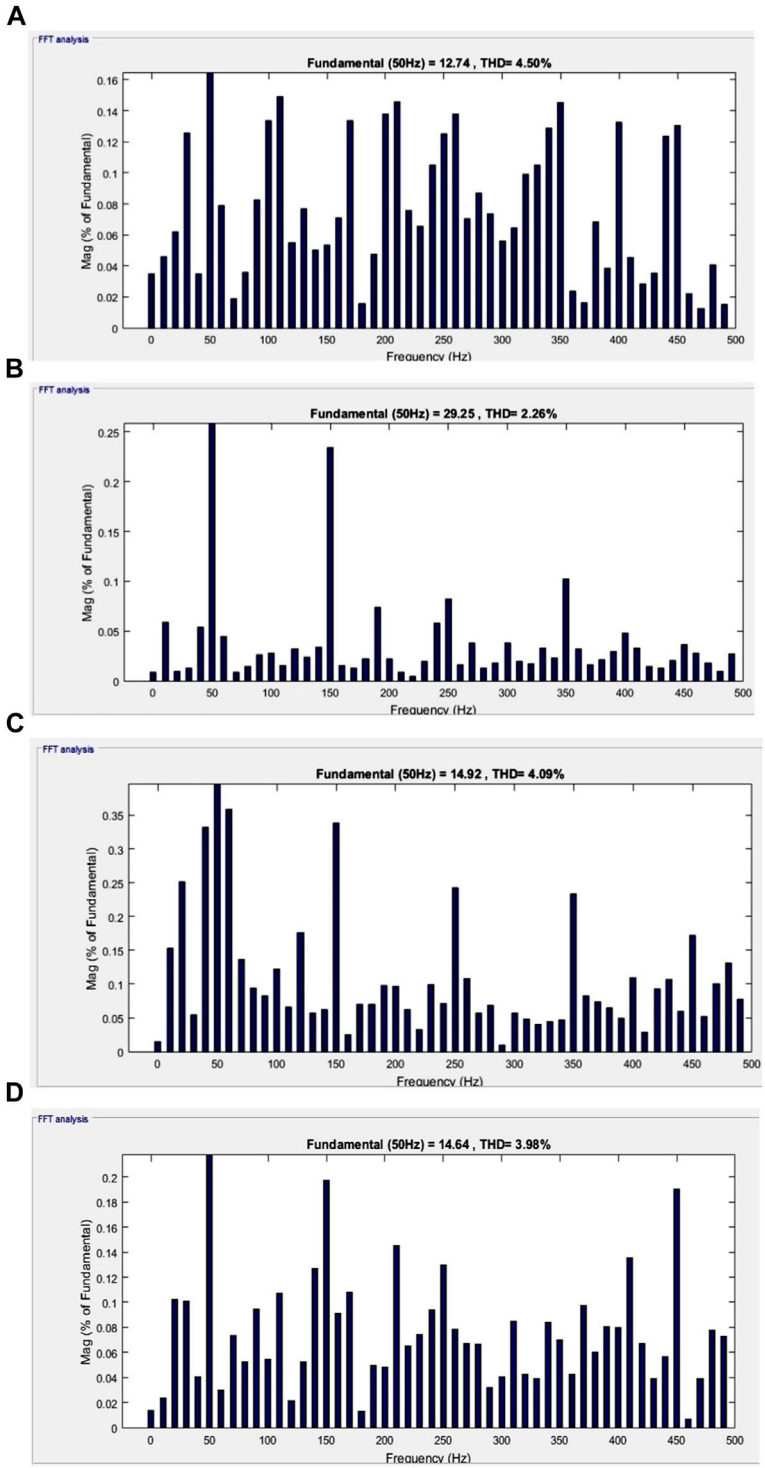

FIGURE 17
Current %THD spectrum for cases.

6 Conclusion

An intelligent ANFIS regulation is employed to effectively manage power flow in a system comprising Grid, RES, BESS and EVs. Here, UPQC is adopted to handle PQ issues to provide constant DC link voltage during varying loads, wind speeds, and irradiation conditions. In addition, the EMVPA method is employed to tune the gain values of PIDC, while also making an appropriate choice of filter parameters. The proposed power management system aims to meet the load demand and support

the required number of EVs. This work, simultaneously handles PQ issues and power management effectively. It effectively suppresses voltage disturbances, swells, sags, and defects in the current waveforms. However, with this proposed technique, the THD values for voltages and currents have been measured and found to be less than 5%. Future research can build upon the results of this study by incorporating metaheuristic algorithms to enhance the effective management of power flow even more.

Data availability statement

The original contributions presented in the study are included in the article/Supplementary Material, further inquiries can be directed to the corresponding author.

Author contributions

KS: Methodology, Writing–original draft. SG: Conceptualization, Software, Writing–original draft. SB: Formal Analysis, Writing–review and editing. PB: Writing–review and editing. GR: Investigation, Writing–review and editing. AP: Supervision, Writing–review and editing. SS: Funding acquisition, Writing–review and editing.

Funding

The author(s) declare that no financial support was received for the research, authorship, and/or publication of this article.

Conflict of interest

The authors declare that the research was conducted in the absence of any commercial or financial relationships that could be construed as a potential conflict of interest.

Publisher's note

All claims expressed in this article are solely those of the authors and do not necessarily represent those of their affiliated organizations, or those of the publisher, the editors and the reviewers. Any product that may be evaluated in this article, or claim that may be made by its manufacturer, is not guaranteed or endorsed by the publisher.

References

Amirullah, U. B., Surabaya, A., Adiananda, O., Penangsang, A., Soeprijanto, U. B., Surabaya, I. T. S., et al. (2020). Load active power transfer enhancement using UPQC-PV-BES system with fuzzy logic controller. *Int. J. Intell. Eng. Syst.* 2 (13), 329–349. doi:10.22266/ijies2020.0430.32

Ashok Kumar, L., and Indragandhi, V. (2020). Power quality improvement of grid connected wind energy system using facts devices. *Interanational J. Ambient Energy* 6 (41), 631–640. doi:10.1080/01430750.2018.1484801

Chellaswamy, C., and Ramesh, R. (2017). Future renewable energy option for recharging full electric vehicles. *Renew. Sustain. Energy Rev.* 76, 824–838. doi:10.1016/j.rser.2017.03.032

Elavarasan, R. M. (2020). 'Comprehensive review on India's growth in renewable energy technologies in comparison with other prominent renewable energy based countries. *J. Sol. Energy Eng.* 3 (142), 1–11. doi:10.1115/1.4045584

Ganesan, A., and Srinath, S. (2019). Optimal controller for mitigation of harmonics in hybrid shunt active power filter connected distribution system: an EGOANN technique. *J. Renew. Sustain. Energy* 11. doi:10.1063/1.5085028

Khosravi, N., Abdolmohammadi, H. R., Bagheri, S., and Miveh, M. R. (2021a). Improvement of harmonic conditions in the AC/DC microgrids with the presence of filter compensation modules. *Renew. Sustain. Energy Rev.* 143, 110898, 110898. doi:10.1016/j.rser.2021.110898

Khosravi, N., Abdolmohammadi, H. R., Bagheri, S., and Miveh, M. R. (2021b). A novel control approach for harmonic compensation using switched power filter compensators in micro-grids. *IET Renew. Power Gener.* 15, 3989–4005. doi:10.1049/rpg2.12317

Khosravi, N., Echalih, S., Baghbanzadeh, R., Hekss, Z., Hassani, R., and Messaoudi, M. (2022). "Enhancement of power quality issues for a hybrid AC/DC microgrid based on optimization methods," in *IET Renewable power generation*. doi:10.1049/rpg2.12476

Khosravi, N., Echalih, S., Hekss, Z., Baghbanzadeh, R., Messaoudi, M., and Shahideipour, M. (2023). A new approach to enhance the operation of M-UPQC proportional-integral multiresonant controller based on the optimization methods for a stand-alone AC microgrid. *IEEE Trans. Power Electron.* 38 (3), 3765–3774. doi:10.1109/TPEL.2022.3217964

Kong, P. Y., and Karagiannidis, G. K. (2016). Charging schemes for plug-in hybrid electric vehicles in smart grid: a survey. *IEEE Access* 4, 6846–6875. doi:10.1109/access.2016.2614689

Madurai Elavarasan, R., Afridhis, S., Vijayaraghavan, R. R., Subramaniam, U., and Nurunnabi, M. (2020a). SWOT analysis: a framework for comprehensive evaluation of drivers and barriers for renewable energy development in significant countries. *Energy Rep.* 6, 1838–1864. doi:10.1016/j.egyr.2020.07.007

Madurai Elavarasan, R., Selvamanohar, L., Raju, K., Vijayaraghavan, R. R., Subburaj, R., Nurunnabi, M., et al. (2020b). A holistic review of the present and future drivers of the renewable energy mix in Maharashtra, state of India. *Sustainability* 16 (12), 6596. doi:10.3390/su12166596

Mahaboob, S., Ajithan, S. K., and Jayaraman, S. (2019). Optimal design of shunt active power filter for power quality enhancement using predator-prey based firefly optimization. *Swarm Evol. Comput.* 44, 522–533. doi:10.1016/j.swevo.2018.06.008

Mansoor, M. A., Hasan, K., Othman, M. M., Noor, S. Z. B. M., and Musirin, I. (2020). Construction and performance investigation of three phase solar PV and battery energy storage system integrated UPQC. *IEEE Accesses* 8, 103511–103538. doi:10.1109/access.2020.2997056

Mirzapour, O., Karimi-Arpanahi, S., and Oraee, H. (2018). "Evaluating grid harmonics effect on induction motor using reduced thermal model," in 2018 Smart Grid Conference (SGC), Sanandaj, Iran, November 28th and 29th 2018, 1–5. doi:10.1109/SGC.2018.8777879

Mohamed, S. A. (2020). Enhancement of power quality for load compensation using three different FACTS devices based on optimized technique. *Int. Trans. Electr. Energy Syst.* 3 (30), 12196. doi:10.1002/2050-7038.12196

Nagireddy, V. V., Kota, V. R., and Ashok Kumar, D. V. (2018). Hybrid fuzzy back-propagation control scheme for multilevel unified power quality conditioner. *Ain Shams Eng. J.* 9 (4), 2709–2724. doi:10.1016/j.asej.2017.09.004

Nunes, P., and Brito, M. C. (2017). Displacing natural gas with electric vehicles for grid stabilization. *Energy* 141, 87–96. doi:10.1016/j.energy.2017.09.064

Okwako, O. E., Lin, Z.-H., Xin, M., Premkumar, K., and Rodgers, A. J. (2022). Neural network controlled solar PV battery powered unified power quality conditioner for grid connected operation. *Energies* 15 (2022), 6825. doi:10.3390/en15186825

Omid Mirzapour, Rui, X., and Sahraei-Ardakani, M. (2023). Transmission impedance control impacts on carbon emissions and renewable energy curtailment. *Energy* 278, 127741, 127741. doi:10.1016/j.energy.2023.127741

Paramanik, S., Sarker, K., Chatterjee, D., and Goswami, S. K. (2019). "Smart grid power quality improvement using modified UPQC," in Proc. Devices for Integr. Circuit (DevIC), Kalyani, India, 19-20 May 2021, 356–360.

Pazouki, S., and Haghifam, M.-R. (2021). Optimal planning and scheduling of smart homes' energy hubs. *Electr. Energy Syst.* 31, e12986. doi:10.1002/2050-7038.12986

Pazouki, S., and Olamaei, J. (2019). The effect of heterogeneous electric vehicles with different battery capacities in parking lots on peak load of electric power distribution networks. *Int. J. Ambient Energy* 40 (7), 734–738. doi:10.1080/01430750.2017.1423382

Rajesh, P., Shajin, F. H., and Umasankar, L. (2021). A novel control scheme for PV/WT/FC/battery to power quality enhancement in micro grid system: a hybrid technique. *Energy Sources, Part A Recovery, Util. Environ. Eff.*, 1–17. doi:10.1080/15567036.2021.1943068

Ramadevi, A., Srilakshmi, K., Kumar Balachandran, P., Colak, I., Dhanamjayulu, C., and Khan, B. (2023). Optimal design and performance investigation of artificial neural network controller for solar- and battery-connected unified power quality conditioner. *Int. J. Energy Res.* 2023, 1–22. Article ID 3355124. doi:10.1155/2023/3355124

Renduchintala, U. K., Pang, C., Tatikonda, K. M., and Yang, L. (2021). ANFIS-fuzzy logic based UPQC in interconnected microgrid distribution systems: modeling, simulation and implementation. *J. Eng.* 21 (1), 6–18. doi:10.1049/tje2.12005

Sakthivel, A., Vijayakumar, P., Senthilkumar, A., Lakshminarasimman, L., and Paramasivam, S. (2015). Experimental investigations on ant colony optimized pi control algorithm for shunt active power filter to improve power quality. *Control Eng. Pract.* 42, 153–169. doi:10.1016/j.conengprac.2015.04.013

Seyed Alizadeh, S. M., Bagherzadeh, A., Bahmani, S., Nikzad, A., Aminzadehsarikhanbeglou, E., and Tatyana Yu, S. (2021). Retrograde gas condensate reservoirs: reliable estimation of dew point pressure by the hybrid neuro-fuzzy connectionist paradigm. *ASME. J. Energy Resour. Technol. June* 144 (6), 063007. doi:10.1115/1.4052167

Shafiullah, G. M., Arif, M. T., and Oo, A. M. T. (2018). Mitigation strategies to minimize potential technical challenges of renewable energy integration. *Sustain. Energy Technol. Assessments* 25, 24–42. doi:10.1016/j.seta.2017.10.008

Srilakshmi, K., Krishna Jyothi, K., Kalyani, G., and Sai Prakash Goud, Y. (2023a). Design of UPQC with solar PV and battery storage systems for power quality improvement. *Cybern. Syst.*, 1–30. doi:10.1080/01969722.2023.2175144

Srilakshmi, K., Pandian, A. N., and Palanivelu, A. (2023b). Fuzzy based hybrid controller for UPQC with wind and battery storage systems. *Int. J. Electron.*, 1–26. doi:10.1080/00207217.2023.2245193

Srilakshmi, K., Srinivas, N., Balachandran, P. K., Reddy, J. G. P., Gaddameedhi, S., Valluri, N., et al. (2022a). Design of soccer league optimization based hybrid controller for solar-battery integrated UPQC. *IEEE Access* 10, 107116–107136. doi:10.1109/ACCESS.2022.3211504

Srilakshmi, K., Sujatha, C. N., Balachandran, P. K., Mihet-Popa, L., and Kumar, N. U. (2022b). Optimal design of an artificial intelligence controller for solar-battery integrated UPQC in three phase distribution networks. *Sustainability* 14 (21), 13992. doi:10.3390/su142113992

Srilakshmia, K., Ravi Babua, P., and Aravindhababub, P. (2020). An enhanced most valuable player algorithm based optimal power flow using Broyden's method. *Sustain. Energy Technol. Assessments* 42, 1008. doi:10.1016/j.seta.2020.100801

Vivas, F. J., Segura, F., Andújar, J. M., Palacio, A., Saenz, J. L., Isorna, F., et al. (2020). Multi-objective fuzzy logic-based energy management system for microgrids with battery and hydrogen energy storage system. *Electronics* 7 (9), 1074. doi:10.3390/electronics9071074

Zhao, X., Chai, X., Guo, X., Ahmad, W., Wang, X., and Zhang, C. (2021). Impedance matching-based power flow analysis for UPQC in three-phase four-wire systems. *Energies* 14 (2021), 2702. doi:10.3390/en14092702

Nomenclature

RES	Renewable energy sources
PIDC	Proportional integral derivate controller
PQ	Power quality
UPQC	Unified PQ Conditioner
EMVPA	Enhanced most valuable player algorithm
SPV	Solar photovoltaic
WES	Wind energy systems
BESS	Battery energy storage system
EVs	Electric vehicles
U-SWBEV	UPQC with RES, EV and Battery
ANFIS	Artificial neuro-fuzzy interface system
ANN	Artificial neural network
FL	Fuzzy logic
FACTS	Flexible Alternating Current Transmission Systems
UPFC	Unified Power Flow Controller
THD	Total Harmonic Distortion
SVC	Static Var Compensator
SOC	Short circuit current
DVR	Dynamic Voltage Restorer
DSTATCOM	Distribution Static Synchronous Compensator
OCV	Open circuit voltage
SHAPF	Shunt active power filters
VSC	Voltage Source Converters
GA	Genetic Algorithm
PSO	Particle swarm optimization
ACO	Ant colony optimization
COV	Cut of voltage
NOV	Nominal Voltage
DLCV	DC Link Voltage
SOC	State of charge of battery
MSF	Membership Function
ST	Station
PLL	Phase-Locked Loop
PWM	Pulse Width Modulation
PSF	Performance score function
MVP	Most Valuable Player
FP	Franchise player
P&O	Perturb and observe method
MPPT	Maximum power point tracking technique
LPF	Low pass filter
FF	Fitness function
MNI	Maximum number of iterations
V_{S_abc}	Source voltage inphase
i_{S_abc}	Source current inphase
i_{sh_abc}	Shunt filter supplied in phases
V_{l_abc}	Load voltage in phases
V_{se_abc}	Series injected voltage in phase
$V^{ref}_{se\_dq}$	Series filter reference voltage in dq
$i^{ref}_{sh\_abc}$	Reference injected SHAPF current in phases
i_{l_abc}	Load current in phases
R_{sh}	Shunt filter resistance
R_{se}	Series filter resistance
L_{sh}	Shunt filter inductance
L_{se}	Series filter inductance
C_{dc}	DC link capacitor
V_{dc}	Voltage across DC link capacitor
i_{ph}	Photo source current
i_d	Diode Forward conducting current
$R_{s,PV}$ **and** $R_{sh,PV}$	Series and parallel resistances of cell
$i_{sh,PV}$	Parallel current of PV cell
i_{PV}	PV cell output current
$i_{PV,m}$, $V_{PV,m}$	Module current and voltage
$i_{s,PV}$	Reverse saturation current
i_{rs}	Reverse saturation current
V_{oc}	Open circuit voltage
N_s	Number of series connected PV cell
N_p	Number of parallel connected PV cell
G	Solar irradiance (W/m^2)
T	Variation in PV cell temperature
P_{PV}	Output PV power
P_{BS}	Battery output power
η	Diode ideal factor
k	Boltzmann's constant
i_{mo}	Module current
Q	Battery's capacity
R	Internal resistance of battery
i_{BESS}	Battery current
V_{BESS}	Battery voltage
P_{BESS}	Battery power
ω	Rotor's rotational velocity
K	Polarization value

V_w	Wind speed
P_w	Wind power
P_L	Load power
P_{EV}	EV power
R_b	Blade's radius
R_{st}	Tip speed ratio
ρ	Air density
T_{mop}	Torque output
P_{mop}	Mechanical power output
C_p	Coefficient of power
Nr	Speed ratio
θ_p	Blade's pitch angle
V_{dc}^{ref}	Reference value of DLCV
K_p, K_i, K_d	Gain values of PIDC
Δi_{dc}	Error current of SHAPF
$i_{l\_d}\, i_{l\_q}$	Load current in dq
$V_{s\_d}^{ref}\, V_{s\_q}^{ref}$	Reference source current in dq
$V_{l\_abc}^{ref}$	Reference load voltage in phase
$V_{s\_d}\, V_{s\_q}$	Source voltage in dq
I_n	Individual harmonic current distortion
I_1	Fundamental harmonic current distortion
I_2	2nd harmonic current distortion
γ	Euclidean distance

frontiers | Frontiers in Energy Research

TYPE Original Research
PUBLISHED 01 February 2024
DOI 10.3389/fenrg.2024.1355867

OPEN ACCESS

EDITED BY
Praveen Kumar Balachandran,
Vardhaman College of Engineering, India

REVIEWED BY
Sudhakar Babu Thanikanti,
Chaitanya Bharathi Institute of Technology, India
Kasi Ramakrishnareddy Ch,
Vasavi College of Engineering, India
Pratikanta Mishra,
SRM University, India

*CORRESPONDENCE
Kareem M. AboRas,
kareem.aboras@alexu.edu.eg
Amr Yousef,
a.yousef@ubt.edu.sa
Mukesh Pushkarna,
mukesh.pushkarna@gla.ac.in

RECEIVED 14 December 2023
ACCEPTED 11 January 2024
PUBLISHED 01 February 2024

CITATION
Pushkarna M, Govardhan Rao KV, Goud BS, Kumar MK, Reddy CR, Kotb H, AboRas KM, Alharthi YZ and Yousef A (2024), A new-fangled connection of UPQC tailored power device from wind farm to weak-grid.
Front. Energy Res. 12:1355867.
doi: 10.3389/fenrg.2024.1355867

A new-fangled connection of UPQC tailored power device from wind farm to weak-grid

Mukesh Pushkarna[1]*, Kambhampati Venkata Govardhan Rao[2], B. Srikanth Goud[3], M. Kiran Kumar[4], Ch. Rami Reddy[5,6], Hossam Kotb[7], Kareem M. AboRas[7]*, Yahya Z. Alharthi[8] and Amr Yousef[9,10]*

[1]Department of Electrical Engineering, GLA University Mathura, Mathura, India, [2]Department of Electrical and Electronics Engineering, St. Martin's Engineering College, Secunderabad, India, [3]Department of Electrical and Electronics Engineering, Anurag University, Hyderabad, India, [4]Department of Electrical and Electronics Engineering, Koneru Lakshmaiah Education Foundation, Guntur, India, [5]Department of Electrical and Electronics Engineering, Joginpally B R Engineering College, Hyderabad, India, [6]Applied Science Research Center, Applied Science Private University, Amman, Jordan, [7]Department of Electrical Power and Machines, Faculty of Engineering, Alexandria University, Alexandria, Egypt, [8]Department of Electrical Engineering, College of Engineering, University of Hafr Albatin, Hafr, Saudi Arabia, [9]Electrical Engineering Department, University of Business and Technology, Jeddah, Saudi Arabia, [10]Engineering Mathematics and Physics Department, Faculty of Engineering, Alexandria University, Alexandria, Egypt

A significant portion of wind power conversion systems worldwide comprise wind farms (WFs) that use Squirrel Cage Induction Generator (SCIG) and are directly linked to the power grid. In facilities that generate electrical energy at a moderate level, WFs are connected by means of distribution systems that use medium voltage (MV). It is not uncommon for such a system to produce a scenario in which the amount of electricity generated corresponds to the grid's transit volume. When a wind farm's wind power generation system is connected to a weak grid, the lack of potential control of the Point of Common Coupling (PCC) is a primary issue. This strategy is called a "Wind Farm with Weak Grid Connection." Therefore, the amalgamation of weak grids, fluctuating electricity from wind, and variations in load on the system cause disruptions in the PCC voltage, further degrading the Power Quality (PQ) and the WF stability. Either the control method at the production level or the compensating strategies at the PCC level can improve this situation. If wind farms are built on SCIG and are directly linked to the grid, it is essential to utilise the last substitute. The technology known as Custom Power Devices (CUPS), proved extremely helpful for this type of application. This study presents a compensation technique based on a specific CUPS device, known as the Unified Power Quality Compensator (UPQC), as a possible solution. The potential terminals of WF needed to be regulated, and the voltage fluctuations on the grid side required to be reduced, so a custom-made control strategy for the UPQC device was designed internally. The control of power, such as active and reactive in the UPQC's series and shunt converters, as well as the transmission of power via the UPQC DC-Link between converters, are the foundation of the internal control strategy that has been developed. Compared to other bespoke tactics that use reactive power, this strategy increases the UPQC's capability to provide compensation. The suggested study calculates THD using a FUZZY controller. The results are compared to PI controller results. Simulation findings show how the suggested compensating strategy can minimise

THD values and improve wind farm power and stability. The simulations suggest that the proposed compensating strategy enhances WF power and stability.

KEYWORDS

wind energy, UPQC, SCIG, voltage fluctuation, feeble grid, fuzzy

1 Introduction

The location of wind-generated electricity generating depends on wind energy. High-voltage (HV) transmission lines are usually far from these facilities (Xie and Sun, 2022). If the facility has medium power, medium voltage (MV) distribution wires will link the WF. The most distinguishing characteristic of these connections is an improved voltage control sensitivity to load variations (Huang et al., 2021). Therefore, the capability of the scheme to normalize potential at the PCC, which is the point at which the electrical system and the WF are coupled, is an essential factor in the proper operation of the WF. In addition, it is common knowledge that wind farms produce variable amounts of electric power due to the unpredictable nature of wind resources. These variations harm the consistency and quality of the electricity provided by the electric power systems (Song et al., 2023).

Additionally, SCIG-used wind turbines have been in use since the beginning of energy extraction from wind resources. The supply mains or capacitor banks supply the required reactive power with SCIG (Yang et al., 2024). There are fluctuations in the rotor speed. For example, the power grid's injected (demanded) WF active (reactive) power will fluctuate due to wind disturbances. This will produce variations in the WF terminal potential and the system's impedance. Electrical power turbulences will eventually find their way into the power system (Zhang et al., 2023), which may result in a spectacle known as a "flicker," which is characterised by oscillations in the level of illumination caused by voltage variations. Additionally, the regular operation of the WF is hampered by these disturbances. The effect is significantly more significant when "weak grids" (WG) are specifically considered.

Several potential methods have been proposed in demand to reduce the possible electric variations that can result in a "flicker" at the WF terminals. Updating the electrical grid by raising the power level at short circuits at the PCC is the most popular solution. This decreases system sensitivity to power fluctuations and voltage control issues (Liu et al., 2023).

Electronic equipment for electric power systems has become widespread due to high-power electronics technology. This device reacts faster than line frequency. FACTS and devices give these active compensators tremendous flexibility for controlling power flow in gearbox systems employing Custom Power System (CUPS) devices (Liu et al., 2023). This type of active compensator increased wind energy assimilation in weak systems, as researched (Miaofen et al., 2023).

We propose and test a UPQC-based compensation approach for a SCIG-based WF connected to a weak distribution power grid. This system is based on a study (Li et al., 2022a). The potential at the WF terminal can be controlled and the PCC experiences fewer voltage swings due to the management of the UPQC. These fluctuations are caused by changes in the system load and the pulsating power provided by the WF, respectively. Inoculating the voltage "in phase" with the PCC potential, the series converter with UPQC controls the electrical potential at the WF terminal (Miaofen et al., 2023). This is achieved through voltage injection. Similarly, the parallel converter is utilised to screen the power created by the WF to prevent voltage swings. This function requires the ability to actively and reactively handle electricity. The standard DC link takes active power distribution among various converters (Chen et al., 2022). Simulations were carried out to demonstrate how successful the proposed compensatory strategy not only for UPQC and also verified with fuzzy logic controller.

1.1 Motivation

The literature survey, Table.1, shows that research has been carried out in the area of wind farms (WF) that use SCIG and are directly linked to the power grid. In facilities that generate electrical energy at a moderated level. Only a little research has revealed that wind farms are built on SCIG and are directly linked to the grid. It is essential to utilize for substitute. In this article, the technology known as CUPS, or custom power devices, proved extremely helpful for this type of application.

1.2 Literature review

A compensation technique that is based on a specific CUPS device known as the UPQC is presented in this study as a possible solution. The same is also implemented with a fuzzy logic controller and PI controller.

1.3 Contribution and organization of the paper

The main contribution of this paper is:

- The main technical characteristics of the weak grid are investigated in that WF is connected using distribution systems that use medium voltage (MV).
- The general case study of an electrical system with small WF with the parameters of 36 wind turbines for generating 21.6 MW electrical power.
- A dynamic layout of UPQC with complete switching converter involvement is developed.
- The complete controlling scheme of UPQC with Series and Shunt compensator is simulated.
- A new fuzzy logic controller is introduced into the system. These are tested with MATLAB Simulink to get a stable

TABLE 1 Literature analysis.

S. No.	Observation	Year	References
1	In this article equivalent modeling of doubly fed induction generator (DFIG)-based wind farms, the link between clustering indexes and sub-synchronous oscillation (SSO) modes and the difference in contribution to clustering results are rarely considered. This work presents a weighted fuzzy C-means (WFCM) clustering approach based on index dimension reduction. Furthermore, without considering the controller parameter coupling effects, a multiparameter coupling optimization design technique incorporating the response surface method and the orthogonal experiment method (OEM) is offered for the grid-connected system SSO study	2023	Song et al. (2022a)
2	This article explores the scope of this investigation, the mathematical model of a wind turbine is reduced in complexity by the utilization of a comparable transfer function. This paper also considers the corresponding line loss model of collector lines, classifies and builds up simplified wind turbines, and computes the corresponding amount of converged wind turbines using the improved capacity weighting method to create grid-connected reduced modelling of large-scale wind farms	2023	Song et al. (2022b)
3	This article explores how the stability of the power system in dual-fed induction wind turbines could be compromised by weak frequency modulation and input "source" disturbances. The computational model of the energy storage system integrated into the doubly fed wind power generation system compares the rotor kinetic energy and supercapacitor energy storage to supply inertia reaction power and energy. This is being done to fulfil the requirements of the system. After that, an evaluation of the multi-energy coordinated inertia response is carried out	2023	Zhu et al. (2022)
4	This article suggests a Quasi Z-Source Indirect Matrix Converter (QZSIMC) for Permanent Magnet Generator (PMG)-based Direct Drive Wind Energy Conversion Systems (DDWECS) to improve voltage transfer ratio and output voltage management under different loading situations. A three-phase Indirect Matrix Converter connects three Quasi Z-Source (QZS) networks to PMG and load in the QZSIMC. Two PWM control approaches, Carrier Based and Modified Space Vector, are proposed to analyze QZSIMC performance	2023	Lu et al. (2022)
5	This article proposes a football league algorithm-based hybrid controller trained by an artificial neural network controller (S-ANNC) is presented for the shunt active power filter. This study offers a fuzzy logic controller for the UPQC's series active power filter, which is connected to the solar photovoltaic and battery storage systems. A self-tuning filter (STF) and unit vector generation method (UVGM) synchronize phases to improve UPQC performance during unbalanced/distorted supply voltage conditions, eliminating the need for phase-locked loops, low-pass filters, and high-pass filters. The STF separates harmonic and fundamental components and generates series and shunt filter synchronization phases	2022	Sun et al. (2023)
6	This article deals with the virtual synchronous control (V_{SynC}) technology. Wind turbines (WTs) may improve the damping coefficient, wind power permeability, and equivalent inertia by imitating the behavior of synchronous generators. Due to the challenging DFIG-grid coupling effect and the unusual partial-scale converter construction of the doubly fed induction generator (DFIG), grid-connected V_{SynC}-based DFIG WTs have yet to receive much attention. Furthermore, unsteady V_{SynC} modes may interact with the wind power system under unfavorable grid circumstances, influencing the dynamic characteristics of the DFIG and the system's stability	2021	Yang et al. (2023)
7	This article explores the dynamic behavior of a grid-connected wind farm is described. The wind farm employs induction generators from squirrel cages, but the grid uses steam turbines. An energy capacitor device maintains the stability of the wind farm when the wind speed varies. The grid was linked to various load sizes to test the energy capacitor system controllers. Considering the participation of the grid load, the variations in the time constant of the integrated DC-DC chopper of the energy capacitor system were investigated	2021	Shirkhani et al. (2023)
8	This article explores the regional grid and DFIG-based wind farms can all transfer wind-thermal-bundled electricity employing a voltage source converter-based HVDC (VSC-HVDC). Together, the sending-end converter (SEC) of VSC-HVDC with PQ-control is susceptible to a new medium-frequency electrical oscillation since the local grid is often weak. This oscillation is caused by the interplay of the DFIG, local grid, and SEC; however, its exact mechanism is unclear. This paper derives an explicit analytic expression for the VSC-HVDC sending-end converter (SEC) sequence impedance model with the PQ-control outer loop and PLL. It then uses an intuitive analysis of the system impedance frequency characteristics to investigate the oscillation process	2021	Wang et al. (2023)
9	This article deals the frequent oscillations that the weakly grid-tied PMSG wind farms cause could pose a significant threat to the safety of the power system. The impedance-based technique is frequently used since it effectively improves the system; however, this method does not consider the PMSG's function as a black box and merely reflects the quality of the system's output on the outside. To enhance the research that has been done previously, this work proposes a unique impedance-based analytical method that can be used to examine weak-grid-tied PMSG wind farms from the perspective of control interaction	2021	Wang et al. (2022a)
10	This article explores the Sub-synchronous resonance (SSR). It is probable because of the impedance interactions between the wind farm, the weak grid, and the line-commutated converter-based high-voltage direct-current (LCC HVDC) at the sending end. The mechanism and characteristics of this SSR are analyzed using the impedance technique. SSR happens when the electricity generated by wind farms grows or the power used for LCC HVDC transmission drops. The studied technology quickly generates SSR as the transmitting end's grid stiffness decreases	2021	Lin et al. (2023)
11	This article provides a steady-state analytic approach to assess the viability of WPP installation in site-specific locations based on grid connection parameters that transmission system operators often supply, such as reactance over resistance (X_{oR}) and short circuit ratio (SCR). The maximum active power transfer to the grid, the reactive power adjustment required for a stable and trustworthy grid connection under steady-state conditions, and weak grid situations are all determined by this feasibility study	2020	Wang et al. (2022b)

(Continued on following page)

TABLE 1 (*Continued*) Literature analysis.

S. No.	Observation	Year	References
12	This article deals about suppresses SSR using a synchronous compensator and a battery energy storage system (STATCOM/BESS) linked to the grid. A rising grid stiffness control method is presented, analogous to a virtual synchronous generator (VSG) for STATCOM/BESS with low active and high reactive power	2020	Li et al. (2022b)
13	In this study, an analytical investigation is performed to investigate how the weak grid connection influences the torsional sub-synchronous oscillations (SSOs) created by a grid-connected DFIG in a power system. These oscillations are caused by rotational inertia. The phase-locked loop (PLL) or DC voltage regulation is the primary focus of the investigation as it relates to the grid-connected DFIG operating in the SSO mode. A theoretical investigation is carried out to demonstrate that a poor grid connection intensifies the modal resonance effect between DFIGs and synchronous generators' torsional dynamics. When the grid connection is weak, the amplifying impact of the weak grid con- section manifests as a decrease in the damping of the SSO mode of DFIG and an increase in the associated residue. Because of this, the DFIG has a more significant potential to create torsion SSOs under a poor grid connection, which might result in the system's instability in the worst possible scenario	2020	Duan et al. (2023)
14	This article of work aims to investigate the instability of the DFIG system while it is experiencing a weak grid failure by developing a micro-signal state-space model. Modal analysis reveals that the phase-locked loop (PLL), the rotor current control loop, and the terminal voltage are the factors that have the most significant influence on the dominating unstable poles that occur during the fault	2020	Xiao et al. (2023)
15	This study analyses how the control settings and active power outputs of grid-connected full-converter wind farms with low power affect sub-synchronous oscillation. Using Eigenvalue and participation factor analysis, we discovered the system's primary oscillation modes. Using the Eigenvalue technique, an investigation of the impact of control settings and active power output on the damping of sub-synchronous oscillations is carried out	2020	Hao et al. (2020)
16	A generic model and comparative study of grid-connected wind farms employing DFIGs in weak grids is presented in this paper. DFIG in a weak grid is benchmarked using a complete model. The model includes a generator, rotor side, converter, phase-locked loop, and mechanical parts. Two simplified models of grid-connected DFIG-based wind farms in a weak grid are compared to the full model using linear system analysis to study sub-synchronous oscillation (SSO) and its causes	2020	Yan et al. (2020)
17	In this study a wind energy generating system (WEGS) that can reach peak output in variable wind speeds without frequency variations was studied. The machine-side voltage source converter (MSVSC) and utility grid-side voltage source converter (UGVSC) are successive VSCs positioned across the DC-link capacitor. These VSCs adapt generator speed to intermittent wind speeds. This study's hybrid generalized integrator control can improve power quality, eliminate sub-harmonic oscillations, and switch UGVSC. A fuzzy logic controller (FLC) controls a wind turbine's salient pole synchronous generator (SG) speed. The FLC monitors reference speed despite restricted bandwidth and high overshoot transients. MSVSC switching uses field-oriented control	2020	Chishti et al. (2020)
18	This study examined the SSO mechanism of D-PMSG-based wind farms using impedance-based stability analysis. An impedance model of grid-connected D-PMSG is created utilizing harmonic linearization theory in the first part of this research effort. Next, sub/sup synchronous current coupling is statistically studied for the first time. We explain how grid impedance and wind farm operational factors affect stability using the impedance model and relative stability criteria	2019	Yuan et al. (2019)
19	In this study, The work evaluated the SSO mechanism of D-PMSG-based wind farms using impedance-based stability analysis, a standard method. First, a grid-connected D-PMSG impedance model based on harmonic linearization theory is built, and the sub/sup synchronous current coupling is assessed. The relative stability criterion and impedance model characterize grid impedance and wind farm operational factors' effects on stability	2019	Sang et al. (2019)
20	Integrating large-scale wind power is a challenge for today's electricity networks. Therefore, simpler, more accurate wind farm (WF) models are required. Aggregation is used in WF modeling to save processing time and model complexity. The fully aggregated model (FAM) and multimachine model, which split the WF into many aggregated models for different sections, are used in the literature. This article compares the two aggregation strategies using a small-signal model	2018	Morgan et al. (2018)

operation to improve voltage WF in the weak grid, and THD results are also presented.

This paper is organized with an abstract on keywords. In the first section, the introduction is explained in terms of wind forms with different UPQC and fuzzy techniques, followed by the literature survey and the paper's contribution. The second section discusses the general case study in the electrical system. In the third section, the turbine rotor and disturbance model are discussed. In the fourth section, the proposed layout of the dynamic compensator model of the induction generator is developed. The fifth and sixth section consists of control scheme for UPQC and fuzzy implementation techniques. The seventh section deal with results and discussion The eighth and ninth sections deal with discussion for paper outcome, followed by an explanation of the conclusion.

2 General case study explanation of electrical system

The electrical system being looked at in this research can be seen in Figure 1. The WF comprises 36 wind turbines utilising squirrel cage induction generators, producing 21.6 MW of electrical power. Each turbine is coupled to an electrical grid of a 630 kVA 0.69/33 kV transformer and features attached fixed reactive compensation capacitor banks with a rating of 175kVAr. Based on reference (Liu et al., 2018), this system depicts a real-life scenario.

The indication of the "connection weakness" based on the power ratio during a quick circuit to the power-valued WF. Consequently, while taking into consideration the fact that the short circuit power in MV6 is S_{SC}> *120 MV* A, so this ratio can be calculated with (1).

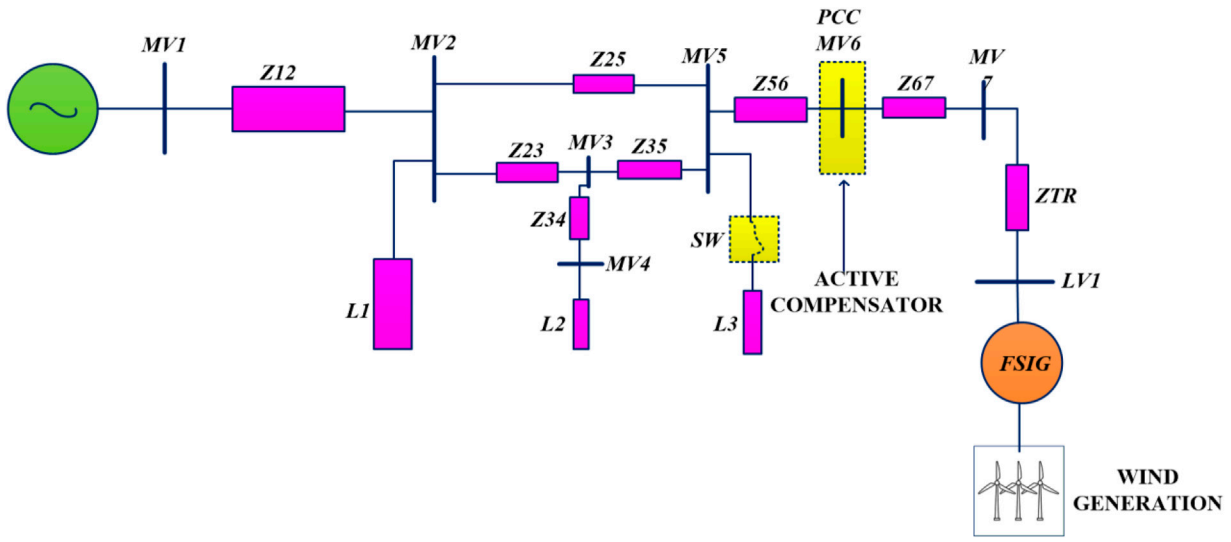

FIGURE 1
A general power system for the case study.

$$r = \frac{S_{SC}}{P_{WF}} \cong 5.5 \tag{1}$$

Any value of $r < 20$ is regarded as having a "weak grid" linkage (Nie et al., 2022).

3 Turbine rotor and associated disturbances model

The following expression determines the amount of electricity obtained from a WT:

$$P = \frac{1}{2} . \rho . \pi . R^2 . v^3 . C_P \tag{2}$$

Where ρ is the air density, R is the radius of the swept area, v is wind speed, and C_P is the power coefficient.

For the considered turbines (600 kW), the values are R = 31.2 m,ρ= 1.225 kg/m^3 *and* C_P calculation is taken from (Damchi and Eivazi, 2022).

The power from the turbines is then combined to create a comprehensive model of the WF, showing that the entire WF is represented by a single corresponding turbine producing electrical potential from wind power, which is the same as the mean totality of the power provided by each turbine is expressed in (3):

$$P_T = \sum_{i=1,2,3.....36} P_i \tag{3}$$

In addition, disruptions in the wind flow can cause the wind speed v in (2) to fluctuate about its usual value. The first is determined by an irregularity in the stream of air that is "seen" from the blades of the turbine because of "tower shadow" and/or edge coat of the atmosphere, and the second is caused by erratic changes that are referred to as "turbulence." Both of these factors can affect the energy produced using the wind turbine. Consider disruption to the airflow induced by the support structure (tower) as part of our analysis. When applied to the mid value of v, the disruption is viewed as a sinusoidal modulation. This modulation has a frequency of N_{rotor} for the three-bladed WT, and the breadth depends on the tower's design. An amplitude modulation of 15% and an average 12 m/s wind speed is used (Rao et al., 2023).

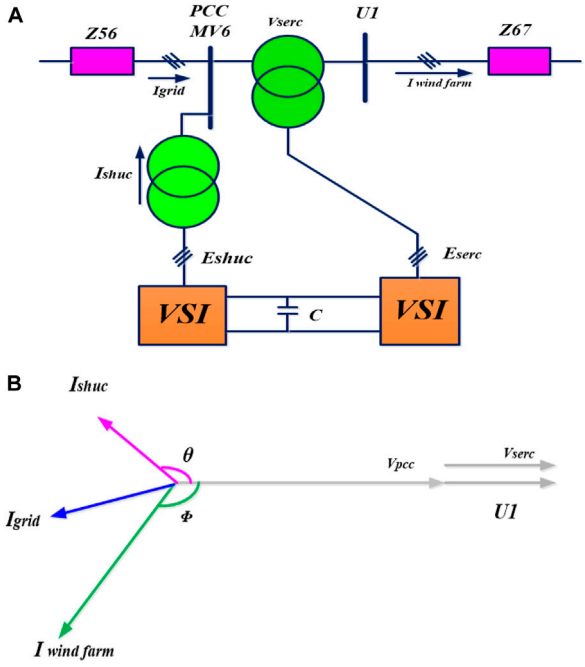

FIGURE 2
(A) representation of UPQC and **(B)** UPQC phasor.

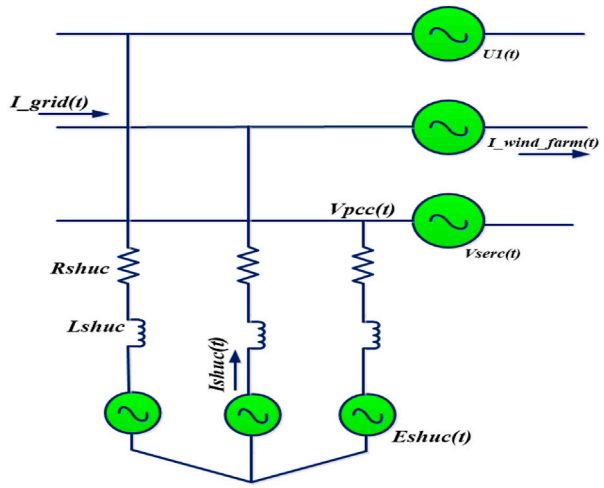

FIGURE 3
Compensator Model for Power Stage at AC side.

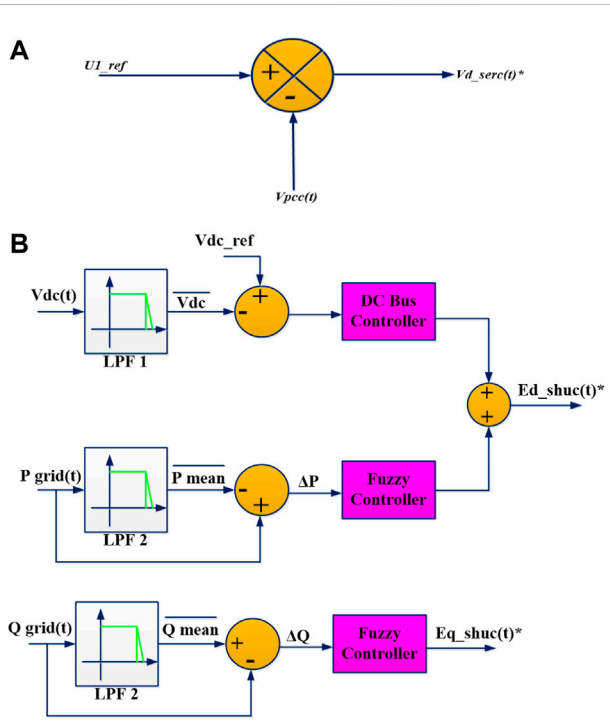

FIGURE 4
(A) controller for series compensator and **(B)** controller for shunt compensator.

In most situations, the effect of the edge coat of the atmosphere is disregarded in favour of the results provided by the shadow effect produced by the tower (Yang et al., 2015). Note that the total of perturbations can occur if the entire turbines operate in the same sequence and in phase, which has the most significant impression on the electrical grid (worst case scenario) because the pulsation of power has the most significant peak in this situation. Therefore, the turbine combination method is acceptable.

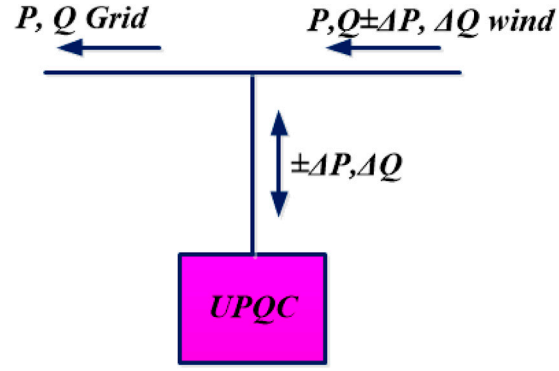

FIGURE 5
Power buffer Concept.

4 Typical layout of dynamic compensator model induction generator

The model used for the SCIG is the one that is included in the Matlab/Simulink, Sim Power Systems package (Venkata Govardhan Rao et al., 2022). Dynamic voltage fluctuations are accounted for by supplying the MV6 (PCC) bus bar with potential in series and active reactive power. This is accomplished with a unified type compensator, a UPQC (Ray et al., 2021). The general layout of this compensator can be seen in Figure 2A, while Figure 1 should be used as a reference for the bus bar and impedance numbering.

The process involves utilising VSI or CSI electrical converters to create three-phase voltages. As for its lower loss of DC link and quicker system response, the VSI converter is preferred over the CSI converter (Srikanth et al., 2023). The UPQC's shunt converter is accountable for injecting current at PCC, as explained in Figure 2B, while the series converter produces electric potential for PCC and UI. The vital theme of the compensator is that the series and shunt VSIs operate using the same DC bus. Thanks to this functionality, the two different types of converters can actively transfer power.

The converters are manufactured using ideal regulated voltage sources since the switching control of the converters is outside the purview of this work, and the higher-order harmonics produced by VSI converters are outside the bandwidth of importance in the simulation analysis. It is completed since the switching converter control is not involved in this task. Figure 3 displays the finalized model of the UPQC system's power side.

$$T = \frac{2}{3}\begin{bmatrix} \sin(\Theta) & \sin\left(\Theta - \frac{2\pi}{3}\right) & \sin\left(\Theta + \frac{2\pi}{3}\right) \\ \cos(\Theta) & \cos\left(\Theta - \frac{2\pi}{3}\right) & \cos\left(\Theta + \frac{2\pi}{3}\right) \\ \frac{1}{2} & \frac{1}{2} & \frac{1}{2} \end{bmatrix} \tag{4}$$

$$\begin{bmatrix} f_d \\ f_q \\ f_0 \end{bmatrix} = T \cdot \begin{bmatrix} f_a \\ f_b \\ f_c \end{bmatrix} \tag{5}$$

Where $fi = a,b,c$ represents either the phase voltage or current, and $fi = d,q,0$ represents that magnitude transformed to the dqo

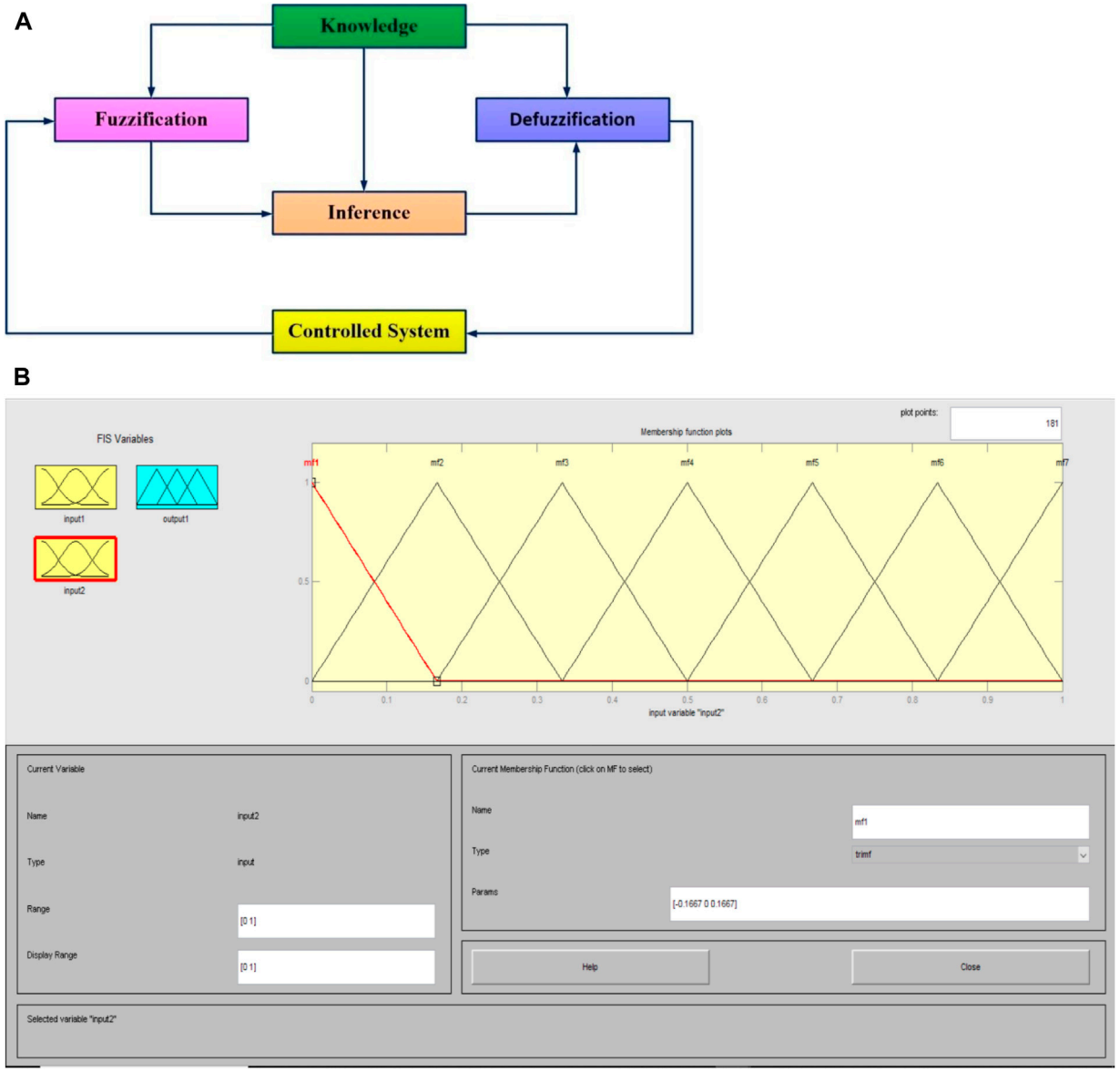

FIGURE 6
(A) Division of fuzzification and **(B)** membership functions of fuzzy controller.

TABLE 2 Fuzzy rules for this case.

E(K), ΔE	NB	NM	NS	ZE	PS	PM	PB
NB	NB	NB	NB	NB	NM	NS	ZE
NM	NB	NB	NB	NM	NS	ZE	PS
NS	NB	NB	NM	NS	ZE	PS	PM
ZE	NB	NM	NS	ZE	PS	PM	PB
PS	NM	NS	ZE	PS	PM	PB	PB
PM	NS	ZE	PS	PM	PB	PB	PB
PB	ZE	PS	PM	PB	PB	PB	PB

From Table PB: positive big, PM: positive medium, PS: positive small, ZE: zero, NS: negative small, NM: negative medium, NB: negative big.

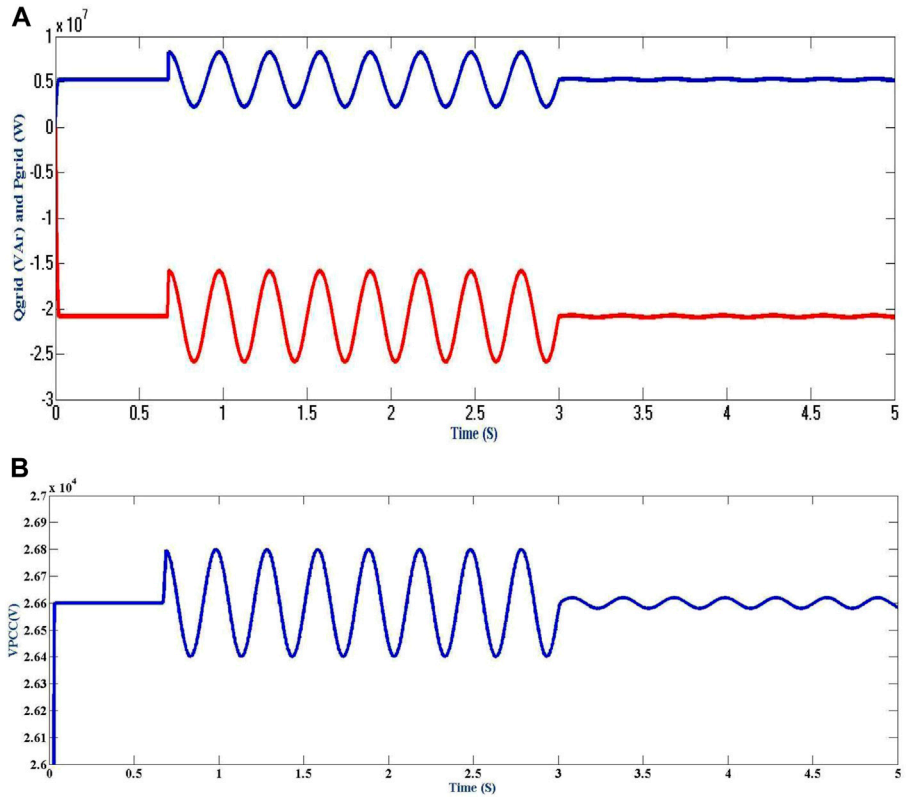

FIGURE 7
(A) Active and reactive power demand's power component at the power grid side and **(B)** Electric Potential at PCC.

space. The controlling of UPQC, with rotating frames using a park's transformation is mentioned in (4) & (5).

It enables the position of a reference frame of the rotating body in the positive direction of the PCC potential space vector. A PLL mechanism determines a reference angle synchronism with the PCC positive sequence fundamental voltage space vector. This makes it possible to get the desired outcome. This study has a PLL that is examined using the "instantaneous power theory".

Under balanced and equilibrium conditions, the synchronous reference frame's electric potential and current vectors do not change. This quality is advantageous for study and detached control.

5 Control scheme for UPQC

The WF terminal voltage is maintained at its nominal level by managing the UPQC serial converter (as in Figure 3), which makes up for variations in the PCC voltage. If this is done, the grid-generated voltage disturbances will not be able to reach the WF facilities. If voltage dips occur at the WF terminals due to this control action, it may have the unexpected impact of increasing the LVRT capacity.

Figure 4A explains the series converter controller block diagram. The PCC electric potential is subtracted from the reference electric potential to produce the injected electric potential, which is aligned in phase with the PCC electric potential. The voltage is injected as a result. On the other hand, the UPQC uses its shunt converter to mesh the pulsations of active and reactive power components, which WF causes. As a result, there will not be any pulsations in the electricity that the WF compensator set injects into the grid. Pulsations cause voltage fluctuations that may propagate throughout the system. This action can be finished with the correct electrical current injection into the PCC. Additionally, this converter has been able to normalize the voltage on the DC bus.

The block architecture of the shunt converter controller is displayed in Figure 4B. The voltage instructions of E_{d_shuC}* and E_{q_shuC}* are produced in this way, depending on the variations ΔP and ΔQ, respectively. The deviations are computed by deducting the mean power from the instantaneous power measured in PCC. Filing by low pass filter calculates the expected values of the active and reactive power components. These filters' bandwidths are altered such that, by the IEC61000-4-15 standard, the fluctuation components for power are chosen as they lie in the flicker band and accept compensation.

Additionally, the control action for the DC–bus voltage loop is contained within E_{d_shuC}*since its components operate at a frequency that is lower than that of the flicker–band.

In the rotating reference frame, the powers P_{shuC} and Q_{shuC} are computed as follows in (6):

$$P_{shuC}(t) = \frac{3}{2} . V_d^{PCC}(t) . I_d^{shuC}(t)$$
$$Q_{shuC}(t) = -\frac{3}{2} . V_d^{PCC}(t) . I_d^{shuC}(t) \quad (6)$$

The equations other than PCC voltage variation, can be expressed as follows in (7):

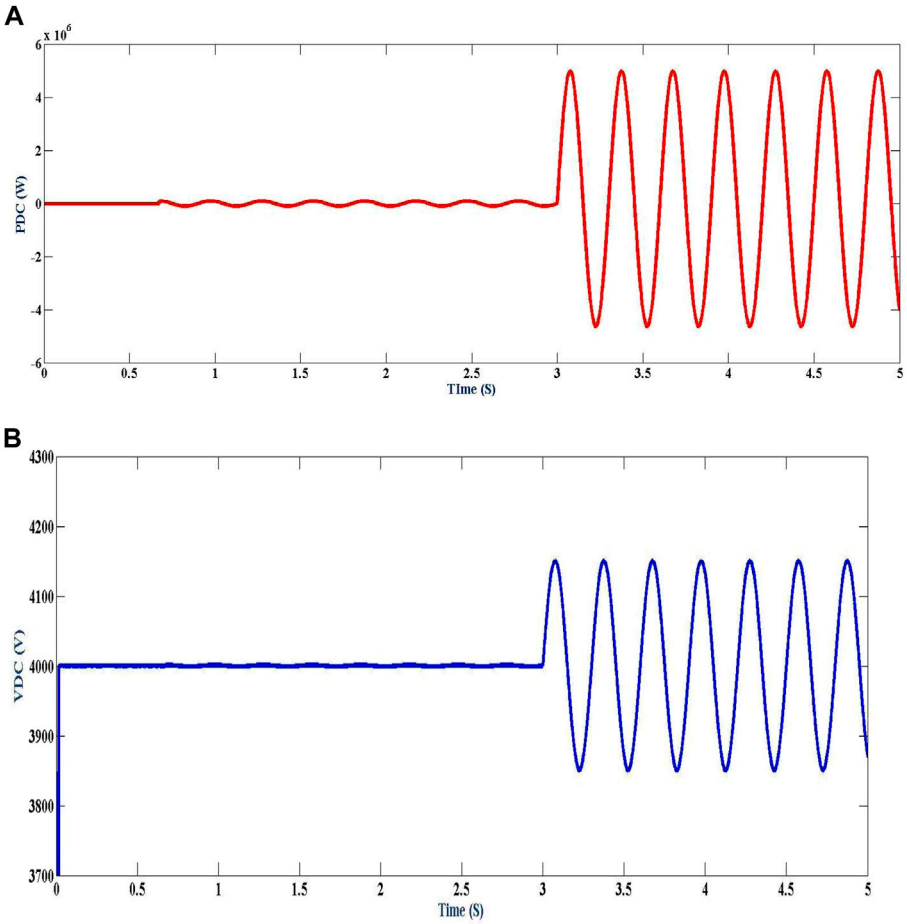

FIGURE 8
(A) Power in the capacitor of DC bus and **(B)** Voltage in the capacitor of DC bus.

$$P_{shuC}(t) = k_p^{'} . I_{d\_shuC}(t)$$
$$Q_{shuC}(t) = k_q^{'} . I_{q\_shuC}(t) \quad (7)$$

Given that the shunt converter is built around a VSI, we must produce sufficient voltage to attain the currents in (6). It is possible by the model of VSI, which is discussed in (Song et al., 2022a), which leads to a linear relationship between the power output and the controlled voltages. Following are the resultant equation in (8):

$$P_{shuC}(t) = k_p^{''} . E_{d-}^{*}(t)_{shuC}$$
$$Q_{shuC}(t) = k_q^{''} . E_{d-}^{*}(t)_{shuC} \quad (8)$$

Proportional controllers have examples of P and Q control loops, whereas the DC–bus loop is an example of a PI controller.

In a nutshell, UPQC is considered a "power buffer" in the suggested strategy, which helps to equalise the power inoculated into the power system grid. This style of operation is conceptually represented by a schematic, which may be found in Figure 5.

It is crucial to remember that the storage element installed on the bus containing UPQC must uphold its mean power at zero because the bus lacks an external DC supply. This is the situation to protect the system's integrity. To do this, a well-designed DC voltage controller is essential.

The concept of power buffer may not be executed with a DVR; however, it is possible to do so with a DSTATCOM. A DVR device is more appropriate in this situation than DSTATCOM's solution since voltage regulation during moderately significant disturbances cannot be effectively managed with just DSTATCOM's reactive power.

6 Implementation of fuzzy logic controller (FLC)

The enormous potential of fuzzy set theory for effectively addressing the problem's uncertainty is evident (Raju and Rao, 2015). It is an outstanding mathematical tool for handling ambiguity-related uncertainties. The concept of fuzzification and de-fuzzification is explained in Figure 6A, and the membership functions of fuzzy controller are depicted in Figure 6B.

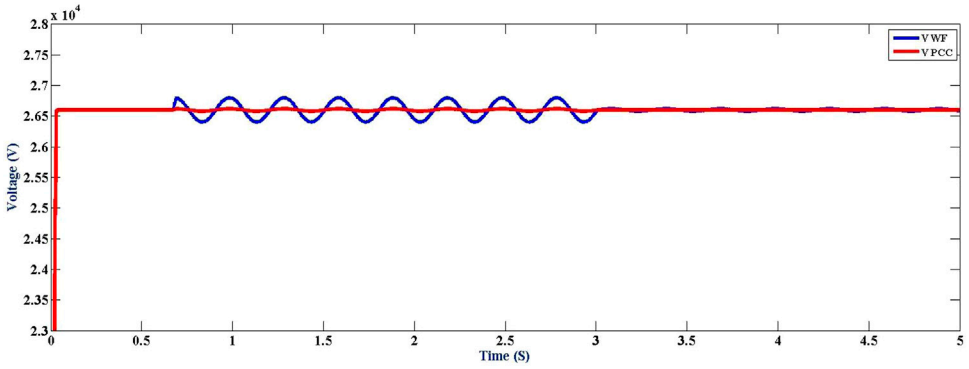

FIGURE 9
Electric Potentials of WF and PCC are shown in phase.

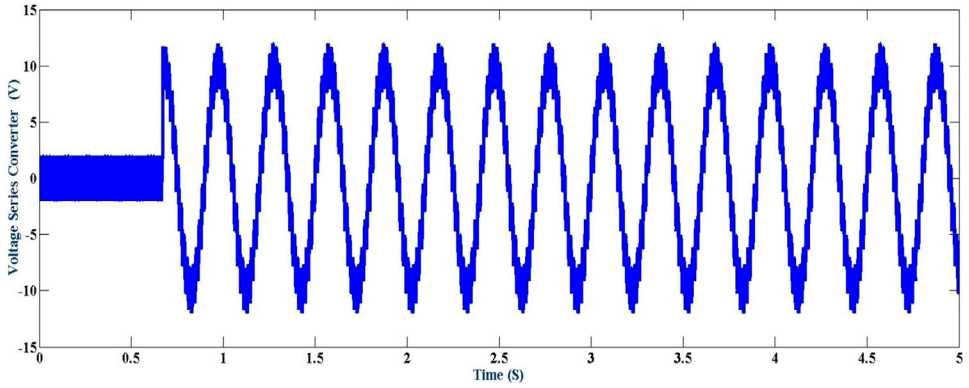

FIGURE 10
Series injected electric potential for the "a" phase.

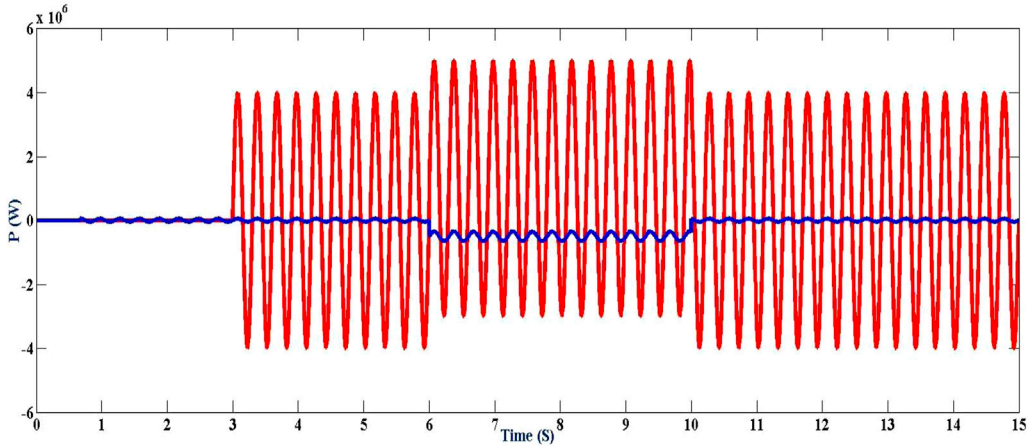

FIGURE 11
DC bus shunt and series active power.

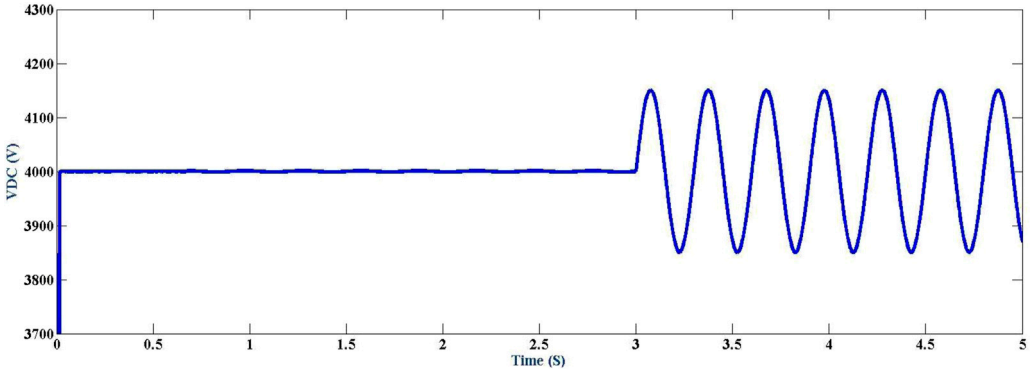

FIGURE 12
Bus potential at DC.

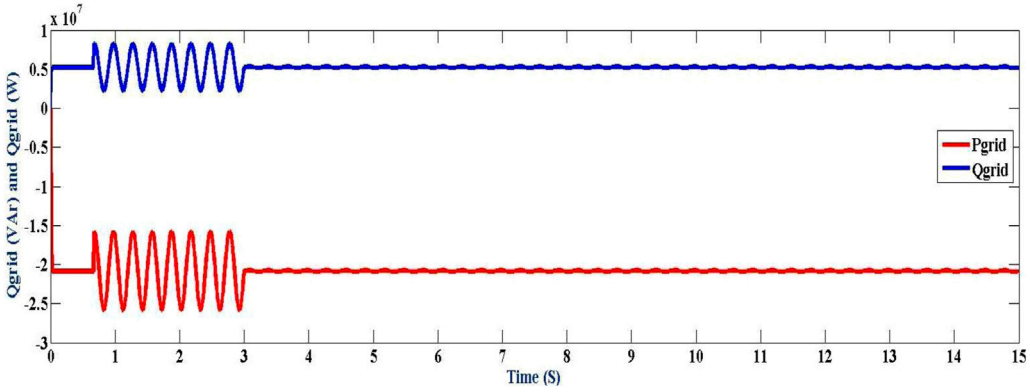

FIGURE 13
Power grid-side active and reactive power consumption.

6.1 Error calculation

The difference between the value as it is now and the reference value that the repeated controller created helps calculate the error signal (*errA*). Additionally, the R_{errA} represents the variance in error in the current sampling and its prior sampling. These current signals are measured and transformed to per unit (p.u.) values for each phase.

6.2 FLC

Three subsections make up the FLC section. The following is a summary of these subsections..

6.3 Fuzzification

The fuzzy linguistic variable, which has a crisply defined border, is created by fuzzifying the numerical input variable measurements, and Table 2 reflects the fuzzy rules for using this fuzzification.

6.4 De-fuzzification

Previously represented as linguistic labels by a fuzzy set, the controller outputs are transformed into actual control (analogue) signals during de-fuzzification. For the fuzzy model's de-fuzzification procedure, the "Sugeno's Weighted Average" method, a particular application of the "Mamdani Model," is employed.

Signal processing: The FLC process output creates the control signals. They are compared to the carrier signal to produce switching signals for converters.

7 Results and discussions

Matlab/Simulink software was used to create the prototypical view of the power system scheme depicted in Figure 1. The

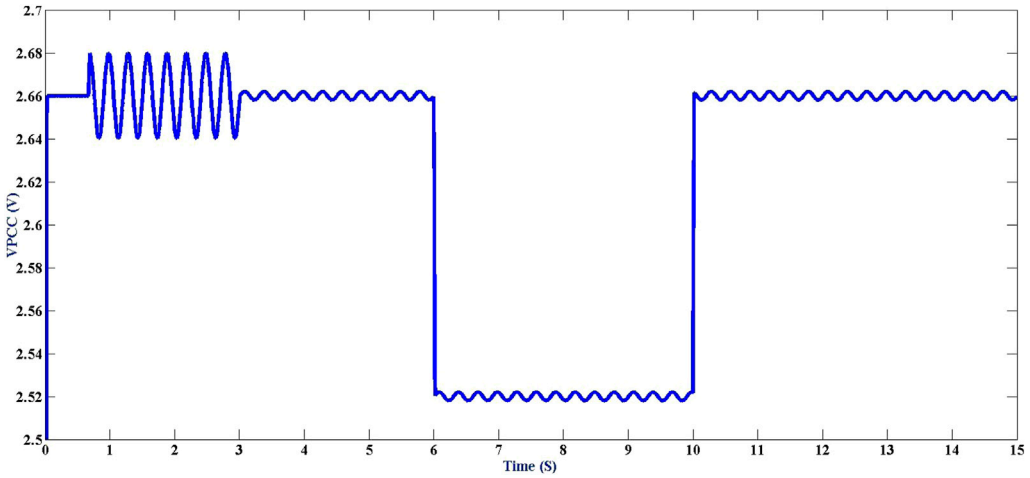

FIGURE 14
Potential at PCC.

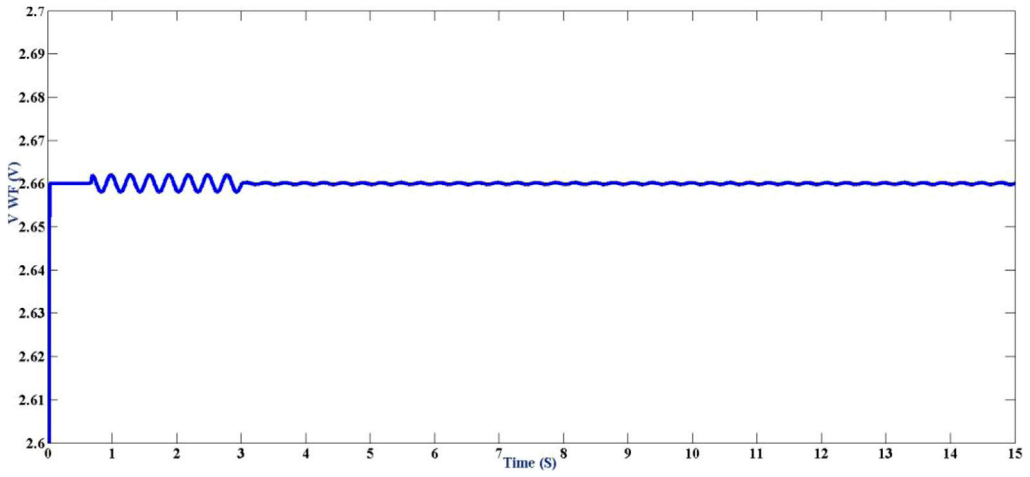

FIGURE 15
WF terminal Potentials.

controllers and the control strategy described in Section III are included in this model. Numerical simulations were carried out to determine and compensate for the voltage fluctuation brought on by variations in wind power and voltage regulation difficulties brought on by a sudden load hook-up.

7.1 Electrical potential fluctuation compensation

Figure 7 displays the simulation results for 0–5 s. The cyclical power pulse the tower shadow effect creates starts when time equals 0.5. As was already established, the tower shadow changes torque, affecting the WF's active and reactive power components. The frequency of power variation at the minimum wind speed is $f = 3.4\ Hz$, and the resulting magnitude of the electric potential variation at PCC is in (9):

$$\frac{\Delta U}{U_{rated}} = 1.50\% \tag{9}$$

For 0.5 to 3, the middle curve of Figure 7A shows this voltage fluctuation. The fluctuation's value exceeds the IEC standard's maximum allowable limit (Zhu et al., 2022). This shows that the WF has a detrimental effect on the System Power Quality even when everything operates smoothly.

P, Q controllers are turned on at time $t = 3.0''$, which causes the pulsations of active and reactive power to slow down. The PCC voltage fluctuation's amplitude has decreased from its prior value of

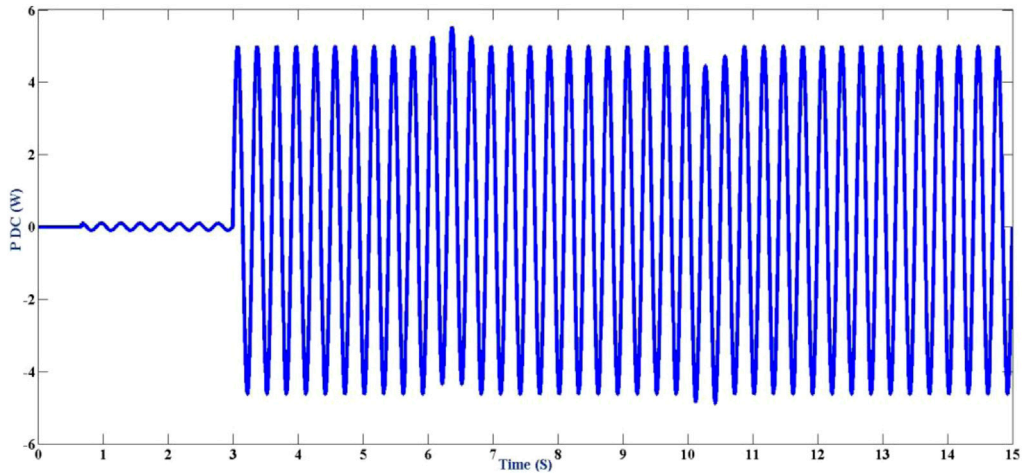

FIGURE 16
Power in the capacitor at the DC bus.

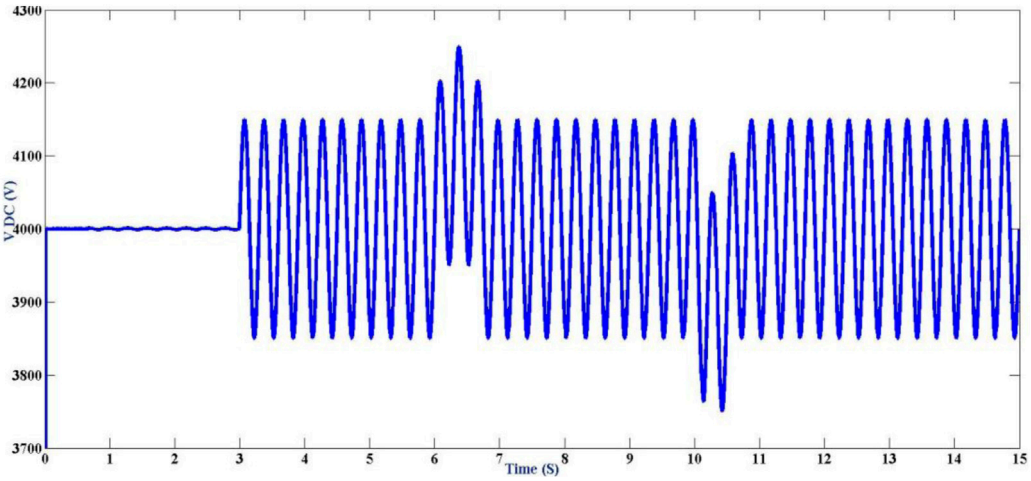

FIGURE 17
Capacitor potential in the DC bus.

1.6% (without correction), which was previously used, to this new amount.

$$\frac{\Delta U}{U_{rated}} = 0.18\% \tag{10}$$

Given that it is less than the set permitted maximum limit of *0.5% at 3.4Hz*, this number complies with the requirements of the IEC standard.

Figure 7A illustrates the active and reactive power and voltage pulses on the DC side of the UPQC. As can be seen from Figure 7A, the series converter needs very little power to run. However, the shunt converter needs a high instantaneous power level from the capacitor to compensate for changes in active power. The DC side power is unaffected by reactive power compensation. The behaviour of the WF terminal potential is depicted in Figure 7B. The series converter action keeps the WF terminal potential constant independent of the PCC voltage's behaviour.

According to VSI's operational features, the voltage level on the DC bus is capped at a specific level. Because the capacitor is in charge of managing the fluctuating active power, the value of the capacitor must be selected so that the DC electric potential "ripple" is in the specified margin.

For instance, a capacitor with a size of $C = 0.42$ F has been considered. It is simple to quickly obtain this high value by utilizing capacitors based on modern technology, known as ultracapacitors.

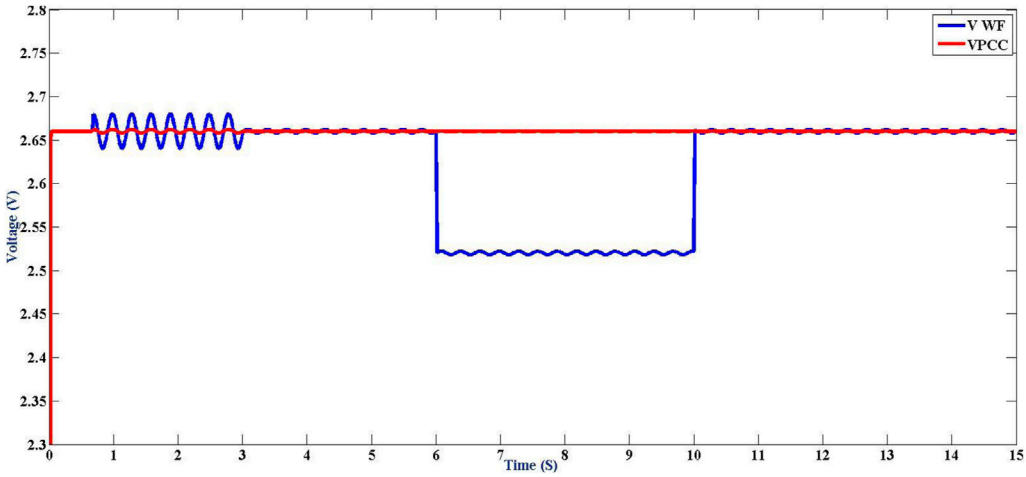

FIGURE 18
Potential at PCC in a phase of WF.

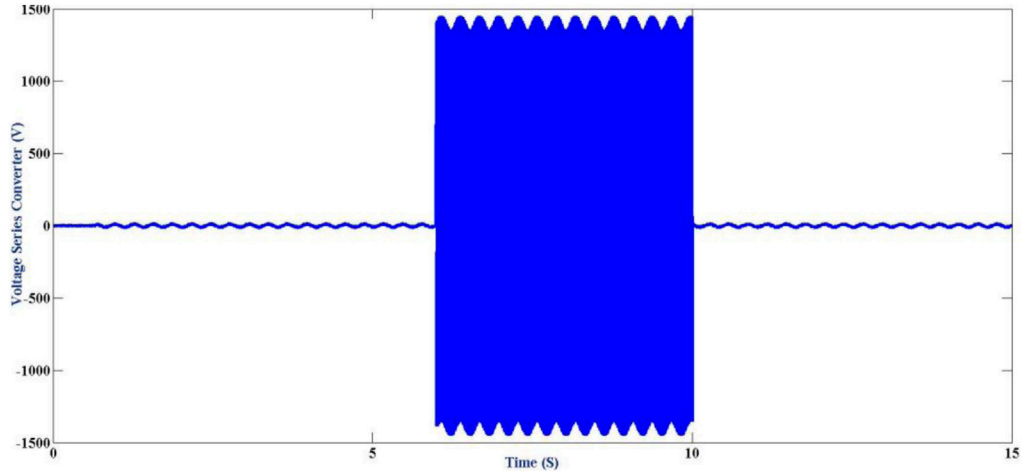

FIGURE 19
Voltage injected in series at "a" phase.

Figure 8A shows the power in the capacitor of the DC bus, and Figure 8B shows the voltage in the capacitor of the DC bus. It is crucial to remember that when the grid's measured current flows towards the park, it is optimistic.

7.2 Regulation of electric potential

The UPQC is used in this section to maintain the steady WF terminal potential while concurrently reducing PCC electric potential variations caused by abrupt engagement or disengagement of loads, power system malfunctions, and other difficulties. At the time $t = 6''$, the switch labelled *SW* to *L3* is closed, which results in a sudden connection of the load in Figure 1. This load has a *PL3* rating of *9.2 MW* and a *QL3* rating of 9.25 MW. After then, the load is disconnected at a time equal to 10 s.

Power in the capacitor terminal voltages and the series injected voltage are displayed in Figure 9 for the "a" phase. Because of the action of the series converter, the figure shows a dramatic shift in the voltage at the PCC terminals, while the voltage at the WF terminals remains practically unchanged. As a result, the active power stage for a series converter is the same as the power for a shunt converter but has the opposite sign. Figure 10 and Figure 11 also explain the DC-bus voltage and the control action of VDC, both of which are extremely obvious. VDC's mean value is maintained at the reference level. However, the ripple is not muted.

The midpoint power injected or engrossed by the series converter is inserted or absorbed by the converter in a shunt as a

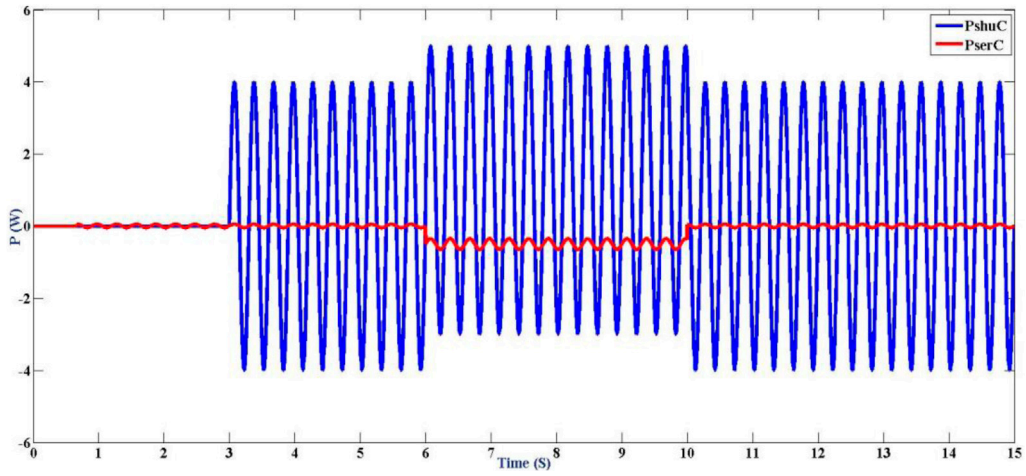

FIGURE 20
The DC bus's shunt power and series power.

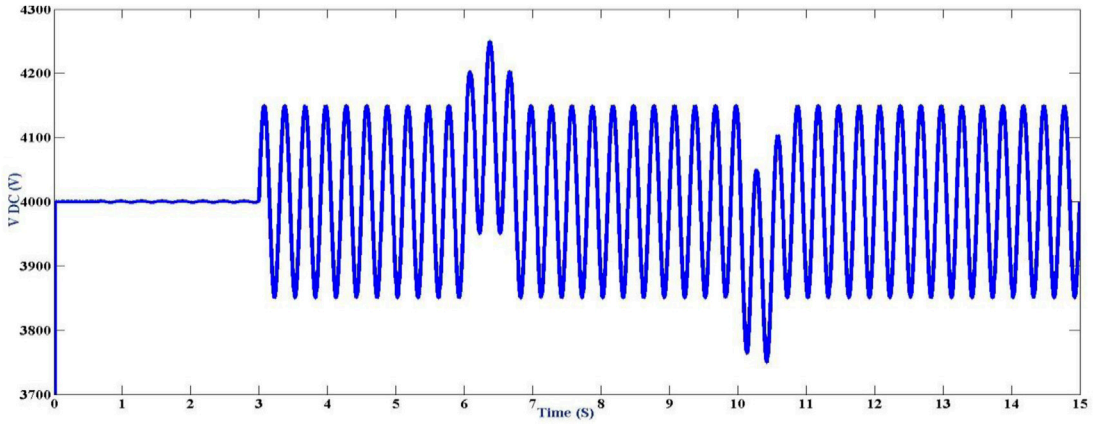

FIGURE 21
DC bus voltage.

result of the functioning of the loop for regulating DC voltage depicted in Figure 12.

7.3 By using a fuzzy controller

The analysis was repeated by using a fuzzy controller and the results can be shown from Figure 13 Figure 14 Figure 15 Figure 16 Figure 17 Figure 18 Figure 19 Figure 20 to Figure 21.

8 Discussion of paper outcome

The UPQC and fuzzy logic controller results clearly illustrate the power demand potential of the PCC series and shunt compensators' injected power. However, here, we proposed a fuzzy logic controller implementation to the same system; with this, we are maintaining all the parameters are the same, but the THD value of the Fuzzy system with the PI controller is meagre, i.e., *2.81%* in comparison to the UPQC system of *5.13%*. Shown in Figure 22A,B, the outcomes of the simulations demonstrate that the proposed compensation technique is beneficial in improving the Quality of power and stability in WF.

9 Conclusion

The article presents a newfangled compensation stratagem built by a UPQC compensator to link SCIG wind farms to feeble power grids. The recommended compensating technique raises the system's power quality by utilizing the wholly DC energy storage and the active power sharing across UPQC converters. The DVR and DSTATCOM compensators do not include these features. The THD of the fuzzy controller improved the UPQC controller. The simulation's outcomes explain that it is possible to regulate the

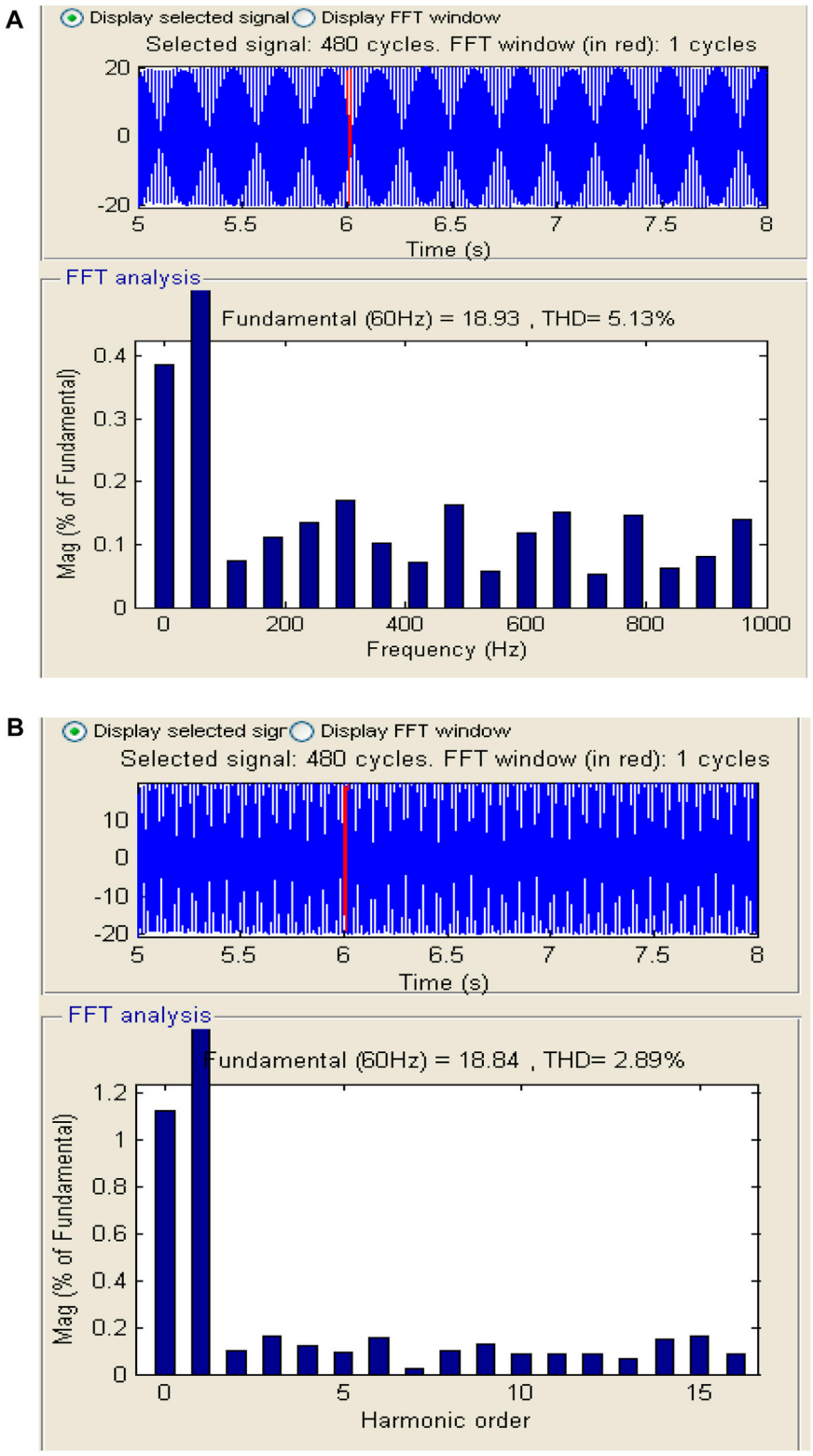

FIGURE 22
(A) FFT analysis with UPQC controller and **(B)** FFT analysis with fuzzy controller.

voltage induced by an unexpected load connection and reject the power fluctuations caused by the "tower shadow effect" with satisfactory results. The research example thus shows that the suggested compensation scheme accomplishes its objectives. The performance levels of the various types of compensators will be compared in future research.

Data availability statement

The original contributions presented in the study are included in the article/Supplementary material, further inquiries can be directed to the corresponding authors.

Author contributions

MP: Conceptualization, Data curation, Formal Analysis, Funding acquisition, Investigation, Methodology, Project administration, Resources, Software, Supervision, Validation, Visualization, Writing–original draft, Writing–review and editing. KG: Conceptualization, Data curation, Formal Analysis, Funding acquisition, Investigation, Methodology, Project administration, Resources, Software, Supervision, Validation, Visualization, Writing–original draft, Writing–review and editing. BS: Conceptualization, Data curation, Formal Analysis, Funding acquisition, Investigation, Methodology, Project administration, Resources, Software, Supervision, Validation, Visualization, Writing–original draft, Writing–review and editing. MK: Conceptualization, Data curation, Formal Analysis, Funding acquisition, Investigation, Methodology, Project administration, Resources, Software, Supervision, Validation, Visualization, Writing–original draft, Writing–review and editing. CR: Conceptualization, Data curation, Formal Analysis, Funding acquisition, Investigation, Methodology, Project administration, Resources, Software, Supervision, Validation, Visualization, Writing–original draft, Writing–review and editing. HK: Conceptualization, Data curation, Formal Analysis, Funding acquisition, Investigation, Methodology, Project administration, Resources, Software, Supervision, Validation, Visualization, Writing–original draft, Writing–review and editing. KA: Software, Supervision, Validation, Visualization, Writing–original draft, Writing–review and editing, Conceptualization, Data curation, Formal Analysis, Funding acquisition, Investigation, Methodology, Project administration, Resources. AY: Conceptualization, Data curation, Formal Analysis, Funding acquisition, Investigation, Methodology, Project administration, Resources, Software, Supervision, Validation, Visualization, Writing–original draft, Writing–review and editing.

Funding

The author(s) declare that no financial support was received for the research, authorship, and/or publication of this article.

Conflict of interest

The authors declare that the research was conducted in the absence of any commercial or financial relationships that could be construed as a potential conflict of interest.

Publisher's note

All claims expressed in this article are solely those of the authors and do not necessarily represent those of their affiliated organizations, or those of the publisher, the editors and the reviewers. Any product that may be evaluated in this article, or claim that may be made by its manufacturer, is not guaranteed or endorsed by the publisher.

References

Chen, C., Wu, X., Yuan, X., and Zheng, X. (2022). A new technique for the subdomain method in predicting electromagnetic performance of surface-mounted permanent magnet motors with shaped magnets and a quasi-regular polygon rotor core. *IEEE Trans. Energy Conversion* 38, 1396–1409. doi:10.1109/TEC.2022.3217042

Chishti, F., Murshid, S., and Singh, B. (2020). Weak grid intertie WEGS with hybrid generalized integrator for power quality improvement. *IEEE Trans. Ind. Electron.* 67 (2), 1113–1123. doi:10.1109/TIE.2019.2898598

Damchi, Y., and Eivazi, A. (2022). Power swing and fault detection in the presence of wind farms using generator speed zero-crossing moment. *Int. Trans. Electr. Energy Syst.* 2022, 1–17. doi:10.1155/2022/2569810

Duan, Y., Zhao, Y., and Hu, J. (2023). An initialization-free distributed algorithm for dynamic economic dispatch problems in microgrid: modeling, optimization and analysis. *Sustain. Energy, Grids Netw.* 34, 101004. doi:10.1016/j.segan.2023.101004

Hao, Y., Liang, J., Wang, K., Wu, G., Joseph, T., and Sun, R. (2020). Influence of active power output and control parameters of full-converter wind farms on sub-synchronous oscillation characteristics in weak grids. *Energies* 5225, 1–17. doi:10.3390/en13195225

Huang, N., Chen, Q., Cai, G., Xu, D., Zhang, L., and Zhao, W. (2021). Fault diagnosis of bearing in wind turbine gearbox under actual operating conditions driven by limited data with noise labels. *IEEE Trans. Instrum. Meas.* 70, 1–10. doi:10.1109/TIM.2020.3025396

Li, P., Hu, J., Qiu, L., Zhao, Y., and Ghosh, B. K. (2022b). A distributed economic dispatch strategy for power–water networks. *IEEE Trans. Control Netw. Syst.* 9 (1), 356–366. doi:10.1109/TCNS.2021.3104103

Li, S., Zhao, X., Liang, W., Hossain, M. T., and Zhang, Z. (2022a). A fast and accurate calculation method of line breaking power flow based on taylor expansion. *Front. Energy Res.* 10. doi:10.3389/fenrg.2022.943946

Lin, L., Zhang, J., Gao, X., Shi, J., Chen, C., and Huang, N. (2023). Power fingerprint identification based on the improved V-I trajectory with color encoding and transferred CBAM-ResNet. *PloS one* 18 (2), e0281482. doi:10.1371/journal.pone.0281482

Liu, H., Wang, W., Cui, J., and Tang, F. (2018). Optimal power factor regulation of dispersed wind farms under diverse load and stochastic wind conditions based on improved firefly algorithm. *Math. Probl. Eng.* 2018, 1–11. doi:10.1155/2018/6203278

Liu, Y., Liu, X., Li, X., Yuan, H., and Xue, Y. (2023). Model predictive control-based dual-mode operation of an energy-stored quasi-Z-source photovoltaic power system. *IEEE Trans. Industrial Electron.* 70 (9), 9169–9180. doi:10.1109/TIE.2022.3215451

Lu, L., Wu, W., Gao, Y., Pan, C., Yu, X., Zhang, C., et al. (2022). Study on current discrepancy and redistribution of HTS non-insulation closed-loop coils during charging/discharging and subsequent transient process toward steady-state operation. *Supercond. Sci. Technol.* 35 (9), 095001. doi:10.1088/1361-6668/ac7dfe

Miaofen, L., Youmin, L., Tianyang, W., Fulei, C., and Zhike, P. (2023). Adaptive synchronous demodulation transform with application to analyzing multicomponent signals for machinery fault diagnostics. *Mech. Syst. Signal Process.* 191, 110208. doi:10.1016/j.ymssp.2023.110208

Morgan, M. Y., El-Deib, A. A., and El-Marsafawy, M. (2018). Wind farm dynamic models assessment under weak grid conditions. *IET Renew. Power Gener.* 12 (12), 1325–1334. doi:10.1049/iet-rpg.2017.0292

Nie, Y., Wang, H., Gao, L., Wu, C., and Xi, M. (2022). Adaptive parameter estimation for static var generators based on wind speed fluctuation of wind farms. *Int. Trans. Electr. Energy Syst.* 2022, 1–12. doi:10.1155/2022/3877777

Raju, K. G., and Rao, K. V. G., "Fuzzy – genetic algorithm approach for fact placement in electrical power system," no. 1, pp. 17, 2015.

Rao, K. V. G., Kiran Kumar, M., and Srikanth Goud, B. (2023). An independently controlled two output half bridge resonant LED driver. *Electr. Power Components Syst.* 0 (0), 1–21. doi:10.1080/15325008.2023.2238695

Ray, P., Ray, P. K., and Kumar Dash, S. (2021). Power quality enhancement and power flow analysis of a PV integrated UPQC system in a distribution network. *IEEE Trans. Industry Appl.* 58 (1), 201–211. doi:10.1109/tia.2021.3131404

Sang, S., Zhang, C., Cai, X., Molinas, M., Zhang, J., and Rao, F. (2019). Control of a type-IV wind turbine with the capability of robust grid-synchronization and inertial response for weak grid stable operation. *IEEE Access* 7, 58553–58569. doi:10.1109/ACCESS.2019.2914334

Shirkhani, M., Tavoosi, J., Danyali, S., Sarvenoee, A. K., Abdali, A., Mohammadzadeh, A., et al. (2023). A review on microgrid decentralized energy/voltage control structures and methods. *Energy Rep.* 10, 368–380. doi:10.1016/j.egyr.2023.06.022

Song, J., Mingotti, A., Zhang, J., Peretto, L., and Wen, H. (2022a). Fast iterative-interpolated DFT phasor estimator considering out-of-band interference. *IEEE Trans. Instrum. Meas.* 71, 1–14. doi:10.1109/TIM.2022.3203459

Song, J., Mingotti, A., Zhang, J., Peretto, L., and Wen, H. (2022b). Accurate damping factor and frequency estimation for damped real-valued sinusoidal signals. *IEEE Trans. Instrum. Meas.* 71, 1–4. doi:10.1109/TIM.2022.3220300

Song, X., Wang, H., Ma, X., Yuan, X., and Wu, X. (2023). Robust model predictive current control for a nine-phase open-end winding PMSM with high computational efficiency. *IEEE Trans. Power Electron.* 38 (11), 13933–13943. doi:10.1109/TPEL.2023.3309308

Srikanth, G., Venkata Sai Kalyani, T., Venkata Govardhan Rao, K., and Sanjeev, G. (2023). Amalgamation of smart grid with renewable energy eources. *International J. of Smart Grid-ijSmartGrid* 7 (2), 103–107. doi:10.20508/ijsmartgrid.v7i2.289.g276

Sun, Q., Lyu, G., Liu, X., Niu, F., and Gan, C. (2023). Virtual current compensation-based quasi-sinusoidal-wave excitation scheme for switched reluctance motor drives. *IEEE Trans. Industrial Electron.*, 1–11. doi:10.1109/TIE.2023.3333056

Venkata Govardhan Rao, K., Kumar, M. K., Goud, B. S., Bajaj, M., Abou Houran, M., and Kamel, S. (2022). Design of a bidirectional DC/DC converter for a hybrid electric drive system with dual-battery storing energy. *Front. Energy Res.* 10 (November), 1–19. doi:10.3389/fenrg.2022.972089

Wang, H., Wang, B., Luo, P., Ma, F., Zhou, Y., and Mohamed, M. A. (2022b). State evaluation based on feature identification of measurement data: for resilient power system. *CSEE J. Power Energy Syst.* 8 (4), 983–992. doi:10.17775/CSEEJPES.2021.01270

Wang, Y., Chen, P., Yong, J., Xu, W., Xu, S., and Liu, K. (2022a). A comprehensive investigation on the selection of high-pass harmonic filters. *IEEE Trans. Power Deliv.* 37 (5), 4212–4226. doi:10.1109/TPWRD.2022.3147835

Wang, Y., Xia, F., Wang, Y., and Xiao, X. (2023). Harmonic transfer function based single-input single-output impedance modeling of LCCHVDC systems. *J. Mod. Power Syst. Clean Energy*. doi:10.35833/MPCE.2023.000093

Xiao, S., Wang, Z., Wu, G., Guo, Y., Gao, G., Zhang, X., et al. (2023). Critical assessment of the delivery methods of chemical and natural postharvest preservatives for fruits and vegetables: a review. *IEEE Trans. Transp. Electrification*, 1–23. doi:10.1080/10408398.2023.2289071

Xie, X., and Sun, Y. (2022). A piecewise probabilistic harmonic power flow approach in unbalanced residential distribution systems. *Int. J. Electr. Power and Energy Syst.* 141, 108114. doi:10.1016/j.ijepes.2022.108114

Yan, C., Yao, W., Wen, J., Fang, J., Ai, X., and Wen, J. (2020). Modelling and comparison analysis of grid-connected DFIG-based wind farm in weak grid. *IET Renew. Power Gener.* 14 (13), 2406–2415. doi:10.1049/iet-rpg.2019.1382

Yang, C., Wu, Z., Li, X., and Fars, A. (2024). Risk-constrained stochastic scheduling for energy hub: integrating renewables, demand response, and electric vehicles. *Energy* 288, 129680. doi:10.1016/j.energy.2023.129680

Yang, J., Zhang, R., Sun, Q., and Zhang, H. (2015). Optimal wind turbines micrositing in onshore wind farms using fuzzy genetic algorithm. *Math. Probl. Eng.* 2015, 1–9. doi:10.1155/2015/324203

Yang, Y., Zhang, Z., Zhou, Y., Wang, C., and Zhu, H. (2023). Design of a simultaneous information and power transfer system based on a modulating feature of magnetron. *IEEE Trans. Microw. Theory Tech.* 71 (2), 907–915. doi:10.1109/TMTT.2022.3205612

Yuan, S., Hao, Z., Zhang, T., Yuan, X., and Shu, J. (2019). Impedance modeling based method for sub/supsynchronous oscillation analysis of D-PMSG wind farm. *Appl. Sci.* 2813, 1–16. doi:10.3390/app9142831

Zhang, X., Gong, L., Zhao, X., Li, R., Yang, L., and Wang, B. (2023). Voltage and frequency stabilization control strategy of virtual synchronous generator based on small signal model. *Energy Rep.* 9, 583–590. doi:10.1016/j.egyr.2023.03.071

Zhu, L., Li, Z., and Hou, K. (2022). Effect of radical scavenger on electrical tree in cross-linked polyethylene with large harmonic superimposed DC voltage. *High. Volt.* 8, 739–748. doi:10.1049/hve2.12302

Nomenclature

WF	Wind Form
SCIG	Squirrel Cage Induction Generator
MV	Medium Voltage
PCC	Point of Common Coupling
PQ	Power Quality
CUPS	Custom Power Devices
UPQC	Unified Power Quality Compensator
DC	Direct Current
THD	Total Harmonic Distortion
PI	Proportional Integral
HV	High Voltage
WG	Weak Grid
FACTS	Flexible AC Transmission System
QZSIMC	Quasi Z-Source Indirect Matrix Converter
PMG	Permanent Magnetic Generator
DDWECS	Direct Drive Wind Energy Conversion Systems
S-ANNC	Soccer Leage Algorithm trained Artificial Neural Network Controller
STF	Self Tuning Filter
UVGM	Unit Vector Generation Method
PWM	Pulse Width Modulation
VSI	Voltage Source Inverter
CSI	Current Source Inverter
PJLL	Phase Locked Loop
LVRT	Low Voltage Ride Through
DSTATCOM	Distribution Static Synchronous Compensator
errA	Error Signal
RerrA	Error Rate Signal
PU	Per Unit
FLC	Fuzzy Logic Controller
DFIG	Doubly-Fed Induction Generator
SSO	Sub-Synchronous Oscillation
WFCM	Weighted Fuzzy C-Means
OEM	Orthogonal Experiment Method
V_{synC}	Virtual Synchronous Control
WTs	Wind Turbines
VSC-HVDC	Voltage Source Converter-Based HVDC
SEC	Sending-End Converter
PMSG	Permanent Magnet Synchronous Generators
SSR	Sub Synchronous Resonance
LCC HVDC	line-commutated converter-based high-voltage direct-current
WPPs	Wind Power Plants
SCR	Short Circuit Ratio
STATCOM	Synchronous Compensator
BESS	Battery Energy Storage System
VSG	Virtual Synchronous Generator
LVRT	ow-Voltage Ride Through
PLL	Phase Locked Loop
WEGS	Wind Energy Generating System
MSVSC	machine-side voltage source converter
UGVSC	Utility Grid Side Voltage Source Converter
SG	Synchronous Generator
D-PMSG	Direct-Drive Permanent Magnet Synchronous Generators
FAM	Fully Aggregated Mode

frontiers | Frontiers in Energy Research

TYPE Original Research
PUBLISHED 19 February 2024
DOI 10.3389/fenrg.2024.1325865

OPEN ACCESS

EDITED BY
Kumaran Kadirgama,
Universiti Malaysia Pahang, Malaysia

REVIEWED BY
Hind Barghash,
German University of Technology in Oman, Oman
Sree Lakshmi Gundebommu,
CVR College of Engineering, India

*CORRESPONDENCE
Praveen Kumar Balachandran,
praveenbala038@gmail.com

RECEIVED 22 October 2023
ACCEPTED 30 January 2024
PUBLISHED 19 February 2024

CITATION
Srilakshmi K, Rao GS, Balachandran PK and Senjyu T (2024), Green energy-sourced AI-controlled multilevel UPQC parameter selection using football game optimization. *Front. Energy Res.* 12:1325865. doi: 10.3389/fenrg.2024.1325865

Green energy-sourced AI-controlled multilevel UPQC parameter selection using football game optimization

Koganti Srilakshmi[1], Gummadi Srinivasa Rao[2], Praveen Kumar Balachandran[3]* and Tomonobu Senjyu[4]

[1]Department of Electrical and Electronics Engineering, Sreenidhi Institute of Science and Technology, Hyderabad, India, [2]Department of Electrical and Electronic Engineering, Velagapudi Ramakrishna Siddhartha Engineering College, Vijayawada, India, [3]Department of Electrical and Electronics Engineering, Vardhaman College of Engineering, Hyderabad, India, [4]Faculty of Engineering, University of the Ryukyus, Nishihara, Japan

The power quality (PQ) has been significantly affected by the integration of intermittent non-conventional sources (NCS) into the local distribution system in addition to the adoption of power electronic technologies to regulate non-linear loads. This article combines the H-bridge cascade five-level unified power quality conditioner (5L-UPQC) with the wind power generation system (WPGS), solar photovoltaic power generation system (SPVGS), and battery storage system (BSS) as an effective approach to address PQ problems. The utilization of the Levenberg–Marquardt backpropagation (LMBP)-trained Artificial neural network controller (ANNC) in the UPQC is recommended for generating appropriate reference signals for the converters. This eliminates the requirement for conventional complex conversions, such as abc, dq0, and αβ. Moreover, the artificial neuro-fuzzy interface system (ANFIS) is recommended for achieving a DC-link balance. Football game optimization (FBGO) is utilized to determine the optimal shunt and series filter characteristics. The major objectives of the proposed system are to reduce the current waveform irregularities, resulting in a decrease in the total harmonic distortion (THD), an enhancement in the power factor (PF), the mitigation of supply voltage imbalances and disturbances, and the maintenance of a steady direct-current link capacitor voltage (DLCV), despite the variations in the load, solar irradiation, and wind velocity. The efficiency of the suggested strategy is assessed using four case studies that involve different loads, variable wind velocities, and source voltage balancing conditions. Based on the simulation studies and obtained results, the suggested method significantly decreases the THD to values of 2.91%, 3.63%, 3.75%, and 3.50%. Additionally, it achieves a power factor of unity, which is considerably lower compared to other multilevel schemes that use the traditional symmetrical reference frame (SRF) and instantaneous reactive power (pq) methods. This design has been executed using the MATLAB/Simulink program.

KEYWORDS

total harmonic distortion, shunt active power filter, series-active power filter, unified power quality conditioner, football game optimization

1 Introduction

In recent years, integrating renewable energy systems, like solar and wind, into the distribution network has been encouraged to reduce the stress on converters and ratings. The output of a traditional square-wave inverter is a square wave with a significant amount of harmonics. This necessitates the use of filters to tailor the output and create a sinusoidal shape. When employing traditional square-wave inverters, the cost and size of the filter rise, which becomes a significant disadvantage. An admirable property of multilevel inverters is that they produce leveled output. Compared to traditional square-wave inverters, leveled output requires smaller filters.

1.1 Motivation for the research work

Lately, there has been a growing emphasis on the role of unified power quality conditioner (UPQC) in distributed power generation systems. The integration of UPQC with a non-conventional source (NCS) has become increasingly crucial compared to the traditional grid-connected voltage source converter (VSC). This approach offers several benefits, including the maintenance of a stable direct-current link capacitor voltage (DLCV) amidst load fluctuations, improvement in the power quality (PQ) on the grid, ensuring the safety of sensitive loads against disturbances from the grid side, and enhancing the fault ride-through capability of the converter during transient events. Notably, UPQC combined with NCS systems is particularly well-suited for three-phase three-wire distribution systems. One key aspect of UPQC is the generation of reference signals. In the existing literature, the methods for generating reference signals for the series and shunt compensators of UPQC have primarily relied on complex techniques, such as the dq and instantaneous reactive power (pq) theory. However, in an effort to circumvent these complexities, electrical engineers are increasingly turning to artificial intelligence controllers.

1.2 Literature review

The solar-integrated UPQC was developed to address PQ issues efficiently. In order to obtain the most power and maintain the DLCV balance, a unique fuzzy-based proportional integral controller (PIC) was created for the maximum power tracking technique (Yang et al., 2019). In addition, an innovative hybrid-enhanced method for the shunt active power filter (SHAPF) connected with the artificial neural network (ANN) technology was introduced to minimize current waveform flaws and boost PQ in the distribution network (Ganesan and Srinath, 2019). The best tuning of a fractional-order proportional integral controller for reactive power and harmonic compensation under balanced and unbalanced loading conditions was then used to construct the particle swarm optimization (PSO) and gray-wolf optimization (GWO)-based optimal SHAPF, which was then tested experimentally (Mishra et al., 2020). However, using hysteresis and pulse-width modulation (PWM) approaches, the effectiveness of wind systems associated with UPQC was investigated under various loads and problematic conditions (DheyaaIed and Goksu, 2022). Additionally, using the technique of impedance matching, the flow of power in UPQC was examined on a three-phase system under various working conditions (Zhao et al., 2021).

Additionally, the power flow analysis of UPQC was investigated on a three-phase distribution grid under various operating situations using the method of impedance matching (Yap et al., 2017). Moreover, the fuzzy-based hybrid technique was adopted to achieve the maximum out of the photovoltaics (PVs). However, to reduce complexity, the ANN was considered for UPQC reference signal generation to solve PQ issues (Srilakshmi et al., 2023). To reduce the current total harmonic distortion (THD), the intelligent fuzzy-tuned PIC was created for the hybrid shunt active and passive filters. By utilizing Clarke's transformation, the performance study was carried out for various loads (Lin and Simachew, 2022). Solar-supplied UPQC was also introduced to lower the THD of the supply current at voltage variations, like sag and swell, by utilizing the ANN. Additionally, under various load conditions, the developed approach was contrasted with symmetrical reference frame (SRF) and pq methods (Okech et al., 2022). An evolutionary PSO and GWO algorithm was proposed to select optimal K_p and K_i values of the PIC of the SHAPF to minimize the THD and manage reactive power, respectively (Mishra et al., 2022). However, to regulate DLCV and to handle power, the feed-forward ANN has been suggested for PV/wind-associated UPQC (Chandrasekaran et al., 2021).

To lower THD in the grid current waveform, the H-bridge inverter-based single phase SHAPF with a modified predictive current control approach was introduced (Belqasem et al., 2022). Furthermore, the microgrid-connected multilevel D-STATCOM was developed to eliminate voltage and current distortions effectively (Sarker et al., 2020). Furthermore, a comprehensive study was carried out on various phase synchronization techniques that were used to control the working of the SHAPF (Yap et al., 2019). The novel technique was introduced for the UPQC to improve the power quality to regulate energy transfer between sources and loads (Szromba, 2020).

For the AC–DC microgrid system, intelligent hybrid controllers, such as fuzzy-PIC and fuzzy PID controllers, were developed to increase the PQ and stabilize the voltage in the presence of D-STATCOM (NafehHeikalEl-Sehiemy and Salem, 2022). However, the GWO was suggested to optimize the gain values of PIC-based UPQC to reduce the THD for both linear and non-linear loads (Marcel et al., 2023). Hysteresis current control was used for pulse generation, stabilizing the DLCV for SHAPF to effectively deal with PQ issues. Additionally, linear and non-linear loads were considered to study the performance (Imam et al., 2020). Biogeography-based optimization (BBO) was selected to obtain optimal gain values of the PIC and for fast action in fault identification with higher accuracy with the motive of stabilizing DLCV fluctuations (Sayed et al., 2021).

The hybrid fuzzy-ANN control technique has been adopted for UPQC to minimize the current THD and voltage fluctuations and improve the network usage (Renduchintala et al., 2021). The improved bat and moth–flame metaheuristic optimization methods were hybridized to solve the PQ issues by the optimal selection of the gain values of PIC (Rajesh et al., 2021). The fuzzy logic controller (FLC) was developed for the series-active power filter (SeAF) of the distribution network to minimize the current- and voltage-related PQ problems (Pazhanimuthu and Ramesh, 2018).

The predator–prey firefly algorithm was selected for the optimal selection of the gain values of the PIC adapted to the

TABLE 1 Literature survey.

Reference/ year	Control		PQ issues				Loads	
[No]/year	Reference signal generation	Controller	THD	DLCV balancing	Supply voltage sag and swell	Supply voltage disturbance	Non-linear sensitive load	Unbalanced load
Mishra et al. (2020)/ 2020	pq theory	FOPID	✓				✓	✓
DheyaaIed and Goksu. (2022)/2022	SRF	PIC	✓					
Srilakshmi et al. (2023)/2023	ANN	ANN	✓	✓	✓	✓	✓	✓
Lin and Simachew. (2022)/2022	SRF	Fuzzy-PI	✓	✓			✓	
Chandrasekaran et al. (2021)/2021	ANN	ANN	✓		✓		✓	✓
Sayed et al. (2021)/ 2021	SRF	PI-BBO	✓		✓		✓	✓
Rajesh et al. (2021)/ 2021	SRF	ANFIS	✓				✓	✓
Pazhanimuthu and Ramesh. (2018)/ 2018	pq	Fuzzy	✓		✓		✓	
Sahithullah et al. (2019)/2019	SRF	PPFFA	✓				✓	✓
(Sakthivel et al., 2015)/2019	SRF	PI-ACO	✓				✓	✓
Sudheer and Kota. (2017)/2017	ANN	ANN	✓	✓	✓		✓	✓
Ramadevi et al. (2023)/2023	SRF	FF-ANN	✓	✓	✓	✓	✓	✓
Proposed 5L-UPVBES	**ANFIS**	**ANFIS**	✓	✓	✓	✓	✓	✓

The bold values shows the proposed method (to highlight the best result).

SHAPF to reduce the THD and to enhance the power factor (PF) (Sahithullah et al., 2019). Soccer match optimization for the optimal selection of weights for the ANN controller was suggested for PV/battery-associated UPQC to solve PQ issues (Koganti et al., 2022). The ant colony optimization (ACO) algorithm was chosen for selecting the K_p and K_i values of the PIC for the SHAPF to reduce the THD under several loading conditions (Sakthivel et al., 2015). An adaptive novel hysteresis band with the FLC was suggested to the PV-powered nine-level VSC of UPQC to receive fluctuation-free signals (Hassan et al., 2022). Next, the soccer match algorithmic approach was suggested for the appropriate choice of PIC gain values for UPQC to successfully handle both voltage fluctuations and current distortions (Srilakshmi et al., 2022).

For UPQC, the hybrid control strategy combining the FLC and ANN features was suggested as a way to lessen the flaws in the grid's voltage and current waveforms while still maintaining DLCV for dynamic loads (KogantiKrishna and Reddy Salkuti, 2022). The ANN-based method was suggested for five-level UPQC to control the PQ problems (Sudheer and Kota, 2017). The firefly-based optimization algorithm was used to train the ANNC, which was developed for the shunt VSC for the PV/battery UPQC to reduce the mean-square error (MSE) and minimize the THD (Ramadevi et al., 2023). The self-tuning filter-based method was developed for UPQC integrated with renewable sources to address PQ issues (Mansoor et al., 2023). The Levenberg–Marquardt backpropagation (LMBP)-trained ANN controller was adopted for UPQC to mitigate the current- and voltage-related PQ problems efficiently (Zhou et al., 2006).

Moreover, a special improved UPQC with several objectives and variables that can be optimized using the BHO and PSO techniques to alter the PIC variables has been designed to decrease the system THD (Khosravi et al., 2023). Furthermore, a suggestion was made to use power-compensating approaches to connect the AC/DC microgrid to the grid in order to lower the harmonic amplitudes. This entails maximizing the gain coefficients in specific filter compensation apparatuses. The PIC's optimized coefficients were linked to the cost

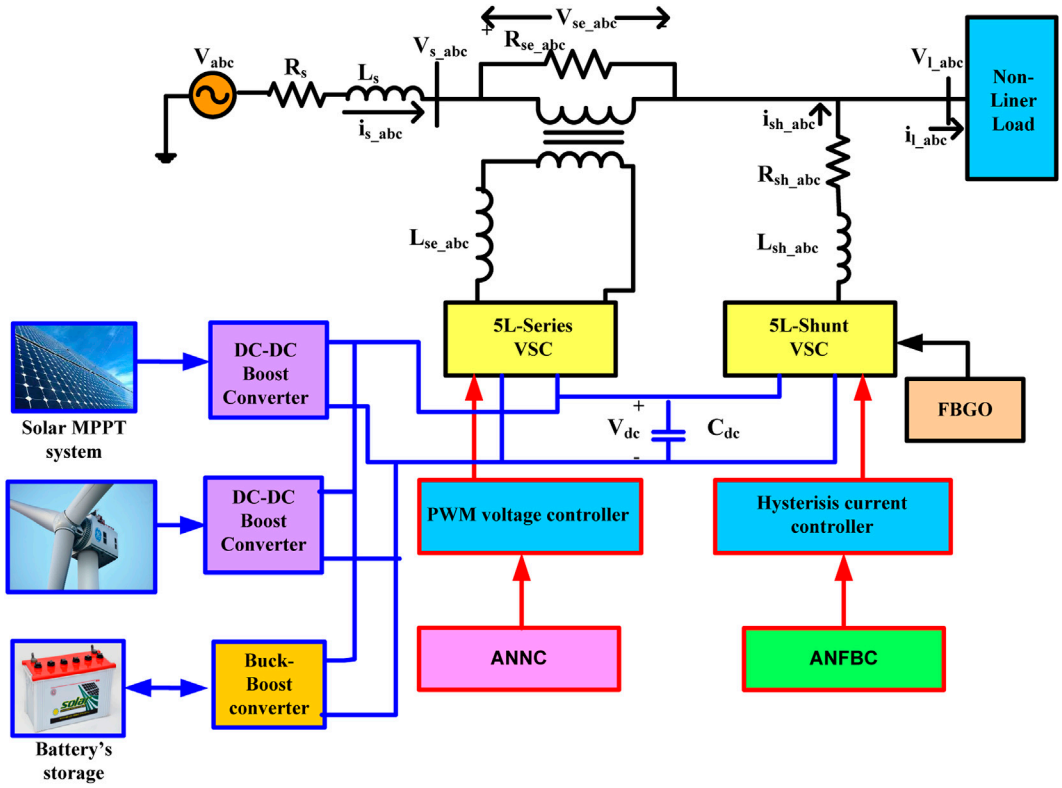

FIGURE 1
Proposed 5L-MUPQC configuration.

functions that took into account the inaccuracy of the controller, voltage harmonics, and current harmonics (Khosravi et al., 2021).

1.3 Key contribution

The literature listed in Table 1 makes it abundantly evident that the majority of the works mostly concentrated on different controllers using the pre-existing traditional control methods for UPQC that included complicated Park's and Clarke's transformations. In addition to an artificial neuro-fuzzy interface system (ANFIS) controller for DC-link balancing, this publication develops ANN-based reference signal generation for the PV/battery-coupled DC-link UPQC.

The novelty of this manuscript is highlighted in the steps below:

- ➢ Introducing the Levenberg–Marquardt-trained ANNC for generating effective reference signals in order to eliminate the necessity of complex abc–dq0–αβ0 conversions, i.e., SRF and pq theories in UPQC.
- ➢ The optimal selection of the H-bridge cascade 5L-UPQC shunt and series filter parameters for effectively reducing the imperfections in the current waveforms effectively using football game optimization (FBGO).
- ➢ Proposing the hybrid ANFIS controller to maintain a constant DLCV.
- ➢ Incorporating solar power with storage systems of the DC link of 5L-UPQC to reduce the stress and burden on the VSC, which supports and meets the load demand and maintains a constant DLCV during load variations.
- ➢ The objective of the proposed system is to diminish the source current THD and eliminate the grid voltage side troubles, like disturbance, swell, and sag.
- ➢ Additionally, the suggested ANFIS for 5L-UPQC in association with the PV, wind, and battery storage system (BSS) (5L-MUPQC) is examined on four test cases for several types of loads, solar irradiation, and wind velocity to show its superior performance.

This paper is structured as follows: Section 2 shows the modeling of 5L-UPQC, Section 3 explains the proposed control scheme, Section 4 demonstrates the results and discussion, and Section 5 concludes the manuscript.

2 Modelling of the developed 5L-MUPQC

Figure 1 shows the proposed 5L-UPQC configuration, which connects the PVs and batteries to the DC link of UPQC. Combining series and shunt VSCs creates UPQC. By supplying the appropriate compensation voltage via the injecting transformer and the inductor, the SHAPF seeks to resolve grid-side voltage-related issues. The SHAPF is similarly connected to the grid via the interface inductance.

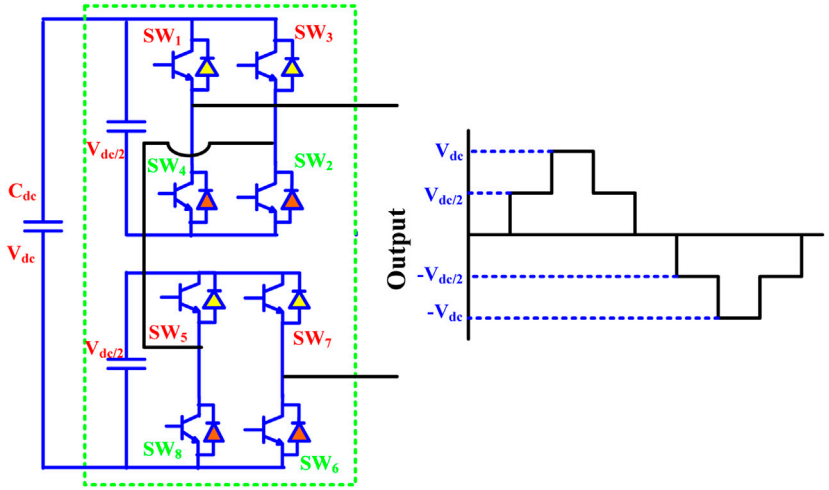

FIGURE 2
Single-phase 5L-cascade H-bridge UPQC with the output.

TABLE 2 On/off of switches considered for 5L-cascaded H-bridge UPQC.

Output voltage	SW1	SW2	SW3	SW4	SW5	SW6	SW7	SW8
V_{dc}	1	1	0	0	1	1	0	0
$V_{dc/2}$	1	1	0	0	1	0	1	0
0	1	0	1	0	1	0	1	0
$-V_{dc/2}$	0	0	1	1	1	0	1	0
V_{dc}	0	0	1	1	0	0	1	1

Note*: 0 = off; 1 = on.

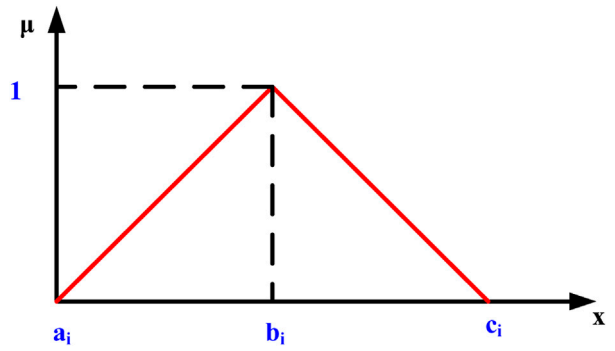

FIGURE 3
Triangular membership function (MSF).

By injecting a sufficient compensating current, the SHAPF seeks to decrease the current waveform harmonics and maintain the DLCV constant with a minimal settling time.

One of the best structures is the multilevel inverter cascaded H-bridge topology, which requires no clamping tools or components. Although the cascaded H-bridge topology's layout is straightforward, more DC sources are needed to power each single H-bridge cell. Two H-bridge cells are cascaded into a five-level H-bridge structure, and every single H-bridge cell is powered by a DC source. Figure 2 displays a multilevel inverter five-level cascaded H-bridge arrangement; it also displays the cascaded H-bridge's 5L voltage output in the phase. The five-level output is produced by sequentially triggering power switches as the whole DC-link voltage is divided across two H-bridge cells. Figure 2 shows the power switches used for five-level cascaded H-bridge, and its switching order is given in Table 2.

2.1 Selection of C_{dc}

The value of C_{dc} can be calculated by Eq. 1:

$$C_{dc} = \frac{\pi^{*} i_{sh}}{\sqrt{3}\omega V_{cr,pp}}. \quad (1)$$

V_{dc}^{ref} is chosen within the suggested system's permissible rating range.

2.2 Selection of L_{sh} and L_{se}

The shunt VSC is linked to the network through an inductor (L_{sh}), given by Eq. 2, which relies on the switching frequency, ripple current, and DLCV; it is given as follows:

TABLE 3 DC-link power distribution.

Mode of operation	Action taken
Mode-1: When no *SPG* and *WPG*	BES only will provide power to P_{DC}
Mode-2: When *SPG* and *WPG* = P_{DC}	Solar PV and wind will supply power P_{DC}
Mode-3: When *SPG* and *WPG* <P_{DC}	Difference sum of the power will be provided by the battery until it reaches $SOCB_{\min}$
Mode-4: When *SPG* and *WPG* >P_{DC}	Excessive solar power is used to charge the battery system until it reaches $SOCB_{\max}$

TABLE 4 NCS ratings.

Device	Parameter/source	Value chosen
WS	Power at output	3 MW
	Velocity of wind	11 m/s
	Pitch integral gain controller K_i	5
	Pitch proportional gain controller K_p	25
	Max rate of change of PA	45 deg
	Pitch angle	25 deg./second
Li-ion BSS	Rated-capacity of the battery	450 Ah
	Maximum battery capacity	550 Ah
	Voltage	650 V
	Full-charged voltage	757 V
SPVG	Output power	214.92 W
	Open circuit voltage	48.3 V
	Short-circuit current	5.8 A
	Voltage/current under max power	39.80 V/5.40 A

$$L_{sh} = \frac{\sqrt{3}\, m V_{dc}}{12\, a_f\, f_{sh}\, I_{cr,pp}}, \tag{2}$$

assuming m is 1, a_f is 1.5, and f_{sh} is 10 kHz. Similarly, L_{se} is given by Eqs 3, 4

$$K_{se} = \frac{V_{L-L}}{\sqrt{3}\, V_{se}}, \tag{3}$$

$$L_{se} = \frac{\sqrt{3}\, m V_{dc} K_{se}}{12\, a_f\, f_{se}\, I_{cr,pp}}. \tag{4}$$

Assuming f_{se} as 10 kHz, the series inductance depends on the ripple current.

2.3 External support for 5L-MUPQC at the DC link

The solar/battery-fed DC link is proposed for the diode-clamped 5L-UPQC. It consists of a hybrid solar and battery energy system to regulate the DLCV at changing loads. External support can reduce the converter ratings and stress by lowering the utility's demands. The equation for the power demand of the suggested technique is given in Eq. 5:

$$P_{PV} + P_W + P_{BSS} - P_{Load} = 0. \tag{5}$$

The PV model used in this work was selected from the Simulink library. To create the necessary quantity of voltage and current, the PV modules are connected in series to form a string. Some of these strings are then connected in parallel. Here, Eq. 6 describes the solar output. Figure 3 illustrates the PV cell properties for a fixed temperature and changing irradiance. The incremental conductance-based MPPT is adopted to extract the maximum output from the PV system (Srilakshmi et al., 2023):

$$P_{PV} = V_{PV} \times i_{PV}. \tag{6}$$

Moreover, the BSS aids in supporting the DLCV's stabilization. The cells are stacked in parallel or series in a battery to provide the necessary voltage and current. Since Li-ion batteries have benefits like slower discharge and inexpensive maintenance costs, this work chooses them from the Simulink library. The state of charge of the battery (*SOCOB*) (Koganti et al., 2022) is expressed in Eq. 7:

$$SOCOB = 80\left(1 + \int i_{BSS}\, dtQ\right). \tag{7}$$

The SPG will choose whether to charge or discharge the battery while adhering to the restrictions stated by Eq. 8. Figure 5 depicts the battery's drain. Table 3 displays the power division at DC's link capacitor, and Table 4 provides the ratings selected for PV, battery, and wind systems. Figure 4 shows the control mechanism for the solar, wind, and battery system fed to the DC link.

$$SOCOB_{\min} \le SOCOB \le SOCOB_{\max}. \tag{8}$$

The wind-generated AC voltage is rectified into the DC voltage, which is then boosted through a boost converter. A permanent magnet synchronous machine was considered in the present work. Wind power generation (KogantiKrishna and Reddy Salkuti, 2022) is given by Eqs 9–13:

$$P_m = 1/2\pi\, \rho\, C_p(\lambda, \beta)\, R^2\, V^3, \tag{9}$$

$$\lambda = \frac{\omega_m R}{v}, \tag{10}$$

$$\omega_m = \omega_t\, G_r, \tag{11}$$

$$C_p(\lambda, \beta) = 0.23\left(\frac{116}{\lambda_1} - 0.48\beta - 5\right)\exp^{\frac{-12.5}{\lambda_1}}, \tag{12}$$

$$\lambda_1 = \left(\frac{1}{\frac{1}{\lambda - 0.02\beta} - \frac{0.0035}{3\beta + 1}}\right). \tag{13}$$

3 Proposed control scheme

Generally, chances take place at the distribution side during dynamic load variations. For a brief period, the system must be restored to its

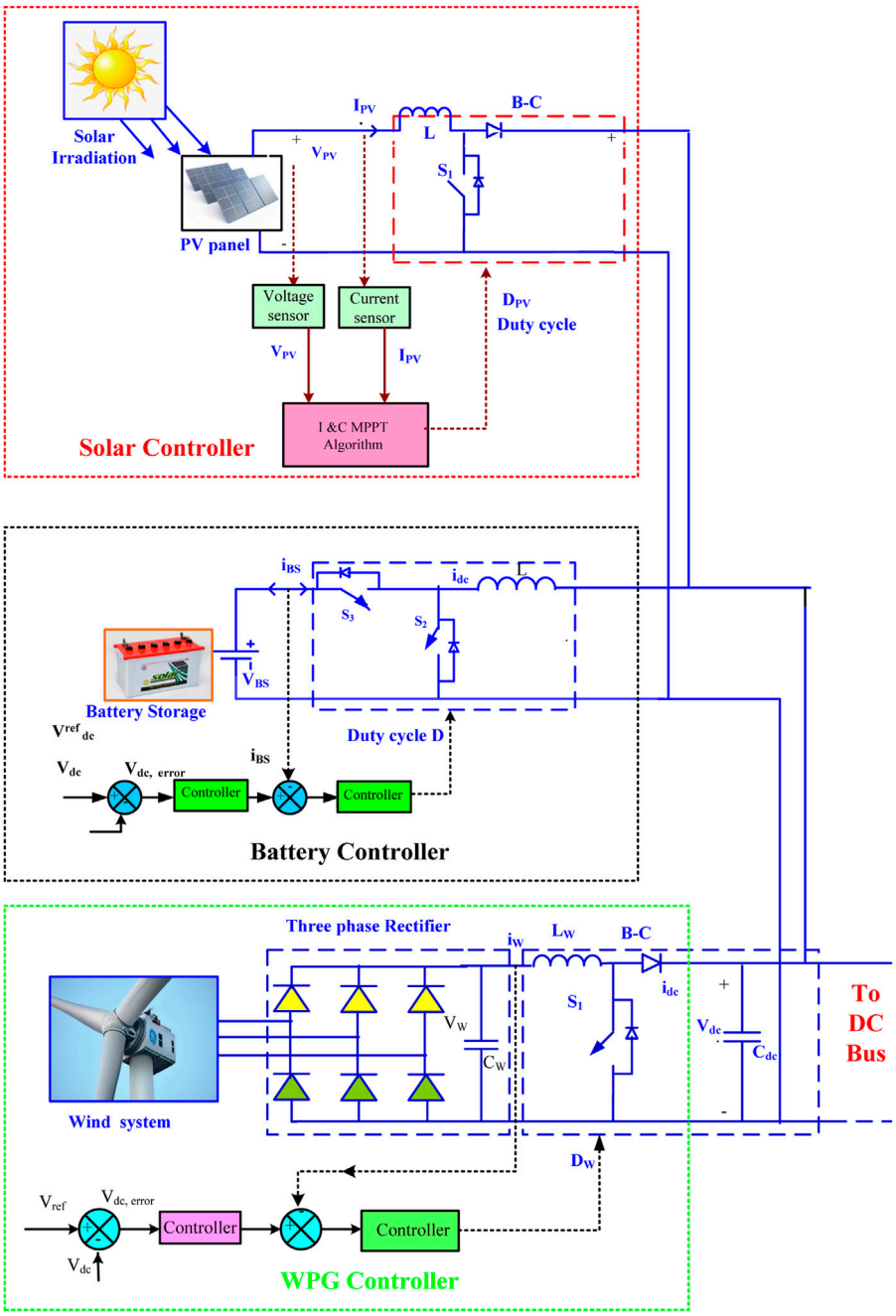

FIGURE 4
Control of photovoltaic (PV), wind, and battery systems with boost and buck–boost converters.

initial value in order to function normally. Here, using the recommended ANNC, the PWM hysteresis current control for the shunt VSC and gate pulses for the series VSC are produced by the PWM technique.

3.1 Shunt VSC

The major goal of the SHAPF is to manage the DLCV under faults and dynamic loading circumstances and to suppress current signal distortions by injecting the compensating current. The output layer (OL), input layer (IL), and hidden layer (HL) components of the ANN make up its structure, where the IL gathers data supplied as input and sends it to the HL. When linked between the IL and the HL, it is afterward multiplied by the appropriate weights on the connected links. Here, calculations are performed with a chosen bias on the HL, and the outcomes are gathered in the OL.

In this case, the LMBP-based ANN is chosen. To get the desired output, the weights of the link are adjusted during training by analyzing the mistake. For ANN training, where the performance function is the MSE, the LMBP training method is used. The LMBP algorithm updates the weights using the obtained derivatives, which has the advantages of rapid convergence and effective learning.

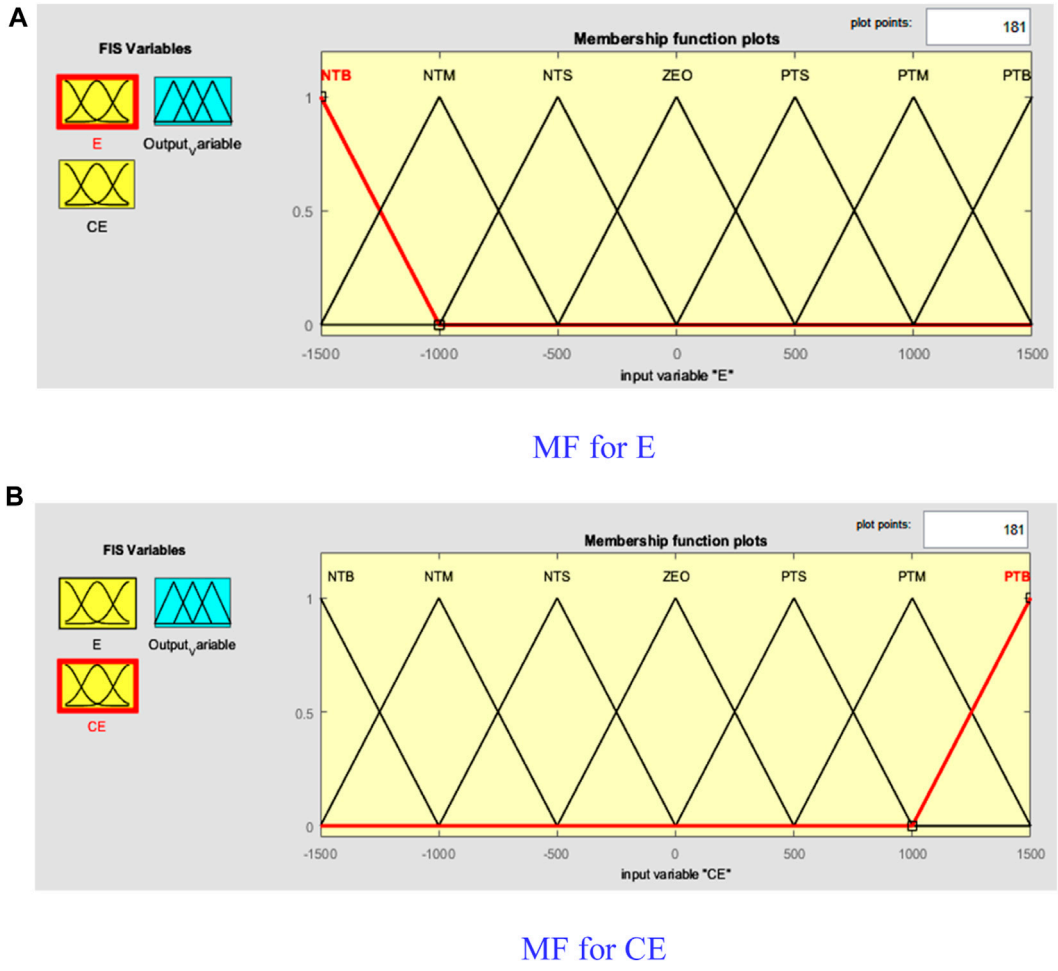

FIGURE 5
Fuzzy MSF for **(A)** E, **(B)** CE.

3.1.1 ANFIS

It is advised that the ANFIS keeps the DLCV constant. The proposed ANFIS combines fuzzy logic and ANN elements to create an intelligent hybrid controller. However, in order to keep the DLCV constant, the obtained DLCV—whose output, E, and CE are taken into consideration—is compared to the selected reference DLCV. As seen in Figure 5, the inputs given to the ANNC are first trained based on the Gaussian membership function (MSF) to yield the best results. The ANFIS is primarily composed of five layers: the first layer, called fuzzification, produces the fuzzy MSF, which is given by Eq. 14 and is depicted in Figure 5.

$$\begin{matrix} \mu_{Ai}(x), i = 1, 2. \\ \mu_{Bj}(y), j = 1, 2.' \end{matrix} \tag{14}$$

where $\mu_{Ai}\mu_{Bj}$ are the MSF outputs obtained from the first layer. The representation of the triangular MSF is exhibited by Eq. 15:

$$\mu_{Ai}(x) = \max\left(\min\left(\frac{x - a_i}{b_i - a_i}, \frac{c_i - x}{c_i - b_i}\right), 0\right), \tag{15}$$

where b_i is the fuzzy set i's point of greatest support and x_{max}–x_{min} (high and low bonds) is the range (world of discourse) of x. The inputs that are taken into consideration are the negative-big (NEB), negative-medium (NEM), zero (ZOE), positive-small (PES), positive-big (PEB), positive-medium (PEM), and negative-small (NES) input. MF's inputs are displayed in Figure 5. We can see the fuzzy rule base in Table 5.

TABLE 5 Lower and upper bounds of variables.

Decision variable	R_{sh} (Ω)	L_{sh} (mH)	R_{se} (Ω)	L_{se} (mH)
Lower	0	0.01	0	0.01
Upper	0.5	10	2	10

Furthermore, the AND operator is used in the second layer (where fuzzy rule weighting is carried out) to calculate the firing strength w_i by accounting for the MSF produced in the initial layer, the result of which is ascertained using Eq. 16:

$$w_k = \mu_{Ai}(x)^*\mu_{Bj}(y)i, j = 1, 2. \tag{16}$$

The third layer is where the values from the previous layer are normalized. Normalization is achieved at each node in this layer by computing the ratio, as given in Eq. 17, of the firing strength (true

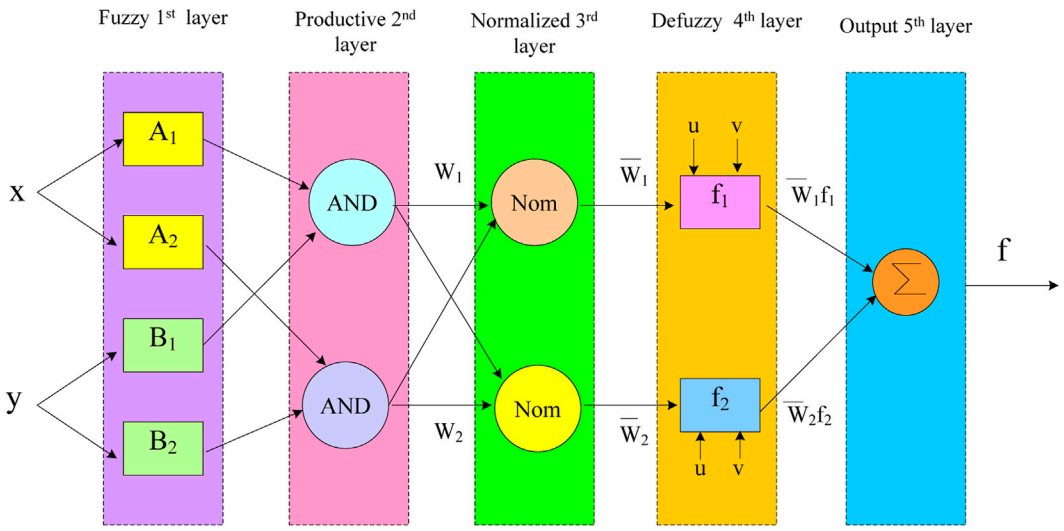

FIGURE 6
Structure of the artificial neuro-fuzzy interface system (ANFIS).

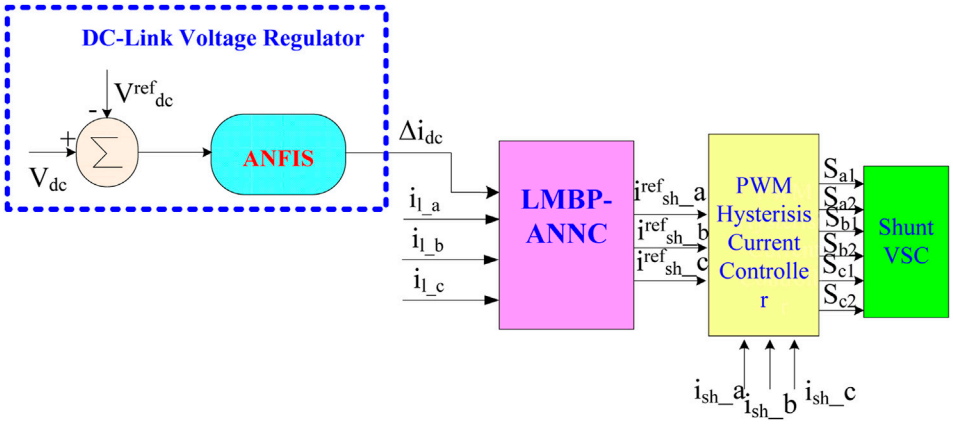

FIGURE 7
Control of the shunt converter.

values) of the kth rule to the sum of the firing strengths of all other rules:

$$\overline{w_k} = \frac{w_k}{w_1 + w_2} k = 1, 2. \tag{17}$$

The self-adaptive capability of the ANNC is executed through the application of the inference parameters (p_k, q_k, r_k) in the fourth layer, which produces an output as defined in Eq. 18:

$$\overline{w_i} f_i = \overline{w_i}(p_k u + q_k v + r_k). \tag{18}$$

As shown in Eq. 19, the inputs are finally combined in the fifth layer to provide the final required total output of the ANFIS. The suggested ANFIS's configuration and the MSF for inputs 1 and 2 are shown in Figure 6.

$$f = \sum_i \overline{w_i} f_i. \tag{19}$$

In this work, the ANFIS is trained to keep the DLCV stable and to generate reference current signals. However, for keeping the DLCV constant, the reference DLCV (V^{ref}_{dc}) is compared with the actual DLCV (V_{dc}); its error is chosen as input data, Δi_{dc}. Subsequently, the load currents (i_{l_abc}) and the DC loss component (Δi_{dc}) are regarded as the input, whereas the reference currents ($i^{ref}_{sh\_abc}$) are regarded as target data, as depicted in Figure 7. Figure 8 shows the selected neurons' structure.

3.2 Series VSC

The main function of the series filter is to reduce source voltage signal imperfections by injecting an appropriate compensating voltage to keep the load voltage constant. The suggested series VSC reference signal production strategy is shown in Figure 9, and the construction of an ANN with an HIL of 200 neurons is

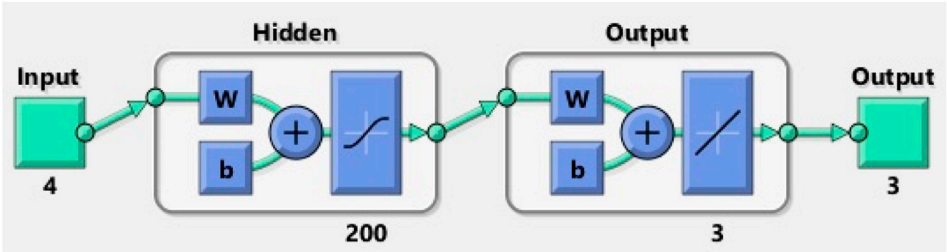

FIGURE 8
ANNC for referencing the current generation.

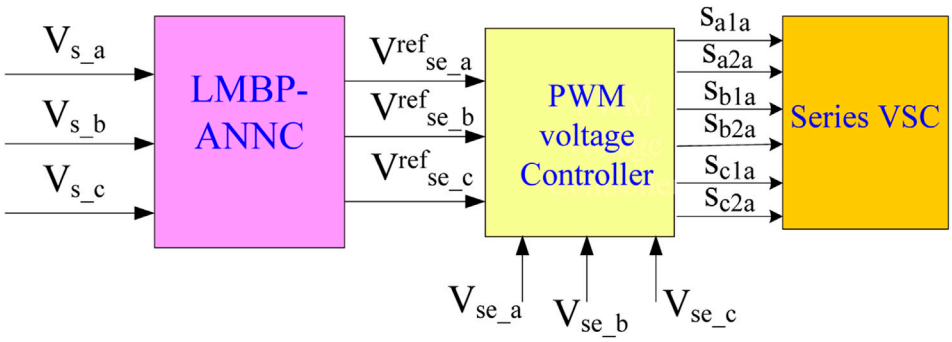

FIGURE 9
Series voltage source converter (VSC) controller.

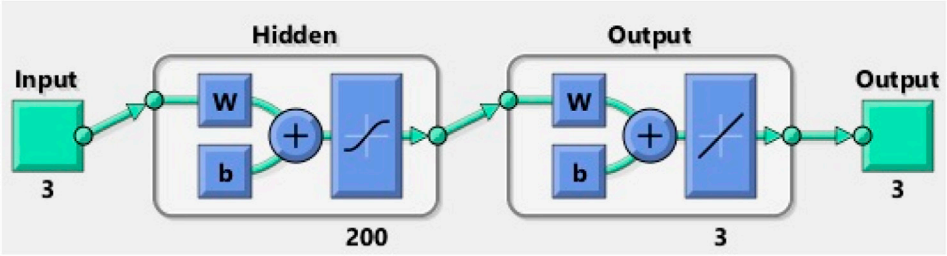

FIGURE 10
Structure of the ANNC for reference voltage generation.

shown in Figure 10. The supply voltages (V_{s_abc}) are regarded as data for the input to produce the reference voltage signals ($V^{ref}_{se\_abc}$), whereas the reference voltage is regarded as the goal data to the ANN. Moreover, the PWM produces pulses for a series converter.

4 FBGO-based shunt and series filter parameter selection

FBGO is a metaheuristic optimization algorithm that simulates the behaviors of football players. Within this framework, a team of players is established, and the position of each player corresponds to a solution point on the football field. The evaluation of each player's performance is based on the performance function (PEF), which is derived from the objective function (Eq. 26). The movements of these players, guided by a team coach, mimic the process of obtaining the ball and reaching a goal, involving two distinct phases: random walk and coaching. The proposed method is used to determine the optimal values of resistance and inductances of shunt and series filters (variables) with the goal of minimizing the THD. Each player is defined to denote the problem variables, as given in Eq. 20. The upper and lower bounds of variables are given in Table 5.

$$P_i = L_{sh}, L_{se}, R_{sh}, R_{se}, \tag{20}$$

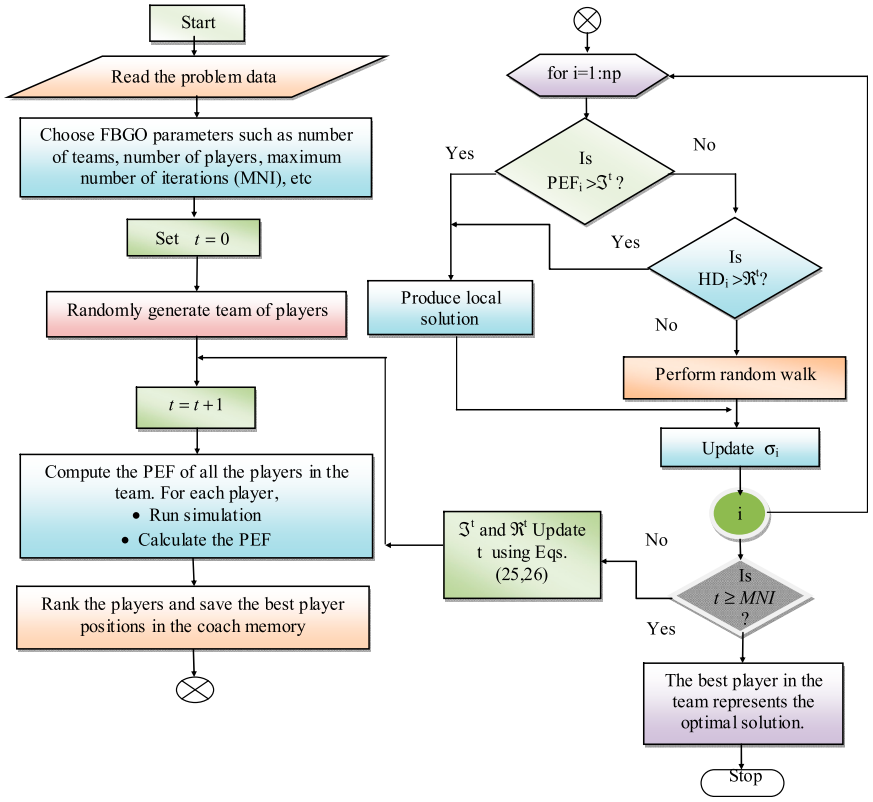

FIGURE 11
Flowchart of football game optimization (FBGO) for the proposed system.

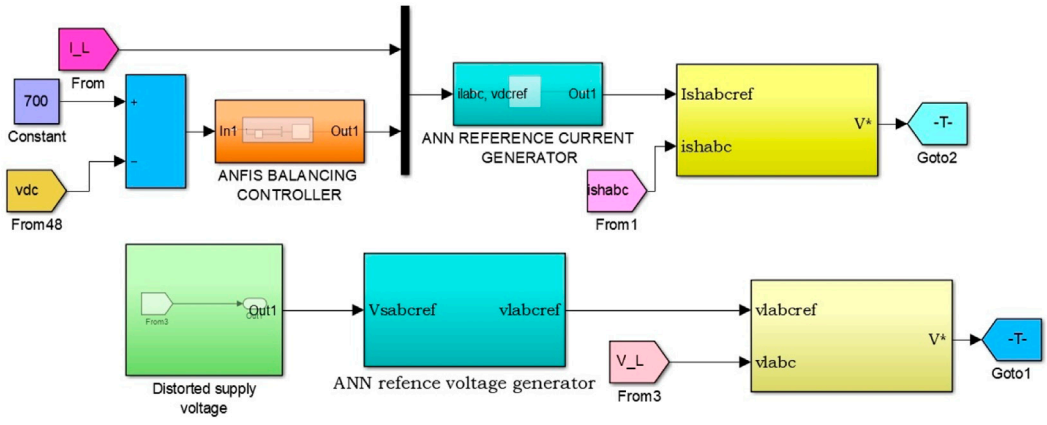

FIGURE 12
Simulink models of proposed M-UPQC with the ANFIS controller.

$$PEF = \frac{1}{1 + THD}. \tag{21}$$

The random player movements, under the supervision of a team coach, follow a two-step process to accomplish the tasks of retrieving the ball and reaching the goal, as detailed below.

4.1 Random walk

Individually, every player embarks on a random walk, aiming to locate a position closer to the ball with the aspiration of scoring a goal. During this phase, there are no specific instructions or guidance from the coach.

TABLE 6 5L-UPQC parameters with loads.

Grid supply	V_s, 415 V; f, 50 Hz; R_s, 0.1 Ω; and L_s, 0.15 mH
SHAPF	Hysteresis-controller band: 0.01
DC link	C_{dc}, 9400 μF; V_{dc}^{ref} = 700V
Loads	1. Balanced 3 Φ rectifier type load: L = 1 mH and R = 10Ω
	2. Balanced 3 Φ rectifier type load: L = 0.5 mH and R = 5Ω
	3. Balanced load: p = 1000 W and Q = 500 Var
	4. Unbalanced 3 Φ RL-type load: R1 and L1 = 10 Ω and 1.50 mH; R2 and L2 = 20 Ω and 3.5 mH; and R3 and L3 = 15 Ω and 2.5 mH

TABLE 7 Test cases studies considered for different loads.

Condition	Case 1	Case 2	Case 3	Case 4
Balanced V_S	✓	✓		
Unbalanced V_S			✓	✓
Steady-state voltage			✓	✓
Steady-state current			✓	✓
V_{Sag}	✓			
V_{Swell} and disturbance		✓		
Current during V_{Sag}, V_{Swell}, and disturbance	✓	✓		
Constant wind velocity of 11 m/s	✓			✓
Variable wind velocity		✓	✓	
Constant solar irradiation 1000 W/m^2	✓	✓		
Variable solar irradiation			✓	✓
Load 1	✓		✓	✓
Load 2		✓	✓	
Load 3	✓			
Load 4		✓		✓

$$P_i^t = P_i^{t-1} + \delta_i\sigma + \gamma\left(P_B^t - P_i^{t-1}\right). \tag{22}$$

σ_i is reduced for every iteration by $\sigma_i = \sigma_i\Theta$.

4.2 Coaching

The player heightens the pressure on their opponent by advancing as directed by the game coach, taking into account the hyper distance (HD) between players, which is determined by Eq. 23:

$$HD_i = \left\|P_i^{t-1} - P_{best}^{t-1}\right\|. \tag{23}$$

Players whose HD values exceed a certain threshold, denoted as "$\mathfrak{R}$", are directed to relocate themselves closer to the optimal nearby positions, $P_{near-best}^{t-1}$, by Eq. 24:

$$P_i^t = P_{near-best}^{t-1} + \sigma_i\delta. \tag{24}$$

The value of "$\mathfrak{R}$" is slowly reduced toward its designated minimum value ($\mathfrak{R}_{\min}$) through Eq. 25, and η resembles the constant.

$$\mathfrak{R}^t = \mathfrak{R}_{\min} + \eta\left(\mathfrak{R}^{t-1} - \mathfrak{R}_{\min}\right). \tag{25}$$

In the substitution plan, the team coach replaces ineffective players with better players to improve the chances of achieving a goal. Each proficient player, whose PEF exceeds the cost constraint value ($\mathfrak{F}$), is exchanged for a nearby skilled player, according to the coach's memory (CM), using Eq. 5. $\mathfrak{F}$ will gradually be reduced as the iteration moves, as defined by Eq. 26:

$$\mathfrak{F}^t = \mathfrak{F}_{\min} + \varepsilon\left(\mathfrak{F}^{t-1} - \mathfrak{F}_{\min}\right), \tag{26}$$

where ε indicates the succession constant. If the new player strays from the soccer field, they are returned to the field through the use of Eq. 24.

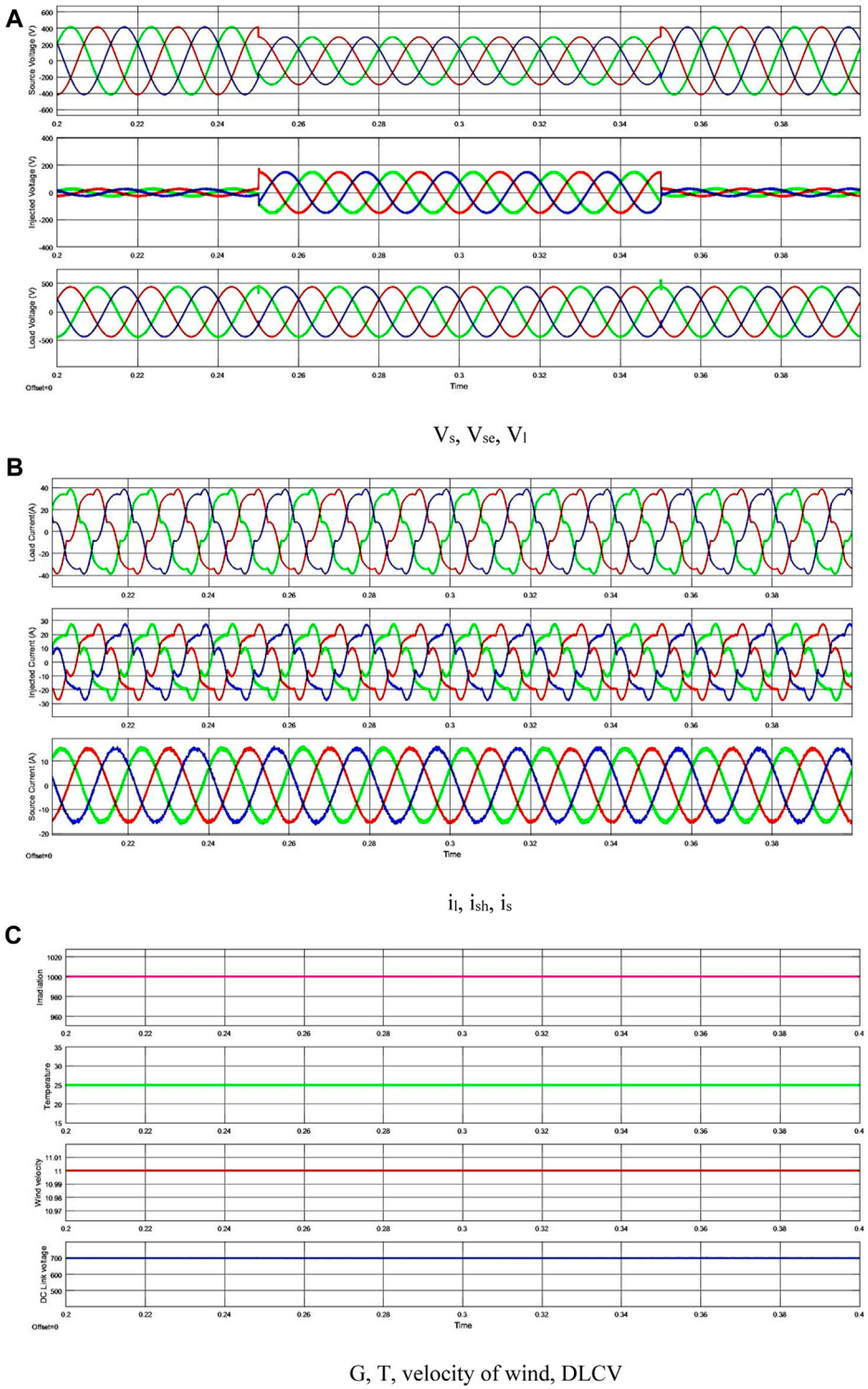

FIGURE 13
Waveforms for the first case study.

4.3 Solution process

A set of players is initially generated with random values, and their PEFs are calculated using Eq. 21. Following this, they are ranked based on their PEF. The HD between each player and the most efficient player is computed. Subsequently, the random walk and coaching steps are carried out using Eqs 22, 23, respectively. The entire cycle, encompassing the PEF evaluation, HD computation, and the execution of random walks and coaching, constitutes the iteration. This process is repeated until convergence is achieved. The player with

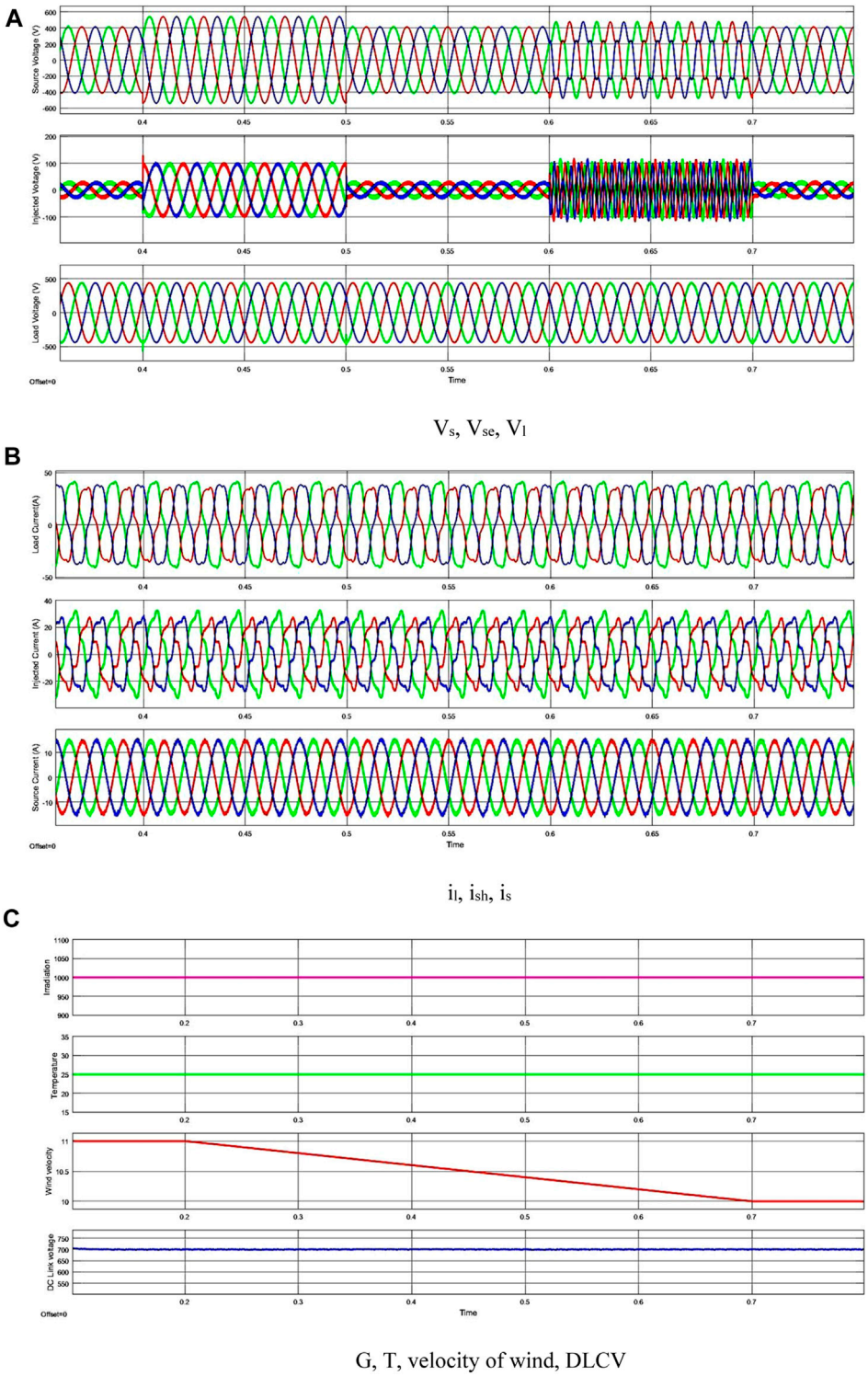

FIGURE 14
Waveforms for the second case study.

the highest PEF is identified as the optimal player once convergence is reached. Figure 11 gives the flowchart of the algorithm for the solution. FBGO has a higher efficiency with faster convergence; it is capable of solving multi-objective and complex engineering problems effectively. Moreover, it has its own limitations, like being a computational burden.

5 Results and discussions

Using MATLAB 2016a, the suggested M-UPQC with ANFBC was created. Figure 12 displays the suggested method's Simulink model. Table 6 also shows the system and the UPQC parameters

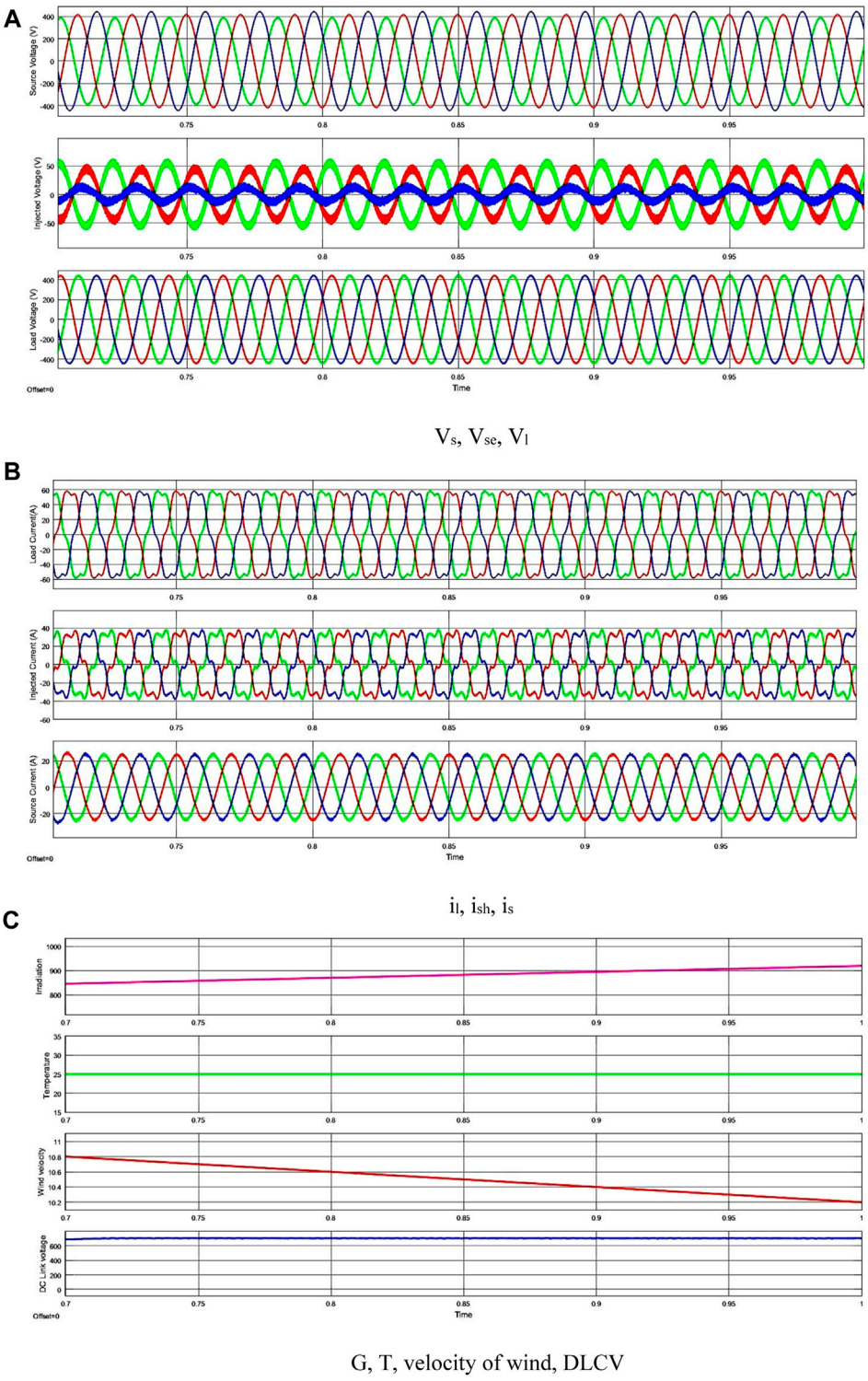

FIGURE 15
Waveforms for the third case study.

with the loads being taken into account. To demonstrate the improved performance of the designed system, Table 7 presents four different case studies with various combinations of non-linear loads and PQ issue conditions with variable wind velocity, solar irradiation, and so on. In this instance, the voltage source (VS) is chosen as an unequal phase supply for instances 3 and 4 and a balanced phase supply for studies 1 and 2. Cases 1 and 2 take into account the voltage sag, voltage swell, and voltage disturbance difficulties. Therefore, the goals were to minimize the THD, increase the PF, and maintain a constant DLCV. With the

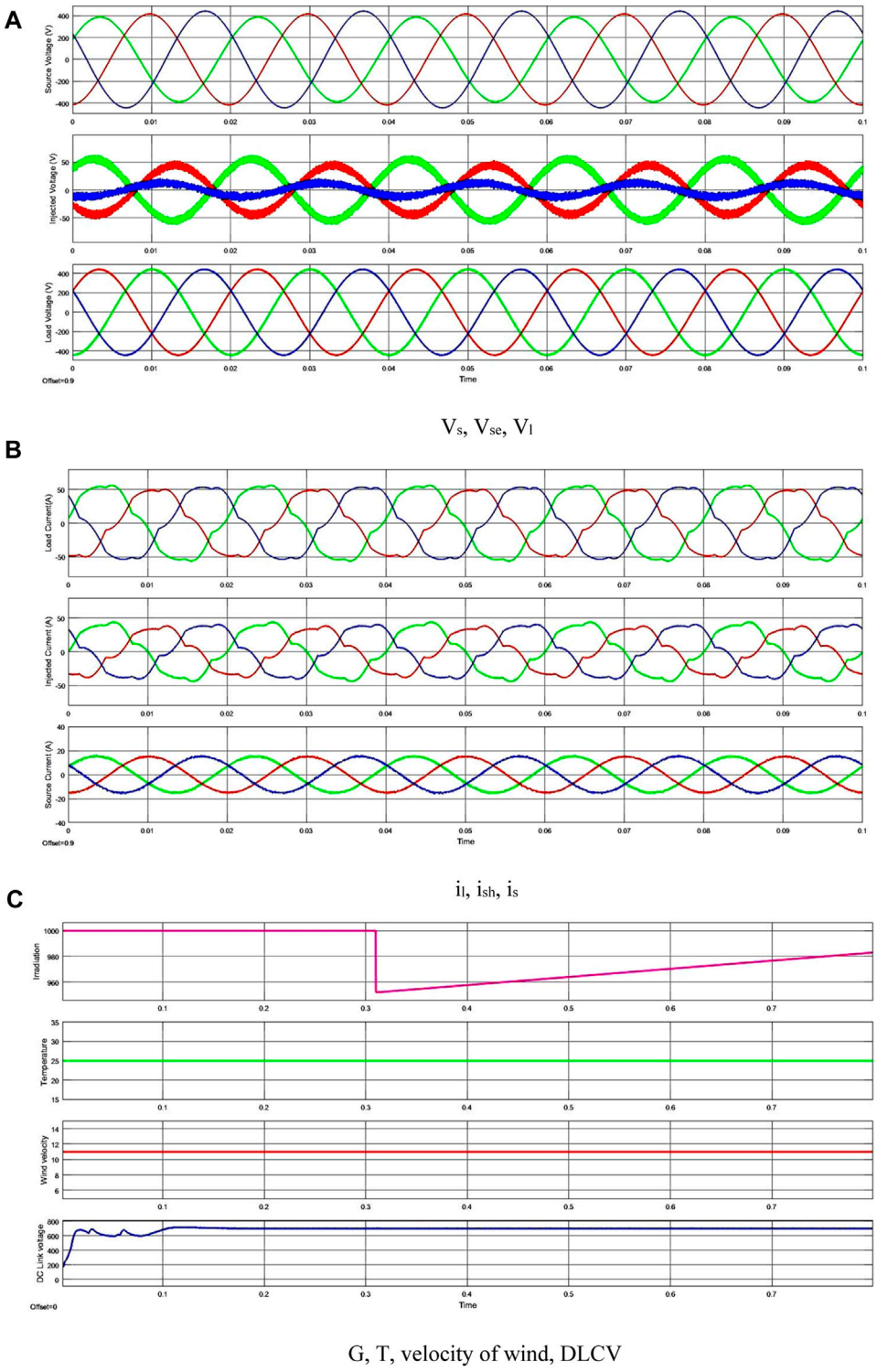

FIGURE 16
Waveforms of the suggested system for case 4.

purpose of demonstrating the effectiveness of the suggested ANFBC, synchronous reference frame theory (SRFT) comparison analysis was performed. Using Eq. 27, the PF is calculated from the THD.

$$THD = \frac{\left(\sqrt{I_2^2 + I_3^2 + ...I_n^2}\right)}{I_1}. \quad (27)$$

The voltage sag/swell ($V_{sag/swell}$) is evaluated by Eq. 28:

TABLE 8 THD and PF comparison.

Case	Method	THD	PF		
			Phase a	Phase b	Phase c
1	No UPQC	17.34	0.7764	0.7575	0.7752
	5L-UPQC with SRFT	3.74	0.9899	0.9845	0.9864
	5L-UPQC with pq	3.23	0.9866	0.9888	0.9841
	2L-UPQC with PM	3.48	0.9887	0.9878	0.9889
	3L-UPQC with PM	3.42	0.9877	0.9866	0.9974
	5L-UPQC with PM and GA	3.11	0.9997	0.9984	0.9995
	5L-UPQC with PM and ACO	3.01	0.9994	0.9991	0.9997
	5L-UPQC with PM and FBGO	**2.91**	**0.9989**	**1**	**1**
2	No UPQC	15.34	0.8664	0.8475	0.8652
	5L-UPQC with SRFT	3.88	0.9985	0.9988	0.9967
	5L-UPQC with pq	3.74	0.9867	0.9816	0.9822
	2L-UPQC with PM	3.86	0.9824	0.9865	0.9878
	3L-UPQC with PM	3.79	0.9924	0.9987	0.9991
	5L-UPQC with PM and GA	3.76	0.9996	0.9999	0.9998
	5L-UPQC with PM and ACO	3.64	0.9998	0.9999	1
	5L-UPQC with PM and FBGO	**3.63**	**1**	**0.9999**	**1**
3	No UPQC	27.90	0.8145	0.8998	0.7117
	5L-UPQC with SRFT	3.66	0.9988	0.9998	1
	5L-UPQC with pq	3.51	0.9845	0.9877	0.9855
	2L-UPQC with PM	3.62	0.9968	0.9979	0.9899
	3L-UPQC with PM	3.89	0.9888	0.9874	0.9854
	5L-UPQC with PM and GA	3.71	0.9997	1	0.9998
	5L-UPQC with PM and ACO	3.88	0.9995	0.9997	1
	5L-UPQC with PM and FBGO	**3.75**	**0.9999**	**1**	**0.9989**
4	No UPQC	19.86	0.6412	0.7012	0.7551
	5L-UPQC with SRFT	3.64	0.9981	0.9999	0.9985
	5L-UPQC with pq	3.78	0.9954	0.9955	1
	2L-UPQC with PM	3.78	0.9824	0.9821	0.9878
	3L-UPQC with PM	3.75	0.9997	0.9998	1
	5L-UPQC with PM and GA	3.78	1	0.9988	0.9998
	5L-UPQC with PM and ACO	3.68	1	0.9988	0.9998
	5L-UPQC with PM and FBGO	**3.50**	**1**	**0.9998**	**0.9998**

*PM, proposed ANN-based reference signal generation method.
The bold values shows the proposed method (to highlight the best result).

$$V_{sag/swell} = \frac{V_l - V_S}{V_l} = \frac{V_{se}}{V_l}. \quad (28)$$

The injected voltage by the series filter is calculated by Eq. 29:

$$V_{se} = V_l - V_S. \quad (29)$$

The injected current by the shunt filter is calculated by Eq. 30:

$$i_{sh} = i_i - i_S. \quad (30)$$

In case 1, the VS is initially considered to be balanced. To assess the performance of the SHAPF, a 30% balanced sag was

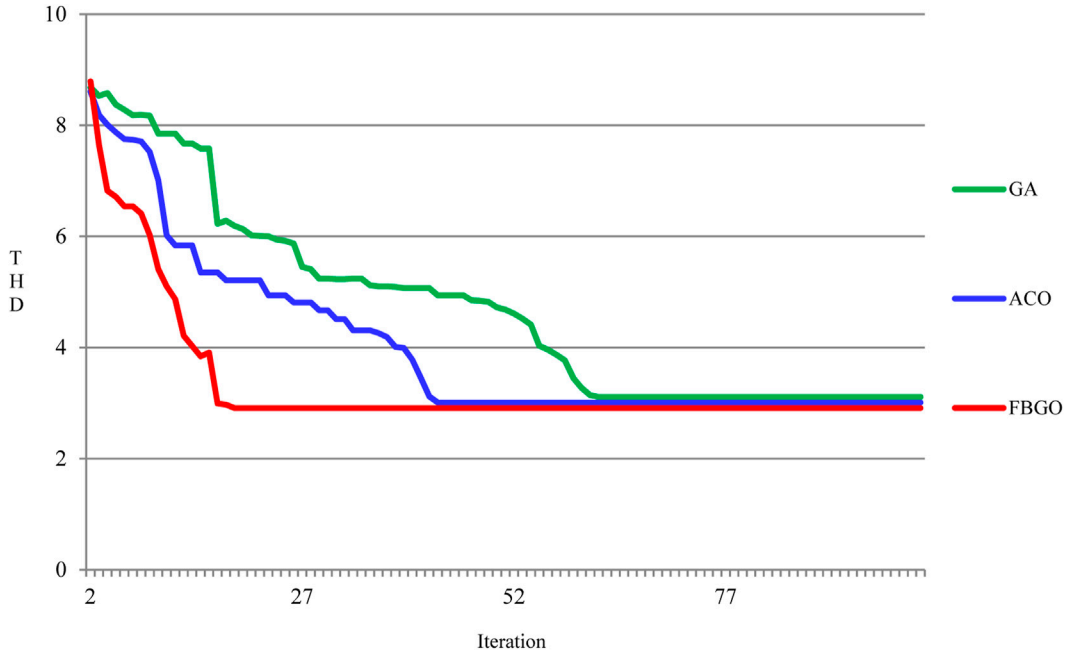

FIGURE 17
Case 1 convergence plot.

TABLE 9 Comparison of the design parameters.

Case	Method	R_{sh}	R_{se}	L_{sh}	L_{se}
1	5L-UPQC with PM and GA	0.01	1.45	1.32	5.2123
	5L-UPQC with PM and ACO	0.04	0.01	0.63	0.1581
	5L-UPQC with PM and FBGO	0.05	1.8	0.91	0.0321
2	5L-UPQC with PM and GA	0.21	0.21	3.45	3.0721
	5L-UPQC with PM and ACO	0.11	1.41	1.08	5.0464
	5L-UPQC with PM and FBGO	0.03	0.03	1.68	9.7308
3	5L-UPQC with PM and GA	0.37	1.61	4.29	2.0387
	5L-UPQC with PM and ACO	0.18	0.45	6.12	1.02
	5L-UPQC with PM and FBGO	0.08	1.72	0.32	3.24
4	5L-UPQC with PM and GA	0.37	1.01	9.21	4.1397
	5L-UPQC with PM and ACO	0.19	1.42	5.12	0.0132
	5L-UPQC with PM and FBGO	0.09	1.11	0.18	0.0736

intentionally introduced into the source voltage between the time interval of 0.25 and 0.35 s, as depicted in Figure 13A. However, the ANNC system effectively detects the voltage dip, applies a suitable compensating voltage through the coupling transformer, and maintains a consistent voltage at the load terminals. To further evaluate the performance of the SHAPF with the proposed ANFIS and FBGO optimally selected filter parameters, both loads 1 and 3 were considered simultaneously.

As shown in Figure 13B, the load current waveform exhibited contamination and non-sinusoidal behavior but remained balanced. The suggested approach mitigates the irregularities in the current waveform, leading to a reduction in the current's THD from 17.34% to 2.91% while concurrently raising the PF from 0.7764 to nearly unity. Furthermore, the proposed method sustains a steady DLCV for the load under the conditions of 11 m/s wind velocity, 1000 W/m^2 irradiation, and a constant temperature of 25°C, as represented in Figure 13C.

In case 2, similar to case 1, the source voltage is initially assumed to be balanced. To examine the working of the SHAPF under the conditions of a 30% swell and disturbance, these events are introduced during the time intervals of 0.4–0.5 s and 0.6–0.7 s, respectively. However, it is evident from Figure 14A that the ANNC effectively recognizes the voltage increase and disturbance, subsequently eliminating them by introducing the necessary compensating voltage.

The load current was found to be non-sinusoidal and unbalanced due to the presence of loads 2 and 4, as depicted in Figure 14B. Nevertheless, the proposed method manages to reduce the THD of the current from 15.34% to 3.63%, which is lower when compared to the SRFT and pq methods and raises the PF from 0.8664 to unity. It is important to note that the wind velocity and load fluctuations are considered simultaneously, with constant irradiation and temperature. However, the suggested approach maintains a steady DLCV of 700 V, as shown in Figure 14C.

In case 3, the source voltage is intentionally taken to be unbalanced, and the performance of the SHAPF is assessed under stable-state voltage conditions, as demonstrated in Figure 15A. Nevertheless, the ANNC effectively recognizes the inequalities in the phase voltage and rectifies it by inserting the necessary voltage. To examine the operation of the SHAPF, loads 1 and 2 are considered, resulting in the observation of a significantly contaminated yet balanced load current waveform, as seen in Figure 15B. The proposed system successfully rectifies the

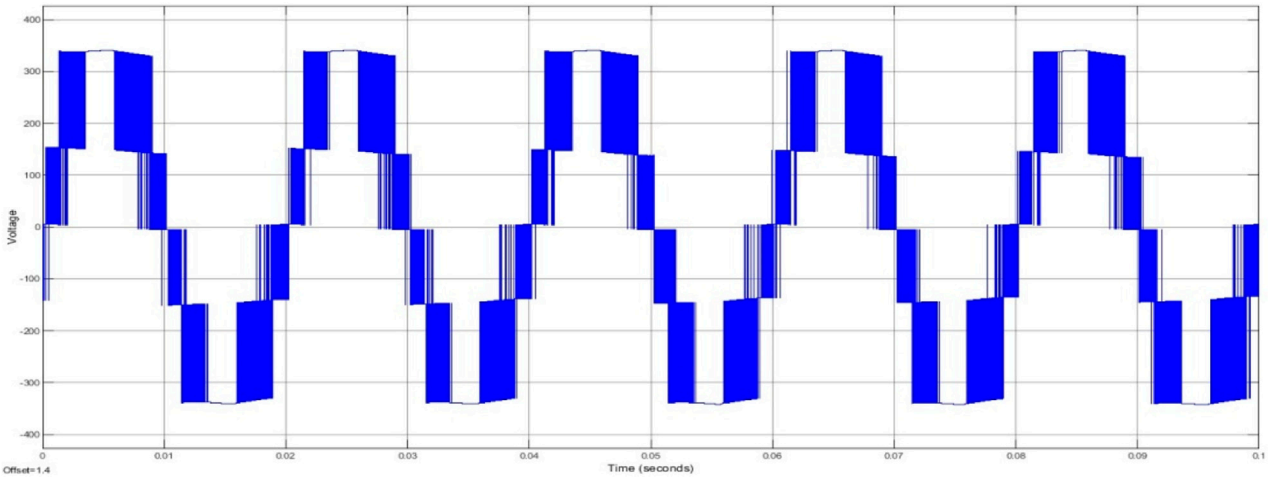

FIGURE 18
Switching voltage of 5L-UPQC.

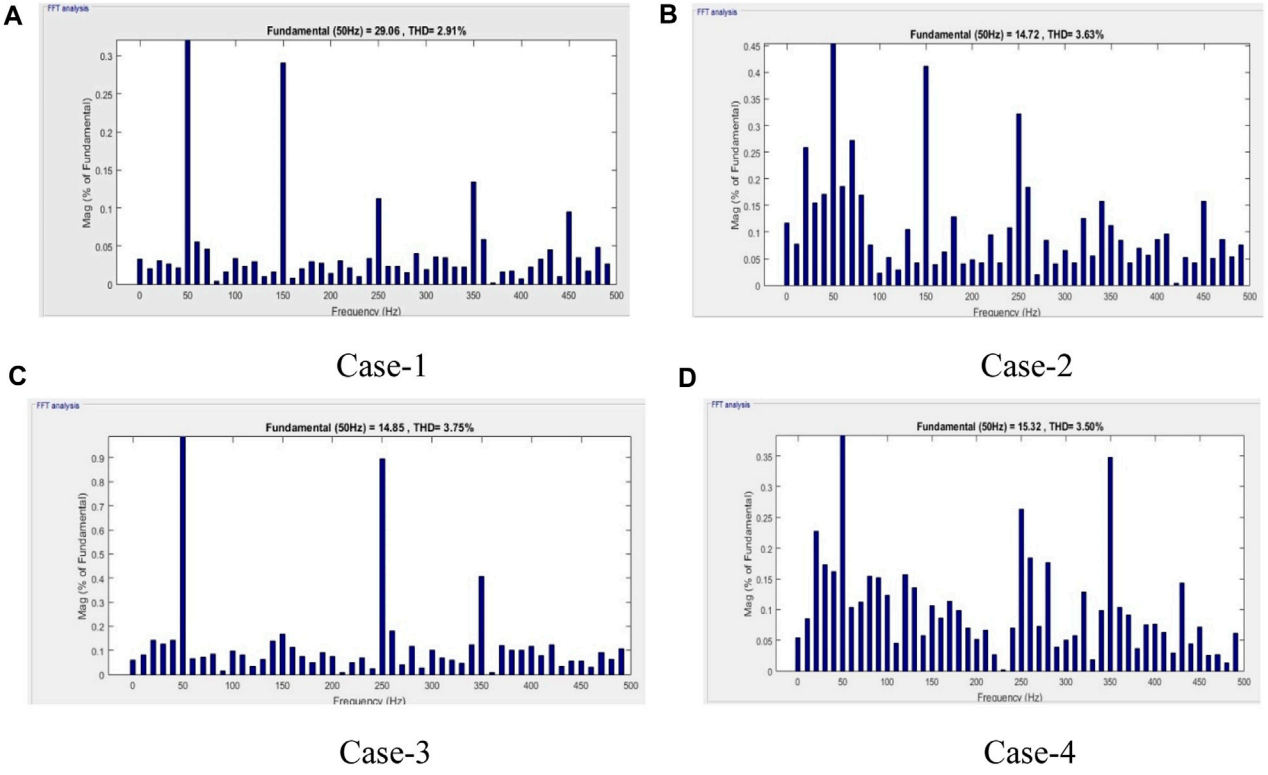

FIGURE 19
THD spectrum.

imperfections in the current waveform. The THD of the current is reduced from 27.90% to 3.75%, and the PF is elevated from 0.8145 to 0.9999. Furthermore, the suggested controller maintains a constant DLCV during variations in the load and solar irradiation, alongside a consistent wind velocity, as depicted in Figure 15C.

In case 4, the source voltage is intentionally set to be unbalanced, and the ANNC-controlled SHAPF adeptly identifies inequalities and successfully rectifies them, as depicted in Figure 16A. In this scenario, the simultaneous connection of loads 1 and 4 results in a contaminated and unbalanced load-current waveform, as illustrated in Figure 16B. However, the proposed SHAPF with FBGO functions efficiently, leading to a reduction in the THD of the current from 19.86% to 3.50% and a rise in the PF from 0.6412 to unity. Furthermore, the suggested controller successfully maintains

a consistent DLCV during load variations, as demonstrated in Figure 16C.

Table 8 provides a comparison of the THD and the PF between the proposed method and other techniques such as SRFT and pq theories with 5L and three levels of UPQC. Table 8 demonstrates that the proposed method significantly reduces the THD and boosts the PF in comparison to the other approaches. Figure 17 illustrates the convergence graph of the proposed FBGO in comparison to the genetic algorithm (GA) and ACO. This plot clearly demonstrates that the proposed FBGO achieves the lowest THD value in just 17 iterations, which is notably less when compared to the GA (62 iterations) and ACO (43 iterations). Moreover, Table 9 provides the optimized values of control variables. The output voltage of five-level UPQC is represented in Figure 18. Lastly, Figure 19 presents the FFT analysis of the current for the proposed system in the second case.

6 Conclusion

In this research, an approach based on ANNC is introduced for a 5L-UPQC interconnected with solar, wind, and battery sources. The ANN controller, trained with the Levenberg–Marquardt algorithm, is employed within the UPQC system to generate reference signals for the converters. This obviates the need for conventional transformations, like abc, dq0, and αβ. Furthermore, the optimization of filter parameters is achieved through football game optimization, and an ANFIS is proposed for the SHAPF to maintain a stable DLCV balance. The proposed 5L-UPQC system effectively sustains a constant DLCV, despite variations in loads, solar irradiation, and wind conditions. It successfully mitigates current harmonics, enhances the shape of the current waveform, resulting in an improved power factor, and effectively eliminates fluctuations in the grid voltage, such as interruptions, sags, swells, and disturbances. In the future, this approach can be extended to multilevel UPQC systems employing reduced switches.

Data availability statement

The raw data supporting the conclusion of this article will be made available by the authors, without undue reservation.

Author contributions

KS: conceptualization, investigation, methodology, and writing–original draft. GR: formal analysis, software, and writing–review and editing. PB: formal analysis, investigation, resources, software, supervision, and writing–review and editing. TS: funding acquisition, resources, visualization, and writing–review and editing.

Funding

The author(s) declare that no financial support was received for the research, authorship, and/or publication of this article.

Conflict of interest

The authors declare that the research was conducted in the absence of any commercial or financial relationships that could be construed as a potential conflict of interest.

Publisher's note

References

Belqasem, A., Rameshkumar, K., Vairavasundaram, I., and Ramachandran, S. (2022). A novel single-phase shunt active power filter with a cost function based model predictive current control technique. *Energies* 15, 4531. doi:10.3390/en15134531

Chandrasekaran, K., Selvaraj, J., Clement Raj Amaladoss, L. V., and Veerapan, L. (2021). Hybrid renewable energy based smart grid system for reactive power management and voltage profile enhancement using artificial neural network. *Energy Sources, Part A Recovery, Util. Environ. Eff.* 43 (No. 19), 2419–2442. doi:10.1080/15567036.2021.1902430

DheyaaIed, M., and Goksu, G. (2022). Design and control of three-phase power system with wind power using unified power quality conditioner. *Energies* 15, 7074. doi:10.3390/en15197074

Ganesan, A., and Srinath, S. (2019). Optimal controller for mitigation of harmonics in hybrid shunt active power filter connected distribution system: an EGOANN technique. *J. Renew. Sustain. Energy* 11. doi:10.1063/1.5085028

Hassan, K., Makdisie, C., IssamHoussamo, and Mohammed, N. (2022). New modulation technique in smart grid interfaced multilevel UPQC-PV controlled via fuzzy logic controller. *Electronics* 11, 919. doi:10.3390/electronics11060919

Imam, A. A., Kumar, R. S., and Yusuf, A. (2020). Modeling and simulation of a PI controlled shunt active power filter for power quality enhancement based on P-Q theory. *Electronics* 9, 637. doi:10.3390/electronics9040637

Khosravi, N., Abdolmohammadi, H. R., Bagheri, S., and Miveh, M. R. (2021). Improvement of harmonic conditions in the AC/DC microgrids with the presence of filter compensation modules. *Renew. Sustain. Energy Rev.* 143, 110898. doi:10.1016/j.rser.2021.110898

Khosravi, N., Echalih, S., Hekss, Z., Baghbanzadeh, R., Messaoudi, M., and Shahideipour, M. (2023). A new approach to enhance the operation of M-UPQC proportional-integral multiresonant controller based on the optimization methods for a stand-alone AC microgrid. *IEEE Trans. Power Electron.* 38 (3), 3765–3774. doi:10.1109/TPEL.2022.3217964

Koganti, S., Sujatha, C. N., Kumar Balachandran, P., Mihet-Popa, L., and Kumar, N. U. (2022). Optimal design of an artificial intelligence controller for solar-battery integrated UPQC in three phase distribution networks. *Sustainability* 14 (21), 13992. doi:10.3390/su142113992

KogantiKrishna, S. J. K., and Reddy Salkuti, S. (2022). Design of multi-objective-based artificial intelligence controller for wind/battery-connected shunt active power filter. *Algorithms* 15 (8), 256. doi:10.3390/a15080256

Lin, T.-C., and Simachew, B. (2022). Intelligent tuned hybrid power filter with fuzzy-PI control. *Energies* 15, 4371. doi:10.3390/en15124371

Mansoor, M. A., Hasan, K., Othman, M. M., Noor, S. Z. B. M., and Musirin, I. (2023). Construction and performance investigation of three phase solar PV and battery energy storage system integrated UPQC. *IEEE Accesses* 8, 103511–103538. doi:10.1109/ACCESS.2020.2997056

Marcel, N., Claudiu-Ionel, N., Dumitru, S., and Adrian, V. (2023). Comparative performance of UPQC control system based on PI-GWO, fractional order controllers, and reinforcement learning agent. *Electronics* 12, 494. doi:10.3390/electronics12030494

Mishra, A. K., Soumya, R. D., Prakash, K., Mohanty, A., and Mishra, D. K. (2020). PSO-GWO optimized fractional order PID based hybrid shunt active power filter for

power quality improvements. *IEEE Access* 8, 74497–74512. doi:10.1109/access.2020.2988611

Mishra, A. K., Soumya, R. D., Ray, P. K., Kumar Mallick, R., Mohanty, A., and Dillip, K. (2022). PS-O-GW-O optimized fractional order PID based hybrid shunt active power filter for power quality improvements. *IEEE Access* 8, 74497–74512. doi:10.1109/access.2020.2988611

NafehHeikalEl-Sehiemy, A. A. A. R. A., and Salem, W. A. A. (2022). Intelligent fuzzy-based controllers for voltage stability enhancement of AC-DC micro-grid with D-STATCOM. *D-STATCOM* 61 (3), 2260–2293. doi:10.1016/j.aej.2021.07.012

Okech, E. O., Zhang-Hui, L., Mali, X., Kamaraj, P., and Alukaka, J. R. (2022). Neural network controlled solar PV battery powered unified power quality conditioner for grid connected operation. *Energies* 15, 6825. doi:10.3390/en15186825

Pazhanimuthu, C., and Ramesh, S. (2018). Grid integration of renewable energy sources (RES) for power quality improvement using adaptive fuzzy logic controller based series hybrid active power filter (SHAPF). *J. Intelligent Fuzzy Syst.* 35, 749–766. doi:10.3233/jifs-171236

Rajesh, P., Shajin, F. H., and Umasankar, L. (2021). A novel control scheme for PV/wt/FC/battery to power quality enhancement in micro grid system: a hybrid technique. *Energy Sources, Part A Recovery, Util. Environ. Eff.* 1–17. doi:10.1080/15567036.2021.1943068

Ramadevi, A., Srilakshmi, K., Kumar, P., Colak, I., Dhanamjayulu, C., and Khan, B. 2023, Optimal design and performance investigation of artificial neural network controller for solar- and battery-connected unified power quality conditioner. *Int. J. Energy Res.* 2023, 1-22. doi:10.1155/2023/3355124

Renduchintala, U. K., Pang, C., Tatikonda, K. M., and Yang, L. (2021). ANFIS-Fuzzy logic based UPQC in interconnected microgrid distribution systems: modeling, simulation and implementation. *J. Eng.* 2021, 6–18. doi:10.1049/tje2.12005

Sahithullah, M., Kumar Ajithan, S., and Jayaraman, S. (2019). Optimal design of shunt active power filter for power quality enhancement using predator-prey based firefly optimization. *Swarm Evol. Comput.* 44, 522–533. doi:10.1016/j.swevo.2018.06.008

Sakthivel, A., Vijayakumar, P., SenthilkumarLakshminarasimman, A. L., and Paramasivam, S. (2015). Experimental investigations on ant colony optimized pi control algorithm for shunt active power filter to improve power quality. *Control Eng. Pract.* 42 (42), 153–169. doi:10.1016/j.conengprac.2015.04.013

Sarker, K., Chatterjee, D., and Goswami, S. K. (2020). A modified PV-wind-PEMFCS-based hybrid UPQC system with combined DVR/STATCOM operation by harmonic compensation. *Int. J. Model. Simul.* 41 (No.4), 243–255. doi:10.1080/02286203.2020.1727134

Sayed, J. A., Sabha, R. A., and Ranjan, K. J. (2021). Biogeography based optimization strategy for UPQC PI tuning on full order adaptive observer based control. *IET Generation, Transm. Distribution* 15, 279–293. doi:10.1049/gtd2.12020

Srilakshmi, K., Jyothi, K. K., Kalyani, G., and Sai Prakash Goud, Y. (2023). Design of UPQC with solar PV and battery storage systems for power quality improvement. *Cybern. Syst. Int. J.*, 1–30. doi:10.1080/01969722.2023.2175144

Srilakshmi, K., Srinivas, N., Balachandran, P. K., Reddy, J. G. P., Gaddameedhi, S., Valluri, N., et al. (2022). Design of soccer league optimization based hybrid controller for solar-battery integrated UPQC. *IEEE Access* 10, 107116–107136. doi:10.1109/access.2022.3211504

Sudheer, V., and Kota, V. R. (2017). Implementation of artificial neural network based controller for a five-level converter based UPQC. *Alexandria Eng. J.* 57 (Issue 3), 1475–1488. doi:10.1016/j.aej.2017.03.027

Szromba, A. (2020). The unified power quality conditioner control method based on the equivalent conductance signals of the compensated load. *Energies*, 13.

Yang, D., MaGaoMa, Z. X. Z., and Cui, E. (2019). Control strategy of intergrated photovoltaic-UPQC system for DC-bus voltage stability and voltage sags compensation. *Energies* 12, 4009. doi:10.3390/en12204009

Yap, H., MohdRadzi, M. A., Hassan, M. K., and Mailah, N. F. (2017). Control algorithms of shunt active power filter for harmonics mitigation: a review. *Energies* 10 (No.12), 2038. 2038. doi:10.3390/en10122038

Yap, H., MohdRadzi, M. A., Zainuri, M. A. A. M., and Md Zawawi, M. A. (2019). Shunt active power filter: a review on phase synchronization control techniques. *Electronics* 8, 791. doi:10.3390/electronics8070791

Zhao, X., Chai, X., Guo, X., Ahmad, W., Wang, X., and Zhang, C. (2021). Impedance matching-based power flow analysis for UPQC in three-phase four-wire systems. *Energies* 14, 2702. doi:10.3390/en14092702

Zhou, M., Wan, J.-Ru, Wei, Z.-Q., and Cui, J. (2006). "Control method for power quality compensation based on levenberg-marquardt optimized BP neural networks," in 2006 CES/IEEE 5th International Power Electronics and Motion Control Conference, Shanghai, China, August, 2006.

Nomenclature

5L-UPQC	**Five-level UPQC**
FBGO	Football game optimization
NCS	Non-conventional sources
PV	Photovoltaic
BSS	Battery storage system
PQ	Power quality
WPGS	Wind power generation system
ANN	Artificial neural network
UPQC	Unified power quality conditioner
LMBP	Levenberg–Marquardt backpropagation
ANFIS	Artificial neuro-fuzzy interface system
pq	Instantaneous reactive power
DLCV	Direct-current link capacitor voltage
SRFT	Synchronous reference frame theory
THD	Total harmonic distortion
PF	Power factor
GA	Genetic algorithm
PSO	Particle swarm optimization
PIC	Proportional integral controller
SHAPF	Shunt active power filter
GWO	Gray wolf optimization
PWM	Pulse-width modulation
BBC	Buck–boost converter
SMC	Sliding mode control
FLC	Fuzzy logic controller
VSC	Voltage source converter
MSE	Mean-square error
BBO	Biogeography-based optimization
SeAF	Series-active power filter
BC	Boost converter
ACO	Ant colony optimization
SCC	Short-circuit current
FOPID	Fractional-order proportional integral derivate
MSF	Membership function
FF-ANN	Firefly-based ANN
PPFFA	Predator–prey firefly algorithm
SPVGS	Solar photovoltaic power generation system
$\mathbf{V_{LL}}$	Line-to-line rms voltage
CE	Change in error
OL	Output layer of the ANN
IL	Input layer of the ANN
HL	Hidden layer of the ANN
E	Error
PEF	Performance function
PF	Power factor
HD	Hyper distance
CM	Coach's memory
L_{se}	SeAF inductance
V_{S_abc}	Source voltage for abc phases
V_m	Peak voltage of the system
$R_S L_S$	Grid resistance and inductance
m	Modulation index
V_{l_abc}	Load voltage for phases a, b, and c
C_{dc}	DC-link capacitance
V_{se_abc}	Voltage injected by the series filter in abc
$V_{se\_abc}^{ref}$	Reference compensated voltage in abc phases
i_{S_abc}	Source current for abc phases
i_{l_abc}	Load current for abc phases
R_{sh}	SHAPF resistance
$f_{sh} f_{se}$	Switching frequency
$V_{cr,pp}$	Peak-to-peak voltage ripple
V_{dc}	DC-link voltage
a_f	Overloading factor
V_{dc}^{ref}	Reference DLCV
i_{sh_abc}	Shunt filter compensated current in abc phases
Δi_{dc}	DC-link output error
$i_{sh\_abc}^{ref}$	Shunt filter reference compensated current in abc phases
i_{dc}^{ref}	Reference DC current
R_{se}	SeAF resistance
$V_{dc,err}$	DLCV error
$i_{BS,er}{}^{*}$	Reference battery error current
i_{ph}	Photocurrent source
i_{PV}	PV cell output current
L_{sh}	SHAPF inductance
i_d	Forward diode-carrying current
P_{dc}	DC-link power
$\mu_{Ai} \mu_{Bi}$	Membership functions of fuzzy
SOCOB	State of charge of the battery
$P^t{}_i$	$P^t{}_i$ indicates the ith position of the player
δ, γ	Random numbers
σ_i	Step size
Θ	Constant
$\mathbf{P^t{}_B}$	Position of the player containing the ball at the instant t

frontiers | Frontiers in Energy Research

TYPE Original Research
PUBLISHED 01 March 2024
DOI 10.3389/fenrg.2024.1335111

OPEN ACCESS

EDITED BY
Sudhakar Kumarasamy,
Universiti Malaysia Pahang, Malaysia

REVIEWED BY
Priya Ranjan Satpathy,
Council of Scientific and Industrial Research (CSIR), India
Surender Reddy Salkuti,
Woosong University, Republic of Korea

*CORRESPONDENCE
Praveen Kumar Balachandran,
praveenbala038@gmail.com
Devakirubakaran Samithas,
kirubathas@gmail.com

RECEIVED 08 November 2023
ACCEPTED 15 February 2024
PUBLISHED 01 March 2024

CITATION
Aljafari B, Balachandran PK, Samithas D, Thanikanti SB and Nwulu NI (2024), Modeling and simulation of a Renzoku puzzle pattern-based PV array configuration for a partially shaded PV system.
Front. Energy Res. 12:1335111.
doi: 10.3389/fenrg.2024.1335111

Modeling and simulation of a Renzoku puzzle pattern-based PV array configuration for a partially shaded PV system

Belqasem Aljafari[1], Praveen Kumar Balachandran[2]*, Devakirubakaran Samithas[3,4]*, Sudhakar Babu Thanikanti[5] and Nnamdi I. Nwulu[6]

[1]Department of Electrical Engineering, College of Engineering, Najran University, Najran, Saudi Arabia, [2]Department of Electrical and Electronics Engineering, Vardhaman College of Engineering, Hyderabad, India, [3]Center for Electric Mobility, Department of Electrical and Electronics Engineering, SRM Institute of Science and Technology, Chennai, Tamil Nadu, India, [4]Center for Nonlinear Systems, Chennai Institute of Technology, Chennai, India, [5]Department of Electrical and Electronics Engineering, Chaitanya Bharathi Institute of Technology, Hyderabad, India, [6]Center for Cyber Physical Food, Energy and Water Systems, University of Johannesburg, Johannesburg, South Africa

The world depends heavily on electrical energy for accessing technologies. For the generation of electricity, technology can utilize renewable energy sources like solar energy and wind energy. Solar photovoltaic (PV) systems occupy space among consumers due to their feasibility, flexibility, cost, and simple implementation procedures. The solar PV system experiences many factors causing power loss like partial shading, hotspots, and diode failure. In this work, a new static PV array configuration, named Renzoku puzzle pattern-based array configuration, is proposed. This proposed configuration technique was designed to overcome the drawbacks of the previously proposed array configurations in terms of power generation, fewer mismatch losses, a high shade-dispersion rate, and consistent performance under any level of partial shading. The proposed array configuration has been validated using both simulation and hardware. The simulation is carried out in a 9 × 9 PV array in MATLAB/Simulink®. The performance analysis, results, and corresponding characteristic curves are presented in this manuscript.

KEYWORDS

photovoltaic effect, mismatch loss, compensation current, partial shading, reconfiguration, puzzle pattern

1 Introduction

Due to fossil fuel depletion and the global shift to low-carbon energy, distributed renewable energy generation has increased over the past decade (Viebahn et al., 2015; Bryant et al., 2024). In 2021, China's National Energy Administration reported 107.5 GW of distributed solar energy generation infrastructure, an increase of 29 GW from 2020 (Wang et al., 2024). Distributed PV solar power generation is becoming more important in green energy (Yang et al., 2020).

Despite their importance, distributed photovoltaic (PV) systems face technical challenges, especially array mismatch losses. These losses occur when the PV module current–voltage (I–V) characteristics vary within an array. Connecting PV modules in series

can limit current to the lowest-current module, causing mismatch losses that reduce PV array power generation. Mismatch losses introduce multiple power–voltage (P–V) peaks, complicating maximum power point tracking (Lappalainen and Valkealahti, 2017).

In order to ensure dependable operation and maximize power generation, monitoring a PV system is essential (Alwar et al., 2022). This monitoring also enables performance evaluation and troubleshooting (Aghaei et al., 2020). For the purpose of this study, field sensors were utilized to perform real-time measurements of the voltage and current of PV modules. Maximizing power generation under mismatched loss conditions is the goal of the dynamic topology optimization that has been proposed (Devakirubakaran et al., 2023). This optimization will influence the awareness of PV system generation systems.

The reconfiguration of PV arrays is an efficient method for preventing mismatch losses in total-cross-tied (TCT) and series–parallel (SP) topologies when mismatch conditions (MCs) are present (Mohammadnejad et al., 2016; Pendem and Mikkili, 2018; Sagar et al., 2020; Ye et al., 2023). This strategy involves modifying the interconnections between PV modules in accordance with the levels of irradiance, with the goals of lowering mismatch losses and improving the performance of the PV systems. In the TCT topology, photovoltaic modules are connected in parallel and series rows, whereas in the SP topology, PV modules are connected in series and PV strings are connected in parallel. These strategies included both physical relocation and electrical array reconfiguration.

In order to physically relocate photovoltaic modules, it is necessary to move them without affecting their electrical connections (Srinivasan et al., 2020). For the purpose of distributing shading effects across the PV array, a pattern that can be reconfigured is utilized during the installation process (Prince Winston et al., 2020a; Prince Winston et al., 2020b). When it comes to physical relocation reconfiguration, the Sudoku puzzle method is a well-known approach that has been demonstrated in references. Through the process of rearranging modules, this technique enhances the generation of power in partially shaded, 9 × 9 TCT-interconnected photovoltaic arrays. It is important to note that the effectiveness of the Sudoku-based reconfiguration is limited because it can only move PV modules in columns and not rows. Other puzzle-based methods, such as Futoshiki and Magic Square, are capable of exhibiting limitations that are comparable to these. On the other hand, a dominance square-based array reconfiguration scheme (Dhanalakshmi and Rajasekar, 2018a; Dhanalakshmi and Rajasekar, 2018b) was proposed in the reference for a 5 × 5 TCT topology. This scheme offers a novel approach in comparison to different solutions that have been proposed in the past. Additionally, the Calcudoku method (Aljafari et al., 2023) and competence square arrangement method (Dhanalakshmi and Rajasekar, 2018a), spiral pattern-based configuration (Cherukuri et al., 2021), and L-shaped propagated array configuration (Srinivasan et al., 2021), as demonstrated in reference, outperformed the dominance square solution. Another innovative approach that was proposed in the reference involves the arrangement of photovoltaic arrays numerically and alphabetically in order to reduce shading effects and distribute shadow patterns.

Reconfigurations that are based on physical relocation, such as Sudoku, Competence Square, and Dominance Square, have their limitations. They require modules to be arranged in rows and columns that are equal, which may not be possible given the actual layout of the PV array. In addition, photovoltaic modules undergo non-uniform aging, which results in a gradual decrease in power generation over time. It is necessary to perform periodic physical reconfigurations as a result of this, which results in high labor costs. These methods lack the flexibility to address the impact of multiple partial shadows and random module defects on PV arrays.

On the other hand, environmental or electric parameter-based array reconfiguration (EAR) strategies make use of switches in order to alter the electrical connection of the photovoltaic array. Through the utilization of global EAR strategies such as particle swarm optimization and genetic algorithms, every module is able to switch electrical connections, thereby increasing the amount of power that is produced (Babu et al., 2018; Durango-Flórez et al., 2022). These techniques, on the other hand, call for a greater number of switches and more complex control algorithms, which drive up the costs. Local reconfiguration, which makes use of a switching matrix to connect adaptive modules with different electrical connections to fixed modules, has the potential to reduce the number of switches; however, it may not be effective in areas with large shadows or in situations where fixed modules have shadows. The uncertain power generation affects the stability of the grid, which also requires power management algorithms (Prasad et al., 2022).

To summarize, physical relocation is a simple option that does not necessitate the utilization of switches or sensors. However, due to the uneven aging of PV modules, it necessitates repeated efforts. When it is functioning under MCs, its effectiveness is hindered by a number of issues, such as the presence of various shadows, the presence of non-uniform aging, and the failure of modules (Thanikanti et al., 2023). Even in the presence of significant shading, its utility is limited because of these concerns. It is necessary to conduct additional studies into the EAR technique in order to reduce the number of switches that are utilized and improve the efficiency of power generation under the majority of mechanical configurations.

The contribution of this work to the field is the development of a novel array configuration approach that is inspired by the concept of the Renzoku puzzle pattern. The term “Renzoku” comes from the Japanese phrase “to the neighbors,” and this pattern is similar to puzzles such as Futoshiki, in which the number that is closest to the player is selected to be the surrounding shell. Using this method, the array layout chooses the photovoltaic modules that are closest to each other and have optimal spacing between them, much like solving a square puzzle. Certain rules define the pattern of the Renzoku puzzle, which are as follows:

- The numbers range from one to the size of the grid; for example, for a 9 × 9 puzzle, the numbers run from one to nine.
- Only one instance of any number can be found in each row and in any given column.
- In the event that there is a dot between two cells, it signifies that the numbers included within those cells should be consecutive; otherwise, they should not be sequential.
- After numeral 9, letters such as A, B, and C are utilized for more complex puzzles.

The array layout approach that has been developed optimizes the arrangement of photovoltaic modules by applying these

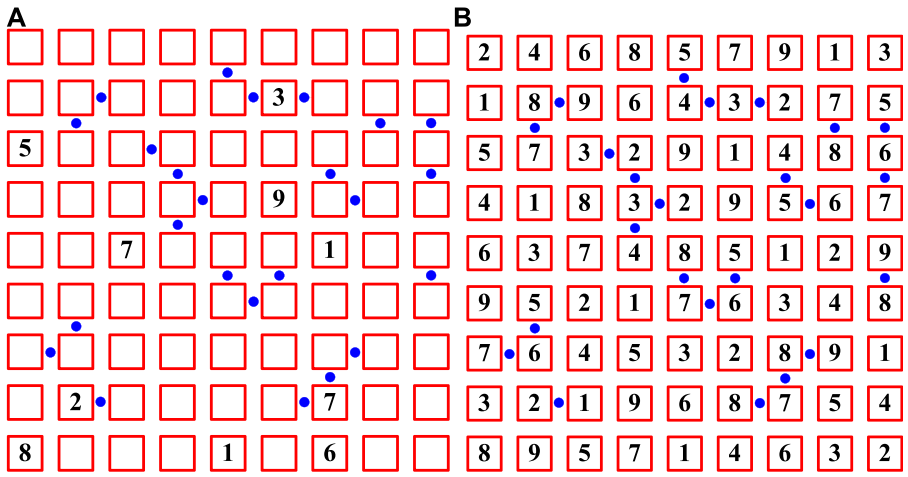

FIGURE 1
(A) 9 × 9 Renzoku puzzle; **(B)** solved 9 × 9 Renzoku puzzle.

guidelines. This ensures that space is utilized effectively and improves the overall performance of the photovoltaic system. This novel methodology provides a strategy that is both systematic and structured for array setup, which makes it possible to improve power generation in a variety of applications.

The remainder of this research article is arranged as follows: Section 2 describes the proposed methodology; Section 3 presents the performance analysis of the proposed array configuration, including power output, efficiency, and the percentage of mismatch loss generation; and finally, Section 4 concludes the research article.

1.1 Proposed Renzoku PV array configuration

The amount of photovoltaic power generated is directly proportional to the amount of direct sunlight that reaches the panel surface. The direction of the sunlight, or the number of photons striking the PV surface, determines the number of free electrons released from the PV cell. Eq. 1 provides a PV cell current output equation (Nguyen and Nguyen, 2015; Ma et al., 2019). When several cells or modules are linked in series, Eq. 2 indicates the current output.

$$I_m = I_L - I_{sat}\left[exp\left(\frac{V + IR_s}{nN_sV_{th}}\right) - 1\right] - \frac{V + IR_s}{R_{sh}}. \quad (1)$$

The voltage is added in series and the current is added in parallel on the different connections of PV cells connected as an array.

$$I_{maximum} = \text{minimum}\,(I_{PV}). \quad (2)$$

When multiple cells are connected in series and a single PV module is affected by the partial shading, it alone operates with the minimum current. This current will be available at the output terminal as per Equation 2. The entire row's current will be reduced due to the shaded panel.

The proposed array configuration is framed based on the Renzoku puzzle pattern. Renzoku means "to the neighbors," whereas this puzzling pattern is like Futoshiki, and the rule chooses the nearest number as the neighbor shell. So, this form of array configuration selects the nearest PV modules with the optimum distance. This puzzling pattern can be applied to any kind of square puzzle. The Renzoku puzzle has certain rules, as follows:

- The numbers range from one to the size of the grid; for example, one to nine for a 9 × 9 puzzle.
- Each number must appear just once in each row and column.
- A dot between two cells signifies that the numbers in those cells should be sequential. The numerals should not be sequential if there is no dot.
- For larger problems, the letters (A, B, C, and so on) come after the digit 9.

In this work, a 9 × 9 PV array has been selected for testing and analyzing the proposed Renzoku puzzle pattern-based PV array configuration. An unsolved 9 × 9 Renzoku puzzle is shown in Figure 1A. Only eight squares among the ninety-one squares had the values, and the values of other squares needed to be obtained by solving the puzzle. The only clue for solving the puzzles is to follow the dots placed between the squares. In this puzzle, the square at the position of the second row and sixth column has a value of 3, surrounded by dots. These dots indicate the neighboring cells, i.e., 27 and 25 should be 2 or 4. By following these dots, the entire puzzle can be solved. Figure 1B shows the solved 9 × 9 Renzoku puzzle. The puzzle should be solved based on the dots and the rules of Renzoku puzzles. The array formation on the Renzoku puzzle can be done by adding a number ranging from 1 to the size of the grid in each column. Figure 2 shows the final matrix diagram of the 9 × 9 PV array. The proposed array configuration has been validated using the MATLAB/Simulink® model. The performance of the proposed array configuration has been compared with the conventional array configurations.

The Renzoku puzzle pattern-based configuration can be defined by the following steps:

21	42	63	84	55	76	97	18	39
11	82	93	64	45	36	27	78	59
51	72	33	24	95	16	47	88	69
41	12	83	34	25	96	57	68	79
61	32	73	44	85	56	17	28	99
91	52	23	14	75	66	37	48	89
71	62	43	54	35	26	87	98	19
31	22	13	94	65	86	77	58	49
81	92	53	74	15	46	67	38	29

FIGURE 2
Matrix diagram of the 9 × 9 PV array from the Renzoku puzzle pattern.

- Define the grid size: determine the size of the grid based on the number of PV modules that are available or planned to be installed. For example, a 9 × 9 grid will have 81 PV modules.
- Assign numbers to PV modules: assign numbers to each PV module in the grid, starting from 1 and ranging up to the size of the grid. For a 9 × 9 grid, the numbers will range from 1 to 81.
- Ensure unique numbers: ensure that each number appears only once in each row and column of the grid. This ensures that each PV module is uniquely identified within the array.
- Sequential numbers: place a dot between two cells to indicate that the numbers in those cells should be sequential. This helps in arranging the PV modules in a sequential order, optimizing the distance between them.
- Arrange PV modules: arrange the PV modules in the grid according to the Renzoku puzzle pattern. Start with the nearest number as the neighbor shell, ensuring that the distance between neighboring PV modules is optimal.
- Extend to larger problems: for larger PV arrays, use letters (A, B, C, and so on) after the digit 9 to continue the numbering sequence. Ensure that each letter is used only once in each row and column, similar to the numbering scheme for smaller grids.
- Iterate for optimization: iterate over the array configuration to optimize the placement of PV modules, ensuring maximum efficiency and power generation.

2 Simulation model and shading patterns

The simulation of the PV cell is performed using the mathematical equation of the single-diode model. Figure 3A illustrates the Simulink model of a single PV cell, depicting specifications such as short circuit current (ISC), open circuit voltage (VOC), maximum output current (IM), maximum output power (PM), temperature (T), and irradiation (S). Figure 3B shows the simulink model of the proposed array configuration with other conventional configurations. The PV cells are interconnected in series and parallel based on the desired configuration. Figure 4B showcases a 9 × 9 PV array with different array configurations, including series–parallel (S-PAC), total cross-tied (TCT-AC), Sudoku puzzle array configuration (SUPAC), L-shaped propagated array configuration (LSPAC), and the proposed Renzoku puzzle pattern array configuration (RPPAC). The interconnections between the PV cells vary depending on the array configuration type. The irradiation block represents the input irradiation value for the PV array. Within this block, the shading pattern is created, and the irradiation is distributed to the PV modules using the Goto blocks in Simulink.

3 Results and analysis

The proposed Renzoku puzzle pattern array configuration's performance was evaluated under eight different shading conditions, which are commonly encountered. The shading conditions are depicted in Figure 4. Figure 4A represents random shading, where shading occurs sporadically without any uniform pattern due to temporary objects obstructing sunlight from reaching the PV surface. The extent of shading can vary between 5% and 80%, depending on the type of object causing the shading. Figure 4B illustrates diagonal shading caused by taller and narrower objects positioned near the PV system. This type of shading results in one shaded panel in each row and column, leading to increased mismatch losses due to varying irradiation levels across rows and columns. L-shaped shading conditions are shown in Figure 4C, causing shading in each row and column. This shading pattern significantly impacts the performance of all array configurations, particularly series–parallel and TCT, due to the high shading levels in rows and columns. The Sudoku and L-shaped array configurations can mitigate this issue to some extent. It is essential to assess the performance of the proposed configuration under this shading condition to determine its effectiveness. The frame shading condition, illustrated in Figure 4D, shades all sides of the PV array. Under this shading condition, the series–parallel and TCT configurations exhibit high mismatch losses. On the other hand, the Sudoku, L-shaped, and proposed array configurations demonstrate better resistance to this shading condition and generate higher power output.

The short and narrow shading condition is depicted in Figure 4E, which occurs when nearby buildings, towers, trees, or new infrastructure cast shadows. The shading conditions are further classified based on their length and breadth into short and narrow (SN), short and wide (SW), long and narrow (LN), and long and wide (LW). Figure 4F illustrates the short and wide shading condition, where the breadth of the object causing the shade is greater compared to the short and narrow shading condition. Similarly, Figures 4G, H represent the shading

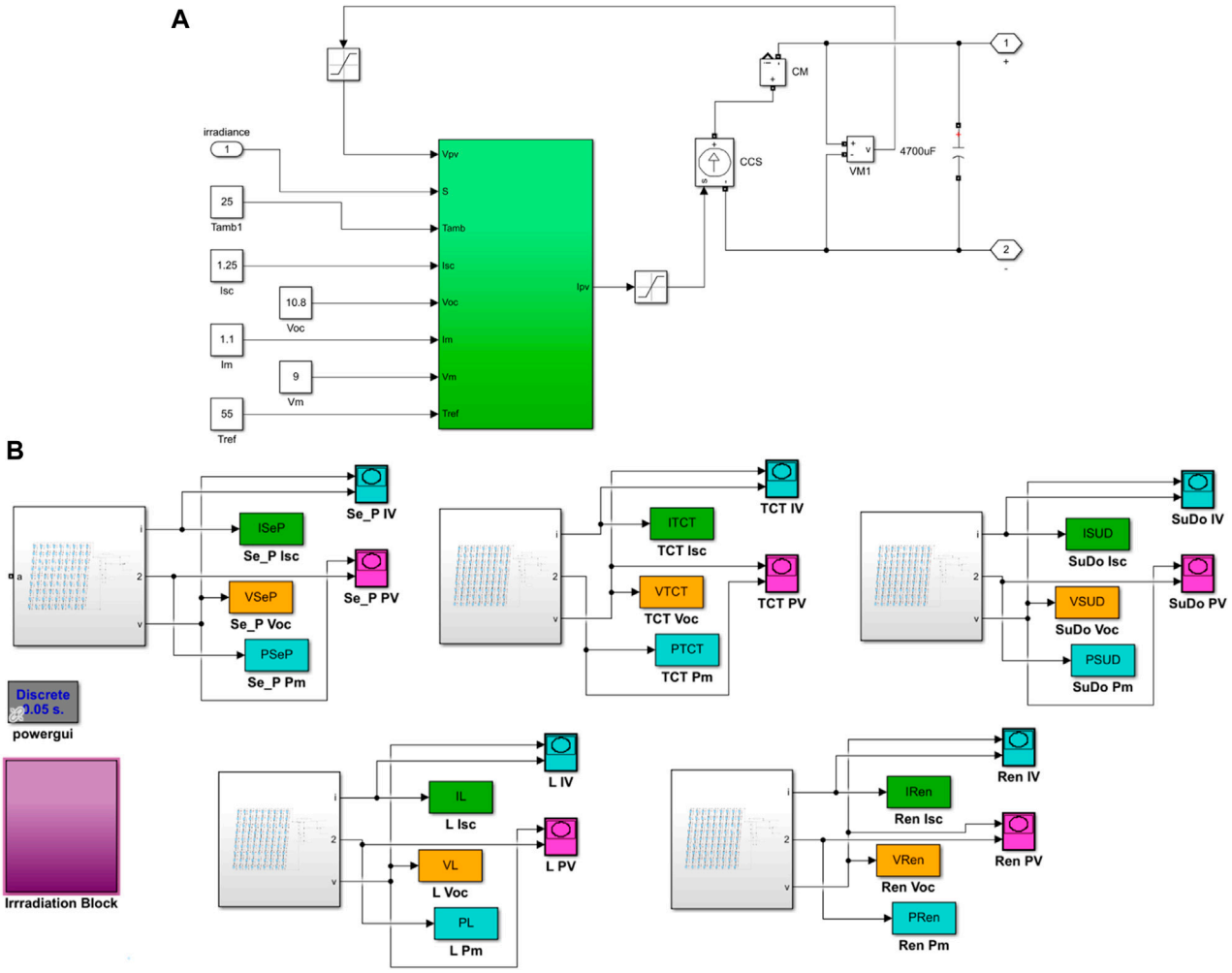

FIGURE 3
(A) Simulink of a single diode model of a PV cell. **(B)** Simulink model of the proposed array configuration with conventional configurations.

conditions of long and narrow and long and wide conditions, respectively. The LN and LW shading conditions involve objects or shade-causing elements with extended height. The shading levels in these four shading conditions are higher and more complex compared to the other shading conditions discussed previously. Conventional array configurations, such as series–parallel and total cross-tied configurations, experience greater power losses under these eight shading conditions. On the other hand, recently developed PV array configurations like the Sudoku and L-shaped propagated configurations have shown the ability to reduce power losses compared to conventional methods.

In this work, a comprehensive analysis is conducted on the proposed Renzoku array configuration under these eight shading conditions. The performance of the proposed configuration is compared with four other array configurations, and the corresponding data are presented in Table 1. To validate the performance of the proposed array configuration, measurements were taken for short-circuit current, maximum power output, power conversion efficiency, and mismatch loss between PV rows. These metrics serve as indicators of the performance and effectiveness of the proposed configuration.

The term mismatch loss can be defined as the power difference between the maximum and minimum power-generating PV rows. By measuring the mismatch loss between the PV rows, the shade dispersion level can be measured. The shade dispersion level of the PV array can define the quality of the PV array configuration. If the PV array is operated with the minimum mismatch losses, power generation can be enhanced. In any kind of shading circumstance, the PV array should be operated with the minimum mismatch losses, and the array configuration method that achieves this constraint would be the best PV array configuration.

In the random shading condition, the proposed Renzoku array configuration generates more power compared to the other PV array configurations. It generates 414 W of power, and the mismatch loss is 27.6%. The LSPAC generates an output power of 378 W with a mismatch loss of 27.6%, which is slightly higher than the proposed configuration, and it reflects on the power output. The SUPAC generates the third-highest power generation and is very close to the

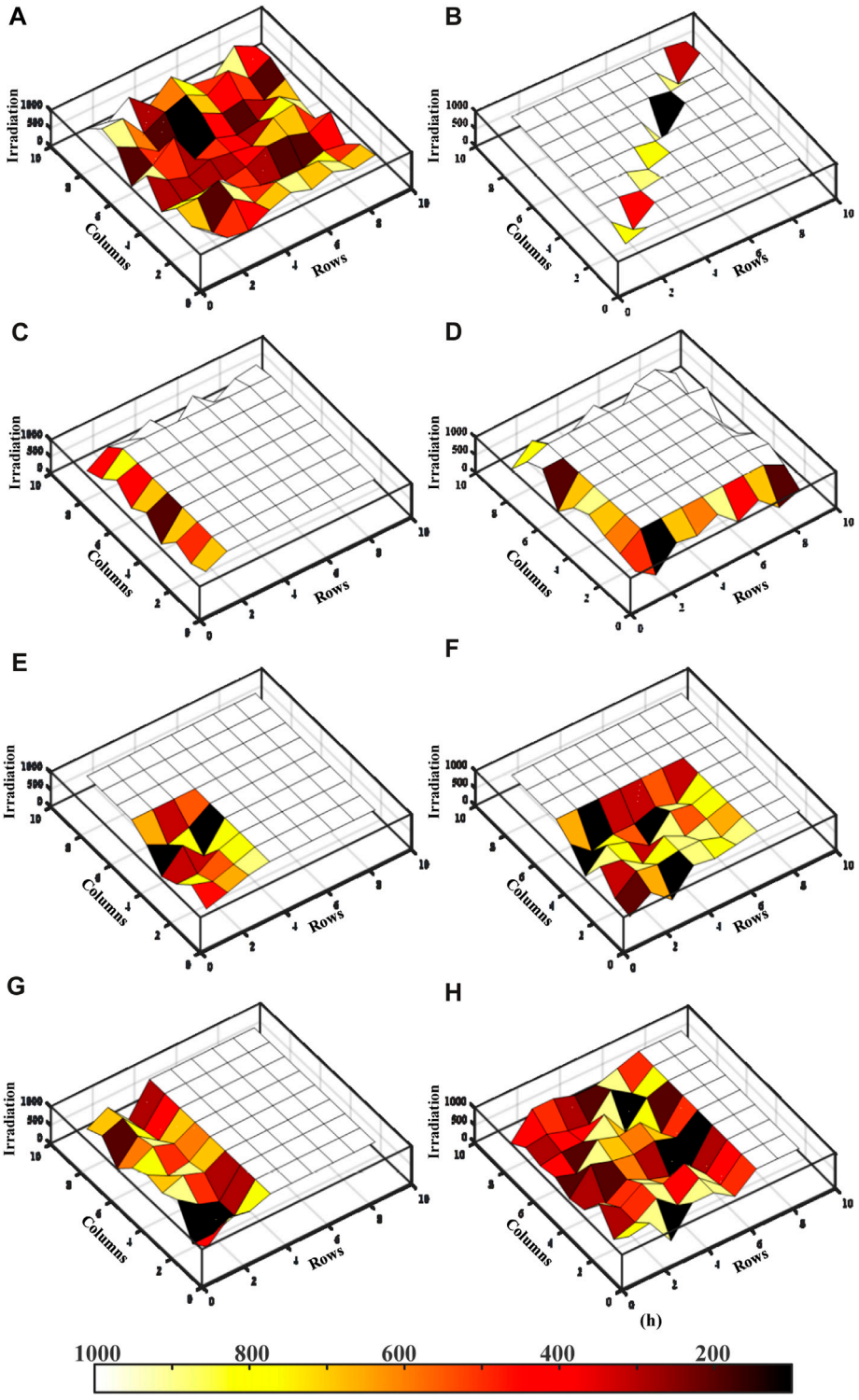

FIGURE 4
(A) Random shading. **(B)** Diagonal shading. **(C)** L-shaped shading. **(D)** Frame shading. **(E)** Short and narrow shading. **(F)** Short and wide shading. **(G)** Long and narrow shading. **(H)** Long and wide shading.

LSPAC, and the power output is 369 W with 35.9% mismatch losses. The TCT-AC and S-PAC configurations generate minimum power, among other configurations. The results of these configurations under random-type shading conditions are given in Table 1, and the corresponding P–V and I–V characteristic curves are shown in Figure 5.

TABLE 1 Performance of the proposed array configurations in different shading types.

S No.	Shade pattern	Array topology	Short-circuit current (ISC)	Output current (IM)	Output power (PM)	Power efficiency (η) (%)	Mismatch power loss (%)	Best configuration
1	Random	S-PAC	2.25	1.98	162	20.0	77.5	RPPAC
		TCT-AC	4.63	4.07	333	41.1	43.9	
		SUPAC	5.13	4.51	369	45.6	35.9	
		LSPAC	5.25	4.62	378	46.7	27.6	
		RPPAC	5.75	5.06	414	51.1	23.3	
2	Diagonal	S-PAC	7.88	6.93	567	70.0	30.0	TCT-AC, LSPAC, and RPPAC
		TCT-AC	10.25	9.02	738	91.1	7.9	
		SUPAC	7.88	6.93	567	70.0	30.0	
		LSPAC	10.25	9.02	738	91.1	7.9	
		RPPAC	10.25	9.02	737	91.1	8.9	
3	L-shaped	S-PAC	6.50	5.72	468	57.8	41.7	SUPAC, LSPAC, and RPPAC
		TCT-AC	6.50	5.72	468	57.8	40.9	
		SUPAC	9.75	8.58	702	86.7	9.3	
		LSPAC	9.75	8.58	702	86.7	9.3	
		RPPAC	9.75	8.58	702	86.7	9.3	
4	Frame	S-PAC	3.75	3.30	270	33.3	66.4	RPPAC
		TCT-AC	5.63	4.95	405	50.0	49.4	
		SUPAC	8.13	7.15	585	72.2	19.8	
		LSPAC	7.75	6.82	558	68.9	24.4	
		RPPAC	8.75	7.70	629	η77.8	15.7	
5	SN	S-PAC	8.50	7.48	612	75.5	24.4	RPPAC
		TCT-AC	9.00	7.92	648	80.0	20.0	
		SUPAC	9.25	8.14	666	82.2	17.8	
		LSPAC	9.50	8.36	684	84.4	13.6	
		RPPAC	9.88	8.69	710	87.8	8.1	
6	SW	S-PAC	6.00	5.28	432	53.3	46.7	RPPAC
		TCT-AC	7.13	6.27	513	63.3	36.7	
		SUPAC	8.00	7.04	576	71.1	25.6	
		LSPAC	9.00	7.92	648	80.0	16.3	
		RPPAC	9.13	8.03	656	81.1	8.8	
7	LN	S-PAC	8.00	7.04	576	71.1	28.1	RPPAC
		TCT-AC	8.13	7.15	585	72.2	21.7	
		SUPAC	8.50	7.48	612	75.5	19.0	
		LSPAC	8.75	7.70	630	77.8	17.6	
		RPPAC	9.13	8.03	656	81.1	9.9	
8	LW	S-PAC	4.75	4.18	342	42.2	56.6	RPPAC
		TCT-AC	5.75	5.06	414	51.1	35.2	

(Continued on following page)

TABLE 1 (*Continued*) Performance of the proposed array configurations in different shading types.

S No.	Shade pattern	Array topology	Short-circuit current (ISC)	Output current (IM)	Output power (PM)	Power efficiency (η) (%)	Mismatch power loss (%)	Best configuration
		SUPAC	6.38	5.61	459	56.7	33.8	
		LSPAC	6.88	6.05	495	61.1	23.6	
		RPPAC	7.50	6.60	539	66.7	11.8	

In the diagonal shading condition, the proposed RPPAC, TCT-AC, and LSPAC configurations perform similarly. The diagonal shading pattern shades only one PV module in one PV row. Therefore, the shade dispersion in the TCT-AC, LSPAC, and proposed RPPAC is almost equal, whereas the SUPAC and S-PAC are highly influenced by this shading pattern due to the shade accumulation on a single row of the SUPAC and shade accumulation on each column of the S-PAC. The P-V and I-V characteristic curves of all PV array configurations are shown in Figure 6.

The L-shaped shading causes more power losses in the TCT-AC method. As the L-shaped shading shades a complete PV row and column, the S-PAC and TCT-AC experiences more power loss. The neighboring PV module in the PV row in TCT-AC is completely shaded, which reduces current generation. This shaded PV row was connected in series with the other PV arrays, which caused more mismatch losses between the PV rows. In S-PAC, one PV module in each column is affected by shading, which results in mismatch losses in each string. So, the S-PAC and TCT-AC will experience more power losses compared with the SUPAC, LSPAC, and proposed RPPAC. The S-PAC and TCT-AC generate a power output of 468 W, with 5.72 A of maximum current output. The SUPAC, LSPAC, and proposed RPPAC configurations generated a power output of 702 W with 8.58 A of maximum current.

The proposed RPPAC outperforms all other existing methods under the frame shading conditions, which are the short and narrow, short and wide, long and narrow, and long and wide shading conditions. As these abovementioned shading conditions vary from moderate to high levels of shading, existing array configurations fail to resist. The proposed array configuration chooses the PV modules for each PV row from the various locations of the conventional PV array so that it can disperse the shading uniformly over the PV array, and the shade dispersion rate is greater than the conventional array configurations. The frame shading shades all corners of the PV array.

In frame shading conditions, the proposed RPPAC configuration generates 629 W of power output with 8.75 A of short circuit current, whereas the other configurations, such as LSPAC, SUPAC, TCT-AC, and S-PAC, generate power outputs of 558 W, 585 W, 405 W, and 270 W, respectively. The SN and LN shading patterns are shades of 25%–40% of the PV panel surface. The S-PAC PV array generates 612 W of power under SN and 576 W of power under LN shading conditions. The SUPAC and LSPAC methods are efficient for minimizing the power loss associated with the SN and LN shading conditions. The TCT-AC has 80% efficiency under SN and 72.2% under LN shading. However, another configuration has similar performance in both of these narrow shading patterns, which can be observed from the mismatch losses. The efficiency of these configurations dropped under N shading conditions. The proposed RPPAC also has a similar kind of mismatch loss as the SUPAC and LSPAC. However, it has 4% greater efficiency than SUPAC and LSPAC. The proposed RPPAC has 710 W power output in SN shading, which is the highest among others, whereas the LSPAC method has the second-highest power output of 684 W. In LN shading, the proposed configuration has the highest power generation of 656 W and the LSPAC has the second-highest generation of 630 W.

Under the SW and LW shading patterns, the proposed RPPAC and LSPAC configurations perform with a smaller deviation, but both of them generate higher output power than other array configurations. The S-PAC has the lowest performance in both SW and LW shadings, which shows poor shade dispersion ability, whereas in TCT, the power generation is enhanced. In SUPAC, the performance has been further enhanced, and in LSPAC, it has the maximum power. However, the proposed RPPAC method has more shade dispersion ability than LSPAC. The LSPAC method generates 648 W in SW shading and 495 W in LW shading. The proposed RPPAC generates 656 W and 539 W of power output under SW and LW shading, respectively. All five array configurations are simulated in MATLAB/Simulink® to analyze and validate the performance of the proposed configuration method, and the corresponding results are given in Table 1; the power(P)–voltage(V) and current(I)–voltage(V) characteristic curves are plotted in Figures 5, 6, respectively.

4 Comparative analysis

According to the literature and the analysis of various PV array configurations, the L-shaped PV array configuration generates maximum power. The LSPAC method disperses the maximum amount of shading, which can be enhanced further using the proposed RPPAC method. This proposed configuration

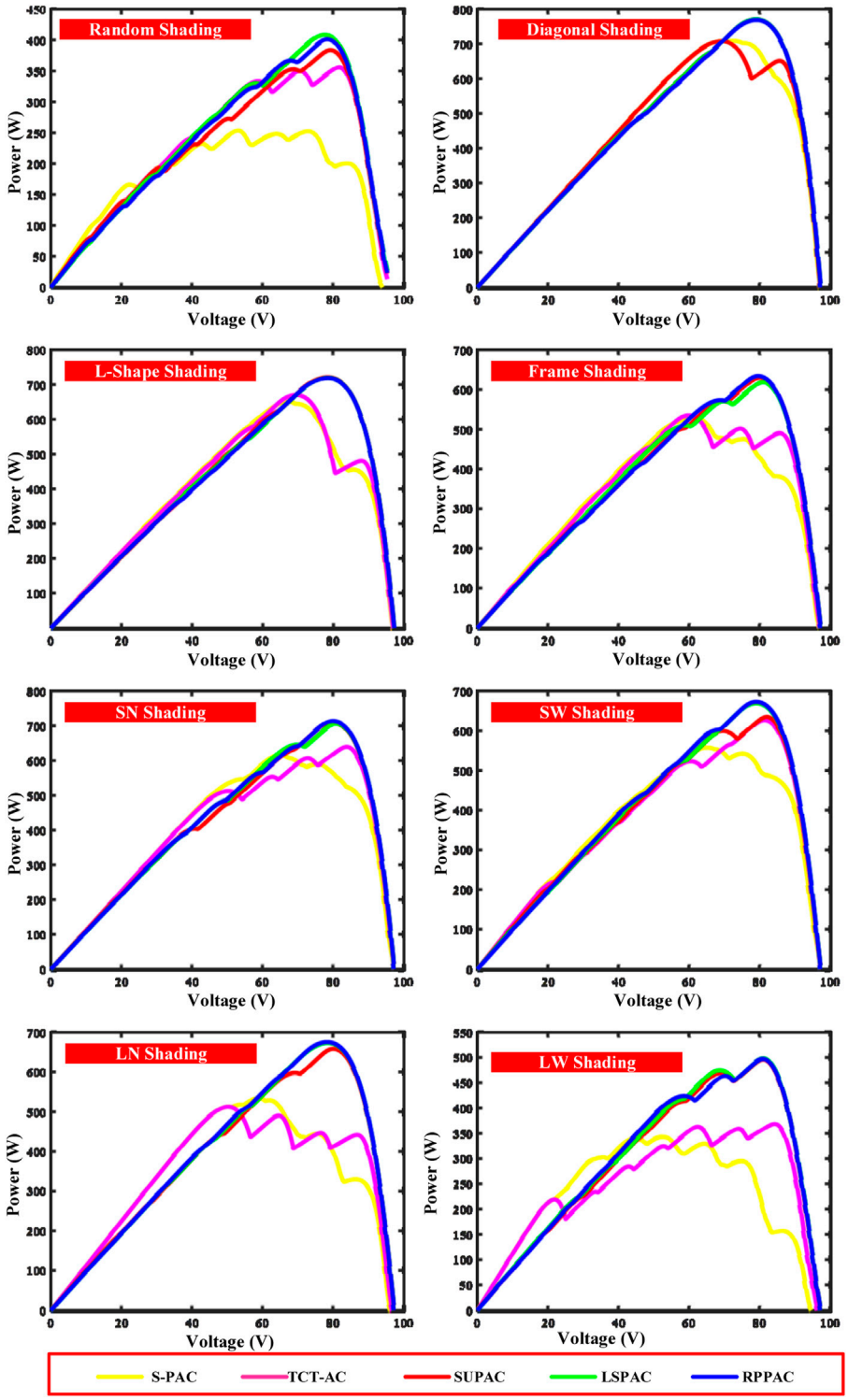

FIGURE 5
P–V characteristic curves.

method follows the Renzoku puzzle pattern, which can disperse more shading than the LSPAC. The performance of the S-PAC, TCT-AC, SUPAC, LSPAC, and proposed RPPAC was analyzed using MATLAB/Simulink®. According to the observed results, the proposed RPPAC performed better than the other four configurations. The power output comparison under various shading conditions is shown in Figure 7. In diagonal shading conditions, the TCT-AC, LSPAC, and proposed RPPAC methods

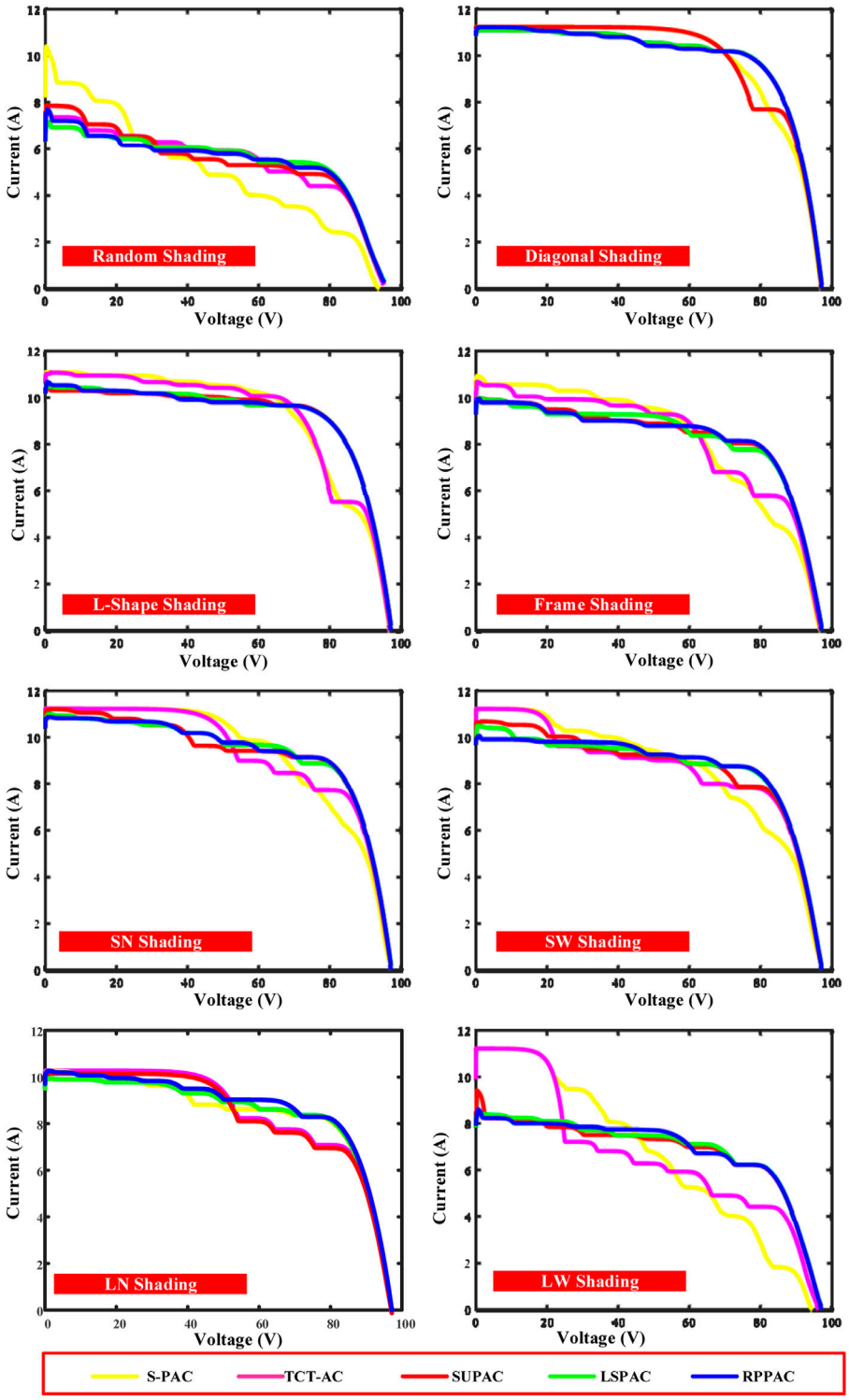

FIGURE 6
I–V characteristic curves.

generated the maximum output power. In L-shaped shading conditions, SUPAC, LSPAC, and RPPAC methods generated the maximum output power. In the other six shading conditions, the proposed RPPAC method generated the maximum output power, whereas the LSPAC method produced the second-highest power output.

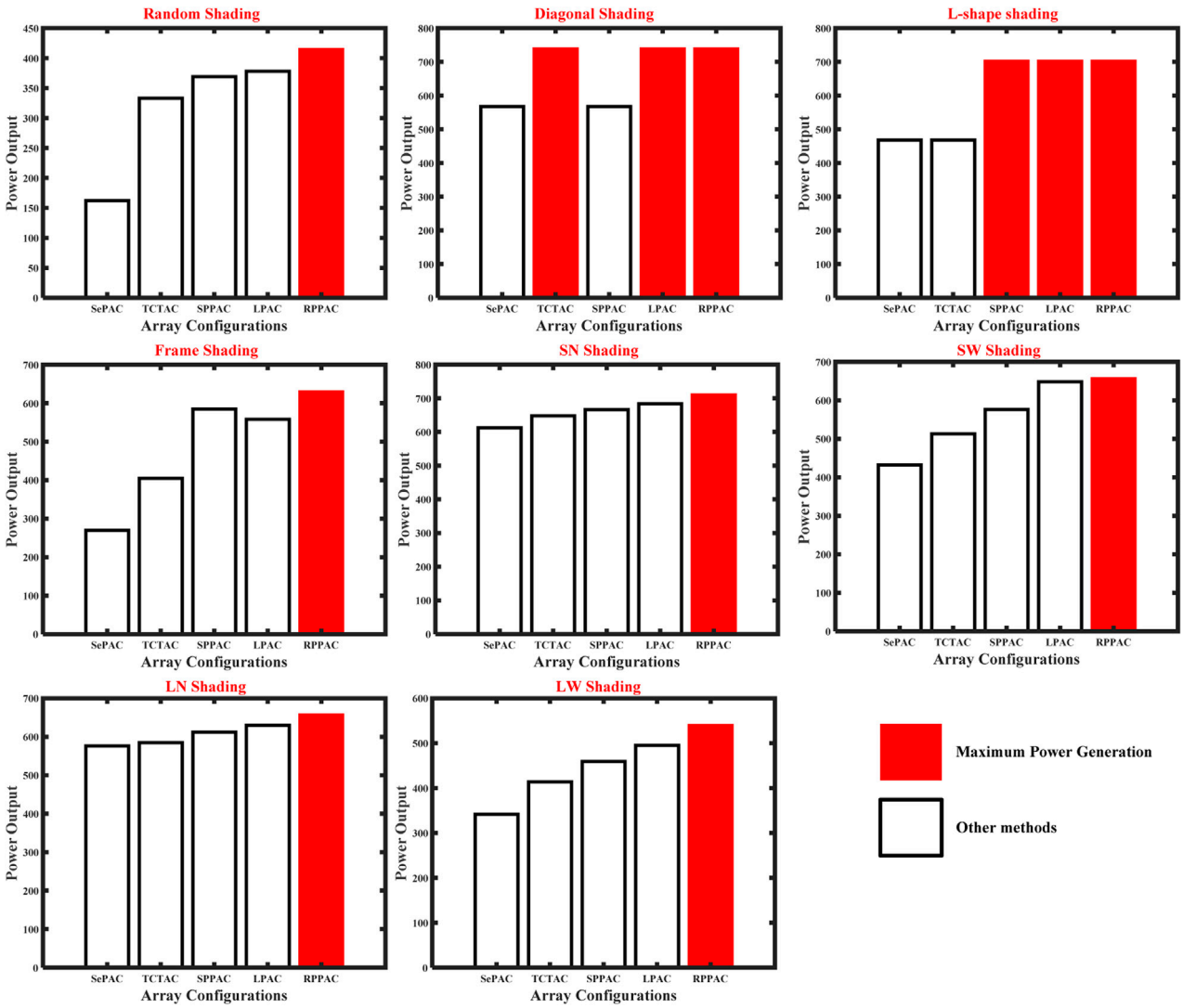

FIGURE 7
Power output comparison chart.

5 Conclusion

In this work, a novel array configuration method called RPPAC was introduced to address the limitations of the existing methods. The performance of the proposed RPPAC was evaluated under eight different shading conditions commonly encountered in photovoltaic systems. The analysis was conducted on a 9 × 9 PV array using MATLAB/Simulink®. The performance of the proposed RPPAC was compared with other established methods, including S-PAC, SUPAC, TCT-AC, and LSPAC. The results and characteristic curves demonstrated that the RPPAC method offers a unique solution for mitigating the effects of partial shading in PV arrays. Compared to the conventional configurations, the proposed RPPAC method exhibited an average efficiency improvement of 30%. Additionally, it outperformed recently developed configurations such as LSPAC, achieving 5%–10% higher efficiency. Notably, the implementation of the proposed configuration did not require any additional setup, although it necessitated a higher quantity of cables for interconnecting the PV modules. These findings highlight the effectiveness and superiority of the proposed RPPAC method in overcoming partial shading issues in PV arrays, offering improved efficiency without the need for major modifications to the existing setup.

Data availability statement

The original contributions presented in the study are included in the article/Supplementary material; further inquiries can be directed to the corresponding author.

Author contributions

BA: Formal Analysis, Investigation, Resources, Writing–original draft. PB: Conceptualization, Writing–review and editing. DS: Methodology, Writing–original draft. ST: Methodology, Writing–review and editing. NN: Resources, Supervision, Writing–review and editing.

Funding

The author(s) declare that no financial support was received for the research, authorship, and/or publication of this article.

Acknowledgments

Authors would like to acknowledge the support of the Deputy for Research and Innovation- Ministry of Education, Kingdom of Saudi Arabia for this research through a grant (NU/IFC/2/SERC/-/25) under the Institutional Funding Committee at Najran University, Kingdom of Saudi Arabia.

Conflict of interest

The authors declare that the research was conducted in the absence of any commercial or financial relationships that could be construed as a potential conflict of interest.

Publisher's note

All claims expressed in this article are solely those of the authors and do not necessarily represent those of their affiliated organizations, or those of the publisher, the editors, and the reviewers. Any product that may be evaluated in this article, or claim that may be made by its manufacturer, is not guaranteed or endorsed by the publisher.

References

Aghaei, M., Kumar, N. M., Eskandari, A., Ahmed, H., de Oliveira, A. K. V., and Chopra, S. S. (2020). "Solar PV systems design and monitoring," in *Photovoltaic solar energy conversion* (Germany: Elsevier), 117–145. doi:10.1016/B978-0-12-819610-6.00005-3

Aljafari, B., S, D., C, B., Balachandran, P. K., and Babu, T. S. (2023). Power enhanced solar PV array configuration based on calcudoku puzzle pattern for partial shaded PV system. *Heliyon* 9 (5), e16041. doi:10.1016/j.heliyon.2023.e16041

Alwar, S., Samithas, D., Boominathan, M. S., Balachandran, P. K., and Mihet-Popa, L. (2022). Performance analysis of thermal image processing-based photovoltaic fault detection and PV array reconfiguration—a detailed experimentation. *Energies* 15 (22), 8450. doi:10.3390/en15228450

Babu, T. S., Ram, J. P., Dragicevic, T., Miyatake, M., Blaabjerg, F., and Rajasekar, N. (2018). Particle swarm optimization based solar PV array reconfiguration of the maximum power extraction under partial shading conditions. *IEEE Trans. Sustain. Energy* 9 (1), 74–85. doi:10.1109/TSTE.2017.2714905

Bryant, S. T., Straker, K., and Wrigley, C. (2024). The need for sectoral transition design: a case of the shift to renewable energy. *Technol. Forecast. Soc. Change* 198, 122930. doi:10.1016/j.techfore.2023.122930

Cherukuri, S. K., Balachandran, P. K., Kaniganti, K. R., Buddi, M. K., Butti, D., Devakirubakaran, S., et al. (2021). Power enhancement in partial shaded photovoltaic system using spiral pattern array configuration scheme. *IEEE Access* 9, 123103–123116. doi:10.1109/ACCESS.2021.3109248

Devakirubakaran, S., Verma, R., Bharatiraja, C., and Mihet-Popa, L. (2023). Performance evaluation of static PV array configurations for mitigating mismatch losses. *IEEE Access*, 1. doi:10.1109/ACCESS.2023.3274684

Dhanalakshmi, B., and Rajasekar, N. (2018a). A novel Competence Square based PV array reconfiguration technique for solar PV maximum power extraction. *Energy Convers. Manag.* 174, 897–912. doi:10.1016/j.enconman.2018.08.077

Dhanalakshmi, B., and Rajasekar, N. (2018b). Dominance square based array reconfiguration scheme for power loss reduction in solar PhotoVoltaic (PV) systems. *Energy Convers. Manag.* 156, 84–102. doi:10.1016/j.enconman.2017.10.080

Durango-Flórez, M., González-Montoya, D., Trejos-Grisales, L. A., and Ramos-Paja, C. A. (2022). PV array reconfiguration based on genetic algorithm for maximum power extraction and energy impact analysis. *Sustainability* 14 (7), 3764. doi:10.3390/su14073764

Lappalainen, K., and Valkealahti, S. (2017). Effects of irradiance transition characteristics on the mismatch losses of different electrical PV array configurations. *IET Renew. Power Gener.* 11 (2), 248–254. doi:10.1049/iet-rpg.2016.0590

Ma, T., Gu, W., Shen, L., and Li, M. (2019). An improved and comprehensive mathematical model for solar photovoltaic modules under real operating conditions. *Sol. Energy* 184, 292–304. doi:10.1016/j.solener.2019.03.089

Mohammadnejad, S., Khalafi, A., and Ahmadi, S. M. (2016). Mathematical analysis of total-cross-tied photovoltaic array under partial shading condition and its comparison with other configurations. *Sol. Energy* 133, 501–511. doi:10.1016/j.solener.2016.03.058

Nguyen, X. H., and Nguyen, M. P. (2015). Mathematical modeling of photovoltaic cell/module/arrays with tags in Matlab/Simulink. *Environ. Syst. Res.* 4 (1), 24. doi:10.1186/s40068-015-0047-9

Pendem, S. R., and Mikkili, S. (2018). Modeling, simulation and performance analysis of solar PV array configurations (Series, Series–Parallel and Honey-Comb) to extract maximum power under Partial Shading Conditions. *Energy Rep.* 4, 274–287. doi:10.1016/j.egyr.2018.03.003

Prasad, T. N., Devakirubakaran, S., Muthubalaji, S., Srinivasan, S., Bajaj, M., Zawbaa, H. M., et al. (2022). Power management in hybrid ANFIS PID based AC–DC microgrids with EHO based cost optimized droop control strategy. *Energy Rep.* 8, 15081–15094. doi:10.1016/j.egyr.2022.11.014

Prince Winston, D., Ganesan, K., Samithas, D., and Baladhanautham, C. B. (2020a). Experimental investigation on output power enhancement of partial shaded solar photovoltaic system. *Energy Sources, Part A Recovery, Util. Environ. Eff.* 17, 1–17. doi:10.1080/15567036.2020.1779872

Prince Winston, D., Kumaravel, S., Praveen Kumar, B., and Devakirubakaran, S. (2020b). Performance improvement of solar PV array topologies during various partial shading conditions. *Sol. Energy* 196, 228–242. doi:10.1016/j.solener.2019.12.007

Sagar, G., Pathak, D., Gaur, P., and Jain, V. (2020). A Su Do Ku puzzle based shade dispersion for maximum power enhancement of partially shaded hybrid bridge-link-total-cross-tied PV array. *Sol. Energy* 204, 161–180. doi:10.1016/j.solener.2020.04.054

Srinivasan, A., Devakirubakaran, S., and Meenakshi Sundaram, B. (2020). Mitigation of mismatch losses in solar PV system – two-step reconfiguration approach. *Sol. Energy* 206, 640–654. doi:10.1016/j.solener.2020.06.004

Srinivasan, A., Devakirubakaran, S., Sundaram, B. M., Balachandran, P. K., Cherukuri, S. K., Winston, D. P., et al. (2021). L-shape propagated array configuration with dynamic reconfiguration algorithm for enhancing energy conversion rate of partial shaded photovoltaic systems. *IEEE Access* 9, 97661–97674. doi:10.1109/ACCESS.2021.3094736

Thanikanti, S. B., Aljafari, B., and Colak, I. (2023). A dynamic mismatch loss mitigation algorithm with dual input dual output converter for solar PV systems. *Sol. Energy Mater. Sol. Cells* 251, 112163. doi:10.1016/j.solmat.2022.112163

Viebahn, P., Soukup, O., Samadi, S., Teubler, J., Wiesen, K., and Ritthoff, M. (2015). Assessing the need for critical minerals to shift the German energy system towards a high proportion of renewables. *Renew. Sustain. Energy Rev.* 49, 655–671. doi:10.1016/j.rser.2015.04.070

Wang, F., Zhuang, L., Cheng, S., Zhang, Y., and Cheng, S. (2024). Spatiotemporal variation and convergence analysis of China's regional energy security. *Renew. Sustain. Energy Rev.* 189, 113923. doi:10.1016/j.rser.2023.113923

Yang, Y., Campana, P. E., and Yan, J. (2020). Potential of unsubsidized distributed solar PV to replace coal-fired power plants, and profits classification in Chinese cities. *Renew. Sustain. Energy Rev.* 131, 109967. doi:10.1016/j.rser.2020.109967

Ye, C.-E., Tai, C.-C., and Huang, Y.-P. (2023). Disperse partial shading effect of photovoltaic array by means of the modified complementary SuDoKu puzzle topology. *Energies* 16 (13), 4910. doi:10.3390/en16134910

frontiers | Frontiers in Energy Research

TYPE Original Research
PUBLISHED 13 March 2024
DOI 10.3389/fenrg.2024.1381376

OPEN ACCESS

EDITED BY
Praveen Kumar Balachandran,
Vardhaman College of Engineering, India

REVIEWED BY
Sudhakar Babu Thanikanti,
Chaitanya Bharathi Institute of Technology, India
Shitharth Selvarajan,
Leeds Beckett University, United Kingdom

*CORRESPONDENCE
Mouna Ben Smida,
mouna.bensmida@esprim.tn
Ahmad Taher Azar,
aazar@psu.edu.sa
Ibrahim A. Hameed,
ibib@ntnu.no

RECEIVED 03 February 2024
ACCEPTED 29 February 2024
PUBLISHED 13 March 2024

CITATION
Ben Smida M, Azar AT, Sakly A and Hameed IA (2024), Analyzing grid connected shaded photovoltaic systems with steady state stability and crow search MPPT control.
Front. Energy Res. 12:1381376.
doi: 10.3389/fenrg.2024.1381376

Analyzing grid connected shaded photovoltaic systems with steady state stability and crow search MPPT control

Mouna Ben Smida[1]*, Ahmad Taher Azar[2,3,4]*, Anis Sakly[1] and Ibrahim A. Hameed[5]*

[1]National Engineering School of Monastir, University of Monastir, Tunis, Tunisia, [2]College of Computer and Information Sciences, Prince Sultan University, Riyadh, Saudi Arabia, [3]Automated Systems and Soft Computing Lab (ASSCL), Prince Sultan University, Riyadh, Saudi Arabia, [4]Faculty of Computers and Artificial Intelligence, Benha University, Benha, Egypt, [5]Department of ICT and Natural Sciences, Norwegian University of Science and Technology, Alesund, Norway

The field of research in maximum power point tracking (MPPT) methods is making significant progress with a wide range of techniques, from simple yet inefficient approaches to more complex but effective ones. Therefore, it is important to suggest a simple and effective strategy to control the global maximum power point (GMPP) of a photovoltaic (PV) system especially under partial shading conditions (PSC). This paper proposes a novel metaheuristic MPPT called the Crow Search Algorithm (CSA) to ameliorate the tracking performance of a grid connected shaded PV system. The CSA is a nature inspired method based on the intelligent behaviors of crows in its search process for hidden food sources. This novel method succeeds to mitigate the adverse impacts of partial shading on the performance of PV systems by accurately tracking the GMPP. Based on the small-signal dynamic model, the stability of the proposed system is analyzed. Simulation results for three different levels of partial shading, including zero, weak, and severe shading, demonstrate the better performance of the suggested CSA compared to fuzzy logic controller (FLC) and Inc-Cond techniques. In fact, the comparison is carried out in terms of simplicity of implementation, high efficiency, and low power loss, decreasing considerably the convergence time.

KEYWORDS

global maximum power point tracking, photovoltaic system, crow search algorithm, partial shading conditions, small signal stability

1 Introduction

Renewable energy sources have a vital importance in electric power generation due to shortage and environmental impacts of conventional fuels. Several studies expect that more than 45% of the global energy supply will be generated by solar energy. However, the performance of photovoltaic (PV) system is strongly dependent on weather and climate change. Besides, a major interest has been given to the study of possible optimal autonomous exploitation of the PV source regardless the climatic conditions. In this framework, optimization algorithms are an appropriate tool for solving complex problems in the field of renewable energy systems. But the developed Maximum Power Point Tracking (MPPT) algorithms are frequently very reliant on the accuracy of the

mathematical model in relation to the generator and on the weather, particularly if partial shading occurs. Partial shading results in power inefficiency and keeps a photovoltaic system from performing at its best. Authors in (Eltamaly et al., 2018) have classified MPPT methods into conventional, soft computing, and hybrid methods.

Conventional techniques like Incremental Conductance (IC), Extremum Seeking Control (ESC), Hill Climbing (HC), perturb and Observe (P&O), Fractional Short Circuit (FSC), Fractional Open Circuit (FOC) and others are effective when used in consistent temperature and irradiation conditions (Ahmed and Salam, 2015).

However, they fail to track the Maximum Power Point (MPP) under Partial Shading Conditions (PSC) caused by the non-uniform irradiation of the PV arrays. The problem becomes complex in shaded conditions since the PV array exhibits several local maxima (LMs) (Maki and Valkealahti, 2012). The current MPPT efficiency is reduced when there are multiple peaks because they can't distinguish the global maximum (GM) between the LMs.

In order to overcome the limitations of conventional techniques, soft computing techniques have been developed in literature. These methods comprise the metaheuristic and the artificial intelligence techniques. The application of intelligent algorithms is prevalent whether for system modeling, identification, or control. They may be considered as alternative solutions due to their flexibility to changes in system conditions, and their resilience to disturbances and modeling errors.

Authors in (Kermadi et al., 2020a) have developed a detailed review of shaded PV system MPPT algorithms. Concerning Artificial Intelligence (AI) based MPPT, an enhanced MPPT technique was proposed by Yilmaz et al. in (Yilmaz et al., 2019) to improve accuracy in PV systems under fluctuating atmospheric conditions. while Salah and Ouali (Salah and Ouali, 2011) compared a FLC and an artificial neural network (ANN) based techniques in maximum power point tracker for PV systems and confirmed through simulations result the superior performance and efficiency of FLC over ANN in tracking capabilities. Compared with conventional techniques these AI methods offer better performances and boost the PV energy production's efficiency as presented in (BOUNECHBA et al., 2014).

In spite of their advantages, these methods heavily rely on the specific attributes of the photovoltaic (PV) system and necessitate prior knowledge of the model specifications. According to Karatepe and Hiyama (Karatepe and Hiyama, 2009), both FLC and ANN exhibit limitations in effectively tracing the Global Maximum Power Point (GMPP) under PSCs.

Within this framework, numerous researchers have delved into the challenge of MPPT challenge using metaheuristic optimization techniques. High efficiency and a fair computational cost are guaranteed by these "smart" procedures during the resolution process (Wang et al., 2020). Kermadi et al. proposed several of the most effective metaheuristic optimization techniques in the literature in (Kermadi et al., 2020a) as: Genetic Algorithm (GA), Particle Swarm Optimization (PSO), Artifcial Bee Colony (ABC), Bat Algorithm (BA), Grey Wolf Optimization, Cuckoo Search (CS), (GWO), Firefly Algorithm (FA), Flower Pollination Algorithm (FPA), and Dragonfy Optimization Algorithm (DFO), Firefly Algorithm (FA) and Whale Optimization Algorithm (WOA). These methods are able to decrease the deficiencies of AI-based and traditional MPPT techniques.

Shaiek et al. in (Miyatake et al., 2011) suggested A GA based MPPT technique for shaded PV systems and simulation results proved that the suggested method outperforms conventional methods in following the GMPP under PSCs. Miyatake et al. (Ishaque and Salam, 2012) introduced PSO for experimental MPPT studies, and many researchers suggested improvements in standard PSO technique including Deterministic PSO (DPSO) in (Chowdhury and Saha, 2010), Adaptive Perceptive PSO (APPSO) in (Ram and Rajasekar, 2017) and Leader PSO (LPSO) in (Ahmed and Salam, 2014). These modified PSO methods offer better performances, but they are extremely sophisticated including an important number of variables.

Combining simulation and experimental data, authors (Sundareswaran et al., 2014) verified the Cuckoo Search algorithm's (CS) ability to track GMPP under rapid changes of irradiance and temperature. In (Mohanty et al., 2015) an evolutionary ABC technique has been developed for a Photovoltaic Generator (PVG) under PSC while Mohanty et al. (Kaced et al., 2017) confirmed experimentally the efficacious application of GWO method for resistive and inductive loads under shade conditions.

Authors in (Wu and Yu, 2018) employed the BA method to address shading issues. Their work highlighted the performance of this technique to attain the GMPP as confirmed with validation in experiments as well as simulation. Authors in (Mirza et al., 2019), on the other hand, introduced an enhanced version of the Bat Algorithm (IBAT) for MPPT. This improvement involved the incorporation of an adaptive weight parameter, thereby enhancing the algorithm's capacity for global search. The modified algorithm ensured rapid and accurate GMPP tracking surpasses numerous other MPPT techniques. In (Balaji and Fathima, 2022), It has been observed by Mirza et al. that the majority of soft computing techniques in literature only address the basic Partial Shading (PS) problem, with little attention paid to the Dynamic partial Shading (DPS) problem. In order to address the PS and DPS concerns, they therefore proposed solutions for these bio-inspired soft computing-based methodologies by proposing ACOA, DFO, and GRNNFFOA MPPT techniques.

Despite the impressive advantages of the aforementioned meta-heuristic methods, the majority of them have limitations such as software complexity and numerous tuning variables. To address these problems, researchers proposed combining two approaches into a hybrid method that retains the merits of each (Lian et al., 2014). In (Sundareswaran et al., 2015) Lian et al. combined both P§O and PSO algorithms in order to reduce the convergence time of the particles search space.

In the same vein, authors in (Mohamed et al., 2019), based on the advantages of P&O, ameliorated the GA response and proposed a hybrid GA-P&O technique under PSC. Mohamed et al. (Askarzadeh, 2016a) implemented PSO-GSA technique for tracking the GMPP and compared it to GWO, Moth-Flame Optimization (MFO) and Salp Swarm Algorithm (SSA) methods. Simulation results demonstrated the stability, success rate, and tracking efficiency of the suggested hybrid technique. Moreover, despite their excellent performances, the modified and the hybrid methods are more complex and increase the complexity of the system.

Among the methods mentioned earlier, a new population based metaheuristic algorithm called Crow Search Algorithm (CSA) has been developed by Askarzadeh (Hinojosa et al., 2018) to solve global

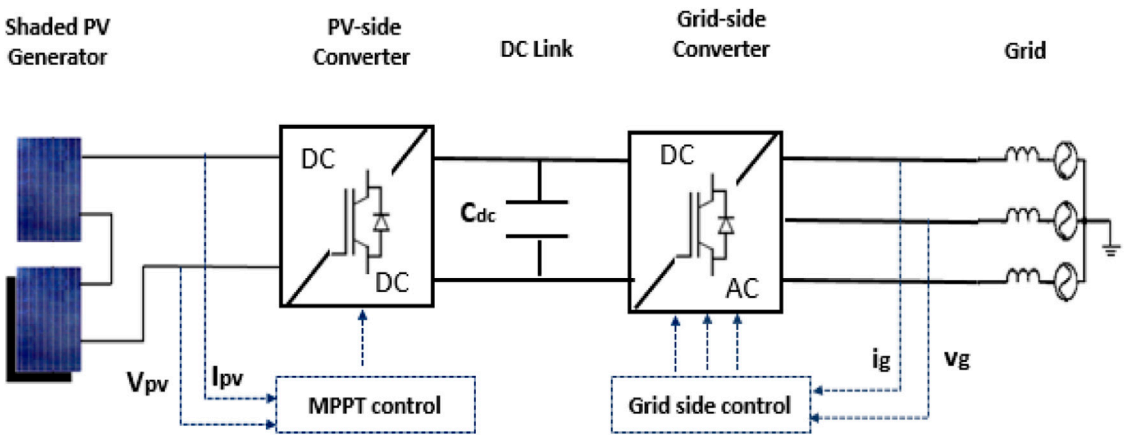

FIGURE 1
System configuration of a two-stage grid connected PV.

optimization problem. This technique is derived from the food stealing behavior of crows (Houam et al., 2021).

Its promising results in global optimization issues have encouraged its application in solving real-nonlinear and multimodal optimization problems in various engineering fields.

Moreover, Moghaddam et al. has suggested CSA in (Moghaddam et al., 2019) for designing a stand-alone hybrid PV/wind/battery system. Houam et al. [29] have developed an efficient metaheuristic technique to control MPP of a partially shaded standalone PV systems using CSA and they exclusively analyze the stability of the PV generator. Motivated by the aforementioned limitations, the present paper proposes the development and the stability analysis of a two-stage grid connected shaded PV system. Tracking the GMPP of a shaded PV generator is optimized by an intelligent approach based on CSA and compared with both a conventional and an AI method.

The paper is structured as follows: section 2 presents the detailed mathematical model of the studied structure. Considering the dynamics of the PV generation, a small-signal model of a two-stage grid connected PV system was built in section 3. The small-signal stability analysis method was used to analyze the influence of the PV generation. The effect of partial shading on PV characteristics and the theories of the Inc-Cond, the FLC and the suggested CSA based MPPT algorithms are introduced in Section 4 and 5, respectively. The simulation studies are performed and discussed in Sections 6. Final conclusions are presented in Section 7.

2 System modeling

In this study, a two stage connected converter system, as shown in Figure 1, is used. As the front stage to shift the PV output voltage to a high level for the grid-connected inverter. The power system consists of a shaded PV generator, a boost converter and a three-phase inverter.

2.1 PV generator

The photovoltaic system under study consists of two PV arrays connected in series, with one of them being shaded. When subjected to uniform climatic conditions, the entire system generates a power output of 2000W. Figure 2 provides the P-V (power-voltage) and I-V (current-voltage) characteristics of the system and the used parameters of the studied PV system are shown in Table 1.

The accurate model of a PV cell is very complicated, and some parameters are difficult to measure directly. Thus, it is not convenient for research and application. By simplifying calculation equations, a practical engineering model was used in this paper.

The current cell is described by:

$$I = I_{sc}\left[1 - C_1\left(e^{\frac{U}{C_2 U_{oc}}} - 1\right)\right] \tag{1}$$

The expressions of C1 and C2are given by:

$$C_1 = \left(1 - \frac{I_m}{I_{sc}}\right)\exp^{\frac{U}{C_2 U_{oc}}} \tag{2}$$

$$C_2 = \frac{\frac{U_m}{U_{oc}}}{Ln\left(1 - \frac{I_m}{I_{sc}}\right)} \tag{3}$$

Where Isc is the short-circuit current, Uoc is the open-circuit voltage, Im and Um are the current and the voltage at the maximum power, respectively.

The voltage and the current of PV array are written as:

$$\begin{cases} U_{pv} = N_s U \\ I_{pv} = N_p I \end{cases} \tag{4}$$

Then the PV current is deduced as:

$$I_{pv} = N_p I_{sc}\left[1 - C_1\left(e^{\frac{U}{N_s C_2 U_{oc}}} - 1\right)\right] \tag{5}$$

2.2 DC/DC converter

A boost converter controlled by a MPPT control system ensures the connection between the GPV and the DC bus. Its configuration is given in Figure 3.

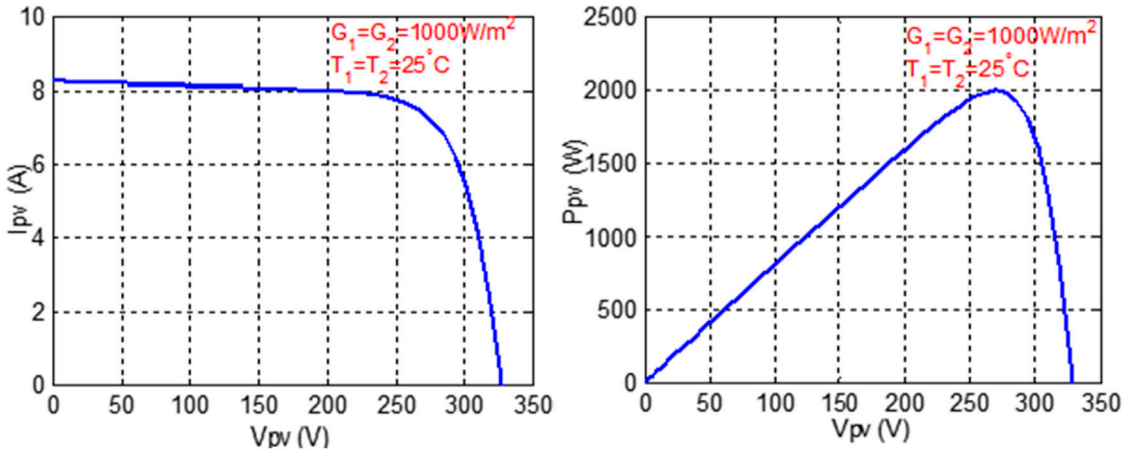

FIGURE 2
I-V and P-V characteristics of the PV system under nominal conditions.

TABLE 1 Parameters of the solar module.

Parameter	Value
Voltage at MPP VMPP	26.3V
Current at MPP IMPP	7.61A
Open circuit voltage Voc	32.9V
Short circuit current Isc	8.21A
Number of serial cells N	54
Number of parallel cells Np	10
Serial Resistance Rs	0.001Ω
Parallel Resistance Rsh	5Ω

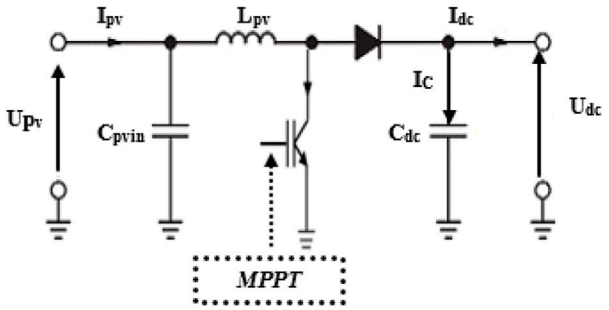

FIGURE 3
Boost configuration.

The output voltages and current of the boost converter during steady state are expressed as follows:

$$\begin{cases} U_{dc} = \dfrac{U_{pv}}{1-D} \\ I_{dc} = (1-D).I_{pv} \end{cases} \quad (6)$$

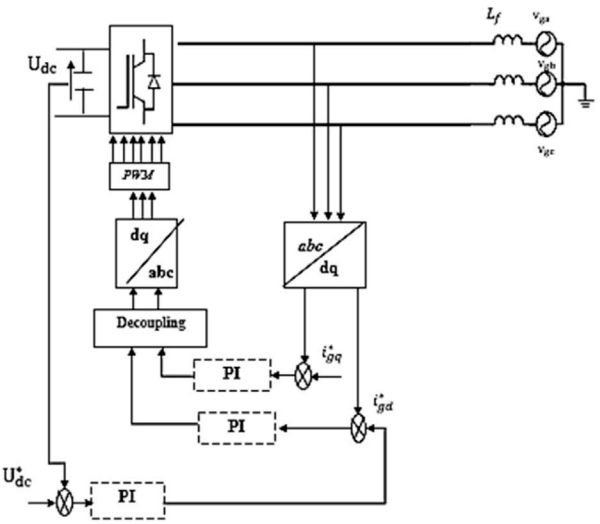

FIGURE 4
Grid side controllers' configuration.

The DC Bus capacitor voltage is given by:

$$C_{dc}\frac{dU_{dc}}{dt} = I_c \quad (7)$$

where Ic is the capacitor current.

2.3 Gride side modeling

Assuming that the loss of both the boost converter and the inverter can be ignored. Then, the output power of a PV array is equal to the sum of the power of a DC capacitor and the output power of an inverter and in order to mitigate the harmonics injected into the grid, a filter comprising an inductance Lf is employed. The dynamic model of the grid is then given by:

10.3389/fenrg.2024.1381376

$$\begin{cases} V_{g_d} = V_{i_d} + L_f \dfrac{di_{g_d}}{dt} + \omega L_f i_{g_q} \\ V_{g_q} = V_{i_q} + L_f \dfrac{di_{g_q}}{dt} - \omega L_f i_{g_d} \\ U_{dc}.C\dfrac{dU_{dc}}{dt} = I_C U_{dc} + \dfrac{3}{2} V_{g_d} i_{g_d} \end{cases} \quad (8)$$

Where i_{gd} and i_{gq} represent the d-q grid current components and V_{gd} and V_{gq} are the d-q inverter voltage components.

The inverter's main objective is to regulate the voltage of the DC bus and manage the power exchanges with the grid. Additionally, controlling this converter allows for the establishment of currents at the frequency of the grid. The value of igq was set to zero. The voltage and current control equations were provided as Eq. 9.

$$\begin{cases} i_{gd}{}^{*} = K_{p1}\left(U_{dc}^{*} - U_{dc}\right) + K_{I1}\int \left(U_{dc}^{*} - U_{dc}\right)dt \\ i_{gq}^{*} = 0 \\ v_{id}^{*} = K_{p2}\left(i_{gd}^{*} - i_{gd}\right) + K_{I2}\int \left(i_{gd}^{*} - i_{gd}\right)dt - \omega L_f i_{gq} + v_{gd} \\ v_{iq}^{*} = K_{p2}\left(i_{gq}^{*} - i_{gq}\right) + K_{I2}\int \left(i_{gq}^{*} - i_{gq}\right)dt - \omega L_f i_{gd} + v_{gq} \end{cases} \quad (9)$$

Figure 4 displays the configurations of voltage and current controllers.

3 Small signal stability analysis model of a two-stage PV grid-connected converter system

This part examines the stability of the PV power system under consideration. The entire small-signal model of the system is required for studying system stability. In fact, investigations of tiny signal stability are often based on a linearized system around an operational point. The dynamic system's differential equations are linearized, and the system eigenvalues are calculated using the characteristic equation.

The state variables of the controllers are introduced R_{dc}, R_{id} and R_{iq} where:

$$\begin{cases} \dfrac{dR_{dc}}{dt} = U_{dc}^{*} - U_{dc} \\ \dfrac{dR_{id}}{dt} = i_{gd}^{*} - i_{gd} \\ \dfrac{dR_{iq}}{dt} = i_{gq}^{*} - i_{gq} \end{cases} \quad (10)$$

Linearizing (1)–(10) around steady-state values, the overall system's differential equations are provided by:

$$\frac{d\Delta x}{dt} = A\Delta x + B\Delta u \quad (11)$$

Where:

$$X = \left[\, U_{dc}\ R_v\ R_{id}\ R_{iq}\ i_{gd}\ i_{gq} \right]^{T} \quad (12)$$

$$U = \left[v_{gd}\ v_{gq} \right] \quad (13)$$

The eigenvalues of matrix A are defined as: .

$$\delta_i = \sigma_i \pm i\omega_i \quad (14)$$

The oscillation frequency, Hz, and the damping ratio are given by:

$$\begin{cases} f = \dfrac{\omega_i}{2\pi} \\ \xi = \dfrac{-\sigma_i}{\sqrt{\sigma_i{}^2 + \omega_i{}^2}} \end{cases} \quad (15)$$

The derivation of the A and B matrices will be discussed in the following paragraph.

3.1 Derivation for A and B matrices

$$\begin{cases} \dfrac{dUdc}{dt} = \dfrac{N_p I_{sc}\left[1 - C_1\left(e^{\frac{U}{N_s C_2 U_{oc}}} - 1\right)\right]}{C_{dc}} - \dfrac{3v_{gd}}{2C_{dc}U_{dc}} i_{gd} \\ \dfrac{dR_v}{dt} = K_{p1}\left(U_{dc}^{*} - U_{dc}\right) + K_{i1}R_{id} - i_{gd} \\ L_f \dfrac{di_{gd}}{dt} = v_{id} + k_{p2}\left[K_{p1}\left(U_{dc}^{*} - U_{dc}\right) + K_{i1}R_{dc} - i_{gd}\right] + K_{i2}R_{id} - v_{id}^{*} \\ L_f \dfrac{di_{gq}}{dt} = v_{iq} + K_{p2}\left(0 - i_{gq}\right) + K_{i2}R_{iq} - v_{iq}^{*} \end{cases} \quad (16)$$

Linearizing (10) and (16) around steady-state values, (17) is given by:

$$\begin{cases} \dfrac{d\Delta U_{dc}}{dt} = \dfrac{3v_{gd}i_{gd}}{2C_{dc}U_{dc}{}^2}\Delta Udc - \dfrac{N_p I_{sc}\left[1 - C_1\left(e^{\frac{U}{N_s C_2 U_{oc}}} - 1\right)\right]}{C_{dc}U_{dc}}\Delta Udc - \dfrac{3v_{gd}}{2C_{dc}U_{dc}}\Delta i_{gd} \\ \dfrac{d\Delta R_{dc}}{dt} = -\Delta U_{dc} \\ \dfrac{d\Delta R_{id}}{dt} = -K_{p1}\Delta U_{dc} + K_{i1}\Delta R_{dc} - \Delta i_{gd} \\ \dfrac{d\Delta R_{iq}}{dt} = -\Delta i_{gq} \\ \dfrac{d\Delta i_{gd}}{dt} = -\dfrac{K_{p1}K_{p2}}{L_f}\Delta U_{dc} + \dfrac{K_{i1}K_{p2}}{L_f}\Delta R_{dc} - \dfrac{K_{p2}}{L_f}\Delta i_{gd} + \dfrac{K_{i2}}{L_f}\Delta R_{id} \\ \dfrac{d\Delta i_{gq}}{dt} = -\dfrac{K_{p2}}{L_f}\Delta i_{gq} + \dfrac{K_{i2}}{L_f}\Delta R_{iq} \end{cases} \quad (17)$$

Thus, the state matrix A and the output matrix B are as follows:

$$A = \begin{bmatrix} \dfrac{3v_{gd}i_{gd}}{2C_{dc}U_{dc}{}^2} - \dfrac{N_p I_{sc}\left[1 - C_1\left(e^{\frac{U}{N_s C_2 U_{oc}}} - 1\right)\right]}{C_{dc}U_{dc}} & 0 & 0 & 0 & -\dfrac{3v_{gd}}{2C_{dc}U_{dc}} & 0 \\ -1 & 0 & 0 & 0 & 0 & 0 \\ -K_{p1} & K_{i1} & 0 & 0 & -1 & 0 \\ 0 & 0 & 0 & 0 & 0 & -1 \\ \dfrac{K_{p1}K_{p2}}{L_f} & \dfrac{K_{i1}K_{p2}}{L_f} & \dfrac{K_{i2}}{L_f} & 0 & -\dfrac{K_{p2}}{L_f} & 0 \\ 0 & 0 & 0 & \dfrac{K_{i2}}{L_f} & 0 & -\dfrac{K_{p2}}{L_f} \end{bmatrix} \quad (18)$$

$$B = \begin{bmatrix} \dfrac{-3i_{gd}}{2C_{dc}U_{dc}} & 0 & 0 & 0 & 0 & 0 \\ 0 & 0 & 0 & 0 & 0 & 0 \end{bmatrix} \quad (19)$$

Table 2 shows the parameters of the explored system. The eigenvalues of the state matrix A are computed as shown in Table 3 Five eigenvalues were obtained with negative real part. According to Lyapunov, this system is small signal marginally stable.

TABLE 2 Studied system parameters.

Parameter	Value
Boost converter capacity Cpv	220 μF
Boost converter inductance Lpv	1.8 mH
DC bus capacitor Cdc	80,010–6 F
Grid Inductance Lf	0.16 H
Proportional Constant Kp1,Kp2	1,000
Integral Constant KI1,KI2	24

4 Effect of partial shading on PV characteristics

The issue of shading arises when different lighting conditions expose the system. It is important to note that the systems electrical performance depends on both the cell specifications and the conditions of irradiation. Shaded modules, acting as a load utilize a portion of the generated power, that influences the behavior of the system leading potentially to hot spot problems.

Hot spotting represent a performance concern, in PV modules where certain solar cells become significantly heated due to mismatches resulting in reduced output power. This phenomenon occurs when dividual cells or groups of them operate at aberrant temperatures and activate at bias, squandering the power that was intended to provide the stimulus. Additionally, these hot areas cause PV panels to age and can sustain irreversible damage. To mitigate spotting effects bypass diodes are commonly employed in parallel, with PV modules. The purpose is to raise the total short circuit current and open circuit voltage by limiting the reverse voltage across spotted or shaded solar cells.

Two irradiations are simulated for the system under study: G1 and G2. The I-V and P-V characteristics, which consist of two extremums, are displayed in Figure 5. It is observed that the second generator's illumination has an impact on the system's overall appearance, especially on the second extremum, which may represent a Local Maximum (LM) or a Global Maximum (GM).

TABLE 3 State matrix eigenvalues.

Eigenvalues	Values	Oscillation frequency	Damping ratio
δ_1	−25030 + 26140i	4160.3	−0.6916
δ_2	−25030-26140i	4160.3	−0.6916
δ_3	0	0	1
δ_4	0	0	1
δ_5	0	0	1
δ_5	−50000	0	1

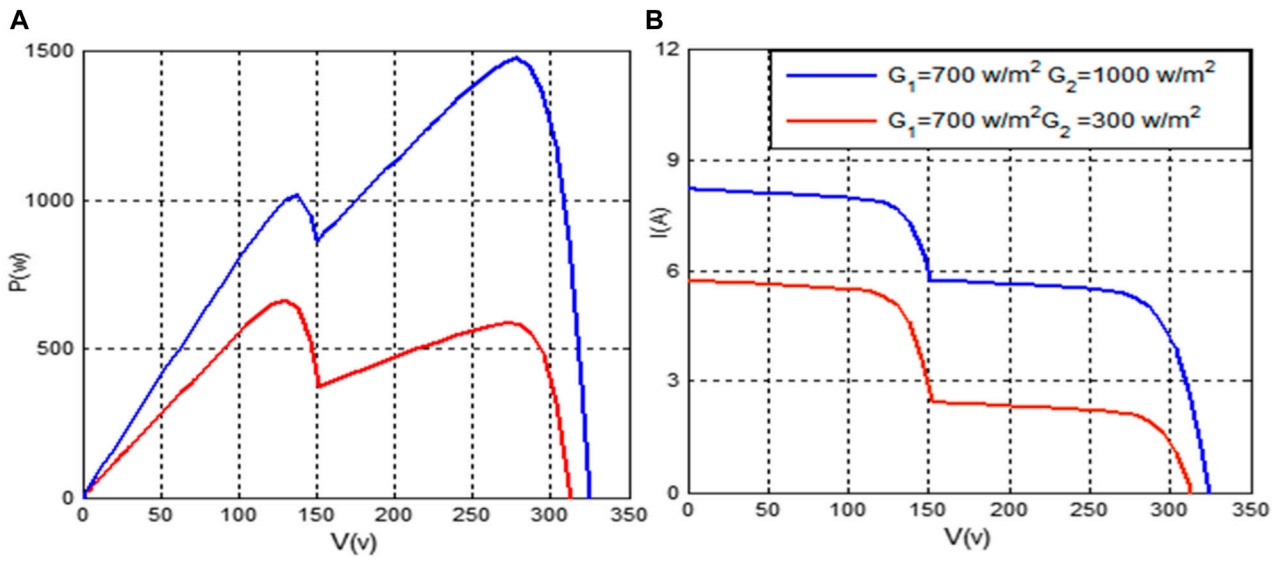

FIGURE 5
Characteristics of the studied Shaded PV generator **(A)** I-V Characteristic **(B)** P-V Characteristic.

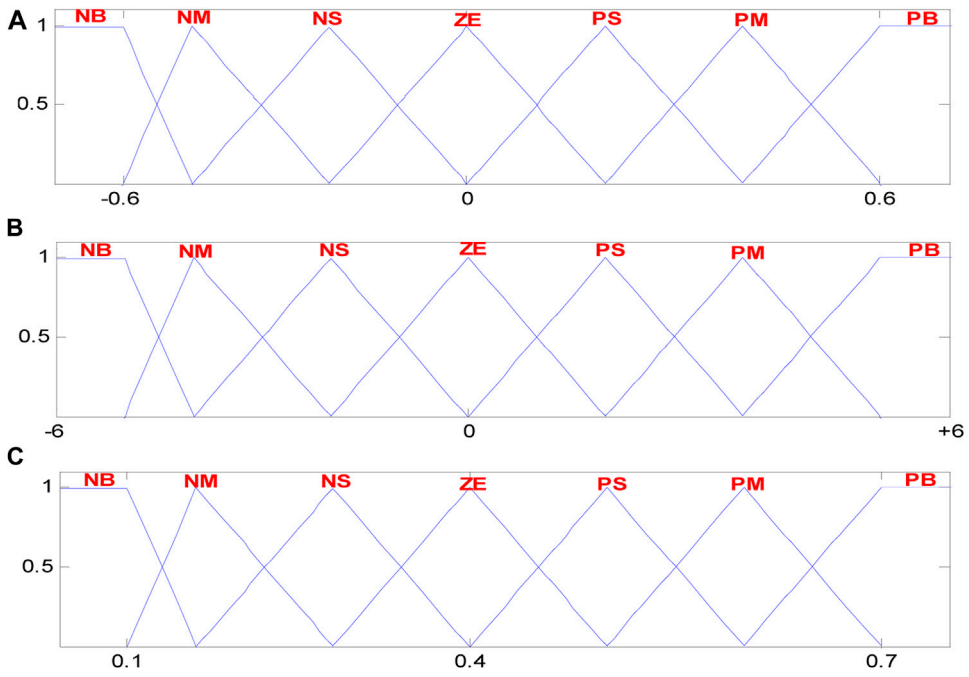

FIGURE 6
Membership functions **(A)** input variable E(n) **(B)** input variable Δ E(n) **(C)** output variable α.

TABLE 4 The fuzzy controller's forty-nine rules.

α	E(n)							
ΔE(n)		NB	NM	NS	ZE	PS	PM	PB
	NB	ZE	ZE	ZE	NB	NB	NB	NB
	NM	ZE	ZE	ZE	NM	NM	NM	NM
	NS	NS	ZE	ZE	NS	NS	NS	NS
	ZE	NM	NS	ZE	ZE	ZE	PS	PM
	PS	PM	PS	PS	PS	ZE	ZE	ZE
	PM	PM	PM	PM	ZE	ZE	ZE	ZE
	PB	PB	PB	PB	ZE	ZE	ZE	ZE

5 Implementation of MPPT methods for optimization problem

5.1 Inc-Cond technique

The Inc-Cond technique is the commonly employed MPPT method. It adjust continuously the output voltage of the generator by comparing the instantaneous conductance $\frac{I_{pv}}{V_{pv}}$ to its negative local variation $\frac{\Delta I_{pv}}{\Delta V_{pv}}$ in order to regulate the operating point on the I-V characteristic to the MPP corresponding voltage.

5.2 Fuzzy MPPT controller

Given that the fuzzy logic approach is acknowledged as a model-free technique, dealing with imprecise inputs and handling non-linearity, the FLC based MPPT strategy is developed to improve the PV response.

The inputs and variables of the suggested controller are: E and ΔE, given by Eqs 3, 4, where P_{pv} (n) and V_{pv} (n) represent the output power and voltage of the PV generator at the sampling instant n.

$$E(n) = \frac{P_{pv}(n) - P_{pv}(n-1)}{V_{pv}(n) - V_{pv}(n-1)} \quad (20)$$

$$\Delta E(n) = E(n)\text{-}E(n\text{-}1) \quad (21)$$

The fuzzification step, requires seven fuzzy levels called NB (negative big), NM (negative medium), NS (negative small), ZE (zero), PS (positive small), PM (positive medium) and PB (positive big).

The memberships functions of the input and output variables are given in Figure 6.

Table 4 presents the 49 fuzzy rules used in the FLC inference approach.

5.3 Crow search algorithm

Crows are considered as highly intelligent birds, which are able to evoke faces and inform each other when an inauspicious one approaches. They exhibit remarkable abilities to sophisticated communication techniques and long-term memories, allowing them to recall their food's hiding place. Moreover, crows tracks other crows or birds to discover the location of their hidden food in order to steal it. Conversely, when a crow becomes aware of being tracked, it resorts to changing its position to deceive others and maintain the secrecy of its own hidden food.

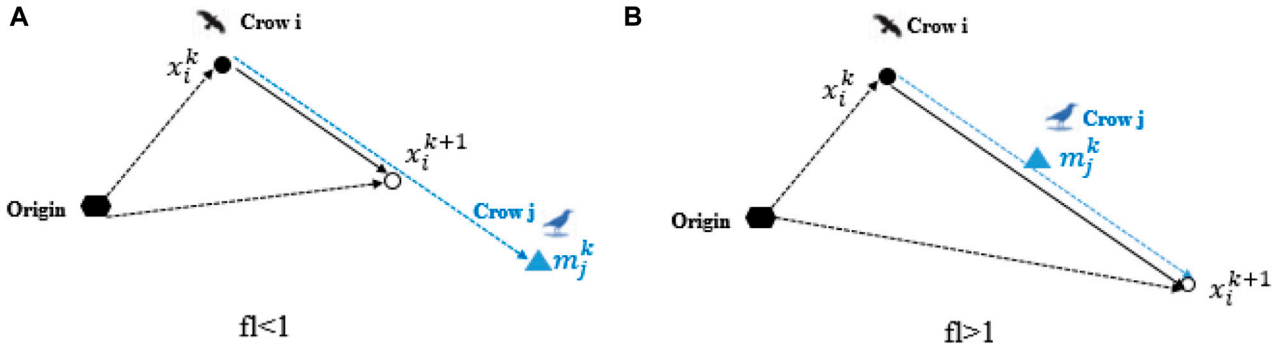

FIGURE 7
Intelligent movement for the crows **(A)** fl < 1 **(B)** fl > 1.

This paper introduces a newly developed population-based metaheuristic algorithm called CSA based on the intelligent behaviors mentioned earlier.

The following is a summary of the CSA's tenets:

- Crows live in flocks and memorize the locations of their hiding spots.
- Crows stalk people to smuggle food from them.
- Crows conceal their food by moving in unpredictable ways.

Step 1: Setting up changeable parameters and decision variables

Decision variables are defined for the optimization problem, and the values of the CSA's adjustable parameters (N, fl, itermax, and AP) are found where:

N: size of flock.
the greatest number of iterations, or itermax.
fl stands for flight length.

Step2: Initialization of crows' position and memory

In a one-dimensional environment including N crows randomly positioned, each decision variables, is characterized by a position x_i^k and a memory m_i^k for a specified iteration k.

$$x_i = [x_1 \ldots\ldots\ldots x_N] \quad (22)$$

$$m_i = [m_1 \ldots\ldots\ldots m_N] \quad (23)$$

Every crow's memory is initialized with the presumption that they have concealed their food at their original locations.

Step3: evaluation of fitness function position and memory

The quality of the initial position is evaluated through a fitness function.

Step4: Generation of new position

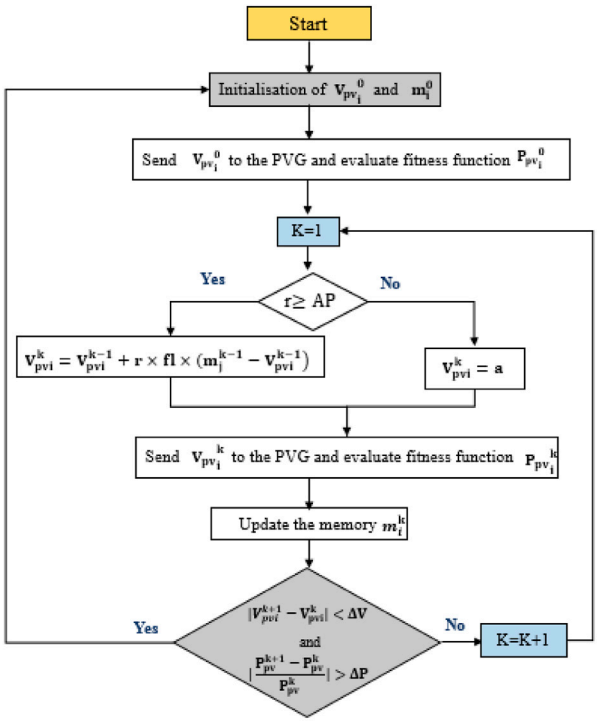

FIGURE 8
Flowchart of the proposed CSA technique.

In order to generate a new position and assuming that at at iteration k crow i tries to follow crow j to identify its hidden location of food. At this moment, depending on the value of the AP parameter, the position of crows are updated as follow:

State1: r ≥ AP

Where r is a random number varying between [0 1].

This situation signifies that crow j is unconscious that crow i is following it hence the position of crow i at an iteration (k+1) is updated according to the following equation:

$$x_i^{k+1} = x_i^k + r \times fl \times \left(m_j^k - x_i^k\right) \quad (24)$$

TABLE 5 Tuning parameters of the proposed MPPT methods.

Inc-Cond (ms)	FLC (ms)	CSA
Ts = 20	Ts = 20	AP = 0.02
		Fl = 1.5
		Ts = 20 ms

State2: r < AP

During this state, crow j is conscious that crow i is following it so it tries to trick it by moving randomly in the research space referring to the given equation:.

$$x_i^{k+1} = \text{a: random location}$$

The schematic of the update states and the effect of fl on the search capability are described in Figure 7.

Step 5: Assessment of the fitness function for newly created positions

After updating the position of each crow, the objective function of each new position is evaluated.

Step 6: update memory

The fitness values for each vector, both past and present, are used to update the memory. as follows:

$$m_i^{k+1} = \begin{cases} x_i^{k+1} & \text{if fitness}\left(x_i^{k+1}\right) > \text{fitness}\left(x_i^{k}\right) \\ m_i^{k} & \text{otherwise} \end{cases} \quad (25)$$

The four initial values of the vectors positions and memory are applied successively.

They are given by:

$$V_{pv_i}^{\ 0} = \left[V_1^0\ V_2^0\ V_3^0\ V_4^0\right] = [0.2 \quad 0.4 \quad 0.6 \quad 0.8] \times 2V_{oc} \quad (26)$$

$$m_i^0 = \left[m_1^0\ m_2^0\ m_3^0\ m_4^0\right] = [0.2 \quad 0.4 \quad 0.6 \quad 0.8] \times 2V_{oc} \quad (27)$$

The evaluation of the quality of initial positions is computed by using the expression of the fitness function below:

$$P_{pv_i}^{\ k} = V_{pvi}^k \times I_{pv} \quad (28)$$

The boost converter's duty cycle and output voltage are correlated in the following way:

$$\alpha_i^k = 1 - \frac{V_{pvi}^k}{2V_{oc}} \quad (29)$$

To update the positions and the memory of the four crows the expressions below are used:

$$V_{pvi}^{(k+1)} = \begin{cases} V_{pvi}^k + r \times fl \times \left(m_j^k - V_{pvi}^k\right) & \text{if } r \geq AP \\ a \quad \text{if } r < AP \end{cases} \quad (30)$$

In reality, the CSA needs to be reinitialized to find the new MPP in such circumstances of abrupt changes in the operating point brought on by variations in solar insolation. If this procedure is not followed, the global maximum and the local one cannot be updated automatically. The suggested criterion to reinitialize the MPPT technique is realized using variations in output voltage and output power as explained by Eqs (31), (32) respectively.

$$\left|V_{pvi}^{k+1} - V_{pvi}^k\right| < \Delta V \quad (31)$$

$$\left|\frac{P_{pv}^{k+1} - P_{pv}^k}{P_{pv}^k}\right| > \Delta P \quad (32)$$

Figure 8 shows the different CSA implementation processes for global optimization problem-based MPPT.

6 Results and discussion

In order to demonstrate the effectiveness of the suggested CSA technique in mitigating the negative impacts of PSC on the MPPT controller's performance in grid connected PV system, simulation studies using MATLAB/SIMULINK environment have been carried out. These studies encompassed three distinct partial shading scenarios. The tuned parameters of the proposed methods are displayed in Table 5. Three simulation scenarios were selected to assess the efficiency of the CSA-based MPPT technique in comparison with the Inc-Cond and FLC-based MPPT techniques, as depicted in Figure 9.

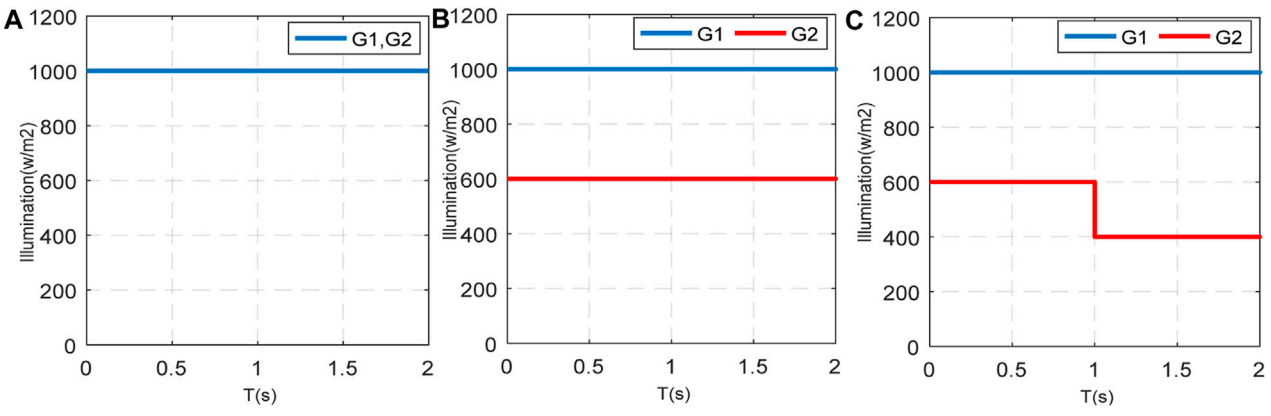

FIGURE 9
Illumination cases **(A)**. First case, **(B)** second case **(C)** Third case.

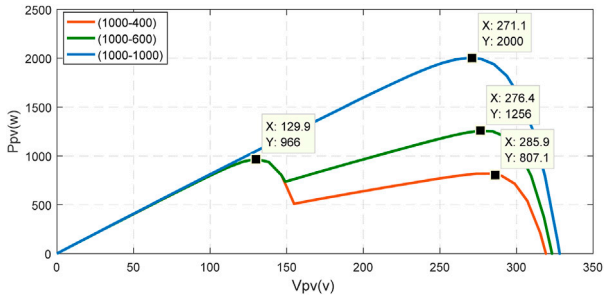

FIGURE 10
P-V characteristics of the PVG under different cases.

- First scenario: Under this specific scenario, both PVG1 and PVG2 experience identical uniform irradiation levels of 1000W/m^2.
- Second scenario: In this particular situation, partial shading is introduced to PVG2.**:** The PVG1 is exposed to 1000w/m^2 while the second PVG is subjected to 600 w/m^2.
- Third scenario: This case involves evaluating the proposed CSA-based MPPT technique under suddenly variation of the illumination.

The P-V characteristics of the PVG under various circumstances are displayed in Figure 10.

7 Discussion and analysis

Based on the acquired simulation results which are shown in Figures 11–13 an accurate comparison study between the three proposed algorithms is explained in Table 6. The bold value provided in Table 6 represent the extracted power and the mismatch power loss of the studied CSA method. The performance indices considered include the extracted Pv power and the mismatch power loss (MML) which is given by:

$$\mathrm{MML} = \frac{\text{Maximum Extracted Power}}{\sum_{i=1}^{N} P_{max}(i)} \times 100 \qquad (33)$$

Case (1): In this case, PVG1 and PVG2 are subjected to the same uniform irradiation (1000W/m^2). The P–V characteristic exhibits a singular GMPP peak at 2000W as presented in Figure 10. CSA method achieved after 0.31Sec the GMPP at 2000 W, without any steady state oscillations, while FLC and Inc-Cond methods reached 1950W and 1980W respectively after 0.68 s and.0.65 s with small steady state oscillations. It is noted that the response of CSA technique presents also less oscillations in the transient phase compared to that generated by other methods. Comparing to Inc–Cond and FLC methods, the CSA technique is more accurate, in fact the rate of oscillation and fluctuation noted in the response is reduced.

Case (2): the PVG1 is exposed to 1000w/m2 while the second PVG is subjected to 600 w/m2. This case yielded two peaks on the

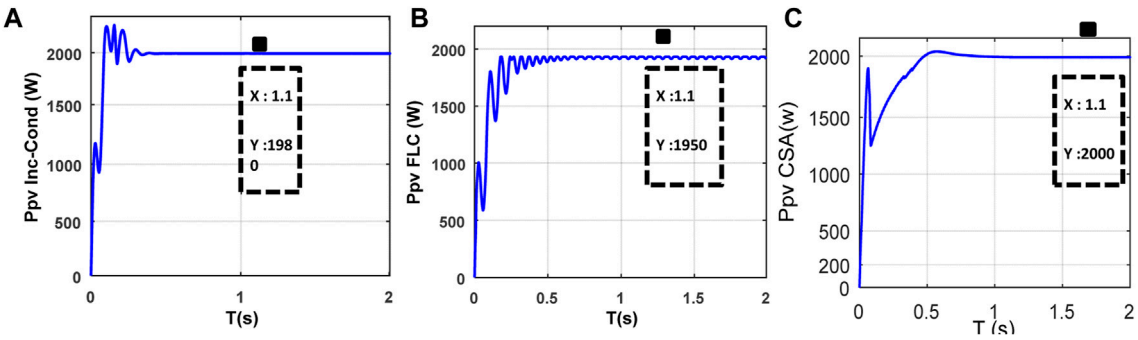

FIGURE 11
Simulated System responses under case (1). **(A)** Inc-Cond **(B)** FLC **(C)** CSA.

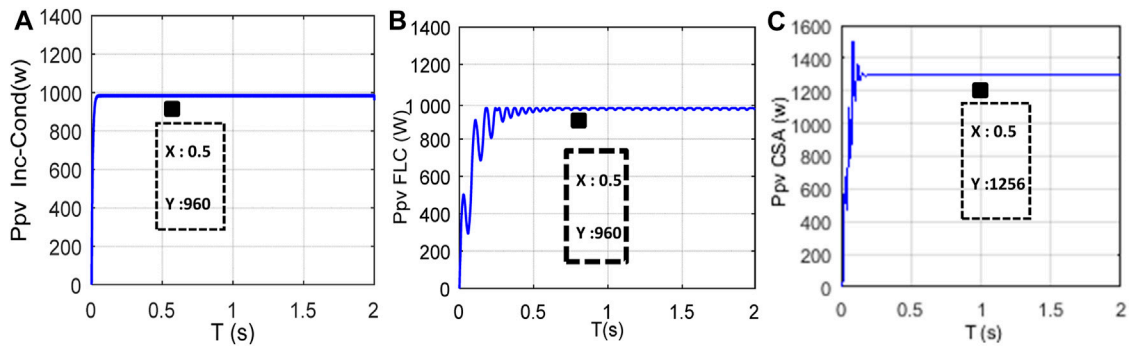

FIGURE 12
Simulated System responses under case (2) **(A)** Inc-Cond **(B)** FLC **(C)** CSA.

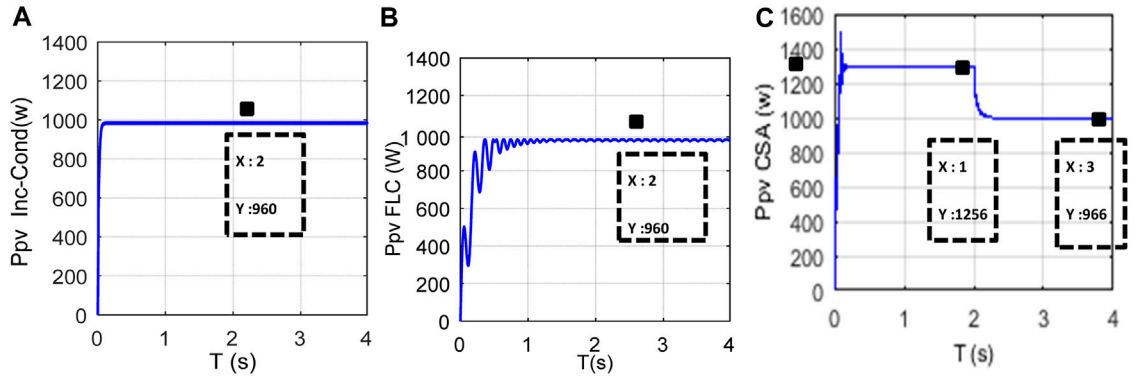

FIGURE 13
Simulated System responses under case (3) **(A)** Inc-Cond **(B)** FLC **(C)** CSA.

TABLE 6 statistical results of the used MPPT methods in the critical case 3 of PSC.

		Case1	Case2	Case3	
				(0-1)s	(1-2)s
GMPP		2000	1256	1256	966
PMPP	**CSA**	**2000**	**1256**	**1256**	**966**
	FLC	1950	960	960	960
	Inc-Cond	1980	960	960	960
MML	**CSA**	**100%**	**56.52%**	**56.52%**	**100%**
	FLC	97.5%	43.20%	43.20%	43.20%
	Inc-Cond	99%	43.20%	43.20%	43.20%

P–V curve as presented in Figure 10: the first one is a LMPP at 966w and the second one is a GMPP at 1256w. Figure 12 shows that CSA method converged to the GMPP of 1256 W after 0.49 s while both FLC and Inc_Cond stuck around the LMPP, they stopped at the first peak encountered. The FLC converged to 960w after 0.4s while the conventional Inc Cond reached 950W after 0.2s. Therefore, only the first local or global maximum—that is considered as the maximum power point for the shaded system—is achieved by these techniques, and they are unable to reach the global maximum if it is situated at the second level.

Case (3): In this case, there are two sequences in the variation's illumination scenario shown in Figure 9C. While the value of G2 varies from 600W/m2 to 400W/m2 at t = 1s, value of G1 is kept constant at 1000w/m2. Two GMPP are present in the PV characteristics. The first one is on the right side with 1256w and the second one is in the left side with 966w. The CSA technique succeeds in reaching the GMPP in every sequence and its response varies from 1256w to 966w.

It is clear from the above discussion that both Inc-Cond and FLC remain fixed around the LMPP, which is always powered lower than the GMPP. This significantly lowers the power provided by the PV system and contributes to the hot spot that forms on the shaded PV modules.

8 Conclusion

This present paper introduces the Crow Search Algorithm (CSA), a meta-heuristic optimization technique designed to address the adverse impacts of partial shading on the accurate pursuing the optimal maximum power point in a two stage grid connected PV system. A small-signal model of the studied system was considered to analyze the stability using Lyaponov function. The digital simulation results illustrated the exceptional capability of CSA technique in effectively tracking the GMPP across three different partial shading scenarios. Despite the dynamic shifts in climatic conditions, the recommended CSA technique demonstrated remarkable effectiveness in tracking the GMPP even in intricate shading scenarios. The CSA technique reduces the total power loss and extracts the maximum power from the studied PVG. The obtained results of the latter MPPT method are compared also with the FLC and Inc-Cond methods and they recorded better performance in terms of mismatch power loss with an average of 78.26%, for the three scenarios of simulation, whereas 56.77% and 57.15% were recorded for FLC and Inc-Cond techniques. Ultimately, a qualitative assessment utilizing statistical analysis validated the superior performance of the CSA technique.

Data availability statement

The original contributions presented in the study are included in the article/Supplementary materials, further inquiries can be directed to the corresponding authors.

Author contributions

MB: Conceptualization, Formal Analysis, Investigation, Methodology, Resources, Software, Writing–original draft, Writing–review and editing. AA: Conceptualization, Formal Analysis, Investigation, Methodology, Validation, Visualization, Writing–original draft, Writing–review and

editing. AS: Formal Analysis, Investigation, Methodology, Resources, Software, Validation, Writing–original draft, Writing–review and editing, Writing–review and editing. IH: Formal Analysis, Funding acquisition, Investigation, Methodology, Resources, Validation, Writing–original draft, Writing–review and editing.

Funding

The author(s) declare financial support was received for the research, authorship, and/or publication of this article. This research was funded by the Norwegian University of Science and Technology.

Acknowledgments

The authors would like to acknowledge the support of the Norwegian University of Science and Technology for paying the Article Processing Charges (APC) of this publication. The authors would like to thank Prince Sultan University, Riyadh, Saudi Arabia for their support. Special acknowledgment to Automated Systems and Soft Computing Lab (ASSCL), Prince Sultan University, Riyadh, Saudi Arabia. In addition, the authors wish to acknowledge the editor and anonymous reviewers for their insightful comments, which have improved the quality of this publication.

Conflict of interest

The authors declare that the research was conducted in the absence of any commercial or financial relationships that could be construed as a potential conflict of interest.

Publisher's note

All claims expressed in this article are solely those of the authors and do not necessarily represent those of their affiliated organizations, or those of the publisher, the editors and the reviewers. Any product that may be evaluated in this article, or claim that may be made by its manufacturer, is not guaranteed or endorsed by the publisher.

References

Ahmed, J., and Salam, Z. (2014). A maximum power point tracking (MPPT) for PV system using cuckoo search with partial shading capability. *Appl. Energy* 119, 118–130. doi:10.1016/j.apenergy.2013.12.062

Ahmed, J., and Salam, Z. (2015). A critical evaluation on maximum power point tracking methods for partial shading in PV systems. *Renew. Sustain Energy Rev.* 47, 933–953. doi:10.1016/j.rser.2015.03.080

Askarzadeh, A. (2016a). A novel metaheuristic method for solving constrained engineering optimization problems: crow searchalgorithm. *Comput. Struct.* 169, 1–12. doi:10.1016/j.compstruc.2016.03.001

Balaji, V., and Fathima, A. P. (2022). Hybrid algorithm for MPPT tracking using a single current sensor for partially shaded PV systems. *Sustain. Energy Technol. Assessments* 53, 102415. doi:10.1016/j.seta.2022.102415

Bounechba, H., Bouzid, A., Nabti, K., and Benalla, H. (2014). Comparison of perturb and observe and fuzzy logic in maximum power point tracker for PV systems. *Energy Procedia* 50, 677–684. doi:10.1016/j.egypro.2014.06.083

Chowdhury, S. R., and Saha, H. (2010). Maximum power point tracking of partially shaded solar photovoltaic arrays. *Sol. Energy Mater Sol. Cells* 94 (9), 1441–1447. doi:10.1016/j.solmat.2010.04.011

Eltamaly, A. M., Farh, H. M., and Othman, M. F. (2018). A novel evaluation index for the photovoltaic maximum power point tracker techniques. *Sol. Energy* 174, 940–956. doi:10.1016/j.solener.2018.09.060

Hinojosa, S., Oliva, D., Cuevas, E., Pajares, G., Avalos, O., and Gálvez, J. (2018). Improving multi-criterion optimization with chaos: a novel multi-objective chaotic crow search algorithm. *Neural Comput.* 29 (8), 319–335. doi:10.1007/s00521-017-3251-x

Houam, Y., Terki, A., and Bouarroudj, N. (2021). An efficient metaheuristic technique to control the maximum power point of a partially shaded photovoltaic system using crow search algorithm (CSA). *J. Electr. Eng. Technol.* 16, 381–402. doi:10.1007/s42835-020-00590-8

Ishaque, K., and Salam, Z. (2012). A deterministic particle swarm optimization maximum power point tracker for photovoltaic system under partial shading condition. *IEEE Trans. Ind. Electron* 60 (8), 1–3206. doi:10.1109/tie.2012.2200223

Kaced, K., Larbes, C., Ramzan, N., Bounabi, M., and Dahmane, Z. e. (2017). Bat algorithm based maximum power point tracking for photovoltaic system under partial shading conditions. *Sol. Energy* 158, 490–503. doi:10.1016/j.solener.2017.09.063

Karatepe, E., and Hiyama, T. (2009). Artificial neural network-polar coordinated fuzzy controller based maximum power point tracking control under partially shaded conditions. *IET Renew. Power Gener.* 3 (2), 239–253. doi:10.1049/iet-rpg:20080065

Kermadi, M., Salam, Z., Eltamaly, A. M., Ahmed, J., Mekhilef, S., Larbes, C., et al. (2020a). Recent developments of MPPT techniques for PV systems under partial shading conditions: a critical review and performance evaluation. *IET Renew. Power Gener.* 14 (17), 3401–3417. doi:10.1049/iet-rpg.2020.0454

Lian, K., Jhang, J., and Tian, I. (2014). A maximum power point tracking method based on perturb-and-observe combined with particleswarm optimization. *IEEE J. Photovolt.* 4 (2), 626–633. doi:10.1109/jphotov.2013.2297513

Maki, A., and Valkealahti, S. (2012). Power losses in long string and parallel-connected short strings of series-connected silicon-based photovoltaic modules due to partial shading conditions. *IEEE Trans. Energy Convers.* 27, 173–183. doi:10.1109/tec.2011.2175928

Mirza, A. F., Ling, Q., Javed, M. Y., and Mansoor, M. (2019). Novel MPPT techniques for photovoltaic systems under uniform irradiance and Partial shading. *Sol. Energy* 184, 628–648. doi:10.1016/j.solener.2019.04.034

Miyatake, M., Veerachary, M., Toriumi, F., Fujii, N., and Ko, H. (2011). Maximum power point tracking of multiple photovoltaic arrays: a PSO approach. *IEEE Trans. Aerosp. Electron Syst.* 47 (1), 367–380. doi:10.1109/taes.2011.5705681

Moghaddam, S., Bigdeli, M., Moradlou, M., and Siano, P. (2019). Designing of standalone hybrid PV/wind/battery system using improved crow search algorithm considering reliability index. *Int. J. Energy Environ. Eng.* 10 (4), 429–449. doi:10.1007/s40095-019-00319-y

Mohamed, M. A., Diab, A. A. Z., and Rezk, H. (2019). Partial shading mitigation of PV systems via different meta-heuristic techniques. *RenewEnergy* 130, 1159–1175. doi:10.1016/j.renene.2018.08.077

Mohanty, S., Subudhi, B., and Ray, P. K. (2015). *A new MPPT design using grey wolf optimization technique for photovoltaic system under partial.*

Ram, J. P., and Rajasekar, N. (2017). A new robust, mutated and fast tracking LPSO method for solar PV maximum power point tracking under partial shaded conditions. 201:45–59. doi:10.1016/j.apenergy.2017.05.102

Salah, C. B., and Ouali, M. (2011). Comparison of fuzzy logic and neural network in maximum power point tracker for PV systems. *Electr. Power Syst. Res.* 81 (1), 43–50. doi:10.1016/j.epsr.2010.07.005

Sundareswaran, K., Sankar, P., Nayak, P. S. R., Simon, S. P., and Palani, S. (2014). Enhanced energy output from a PV system under partial shaded conditions through artificial bee Colony. *IEEE Trans. Sustain Energy* 6 (1), 198–209. doi:10.1109/tste.2014.2363521

Sundareswaran, K., Vigneshkumar, V., and Palani, S. (2015). Development of a hybrid genetic algorithm/perturb and observe algorithm for maximum power point tracking in photovoltaic systems under non-uniform insolation. *IET Renew. Power Gen.* 9 (7), 757–765. doi:10.1049/iet-rpg.2014.0333

Wang, Z., Luo, Q., and Zhou, Y. (2020). Hybrid metaheuristic algorithm using butterfly and flower pollination base on mutualism mechanism for global optimization problems. *Eng. Comput.* 37, 3665–3698. doi:10.1007/s00366-020-01025-8

Wu, Z., and Yu, D. (2018). Application of improved bat algorithm for solar PV maximum power point tracking under partially shaded condition. *Appl. Soft Comput.* 62, 101–109. doi:10.1016/j.asoc.2017.10.039

Yilmaz, U., Turksoy, O., and Teke, A. (2019). Improved MPPT method to increase accuracy and speed in photovoltaic systems under variable atmospheric conditions. *Int. J. Electr. Power Energy Syst.* 113, 634–651. doi:10.1016/j.ijepes.2019.05.074

frontiers | Frontiers in Energy Research

TYPE Original Research
PUBLISHED 27 March 2024
DOI 10.3389/fenrg.2024.1370412

OPEN ACCESS

EDITED BY
Enrico Maria Vitucci,
University of Bologna, Italy

REVIEWED BY
Dheeraj Joshi,
Delhi Technological University, India
Nishant Kumar,
Indian Institute of Technology Jodhpur, India

*CORRESPONDENCE
Shitharath Selvarajan,
s.selvarajan@leedsbeckett.ac.uk

RECEIVED 14 January 2024
ACCEPTED 13 March 2024
PUBLISHED 27 March 2024

CITATION
Srilakshmi K, Sundaragiri D, Gaddameedhi S, Vangalapudi R, Balachandran PK, Colak I and Selvarajan S (2024), Simulation of grid/standalone solar energy supplied reduced switch converter with optimal fuzzy logic controller using golden BallAlgorithm. *Front. Energy Res.* 12:1370412. doi: 10.3389/fenrg.2024.1370412

Simulation of grid/standalone solar energy supplied reduced switch converter with optimal fuzzy logic controller using golden BallAlgorithm

Koganti Srilakshmi[1], Dheeraj Sundaragiri[2], Sravanthy Gaddameedhi[1], Ramprasad Vangalapudi[1], Praveen Kumar Balachandran[3], Ilhami Colak[4] and Shitharath Selvarajan[5]*

[1]Department of Electrical and Electronics Engineering, Sreenidhi Institute of Science and Technology, Hyderabad, Telangana, India, [2]Department of Computer Science and Engineering, Sreenidhi Institute of Science and Technology, Hyderabad, Telangana, India, [3]Department of Electrical and Electronics Engineering, Vardhaman College of Engineering, Hyderabad, Telangana, India, [4]Department of Electrical and Electronics Engineering, Faculty of Engineering and Architectures, Nisantasi University, Istanbul, Türkiye, [5]Cyber Security and Digital Forensics, School of Built Environment, Engineering and Computing, Leeds Beckett University, Leeds, United Kingdom

This article presents the utilization of a shunt active power filter (SHAPF) in combination with an Energy Storage System (ESS) and a Solar Energy System (SES). Voltage source converters (VSC) are connected in parallel to a direct current (DC) bus. The membership function (MSF) of fuzzy logic controller (FLC) for the shunt control system is optimally adjusted using the golden balloptimization algorithm (GBOA). The present effort aims to achieve the following primary objectives: 1) Quick implementation to stabilize the voltage of the DC Link capacitor (DCLCV); 2) Mitigation of harmonics and improvement of power factor (PF); 3) Satisfactory performance under load as well as solar power varying conditions. The effectiveness of the optimally designed controller is evaluated by studying four test scenarios with grid and standalone conditions. The results are then compared to the existing sliding mode (SMC) and fuzzy logic controllers (FLC).

KEYWORDS

fuzzy logic controller, golden ball optimization algorithm, solar system, battery system, reduced switch converter

1 Introduction

Promoting the insertion of sources of clean energy, such as wind and solar energy, into the network of distribution has been encouraged over the past few years to reduce the burden on converters and ratings. The word “reduced switch” refers to achieving its objectives with a reduced number of switches in comparison to conventional systems. This reduction in the number of switches can lead to benefits such as lower cost, reduced power losses, and improved reliability. Like other active power filters, reduced Switch Shunt Active Power Filters play a crucial role in maintaining a stable and high-quality electrical power

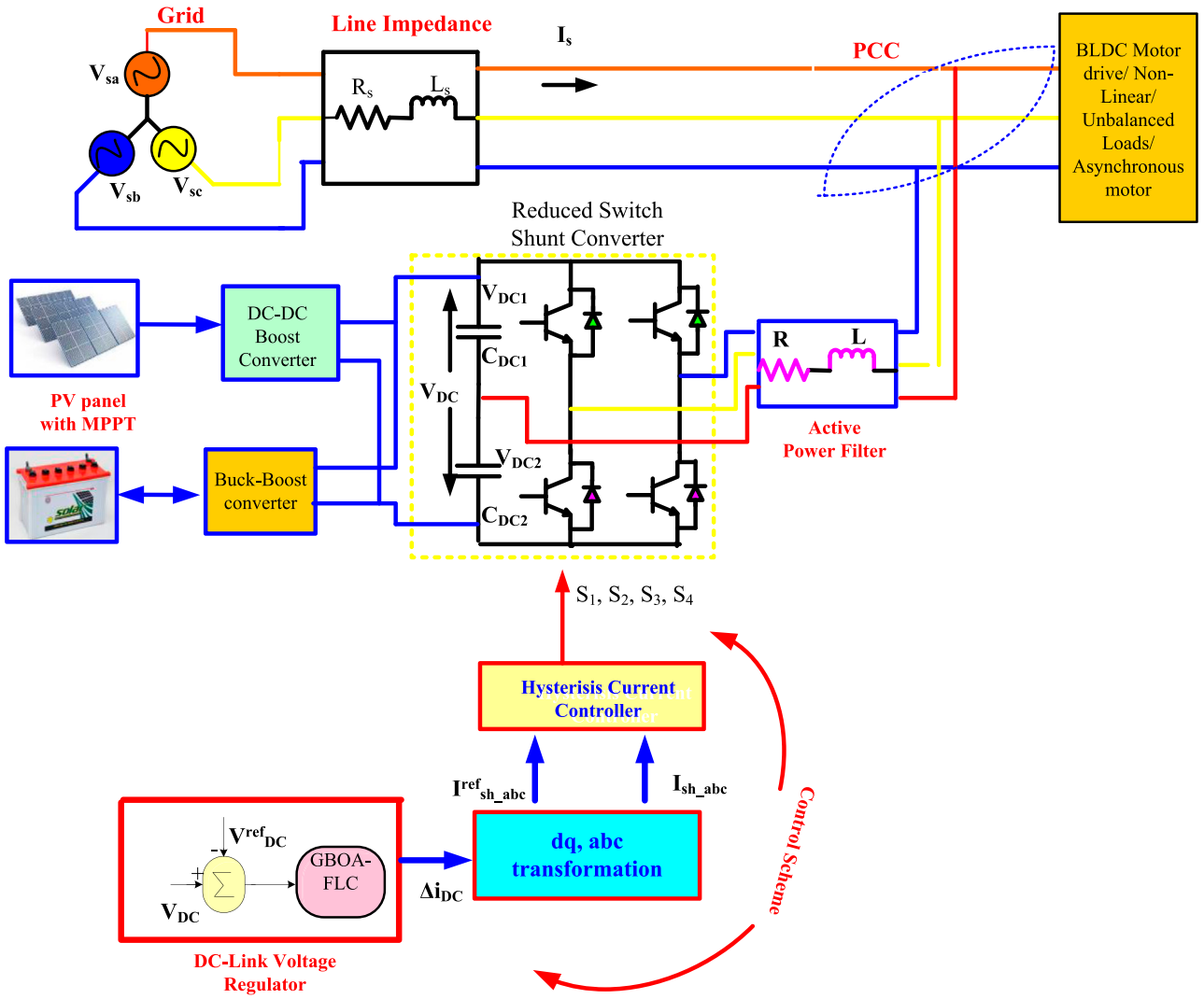

FIGURE 1
Reduced switch VSC.

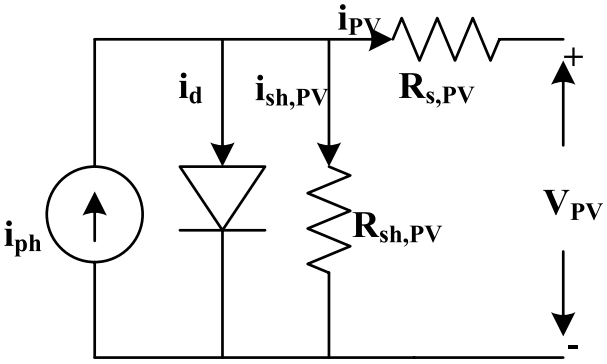

FIGURE 2
PV single-cell model.

supply in modern power systems. Their design and operation may vary based on specific requirements and the characteristics of the power system.

1.1 Motivation

The significance of SHAPF in distributed power generation systems and micro-grids has lately garnered attention. The integration of SHAPF with alternative sources of energy has become increasingly important compared to the traditional grid-connected VSC. This strategy has several benefits, including the capacity to keep a steady (DCLCV) despite load swings enhance Power Quality (PQ) on the grid, safeguard sensitive equipment from disturbances originating from the grid, and enhance the converter's ability to withstand transient events. Besides, the 3-phase, 3-wire distribution networks are particularly suitable for utilizing shunt filters with clean energy sources. Most of the techniques described in current literature papers are with conventional proportional integral controller (PIC), SMC, and artificial intelligence (AI) methods involving various loads. However, these methods have not successfully obtained optimized values during change in irradiation and load.

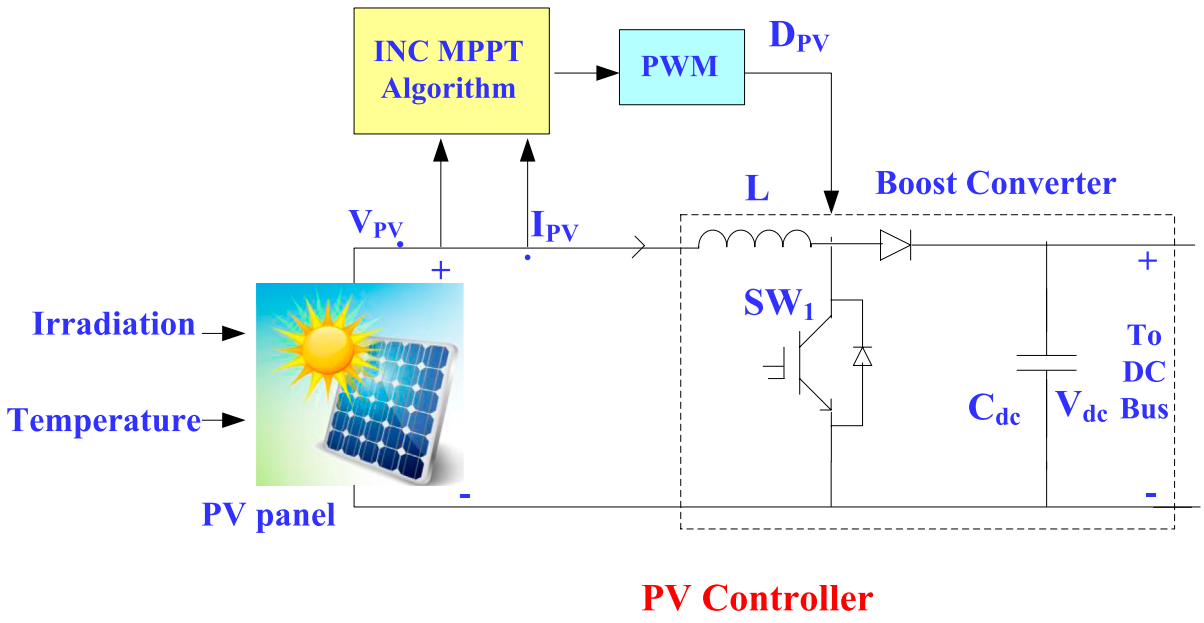

FIGURE 3
Control of SES system.

1.2 Literature survey

A novel automated transition mechanism has been devised for the SES and ESS tie UPQC to address PQ challenges in grid and island modes effectively. Moreover, the system's function was validated using empirical data (Devassy and Singh, 2020). An evaluation was undertaken to assess the performance of the SES and ESS for UPQC utilizing the Adaptive Neuro-Fuzzy Inference System (ANFIS) technique. This system was designed to improve PQ. The evaluation was conducted under different demand and supply instances (Dheeban and MuthuSelvan, 2021). In addition, it was proposed to combine UPQC with PV systems using an adaptive compensation technique. This technique utilizes the variable leaky least mean square (VLLMS) algorithm to eliminate the need for a low-pass or moving average filter. Instead, it extracts the fundamental components from the distorting input voltage and load current. It generates a reference signal to regulate the VSCS switching operations in the UPQC (Ray et al., 2022). Simultaneously, a computational challenge was presented to identify the optimal positions and setups for grid-connected PV systems. The purpose is to enhance the reliability of power generation by maximizing the efficiency of PV systems in diverse scenarios with varying generation probabilities (Tawfiq et al., 2021).

The adaptive distributed power control technique was proposed to address problems such as THD and voltage aberrations. This technique involves using two H-connected arrangements, each consisting of eight switches, for the 3-ω UPQC (Mohanraj and Prakash, 2020). Additionally, the PPDM was implemented for the UPQC in the context of a multilayer Cascaded Inverter. The principal objective is to reduce fluctuation in voltage (sag and swell), manage harmonics, and maintain a stable DCLCV (Vinothkumar and Kanimozhi, 2021). A performance comparison was conducted between the P & O and PSO algorithms to get maximum power point tracking system (MPPT) for the PV system during changes in irradiance. The micro-inverter adjusts to partial circumstances (Jaber and Shakir, 2021a). Furthermore, a multi-level cascade UPQC was developed to mitigate voltage supply abnormalities and THD by utilizing PV, wind, and Proton Exchange Membrane Fuel Cells (PEMFCS) as power sources (Sarker et al., 2020).

The UPQC system, associated with ESS and SES, was suggested to mitigate THD and resolve grid voltage problems (AlifMansor et al., 2020). Besides, the study investigated several control techniques and algorithms for UPQC to improve PQ. As a result, a flexible control strategy was recommended (SaiSarita et al., 2021). The SES-supplied Synchronous Uninterruptible Active Power Filter was developed to control reactive power effectively and minimize THD in current waveforms. However, to generate appropriate reference currents, the Maxikalman filter was designed (Das et al., 2021). Meanwhile, ANN controller, utilizing feed-forward training, was implemented in a UPQC system connected to SES and WES sources. This controller was used for voltage regulation and control of reactive power inside the grid (Chandrasekaran et al., 2021).

The UPQC was employed to correct voltage imbalances, reduce current harmonics imperfections, and improve network efficiency. This was accomplished by incorporating an adaptive ANFIS controller (Renduchintala et al., 2021). The FLC was suggested for incorporating the series filter into the grid-tie three-phase distribution system to tackle power quality issues such as voltage fluctuations, decreased total harmonic distortion of the current signal, and continuous maintenance of DCLCV stability (Pazhanimuthu and Ramesh, 2018). However, a specialized SRFT technique utilizing a PIC was designed specifically for the synchronous uninterruptible SHAPF connected with the fuel cell. The main goal is to decrease the existing harmonics with DCLCV

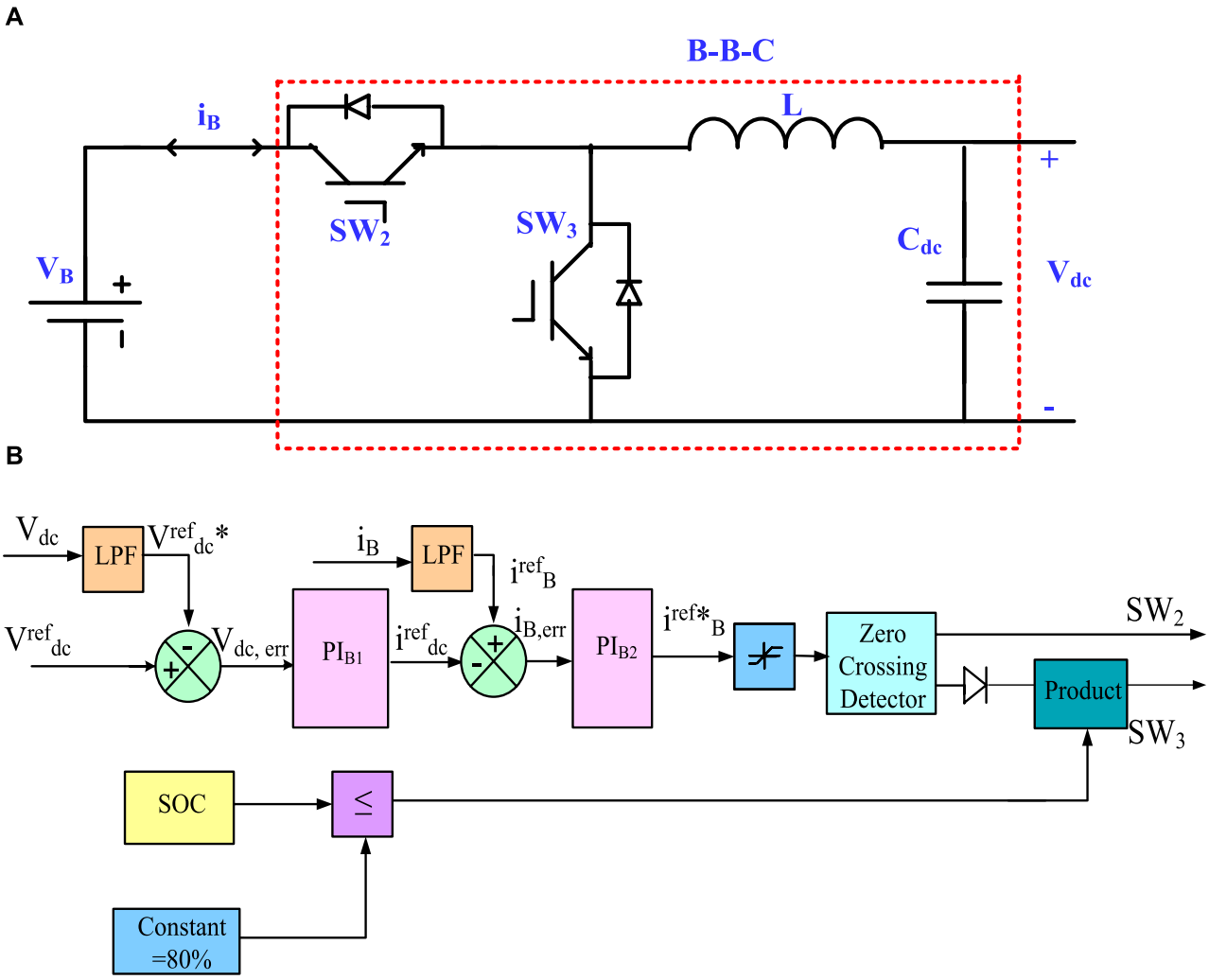

FIGURE 4
ESS. **(A)** ESS configuration at DC link **(B)** ESS controller.

TABLE 1 Power dispersion at DC link.

Modes of operation	Action taken
Mode-1: When No SES	Only ESS will supply power to P_L
Mode-2: When SES = P_L	Solar PV supply power to P_L
Mode-3: When SES< P_L	The battery will supply the cumulative difference in power until till $SOCB_{min}$
Mode-4: When SES> P_L	The surplus solar electricity is utilized to charge the Battery system until it reaches $SOCB_{max}$

stable (K Krishna et al., 2020). The idea entailed the integration of intelligent Fuzzy-PI and Fuzzy-PID controllers into an AC-DC micro-grid to address PQ issues and enhance voltage stability. Moreover, the effectiveness of the controllers was demonstrated through two scenarios involving different levels of loads (Abdelnasser et al., 2022).

An adaptive full-order technique is proposed to improve UPQC by reliably detecting faults in dynamic load variations and grid circumstances. In addition, a BBO metaheuristic technique was utilized to tune the gain parameters of the PIC to stabilize DCLCV oscillations (Sayed et al., 2021) efficiently. On other hand, the experimental setup of a full bridge DC-DC converter was examined along with a snubber circuit (Jaber and Shakir, 2021a). A novel hybrid control approach was developed by integrating the Improved Bat Algorithm and Moth Flame Algorithm to tackle power quality concerns in a micro-grid system effectively. The objective of this strategy is to reduce the error function that is linked to power variations. Fine-tuning the Kp and Ki parameters optimally can minimize the operational expenses associated with renewable energy sources (Rajesh et al., 2021). A

TABLE 2 SES and ESS ratings.

Equipment	Factor	Value chosen
PV single panel (Sun power SPR-305E-WHT-D)	PV cells connected in parallel, series	66, 5
	Maximum PV Output power	305.22W
	Under max power the current/voltage	5.58A/54.7V
	Voltage under open circuit condition	64.2V
	Current under short circuit condition	5.96A
Li-ion battery	Fully charge voltage	350V
	Rated Capacity of battery	35Ah

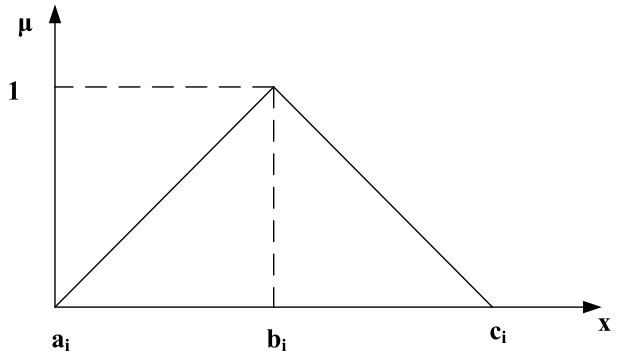

FIGURE 5
Triangular MSF.

hybrid control system incorporating fuzzy back-propagation was used to a 5-level UPQC to decrease THD and improve the power factor (Nagireddy et al., 2018). In addition, a unique method was proposed to combine sequence-component identification with unit vector-template creation for the double-stage SES UPQC. This method aims to address PQ problems (Nkado et al., 2021).

A novel control method utilizing a damped fifth-order generalized integrator was proposed for grid-integrated solar photovoltaic (PV) systems. Furthermore, the GMPPT utilizes the HPO algorithm. A grid-integrated partially shaded PV array with a single-stage topology, consisting of three phases and three wires, was built. The HPO algorithm exhibits speedy and accurate global maximum power peak seeking behaviour, resulting in good steady-state and dynamic performances, even under rapid solar irradiance change (Kumar et al., 2019). On the other hand, a technology called adaptive Maximize-M Kalman filter is utilized for better optimal control. In order to optimize the amount of power extracted from a solar PV panel, a grid-integrated solar PV system utilizes a learning-based hill-climbing algorithm (Kumar et al., 2020).

However, a model predictive control algorithm is used to manage and control the power transmission between a solar PV system and the grid efficiently. The double stage three-phase design is regulated utilizing a model predictive control technique that considers the power converters' switching states to anticipate the next control variable. The control utilizes a modified-dual second-order generalized-integrator to estimate the power demands, taking into account the continuously changing system parameters (Saxena et al., 2021). Meanwhile, a novel voltage sensorless model predictive control approach was proposed for efficient and rapid maximum power extraction from a PV array in a solar-powered on-board electric vehicle (EV) charging system. The VSPC system employs the initial model predictive control technique, utilizing a PV array to forecast the system's condition within a specific time frame and to eliminate the need for a voltage sensor (Kumar et al., 2023).

Besides, a novel command authentication strategy was developed to detect and mitigate false data injection attacks targeting the system centralized economic dispatch control signals (Siu et al., 2022). A revolutionary hill climbing MPPT algorithm was created using a parabolic curve fitting to efficiently harvest the maximum power from solar PV panels. This algorithm was designed for residential customers and can adapt to changing environmental circumstances. Furthermore, the advanced PCHC algorithm has been combined with an innovative decreased sensor-based method, in which a solitary current sensor is employed to charge the solar-powered battery (Kumari et al., 2023).

However, the hybrid fuzzy-sliding mode control (HFSMC) based maximum-power-point tracking system (MPPTs) is adopted for solar PV system to extract maximum output (Srilakshmi et al., 2023). Besides, the design of Unified Power Quality Conditioner (UPQC) through the optimal selection of the active filter and PID Controller parameters using the enhanced most valuable player algorithm (EMVPA) was suggested to handle PQ issues (SrilakshmiKoganti et al., 2024). Besides, the soccer league algorithm-based optimal tuned hybrid controller for the UPQC was designed for PQ enhancement (Srilakshmi et al., 2022). On the other hand, the optimal training of neural network controller was proposed for the UPQC to handle PQ problems (AlapatiRamadevi et al., 2023). The Optimal design of artificial neuro fuzzy controller member ship function was carried out with the firefly and harmony search algorithms (Srilakshmi et al., 2024).

1.3 Key contribution

The following steps emphasize the contribution of this manuscript:

- Introducing the SHAPF using the nature-inspired metaheuristic GBOA.

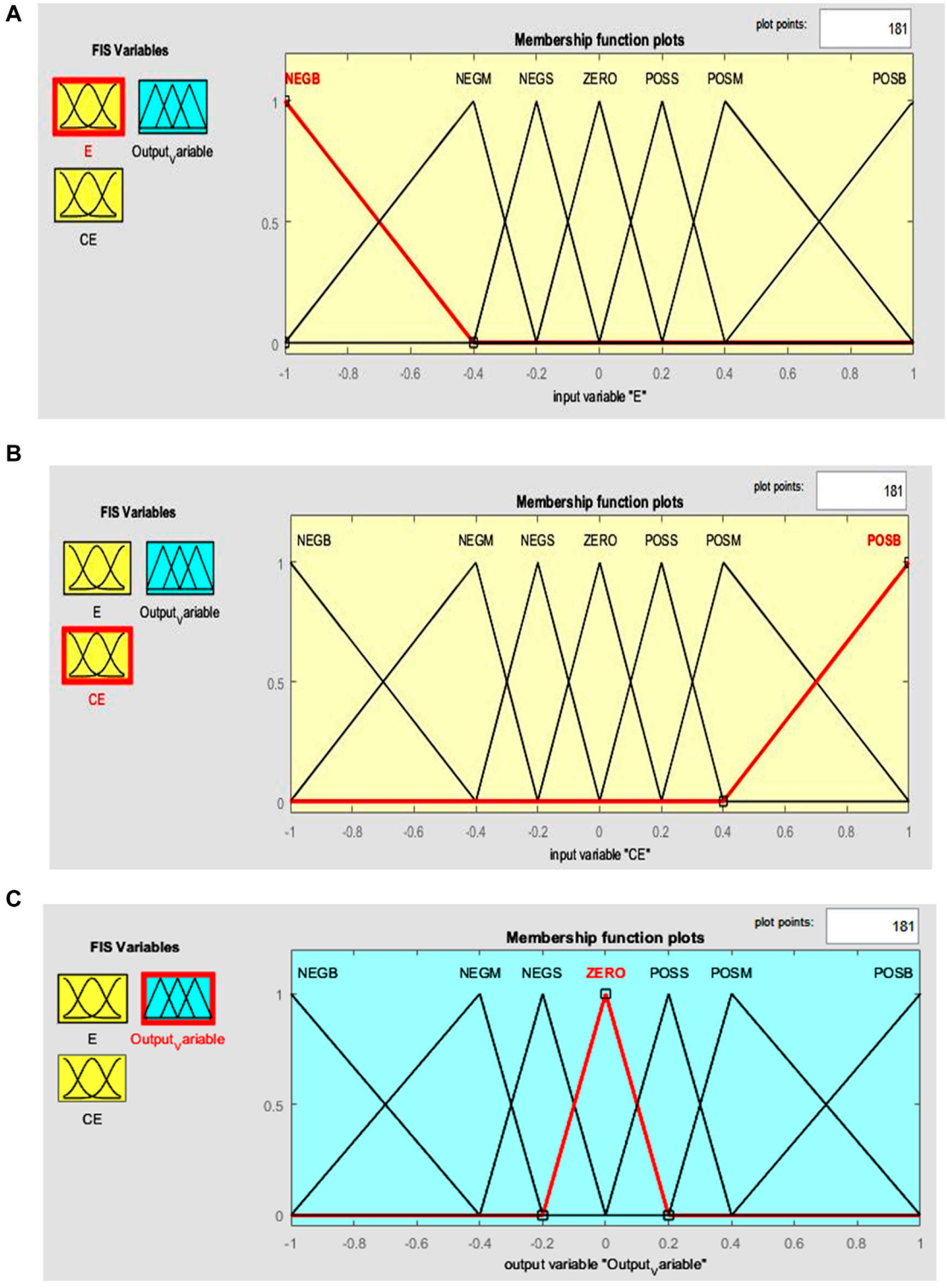

FIGURE 6
Optimal MSF with GBOA. **(A)** E **(B)** CE **(C)** Output.

- Design of reduced switch SHAPF.
- Optimal selection of MSF parameters for reduced switch SHAPFwith GBOA in order to minimize imperfections in the current waveforms and appropriate power supply to the load.
- Integrating the SES and ESS into the DC connection of the proposed reduced switch VSC reduces the burden and stress on the filter. This integration will also enable the filter to fulfill load demands and maintain a steady DCLCV even during changes in demand and irradiation.

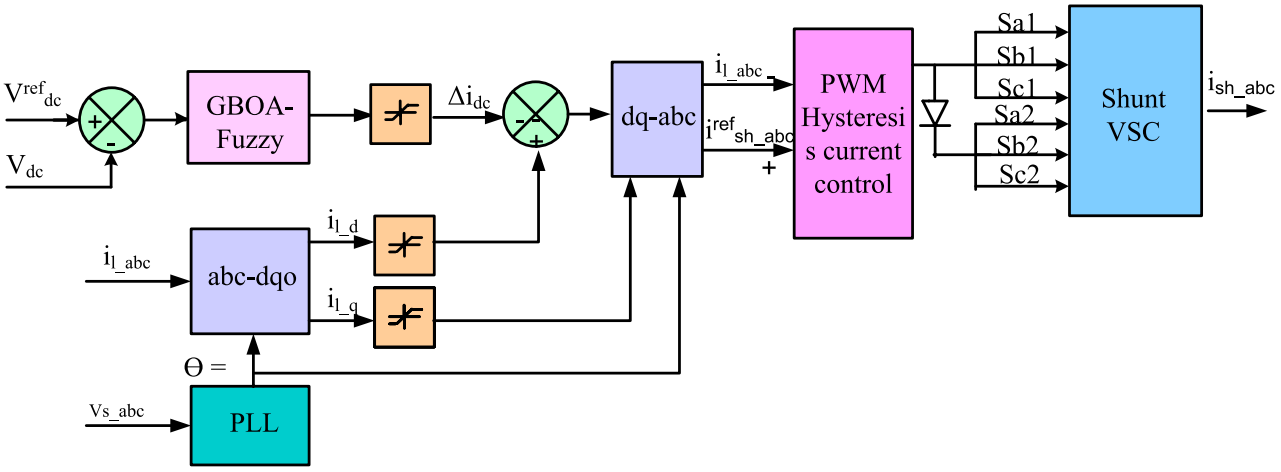

FIGURE 7
Hybrid controller for shunt converter.

➢ The proposed strategy is to enhance power factor, achieve consistent direct current line current variation within a brief timeframe, and minimize total harmonic distortion of the source current. To further show the efficiency of the suggested approach, it is subjected to examination under four different situations, each characterized by changing loads and Sun irradiation levels as well as grid and standalone conditions.

The structure of this paper is as outlined below: Section 2 covers the reduced switch VSC, focusing on its external sources. Section 3 describes the recommended control system with GBOA. Section 4 gives the outcomes and discussions. Finally, Section 5 ends the manuscript.

2 System design and modeling

Figure 1 depicts the block diagram of the SHAPF connected to the DC link, along with ESS and SES. When coupled in parallel to the load, the inverter acts as SHAPF to compensate the harmonics in the load current while simultaneously maintaining DCLCV. In the conventional inverter configuration, a more significant number of switches are needed. This work utilizes a simplified switch configuration for an inverter of a SHAPF. The Modified low Switch SHAPF technique decreases the number of switches in the Bridged VSC from six to four. Split capacitors are used to connect the third phase. Figure 1 depicts the proposed VSC, with various load types.

2.1 Design of SHAPF

The fundamental role of SHAPF is to provide a distortion-free supply current by injecting the required amount of current at the point of common coupling (PCC). The control circuit uses Eqs 1–4, to calculate the necessary magnitude of compensated current.

$$i_s = i_l - i_{sh} \tag{1}$$

$$V_s = V_m \sin wt \tag{2}$$

$$i_l = \sum_{n=1}^{\infty} i_n \sin(nwt + \varphi_n) = i_1 \sin(wt + \varphi_1) + \sum_{n=1}^{\infty} i_n \sin(nwt + \varphi_n) \tag{3}$$

$$P_L = V_s{}^{*} i_l \tag{4}$$

Where, “Vm” denotes the amplitude voltage of the sinusoidal signal, “n” resembles the nth harmonic current, “il” indicates load current, “ish” gives the shunt filter compensating current, PLis the load power, Eq 5 can be utilized to obtain the numerical value of Cdc

$$C_{dc} = \frac{\pi^{*} i_{sh}}{\sqrt{3}\omega V_{cr,pp}} \tag{5}$$

The V_{dc}^{ref} selection is made from the available ratings provided by the proposed method. The choice is determined by the peak-to-peak voltage ripple ($V_{cr,pp}$) and the shunt adjusting current. The inductor (Lsh) links the shunt VSC to the network and its characteristics are determined by the DCLCV, switching frequency, and ripple current as mentioned in Eq. 6:

$$L_{sh,\min} = \frac{\sqrt{3}\, m\, V_{dc}}{12\, a_f\, f_{sh}\, I_{cr,pp}} \tag{6}$$

The value of (L_{sh}) is determined by the switching frequency (f_{sh}) is 10 kHz, the peak-to-peak ripples ($I_{cr,pp}$), the overloading factor (a_f) is 1.5with the assumption that the modulation depth (m) is 1.

2.2 Mathematical modelling of the external sources and modes of operation

The reduced switch VSC is recommended for employing the SES and ESS to supply the DC link. The DCLCV is regulated by a sustainable energy source with the support of ESS assistance during fluctuations in power demand. These external sources of

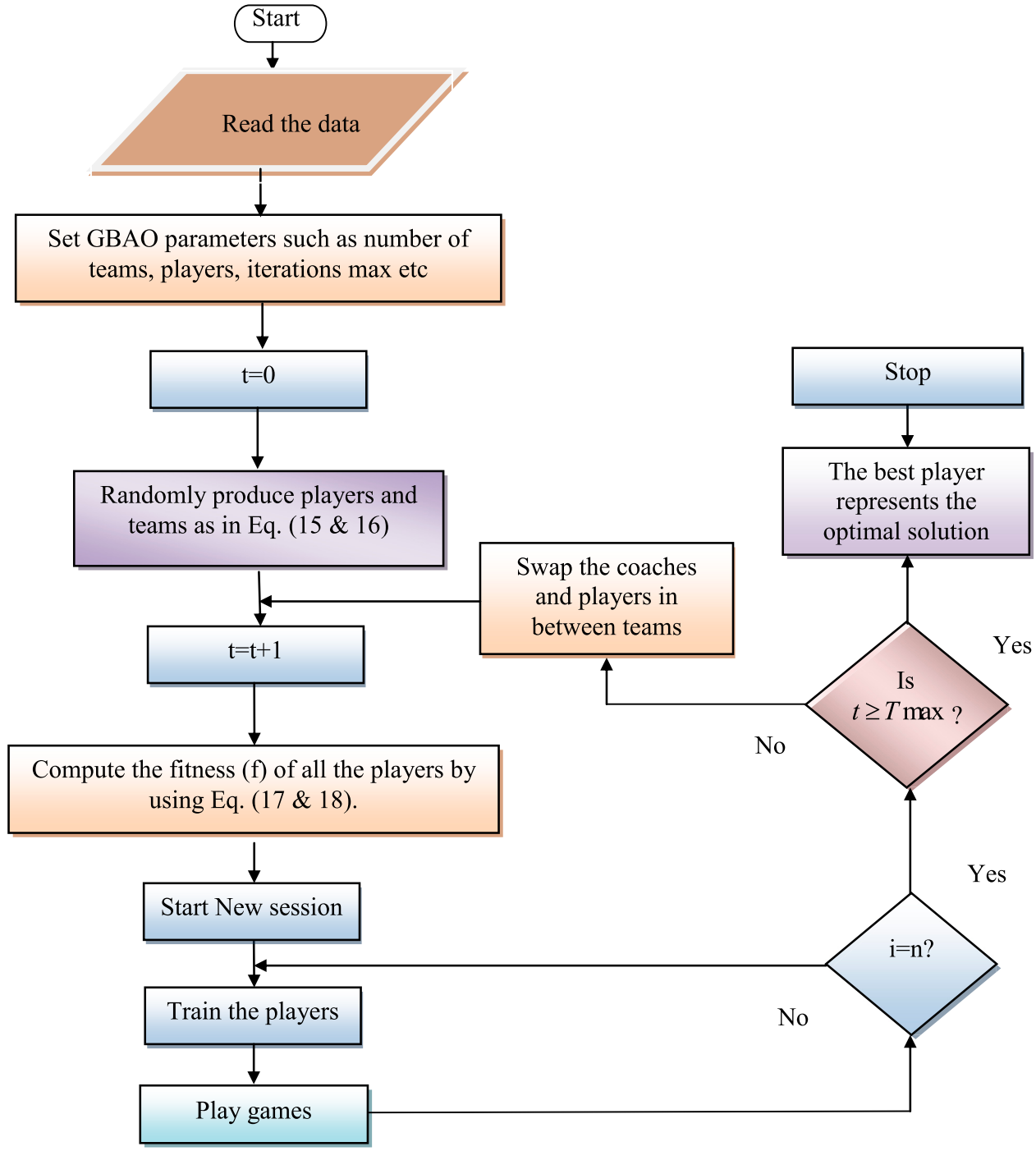

FIGURE 8
Flow chart of GBOA.

TABLE 3 System with SHAPF parameters.

Grid supply	V_s: 415Volts; f: 50Hertz R_s: 0.1Ω; L_s: 0.15 mH
SHAPF	R_{sh}: 0.0010 Ω; L_{sh}: 2.15 mH
DClink	C_{dc}: 9,400 microfarad; V_{dc}^{ref} = 700Volts

TABLE 4 Cases studies under 250 c solar Temperature.

	Case study 1	Case study 2	Case study 3	Case study 4
Grid Connected	✓	✓	✓	
Standalone				✓
Fixed solar irradiation (1000 W/m2)	✓			✓
Fixed solar irradiation (800 W/m2)		✓		
Variable solar irradiation			✓	
Load-1: Balanced bridged rectifier non-linear load: 60Ω and 30 mH	✓		✓	✓
Load 2: Unbalanced RL branch Load R1 = 10 Ω, R2 = 40 Ω and R3 = 80Ω L1 = 1.5mH, L2 = 3.5 mH and L3 = 2.5 mH		✓	✓	
Load 3: BLDC Motor drive	✓	✓	✓	✓
Load 4: Asynchronous Motor	✓			
Load 5: Active and Reactive power load p = 2000 W, 5000Vars		✓	✓	
THD	✓	✓	✓	
Power Factor	✓	✓	✓	
DC link voltage settling time (sec)	✓	✓	✓	✓

TABLE 5 Comparison of %THD.

Ref []/Controller	Case-1	Case-2	Case-3
Without SHAPF	28.99	11.36	27.33
PIC	6.01	5.12	6.12
FLC	4.48	3.99	4.89
SMC	4.91	3.54	4.97
GBOA-FLC	2.27	2.24	4.55

supply reduce converter ratings and stress by alleviating the demands imposed by the utility. Eq. 7 yields the recommended technique's PL.

$$P_{PV} \pm P_{BSS} + P_G = P_L \tag{7}$$

2.2.1 SES

The PV version employed in this investigation was selected from the Simulink library. However, to achieve the necessary voltage and current, the PV modules are connected in a series arrangement to form a string. Consequently, several of the above strings are joined together in parallel. Every PV cell within the module is constructed with a simpler circuit comprising just one diode, as depicted in Figure 2.

The PV cell's output current is determined by applying Kirchhoff's law as stated in Eq. 8

$$i_{PV} = i_{ph} - i_d - i_{sh,PV} \tag{8}$$

Eq. 9 links the PV modules in both series and parallel configurations, forming an array and Eq. 10 gives the PV current.

$$i_{PV,m} = i_{ph}N_p - i_{S,PV}N_p\left[\exp\left(\frac{Q\left(V_{PV} + N_s/N_p\left(i_{PV,m}R_{S,PV}\right)\right)}{N_s\eta kT_C}\right) - 1\right] - \frac{V_{PV,m} + N_s/N_p\left(i_{PV,m}R_{S,PV}\right)}{N_s/N_p\left(R_{sh,PV}\right)} \tag{9}$$

Here,

$$i_{ph} = \left(i_{ph,n} + K_1\Delta T_C\right)\frac{G}{G_n} \tag{10}$$

Here, "PPV, VPV, iPV" resembles solar output power, voltage and current. "iph, id, ish,PV" gives photo current, diode current and shunt PV current. "Np, Ns, T, G" indicates number of cells in parallel, series, temperature and irradiation. Suffix "m" indicates module.

Eq. 11 describes the solar output whose controller is given in the Figure 3. The FLC-basedMPPT method (Discussed in Section 3 in detail) was adopted in this work to extract maximum output.

$$P_{PV} = V_{PV} \times i_{PV} \tag{11}$$

2.2.2 ESS

The lithium-ion ESS offers advantages such as low self-discharge and minimal maintenance requirements. The battery can undergo charging or discharging processes utilizing switches SW1 and SW2, as depicted in Figure 4A. Eq. 12 represents the state-of-charge (SOCB) of the battery.

$$SOCB = 80\left(1 + \int i_{BS}\,dtQ\right) \tag{12}$$

The battery's ability to charge or discharge depends upon the quantity of SES and SOCB limits.

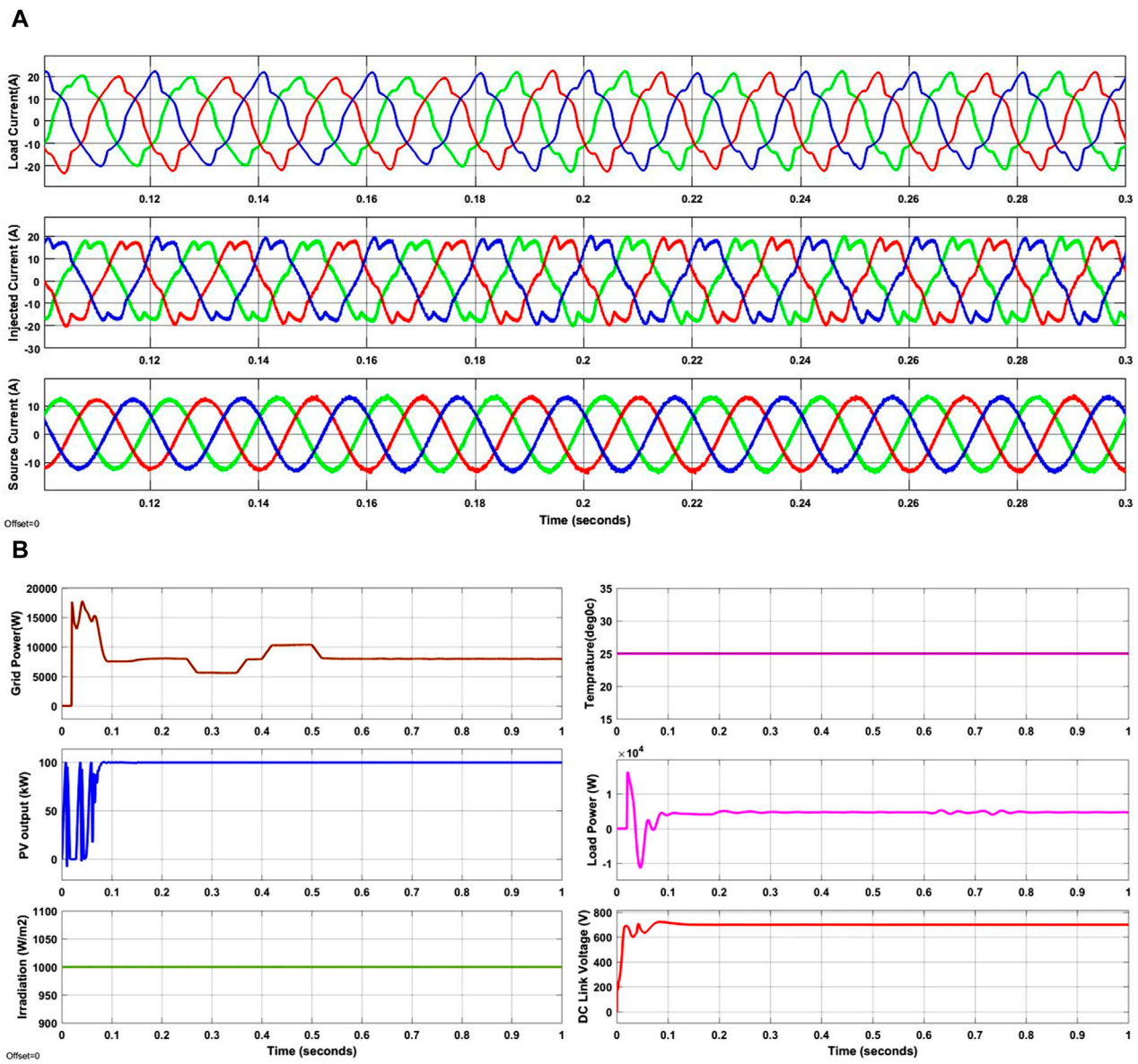

FIGURE 9
Waveforms of the suggested method for case one. **(A)** i_l, i_{sh}, i_s **(B)** Grid power, P_{PV}, G, T, P_L, DCLCV.

$$SOCB_{\min} \le SOCB \le SOCB_{\max} \quad (13)$$

In this Eq. 13, the symbol "SOCB" represents the battery's state of charge and current. "SOCBmax" and "SOCBmin" show the maximum and minimum permissible values for the state of charge of the battery. Figure 4B depicts the control circuit regulating the battery operation concerning the desired DCLCV. Table 1 presents the power management of SES and ESS in conjunction with the grid and load. Table 2 displays the selected SES and ESS values for the project.

3 Control scheme

The primary objectives of SHAF are to maintain the DCLCV at a consistent level and mitigate waveform abnormalities by providing an optimal current. It does the following frame conversions: (i) abc to dq0 and *vice versa* (ii) GBOA-based Fuzzy is developed to fulfill the specific objectives. As the published works already contain conversions, this paper focuses on highlighting the control approach of the proposed GBOA-based Fuzzy.

3.1 FLC

The FLC is advised to keep the DLCV steady. The reference voltage is compared to the actual voltage for DLCV stabilization, and its error is expressed as Error (E), Change in Error (CE), and Output (O), with Two Input Single Output (TISO). The following are regarded as inputs and outputs: Negative-Big (NGTB), Negative

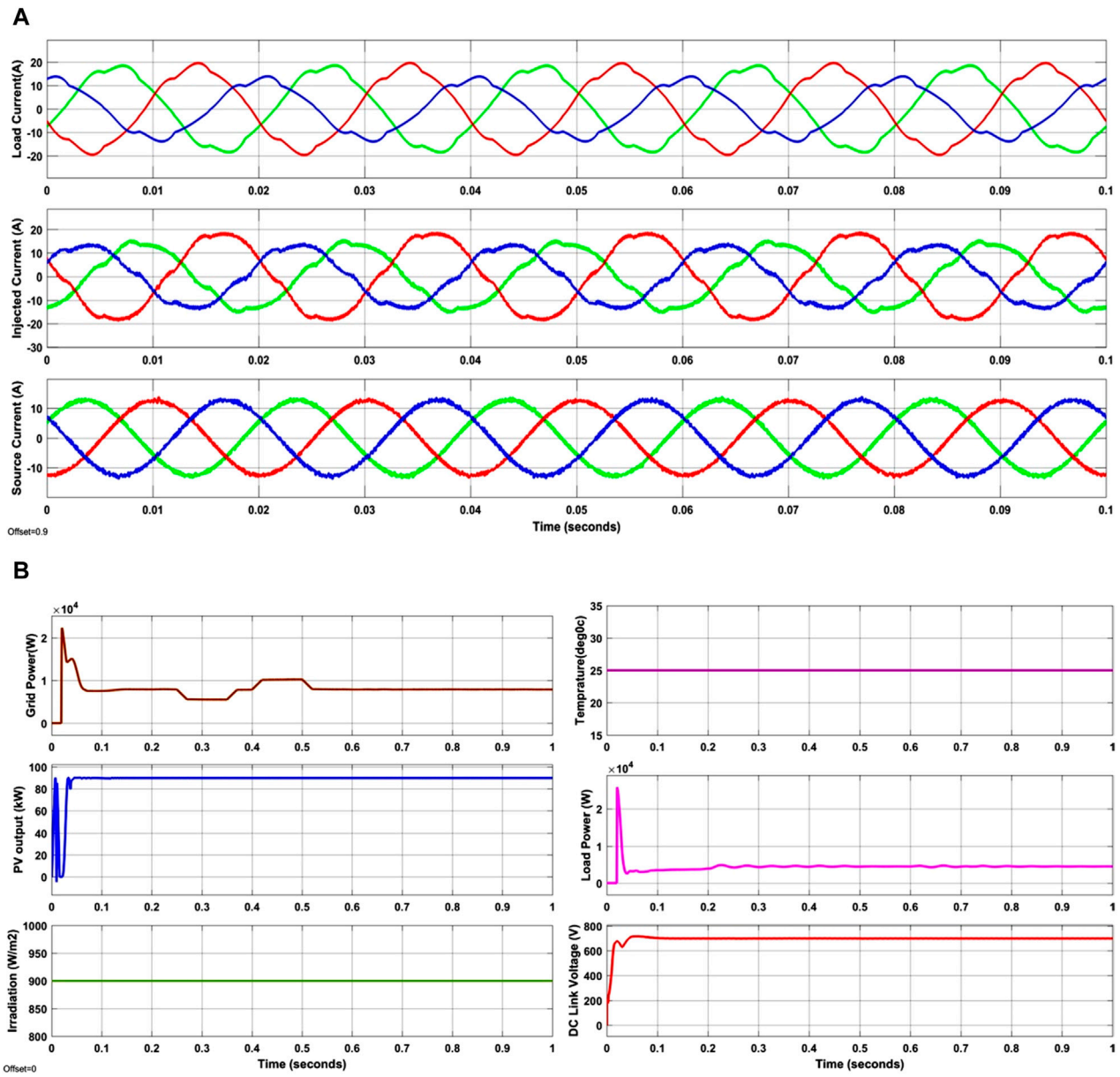

FIGURE 10
Waveforms of the suggested system for case two. **(A)** i_l, i_{sh}, i_s **(B)** Grid power, P_{PV}, G, T, P_L, DCLCV.

medium (NGTM), Zero (ZERO), Positive small (POSS), Positive big (POSB), Positive medium (POSM), and Negative-small (NGTS).

Here, the GBOAis adopted to optimize MSF parameters, the problem was set up for a triangular MSF (The same argument can be extended to two input MSF and output in the present work) as follows: Define the span given by Eq. (14). of the MSF using ai, bi and ci as in Figure 5.

$$triangle(x;a,b,c) = \begin{cases} 0 & x_{\min} \le a \\ \dfrac{x-a}{b-a} & a \le x \le b \\ \dfrac{c-x}{c-b} & b \le x \le c \\ 0 & c \le x_{\max} \end{cases} \quad (14)$$

Where, the range (Universe of discourse) of x is xmax - xmin (upper and lower bonds) which are considered as 1 and -1 (normalized) and i is the fuzzy set. The task is to improve the performance of the FLC by optimizing the MSF parameters.

3.2 GBOA based MSF selection

The GBOA method is a meta-heuristic that utilizes several populations. Like other population-based methodologies, GB initiates its execution by generating a population of solutions. Subsequently, it allocates the various problem-solving approaches into distinct teams, each operating autonomously and engaging in a competitive confrontation.

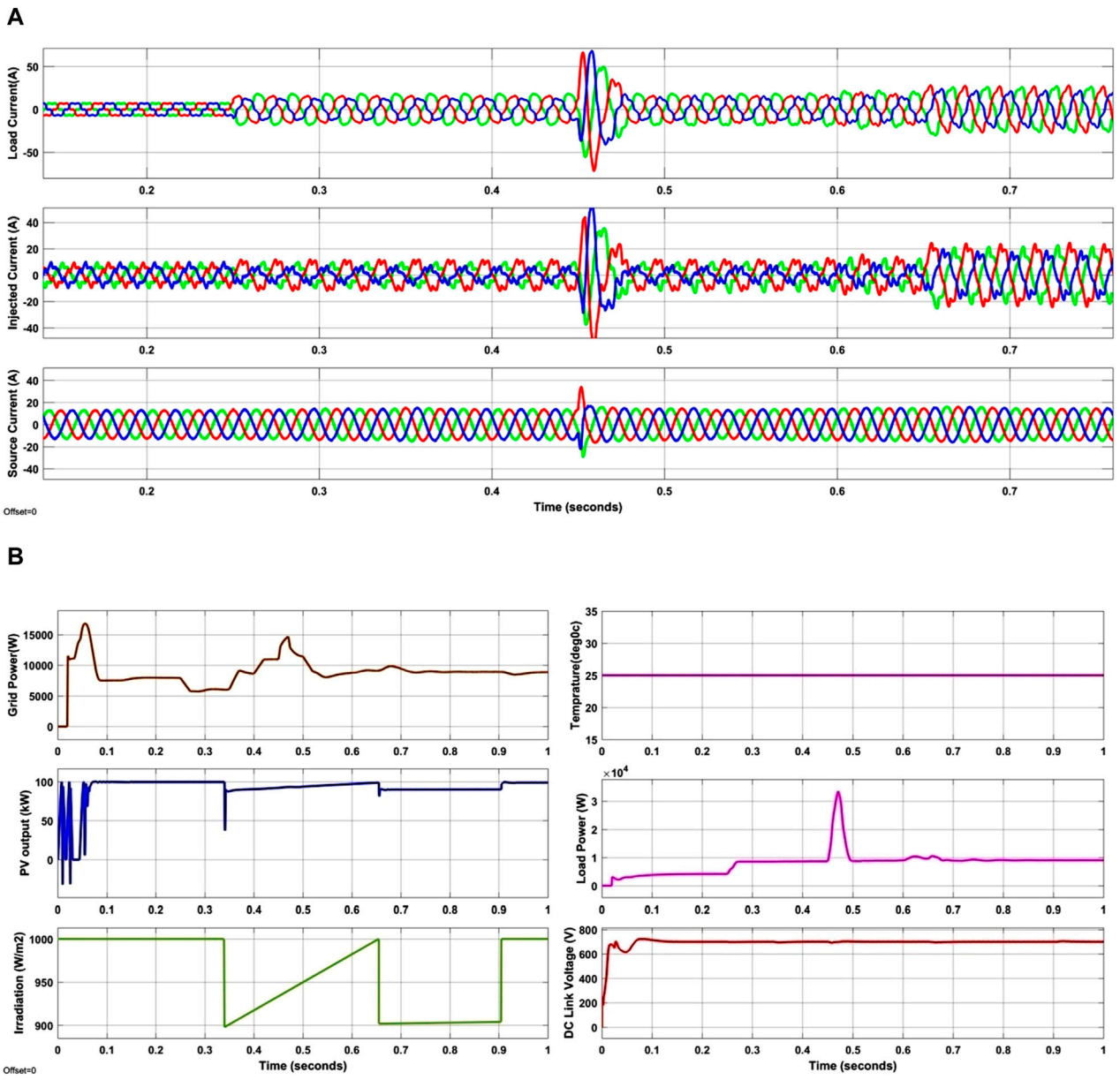

FIGURE 11
Waveforms of the suggested system for case three. **(A)** i_l, i_{sh}, i_s **(B)** Grid power, P_{PV}, G, T, P_L, DCLCV.

This competition is crucial in determining the transfer of solutions among teams and establishing the training model for each team.

The MSF control valuables a, b, c are arranged in the form of a matrix [f] of size (N × L), are K-number of parameters [u1,u2, ···,uK]. GBOA was developed from the inspiration of soccer games, where players in different teams attempt to play well to score goals and become the captain, in addition to winning the trophy. In this approach, a population of players are randomly generated and grouped into several teams. Each player in any team possessing different skills represents a solution of the clustering problem as,

$$Pij = \left[x_{ij}^{1}, x_{ij}^{2}, ..., x_{i}^{nv} j\right] \rightarrow [u_1, u_2....u_K] \\ = [(u_{11}, u_{12}....u_{1L}), (u_{11}, u_{12}....u_{1L})....., (u_{K1}, u_{K2}....u_{KL}) \quad (15)$$

Here in Eq. 15, uk denotes the k-th parameter, Pijis the j-th artificial player of the i-th team, and ukj is the j-th value of the k-th parameter. m and n represent the number of teams and the number of players in team, i. e., MSF variables that need to be optimized, respectively. Each player's contribution to a team is based on their abilities, which are assessed using a fitness function. The players with their teams comprise the population represented by Eq. 16,

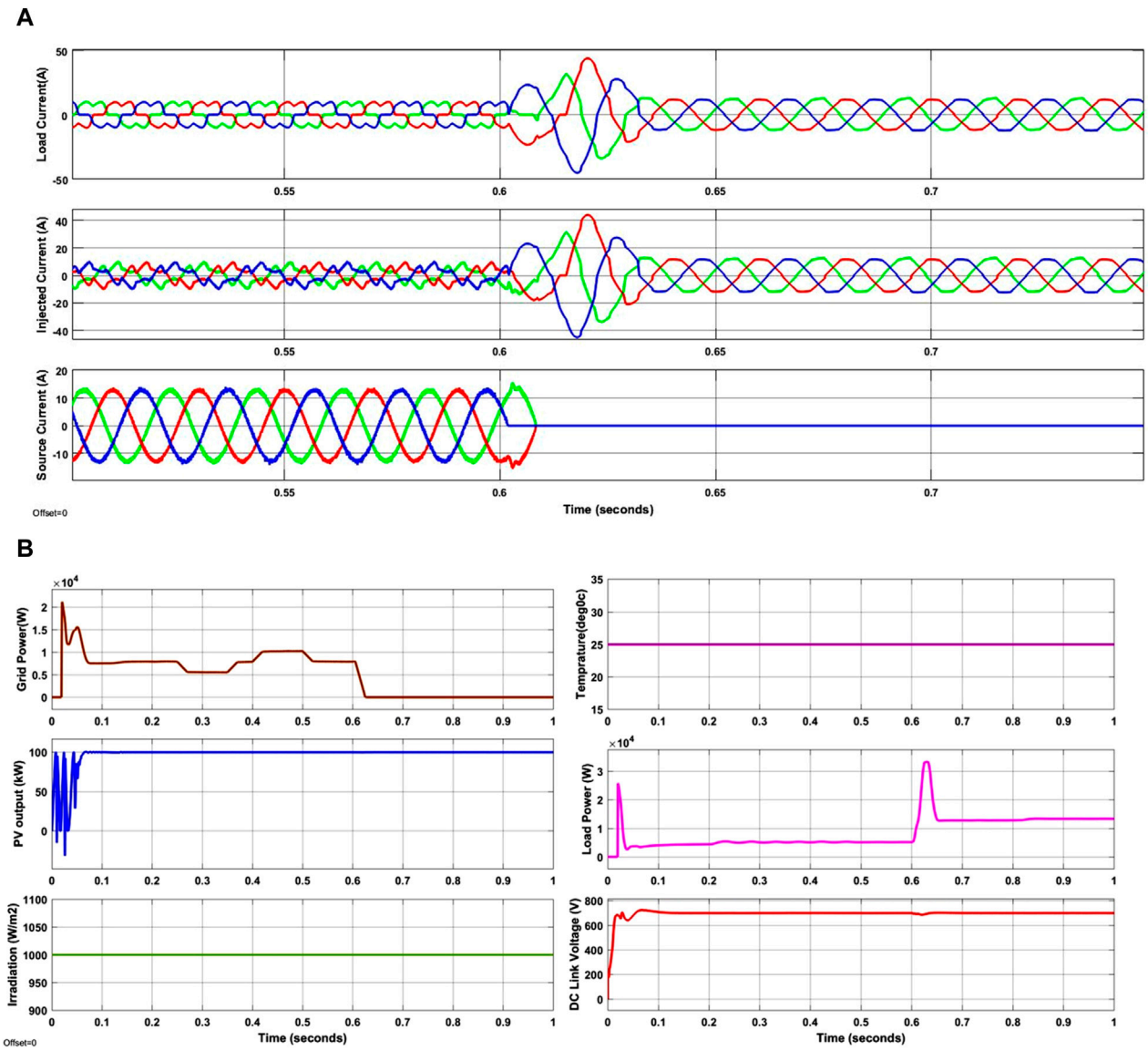

FIGURE 12
Waveforms of the suggested system for case four. **(A)** i_l, i_{sh}, i_s **(B)** Grid power, P_{PV}, G, T, P_L, DCLCV.

$$Population = \begin{bmatrix} T_1 \rightarrow \begin{Bmatrix} P_{11} \\ P_{12} \\ . \\ P_{1n} \end{Bmatrix} \\ T_2 \rightarrow \begin{Bmatrix} P_{21} \\ P_{22} \\ . \\ P_{2n} \end{Bmatrix} \\ . \\ . \\ T_m \rightarrow \begin{Bmatrix} P_{m1} \\ P_{m2} \\ . \\ P_{mn} \end{Bmatrix} \end{bmatrix} \tag{16}$$

Thus, the fitness function is customized using the minimization function of the issue as mentioned in Eq. 17,

$$Fitness\,function = \frac{1}{1 + MSE} \tag{17}$$

Where, is the actual output, indicated is the predicted output, and n is the total number of instances. The mean square error is then calculated using Eq. 18. where, O is the actual ouput, $\bar{O}$ indicated the predicted one, and n is the total number of instances.

$$MSE = \frac{1}{n}\sum_{p=1}^{m}\left(O_p - \bar{O}_p\right)^2 \tag{18}$$

The process describes to solve the MSF optimization. The global best solution are those that rank highest after optimization. Figure 6 shows the GBOA-based fuzzy optimal MSF. GBOA begins by generating the initial population and distributing the players, or solutions, among the system's subpopulations, or teams. After this preliminary stage is finished, the first season starts. Weeks make up a

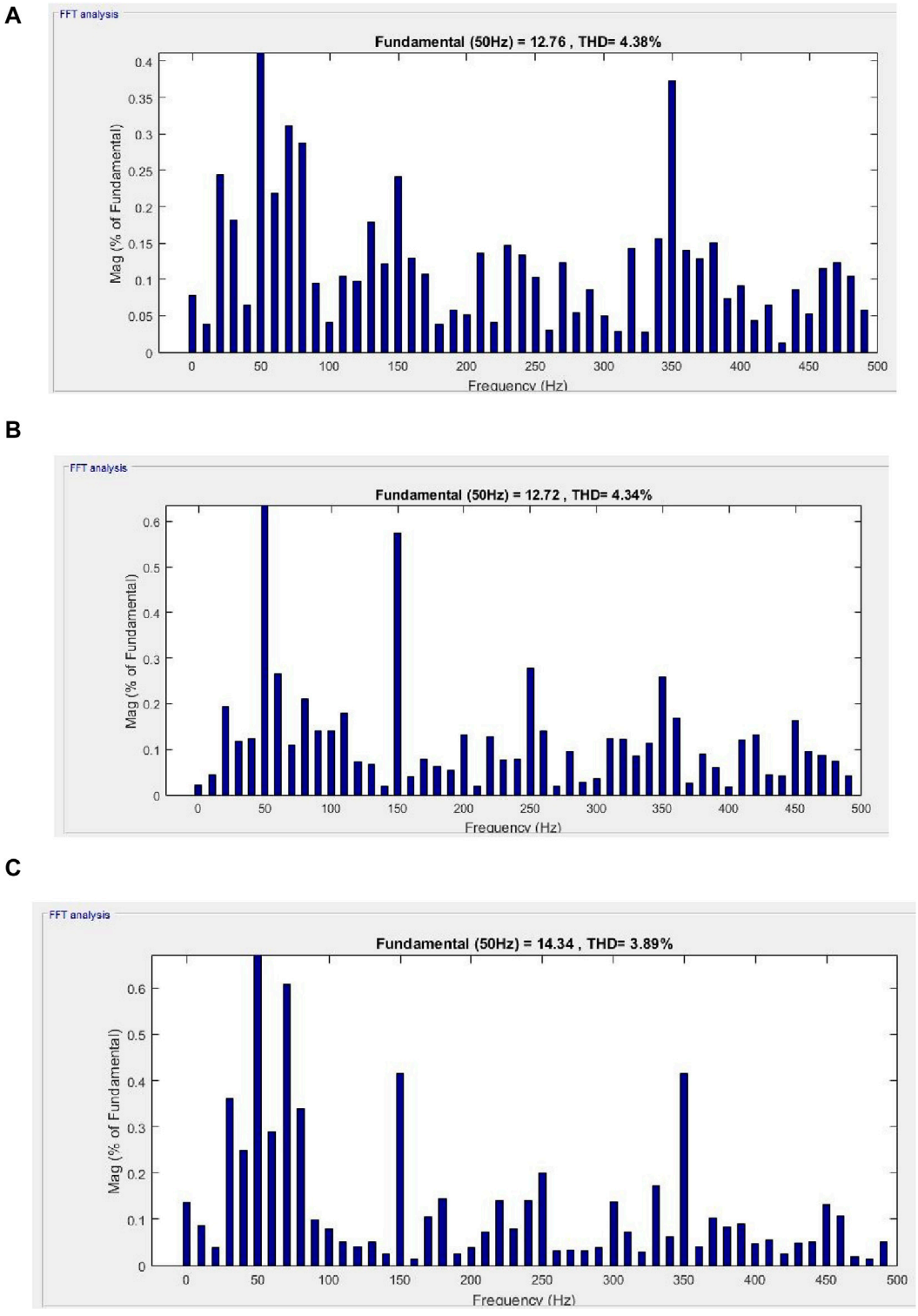

FIGURE 13
FFT spectrum for grid connected source current of three cases. **(A)** Case-1 **(B)** Case-2 **(C)** Case-3.

season, during which the teams practice and play one another to create a league competition. Following the season, there is a transfer window during which coaches and players can join new teams. Until the termination requirement is satisfied, this process is repeated. This work selected 4 teams and 12 players in each team and 10 times training of maximum 100 iterations (Tmax).

The load current is converted to the dq0 frame using the pharos approach, while the grid voltage sets the phasor through PLL. The

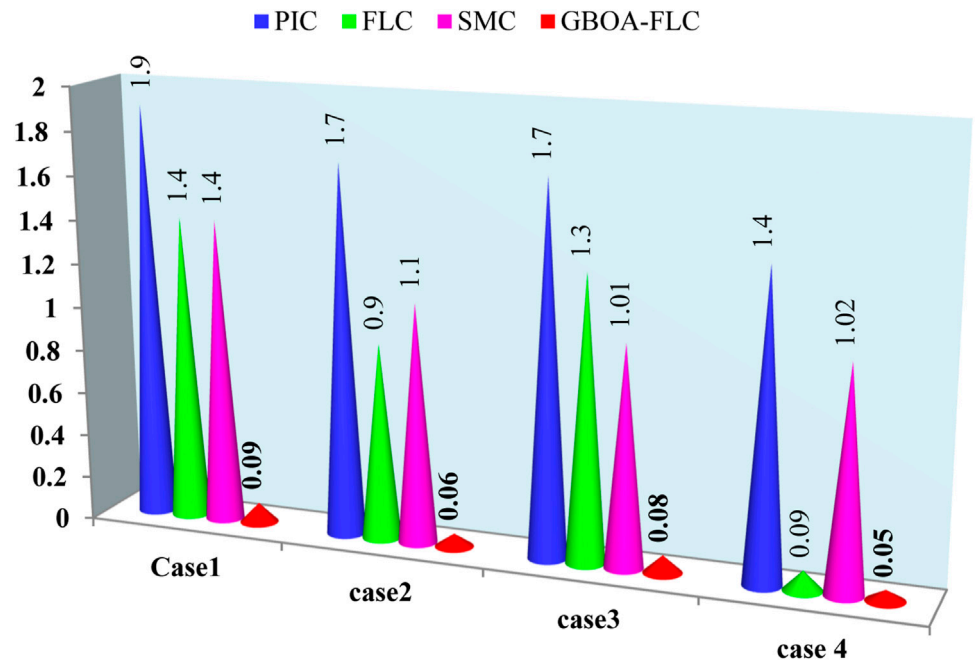

FIGURE 14
Comparison plot of time taken in sec to reach DCLCV stable.

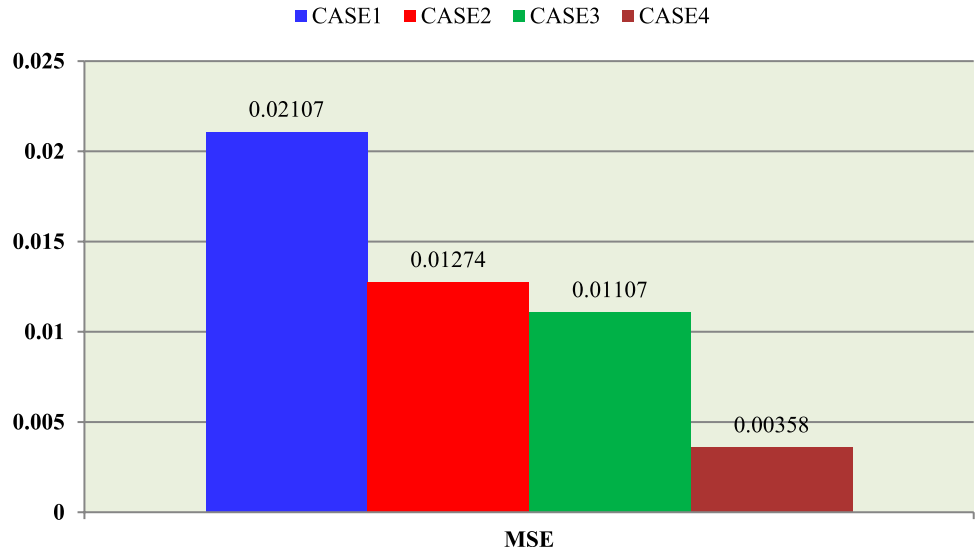

FIGURE 15
MSE for case studies.

performance of the SHAPF relies on the production of the reference current and the control of the DCLCV. However, as the load varies, it can lead to fluctuations in power flow, which in turn causes variations in DCLCV. To achieve stability in the DCLCV, the SHAPF must match the switching losses. The dth fraction of the load current is merged with the error obtained from the FLC. The dq0 components are converted into the abc reference frame and subsequently compared with the current at the load, and a hysteresis current controller is adapted to provide the necessary gate signals. Figure 7 depicts the regulation of SHAPF using the recommended controller. Figure 8 illustrates the flowchart of the suggested GBOA optimization technique.

4 Simulation and results

The given approach was tested using a 3-phase distribution system. Table 3 presents a record of the various parameters of the

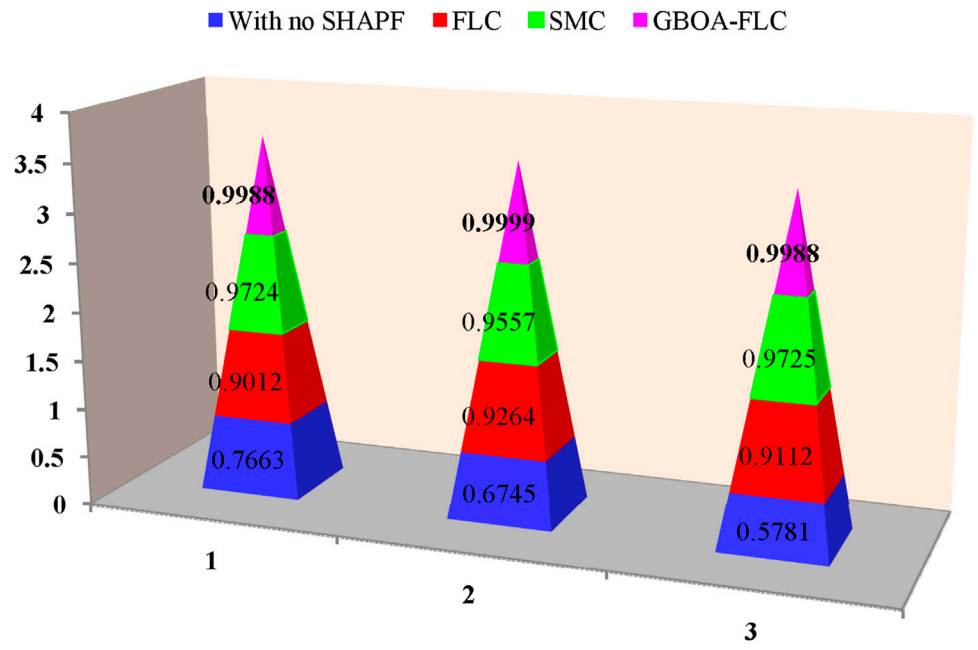

FIGURE 16
Power factor comparison.

system's configuration. To evaluate the effectiveness of the GBOA selected MSF of FLC-based SHAPF, four different test situations were chosen for grid/standalone conditions. These cases involved various combinations of harmonic loads, such as a three-phase rectifier load, an imbalanced load, an asynchronous motor load, an active/reactive power load, and BLDC Motor drive with fixed and variable SES. The details of these case studies may be seen in Table 4. The THD of the entire system were measured and compared with the commonly used SMC and FLC methods in Table 5 for each test scenario, both with and without the usage of SHAPF.

The suggested system's waveforms for cases 1–4 are shown in Figures 9–12. These represent the load voltage (Vl), DCLCV (Vdc) voltages, irradiation (G), and temperature (T).

Table 4 demonstrates that in case 1, when Load1, Load 3 and Load 4 are connected, the current in the load is not sinusoidal. However, it is balanced with a power factor of 0.7663 and a THD of 28.99%. Figure 9A shows that the proposed system offers a distortion-free supply current. In addition to the existing waveforms, there is a notable decrease in the THD, as indicated in Table 5. By introducing the suitable shunt currents, the power factor increased from 0.7663 to 0.9988 and the THD of the load current dropped from 28.99% to 2.27%—a lower value compared to other methods and documented techniques. As depicted in Figure 9B, the proposed method successfully achieved a stable DCLCV within a time frame of less than 0.09 s. However, it is also clearly visible that during supply changes the solar under fixed G of 1000 W/m2 and 250c temperature conditions is satisfying load demand effectively.

As seen in Figure 10A, the load current in case 2 was extremely imbalanced and non-sinusoidal due to the loads. As depicted in Figure 10A, the current waveform at load in case 2 exhibited a significant imbalance with non-sinusoidal pattern. The PF of the load current is observed to be 0.6745, whereas THD is 11.36% without a compensating device. Figure 10A demonstrates the ability of the designed system to generate sinusoidal grid current by eliminating harmonics and injecting the necessary amount of shunt compensating current. The PF is increased to almost 1 and the THD of the load current decreased from 11.36% to 2.24%. Moreover, it is clear that the proposed method settles the DCLCV at a consistent level of 0.06 s, during the change in grid supply; the Solar System provides the required power to satisfy the load demand as shown in Figure 10B.

Besides, case-3 demonstrates the dynamic behaviour a similar trend in reducing the THD and increasing the PF. The load current is initially non-sinusoidal and balanced till 0.25 s due to load 1. Later, at 0.25 s, load 2 is connected, due to which it exhibited non-synoidal and unbalanced. Lastly, at 0.45 s load 3 is connected, due to which the magnitude of current increases with imperfections. Lastly, at 0.65 s load 5 is connected. Figure 11A demonstrates that the proposed solution efficiently rectifies the shortcomings in the present waveform. Furthermore, Figure 11B indicates that the proposed technique effectively maintains the stability of DCLCV within a short span of 0.05 sec. Besides, it is visible that the demand is satisfied successfully during both the grid power and solar power variations.

The case 4 provides the study during grid and standalone conditions with loads 1 and 3 acting simultaneously. From Figure 12A, B it is clearly visible that the proposed system supplies distortion-free supply current till 0.6 s and successfully satisfies load demand with the grid's support. Later, from 0.6 s it works under the islanded mode of operation where the grid current is zero. However, it satisfies load demand with the support of the

Solar System. Additionally, it also reaches DCLCV stability with a very low time period of 0.05 s.

This study involves conducting FFT analysis on all test cases. However, this particular component focuses on the results of test case 3, which involved various types of non-linear and unbalanced loads in conjunction with a BLDC Motor drive. The current harmonic spectra are depicted for each scenario in Figure 13. Figure 14 displays the recorded time required for the stable-state DCLCV and various control systems. This shows that the BGOA-tuned PIC-based SHAPF achieves steady-state DCLCV in under 0.02 s. Figure 15 illustrates MSE for various case studies considered and the power factor comparison for all four cases is shown in Figure 16. The talks above demonstrate that the proposed technique is highly effective in reducing total THD, enhancing PF, and ensuring the stability of the DCLCV.

5 Conclusion

In this paper, the reduced switch shunt VSC was created for the SHAPF. The GBOA was developed to optimize the selection of MSF and FLC for the proposed shunt converters. The ESS controller and different SHAPF, solar, and ESS components were also included in the modeling process. This facilitated prompt intervention in adjusting the DCLCV, reducing the THD of source currents, and enhancing the power factor. By analyzing three test scenarios with varying load topologies, fixed and variable G, the proposed controller effectively reduces THD to levels that fall within acceptable limits and significantly improves the power factor to close to unity. These controllers performed better than the commonly employed FLC and SMC controllers. In addition, the suggested system demonstrated a faster stable DCLCV attainment than alternative techniques. Subsequent research on the proposed model could focus on enhancing the design parameters of the model by approaching the design challenge as optimization problem and employing metaheuristic optimization techniques.

Data availability statement

The original contributions presented in the study are included in the article/supplementary material, further inquiries can be directed to the corresponding author.

Author contributions

KS: Conceptualization, Methodology, Writing–original draft. DS: Software, Writing–review and editing. SG: Conceptualization, Methodology, Writing–original draft. RV: Data curation, Investigation, Writing–original draft. PB: Supervision, Writing–review and editing. IC: Supervision, Writing–review and editing. SS: Funding acquisition, Writing–review and editing.

Funding

The author(s) declare that no financial support was received for the research, authorship, and/or publication of this article.

Conflict of interest

The authors declare that the research was conducted in the absence of any commercial or financial relationships that could be construed as a potential conflict of interest.

Publisher's note

References

Abdelnasser, A., Nafeh, A. H., El-SehiemyRagab, A., and Waleed, A. A. S. (2022). Intelligent fuzzy-based controllers for voltage stability enhancement of AC-DC micro-grid with D-STATCOM. *Alexandria Eng. J.* 61, 2260–2293. doi:10.1016/j.aej.2021.07.012

AlapatiRamadevi, K. S., Praveen Kumar Balachandran, I. C., Dhanamjayulu, C., Khan, B., and Khan, B. (2023). Optimal design and performance investigation of artificial neural network controller for solar- and battery-connected unified power quality conditioner. *Int. J. Energy Res.* 2023, 1–22. Article ID 3355124. doi:10.1155/2023/3355124

AlifMansor, M., Hasan, K., Murtadha Othman, M., Noor, S. Z. B. M., and Musirin, I. (2020). Construction and performance investigation of three-phase solar PV and battery energy storage system integrated UPQC. *IEEE Access* 8, 103511–103538. 2997056. doi:10.1109/access.2020.2997056

Chandrasekaran, K., Selvaraj, J., Amaladoss, C. R., and Veerapan, L. (2021). Hybrid renewable energy based smart grid system for reactive power management and voltage profile enhancement using artificial neural network. *Energy Sources, Part A Recovery, Util. Environ. Eff.* 43 (No. 19), 2419–2442. doi:10.1080/15567036.2021.1902430

Das, S. R., Ray, P. K., Mohanty, A., and Panda, G. (2021). "Power quality enhancement in PV and battery storage based microgrid using hybrid active filter," in 2020 3rd International Conference on Energy, Power and Environment: Towards Clean Energy Technologies, China, 5th-7th March, 2021 (IEEE), 5–7.

Devassy, S., and Singh, B. (2020). Performance analysis of solar PV array and battery-integrated unified power quality conditioner for micro grid systems. *IEEE Trans. Industrial Electron.* 5 (Issue), 4027–4035. doi:10.1109/TIE.2020.2984439

Dheeban, S. S., and MuthuSelvan, N. B. (2021). ANFIS-based power quality improvement by photovoltaic integrated UPQC at the distribution system. *IETE J. Res.*, 1–19. doi:10.1080/03772063.2021.1888325

Jaber, S., and Shakir, A. M. (2021a). Design and simulation of a boost-microinverter for optimized photovoltaic system performance. *Int. J. Smart Grid* 5 (No. 2), 1–9. doi:10.20508/ijsmartgrid.v5i2.189.g145

K Krishna, V., Dash, S. K., and Geshma, K. (2020nd). "Development and analysis of power quality by using fuel cell based shunt active power filter," in International Conference on Innovative Mechanisms for Industry Applications (ICIMIA), 5-7 March 2020, USA, 5-7 March, 2020 (IEEE).

Kumar, N., Singh, B., and BijayaKetanPanigrahi, (2019). Grid synchronisation framework for partially shaded solar PV-based microgrid using intelligent control strategy. *Transm. Distribution* 13 (No 6), 829–837. doi:10.1049/iet-gtd.2018.6079

Kumar, N., Singh, B., and Panigrahi, B. K. (2023). Voltage sensorless based model predictive control with battery management system: for solar PV powered on-board EV charging. *IEEE Trans. Transp. Electrification* 9 (2), 2583–2592. doi:10.1109/TTE.2022.3213253

Kumar, N., Singh, B., Wang, J., and Panigrahi, B. K. (2020). A framework of L-HC and AM-MKF for accurate harmonic supportive control schemes. *IEEE Trans. Circuits Syst. I Regul. Pap.* 67 (12), 5246–5256. doi:10.1109/TCSI.2020.2996775

Kumari, P., Kumar, N., and Panigrahi, B. K. (2023). A framework of reduced sensor rooftop SPV system using parabolic curve fitting MPPT technology for household consumers. *IEEE Trans. Consumer Electron.* 69 (1), 29–37. doi:10.1109/TCE.2022.3209974

Mohanraj, M. R., and Prakash, R. (2020). A unified power quality conditioner for power quality improvement in distributed generation network using adaptive distributed power balanced control (ADPBC). *Int. J. Wavelets, Multi-resolution Inf. Process.* 18 (No. 01), 1941021. doi:10.1142/s0219691319410212

Nagireddy, V. V., Kota, V. R., and Ashok Kumar, D. V. (2018). Hybrid fuzzy back-propagation control scheme for multilevel unified power quality conditioner. *Ain Shams Eng. J.* 9 (4), 2709–2724. doi:10.1016/j.asej.2017.09.004

Nkado, F., Nkado, F., Oladeji, I., and Zamora, R. (2021). Optimal design and performance analysis of solar PV integrated UPQC for distribution network, EJECE. *Eur. J. Electr. Eng. Comput. Sci.* 5 (5), 1–8. doi:10.24018/ejece.2021.5.5.361

Pazhanimuthu, C., and Ramesh, S. (2018). Grid integration of renewable energy sources (RES) for power quality improvement using adaptive fuzzy logic controller-based series hybrid active power filter (SHAPF). *J. Intelligent Fuzzy Syst.* 35 (No. 1), 749–766. doi:10.3233/jifs-171236

Rajesh, P., Shajin, F. H., and Umasankar, L. (2021). A novel control scheme for PV/wt/FC/battery to power quality enhancement in micro grid system: a hybrid technique. *Util. Environ. Eff.*, 1–17. doi:10.1080/15567036.2021.1943068

Ray, P., Ray, P. K., and Dash, S. K. (2022). Power quality enhancement and power flow analysis of a PV integrated UPQC system in a distribution network. *IEEE Trans. onIndustry Appl.* 1 (58), 201–211. doi:10.1109/TIA.2021.3131404

Renduchintala, U. K., Pang, C., Tatikonda, K. M., and Yang, L. (2021). ANFIS-fuzzy logic based UPQC in interconnected microgrid distribution systems: modeling, simulation and implementation. *J. Eng.* 21 (No.1), 6–18. doi:10.1049/tje2.12005

SaiSarita, N. C., Suresh Reddy, S., and Sujatha, P., "Control strategies for power quality enrichment in Distribution network using UPQC", 2021.

Sarker, K., Chatterjee, D., and Goswami, S. K. (2020). A modified PV-wind-PEMFCS-based hybrid UPQC system with combined DVR/STATCOM operation by harmonic compensation. *Int. J. Model. Simul. World Sci.* 41 (No.4), 243–255. doi:10.1080/02286203.2020.1727134

Saxena, V., Kumar, N., Singh, B., and Panigrahi, B. K. (2021). An MPC based algorithm for a multipurpose grid integrated solar PV system with enhanced power quality and PCC voltage assist. *IEEE Trans. Energy Convers.* 36 (2), 1469–1478. doi:10.1109/TEC.2021.3059754

Sayed, J. A., Sabha, R. A., and Ranjan, K. J. (2021). Biogeography based optimization strategy for UPQC PI tuning on full order adaptive observer-based control. *IET Generation, Transm. Distribution* 15, 279–293. doi:10.1049/gtd2.12020

Siu, J. Y., Kumar, N., and Panda, S. K. (2022). Command authentication using multiagent system for attacks on the economic dispatch problem. *IEEE Trans. Industry Appl.* 58 (4), 4381–4393. doi:10.1109/TIA.2022.3172240

Srilakshmi, K., Krishna Jyothi, K., Kalyani, G., and SaiPrakashGoud, Y. (2023). Design of UPQC with solar PV and battery storage systems for power quality improvement. *Cybern. Syst.*, 1–30. doi:10.1080/01969722.2023.2175144

Srilakshmi, K., Rao, G. S., Swarnasri, K., Inkollu, S. R., Kondreddi, K., Balachandran, P. K., et al. (2024). Optimization of ANFIS controller for solar/battery sources fed UPQC using an hybrid algorithm. *ElectrEng*. doi:10.1007/s00202-023-02185-8

Srilakshmi, K., Srinivas, N., Balachandran, P. K., Reddy, J. G. P., Gaddameedhi, S., Valluri, N., et al. (2022). Design of soccer league optimization based hybrid controller for solar-battery integrated UPQC. *IEEE Access* 10, 107116–107136. doi:10.1109/ACCESS.2022.3211504

SrilakshmiKoganti, G. S., Reddy, B. S., Praveen Kumar, B., Prasad, R. G., PalaniveluAravindhababu, S. S., et al. (2024). Optimal design of solar/wind/battery and EV fed UPQC for power quality and power flow management using enhanced most valuable player algorithm. *Front. Energy Res.* 11. doi:10.3389/fenrg.2023.1342085

Tawfiq, A. E., El-Raouf, M. O. A., Mosaad, M. I., Gawad, A. F. A., and Farahat, M. A. E. (2021). Optimal reliability study of grid-connected PV systems using evolutionary computing techniques. *IEEE Access* 9, 42125–42139. doi:10.1109/ACCESS.2021.3064906

Vinothkumar, V., and Kanimozhi, R. (2021). RETRACTED ARTICLE: power flow control and power quality analysis in power distribution system using UPQC based cascaded multi-level inverter with predictive phase dispersion modulation method. *J. Ambient Intell. Humaniz. Comput.* 12, 6445–6463. doi:10.1007/s12652-020-02253-y

frontiers | Frontiers in Energy Research

TYPE Original Research
PUBLISHED 08 April 2024
DOI 10.3389/fenrg.2024.1380387

OPEN ACCESS

EDITED BY
Praveen Kumar Balachandran,
Vardhaman College of Engineering, India

REVIEWED BY
Sudhakar Babu Thanikanti,
Chaitanya Bharathi Institute of Technology, India
Priya Ranjan Satpathy,
Council of Scientific and Industrial Research (CSIR), India
Veerpratap Meena,
Malaviya National Institute of Technology, India

*CORRESPONDENCE
Arezki Fekik,
a.fekik@univ-bouira.dz
Ibrahim A. Hameed,
ibib@ntnu.no

RECEIVED 01 February 2024
ACCEPTED 14 February 2024
PUBLISHED 08 April 2024

CITATION
Fekik A, Hamida ML, Azar AT, Ghanes M, Hakim A, Denoun H and Hameed IA (2024), Robust power control for PV and battery systems: integrating sliding mode MPPT with dual buck converters.
Front. Energy Res. 12:1380387.
doi: 10.3389/fenrg.2024.1380387

Robust power control for PV and battery systems: integrating sliding mode MPPT with dual buck converters

Arezki Fekik[1,2]*, Mohamed Lamine Hamida[3], Ahmad Taher Azar[4,5,6], Malek Ghanes[2], Arezki Hakim[3], Hakim Denoun[3] and Ibrahim A. Hameed[7]*

[1]Department of Electrical Engineering, University Akli Mohand Oulhadj-Bouria, Bouira, Algeria, [2]Nantes Université, École Centrale Nantes, CNRS, LS2N, UMR 6004, Nantes, France, [3]Electrical Engineering Advanced Technology Laboratory (LATAGE), Tizi Ouzou, Algeria, [4]College of Computer and Information Sciences, Prince Sultan University, Riyadh, Saudi Arabia, [5]Automated Systems and Soft Computing Lab (ASSCL), Prince Sultan University, Riyadh, Saudi Arabia, [6]Faculty of Computers and Artificial Intelligence, Benha University, Benha, Egypt, [7]Department of ICT and Natural Sciences, Norwegian University of Science and Technology, Trondheim, Norway

This paper presents a comprehensive exploration of an integrated Buck-Boost converter and Sliding Mode Control (SMC) Maximum Power Point Tracking (MPPT) system for optimizing photovoltaic energy conversion. The study focuses on enhancing solar energy extraction efficiency, regulating output currents, and ensuring effective battery utilization. Through a systematic analysis of converter component sizing and operational modes, the paper delves into the intricacies of the Buck-Boost converter. The unique contribution lies in the innovative integration of SMC with the traditional Perturb and Observe (P&O) algorithm, providing robust and adaptive MPPT under varying environmental conditions. Additionally, the paper introduces a battery management system with three distinct modes, namely, Charging, Direct, and Discharging, offering intelligent control over critical scenarios. Simulation results underscore the robustness of the proposed system under diverse conditions, demonstrating its effectiveness in managing power distribution based on battery charge levels, even in scenarios of insufficient solar power. Overall, this research significantly contributes to advancing the understanding of PV/battery systems and offers a practical, sustainable solution for optimizing energy production, distribution, and storage, marking a substantial stride towards a more efficient and sustainable energy future.

KEYWORDS

buck converter, buck-boost converter, PI controller, supervisory control, hybrid power management, SMC-MPPT

1 Introduction

The systems for renewable energy production, such as photovoltaic installations, play a crucial role in the transition towards a more sustainable economy. The use of solar energy through photovoltaic panels offers several significant environmental advantages (Potrč et al., 2021; Fekik and Benamrouche, 2022; Fekik et al., 2023a; Fekik et al., 2023b). Firstly, it reduces dependence on fossil fuels, thereby contributing to mitigating greenhouse gas

emissions responsible for climate change. Additionally, photovoltaic systems do not generate air pollution or toxic waste, minimizing their impact on air and soil quality. However, it is important to recognize that these technologies are not without challenges. The intermittency of solar energy production and the need for efficient storage to address seasonal and diurnal variations pose technical challenges (Hassan et al., 2023; Fachrizal et al., 2024; Khalid, 2024).

The integration of power electronics into photovoltaic systems represents a significant advancement in controlling and optimizing solar energy production. Power electronics provide functionalities such as Maximum Power Point Tracking (MPPT), enabling the best utilization of variations in sunlight to maximize energy production (Meghni et al., 2017; Meghni et al., 2018; Ammar et al., 2019). The continual pursuit of efficiency in photovoltaic systems has led to the development and study of various MPPT techniques. Among the most common methods are Perturb and Observe (P&O), which continuously adjusts the solar panel voltage to maximize output power, and Incremental Conductance, which uses an analysis of the current-voltage characteristic curve to determine the maximum power point (Vinnikov et al., 2021; Mandourarakis et al., 2022; Hai et al., 2023; Katche et al., 2023). Other approaches include the Sequential Search Algorithm, systematically exploring operating points to identify MPPT, and techniques based on artificial intelligence algorithms such as neural networks and genetic algorithms. Each method has its advantages and limitations, including responsiveness to weather changes, implementation complexity, and associated costs. Ongoing research aims to develop more sophisticated MPPT methods, combining traditional approaches with advanced algorithms to optimize solar energy production under various conditions.

Efficient power management in photovoltaic systems (PV) incorporating batteries is a central imperative to maximize the use of renewable resources and ensure a constant availability of energy. This necessity has driven the development of innovative approaches to optimize solar energy production while ensuring efficient storage. In-depth research has highlighted the inherent complexity of variable weather conditions and energy demand fluctuations. Innovative power management strategies, such as the use of advanced MPPT techniques and the integration of intelligent power converters, are at the core of these initiatives. The goal is to optimally balance the production, distribution, and storage of energy, ensuring continuous availability and efficient resource utilization while extending the system components' useful life. Continuous innovation in this field is essential to address evolving challenges and to solidify PV/battery systems as key components of a resilient and sustainable energy infrastructure.

Benhalima et al. (2018) presented enhanced control strategies for autonomous microgrids based on solar photovoltaic systems (SVPAs) and fixed-speed synchronous generators driven by a diesel engine. To achieve this, a sliding mode regulator based on the d-q transformation theory is employed for the voltage source converter (VSC). This approach aims to mitigate harmonics, balance the diesel generator (DG) current, and inject the power generated by SVPA into the local grid.

A two-stage photovoltaic (PV) system that concurrently achieves maximum power point tracking (MPPT) and voltage regulation is presented in Manuel and İnanç (2022). Additionally, it introduces an enhanced version of the perturb and observe (P&O) algorithm, known as artificial potential fields (APF)-P&O. Simulations conducted using MATLAB/Simulink demonstrate the superior efficiency of the APF-P&O method compared to conventional approaches. This integrated approach offers a promising avenue to enhance the overall performance of photovoltaic systems by addressing both MPPT and voltage regulation in a more efficient and synchronized manner.

In the paper Haq et al., 2022, a nonlinear generalized global sliding mode controller (GGSMC) is presented to maximize the power of a photovoltaic array (PV) using a DC-DC buck-boost converter. A feed-forward neural network (FFNN) is employed to provide a reference voltage. The GGSMC is designed to track the reference generated by the FFNN, accounting for variations in temperature and sunlight. The proposed control strategy, in conjunction with a modified sliding mode control, eliminates the convergence phase, ensuring that the sliding mode persists throughout the entire duration.

The primary goal of this research is:

- Develop and evaluate an integrated Buck-Boost converter and Sliding Mode Control (SMC) Maximum Power Point Tracking (MPPT) system.
- Enhance the efficiency of solar energy extraction and regulate output currents.
- Ensure effective utilization of batteries within a photovoltaic system.
- Innovative integration of SMC with the Perturb and Observe (P&O) algorithm.
- Introduce a battery management system with distinct modes, and offer intelligent control in diverse scenarios.
- Contribute significantly to advancing the understanding of PV/battery systems.

In order to provide a comprehensive exploration of the integrated Buck-Boost converter and Sliding Mode Control (SMC) Maximum Power Point Tracking (MPPT) system for optimizing photovoltaic energy conversion, this paper is structured as follows. Section 2 delves into the system modeling, encompassing the modeling of PV cells, the design considerations for the Buck and Buck-Boost converters, and the proposed MPPT strategies. Following this, Section 3 elucidates the battery management aspect of the system. Moving forward, Section 4 presents the results and discussion derived from various tests conducted to evaluate the system's performance. Specific attention is given to Test N°1, Test N°2, and Test N°3. Finally, Section 5 encapsulates the paper with a comprehensive conclusion, summarizing key findings, emphasizing the significance of the proposed system, and suggesting avenues for future research.

2 System modeling

The studied global system is depicted in Figure 1. This configuration consists of a photovoltaic system connected to a Buck converter controlled by an MPPT based on sliding mode control. The Buck converter is linked to batteries and a second Buck-Boost converter controlled in current. The power supply management of the batteries is carried out by a supervisory system adapted to the operating conditions.

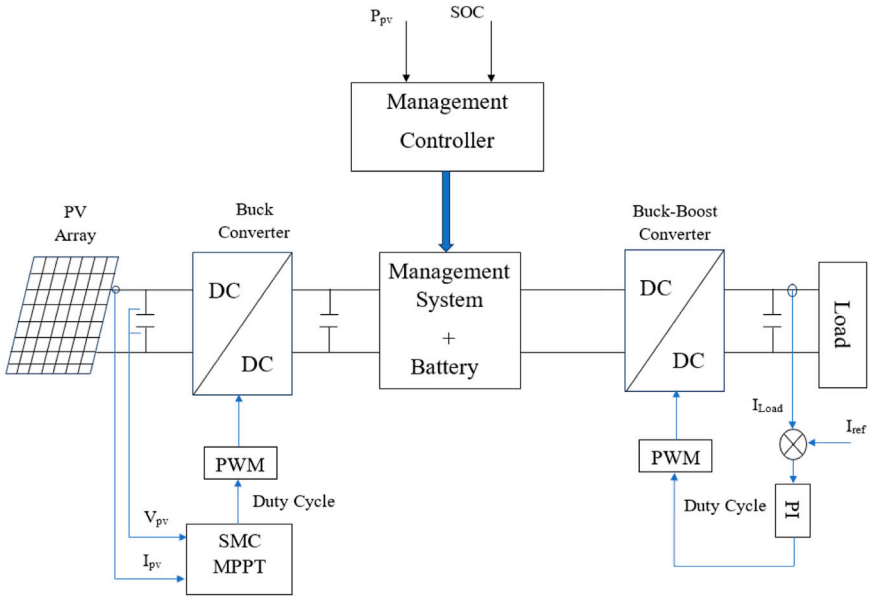

FIGURE 1
Global system.

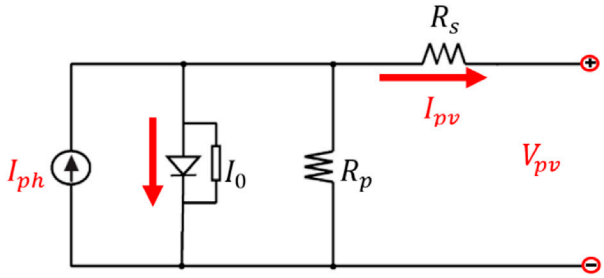

FIGURE 2
PV cell modeling.

2.1 PV cell modeling

Figure 2 illustrates the equivalent circuit of a solar cell. This circuit consists of a current source in parallel with a diode, accompanied by a parallel resistor and a second series resistor. Eq. (1) defines the mathematical model of the current generated by a photovoltaic cell (Fekik et al., 2023b; Fekik et al., 2022b).

$$I_{pv} = \left(I_{ph} - I_s \left(exp\left(\frac{q(V_{pv} + R_s I_{pv})}{NKT} \right) - 1 \right) - \frac{(V_{pv} + R_s I_{pv})}{R_p} \right) \quad (1)$$

Where I_{pv} and V_{pv} represent, respectively, the current and voltage output of a solar cell:

R_p: is the parallel resistance, or shunt resistance, of a solar cell. In practice, the value of the resistance (R_p) is often high, so it can be neglected.

R_s: represents the series resistance.

q: is the charge of an electron (1.602 × 10-19 Coulombs).

TABLE 1 Characteristics of the chosen photovoltaic panel.

P_{max}	I_{SC}	V_{OC}	I_{MPP}	V_{MPP}	N_T	N_s	N_p
330W	9.02A	45.8	8.45	39	10	2	5

I_{ph}: and I_s represent, respectively, the photoelectric current and the saturation current of a diode.

N: is the ideality factor of the diode.

K: is the Boltzmann constant (1.38 × 10^{-23} J/°K).

T: is the temperature of a cell.

The modeling of a photovoltaic panel (PV) can be performed using various methods, ranging from simple analytical models to more complex physical models based on the fundamental equations of physics. A solar module consists of a set of elementary photovoltaic cells, usually connected in series, which are then linked to other modules to form a photovoltaic generator (PVG) with the desired characteristics.

The solar generator with a power of 3,300 Wc will enable the operation of the studied system. In the context of this study, the selection of modules has been oriented towards the 330 Wc-Poly 72-cell modules, and the associated electrical parameters are presented in Table 1 below:

When solar panels are connected in series, the voltage adds up with a constant current. Conversely, if they are connected in parallel, the currents add up, and the voltage remains constant. To achieve the desired characteristics, it is sometimes necessary to combine these two topologies. In the context of this study, we have 10 panels connected in a series-parallel arrangement, allowing us to obtain a PVG with the characteristics presented in Table 2 under standard operating conditions.

TABLE 2 Characteristics of the utilized photovoltaic generator.

P_{max}	I_{SC}	V_{OC}	I_{MPP}	V_{MPP}
3300W	45 .1	91 .6	42.7	78

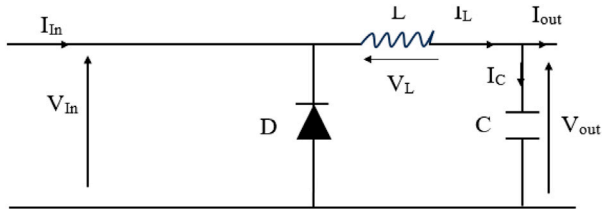

FIGURE 3
Equivalent circuit of the Buck converter for the closed switch K.

2.2 Buck converter

The operating principle of the Buck converter shown in Figure 3 is based on the periodic switching of the switch K to create state transitions that allow energy to be stored in an inductance and released to a load (Radwan et al., 2018; Fang et al., 2021). The switch is typically controlled by a control pulse, which rapidly opens and closes based on a pulse width modulation (PWM) signal.

The choice of a buck converter over a buck-boost converter in battery chargers depends on the specific characteristics of the system and battery charging requirements. The reasons for choosing a buck converter in battery chargers are:

- Stable Input Voltage: If the input voltage of your system is generally higher than the required voltage to charge the battery, a buck converter can effectively lower this voltage to an appropriate level.
- High Efficiency: Buck converters often have higher efficiency than buck-boost converters, especially when the input voltage is close to the output voltage.
- Simplicity of Design: Buck converters tend to have simpler and more cost-effective designs than buck-boost converters. This can be an advantage in applications where complexity needs to be minimized
- Battery Characteristics: If the battery you are charging has a nominal voltage compatible with the input voltage of your system, a buck converter can be a suitable choice without requiring a boost function.

When the switch is closed (0 to DT), the diode is blocked, and the current flows through the inductance, storing energy. When the switch is open (DT to T), the diode conducts, and the current flows through it to the load. The duty cycle of the PWM signal is adjusted to regulate the desired output voltage. However, it is important to note that this device adheres to the principle of energy conservation, so if $V_{in} > V_{out}$, then $I_{in} < I_{out}$. There are two possible topologies resulting from a given position of the switch. By applying Kirchhoff's laws to each, we can derive the equations that define them. It is worth noting that the following modeling is done for continuous conduction mode (Leng and Liu, 2017).

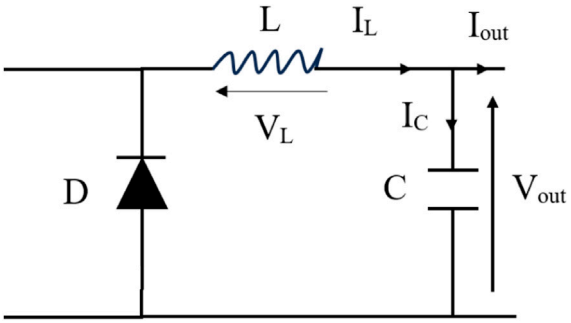

FIGURE 4
Equivalent circuit of the Buck converter for K open.

From 0 to DT: The switch K is closed, and the diode is reverse-biased, as shown in Figure 3.

By applying Kirchhoff's voltage law to this circuit, the following equations (Eqs 2–5) (Ejury, 2013; Lee, 2015).

$$\boldsymbol{V_{in}(t) = V_L(t) + V_{out}(t) \text{ with } V_k(t) = 0v} \tag{2}$$

This implies:

$$\boldsymbol{V_L = V_{in}(t) - V_{out}(t)} \tag{3}$$

Therefore:

$$\boldsymbol{L\frac{di_L(t)}{dt} = V_{in}(t) - V_{out}(t)} \tag{4}$$

Consequently:

$$\boldsymbol{i_L(t) = \frac{V_{in} - V_{out}}{L}\, t + I_{Lmin}} \tag{5}$$

We know that for t = 0, we will have a minimal inductor current I_L, and for t = DT, we will have a maximal inductor current. Therefore, we can deduce the (Eq. 6):

$$\boldsymbol{i_L(DT) = I_{Lmax} = \frac{V_{in} - V_{out}}{L}\, DT + I_{Lmin}} \tag{6}$$

So, the peak-to-peak ripple of the current, denoted as Δi_L, can be determined by the equation (Eq. 7):

$$\boldsymbol{\Delta i_L = I_{Lmax} - I_{Lmin} = \frac{V_{in} - V_{out}}{L}\, DT \text{ with } T = \frac{1}{f_s}} \tag{7}$$

The current ripple in the receiver is directly proportional to the chopping frequency used in pulse width modulation (PWM). Thus, the higher the chopping frequency, the lower the current ripple will be. This implies that a significant increase in the chopping frequency would require the use of fast-switching electronic components, such as MOSFETs, capable of rapid switching to maintain a clean voltage waveform at higher frequencies (Ejury, 2013; Lee, 2015).

From DT to T: The switch K is open, and the diode D is conducting, as shown in Figure 4.

By applying Kirchhoff's voltage law to this circuit, the equation (Eq. 8):

$$\boldsymbol{V_L(t) = -V_{out}(t) \text{ with } V_{out}(t) = V_c(t) \text{ et } V_d(t) = V_c(t)} \tag{8}$$

The equation (Eq. 8) becomes (Eq. 9):

$$-L\frac{di_L(t)}{dt} = V_{out}(t) \tag{9}$$

And the load current is given by equation (Eq. 10)

$$i_L(t) = \frac{V_{out}}{L}t + I_{Lmax} \tag{10}$$

We know that for t = DT, we will have a maximal inductor current I_L, and for t = T, we will have a minimal inductor current. Therefore, we can deduce the equation (Eq. 11):

$$i_L(T) = I_{Lmin} = \frac{-V_{out}}{L}(T - DT) + I_{Lmax} \tag{11}$$

So, the peak-to-peak ripple of the current, denoted as Δi_L, can be determined by the following formula (Eq. 12):

$$\Delta i_L = I_{Lmax} - I_{Lmin} = \frac{V_{out}}{L}(\mathrm{T} - DT) \text{ with } T = \frac{1}{f_s} \tag{12}$$

In steady-state operation, the energy stored in each component of the Buck converter remains constant at the beginning and end of each switching cycle. Therefore, the inductor current I_L flowing through the inductance also remains constant at the beginning and end of each switching cycle. This means that the current in the inductance does not change significantly during a switching period and remains practically stable [33]. The out voltage is given by equation (Eq. 13)

$$\frac{V_{out}}{L}(\mathrm{T} - DT) = \frac{V_{in} - V_{out}}{L}DT \rightarrow \frac{V_{out}}{V_{in}} = D \tag{13}$$

So:

$$D = \frac{V_{out}}{V_{in}} \tag{14}$$

The duty cycle D shown by the equation (Eq. 14) linearly determines the variation in the output voltage. Thus, the output voltage V_{in} is always less than the input voltage because the duty cycle is between 0 and 1. Under ideal conditions where there is no power loss, the average power at the input and output of the circuit is equal if we consider the inductor, diode, and switch as ideal components.

2.2.1 Dimensioning and component selection

This section presents the criteria for choosing each of the main components of the Buck-Boost converter to meet specific specifications and applications. Indeed, oversizing these components will increase the weight and cost of the circuits.

2.2.1.1 Current ripple and inductor selection

It is crucial that the sizing of the inductance L complies with the current allowed by the MOSFET transistor. If one wishes to limit the maximum current ripple Δi_L for a given value, it is essential to choose the switching frequency f_s wisely. Indeed, the higher the switching frequency, the smaller the inductance core can be, which is approved by the following formula (Eq. 15), allowing us to calculate the value of L (Ejury, 2013; Lee, 2015).

$$\Delta i_L = I_{Lmax} - I_{Lmin} = \frac{V_{out}}{L}(\mathrm{T} - DT) \quad with\ T = \frac{1}{f_s} \tag{15}$$

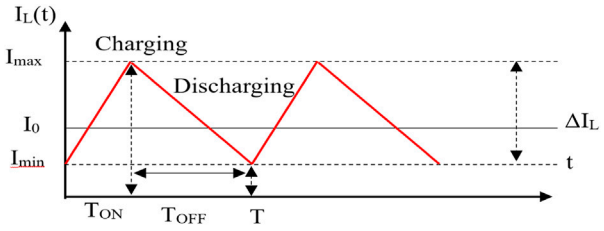

FIGURE 5
Charge and discharge of the output capacitor.

$$\Delta i_L = \frac{V_{out}}{Lf_s}(1 - D) \tag{16}$$

$$\mathrm{L} = \frac{V_{out}}{f_s \Delta i_L}(1 - D) \text{ with } V_{out} = DV_{in} \tag{17}$$

This implies:

$$\mathrm{L} = \frac{V_{in}}{f_s \Delta i_L}(1 - D)D \tag{18}$$

For continuous conduction mode, it is assumed that:

$$\Delta_{I_L} = 2I_{out} \quad \text{with: } I_{out} = \frac{V_{out}}{R} \tag{19}$$

By combining Eqs 18, 19, we obtain a second equation allowing the calculation of the inductance value L, which is dependent on the load value:

$$\mathrm{L} = \frac{R(1 - D)}{2f_s} \tag{20}$$

Generally, a good estimate for the maximum tolerated ripple current of the inductance is 20%–40% of the output current (Ejury, 2013; Lee, 2015). Note that the maximum inductance value can be calculated for a duty cycle of 50%.

2.2.1.2 Voltage ripple and capacitor selection

To maintain the output voltage V_{out} and the current I_{out} constant, even during the opening of the switch, converter topologies typically include a capacitor C. The components of the converter are sized to minimize ripples in output voltages and currents during the switch transition from closing to opening and *vice versa*. To estimate the ripple of the output voltage, it is assumed that the current flowing through the capacitor is equal to the ripple of the current in the inductance. In other words, it is assumed that the ripple of the current flowing through the load R is zero (Choudhary and Saxena, 2014).

It is possible to observe that for each half-switching period, the capacitor stores or releases a charge ΔV_c, leading to a voltage variation across its terminals, as shown in Figure 5. This variation is given by the following formula (Eq. 21):

$$\Delta v_c = \frac{\Delta Q}{C} = \frac{V_{out}}{8LCf^2}(1 - D)D \tag{21}$$

If the current ripple is known, then we have the following formula (Eq. 22):

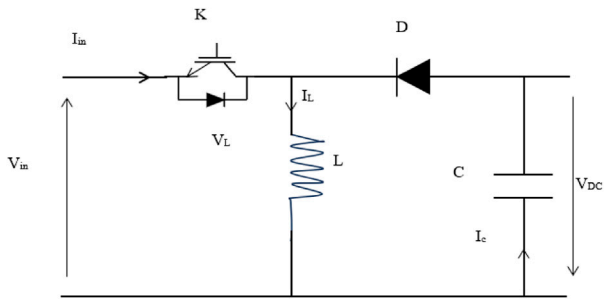

FIGURE 6
A basic schematic of the buck-boost converter.

$$C = \frac{\Delta_{i_L}}{8L\Delta_{V_{out}}f^2} \tag{22}$$

For a duty cycle of 50%, we will have a maximum ripple, and this will allow us to determine the capacitor value that ensures a ripple below this value (Eq. 23):

$$C \geq \frac{V_{in}}{32.L.\Delta V_{C_{max}}.f^2} \tag{23}$$

2.3 Buck boost converter

The DC-DC converter depicted in Figure 6 is a Buck-Boost converter, a variant that controls the output voltage by delivering either a higher or lower voltage compared to the input voltage, based on the specific needs of the application. This converter amalgamates the characteristics of both Buck and Boost converters, making it suitable as an optimal transformer for generating the desired output voltage from an input voltage with reverse polarity. Additionally, it incorporates a diode for ensuring safe operation Ahmed et al., 2023; González-Castaño et al., 2022; Khan et al., 2022; Allahverdinejad et al., 2022).

Therefore, the converter can be configured in two ways, and applying Kirchhoff's laws to each allows for the extraction of equations defining it in the continuous conduction mode (Afshari et al., 2023).

2.3.1 ON-state mode of operation (switch, k, closed)

In this operational mode, the switch K remains closed for a duration of DT, where D is the duty cycle, and T is the time period. With the switch closed, offering zero resistance, the current flows through the inductor, the switch, and back to the DC input source. Throughout this period, the inductor stores energy. As the diode is in a blocked state, the inductor's polarity reverses, enabling the current to pass through the load and the diode before returning to the inductor. Consequently, the direction of the current through the inductor remains constant (Singh et al., 2022).

Applying Kirchhoff's voltage law to the circuit shown in Figure 7 results in the following equations, assuming the ideal characteristics of the components (Singh et al., 2022) (Eqs 24, 25):

$$V_{in}(t) = V_L(t) \tag{24}$$

$$L\frac{di_L(t)}{dt} = V_{in}(t) \tag{25}$$

By integrating the differential Eq. 10, we obtain the solution (Eq. 26):

$$i_L(t) = \frac{V_{in}}{L}t + I_{Lmin} \tag{26}$$

where at $t = 0$, minimum current is $i_L(0) = I_{Lmin}$, and at $t = DT$, the inductor current is at a maximal current I_{Lmax} under the steady state operation of the converter (Eq. 27).

Therefore,

$$i_L(DT) = I_{Lmax} = \frac{V_{in}}{L}DT + I_{Lmin} \tag{27}$$

The peak-to-peak ripple, Δi_L in the current can be determined by utilizing the following equation (Eq. 28):

$$\Delta i_L = I_{Lmax} - I_{Lmin} = \frac{V_{in}}{L} * DT \text{ where } T = \frac{1}{f_s} \tag{28}$$

Next, we define the following:

V_{in} = buck-boost converter input voltage; V_{DC} = buck-boost converter output voltage; V_L = inductor voltage; I_{in} = buck-boost converter input current; I_{DC} = buck-boost converter output current; I_L = Inductor current; I_C = capacitor current.

2.3.2 OFF-state mode of operation (switch, k, open)

In the OFF cycle, from DT to T, the diode D conducts, as depicted in Figure 8. In this phase of current decay within inductor L, corresponding to the opening of switch K, the inductor discharges and redistributes the energy it had stored back to the load.

Applying Kirchhoff's voltage law to this circuit yields the following equations (Eqs 29, 30) (Singh et al., 2022):

$$V_L(t) = -V_{DC}(t) \text{ with } V_{DC}(t) = V_c(t) \tag{29}$$

$$V_L(t) = -L\frac{di_L(t)}{dt} = V_{DC}(t) \tag{30}$$

Solving the equations with the same approach as during the ON state, the inductor current is expressed by the equation (Eq. 31)

$$i_L(t) = \frac{V_{DC}}{L}t + I_{Lmax} \tag{31}$$

Also, the inductor current I_L, at t = T is given by the following equation (Eq. 32):

$$i_L(T) = I_{Lmin} = \frac{-V_{DC}}{L}(T - DT) + I_{Lmax} \tag{32}$$

And the peak-to-peak ripple current Δi_L is determined by the following equation (Eq. 33):

$$\Delta i_L = I_{Lmax} - I_{Lmin} = \frac{V_{DC}}{L}(T - DT) \tag{33}$$

The duty cycle can be derived as follows (Eq. 34):

$$\frac{V_{in}}{L}\text{DT} = \frac{-V_{DC}}{L}(1 - D)T \rightarrow \frac{-V_{DC}}{V_{in} - V_{DC}} = D \tag{34}$$

Knowing that the output voltage is inverted, it can be written as shown in the equation (Eq. 35)

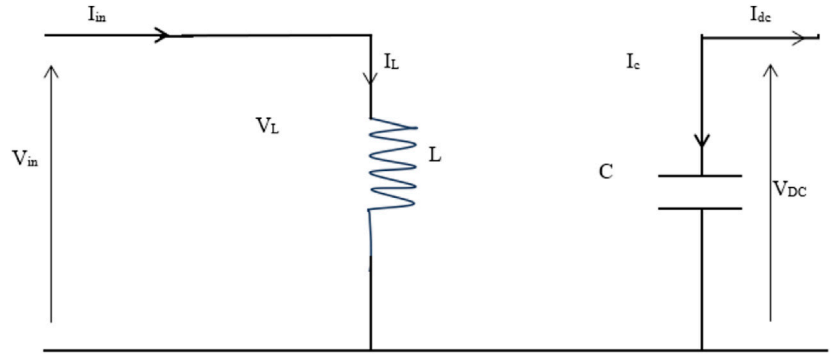

FIGURE 7
Structure of an Equivalent circuit of the buck-boost converter during the on-state.

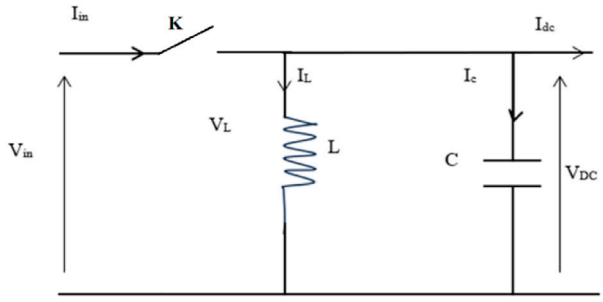

FIGURE 8
Equivalent Circuit of the Buck-Boost Converter during the OFF state.

$$D = \frac{V_{DC}}{V_{in} + V_{DC}} \tag{35}$$

Also, the relationship between the input and the output of the converter is given as follows equation (Eq. 36):

$$V_{DC} = \frac{D}{1 - D} V_{in} \tag{36}$$

The output voltage of the Buck-Boost converter is dictated by both the input voltage and the duty cycle, D (Mayo-Maldonado et al., 2018; Rosas-Caro et al., 2018; Singh et al., 2022). This converter functions as a step-down transformer when the duty cycle is less than 0.5 and as a step-up transformer when the duty cycle exceeds 0.5. Despite its dual functionality, it is commonly referred to as an inverting converter because the output voltage always exhibits the opposite polarity to the input voltage. While the ideal output voltage is expected to be unaffected by the load, practical considerations require regulation to offset fluctuations in the input voltage and imperfections in real components.

2.3.3 Current ripple and inductor selection

The choice of inductance in a Buck-Boost converter demands careful consideration to enhance efficiency, stability, and overall circuit performance. This optimization process involves utilizing the previously defined equations (Ejury, 2013; Lee, 2015).

Eq. 37 establishes a connection between the change in inductor current (ΔiL), the direct current voltage (VDC), the inductance (L), and the time period (T) minus the product of the duty cycle and the time period (DT). This change in inductor current essentially represents the difference between the maximum and minimum inductor currents is given by equation (Eq. 37).

$$\Delta i_L = I_{Lmax} - I_{Lmin} = \frac{V_{DC}}{L} (T - DT) \tag{37}$$

The given equation articulates the variation in inductor current with respect to the direct current voltage (VDC), the switching frequency (fs), the inductance (L), and the complement of the duty cycle (1 - D) as shown by the equation (Eq. 38):

$$\Delta i_L = \frac{V_{DC}}{f_s L} (1 - D) \tag{38}$$

Eq. 23 can be resolved to find the inductance (L) in relation to the direct current voltage (V_{DC}), switching frequency (fs), change in inductor current (Δi_L), and the complement of the duty cycle (1 - D). Additionally, the expression for V_{DC} is provided in terms of D/(1-D) * V_{in}, as illustrate by the equation (Eq. 39):

$$L = \frac{V_{DC}}{f_s \Delta i_L} (1 - D) \text{ with } V_{DC} = \frac{D}{1 - D} V_{in} \tag{39}$$

Thus, we obtain the equation (Eq. 40):

$$L = \frac{V_{in}}{f_s \Delta i_L} D \tag{40}$$

2.3.4 Voltage ripple and capacitor selection

A. Selecting the suitable capacitor for the Buck-Boost converter typically involves beginning with a standard capacitor value and verifying if it aligns with the converter's specifications. In cases where the voltage ripple exceeds acceptable limits, opting for a larger capacitor is advisable to mitigate the voltage ripple (Ejury, 2013; Lee, 2015).

By examining the current waveform depicted in Figure 9, it becomes feasible to ascertain the fluctuation in voltage across the capacitor, given by the equation (Eq. 17):

$$\Delta Q = \frac{-V_{DC}}{R} DT \tag{41}$$

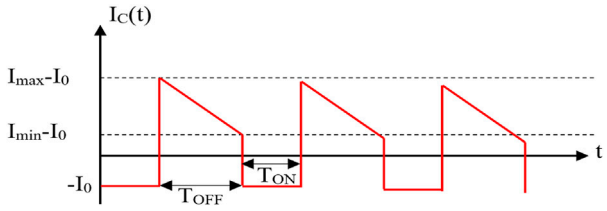

FIGURE 9
Current waveform across the capacitor.

This equation describes the variation in charge (ΔQ) within a circuit element. It equals the negative of the product of the voltage across the element (V_{DC}) and the reciprocal of the resistance (R), multiplied by the change in time (DT), as shown by the equation (Eq. 42):

$$|\Delta V_{DC}| = \frac{\Delta Q}{C} = \frac{V_{DC}}{RC} DT \tag{42}$$

This equation establishes a connection between the absolute value of the change in output voltage ($|\Delta V_{DC}|$) and the ratio of the change in charge (ΔQ) to the capacitance (C). Additionally, it is expressed in terms of the output voltage (V_{DC}), resistance (R), capacitance (C), and the change in time (DT), as given by the equation (Eq. 43):

$$C = \frac{V_{DC}}{R\Delta V_{DC} f_s} D \text{ with } V_{DC} = I_{DC} R \tag{43}$$

In this context, C denotes the capacitance, V_{DC} is the output voltage, R represents the resistance, ΔV_{DC} is the change in output voltage, fs is the switching frequency, and D stands for the duty cycle. This equation establishes a relationship between capacitance, output voltage, resistance, change in output voltage, switching frequency, and duty cycle, as shown by the equation (Eq. 44):

$$C = \frac{I_{DC}}{\Delta V_{DC} f_s} D \tag{44}$$

The provided equation expresses capacitance in terms of the output current (I_{DC}), the change in output voltage (ΔV_{DC}), switching frequency (f_s), and duty cycle (D).

Leveraging the previously discussed equations, we conducted a dimensioning process, as illustrated in Table 3 below. It is noteworthy that our approach differs from the conventional method of fixing a switching frequency (f_s) and then searching for appropriate hardware. Instead, we calculated the suitable frequency based on the available hardware.

3 Proposed MPPT

Numerous algorithms have been suggested to optimize the operation of the PV array at the maximum power point (Mostafa et al., 2020). This paper employs and compares Perturb and Observe (P&O) and Sliding Mode Control (SMC) methods, as elaborated later.

3.1 Classical perturb and observe (P&O)

The Perturb and Observe (P&O) algorithm stands out as the most commonly employed method for tracking the maximum power point. The P&O MPPT technique operates by periodically perturbing the terminal voltage of the PV array, incrementing or decrementing a control parameter by a small amount until reaching the maximum power point. The process involves measuring the power, introducing a small perturbation, measuring the new power, and determining the direction of perturbation based on the sign of the power change. If the change is positive, the control system continues perturbing in the same direction; otherwise, it adjusts the operating point in the opposite direction (Bharambe and Mahajari, 2015; Lamnadi et al., 2016).

However, this method has notable drawbacks. In steady-state operation, the obtained power oscillates around the maximum power point, potentially causing the tracking to deviate under rapidly changing environmental conditions. Additionally, the step size not only defines the range of oscillation around the MPP during steady-state operation but also governs the speed of convergence to the MPP.

3.2 Sliding mode MPPT

The sliding mode control (SMC) process represents a nonlinear controller, falling within the category of dynamic controllers designed to provide robust control for intricate, high-order nonlinear dynamic plants operating in uncertain conditions (Bartoszewicz and Żuk, 2010; Singh et al., 2017; Meng et al., 2018; Vaidyanathan et al., 2019). In conjunction with this, Perturb and Observe (P&O) is utilized to track the maximum power point, acquiring V_{ref} for subsequent comparison with the actual V_{pv} in varying environmental conditions (Mostafa et al., 2020). Subsequently, the current controller, employing I_C, engages the hysteresis loop to generate the signal (u) for toggling the converter between on (1) and off (0).

Regarding the dynamic analysis of SMC:

$$S = (V_{pv} - V_{ref}) * G_1 + I_{in} * G_2 \tag{45}$$

With G_1 and G_2 are constants gain; To implement the proposed technique, (S) must be equal to zero, and dS/dt should also be zero.

From this standpoint, the derivative of equation (Eq. 45) is given by equation (Eq. 46)

$$\frac{dS}{dt} = \left(\frac{dV_{pv}}{dt} - \frac{dV_{ref}}{dt}\right) * G_1 + \frac{dI_C}{dt} * G_2 \tag{46}$$

$$I_C = (I_{pv} - I_{out}) \tag{47}$$

And

$$I_C = C\frac{dV_C}{dt} \tag{48}$$

Deriving Eqs 47 and 48, we arrive at the subsequent expression:

$$\frac{dV_C}{dt} = \frac{I_{pv} - I_{out}}{C} \tag{49}$$

TABLE 3 Dimensioning of the regulation stages used in the system.

Converter	r	D	f_s	L_{min}	C_{min}	Δ_{i_L}	Δv_{out}
Buck	$\frac{V_{out}}{V_{in}}$	$\frac{V_{out}}{V_{in}}$	$\frac{R(1-D)}{2L}$	$\frac{R(1-D)}{2f_s}$	$\frac{\Delta_{i_L}}{8L\Delta_{V_{out}}f^2}$	$\frac{V_{out}}{Lf_s}(1-D)$	$\frac{V_{out}}{8LCf^2}(1-D)D$
	0.61	0.61	6 KHz	300 µH	10000 µF	<15%	<1%
Buck-Boost	$\frac{V_{out}}{V_{in}}$	$\frac{V_{out}}{V_{in}+V_{out}}$	$\frac{R(1-D^2)}{2L}$	$\frac{V_{in}}{f_s\Delta i_L}D$	$\frac{I_{out}}{\Delta V_{out}f_s}D$	$\frac{V_{out}}{f_sL}(1-D)$	$\frac{V_{out}}{RC}DT$
	0.1	0.09	12 KHz	300 µH	10000 µF	<15%	<1%

We have also the equations (Eqs 50–52):

$$\boldsymbol{V_{pv}(t) = V_{in}(t) = V_L(t) + V_{out}(t) \text{ with } V_{out}(t) = V_C} \quad (50)$$

$$\boldsymbol{V_{pv}(t) = V_L(t) + V_C(t)} \quad (51)$$

$$\boldsymbol{\frac{dV_{pv}}{dt} = L\frac{dI_l}{dt} + \frac{I_{pv} - I_{out}}{C}} \quad (52)$$

By substituting Eqs 52 and 48, and Eq. 47 into Eq. 46, we obtain the following expression:

$$\boldsymbol{\frac{dS}{dt} = \left(L\frac{dI_l}{dt} + \frac{I_{pv} - I_{out}}{C} - \frac{dV_{ref}}{dt}\right)*G_1 + \left(\frac{dI_{pv}}{dt} - \frac{dI_l}{dt}\right)*G_2} \quad (53)$$

With

$$\boldsymbol{\frac{di_L(t)}{dt} = \frac{V_{in}(t) - V_{out}(t)}{L} = \frac{\left(\frac{V_{out}}{D}\right) - V_{out}(t)}{L} = \frac{V_{out}}{L}\left(\frac{1-D}{D}\right)} \quad (54)$$

By substituting Eq. 53 into Eq. 54, we can express the relation as given by the equation (Eq. 55):

$$\boldsymbol{\frac{dS}{dt} = \left(V_{out}\left(\frac{1-D}{D}\right) + \frac{I_{pv} - I_{out}}{C} - \frac{dV_{ref}}{dt}\right)*G_1 + \left(\frac{dI_{pv}}{dt} - \frac{V_{out}}{L}\left(\frac{1-D}{D}\right)\right)*G_2 = 0} \quad (55)$$

4 Battery management

This module incorporates a 640Ah capacity battery with a programmable state of charge, accompanied by an intelligent supervisory control system managing battery behavior in critical scenarios using three switches: "Charging," "Direct," and "Discharging."

The charging behavior of the battery (P_{Load}) can be described by the following equations:

When.

P_{pv} exceeds P_{Load} (battery charging) (see Eq. 56):

$$\boldsymbol{P_{Load} = P_{pv} + P_{Bat}} \quad (56)$$

When P_{pv} is less than P_{Load} (battery discharging) (see Eq. 57):

$$\boldsymbol{P_{Load} = P_{pv} - P_{Bat}} \quad (57)$$

where:

P_{Load}: Battery charging power (positive for charging, negative for discharging).

P_{pv}: Photovoltaic power (solar panels).

P_{Bat}: Battery power (positive for discharging, negative for charging, based on charging/discharging conditions and the state of the "Charging," "Direct," "Discharging" switches).

5 Results and discussion

The photovoltaic panel will serve as the power source for the entire system, followed by a Buck-type adaptation stage controlled by a proposed Maximum Power Point Tracking (MPPT) command, along with a load in the form of a battery. Figure 10 below illustrates the voltage-current and power-voltage characteristics of the selected module under standard operating conditions in terms of temperature and irradiation (25°C, 1000 W/m^2):

To gain a preliminary insight into the behavior of the PV generator, consisting of 2 modules in series and 5 in parallel as indicated in Table 1, we have studied its response to variations in temperature and irradiation.

From Figure 11, it can be observed that irradiance has a direct impact on current; as irradiance increases, the current intensity increases, and the I(V) curves shift towards higher values, allowing the module to produce more electrical power.

To test the validity and feasibility of the proposed structure and MPPT technique, three tests will be conducted.

5.1 TestN°1

In this test, the state of charge of the battery (SOC) and the irradiance are kept constant, as shown in Figures 12A,D. The state of the switches is observed, as depicted in Figure 12B,C, F.

It is observed that when the power supplied by the panel is sufficient and constant, as shown in Figure 12E due to constant irradiance (G = 1000 W/m2) to meet the requirements of the load, the battery maintains a constant charge level. This confirms the robustness of the proposed MPPT technique based on the sliding mode. It is also noteworthy that the direct switch is activated, indicating that the load is powered by the PV generators, while the other two switches are deactivated. Figures 12G, H depict the current and voltage at the output of the buck-boost converter, maintained constant at their desired values through regulation ensured by the PI controller.

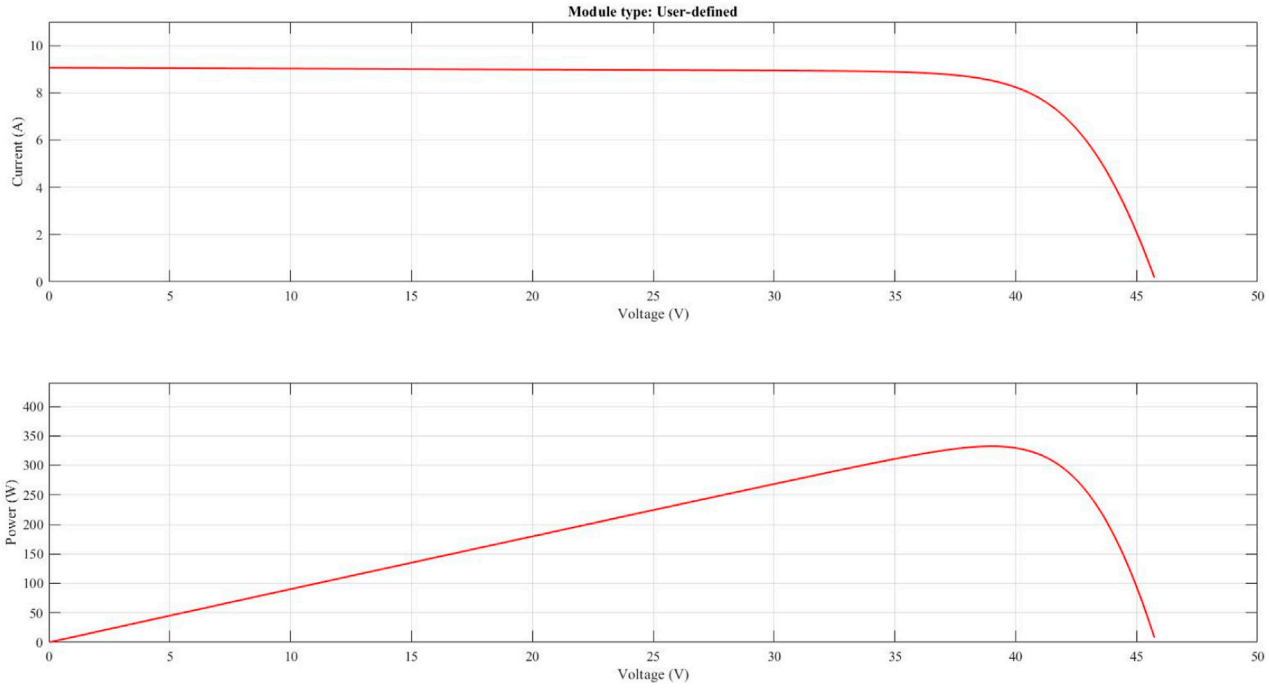

FIGURE 10
Characteristics of I (V) and P (V) for the selected module.

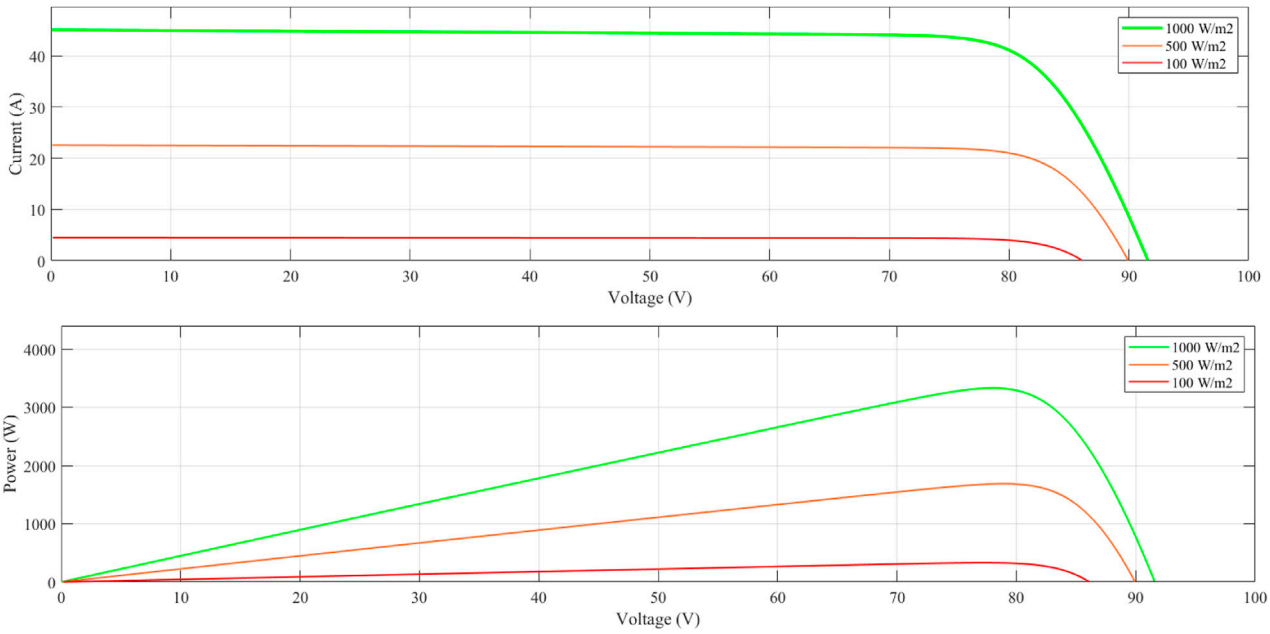

FIGURE 11
Characteristic of the PV generator for different irradiance values.

5.2 TestN°2

In this test, the state of charge of the battery (SOC) is maintained constant, as depicted in Figure 13A, while the irradiance varies according to the profile shown in Figure 13D. The state of the switches is observed, as indicated in Figures 13B,C, F.

When the power provided by the panel exceeds 1500 W and the SOC is constant, the discharge and charge switches are activated (see

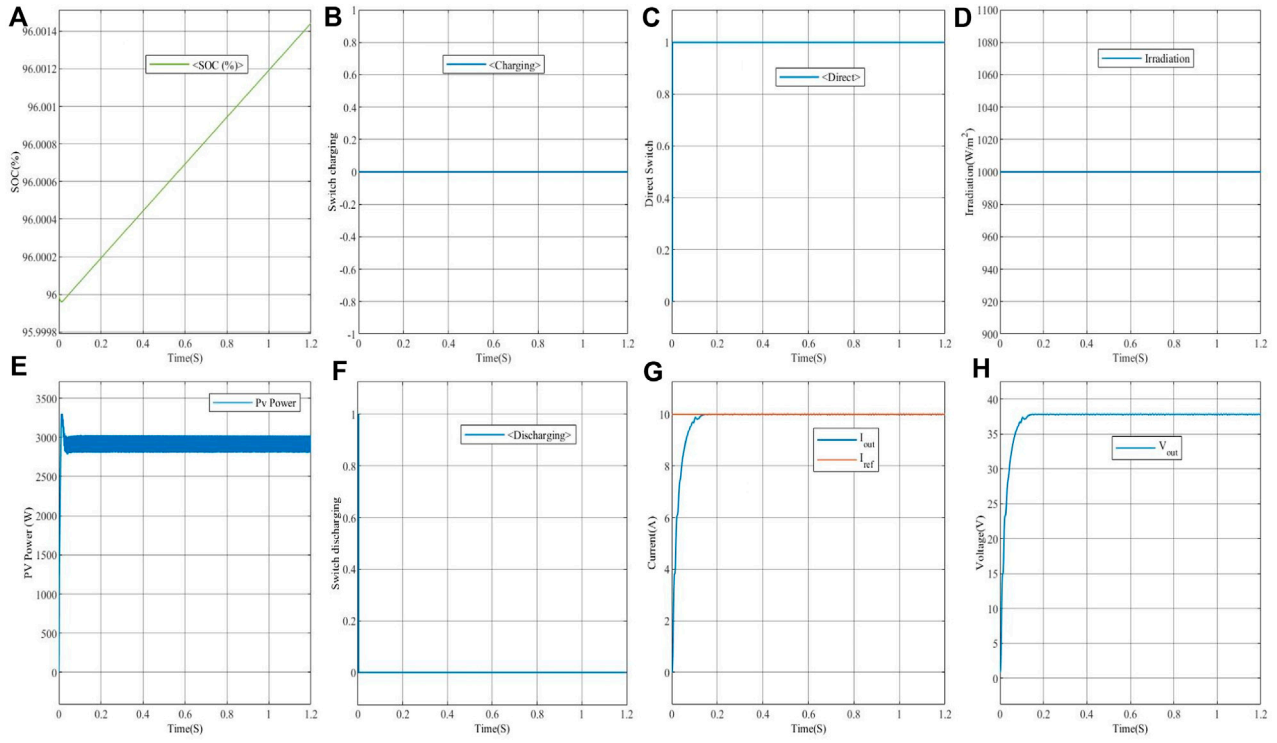

FIGURE 12
Simulation results for a state of charge (SOC) greater than 95% with constant irradiance = 1000 W/m2.

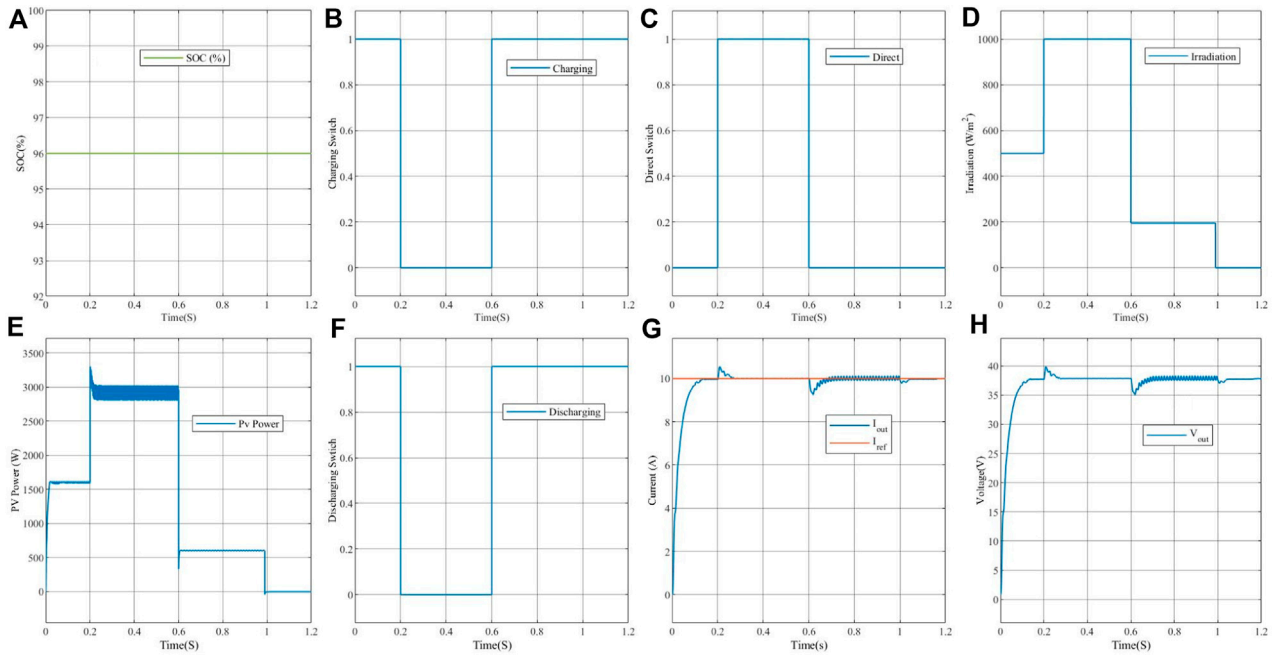

FIGURE 13
Simulation results for a state of charge (SOC) greater than 95% with variable irradiance.

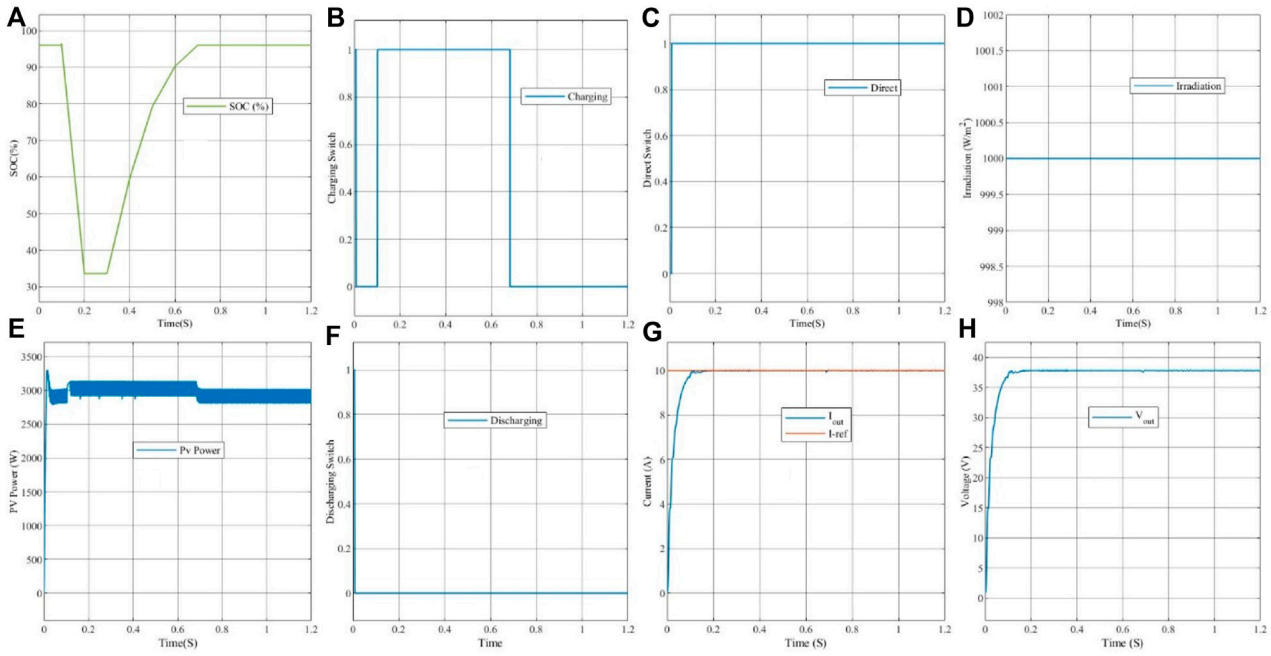

FIGURE 14
Simulation results for a variable state of charge (SOC) with constant irradiance = 1000 W/m2.

Figures 13B,F) to compensate for the power deficiency, ensuring that the current and voltage at the output of the buck-boost converter are maintained at their desired values and the battery remains fully charged.

From time (t = 0.2 to t = 0.6 s), with irradiance G = 1000 W/m2, as shown in Figure 13D, the power supplied by the photovoltaic generator is sufficient. It can be observed that the charge and discharge switches are deactivated, while the Direct switch is activated, as depicted in Figures 13B, C, F. The current and output voltage remain constant after a slight disturbance.

From time (t = 0.6 to t = 1.2 s), when the power supplied by the photovoltaic generator is insufficient, the discharge and charge switches are activated to compensate for the power deficiency from the PV generator with the battery, as shown in Figures 13C, E, F. This ensures that the voltage and current at the output of the buck-boost converter are maintained at their desired levels, as illustrated in Figures 13G, H.

5.3 TestN°3

In this test, the brightness remains constant, as shown in Figure 14D, while the state of charge of the battery (SOC) varies according to the profile presented in Figure 14A. The state of the switches is observed, as illustrated in Figures 14B, C, F. When the state of charge of the battery (SOC) is above 95%, the discharge and charge switches are deactivated (see Figures 14B, F), as there is no lack of power, and the battery's state of charge is satisfactory. The power supplied by the PV generator keeps the current and voltage at the output of the buck-boost converter at their desired values, thus maintaining the battery at its full charge, with the Direct switch activated (see Figure 14C).

From time (t = 0.2 to t = 0.7 s), the state of charge of the battery varies according to the profile shown in Figure 14A. The power supplied by the photovoltaic generator remains sufficient, as shown in Figure 14E, with constant illumination. The activation of the charge switches is noted to charge the battery with the power generated by the PV generator, as shown in Figure 14B. The discharge switch remains deactivated as long as the PV power is sufficient, while the Direct switch is activated, as illustrated in Figure 14C. The current and output voltage remain constant after a slight disturbance.

From time (t = 0.7 to t = 1.2 s), the power supplied by the photovoltaic generator remains sufficient. The deactivation of the discharge and charge switches is observed, while the Direct switch is activated to maintain a constant current and voltage at their desired values.

5.4 TestN°4

In this test, both the brightness and the state of charge of the battery (SOC) remain constant, as indicated in Figures 15A,D. A charge disturbance is introduced from time t = 0.3 to t = 0.6 s, followed by deactivating the disturbance from t = 0.6–1.2 s. The state of the switches is observed, as illustrated in Figures 15B, C, F.

Upon introducing the charge disturbance, a perturbation is observed in the current curve (Figure 15G), stabilizing subsequently at the imposed reference value, I_{ref} = 10A, confirming the robustness of the implemented controller. However, the output voltage at the load exhibits a slight drop due to the charge disturbance. Analysis of the switch states reveals that the power is supplied by the PV panel (Figure 15E).

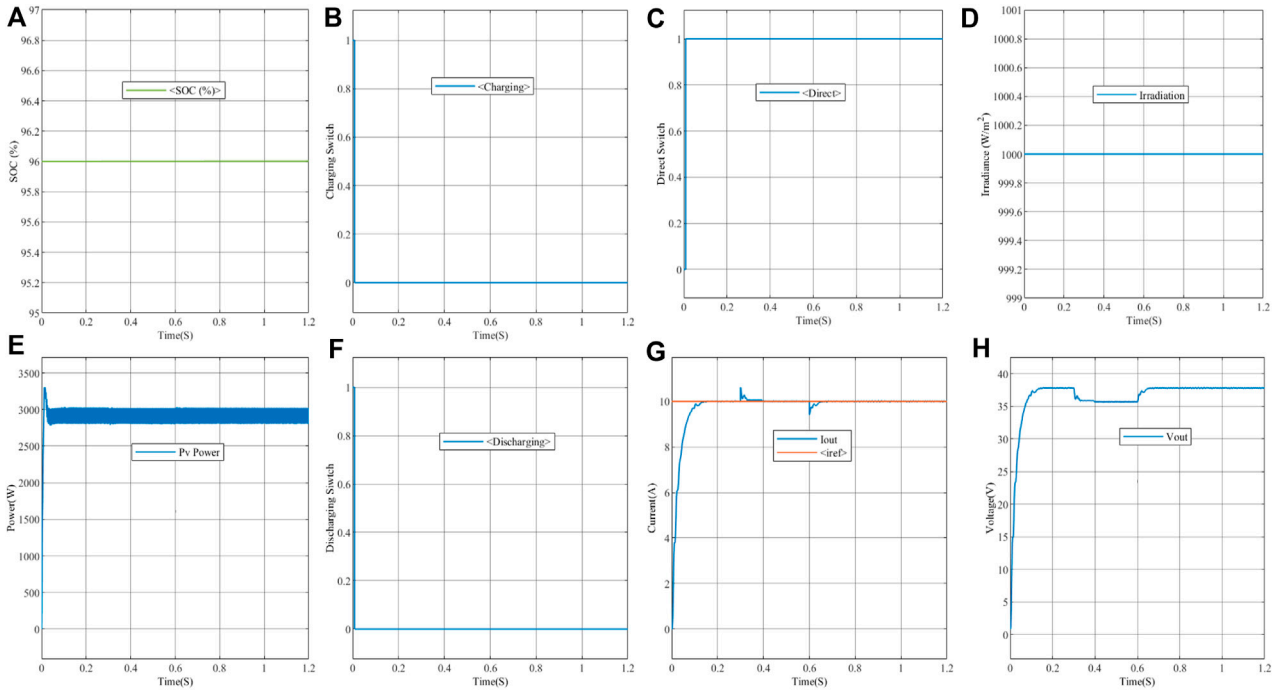

FIGURE 15
Simulation results for a variable load.

This temporary current perturbation can be attributed to the system's response to the load variation, while the slight voltage drop may result from the converter's response to the disturbance. These observations demonstrate the system's ability to maintain stability despite temporary disturbances, thereby validating the effectiveness of the implemented control.

6 Conclusion and future works

This research introduces an innovative approach to power control in PV/battery systems by integrating sliding mode MPPT with advanced energy management through a dual Buck converter. The study focuses on optimizing solar energy extraction, regulating current, and ensuring efficient battery utilization. Simulations conducted on MATLAB with two converters (buck and buck-boost) validate the proposed hybrid topology, contributing significantly to the advancement of sustainable and efficient energy solutions.

The results showcase the robustness of the sliding mode MPPT technique under various conditions. Tests conducted under constant and variable solar irradiance, coupled with State of charge (SOC) variations, demonstrate the system's adaptability and efficiency. The supervisory system effectively manages the power supply of the buck-boost converter based on battery charge levels, addressing specific scenarios such as insufficient solar power.

This study not only advances the understanding of PV/battery power control but also underscores the potential of integrating sliding mode MPPT and dual Buck converters for optimizing energy production, distribution, and storage. The results presented herein pave the way for further exploration and implementation of these innovative techniques in real-world applications, marking a significant stride towards a more sustainable and efficient energy future.

Data availability statement

The original contributions presented in the study are included in the article/supplementary material, further inquiries can be directed to the corresponding authors.

Author contributions

AF: Conceptualization, Data curation, Formal Analysis, Funding acquisition, Investigation, Methodology, Project administration, Resources, Software, Supervision, Validation, Visualization, Writing–original draft, Writing–review and editing. MH: Conceptualization, Data curation, Project administration, Software, Visualization, Writing–original draft, Writing–review and editing. AA: Conceptualization, Formal Analysis, Funding acquisition, Investigation, Methodology, Supervision, Visualization, Writing–original draft, Writing–review and editing. MG: Conceptualization, Formal Analysis, Investigation, Methodology, Resources, Software, Supervision, Validation, Visualization, Writing–original draft, Writing–review and editing. AH: Conceptualization, Data curation, Formal Analysis, Software, Visualization, Writing–original draft. HD: Conceptualization, Methodology, Resources, Software, Validation, Visualization, Writing–original draft, Writing–review and editing. IH:

Conceptualization, Formal Analysis, Funding acquisition, Investigation, Methodology, Project administration, Resources, Writing–original draft, Writing–review and editing.

Funding

The author(s) declare financial support was received for the research, authorship, and/or publication of this article. This research was funded by the Norwegian University of Science and Technology. This research is supported by Automated Systems and Soft Computing Lab (ASSCL), Prince Sultan University, Riyadh, Saudi Arabia.

Acknowledgments

The authors would like to acknowledge the support of the Norwegian University of Science and Technology for paying the Article Processing Charges (APC) of this publication. The authors would like to thank Prince Sultan University, Riyadh, Saudi Arabia for their support. Special acknowledgment to Automated Systems and Soft Computing Lab (ASSCL), Prince Sultan University, Riyadh, Saudi Arabia. In addition, the authors wish to acknowledge the editor and anonymous reviewers for their insightful comments, which have improved the quality of this publication.

Conflict of interest

The authors declare that the research was conducted in the absence of any commercial or financial relationships that could be construed as a potential conflict of interest.

Publisher's note

All claims expressed in this article are solely those of the authors and do not necessarily represent those of their affiliated organizations, or those of the publisher, the editors and the reviewers. Any product that may be evaluated in this article, or claim that may be made by its manufacturer, is not guaranteed or endorsed by the publisher.

References

Afshari, H., Husev, O., and Vinnikov, D. (2023). "A novel isolated buck-boost dc-dc converter with wide range of voltage regulations," in 2023 IEEE 17th International Conference on Compatibility, Power Electronics and Power Engineering (CPE-POWERENG) (Tallinn, Estonia: IEEE), 1–6.

Ahmed, N., Sher, H. A., Al-Durra, A., and Hasanien, H. M. (2023). Comprehensive analysis and design of a switched-inductor type low inductance-requirement DC-DC buck-boost converter for low power applications. *IET Power Electron* 16, 1239–1254. doi:10.1049/pel2.12465

Allahverdinejad, B., Modaberi, S. A., and Ajami, A. (2022). "A non-isolated buck-boost DC–DC converter with continuous input current and wide conversion ratio range for photovoltaic applications," in 2022 13th Power Electronics, Drive Systems, and Technologies Conference (PEDSTC), Tehran, Iran, Islamic Republic of, 01-03 February 2022 (IEEE), 491–497.

Ammar, H. H., Azar, A. T., Shalaby, R., and Mahmoud, M. I. (2019). Metaheuristic optimization of fractional order incremental conductance (FO-INC) maximum power point tracking (MPPT). *Complexity* 2019, 1–13. doi:10.1155/2019/7687891

Bartoszewicz, A., and Żuk, J. (2010). "Sliding mode control—basic concepts and current trends," in 2010 IEEE international symposium on industrial electronics, Bari, Italy, 04-07 July 2010 (IEEE), 3772–3777.

Benhalima, S., Miloud, R., and Chandra, A. (2018). Real-time implementation of robust control strategies based on sliding mode control for standalone microgrids supplying non-linear loads. *Energies* 11 (10), 2590. doi:10.3390/en11102590

Bharambe, V. R., and Mahajari, K. M. (2015). Implementation of P&O MPPT for PV System with using buck dan buck-boost converters. *Int. J. Res. Electr. Eng.* 2 (3), 5–10.

Choudhary, D., and Saxena, A. R. (2014). DC-DC buck-converter for MPPT of PV system. *Int. J. Emerg. Technol. Adv. Eng.* 4 (7), 813–821.

Ejury, J. (2013). Buck converter design. *Infineon Technol. N. Am. (TFNA) Corn. Desion Note* 1, 1–17.

Fachrizal, R., Qian, K., Lindberg, O., Shepero, M., Adam, R., Widén, J., et al. (2024). Urban-scale energy matching optimization with smart EV charging and V2G in a net-zero energy city powered by wind and solar energy. *eTransportation* 20 (1), 100314. doi:10.1016/j.etran.2024.100314

Fang, J. S., Tsai, S. H., Yan, J. J., Chen, P. L., and Guo, S. M. (2021). Realization of DC–DC buck converter based on hybrid ${H_2} $ model following control. *IEEE Trans. Industrial Electron.* 69 (2), 1782–1790. doi:10.1109/tie.2021.3062268

Fekik, A., Azar, A. T., Hameed, I. A., Hamida, M. L., Amara, K., Denoun, H., et al. (2023a). Enhancing photovoltaic efficiency with the optimized steepest gradient method and serial multi-cellular converters. *Electronics* 12 (10), 2283. doi:10.3390/electronics12102283

Fekik, A., and Benamrouche, N. (2022). *Modeling and control of static converters for hybrid storage systems.* United States: IGI GLOBAL, 1–355. doi:10.4018/978-1-7998-7447-8

Fekik, A., Ghanes, M., and Denoun, H. (2023b). *Power electronics converters and their control for renewable energy applications*. 1st edition. Elsevier, 1–337. doi:10.1016/C2020-0-04639-6

Fekik, A., Hamida, M. L., Houassine, H., Azar, A. T., Kamal, N. A., Denoun, H., et al. (2022b). "Power quality improvement for grid-connected photovoltaic panels using direct power control," in *Modeling and control of static converters for hybrid storage systems"* (United States: IGI Global), 107–142. doi:10.4018/978-1-7998-7447-8.ch005

González-Castaño, C., Restrepo, C., Flores-Bahamonde, F., and Rodriguez, J. (2022). A composite DC–DC converter based on the versatile buck–boost topology for electric vehicle applications. *Sensors* 22 (14), 5409–5419. doi:10.3390/s22145409

Hai, T., Zain, J. M., and Muranaka, K. (2023). A novel global MPPT technique to enhance maximum power from pv systems under variable atmospheric conditions. *Soft Comput.*, 1–14. doi:10.1007/s00500-023-09069-w

Haq, I. U., Khan, Q., Ullah, S., Khan, S. A., Akmeliawati, R., Khan, M. A., et al. (2022). Neural network-based adaptive global sliding mode MPPT controller design for stand-alone photovoltaic systems. *Plos one* 17 (1), e0260480. doi:10.1371/journal.pone.0260480

Hassan, Q., Algburi, S., Sameen, A. Z., Salman, H. M., and Jaszczur, M. (2023). A review of hybrid renewable energy systems: solar and wind-powered solutions: challenges, opportunities, and policy implications. *Results Eng.* 20 (1), 101621. doi:10.1016/j.rineng.2023.101621

Katche, M. L., Makokha, A. B., Zachary, S. O., and Adaramola, M. S. (2023). A comprehensive review of maximum power point tracking (mppt) techniques used in solar pv systems. *Energies* 16 (5), 2206. doi:10.3390/en16052206

Khalid, M. (2024). Smart grids and renewable energy systems: perspectives and grid integration challenges. *Energy Strategy Rev.* 51 (1), 101299. doi:10.1016/j.esr.2024.101299

Khan, M. S., Nag, S. S., Das, A., and Yoon, C. (2022). Analysis and control of an input-parallel output-series connected buck-boost DC-DC converter for electric vehicle powertrains. *IEEE Trans. Transp. Electrification* 9 (2), 2015–2025. doi:10.1109/tte.2022.3216610

Lamnadi, M., Trihi, M., Bossoufi, B., and Boulezhar, A. (2016). Comparative study of IC, P&O and FLC method of MPPT algorithm for grid connected PV module. *J. Theor. Appl. Inf. Technol.* 89 (1), 242–253.

Lee, J. (2015). *Basic calculation of a buck converter's power stage. Application Note AN041*. Hsinchu, Taiwan: Richtek Technology Corporation, 1–8.

Leng, Z., and Liu, Q. (2017). "A simple model predictive control for Buck converter operating in CCM," in 2017 IEEE International Symposium on Predictive Control of Electrical Drives and Power Electronics (PRECEDE), Pilsen, Czech Republic, 04-06 September 2017 (IEEE), 19–24.

Mandourarakis, I., Gogolou, V., Koutroulis, E., and Siskos, S. (2022). Integrated maximum power point tracking system for photovoltaic energy harvesting applications. *IEEE Trans. Power Electron.* 37 (8), 9865–9875. doi:10.1109/tpel.2022.3156400

Manuel, N. L., and İnanç, N. (2022). Sliding mode control-based MPPT and output voltage regulation of a stand-alone PV system. *Power Electron. Drives* 7 (1), 159–173. doi:10.2478/pead-2022-0012

Mayo-Maldonado, J. C., Valdez-Resendiz, J. E., Garcia-Vite, P. M., Rosas-Caro, J. C., del Rosario Rivera-Espinosa, M., and Valderrabano-Gonzalez, A. (2018). Quadratic buck–boost converter with zero output voltage ripple at a selectable operating point. *IEEE Trans. Industry Appl.* 55 (3), 2813–2822. doi:10.1109/tia.2018.2889421

Meghni, B., Dib, D., Azar, A. T., Ghoudelbourk, S., and Saadoun, A. (2017). Robust adaptive supervisory fractional order controller for optimal energy management in wind turbine with battery storage. *Stud. Comput. Intell.* 688, 165–202.

Meghni, B., Dib, D., Azar, A. T., and Saadoun, A. (2018). Effective supervisory controller to extend optimal energy management in hybrid wind turbine under energy and reliability constraints. *Int. J. Dyn. Control* 6 (1), 369–383. doi:10.1007/s40435-016-0296-0

Meng, Z., Shao, W., Tang, J., and Zhou, H. (2018). Sliding-mode control based on index control law for MPPT in photovoltaic systems. *CES Trans. Electr. Mach. Syst.* 2 (3), 303–311. doi:10.30941/cestems.2018.00038

Mostafa, M. R., Saad, N. H., and El-sattar, A. A. (2020). Tracking the maximum power point of PV array by sliding mode control method. *Ain Shams Eng. J.* 11 (1), 119–131. doi:10.1016/j.asej.2019.09.003

Potrč, S., Čuček, L., Martin, M., and Kravanja, Z. (2021). Sustainable renewable energy supply networks optimization–The gradual transition to a renewable energy system within the European Union by 2050. *Renew. Sustain. Energy Rev.* 146, 111186. doi:10.1016/j.rser.2021.111186

Radwan, A. G., Emira, A. A., Abdelaty, A., and Azar, A. T. (2018). Modeling and analysis of fractional order DC-DC converter. *ISA Trans.* 82, 184–199. doi:10.1016/j.isatra.2017.06.024

Rosas-Caro, J. C., Valdez-Resendiz, J. E., Mayo-Maldonado, J. C., Alejo-Reyes, A., and Valderrabano-Gonzalez, A. (2018). Quadratic buck–boost converter with positive output voltage and minimum ripple point design. *IET Power Electron.* 11 (7), 1306–1313. doi:10.1049/iet-pel.2017.0090

Singh, A., Gupta, J., and Singh, B. (2022). "Design and control of two stage battery charger for low voltage electric vehicle using high gain buck-boost PFC AC-DC converter," in 2022 IEEE 2nd International Conference on Sustainable Energy and Future Electric Transportation (SeFeT), Hyderabad, India, 04-06 August 2022 (IEEE), 1–6.

Singh, S., Azar, A. T., Ouannas, A., Zhu, Q., Zhang, W., and Na, J. (2017). "Sliding mode control technique for multi-switching synchronization of chaotic systems," in Proceedings of 9th International Conference on Modelling, Identification and Control (ICMIC 2017), Kunming, China, July 10-12, 2017 (IEEE), 880–885.

Vaidyanathan, S., Azar, A. T., Akgul, A., Lien, C. H., Kacar, S., and Cavusoglu, U. (2019). A memristor-based system with hidden hyperchaotic attractors, its circuit design, synchronisation via integral sliding mode control and an application to voice encryption. *Int. J. Automation Control (IJAAC)* 13 (6), 644–667. doi:10.1504/ijaac.2019.102665

Vinnikov, D., Chub, A., Kosenko, R., Sidorov, V., and Lindvest, A. (2021). Implementation of global maximum power point tracking in photovoltaic microconverters: a survey of challenges and opportunities. *IEEE J. Emerg. Sel. Top. Power Electron.* 11 (2), 2259–2280. doi:10.1109/jestpe.2021.3137521

frontiers | Frontiers in Energy Research

TYPE Original Research
PUBLISHED 10 April 2024
DOI 10.3389/fenrg.2024.1375820

OPEN ACCESS

EDITED BY
Sudhakar Babu Thanikanti,
Chaitanya Bharathi Institute of Technology, India

REVIEWED BY
Sisir Kumar Yadav,
Birla Institute of Technology and Science, India
Murali Krishna Tangirala,
Chaitanya Bharathi Institute of Technology, India

*CORRESPONDENCE
Hexu Yang,
yanghexu0608@126.com

RECEIVED 24 January 2024
ACCEPTED 20 March 2024
PUBLISHED 10 April 2024

CITATION
Luo J, Yang H, Zhang L, Liu H, Wang Y and Hao C (2024), A comparative study on the combination of life cycle assessment and ecological footprints: solar photovoltaic power generation vs. coal power generation in Ningxia.
Front. Energy Res. 12:1375820.
doi: 10.3389/fenrg.2024.1375820

A comparative study on the combination of life cycle assessment and ecological footprints: solar photovoltaic power generation vs. coal power generation in Ningxia

Jinni Luo[1], Hexu Yang[1]*, Liangxia Zhang[1], He Liu[2], Yidan Wang[1] and Chen Hao[1]

[1]Ningxia Institute of Science and Technology, Shizuishan, China, [2]Ningxia Belite Chemical Cyanamide Development Co., Ltd, Shizuishan, China

In China, where energy activities, predominantly driven by fossil fuel combustion, account for nearly 90% of the country's greenhouse gas (GHG) emissions and coal power alone contributes over 40%, the shift towards carbon neutrality is a critical national ambition. This study conducts a comprehensive comparison of the environmental impacts of solar photovoltaic power generation (SPPG) and coal power, employing both life cycle assessment and ecological footprint analysis. We meticulously analyze the complete lifecycle of SPPG, pinpointing key stages of GHG emissions, and offer nuanced, localized policy recommendations. Our findings indicate that a 1 kWp SPPG module emits 1,601.18 kg of GHGs over its lifespan, equating to 1.35 kg/kW·h per unit of electricity produced—substantially lower than the 4.81 kg/kW·h emitted by coal power, thus highlighting the latter's heightened environmental detriment. Additionally, this study assesses the ecological footprint of both energy sources in Ningxia. SPPG emerges with an ecological surplus, showcasing a *per capita* footprint of 0.0342 hm^2, compatible with Ningxia's ecological capacity. In stark contrast, coal power exhibits a sustained ecological deficit over the past 5 years, with a growing *per capita* footprint of 0.6529 hm^2, underscoring its unsustainability. This research provides a detailed comparative analysis of the environmental impacts of SPPG and coal power in Ningxia, offering valuable insights for energy policymakers and industry stakeholders. It underscores the urgent need for industrial restructuring towards more sustainable and renewable energy sources, aligning with China's broader objectives of environmental preservation and achieving carbon neutrality.

KEYWORDS

solar photovoltaic power generation, greenhouse gas emissions, ecological footprint, life cycle assessment, carbon mitigation

1 Introduction

The global climate crisis, fuelled by rising greenhouse gas (GHG) emissions, poses an existential threat to our planet. Energy production, a vital cog in the wheel of economic progress, is also one of the primary contributors to this environmental challenge (Zhang and Gao, 2023). Historically, the reliance on fossil fuels for energy has been the principal driver of GHG emissions, contributing significantly to global warming and climate change (Liu et al., 2023). China's energy sector, dominated by coal, has been the backbone of its economic powerhouse status (Gao et al., 2021). Coal power, a significant contributor to China's energy mix, has also been a major source of its GHG emissions, accounting for over 40% of the total emissions (Zhang et al., 2020). This heavy reliance on coal has led to substantial environmental and health concerns, including air pollution and a considerable carbon footprint (Yousri et al., 2021). However, in recent years, there has been a paradigm shift. In September 2020, China announced 'double carbon' target-a pledge to reach a carbon peak before 2030 and achieve carbon neutrality by 2060, commonly referred to as the. This ambitious commitment is a clear signal of China's intention to transition towards a more sustainable energy future and holds substantial implications for global climate change mitigation efforts.

The transition from fossil fuels to renewable energy sources has become a cornerstone of China's strategy to meet its 'double carbon' goals. The urgency of this transition cannot be overstated, given the escalating climate crisis and China's significant role in global GHG emissions. Among various renewable energy options, solar photovoltaic power generation (SPPG) stands out as a particularly promising alternative (Wang et al., 2019). The evaluation of ecological impacts from various energy production methods involves renewable energy approaches, life cycle assessment (LCA), and the ecological footprint methodology. LCA is established as a mature framework that allows for a comprehensive assessment of environmental impacts associated with energy consumption and emissions across the entire lifecycle of renewable energy sources (Ahmed et al., 2020). On the other hand, the ecological footprint has become a widely utilized metric for addressing direct and indirect environmental impacts in studies on environmental sustainability, quantifying the influence of human activities on the ecosystem (Alola et al., 2019).

Previous studies have predominantly focused on either the economic feasibility or technological aspects of renewable energy. For example, studies have explored the environmental repercussions of China's burgeoning solar energy sector, propelled by policy subsidies (Hong et al., 2016; Huang et al., 2017; Yu et al., 2017). The LCA method has been instrumental in evaluating the environmental trade-offs of China's solar photovoltaic industry (Xu et al., 2018). Regarding biomass energy, the last decade has indicated its potential as an interim substitute for fossil fuels (Udomsirichakorn and Salam, 2014), with a growing body of research employing LCA to examine the environmental effects of various biomass fuels, their logistics, and biopower technologies between 2009 and 2020 (Magelli et al., 2009; Song et al., 2017; Hossain and Poon, 2018; Liu et al., 2019). However, less emphasis on the combination evaluation of comparative environmental impacts including both LCA and ecological footprints. This study aims to fill this gap by providing a detailed comparative analysis of the life cycle assessment and ecological footprints of SPPG and coal power generation. The significance of this research lies in its potential to inform policymakers and stakeholders about the environmental implications of energy choices. By evaluating both the GHG emissions and ecological footprints of SPPG and coal power, this study offers a holistic view of their environmental impacts, thereby contributing valuable insights to the discourse on sustainable energy transition in China.

With its abundant light and long sunshine hours, Ningxia province, located in the northwest of China, presents an ideal setting for the development and utilization of SPPG. The region's natural endowments, combined with advancements in solar technology, position it as a key player in China's renewable energy landscape. The development of SPPG in Ningxia not only aligns with the national energy policy but also offers a model for sustainable energy development that can be replicated in other regions.

The objective of this study is to conduct a comparative analysis of the environmental impacts of SPPG and coal power generation systems in Ningxia, focusing on their life cycle assessments and ecological footprints. Then, a comprehensive analysis will be conducted to combine all evaluation indictors. This comparison aims to shed light on the respective environmental burdens of these two energy sources and provide a basis for informed decision-making in China's energy policy. Finally, the paper will conclude with a summary of the key findings and their significance, along with suggestions for future research in this area.

2 Methodology

2.1 System boundary and database

This research uses Ningxia city as a case study. The Ningxia region is very rich in solar energy resources, with an annual average of solar radiation between 4,950 MJ/m^2 and 6,100 MJ/m^2, and the interannual changes in the distribution of solar radiation in the region are relatively stable. And Ningxia is one of the country's three major silica bases, with the world's largest silica and quartz ore resources, its high-quality silicon ore resources reserve of up to 4.28 billion tonnes, and its silicon processing industry chain is more complete, with the production of polysilicon is the most notable. Therefore, the photovoltaic industry chain has been more perfect in Ningxia, which is also one of the factors that photovoltaic can be vigorously developed in this region.

This study focuses on the grid-connected solar photovoltaic (PV) systems in Ningxia, China, emphasizing multicrystalline silicon solar panels due to their established industry presence in the region. There are three main parts of the PV industry chain. Upstream includes the manufacture and acquisition of silicon raw materials, the preparation of polysilicon materials, the ingot casting of polysilicon materials, and the preparation of polysilicon wafers; midstream includes the production of cells, the production of battery modules, and the production of balance-of-systems components; and downstream involves the assembly of its parts to form a complete photovoltaic power generation system. The research delineates the system boundary for lifecycle assessment and ecological footprints, as shown in Figure 1. Based on the life cycle assessment and the life cycle technology framework and characteristics, the following statements are made in response to

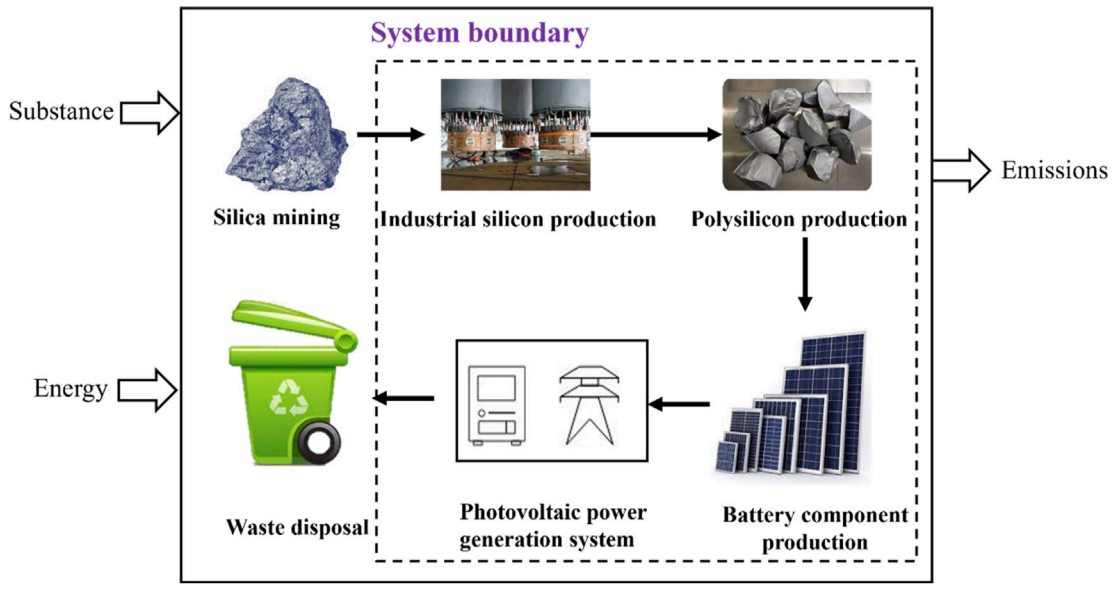

FIGURE 1
System boundary for lifecycle assessment and ecological footprints.

the system boundary diagram drawn above: 1) Production equipment, plant construction, workforce, and transport vehicles not considered; 2) Challenges in estimating transmission distances and energy consumption within Ningxia lead to exclusion of this aspect; 3) Complex components like DC converter boxes excluded due to limited literature and minor impact on overall carbon emissions; 4) Emission-free and pollution-free nature of solar PV systems during operation leads to their exclusion from the lifecycle analysis.

The data sources and statistics of this paper are mainly in the following ways: official websites of domestic PV enterprises, relevant articles and industry reports, and inventory data of similar processes or products. Lifecycle GHG emissions for PV systems are derived by multiplying electrical consumption by the updated emission factor, 0.5810 t CO_2/MWh, as specified by China's climate change authorities for 2021 and 2022 emissions reporting (China Energy Statistical Yearbook, 2021; Ningxia Statistical Yearbook, 2022). Due to data acquisition difficulties, this paper uses literature averages for non-electrical emissions. For simplicity, emissions are expressed as kg CO_2/kWh, and related silicon flow data are compiled in Table 1.

PV power generation, a renewable resource, requires land occupation, varying by layout-distributed PV on rooftops and spare spaces in urban areas, and centralized PV in regions with longer sunlight exposure, as per regional planning. Although both types occupy land, the dispersed nature and complex land use of distributed PV make data collection challenging. Therefore, this study focuses on resource consumption during the manufacturing of PV components in Ningxia, including silica mining, industrial silicon production, and polycrystalline silicon production. After data processing and calculation, the total resource consumption, standard coal consumption and its corresponding carbon emission of the photovoltaic industry chain in Ningxia is shown in Table 2.

For comparison, the emission and ecological footprints of coal power generation system is calculated to evaluate the performance of SPPG system. For the life-cycled assessment, a clean coal-fired project with 2 × 1000 MW ultra-supercritical power plant is used for the case study (Yu et al., 2017). For ecological footprints study, the coal resource consumption in the power generation process of coal-fired power generation in Ningxia is used for analysis and calculation. These data could be checked in the reference and official reports, which will not be presented here.

2.2 Life cycle assessment

The entire photovoltaic power generation system production chain is divided into four stages: raw material production stage, solar photovoltaic module system production stage, transportation stage and waste recycling and disposal stage (Guinee et al., 2011). Based on these four stages, this GHG emission of the system is calculated as follows:

$$Ct = M + P + T + W \tag{1}$$

where C_t is the total carbon emissions of the entire life cycle of the photovoltaic power generation system, kg; M is the total carbon emissions of the raw material production stage, kg; P is the total carbon emissions of the solar photovoltaic module system production stage, kg; T is the total carbon emissions in the transportation stage, kg; W is the total carbon emissions in the waste recycling disposal stage, kg.

The quantification of the GHG emissions from four stages, is conducted by a process-based life cycle assessment method, as presented in Eq. 2:

$$E^P = AD \times EF_{electricity} \tag{2}$$

where E^P is the total GHG emissions; AD refers to the activity amount, such as the consumption amount of silicon (t); $EF_{electricity}$ is the emission factor of different processes.

TABLE 1 Total input and output of multicrystalline silicon SPPG system.

	Input		Output	
	Type	Amount	Type	Amount
Industrial silicon	Silica	26.23 kg	Industrial silicon	9.72 kg
	Charcoal	4.07 kg	CO_2	38.59 kg
	Petroleum coke	6.22 kg	SO_2	6.32 kg
	Graphite electrode	0.97 kg	SiO_2	4.37 kg
	Wood chips sawdust	3.89 kg	NOx	1.91 kg
	Bituminous coal	6.80 kg	CO_2 by electricity consumption	70.36 kg
	Recycled water	1,360.8 kg		
	Electricity	121.11 kW h		
Multicrystalline silicon	Industrial silicon	9.72 kg	Multicrystalline silicon	7.31 kg
	H_2	0.65 kg	HCl	0.83 kg
	Cl_2	10.30 kg	SS	37.85 kg
	NaOH	403.66 kg	COD	33.68 kg
	Cooling water	2012.07 kg	SiO_2	2.08 kg
	Electricity	867.59 kW · h	Chlorides	12.39 kg
			Fluorides	0.29 kg
			CO_2 by electricity consumption	504.07 kg
Silicon wafer	Multicrystalline silicon	7.31 kg	Silicon wafer	240 pieces
	Silicon carbide	17.17 kg	Chlorides	0.09 kg
	Argon	2.41 kg	Fluorides	0.20 kg
	Polyethylene	15.08 kg	COD	2.57 kg
	HF	102.00 g	Solid waste	192.00 kg
	HCl	51.60 g	Waste cutting fluid	3.70 kg
	NaOH	56.88 g	CO_2 by electricity consumption	228.26 kg
	Electricity	392.88 kW · h		
Solar cell	Multicrystalline silicon	240 pieces	Solar cell	1 kWh
	Silver paste	127.2 g	Cl_2	81.23 g
	Aluminum paste	307.2 g	NOx	0.03 g
	SiH_4	166.8 g	VOC	1.17 kg
	NH_3	423.6 g	COD	126.89 g
	HCl	176.4 g	HCl	4.35 g
	NaOH	200.34 g	Chlorides	15.89 g
	HNO_3	1.20 kg	Fluoride gases	20 g
	$POCl_3$	4.8 g	Solid waste	283 g
	HF	946.8 g	CO_2 by electricity consumption	71.81 kg
	N_2	16.06 kg		
	O_2	72.00 g		
	Electricity	123.6 kW · h		

(Continued on following page)

TABLE 1 (*Continued*) Total input and output of multicrystalline silicon SPPG system.

	Input		Output	
	Type	Amount	Type	Amount
Solar panel module	Solar cell	1.12 kwp	Solar panel module	1 kWp
	Copper	0.49 kg	VOC	3.24 g
	EVA film	7.06 kg	Welding fumes	1.04 g
	TPT back sheet	3.64 kg	Solid waste	132 g
	Tempered Glass	62.22 kg	CO_2 by electricity consumption	34 kg
	Aluminum frame	13.12 kg		
	Silicone sealant	40 kg		
	Electricity	58.5 kW · h		

COD: chemical oxygen demand; SS: silicon sheet; VOC; volatile organic compounds; EVA: Ethylene-vinyl acetate; TPT: Tedlar-polyester-tedlar.

TABLE 2 Total coal consumption, standard coal consumption and its corresponding carbon emission of the photovoltaic industry chain in Ningxia.

Year	Total resource consumption (Mt)	Standard coal consumption (Mt)	Corresponding carbon emission (Mt)
2018	2.85	2.04	1.54
2019	2.88	2.06	1.56
2020	3.00	2.14	1.62
2021	3.15	2.25	1.70
2022	2.991	2.08	1.57

TABLE 3 Detailed classifications of the SPPV power generation inventory and coal power generation inventory.

Types	SSPPG	Coal power generation
LF	Silica, wood, water, electricity, silver, aluminum, steel	Wood, steel, cement, water
Fossil energy consumption	Coal, fuel	Coal, oil, natural gas, fuel
global warming	CO_2, N_2O	CO_2, N_2O, CH_4, CO
Photochemical ozone synthesis	VOC、COD	CO、CH_4、NMHC
acidification	SO_2, NO_x, HCl	SO_2, NO_x
Eutrophication	COD、SS	COD、BOD、SS、N、P
smoke	—	TSP

Environmental impact assessment quantitatively evaluates impacts using inventory analysis data on resources, energy, and emissions. This process, governed by the International Society of Environmental Toxicology and Chemistry (ISETC), involves classification, characterization, and valuation. Key impact areas are resource utilization, human health, and ecosystem integrity, encompassing subcategories like mineral and fuel depletion, global warming potential, acidification, photochemical ozone formation, eutrophication, particulate matter, and solid waste management. The analysis should consider emissions that cause multiple types of impacts; if these impacts are independent, they should be included. Based on this model, the study categorizes the lifecycle inventories of SPPV and coal power generation. Key environmental impact categories for solar PV include resource consumption, fossil fuel usage, global warming potential, photochemical ozone creation, acidification, and eutrophication. Detailed classifications of the SPPV power generation inventory and coal power generation inventory are presented in Table 3.

The contribution of pollutant k to a specific environmental impact type t, denoted as ep_k^t, is calculated through the equation:

$$EP^t = \sum Q_k ep_k^t \tag{3}$$

where ep_k^t is the contributing factor of pollutant; k to the type of environmental impact; t is kg/kg (1, 2, 3 . . .).

2.3 Ecological footprints

The ecological footprint serves as a sustainability metric based on terrestrial area (Wackernagel et al., 1999). Defined as the ecological land area needed to absorb the natural resources consumed and waste emitted by a specific population or region, it primarily includes arable land, forest land, land for fossil energy, buildable land, and water bodies. This method is the carbon footprint of energy consumption, which refers to the ratio of carbon emissions to the forest area conversion coefficient, as shown in Eq. 4:

$$C_F = C/S = \sum C_i/S \tag{4}$$

Where C_F represents the carbon footprint of energy consumption (in ten thousand hectares); C denotes the total carbon emissions from energy consumption (in ten thousand tons); and S is the conversion coefficient between carbon emissions and forest area (in tons per hectare), which is set to 6.49 t/hm^2.

The calculation formula of carbon emissions is:

$$C = \sum C_i = \sum P_i/Q_i \tag{5}$$

Where P_i is the consumption of fossil energy; Q_i is the carbon emission coefficient of fossil energy.

Ecological footprint calculations are predicated on the fundamental fact that humans can determine most resources consumed and the quantity of waste produced; these resource flows and waste can be converted into corresponding bioproductive areas (Wackernagel, 1996). Therefore, the ecological footprint of an individual or a nation represents the productive area, including land and water bodies, that supplies all resources consumed and assimilates all waste generated by the populace. Due to the significant variation in bioproductive capacity across unit areas of cropland, fossil fuel land, pasture, and forest, it is necessary to convert different land types into a uniform standard for comparison. This is done by applying equivalence factors to the various bioproductive areas, to yield comparable bioproductive areas. The formula for calculating the ecological footprint is as follows:

$$EF = N \times \sum A_i \times r_j^i = N \times \sum \frac{C_i r_j^i}{p_i} \tag{6}$$

where EF represents the ecological footprint in hm^2; A_i is the *per capita* ecological footprint of the ith type of bioproduct; r_j^i is the equivalence factor for the ith type of land corresponding to the ith type of bioproduct; N is the population of the study area; C_i is the *per capita* annual consumption of the ith bioproduct in joules or kilograms; p_i is the average productivity of the ith bioproduct at the national level in joules per hm^2 or kilograms per hm^2.

The natural conditions and resource endowments of countries and regions vary greatly, as do the production capabilities per unit area of different types of land and the production areas per unit area of the same type of bioproducts. When calculating ecological carrying capacity, it is necessary to adjust the actual area of similar bioproductive lands in different countries and regions to enable comparisons. The formula for ecological carrying capacity is as follows:

$$EC = N \times \sum \left(a_j \times r_j \times y_j\right) \tag{7}$$

where EC represents ecological carrying capacity in hm^2; a_j is the *per capita* actual area of the jth type of land; r_j is the equivalence factor for the jth type of land; y_j is the yield factor for the jth type of land.

The emergence of an ecological deficit is primarily to assess whether a country or region can sustain development through the analysis of ecological footprints and carrying capacity. An ecological deficit occurs when a region's ecological footprint exceeds its carrying capacity, signifying unsustainable practices. Conversely, an ecological surplus within a region indicates sustainable development of the regional ecosystem. The formulas for calculating the ecological deficit or surplus are:

$$ED = EF - EC\,(EC < EF) \tag{8}$$

$$ES = EC - EF\,(EC > EF) \tag{9}$$

where ED represents the ecological deficit; ES represents the ecological surplus; EC is the ecological carrying capacity; EF is the ecological footprint.

3 Results and discussion

3.1 Life cycle assessment

3.1.1 Environmental impacts of solar photovoltaic power generation systems

To synthesize the pollutant emission figures and inventory analysis findings from previous sections on SPPG and coal power generation systems, a qualitative and quantitative analysis is conducted. This process involves transforming direct emission data of various environmental impact factors into potential environmental impact values. Such data characterization allows for a detailed comparative analysis of the two energy sources. The following is a characterization of the inventory data for both solar PV and coal power generation, with the processed results presented in Table 4.

The following clarifications are provided to supplement the data presented:

1 The emission data for the SPPG system represent the results obtained by converting the inventory analysis data from earlier sections to emissions per kilowatt-hour (kWh).
2 Due to the scarcity of literature on resource depletion coefficients and the dated nature of some parameters, their relevance is considered low. Since these coefficients are not central to the core research of this paper, they will not be analysed in detail.
3 The equivalence factors used for calculating the environmental impacts are sourced from reference (Author Anonymous, 2014).

Figure 2 compares the life cycle carbon emissions of different stages in SPPG system. The industrial silicon stage has a total emission value of 838.14 kg $CO_{2\text{-eq}}$, with the highest contribution coming from the base category at 504.07 kg $CO_{2\text{-eq}}$, followed by an additional 228.26 kg $CO_{2\text{-eq}}$, 71.81 kg $CO_{2\text{-eq}}$, and the topmost

TABLE 4 Potential values of various environmental impacts of solar photovoltaic power generation systems.

Type	Environmental interference factors	Characteristic factors	Emissions (kg)
GWP	CO_2	CO_2	1.35E+00
POCP	VOC	C_2H_4	9.86E-04
	SO_2	SO_2	5.31E-03
AP	NO^x		1.61E-03
	HCl		7.01E-04
EP	COD		3.06E-02
	SS		3.18E-02

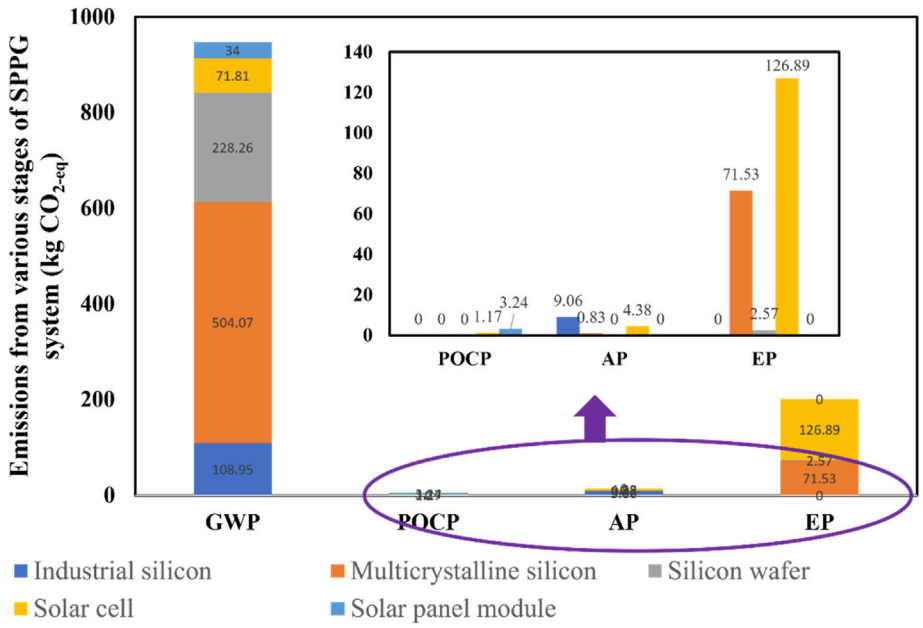

FIGURE 2
Life cycle carbon emissions of SPPG system.

section at 34 kg $CO_{2\text{-eq}}$. The base category is possibly representing the direct emissions from industrial processes, while the stacked segments could represent indirect emissions such as energy consumption, transportation, or other industrial activities. The multicrystalline silicon stage shows significantly lower total emissions, with a negligible contribution from the solar cell component (0.17 kg $CO_{2\text{-eq}}$) and another minor contribution from the base category (3.24 kg $CO_{2\text{-eq}}$). Moving to the silicon wafer stage, the total emissions are minimal, with no contribution from the solar cell component and a small emission value of 0.83 kg $CO_{2\text{-eq}}$ from the base category. The solar panel module stage has a total emission value of 198.42 kg $CO_{2\text{-eq}}$, with the majority coming from the solar cell component at 126.89 kg $CO_{2\text{-eq}}$, followed by the base category at 71.53 kg $CO_{2\text{-eq}}$, and a minimal addition of 2.57 kg $CO_{2\text{-eq}}$ on top.

In conclusion, the industrial silicon stage stands out as the most emission-intensive phase in the solar photovoltaic power generation system, significantly leading in environmental impact in terms of emissions. This highlights that the extraction and processing of silicon, crucial for solar panel production, are major sources of greenhouse gas emissions. In contrast, the multicrystalline silicon and silicon wafer stages have a considerably lower emission contribution, suggesting that these processes are more energy-efficient or inherently less intensive in terms of environmental impact. Moreover, the solar panel module stage, while contributing less to emissions than the industrial silicon stage, still accounts for a noteworthy portion of the total emissions, likely attributed to the final assembly and manufacturing processes of the solar panels. Therefore, to diminish the environmental footprint of solar photovoltaic power generation systems, it is imperative to concentrate efforts on reducing emissions particularly at the industrial silicon stage. This could be achieved through advancements in industrial methodologies or by enhancing energy efficiency within these processes.

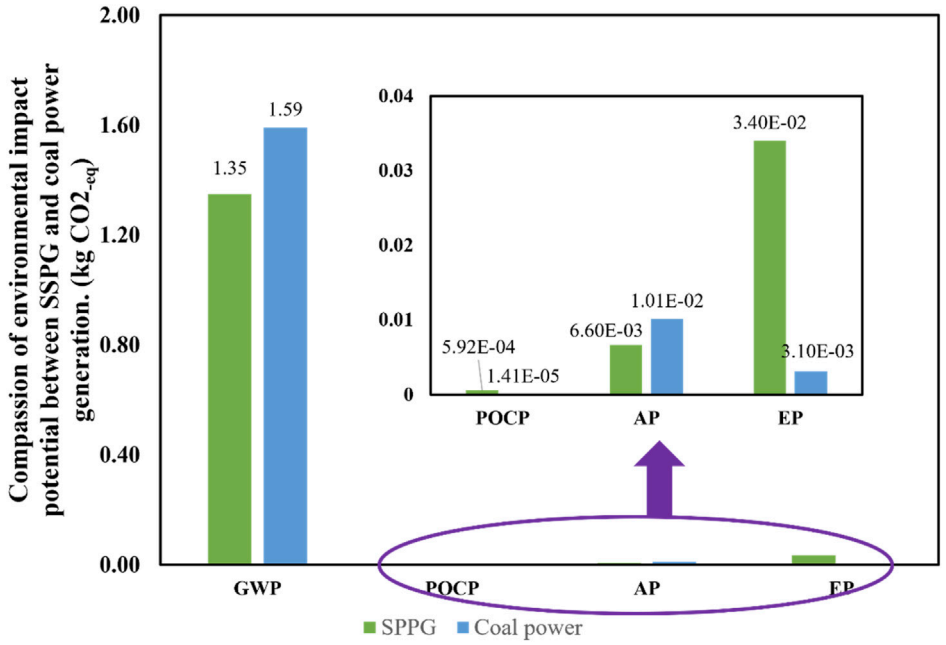

FIGURE 3
Compassion of environmental impact potential between SSPG and coal power generation.

3.1.2 Compassion of coal power system

Figure 3 presents data reveals comparative insights into the environmental impact potential, specifically GWP, POCP, AP, and EP of SPPG and coal power systems. For global warming potential, coal power systems exhibit a slightly higher potential value (1.58E+00) compared to solar PV systems (1.35E+00). This indicates that coal power systems have a greater propensity to exacerbate the greenhouse effect than solar PV systems, aligning with the conventional understanding of coal's impact due to its carbon-intensive nature. When examining the photochemical ozone creation potential, the value for solar PV systems (9.86E-04) is approximately an order of magnitude higher than that of coal power (5.34E-04). The near-negligible potential of coal power in this category suggests that solar PV systems, despite their renewable status, may have a larger contribution to this environmental impact. This could be attributed to the life cycle emissions of volatile organic compounds during the manufacturing processes of solar panels. Regarding acidification potential, solar PV systems present a value (5.31E-03) that is just over half of what is reported for coal power systems (7.66E-03). This indicates that coal power has a more substantial acidifying effect on the environment, which is consistent with the emissions profile of coal combustion, known for releasing sulfur dioxide and nitrogen oxides that contribute to acid rain.

While solar PV systems show a lower potential for global warming and acidification compared to coal power systems, they exhibit a higher potential for photochemical ozone creation. These findings highlight the importance of considering multiple dimensions of environmental impact when assessing the sustainability of energy systems. They also underscore the need for continued innovation and improvement in the production and deployment of solar PV technology to further minimize its environmental footprint.

To facilitate a comparative analysis of greenhouse gas emissions between SPPG and coal power, emissions per unit of electricity generated are standardized, and the contributions of each stage to greenhouse gas emissions for both SPPG and coal power are briefly described and contrasted. The standardization process begins with SPPG emissions. As previously mentioned, all inventory data related to solar PV generation is collected and calculated based on a peak power output of one kWp, which is the amount of electricity generated per hour by a one kWp solar PV system under optimal lighting conditions. The paper calculates the CO2 emissions per kilowatt-hour of electricity generated in the first year of the system's life.

The annual electricity generation is calculated as follows:

$$Ep = H_A \times K \times P_{AZ}$$
$$= 1534.72\text{kW} \cdot \text{h}/m^2 \times 0.775 \times 1 = 1189.41\text{kW} \cdot \text{h}$$

where E_p represents the electricity generated, H_A is the total annual solar radiation on a horizontal plane, and P_{AZ} is the installed capacity of the system.

The total annual solar radiation for Ningxia is taken as the average annual radiation of 4,950–6,100 MJ/m^2," which is 5525 MJ/m or 1,534.72 kWh/m^2.

Next, emissions per kilowatt-hour of electricity generated are used as the comparative unit to account for the emissions per unit of electricity for both energy sources. It was found that solar PV power generation emits 1.35 kg of greenhouse gases per kWh of electricity generated, whereas coal power emits 4.81 kg of greenhouse gases per kWh.

This standardization and comparison demonstrate that per unit of electricity generated, coal power has a significantly higher greenhouse gas emission rate than SPPG, which underlines the greater environmental efficiency of SPPG over coal power in terms of GHG emissions.

3.1.3 Suggestions

Ningxia region, endowed with abundant solar energy resources and minimal overcast days, is exceptionally well-suited for the development of SPPG projects. The region, particularly Shizuishan, is also rich in silicon resources, further enhancing its suitability for PV development. Research indicates that the carbon emission recovery period for the PV industry is significantly shorter than the lifespan of PV power generation, highlighting its substantial advantages in energy conservation and emission reduction. The environmental benefits of PV power are especially notable, warranting robust government support for the sector's growth. Governmental agencies should plan long-term development strategies and policies for the PV industry, standardizing and regulating the sector while encouraging the advancement of PV technologies. Continuous government support, including national subsidies, will promote the development of home-based distributed PV and grid-connected PV stations. Encouraging residents to sell surplus electricity to grid companies can lead to mutual benefits.

In the multicrystalline silicon production phase, which emits the most greenhouse gases, strict standards and regulations are necessary. This includes stringent entry criteria for the multicrystalline silicon industry and the elimination of substandard PV component manufacturers, alongside encouraging the development of new technologies. Research departments should actively develop new techniques to achieve low-cost, low-energy production goals. PV enterprises should carefully plan and manage their costs and carbon emissions to reduce financial burdens. Exploring new technologies for the disposal and recycling of PV waste can save resources and reduce land pollution.

Regarding coal power, a traditional energy source, its stability and technological maturity mean it cannot yet be fully replaced, despite its significant contribution to the greenhouse effect. Coal power enterprises should optimize their coal-fired power generation processes or improve flue gas treatment technologies. As a major source of CO_2 emissions in China, exploring energy-saving and emission-reducing directions, particularly Carbon Capture and Storage (CCS) technology, is critical for the future of fossil fuels (Ladenburg et al., 2024). Besides the above, addressing environmental pollution is crucial. While not the focus of this paper, it is important to mention. The environmental impact of coal power, previously categorized in this paper as resource consumption, fossil fuel usage, global warming, acidification, smog, and eutrophication, requires enhanced management and control, especially in controlling greenhouse gas emissions.

3.2 Ecological footprints

3.2.1 Ecological carrying capacity nalysis

In Figure 4, we can observe specific values that inform the ecological carrying capacity in Ningxia. The *per capita* footprint of coal power generation shows a substantial increase from 0.033458 hm^2 in 2018 to 0.033598 hm^2 in 2022, indicating a consistent pressure on the ecological system. On the other hand, the *per capita* footprint of SPPG remains considerably lower, with values ranging from 0.1069 hm^2 in 2018 to 0.1324 hm^2 in 2022, well below the ecological surplus threshold. The *per capita* forest land area in Ningxia, serving as a measure of ecological carrying capacity, is at 0.112 hm^2. This is crucial as it is used to compare the ecological footprints of both coal power generation and SPPG. The data reveals that the *per capita* footprint for coal power far exceeds this value, whereas PV power's footprint is below, suggesting that SPPG remains within the region's ecological carrying capacity.

While Ningxia's *per capita* forest land area is lower than the national average, indicating a relative scarcity of forest coverage, the region's SPPG has not yet caused an ecological deficit, thanks to its clean energy production and the late start in its development. Despite Ningxia's rich solar resources, the growth of the PV industry must be sustainable to ensure that the ecological footprint does not surpass the ecological carrying capacity in the future, thus avoiding undue environmental stress.

3.2.2 Ecological deficit

Figure 5 demonstrates the *per capita* ecological deficit caused by coal power generation in the Ningxia region from 2018 to 2022. The chart indicates a rising trend in the ecological deficit *per capita* for coal power generation in Ningxia, with specific values for the deficit increasing from 0.5126 hm^2 in 2018 to 0.7353 hm^2 in 2022. This trend reflects the region's increasing installation of thermal power units and rapid socio-economic and industrial development, outpacing the relatively slow growth in ecological supply. This misalignment has led to a widening ecological deficit, with the deficit for the most recent year being a direct consequence of energy conservation and emission reduction measures not keeping pace with adjustments in the overall industrial structure of Ningxia's power sector.

To address this, Ningxia must continue to optimize the installed structure of its power industry, reduce carbon emissions from thermal power units, and reinforce the gains made from converting farmland back to forest. The government should also increase investment in new energy projects like wind and solar photovoltaic power, promoting clean energy to replace traditional fossil fuels, thereby reducing coal consumption and air pollution. Additionally, by adjusting the industrial structure and improving enterprise profitability, Ningxia can foster a shift in its economic development model, effectively alleviating the regional ecological deficit caused by coal power generation.

3.2.3 Suggestions

The development of solar PV power enterprises in the Ningxia region offers significant potential, given its abundant sunlight and rare overcast days, making it an ideal locale for solar power projects. However, several critical factors must be considered for the successful implementation and operation of solar power stations. These include maintenance post-construction, efficiency in power generation, grid integration, the lifespan of solar power plants, and their abandonment rates. Addressing these concerns is essential for businesses in the industry.

At present, the carbon emissions from the production and manufacturing phases of the solar PV industry in Ningxia still

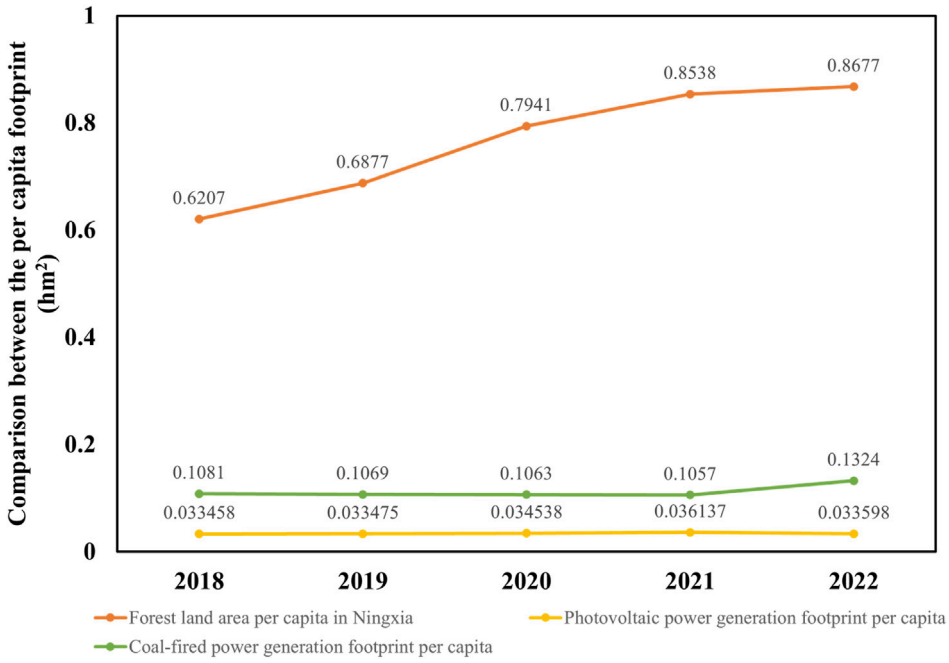

FIGURE 4
Comparison between the *per capita* footprint of photovoltaic power generation and coal-fired power generation in Ningxia and the *per capita* forest land area in Ningxia (Unit: hm^2).

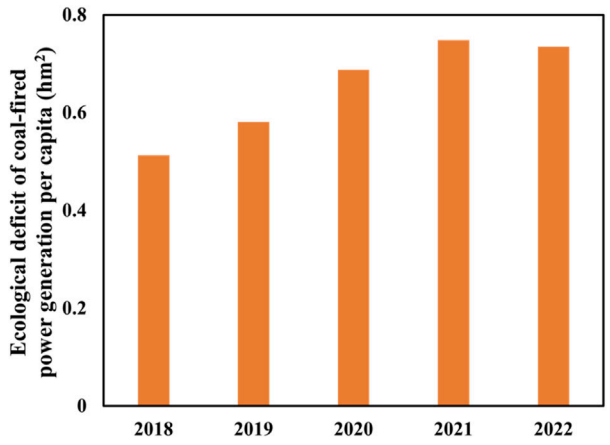

FIGURE 5
Ecological deficit of coal-fired power generation *per capita* in Ningxia from 2018 to 2022.

result in ecological surpluses. The region's rich silicon resources provide a distinct advantage in producing multicrystalline and monocrystalline silicon. However, it is crucial for manufacturers to minimize energy consumption across all processes, encourage the development of new technologies and processes, and phase out substandard PV component producers. Specifically, while Ningxia has made strides in PV equipment manufacturing, there is a need for more effort in developing high-precision and advanced products.

Solar PV companies should also plan meticulously regarding their production costs and carbon emissions. While the current carbon emissions from the solar PV industry in Ningxia indicate an ecological surplus, it is vital not to blindly increase production capacity without considering the region's ecological carrying capacity. PV enterprises should actively seek new technologies for the disposal of solar PV waste, aiming to recycle and reuse various waste materials to conserve resources and reduce land pollution.

Besides SPPG, there are also some suggestions for coal-fired power generation companies. In Ningxia, a region abundant in coal resources, there's an ecological deficit challenge due to the high carbon emissions from thermal power generation, which surpasses the area's ecological carrying capacity. Despite this, thermal power continues to be a significant electricity source. Coal power enterprises in Ningxia should, therefore, prioritize optimizing their thermal units, focusing on shutting down smaller, more polluting ones to address this issue. As a significant contributor to CO_2 emissions, the coal power sector is exploring energy conservation and emission reduction strategies. Among these, CCS technology has emerged as a promising approach to curb emissions in thermal power generation. Ningxia's coal power enterprises are urged to innovate in these technologies and implement them promptly in their operations. Furthermore, with Ningxia's reliance on coal for most of its thermal power, there is an opportunity to delve into clean coal technologies. Transforming and upgrading the coal power industry, coupled with increased investment in integrated coal power projects, is essential for the region's move towards sustainable development in energy.

3.3 Comprehensive analysis

Figure 6 presents a comprehensive comparison of environmental impacts between an SPPG system and a coal power generation system.

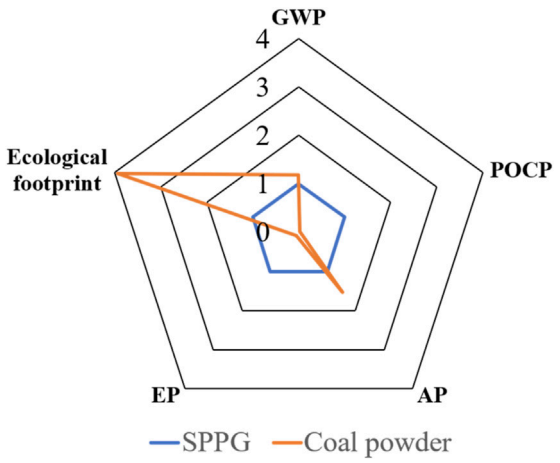

FIGURE 6
Comparison between SPPG system and coal power generation system.

Each axis on the spider chart would represent a different dimensionless parameter related to environmental impacts, such as carbon footprint, energy efficiency, or pollutant emissions. The indexes of SPPG system's performance on each environmental impact parameter is compared against the coal power generation, which is set as the baseline with an index value of 1. This normalization allows for an immediate visual grasp of how each system performs relative to the baseline coal power generation across multiple environmental criteria. The SPPG system, a renewable energy source, generally outperforms coal power in environmental impact, with a GWP that is 17.78% lower. However, in POCP, coal power is unexpectedly more efficient with 97.62% lower impact than SPPG. Coal power also shows a higher AP, at 53.03% above SPPG, while having a slightly better EP. Notably, ecological footprint of coal power generation system is almost 294% greater than SPPG, highlighting SPPG's lower ecological impact. Despite SPPG's advantages, the data reveals specific areas for potential improvement, especially considering the energy repayment ratio, emphasizing lifecycle sustainability.

By focusing on the energy repayment ratio instead of just the energy repayment time, the comparison considers the different lifespans of the power generation methods, which is crucial for an accurate assessment. This approach reflects an understanding that an energy source might take longer to 'repay' its energy investment but may still be more sustainable over a longer lifecycle. In conclusion, the figure demonstrates that the SPPG system is a more environmentally friendly option compared to coal power generation, with strengths in certain environmental impact parameters. However, there is still room for improvement and optimization to maximize its potential benefits over the lifecycle of the power generation system.

4 Implications and future perspectives

In recent years, with the rapid socio-economic development of urban areas, residents have elevated their demands for a better urban ecological environment. Over the past few decades, humanity has embarked on assessing the quality of the ecological environment, yet the measurement and quantification of natural resources remain challenging. Determining whether a region's development is sustainable necessitates objective assessments using scientific models. These models not only accurately depict the developmental status of a region but also provide feasible strategies for regional development and timely planning.

This study focuses primarily on the Ningxia region, located in northwest China, characterized by its small population base and predominantly semi-arid climate. Transitioning from the initial post-establishment power shortages, where urban and rural areas relied on oil lamps, to its current state of widespread electrification, Ningxia now ranks at the forefront of thermal and renewable energy installation capacity in the northwest. This study conducts an ecological footprint model analysis of carbon resource consumption and carbon emissions during the production and manufacturing phases of both photovoltaic power and coal power generation in Ningxia. The research aims to ascertain the ecological gains and losses of photovoltaic and coal power generation in the region and offer suggestions for energy conservation and emission reduction in Ningxia's power industry.

The paper meticulously delineates the system boundary, incorporating a variety of environmental impact potentials along with a full lifecycle evaluation. This approach is a step forward from the early lifecycle assessments of photovoltaic and coal power generation by researchers like Zhang and Zhu (Author Anonymous, 2014). Notably, this study expands on the carbon emissions from electricity consumption and the waste disposal stages of PV production, with an aspiration to make the lifecycle evaluation more comprehensive than previous literature. Compared to the analyses by He (Author Anonymous, 2017) and Sun (Author Anonymous, 2019), which were limited to inventory analyses of different lifecycle stages of photovoltaic and coal power, this paper delves into a more in-depth study and evaluation of environmental impacts.

However, the study faces challenges, particularly in data collection. Due to limitations in knowledge and data gathering, this paper focuses on multicrystalline silicon solar cells and ultra-supercritical thermal power plants. Other types, such as single-crystal silicon solar cells and subcritical power plants, have not been included, presenting an opportunity for future research. Additionally, the difficulty in collecting inventory data for Ningxia's photovoltaic and coal power meant that the study often had to rely on other literature and averages, which might have introduced biases in the results. Future research opportunities also include a more detailed study of the impacts of photovoltaic power, with a focus on assessing the potential environmental impacts and calculating the economic costs and carbon emission recovery periods.

Furthermore, the paper encounters a significant challenge in obtaining accurate data for calculating the ecological footprint and carrying capacity of Ningxia. Complications arise from the need to account for resources consumed in the production of photovoltaic power and coal during power generation. The lack of comprehensive statistics on resource consumption and pollution emissions for both SPPG and coal power generation leads to approximations, potentially reducing the accuracy of the findings. Additionally, variations in fossil resource and energy conversion coefficients and carbon emission factors, due to differences in regional and

production processes, further complicate the analysis. Consequently, future studies should aim to use various methods to collect more accurate data across different industries and products.

Despite the established concepts of ecological and carbon footprints, research focusing on the sustainable development of photovoltaic and coal power in Ningxia is still in its infancy. Addressing this gap, our study, which concentrates on the pollution issues of the power generation industry, contributes to the ongoing discourse on sustainability, particularly in the context of national initiatives for environmental conservation and emission reduction. Nonetheless, due to limitations in capability and time, the study inevitably has shortcomings, with several areas requiring further research and refinement. The future research will seek better methodologies to enhance the scientific rigor and validity of the analysis, fostering a more objective and comprehensive understanding of the environmental impacts of power generation in Ningxia.

5 Conclusion

In response to China's imperative shift from fossil fuels to cleaner energy solutions, this investigation provides an exhaustive evaluation of the environmental impacts associated with the SPPG system relative to traditional coal power generation, with a particular focus on LCA and ecological footprint metrics in the Ningxia region. The study delineates that, throughout its life cycle, the SPPG system is responsible for substantially lower GHG emissions, amounting to 1,601.18 kg $CO_{2\text{-eq}}$ per 1 kWp installation, which equates to 1.35 kg of CO_2 per kilowatt-hour of electricity generated—considerably less than the 4.81 kg/kW·h attributed to coal-powered systems. This disparity highlights the reduced environmental impact of solar power. Further analysis of the ecological footprint demonstrates that solar power generation in Ningxia maintains an ecological surplus, signifying its operation within the ecological carrying capacity of the region. This is in stark contrast to the ecological deficit perpetuated by coal power, which has been on an upward trajectory. Such a contrast accentuates the unsustainability of coal power and the environmental efficacy of the SPPG system. While the SPPG system emerges as the environmentally superior option, the study reveals potential areas for enhancement, particularly where coal power unexpectedly outperforms in categories such as POCP. These findings signal the critical need for ongoing technological refinement and innovation in SPPG to harness its full environmental potential. The insights garnered from this research are instrumental for energy sector decision-makers, advocating for a realignment of the industrial infrastructure towards sustainable and renewable energy sources to support China's overarching objectives of carbon neutrality. The conclusion drawn from this analysis stresses the vital integration of renewable energy adoption with socio-economic development and ecological conservation. Future strategies must underscore the necessity for cutting-edge technology, supportive policy frameworks, and comprehensive assessment mechanisms to foster and facilitate China's sustainable energy transition.

In this study, we utilized Life Cycle Assessment (LCA) and Ecological Footprint accounting methods to assess the environmental impacts of solar photovoltaic (PV) power generation. However, both methods come with inherent limitations. The LCA approach faces challenges in terms of data quality and availability, the diversity of technologies, regional differences, long-term temporal scales, and issues regarding recycling and disposal. These factors may affect the accuracy and reliability of our assessments. Conversely, Ecological Footprint accounting is limited in its methodological consistency, the comprehensiveness of environmental impacts, the scale of analysis, and the incorporation of socio-economic factors. This could lead to limitations in accurately reflecting the full environmental impacts of solar PV systems. Therefore, while these methods offer valuable insights into the environmental aspects of solar PV, these limitations must be considered when interpreting the results. Future research should aim to address these limitations to more accurately evaluate and understand the environmental benefits of solar PV technology.

Data availability statement

The original contributions presented in the study are included in the article/Supplementary Material, further inquiries can be directed to the corresponding author.

Author contributions

JL: Conceptualization, Data curation, Formal Analysis, Methodology, Writing–original draft, Writing–review and editing. HY: Conceptualization, Investigation, Resources, Supervision, Visualization, Writing–review and editing. LZ: Investigation, Project administration, Supervision, Writing–review and editing. HL: Investigation, Methodology, Writing–review and editing. YW: Data curation, Formal Analysis, Investigation, Writing–review and editing. CH: Data curation, Formal Analysis, Investigation, Writing–review and editing.

Funding

The author(s) declare that no financial support was received for the research, authorship, and/or publication of this article.

Acknowledgments

We extend our heartfelt gratitude to the Ningxia research community for their invaluable data contributions and to our peers for their insightful feedback. Special thanks are also due to the funding agencies and institutional support that facilitated the research, demonstrating the collaborative spirit vital for advancements in sustainable energy studies.

Conflict of interest

Author HL was employed by Ningxia Belite Chemical Cyanamide Development Co. Ltd.

The remaining authors declare that the research was conducted in the absence of any commercial or financial relationships that could be construed as a potential conflict of interest.

Publisher's note

All claims expressed in this article are solely those of the authors and do not necessarily represent those of their affiliated organizations, or those of the publisher, the editors and the reviewers. Any product that may be evaluated in this article, or claim that may be made by its manufacturer, is not guaranteed or endorsed by the publisher.

Supplementary material

The Supplementary Material for this article can be found online at: https://www.frontiersin.org/articles/10.3389/fenrg.2024.1375820/full#supplementary-material

References

Ahmed, Z., Zafar, M. W., Ali, S., and Danish, S. (2020). Linking urbanization, human capital, and the ecological footprint in G7 countries: an empirical analysis. *Sustain. Cities Soc.* 55, 102064. doi:10.1016/j.scs.2020.102064

Alola, A. A., Bekun, F. V., and Sarkodie, S. A. (2019). Dynamic impact of trade policy, economic growth, fertility rate, renewable and non-renewable energy consumption on ecological footprint in Europe. *Sci. Total Environ.* 685, 702–709. doi:10.1016/j.scitotenv.2019.05.139

Author Anonymous (2014). Comparative study on life cycle assessment of photovoltaic power generation and coal-fired power generation (in Chinese). *Environ. Sci. Manag.* 39 (10), 86–90.

Author Anonymous (2017). *Research on carbon emission of photovoltaic power generation based on life cycle evaluation (in Chinese).* Nanjing University of Aeronautics and Astronautics.

Author Anonymous (2019). *Comparative study of clean coal-fired power generation and photovoltaic power generation under the perspective of energy input return and economic value (in Chinese).* Beijing: China University of Petroleum.

China Energy Statistical Yearbook (2021). E. sector. Available at: https://www.zgtjnj.org/navibooklist-n3022013309-1.html.

Gao, C., Zhu, S., Na, H., and You, H. (2021). Comprehensive comparison of multiple renewable power generation methods: a combination analysis of life cycle assessment and ecological footprint. *Renew. Sustain. Energy Rev.* 147, 111255. doi:10.1016/j.rser.2021.111255

Guinee, J. B., Huppes, G., Zamagni, A., Masoni, P., Buonamici, R., et al. (2011). Life cycle assessment: past, present, and future. *Environ. Sci. Technol.* 45 (90-6), 90–96. doi:10.1021/es101316v

Hong, J., Chen, W., Qi, C., Ye, L., and Xu, C. (2016). Life cycle assessment of multicrystalline silicon photovoltaic cell production in China. *Sol. Energy* 133, 283–293. doi:10.1016/j.solener.2016.04.013

Hossain, M. U., and Poon, C. S. (2018). Comparative LCA of wood waste management strategies generated from building construction activities. *J. Clean. Prod.* 177, 387–397. doi:10.1016/j.jclepro.2017.12.233

Huang, B., Zhao, J., Chai, J., Xue, B., Zhao, F., and Wang, X. (2017). Environmental influence assessment of China's multi-crystalline silicon (multi-Si) photovoltaic modules considering recycling process. *Sol. Energy* 143, 132–141. doi:10.1016/j.solener.2016.12.038

Ladenburg, J., et al. (2024). Taking the carbon capture and storage, wind power, PV or other renewable technology path to fight climate change? Exploring the acceptance of climate change mitigation technologies – a Danish national representative study. *Renew. Energy*, 220.

Liu, W., Zhu, Q., Zhou, X., and Peng, C. (2019). Comparative analyses of different biogenic CO(2) emission accounting systems in life cycle assessment. *Sci. Total Environ.* 652, 1456–1462. doi:10.1016/j.scitotenv.2018.11.039

Liu, Z., Guo, Z., Song, C., Du, Y., Chen, Q., Chen, Y., et al. (2023). Business model comparison of slum-based PV to realize low-cost and flexible power generation in city-level. *Appl. Energy* 344, 121220. doi:10.1016/j.apenergy.2023.121220

Magelli, F., Boucher, K., Bi, H. T., Melin, S., and Bonoli, A. (2009). An environmental impact assessment of exported wood pellets from Canada to Europe. *Biomass Bioenergy* 33 (3), 434–441. doi:10.1016/j.biombioe.2008.08.016

Ningxia Statistical Yearbook (2022). Ningxia. Available at: https://nxdata.com.cn/files_nx_pub/html/tjnj/2022/indexfiles/indexch.htm?1=1.

Song, S., Liu, P., Xu, J., Chong, C., Huang, X., Ma, L., et al. (2017). Life cycle assessment and economic evaluation of pellet fuel from corn straw in China: a case study in Jilin Province. *Energy* 130, 373–381. doi:10.1016/j.energy.2017.04.068

Udomsirichakorn, J., and Salam, P. A. (2014). Review of hydrogen-enriched gas production from steam gasification of biomass: the prospect of CaO-based chemical looping gasification. *Renew. Sustain. Energy Rev.* 30, 565–579. doi:10.1016/j.rser.2013.10.013

Wackernagel, M. O. L., Bello, P., Linares, A. C., Falf´ an, I. S. L., García, J. M., Méndez Garcia, J., et al. (1999). National natural capital accounting with the ecological footprint concept. *Ecol. Econ.* 29 (375-90), 375–390. doi:10.1016/s0921-8009(98)90063-5

Wackernagel, M. R. W. (1996). *Our ecological footprint:reducing human impact on the earth.* Gabriela Island: New Sociely Publishers.

Wang, C., Zhang, L., Zhou, P., Chang, Y., Zhou, D., Pang, M., et al. (2019). Assessing the environmental externalities for biomass- and coal-fired electricity generation in China: a supply chain perspective. *J. Environ. Manage* 246, 758–767. doi:10.1016/j.jenvman.2019.06.047

Xu, L., Zhang, S., Yang, M., Li, W., and Xu, J. (2018). Environmental effects of China's solar photovoltaic industry during 2011–2016: a life cycle assessment approach. *J. Clean. Prod.* 170, 310–329. doi:10.1016/j.jclepro.2017.09.129

Yousri, D., Mirjalili, S., Machado, J. T., Thanikanti, S. B., elbaksawi, O., and Fathy, A. (2021). Efficient fractional-order modified Harris hawks optimizer for proton exchange membrane fuel cell modeling. *Eng. Appl. Artif. Intell.* 100, 104193. doi:10.1016/j.engappai.2021.104193

Yu, Z., Ma, W., Xie, K., Lv, G., Chen, Z., Wu, J., et al. (2017). Life cycle assessment of grid-connected power generation from metallurgical route multi-crystalline silicon photovoltaic system in China. *Appl. Energy* 185, 68–81. doi:10.1016/j.apenergy.2016.10.051

Zhang, B., and Gao, Y. (2023). The optimal capacity ratio and power limit setting method of the PV generation system based on the IGBT reliability and PV economy. *Microelectron. Reliab.* 148, 115145. doi:10.1016/j.microrel.2023.115145

Zhang, S., Wei, J., Chen, X., and Zhao, Y. (2020). China in global wind power development: role, status and impact. *Renew. Sustain. Energy Rev.* 127, 109881. doi:10.1016/j.rser.2020.109881

frontiers | Frontiers in Energy Research

TYPE Original Research
PUBLISHED 06 May 2024
DOI 10.3389/fenrg.2024.1400651

OPEN ACCESS

EDITED BY
Praveen Kumar Balachandran,
Vardhaman College of Engineering, India

REVIEWED BY
Devakirubakaran S.,
SRM Institute of Science and Technology, India
Prince Winston D.,
Kamaraj College of Engineering & Technology, India

*CORRESPONDENCE
Ahmad Taher Azar,
aazar@psu.edu.sa
Ibrahim A. Hameed,
ibib@ntnu.no

RECEIVED 13 March 2024
ACCEPTED 18 April 2024
PUBLISHED 06 May 2024

CITATION
Baskaran J, Naghapushanam M, Ganapathy M, Meena P, Meena VP, Azar AT and Hameed IA (2024), Cost-effective high-gain DC-DC converter for elevator drives using photovoltaic power and switched reluctance motors.
Front. Energy Res. 12:1400651.
doi: 10.3389/fenrg.2024.1400651

Cost-effective high-gain DC-DC converter for elevator drives using photovoltaic power and switched reluctance motors

J. Baskaran[1], Manimaran Naghapushanam[2], Mahalakshmi Ganapathy[3], P. Meena[4], V. P. Meena[5], Ahmad Taher Azar[6,7,8]* and Ibrahim A. Hameed[9]*

[1]Department of Electrical and Electronics Engineering, PSG Institute of Technology and Applied Research, Coimbatore, India, [2]Department of Electrical and Electronics Engineering, Adhiparasakthi Engineering College, Melmaruvathur, Tamil Nadu, India, [3]Department of Electrical and Electronics Engineering, Agni College of Technology, Chennai, Tamil Nadu, India, [4]Department of Electrical Engineering, Indian Institute of Technology Jodhpur, Jodhpur, Rajasthan, India, [5]Department of Electrical and Electronics Engineering, Amrita School of Engineering, Bengaluru, India, [6]College of Computer and Information Sciences, Prince Sultan University, Riyadh, Saudi Arabia, [7]Automated Systems and Soft Computing Lab (ASSCL), Prince Sultan University, Riyadh, Saudi Arabia, [8]Faculty of Computers and Artificial Intelligence, Benha University, Benha, Egypt, [9]Department of ICT and Natural Sciences, Norwegian University of Science and Technology, Alesund, Norway

Low-cost photovoltaic-powered elevators (PVPEs) have gained ever-increasing attention in the last few years for their advantages in terms of renewable energy and low maintenance costs after installation. In this paper, four high-step-up DC-DC converters for low-voltage sources such as solar photovoltaic, fuel cells, and battery banks are proposed. Their performances are evaluated in terms of optimal capability and high reliability. Among the four proposed architectures, the bootstrap converter is selected for its ability to restrict losses and other redundant parameters. The proposed converter drives the inverter-driven switched reluctance motor (SRM) assembly through a directly coupled method, which eliminates the need for battery banks while aiding in cost reduction. The prototype model is implemented, and results are validated, showing promising performance and thus being very efficacious for application to low-cost PVPEs.

KEYWORDS

photovoltaic systems, SRM, DC-DC boost converters, multilevel-inverter, continuous conduction mode

1 Introduction

The photovoltaic-powered elevator (PVPE) promises to be the invention of the next few years due to its several advantages and characteristics. It is pollution-free and needs less maintenance after installation. It does not need any fuel to be powered up, and its source of power is renewable, clean, and environmentally friendly. The source of power is renewable, clean, and environmentally friendly. It is estimated that in (Cronshaw, 2015) the solar-powered apparatus is going to play the most significant role in human life. As of now, the most important equipment is motors, which utilize non-renewable energy as the main source. We are badly in need of an alternate energy source that would be renewable and reliable—none other than solar PV systems.

One easier way of making electrical energy available during calamities is solar energy. Nevertheless, the solar-powered system available traditionally is too expensive, and most of the energy is lost in conversion. If a few steps were taken to minimize these aspects, then this kind of energy would become a cheaper and maintenance-free system for several years (Caracas et al., 2013; Meghni et al., 2017). In (Raghavendra et al., 2019), the authors propose a unique converter for solar water-pumping assemblies that do not require a battery (Antonello et al., 2016; Raghavendra et al., 2019; Meena and Singh, 2023b; Fekik et al., 2023; Thanikanti et al., 2023). Then, new high-voltage-boosting converters are designed in (Hwu et al., 2012; Hwu and Yau, 2013).

When sunlight intensity crosses 1000 W/m^2, which is roughly equivalent to midday in summer in Germany, for example, or when solar irradiation approaches 1000 W/m^2 at lower temperatures, a module's real power may rise above its nominal power (Sontake and Kalamkar, 2016).Two popular configurations usually employed for PV-powered systems are (i) battery-coupled and (ii) direct-coupled methods. The former approach uses the battery to increase supply over a longer period by acting as a constant voltage source for the system. But for elevators, the longer utilization period will be only during the day, when the Sun shines brightly. Though battery utilization aids in some aspects, it has its own drawbacks, as discussed below. The batteries minimize the performance of the system as the voltage is decided by the battery and not by the solar panel. Therefore, when the Sun's luminosity is high, the nominal power can exceed 1000 W/m^2 (roughly during midday), but the battery lays an obstacle to the maximum utilization of power by the system. Furthermore, the batteries have a 2-year life duration when compared to the PV module's life span of 20 years. In addition, the cost of battery maintenance and replacement is significant. As a result, the total efficiency of the system is diminished, while the PVPE system installation cost is increased. As a result, the battery-coupled system is not employed (Eker, 2005; Meah et al., 2008; Chunting et al., 2010; Tschanz et al., 2010; Vitorino et al., 2010; Malla et al., 2011; Meena and Singh, 2022; Arun et al., 2024; Jagan et al., 2024).

In (Lee et al., 2000), interleaved operation of two or more boost converters is presented in this study for high-power applications to increase output power and reduce output ripple (Lee et al., 2000; Kengne et al., 2023). Two structures, a switched-capacitor (SC)-based boost converter and a two-level inverter, are connected in cascade in this article (Axelrod et al., 2005). To meet safety standards and make maximum use of the PV-generated power, a recent research trend in residential power generation systems is to adopt the PV parallel connected configuration rather than the series-connected design (Li and He, 2010; Meghni et al., 2018; Radwan et al., 2018; Suresh et al., 2019; Sethuraman et al., 2020). This work includes thorough mathematical analysis, detailed converter design, parameter analysis and comparison with other existing converters, and a new hardware prototype with expanded hardware results (Sathyan et al., 2015; Periyanayagam et al., 2020; Kalaiarasi et al., 2021; Meena and Singh, 2023a; Reddy et al., 2023; Meena et al., 2024; Bharatiraja et al., 2016a; Bharatiraja et al., 2016b). From the analyses made above, it is evident that an efficient and low-cost PVPE can be set up if a suitable boost converter is designed while still minimizing the conduction and switching losses for improved performance.

In this paper, we propose a detailed study of four high-step-up boost converters. Then, the most suitable topology is chosen after a careful analysis of the simulation results. In Figure 1, the overall block diagram of the proposed system is shown for better understanding of the proposed topology. The design of four types of high-step-up bootstrap converters and a multilevel inverter energizing the switched reluctance motor (SRM) according to the prevailing necessity are considered the main contributions of the work claimed in this research. The cost-reducing factor has already been discussed adequately.

The rest of this paper is organized as follows: The Section 2 elaborates on the design and selection part of the optimal bootstrap DC-DC converter and its reliable features. The multilevel-inverter-fed SRM drive is designed to provide a dynamic speed response during source variations as well as load surges in the Section 3. Section 4 shows the photovoltaic supply comparison with and without the maximum power point tracking (MPPT) controller that excites the DC-DC converter. Numerical results and hardware implementation are depicted in Section 5, while the paper's conclusions and justifications are briefly highlighted in Section 6.

2 Selection of the DC-DC converters

There are two types of converters available for modifying the power obtained from the solar cells, which are meant for consumer-friendly use. The first is an inverter, which converts the DC into AC at the desired frequency to supply AC appliances. The other one is a DC-to dc converter, which already possesses numerous applications via DC motors for solar water pumping systems and other emerging areas like solar-powered electrical vehicles. In this proposed system, the preferred PVPE is driven by SRM; therefore, we have opted for designing a suitable boost converter and PWM inverter. As a result, various boost converters, starting from the basic conventional converter to newly proposed topologies like interleaved converters, quadruple converters, hybrid interleaved-quadruple converters, and finally bootstrap converters, were designed and simulated in this paper. The results were compared to choose the best converter according to the motor requirements.

2.1 Bootstrap converters

This converter consists of bootstrap capacitors and two boost inductors that allow the converter to work appropriately. The three switches are operated in a fashion where only half bridge and one low side gate drive are triggered. The bootstrap converter simulation circuit is shown in Figure 2.

2.2 Operating modes of the converter

Mode 1, Figure 3: When switches S_1 and S_3 are turned on, the capacitor C_b is immediately charged and the inductors are magnetized because the diode D_0 is reverse biased due to the S_3 switch being turned on.

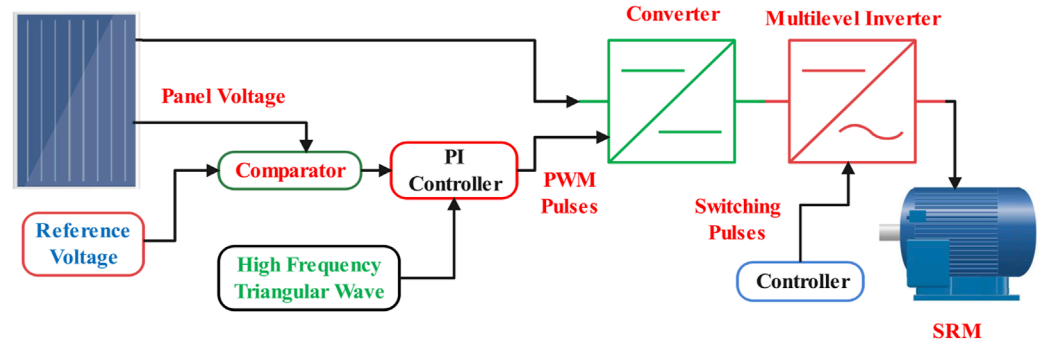

FIGURE 1
Block diagram of the proposed system.

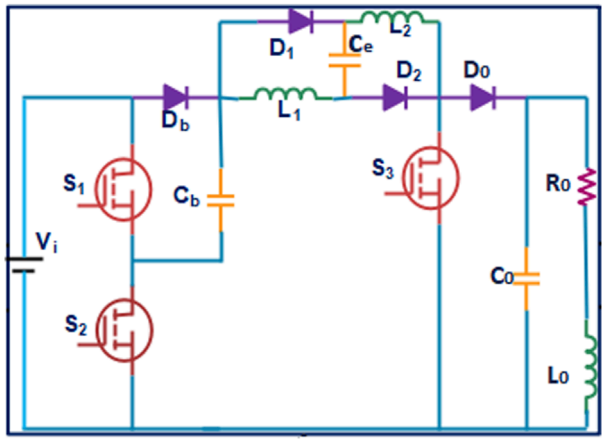

FIGURE 2
The proposed bootstrap converter.

The output capacitor will provide electricity to the load during this time. The voltage across L_1 and L_2 in this mode can be expressed as

$$V_{L1-ON} = V_i + V_{cb}$$

$$V_{L2-ON} = V_i + V_{cb}$$

Mode 2, Figure 4: When switch S_2 is activated, the capacitor C_b is instantaneously charged to the input voltage. The input voltage, together with the energy stored in C_e, L_1 & L_2 feeds the load, causing C_0 to be energized and C_e discharged, L_1, L_2 to be demagnetized.

So V_0 in this mode can be expressed as

$$V_{L1-OFF} = \frac{-D}{1-D} \times V_{L1-ON}$$

$$V_{L2-OFF} = \frac{-D}{1-D} \times V_{L2-ON}$$

The converter is operated in continuous conduction mode; the waveform is shown in Figure 5.The voltage conversion ratio in the continuous conduction mode is given by

$$\frac{V_0}{V_i} = \frac{3+D}{1-D}$$

The output response of the converter and the switching pulses are shown in Figures 6, 7. The input voltage of the converter is 24 V, the output voltage is 72 V, and the switching frequency is 5 kHz. Table 1 shows the comparison of the parameters and the responses of each boost converter. The best-suited converter for the SPWP is selected and implemented in the prototype.

Taking into consideration the input voltage and output voltage, the gain is highest in a hybrid converter. And then, bearing in mind the current limitations due to some saturation facts of SRM, we turn on the interleaved and bootstrap converters. However, a few primary parameters, like the number of inductors, capacitors, and switches that would be able to avoid bulkiness, offer a better power factor, and have low switching losses, can be taken into account when picking a suitable converter among the two. Thus, we chose the bootstrap converter with two inductors, two capacitors, and 3 MOSFET switches, which can offer three times the input voltage with maximum compatibility.

3 Multilevel-inverter fed SRM drive operating principle

The multilevel-inverter-fed SRM drive is designed to provide a dynamic speed response during source variations as well as load surges in this section. Figure 8 illustrates the energy flow diagram of the proposed multilevel inverter topology (Phase A) at various levels. When the DC supply is given to the circuit, all three capacitors $C1$, $C2$ and $C3$ get charged. The DC voltage across the capacitors is equally divided, i.e.,

$$V_{C1} = V_{C2} = V_{C3} = \frac{V_{dc}}{3} \quad (1)$$

To attain the first level in the positive cycle, the switches SA and $X1$ are excited, and the energy flows through $C1 - D1 - X1 - D3 - RL - SA - C1$. For the second level, the current flows through $C2 - D5 - X2 - D7 - SA - C1 - C2$ and $C3 - SC - RL - SA - C1 - C2 - C3$ for the third level. In the negative cycle, for the first level, the current flows from $C3 - SD - RL - D6 - X2 - D8 - C1$, for the second level, the

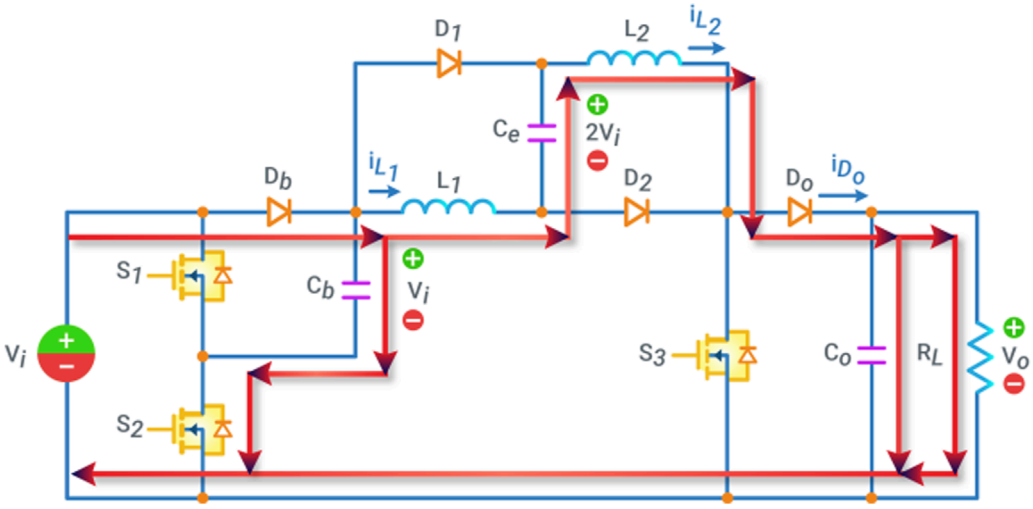

FIGURE 3
Continuous conduction Mode-1.

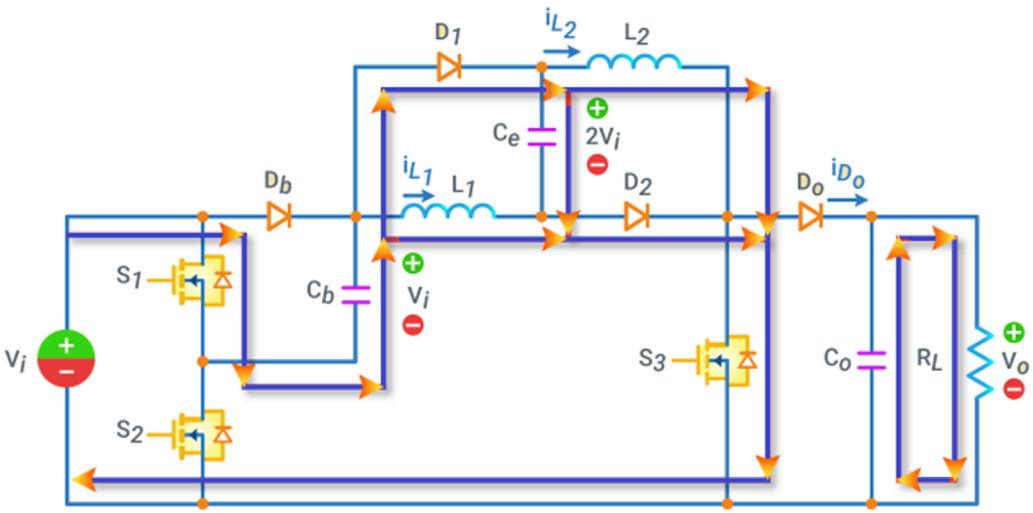

FIGURE 4
Continuous conduction Mode-2.

TABLE 1 Comparison of the results and other factors to deduce the best converter.

Types of boost converter	Input voltage	Output Voltage	Output current	No. Of inductors used	No. Of capacitors used	No. Of switches used	Voltage gain
Conventional	12	24	0.7	1	1	1	2
Interleaved	20	148	2.5	3	1	2	7.5
Voltage Quadruple	24	94	1.8	3	3	2	3.9
Hybrid	24	407	14.2	6	3	5	16.9
Bootstrap	24	72	2.5	2	2	3	3

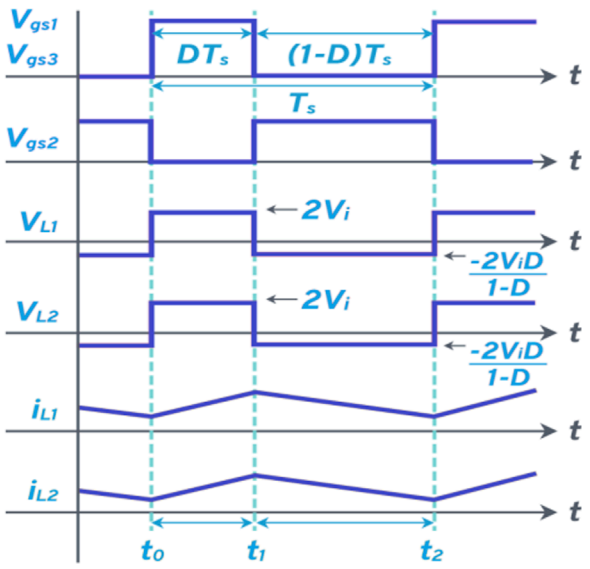

FIGURE 5
Continuous conduction mode waveform of the converter.

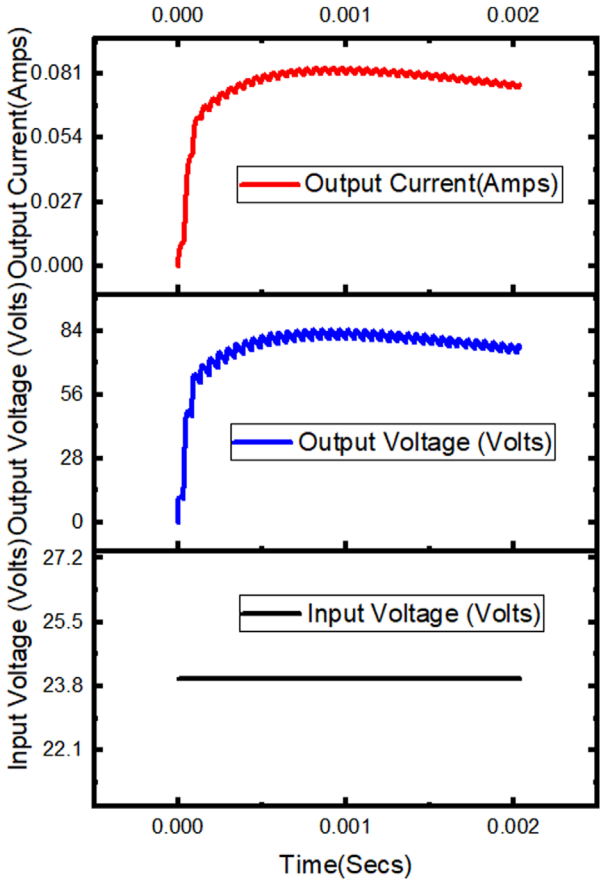

FIGURE 6
Simulation output of a bootstrap converter.

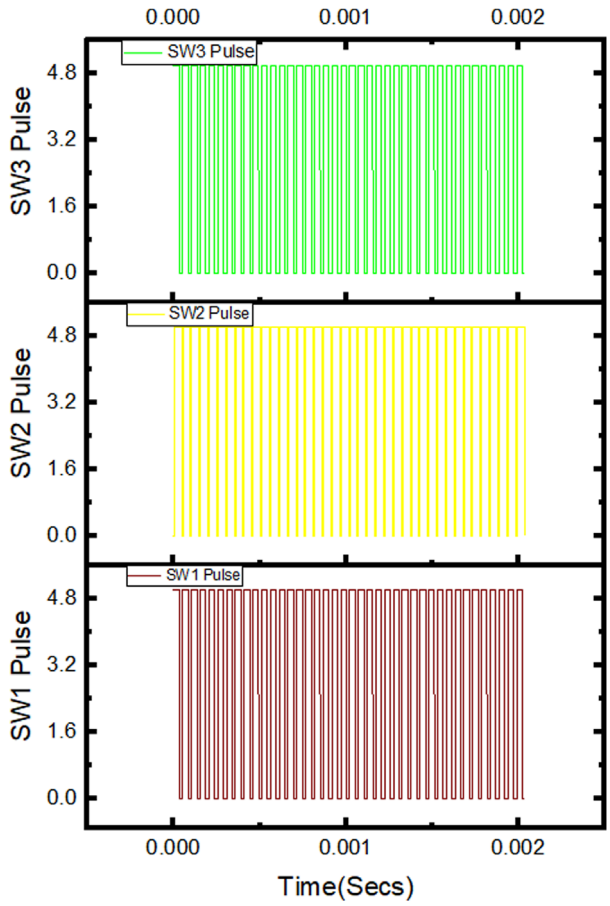

FIGURE 7
Switching pulses of the bootstrap converter.

current flows from $C2-C1-SD-RL-D2-X1-D4-C2$; and $C1-C2-C3-SD-RL-SB-C1$.

In terms of the switching conditions provided in Table 2, the gating pulses for each switch are graphed in Figure 9. In one full cycle of operation, the seven-level output is divided into 16 regions with respect to the firing angle (α_n). For a seven-level switched capacitor-based symmetric multilevel inverter (SCBSMLI), the three positive half cycle levels are triggered at α_1, α_2, and α_3, which lie between 0 and $\pi/2$, and the negative half cycle levels are triggered at $\alpha_9(=\pi+\alpha_1)$, $\alpha_{10}(=\pi+\alpha_2)$, and $\alpha_{11}(=\pi+\alpha_3$, which lies between π and $3\pi/2$. The zero level occurs during $\alpha_0(=0)$ to α_1, α_7 to α_9, and α_{15} to $\alpha_{16}(=2\pi)$.

The switches are turned on in the following regions:

$$SA{:}\alpha_1 < \omega t < \alpha_7$$

$$SB{:}\alpha_{11} < \omega t < \alpha_{13}$$

$$SC{:}\alpha_3 < \omega t < \alpha_5$$

$$SD{:}\alpha_9 < \omega t < \alpha_{15}$$

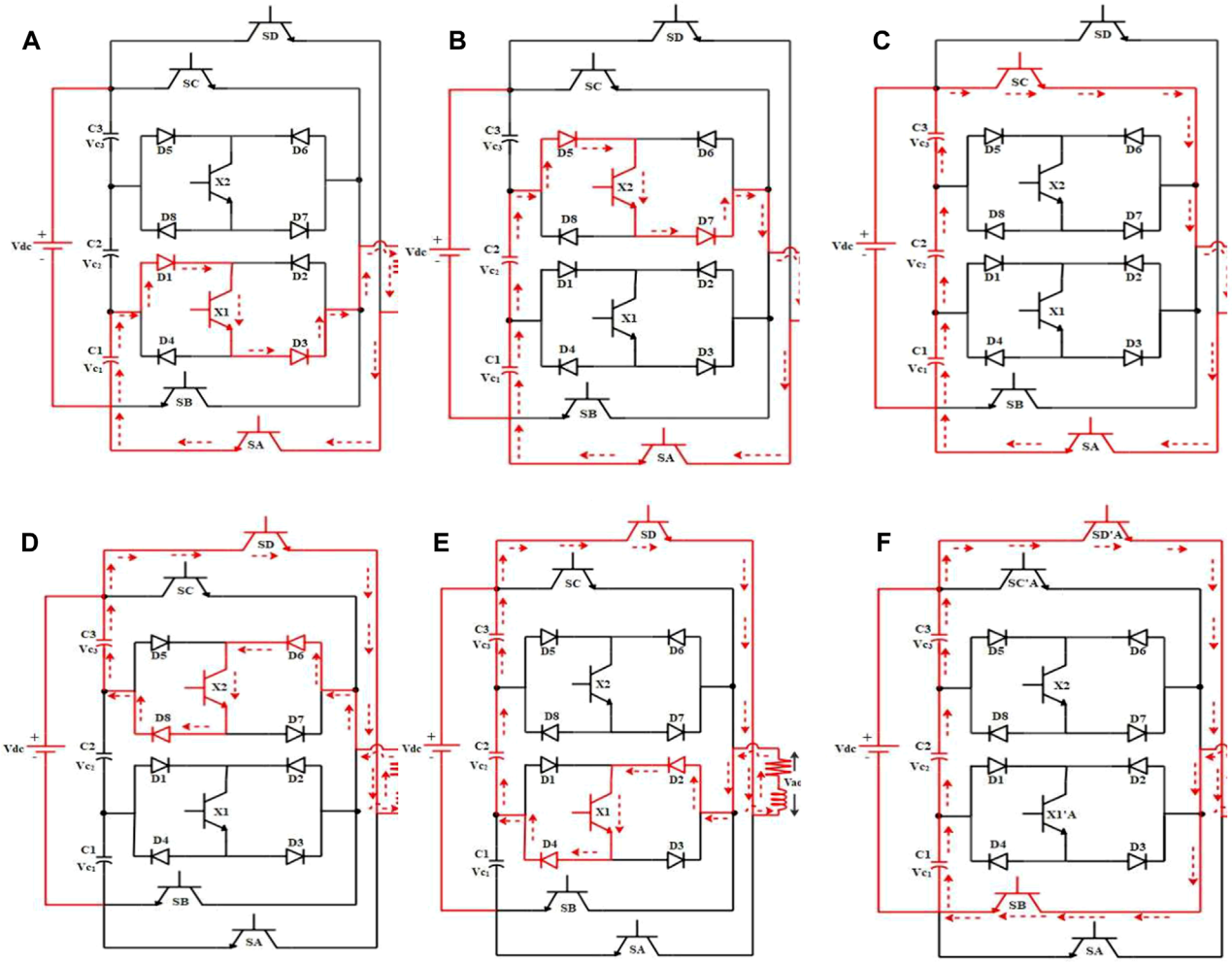

FIGURE 8
Energy Flow diagram of the seven level switched capacitor based symmetric multilevel inverter (SCBSMLI) at **(A)** Positive First level **(B)** Positive Second Level **(C)** Positive Third Level **(D)** Negative First Level **(E)** Negative Second Level **(F)** Negative Third Level.

$$X1:\begin{cases}\alpha_1 < \omega t < \alpha_2\\ \alpha_6 < \omega t < \alpha_7\\ \alpha_{10} < \omega t < \alpha_{11}\\ \alpha_{13} < \omega t < \alpha_{14}\end{cases} \quad (2)$$

$$X2:\begin{cases}\alpha_2 < \omega t < \alpha_3\\ \alpha_5 < \omega t < \alpha_6\\ \alpha_9 < \omega t < \alpha_{10}\\ \alpha_{14} < \omega t < \alpha_{15}\end{cases} \quad (3)$$

The above switching conditions (2) and (3) are rewritten in the term of α_1, α_2 and α_3

$$SA{:}\alpha_1 < \omega t < \frac{\pi}{2} + \alpha_3$$

$$SB{:}\pi + \alpha_3 < \omega t < \frac{3\pi}{2} + \alpha_1$$

$$SC{:}\alpha_3 < \omega t < \frac{\pi}{2} + \alpha_1$$

$$SD{:}\pi + \alpha_1 < \omega t < \frac{3\pi}{2} + \alpha_3$$

$$X1:\begin{cases}\alpha_1 < \omega t < \alpha_2\\ \frac{\pi}{2} + \alpha_2 < \omega t < \frac{\pi}{2} + \alpha_3\\ \pi + \alpha_2 < \omega t < \pi + \alpha_3\\ \frac{3\pi}{2} + \alpha_1 < \omega t < \frac{3\pi}{2} + \alpha_2\end{cases} \quad (4)$$

$$X2:\begin{cases}\alpha_2 < \omega t < \alpha_3\\ \frac{\pi}{2} + \alpha_1 < \omega t < \frac{\pi}{2} + \alpha_2\\ \pi + \alpha_1 < \omega t < \pi + \alpha_2\\ \frac{3\pi}{2} + \alpha_2 < \omega t < \frac{3\pi}{2} + \alpha_3\end{cases} \quad (5)$$

From the above (4) and (5), the AC output voltage of the SCBSMLI is calculated using the Fourier Half Sine series as given in the (6), since the desired output is ultimately as

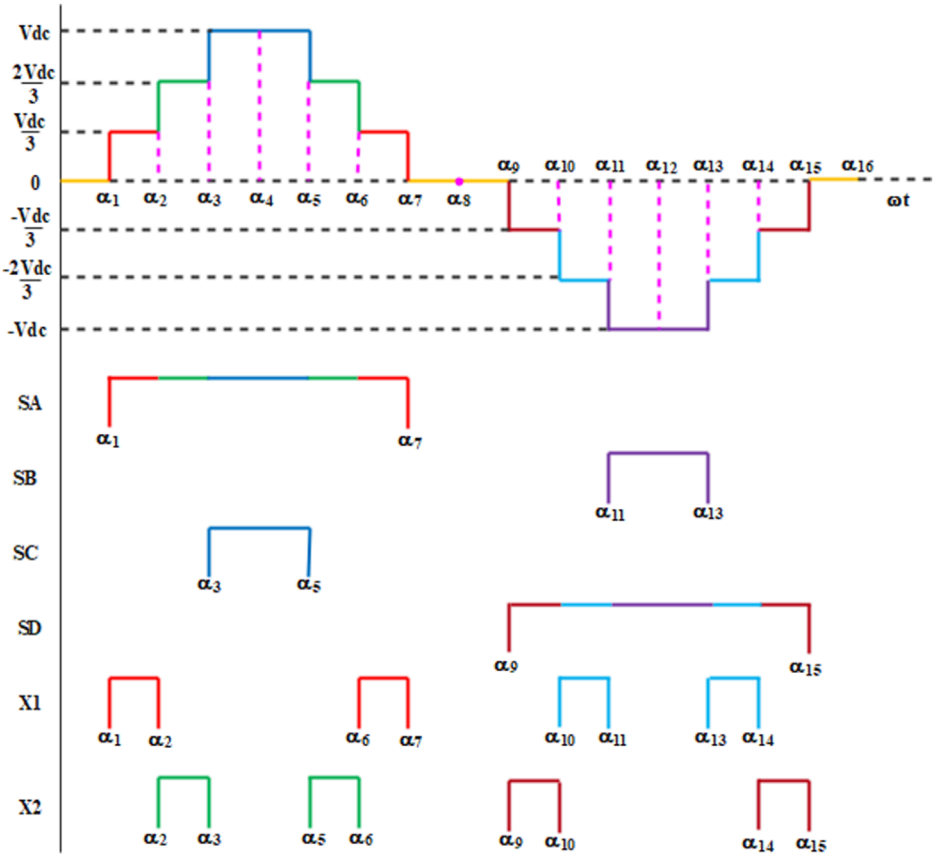

FIGURE 9
Gate pulses of switches SA, SB, SC, SD, X1 and X2.

TABLE 2 Switching Conditions of seven level SCBSMLI.

Level	SA	SB	SC	SD	X1	X2
$+\frac{3V_{dc}}{3}$	1	0	1	0	0	0
$+\frac{2V_{dc}}{3}$	1	0	0	0	0	1
$+\frac{V_{dc}}{3}$	1	0	0	0	1	0
	1	1	0	0	0	0
0	0	0	1	1	0	0
$-\frac{V_{dc}}{3}$	0	0	0	1	0	1
$-\frac{2V_{dc}}{3}$	0	0	0	1	1	0
$-\frac{3V_{dc}}{3}$	0	1	0	1	0	0

$$f(\omega t) = \begin{cases} V_{C1}, & if \ \ \alpha_1 < \omega t < \pi - \alpha_1 \\ V_{C2}, & if \ \ \alpha_2 < \omega t < \pi - \alpha_2 \\ V_{C3}, & if \ \ \alpha_3 < \omega t < \pi - \alpha_3 \end{cases} \tag{6}$$

$$f(\omega t) = \sum_{n=1}^{\infty} b_n sin(n\omega t) \tag{7}$$

where

$$b_n = \frac{2}{\pi}\int_0^{\pi} f(\omega t)\, sin(n\omega t)\, d(\omega t) \tag{8}$$

writing (8) in terms of voltage

$$V_{ac} = \frac{2}{\pi}\int_0^{\pi} V_m sin(\omega t)\, d(\omega t) \tag{9}$$

Substituting (5) in (8)

$$V_{ac} = \frac{2}{\pi}\left[\int_{\alpha_1}^{\pi-\alpha_1} V_{C1} sin(\omega t) + \int_{\alpha_2}^{\pi-\alpha_2} V_{C2} sin(\omega t) + \int_{\alpha_3}^{\pi-\alpha_3} V_{C3} sin(\omega t)\right] \tag{10}$$

Substituting (2) in (9)

$$V_{ac} = \frac{2}{\pi}\left[\int_{\alpha_1}^{\pi-\alpha_1} \frac{V_{dc}}{3} sin(\omega t) + \int_{\alpha_2}^{\pi-\alpha_2} \frac{V_{dc}}{3} sin(\omega t) + \int_{\alpha_3}^{\pi-\alpha_3} \frac{V_{dc}}{3} sin(\omega t)\right] \tag{11}$$

$$V_{ac} = \frac{2V_{dc}}{3\pi}\left[\int_{\alpha_1}^{\pi-\alpha_1} sin(\omega t) + \int_{\alpha_2}^{\pi-\alpha_2} sin(\omega t) + \int_{\alpha_3}^{\pi-\alpha_3} sin(\omega t)\right] \tag{12}$$

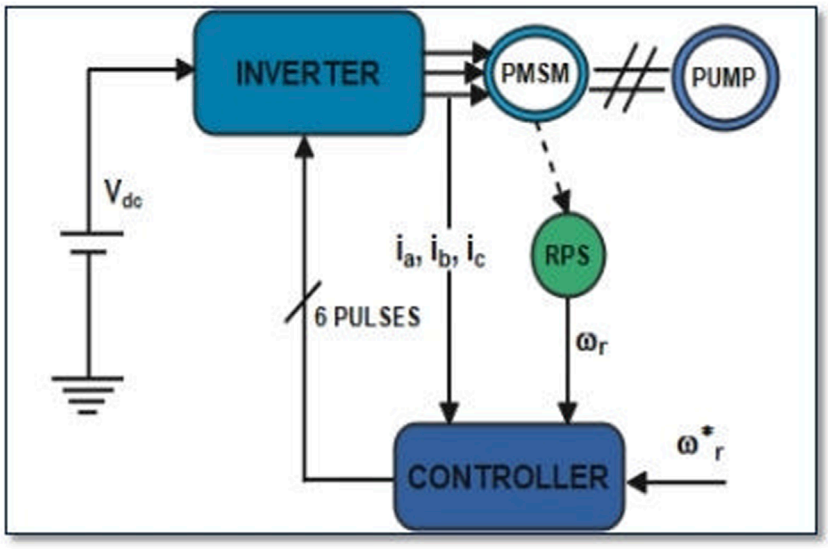

FIGURE 10
Schematic-representation of the PMSM-PUMP drive system.

Integrating and simplifying (10) using trigonometric functions, the AC output voltage is for seven-level SCBSMLI given as

$$V_{ac} = \frac{4V_{dc}}{3\pi}\left[cos\alpha_1 + cos\alpha_2 + cos\alpha_3\right] \tag{13}$$

DC machine-like performance can be achieved for a permanent magnet synchronous motor (PMSM) drive when vector-control or field-oriented control (FOC) is used to achieve decoupling control. It is mentioned that the vector-control decouples the excitation component (i_d) and torque segment (i_q) in PMSM by applying the instant space-vector hypothesis (Pillay and Krishnan, 1989; Bharatiraja et al., 2016a; Bharatiraja et al., 2016b). A high-precision and servo-controlled industrial robot driven by PMSM-Direct Torque Control utilizing composite active vectors is designed in (Yuan et al., 2019). The conceptual framework of antecedents to trends on permanent magnet synchronous generators for wind energy conversion systems has been briefed in (Chokkalingham et al., 2018; Padmanathan et al., 2019; Fekik et al., 2021).

The PMSM-PUMP drive comprises five primary parts: the PMSM, inverter, control unit, temperature sensor, and pump as load. The schematic representation of the drive system is shown in Figure 10. The inverter receives DC supply from the PV panel with a constant-voltage MPPT controller. Thus, the pump receives constant voltage during the day even when fluctuations are experienced in the Sun's radiance insolation.

4 MPPT controller

The proposed system is simulated, and the results are compared with the system simulated without MPPT. The MPPT-controlled bootstrap converter drives the SVM inverter to run the PMSM-PUMP assembly block diagram, as shown in Figure 11. The comparison between the proposed system without MPPT and with MPPT is done after introducing a step change in the insolation from 1,000 to 950, as exhibited in Figure 12.

Following the insolation graph, the other parameters like V_{pv}, P_{pv}, V_{out}, and speed of the motor are obtained and compared with the system without MPPT to show the superiority of the proposed system.

A comparison of output voltage and motor speed with and without MPPT is delineated in Table 3. By using the MPPT controller, the output voltage is enhanced from 385V to 415V, and motor speed is also enhanced from 1200 RPM to 1415 RPM. The panel voltage and power also seem to be improved in the MPPT-controlled system.

From Table 3, it is evident that the system with MPPT is showing better results than the system without MPPT. Also, the desired values are obtained, and the response is stable for the system with the MPPT technique.

TABLE 3 Comparison of output voltage and motor speed with and without MPPT.

CASE	VPV	PPV (W)	V_o	N (RPM) (rpm)
Without MPPT	122 V	591	385 V	1,200
With MPPT	119 V	640	415 V	1,415

5 Experimental setup & results

Thus, after the design of the proposed system, the implementation of the prototype model is carried out. Its results are validated with the proposed topology, and the challenges of implementation are summarized. Figure 13 shows the hardware

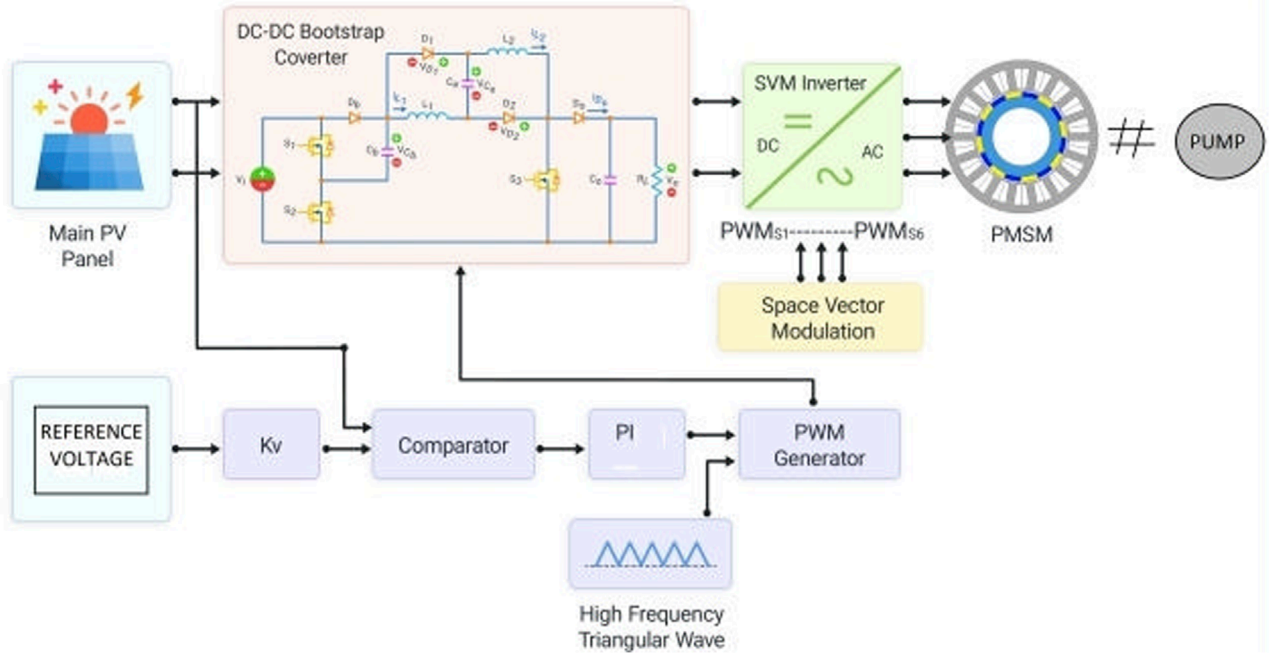

FIGURE 11
Block diagram of bootstrap converter and SVM inverter with MPPT controller.

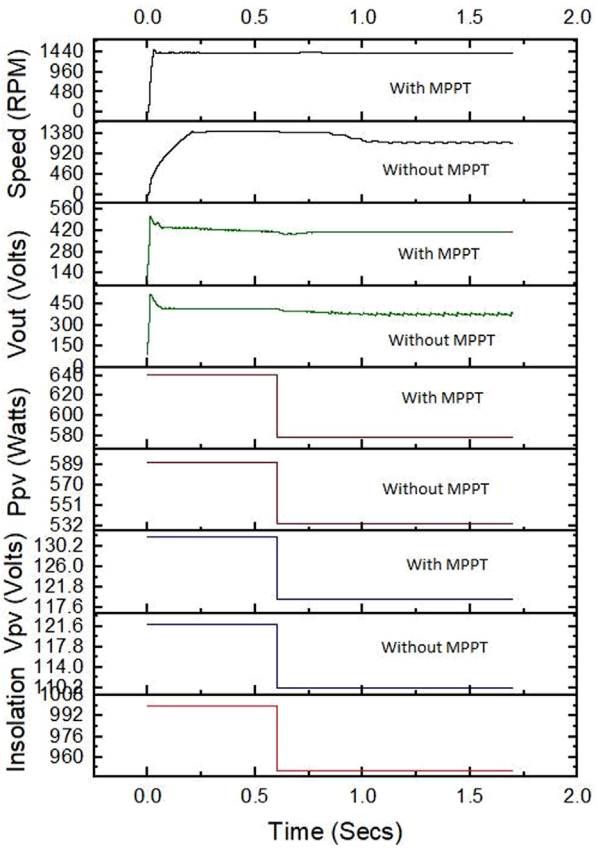

FIGURE 12
Response of the proposed system with and without MPPT.

TABLE 4 Hardware parameters of bootstrap converter.

S. No.	Parameters	Value
1	Power rating	100 *W*
2	Input voltage	24 *V*
3	Switching frequency	195 *KHz*
4	Output voltage	200 *V*
5	Inductors	170 μF
6	Bootstrap capacitor, C_1	100 μF
7	Output capacitors, C_3	60 μF
8	Load resistance	400 Ω
9	Capacitor, C_2	200 μF

setup of the proposed topology. The bootstrap converter is designed, and its output is shown in the DSO. The solar panel supplies the DC voltage for the bootstrap converter, and the constant voltage MPPT technique is employed to offer the required output as per the motor ratings. The motor speed response is converted into serial input, and then it is sent to the COM-8 port of the computer, where it is displayed on the monitor. The hardware parameters of the bootstrap are given in Table 4.

Figure 14 shows the output of the bootstrap converter from the hardware implemented for the purpose of giving constant dc

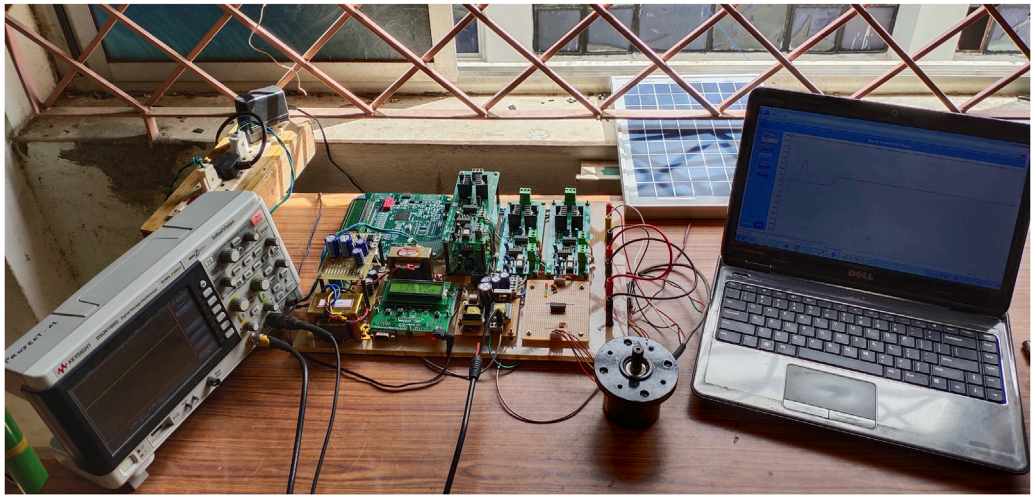

FIGURE 13
Hardware of the proposed topology.

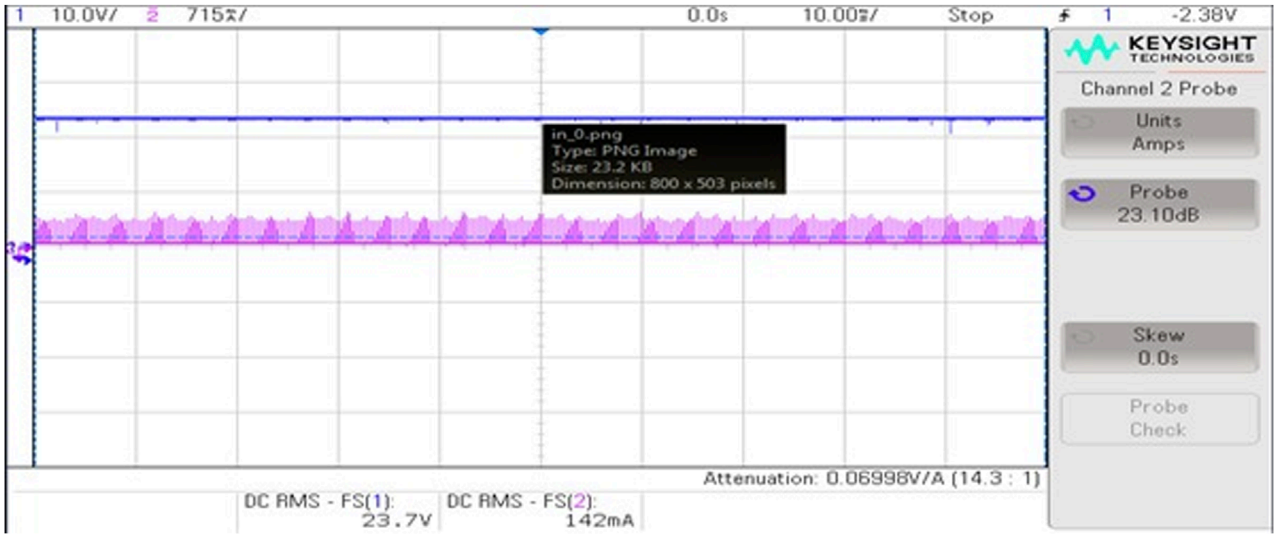

FIGURE 14
Output of the bootstrap converter from the hardware implemented.

voltage equal to 23.7 V and current of 142 mA to the inverter which drives the SRM. Then Figure 15 gives the speed response of the SRM to deliver a constant speed to the ELEVATOR load even if any disturbance occurs.

6 Conclusion and future works

This work has introduced four architectures of DC-DC converters for possible application in low-cost PVPEs. Results and comparisons from simulations show that the proposed bootstrap converter provides an enhanced output and small voltage pressure on the switches. In the projected topology, only two inductors are used for high-voltage output applications. In different operations, the converter just handles two duty ratios. Thus, we can minimize the overall cost of the solar-powered water elevator system by reducing processes like battery installation, maintenance, and further switching losses due to the DC-AC alteration stage. The direct DC-DC boost converter coupled configuration might also provide additional cost reduction. In our solution, the SRM is used as the drive for the elevator. The speed response of the SRM is guarded by a multilevel inverter controller, which ensures the

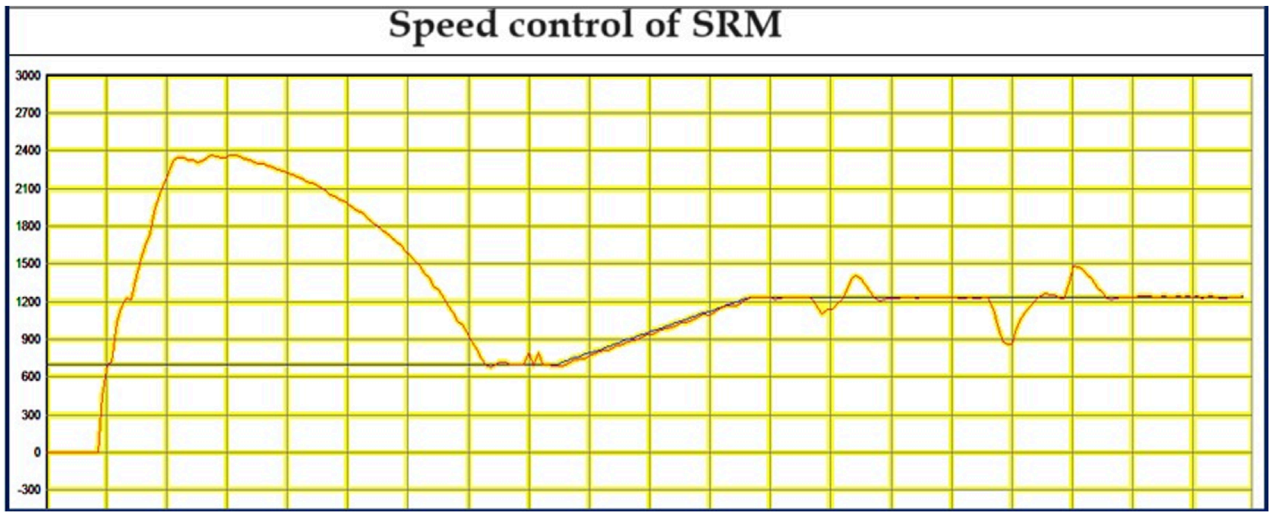

FIGURE 15
The speed response of the SRM with constant speed to the pump with load disturbance.

stability of the whole system. The bootstrap converter supplying DC to the inverter that excites the SRM to drive the prototype is finally implemented.

Future work will focus on refining the proposed bootstrap converter architecture to optimize its efficiency and performance further. Additionally, research will explore integrating advanced control strategies to enhance the overall stability and reliability of the solar-powered water elevator system.

Data availability statement

The original contributions presented in the study are included in the article/Supplementary material, further inquiries can be directed to the corresponding author.

Author contributions

JB: Conceptualization, Formal Analysis, Methodology, Resources, Software, Writing–original draft, Writing–review and editing. MN: Conceptualization, Formal Analysis, Methodology, Resources, Software, Writing–original draft, Writing–review and editing. MG: Conceptualization, Formal Analysis, Methodology, Resources, Software, Writing–original draft, Writing–review and editing. PM: Conceptualization, Formal Analysis, Methodology, Resources, Software, Writing–original draft, Writing–review and editing. VM: Conceptualization, Formal Analysis, Methodology, Resources, Software, Writing–original draft, Writing–review and editing. ATA: Conceptualization, Formal Analysis, Investigation, Methodology, Validation, Writing–original draft, Writing–review and editing. IH: Formal Analysis, Funding acquisition, Investigation, Methodology, Resources, Validation, Writing–review and editing.

Funding

The author(s) declare that financial support was received for the research, authorship, and/or publication of this article. This research was funded by the Norwegian University of Science and Technology.

Acknowledgments

The authors would like to acknowledge the support of the Norwegian University of Science and Technology for paying the Article Processing Charges (APC) of this publication. This research is supported by Automated Systems and Soft Computing Lab (ASSCL), Prince Sultan University, Riyadh, Saudi Arabia. The authors would like to thank Prince Sultan University, Riyadh, Saudi Arabia for their support.

Conflict of interest

The authors declare that the research was conducted in the absence of any commercial or financial relationships that could be construed as a potential conflict of interest.

Publisher's note

All claims expressed in this article are solely those of the authors and do not necessarily represent those of their affiliated organizations, or those of the publisher, the editors and the reviewers. Any product that may be evaluated in this article, or claim that may be made by its manufacturer, is not guaranteed or endorsed by the publisher.

References

Antonello, R., Carraro, M., Costabeber, A., Tinazzi, F., and Zigliotto, M. (2016). Energy-efficient autonomous solar water-pumping system for permanent-magnet synchronous motors. *IEEE Trans. Industrial Electron.* 64, 43–51. doi:10.1109/tie.2016.2595480

Arun, R., Muniraj, R., Karuppiah, N., Kumar, B. P., and Murugaperumal, K. (2024). Automated approach to design predictive pi control scheme for gain margin specification. *Int. J. Syst. Assur. Eng. Manag.*, 1–8. doi:10.1007/s13198-023-02238-y

Axelrod, B., Berkovich, Y., and Ioinovici, A. (2005). A cascade boost-switched-capacitor-converter-two level inverter with an optimized multilevel output waveform. *IEEE Trans. Circuits Syst. I Regul. Pap.* 52, 2763–2770. doi:10.1109/tcsi.2005.852205

Bharatiraja, C., Jeevananthan, S., Latha, R., and Mohan, V. (2016a). Vector selection approach-based hexagonal hysteresis space vector current controller for a three phase diode clamped mli with capacitor voltage balancing. *IET Power Electron.* 9, 1350–1361. doi:10.1049/iet-pel.2015.0184

Bharatiraja, C., Jeevananthan, S., Munda, J. L., and Latha, R. (2016b). Improved svpwm vector selection approaches in ovm region to reduce common-mode voltage for three-level neutral point clamped inverter. *Int. J. Electr. Power & Energy Syst.* 79, 285–297. doi:10.1016/j.ijepes.2016.01.002

Caracas, J. V. M., de Carvalho Farias, G., Teixeira, L. F. M., and de Souza Ribeiro, L. A. (2013). Implementation of a high-efficiency, high-lifetime, and low-cost converter for an autonomous photovoltaic water pumping system. *IEEE Trans. Industry Appl.* 50, 631–641. doi:10.1109/TIA.2013.2271214

Chokkalingham, B., Padmanaban, S., and Blaabjerg, F. (2018). Investigation and comparative analysis of advanced pwm techniques for three-phase three-level npc-mli drives. *Electr. Power Components Syst.* 46, 258–269. doi:10.1080/15325008.2018.1445142

Chunting, M., Correa, M., and Pinto, J. (2010). The ieee 2011 international future energy challenge—request for proposals. *Proc. IFEC*, 1–24.

Cronshaw, I. (2015). World energy outlook 2014 projections to 2040: natural gas and coal trade, and the role of China. *Aust. J. Agric. Resour. Econ.* 59, 571–585. doi:10.1111/1467-8489.12120

Eker, B. (2005). Solar powered water pumping systems. *Trakia J. Sci.* 3, 7–11.

Fekik, A., Azar, A. T., Hameed, I. A., Hamida, M. L., Amara, K., Denoun, H., et al. (2023). Enhancing photovoltaic efficiency with the optimized steepest gradient method and serial multi-cellular converters. *Electronics* 12, 2283. doi:10.3390/electronics12102283

Fekik, A., Azar, A. T., Kamal, N. A., Denoun, H., Almustafa, K. M., Hamida, L., et al. (2021). "Fractional-order control of a fuel cell–boost converter system," in *Advanced machine learning technologies and applications: proceedings of AMLTA 2020* (Springer), 713–724.

Hwu, K., and Yau, Y. (2013). High step-up converter based on coupling inductor and bootstrap capacitors with active clamping. *IEEE Trans. Power Electron.* 29, 2655–2660. doi:10.1109/tpel.2013.2289387

Hwu, K.-I., Chuang, C., and Tu, W. (2012). High voltage-boosting converters based on bootstrap capacitors and boost inductors. *IEEE Trans. Industrial Electron.* 60, 2178–2193. doi:10.1109/tie.2012.2194972

Jagan, V., Maheshwaram, B. C., Usirikapally, M., Balachandran, P. K., Reddy, B. N., Mettu, S., et al. (2024). Analysis of different pwm techniques for enhanced ultrahigh gain z-network topology. *Int. Trans. Electr. Energy Syst.* 2024, 1–14. doi:10.1155/2024/6645798

Kalaiarasi, N., Subhranshu, S. D., Paramasivam, S., Bharatiraja, C., et al. (2021). Investigation on anfis aided mppt technique for pv fed zsi topologies in standalone applications. *J. Appl. Sci. Eng.* 24, 261–269.

Kengne, E. R. M., Kammogne, A. S. T., Siewe, M. S., Tamo, T. T., Azar, A. T., Mahlous, A. R., et al. (2023). Bifurcation analysis of a photovoltaic power source interfacing a current-mode-controlled boost converter with limited current sensor bandwidth for maximum power point tracking. *Sustainability* 15, 6097. doi:10.3390/su15076097

Lee, P.-W., Lee, Y.-S., Cheng, D. K., and Liu, X.-C. (2000). Steady-state analysis of an interleaved boost converter with coupled inductors. *IEEE Trans. industrial Electron.* 47, 787–795. doi:10.1109/41.857959

Li, W., and He, X. (2010). Review of nonisolated high-step-up dc/dc converters in photovoltaic grid-connected applications. *IEEE Trans. industrial Electron.* 58, 1239–1250. doi:10.1109/tie.2010.2049715

Malla, S. G., Bhende, C., and Mishra, S. (2011). "Photovoltaic based water pumping system," in *2011 international conference on energy, automation and signal* (IEEE), 1–4.

Meah, K., Ula, S., and Barrett, S. (2008). Solar photovoltaic water pumping—opportunities and challenges. *Renew. Sustain. Energy Rev.* 12, 1162–1175. doi:10.1016/j.rser.2006.10.020

Meena, V., Gupta, A., and Singh, V. (2024). "Interval modelling based pid controller design for cuk converter," in *AIP conference proceedings* (AIP Publishing), 2966. doi:10.1063/5.0189780

Meena, V., and Singh, V. (2023a). Controller design for a tito doha water treatment plant using the class topper optimization algorithm. *Arabian J. Sci. Eng.* 48, 16097–16107. doi:10.1007/s13369-023-08022-1

Meena, V., and Singh, V. (2023b). "Design of fopid controller for riverol-pilipovik water treatment plant exploiting jaya algorithm," in *2023 international conference on computer, electronics & electrical engineering & their applications (IC2E3)* (IEEE), 1–5.

Meena, V., and Singh, V. P. (2022). Kharitonov polynomial-based interval reduced order modelling of cuk converter. *Int. J. Model. Identif. Control* 41, 231–242. doi:10.1504/ijmic.2022.10052626

Meghni, B., Dib, D., Azar, A. T., Ghoudelbourk, S., and Saadoun, A. (2017). Robust adaptive supervisory fractional order controller for optimal energy management in wind turbine with battery storage. *Fract. order control synchronization chaotic Syst.*, 165–202. doi:10.1007/978-3-319-50249-6_6

Meghni, B., Dib, D., Azar, A. T., and Saadoun, A. (2018). Effective supervisory controller to extend optimal energy management in hybrid wind turbine under energy and reliability constraints. *Int. J. Dyn. Control* 6, 369–383. doi:10.1007/s40435-016-0296-0

Padmanathan, K., Kamalakannan, N., Sanjeevikumar, P., Blaabjerg, F., Holm-Nielsen, J. B., Uma, G., et al. (2019). Conceptual framework of antecedents to trends on permanent magnet synchronous generators for wind energy conversion systems. *Energies* 12, 2616. doi:10.3390/en12132616

Periyanayagam, M., Kumar V, S., Chokkalingam, B., Padmanaban, S., Mihet-Popa, L., and Adedayo, Y. (2020). A modified high voltage gain quasi-impedance source coupled inductor multilevel inverter for photovoltaic application. *Energies* 13, 874. doi:10.3390/en13040874

Pillay, P., and Krishnan, R. (1989). Modeling, simulation, and analysis of permanent-magnet motor drives. i. the permanent-magnet synchronous motor drive. *IEEE Trans. industry Appl.* 25, 265–273. doi:10.1109/28.25541

Radwan, A. G., Emira, A. A., AbdelAty, A. M., and Azar, A. T. (2018). Modeling and analysis of fractional order dc-dc converter. *ISA Trans.* 82, 184–199. doi:10.1016/j.isatra.2017.06.024

Raghavendra, K. V. G., Zeb, K., Muthusamy, A., Krishna, T., Kumar, S. V. P., Kim, D.-H., et al. (2019). A comprehensive review of dc–dc converter topologies and modulation strategies with recent advances in solar photovoltaic systems. *Electronics* 9, 31. doi:10.3390/electronics9010031

Reddy, B. N., Goud, B. S., Kalyan, S., Naga, C., Balachandran, P. K., Aljafari, B., et al. (2023). The design of 2s2l-based buck-boost converter with a wide conversion range. *Int. Trans. Electr. Energy Syst.* 2023, 1–17. doi:10.1155/2023/4057091

Sathyan, S., Suryawanshi, H. M., Ballal, M. S., and Shitole, A. B. (2015). Soft-switching dc–dc converter for distributed energy sources with high step-up voltage capability. *IEEE Trans. Industrial Electron.* 62, 7039–7050. doi:10.1109/tie.2015.2448515

Sethuraman, S. S., Santha, K., Mihet-Popa, L., and Bharatiraja, C. (2020). A modified topology of a high efficiency bidirectional type dc–dc converter by synchronous rectification. *Electronics* 9, 1555. doi:10.3390/electronics9091555

Sontake, V. C., and Kalamkar, V. R. (2016). Solar photovoltaic water pumping system-a comprehensive review. *Renew. Sustain. Energy Rev.* 59, 1038–1067. doi:10.1016/j.rser.2016.01.021

Suresh, K., Chellammal, N., Bharatiraja, C., Sanjeevikumar, P., Blaabjerg, F., and Nielsen, J. B. H. (2019). Cost-efficient nonisolated three-port dc-dc converter for ev/hev applications with energy storage. *Int. Trans. Electr. Energy Syst.* 29, e12088. doi:10.1002/2050-7038.12088

Thanikanti, S. B., Kumar, P., Devakirubakaran, S., Aljafari, B., and Colak, I. (2023). A dynamic mismatch loss mitigation algorithm with dual input dual output converter for solar pv systems. *Sol. Energy Mater. Sol. Cells* 251, 112163. doi:10.1016/j.solmat.2022.112163

Tschanz, D., Lovatt, H., Vezzini, A., and Perrenoud, V. (2010). "A multi-functional converter for a reduced cost, solar powered, water pump," in *2010 IEEE international symposium on industrial electronics (IEEE)* (IEEE), 568–572.

Vitorino, M. A., de Rossiter Corrêa, M. B., Jacobina, C. B., and Lima, A. M. N. (2010). An effective induction motor control for photovoltaic pumping. *IEEE Trans. Industrial Electron.* 58, 1162–1170. doi:10.1109/tie.2010.2054053

Yuan, T., Wang, D., Wang, X., Wang, X., and Sun, Z. (2019). High-precision servo control of industrial robot driven by pmsm-dtc utilizing composite active vectors. *IEEE Access* 7, 7577–7587. doi:10.1109/access.2018.2890539

frontiers | Frontiers in Energy Research

TYPE Original Research
PUBLISHED 13 June 2024
DOI 10.3389/fenrg.2024.1387908

OPEN ACCESS

EDITED BY
Sudhakar Babu Thanikanti,
Chaitanya Bharathi Institute of Technology, India

REVIEWED BY
T. Yuvaraj,
Chennai Institute of Technology, India
Ali Q. Al-shetwi,
Fahd bin Sultan University, Saudi Arabia
P. Balamurugan,
Loyola Institute of Technology, India

*CORRESPONDENCE
Enrico De Tuglie,
enricoelio.detuglie@poliba.it

RECEIVED 18 February 2024
ACCEPTED 29 April 2024
PUBLISHED 13 June 2024

CITATION
Brahmendra Kumar GV, Palanisamy K and De Tuglie E (2024), Ramp-rate control for power quality improvement of renewable grid-integrated microgrid with hybrid energy storage system.
Front. Energy Res. 12:1387908.
doi: 10.3389/fenrg.2024.1387908

Ramp-rate control for power quality improvement of renewable grid-integrated microgrid with hybrid energy storage system

G. V. Brahmendra Kumar[1], K. Palanisamy[1] and Enrico De Tuglie[2]*

[1]School of Electrical Engineering, Vellore Institute of Technology, Vellore, India, [2]Department of Electrical Information Engineering, Polytechnic University of Bari, Bari, Italy

This paper demonstrates an enhancement of power quality for a photovoltaic (PV) system connected to the grid with a hybrid energy storage system (HESS). The proposed system utilizes a ramp-rate control (RRC) strategy to limit severe fluctuations in the PV power output. Battery storage is integrated to store surplus energy generated by the PV system and is used for continuous power application. A high-power density device, known as a supercapacitor (SC), is employed to mitigate transient fluctuations in the battery. The proposed system facilitates smooth PV power generation, stabilizes the DC bus voltage (V_{DC}), and eliminates source current harmonics induced by non-linear loads. The Shunt Active Power Filter (SAPF) discussed in this paper serves two primary purposes. Firstly, it acts as a reactive power buffer, smoothing out fluctuations and reducing current harmonic distortions. Secondly, it enables active power injection into the grid, utilizing a specific renewable solar PV source. The efficiency of the modeled compensation system is demonstrated by the sinusoidal shape of the current and the compensation of reactive power (RPC). The targeted system showcases the effectiveness of the current setup by exhibiting low total harmonic distortion (THD). The multifunctional features of the proposed system were implemented using the MATLAB/Simulink software, and the results were validated using an OP5700 Hardware-in-the-Loop (HIL) test bench. This integration of distributed power generation capabilities not only enhances the overall power quality but also improves the efficient utilization of renewable energy resources (RESs).

KEYWORDS

PV system, hybrid energy storage system, ramp-rate control, shunt active power filter, harmonics, power quality

1 Introduction

Renewable energy is a rapidly growing part of electricity generation because it is non-polluting and environmentally friendly. There is a global trend toward this energy source (Brahmendra Kumar and Palanisamy, 2019; Kumar and Palanisamy, 2023). Such electricity is used locally through conventional means, which are often not used if the local load is not strengthened. Integration of distributed RESs has recently gained interest in research due to the significance of the integration practices, particularly in terms of the impact on electrical power networks. Multiple DG sources can be linked together using the microgrid (MG). A MG is formed by the interconnection of distribution resources, ESSs, and loads. Distributed

generation (DG) systems have the potential to improve distribution, but they also pose some risks, such as power imbalance, voltage variation, and so on. Conventional solar power utilization makes use of stand-alone PV systems, which supply energy directly. In grid-connected renewable systems, power is injected into the grid using Voltage Source Converter (VSCs) and a DC–DC converter. The renewable integration methods face problems in addition to unused power generated during the absence/reduction of load (Khan et al., 2022). The efficiency of RE will be impaired due to their high initial costs and seasonality. In order to resolve this problem, RESs interface power converters can be designed for multiple operations, such as correcting the system power factor, suppressing voltage fluctuations, and reducing current harmonics (Kumar et al., 2019; Kumar et al., 2021). When integrating RESs with the electric grid, the interface device between the sources and the grid plays a critical role as it can generate harmonic components that affect power quality (Panigrahi and Subudhi, 2017). To address this issue and optimize the utilization of RESs, a VSI can be constructed to inject active power from the RES along with ESS. HESSs are indispensable in modern MGs due to the intermittent and fluctuating nature of RESs and loads. In modern MGs, these HESS components are necessary for managing the intermittent behavior of RESs and loads. It also contributes to enhancing the power quality of the grid (Jasim et al., 2023).

The use of non-linear power electronic-based loads and switch mode power supplies has become more popular in present years. Consequently, the quality of delivered power has been negatively affected, leading to harmonic contamination and reactive power components that require compensation. Filters are increasingly being employed to mitigate harmonics and reactive power effects (Tareen and Mekhielf, 2018). The most common method of compensating for existing harmonics and reactive power is the use of passive filters, which are less expensive (Alfaris and Bhattacharya, 2019). The primary issue affecting power quality is the harmonic current and voltage profile. To address these concerns, the most commonly utilized device is an active power filter (APF) for shunt compensation. In (Kuznetsov et al., 2022; Wang et al., 2022), these authors propose a method based on a shunt APF that simultaneously addresses issues such as power factor, current imbalance, and current harmonics. If the PV system is associated to the grid, surplus energy can be fed into the grid once the maximum demand has been met. Consequently, when demand surpasses supply, extra energy is drawn from the grid. Therefore, PV energy functions as an additional power source (Parchure et al., 2017).

The use of sensitive electronic circuits in industries and homes, combined with the challenges posed by privatization and electric power systems, constitutes one of the major difficulties in the electrical industry. Harmonics lead to source voltage distortion and energy loss resulting from undesired current flow into the source. They can also lead to the failure of relays, switches, and other components. Therefore, various techniques must be available to mitigate harmonic effects (Devassy and Singh, 2019). The shunt APF generates equal magnitude and phase opposite harmonics of non-linear loads to cancel out the harmonic currents within the system. It is the most well-known method and is equipped with power electronic devices that have a fast response time and operate with flexibility. In (Beniwal et al., 2018), a shunt APF is used to control and operate a PV-battery-grid-connected system. The major drawback of the system is that sudden changes in load or source can stress the battery. Hence, the SC device is used to remove transient fluctuation in battery current, thereby extending the battery lifetime (Kumar and Palanisamy, 2020).

The control methods proposed in (Devassy and Singh, 2018; Zahedmanesh et al., 2020; Ray et al., 2022; Patel et al., 2023) pertain to the integration of shunt APF with solar PV. These methods offer many advantages, such as improving grid power quality and securing the grid-side disturbances of critical loads. However, they do not include ESS support for fluctuating PV power. Nonetheless, the combination of batteries and RESs allows systems to operate independently when the grid is unavailable and provides safe and continuous power to critical loads. The incorporation of the battery enables RES to supply stable power to the grid even when the PV array fluctuates (Saxena et al., 2017; Liang et al., 2023). However, the authors do not describe the operation and importance of the SC. The SC increases battery lifetime and system performance. Various active power topologies are combined with nonlinear loads to meet power quality requirements. Active filters with hybrid, series, and shunt topologies can provide flexible and high-quality offset for voltage and current distortions (Echalih et al., 2022). To improve the application of modern filtering methods, literature (Rahmani et al., 2015) suggests combining active filters with RESs such as wind and solar. Harmonic mitigation and the performance of APFs are critical to maintaining a constant DC link voltage (V_{DC}). Consequently, numerous control approaches are discussed in the literature (Benchouia et al., 2015).

A PV-based D-STATCOM utilizes the SRF theory to improve power quality in (Golla et al., 2023). It enables better control of RPC, reduces voltage fluctuations, and optimizes solar power utilization. To compensate for reactive power, reduce harmonic distortions, and obtain maximum power from the PV module, a single-phase grid associating PV with an integrated SAPF is proposed in (Sharma et al., 2022). In (Pradeep Reddy et al., 2022), the discussion of the UPQC integrated PV system highlights numerous advantages, including improved grid power quality, protection of critical loads from grid-side disruptions, and increased fault ride-through converter capability during transients. According to a literature review, PV integrated SAPF offers several advantages over traditional methods, such as harmonic removal, stable V_{DC}, and RPC.

The above-mentioned papers discuss power quality improvement in a renewable-grid integrated system based on the shunt APF capability. However, no control methods are discussed to mitigate changes in fluctuating PV power. Consequently, the size and cost of the ESS can increase. Additionally, sudden changes in the battery system can reduce the battery's lifetime. The proposed work presented by the SC aims to mitigate sudden variations in the battery and thus increase the battery's lifetime.

Figure 1 depicts a shunt-connected PV converter with a non-linear load that can operate in both shunt APF mode and real power injection mode. The SAPF is to be associated in parallel with the non-linear load, and the distribution network is to be linked to the point of common coupling (PCC). The output voltage value of the PV system can be adjusted using a DC/DC converter, and the p-q theory is employed to compute the current reference of the shunt

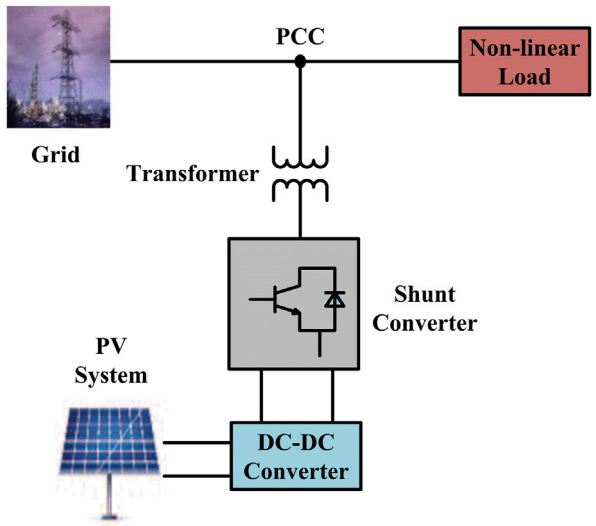

FIGURE 1
Shunt converter fed with a PV system.

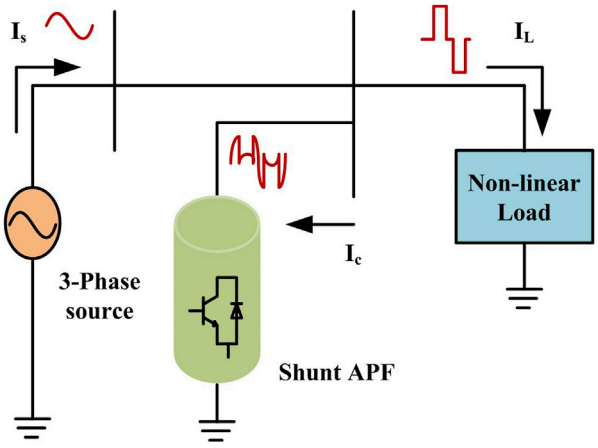

FIGURE 2
Model circuit for shunt APF.

APF. Furthermore, the inverter is utilized as an APF to compensate for reactive power and non-linear load harmonics (Abdullah et al., 2016). The PV interactive shunt APF system performs all of its functions during the day in intense sunlight. Power is required by the load at night, which is obtained from the distribution network when there is no sunlight. In contrast, the inverter system provides RPC, and harmonic currents are filtered (Dashtdar et al., 2022). The key contributions of this work are as follows:

- The shunt APF in this paper provides a reactive power buffer and eliminates current harmonic distortions. Additionally, it also injects active power into the grid from a given renewable solar PV source. It incorporates distributed power generation functionality while also improving power quality.
- The system remains stable under various circumstances, including changes in irradiation and load variations. Consequently, the V_{DC} is maintained at a constant level even with sudden changes in load.
- The performance of the solar PV system is affected by insolation, time of the day, and temperature. System reliability is increased by the RRC, which mitigates PV power fluctuations.
- The battery-based ESS (BESS) is incorporated to provide continuous power flow into the system. The battery system is stressed as a result of the abrupt changes in battery power. Hence, the SC is used to respond to transients in the battery system.
- The combination of battery and SC devices improves the functionality of a grid-integrated system. The PV-HESS-grid network system has an inherent shunt APF capability and maintains the grid voltage and current THD within the IEEE-519 standard limits.

This paper is structured as follows: Section 2 outlines the methodology, which includes subsections on the configuration of the SAPF with a PV system, the configuration of the proposed method, and the control scheme of the proposed system. In Section 3, the results and discussion are provided, along with the implementation of the Hardware-in-the-Loop (HIL) system. The simulation and HIL experimental test-bench results of the proposed control scheme, both with and without a controller, are also presented in this section. Finally, Section 4 contains the conclusions.

2 Methodology

2.1 Shunt APF configuration

A shunt APF is a converter that combines the switching network as well as the filter components. Figure 2 depicts the model circuit for the shunt APF configuration. The high-frequency switch power converter is generally used to control the desired current flow between the DC side and the AC side. The power converter incorporates semiconductor switches as well as storage devices. The typical power converter is basically a VSI, which is low in cost, low in loss, and easy to implement (Fabricio et al., 2018; Kumar and Bansal, 2019). The power filter's structure is based on the VSI control technique, which includes a DC-storage capacitor and the connection of the inverter output to the non-linear load. The anti-parallel diodes are connected to the IGBTs in each of the switches to allow the flow of current in either direction.

The current control scheme is used to control the power flow in the VSI. To transfer active power from RES to the grid and loads, a current-controlled VSI is used. The AC side of the VSI is connected to the grid via the PCC and the DC side is connected to the PV via the HESS. The current-controlled VSI is used to shunt APF to enhance the power quality of the electrical system. The power converter is used to remove current harmonics and compensate for reactive power required by non-linear loads. As a result, grid currents become sinusoidal with a unity power factor. The shunt APF can detect the harmonic currents due to the non-linear load. Then it injects an equal magnitude current in the opposite direction (Hoon et al., 2018), called a compensation current (I_C). It decreases harmonics in load currents (I_L) caused by non-linear loads.

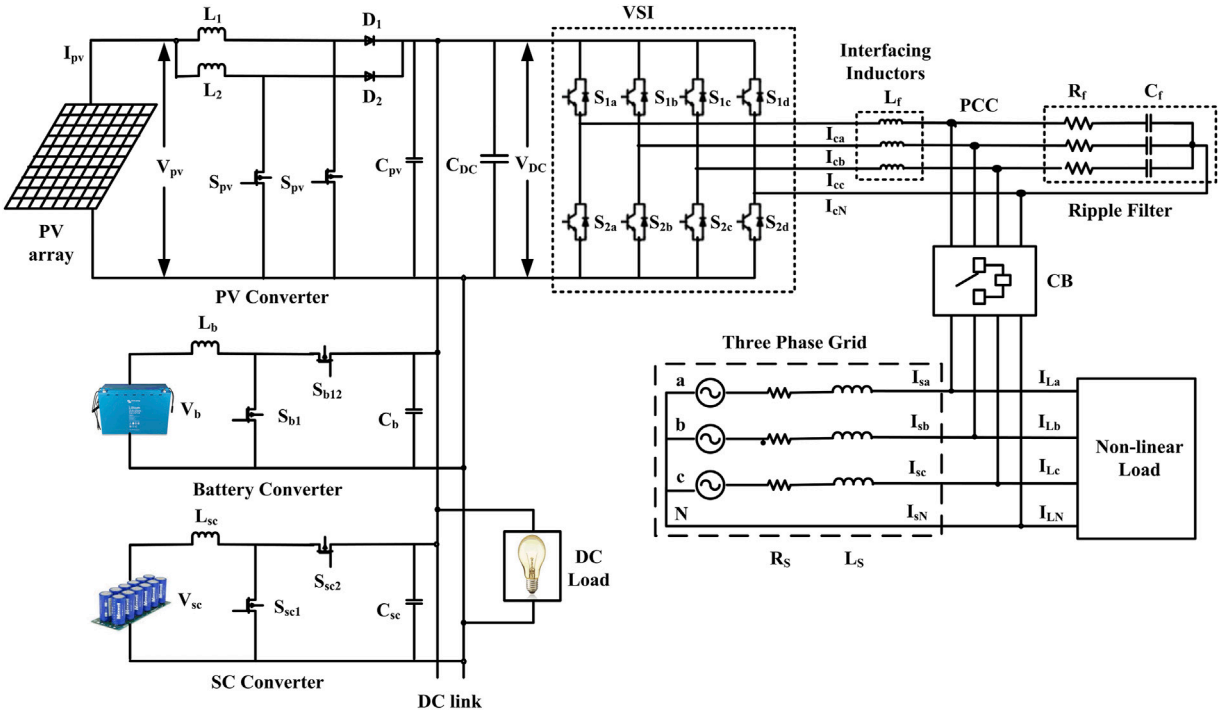

FIGURE 3
Configuration of a renewable-grid connected MG with HESS.

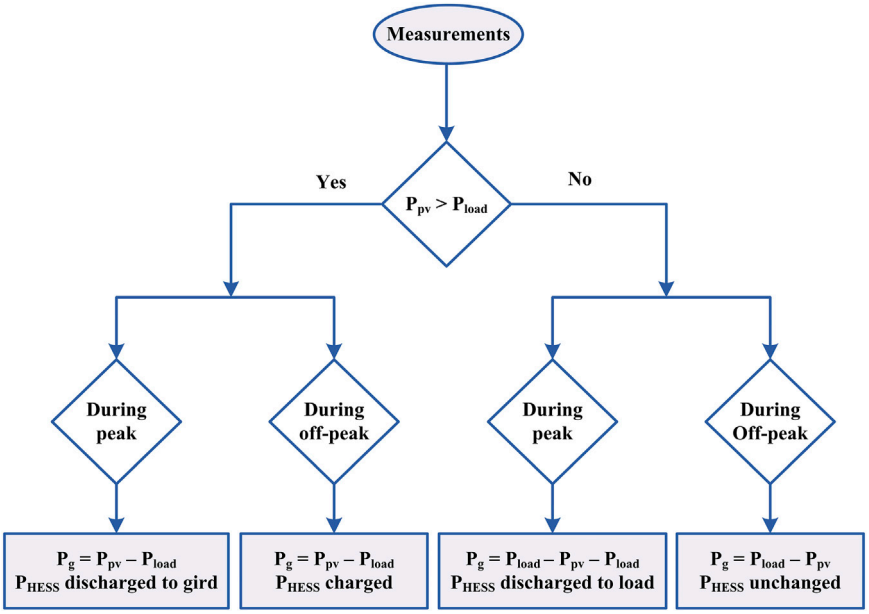

FIGURE 4
Power flow chart of a PV-HESS-grid connected system.

2.2 Configuration of the proposed system

The structure of the system consists of a PV system, BESS, SC, VSI, non-linear load, ripple filter, and DC-bus capacitor. The grid-connected PV system with a HESS configuration is shown in Figure 3. The PV-SAPF system is connected to a three-phase, four-wire power supply. It is designed and simulated for a three-phase grid-integrated PV system and with loads at the PCC. The proposed method aims to provide better compensation and a simpler structure while reducing the number of three-phase

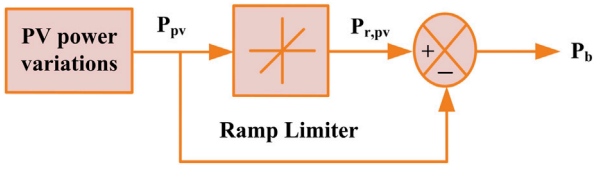

FIGURE 5
RRC block diagram.

power switching devices. The system must extract grid voltage and load current fundamentals.

On the DC grid side, a PV system is associated with an interleaved boost converter (IBC) to obtain peak power from the PV system, and HESS is utilized to balance average and transient power flow. The IBC is used in the system to minimize current ripples, conduction losses, and switch voltage stress. Hence, the system efficiency is improved by saving energy (Kumar and Palanisamy, 2019; Kumar et al., 2020). The BESS and SC are linked to the DC bus with bi-directional converters. Renewable power/load variations affect V_{DC} dynamics. As a result, the SC unit supports the transient power requisite at the DC link, while the battery and grid share average power. It regulates V_{DC} quickly. If the SC is not linked to the system, the battery/grid should supply or absorb the transient power. Consequently, V_{DC} requires longer time to stabilize. Hence, the SC control scheme is crucial for improving V_{DC} dynamics.

Nonlinear and unbalanced loads on the AC grid side are connected to assess the additional functionalities of the proposed scheme, including harmonic compensation, RPC, load balancing, and power factor correction in grid-connected mode. Power quality issues such as reactive power and harmonics from the load can be mitigated using a shunt compensator. The PV system is integrated with the SAPF system at the DC-link. In the PV-SAPF setup, the shunt compensator not only compensates for losses but also harnesses power from the solar PV

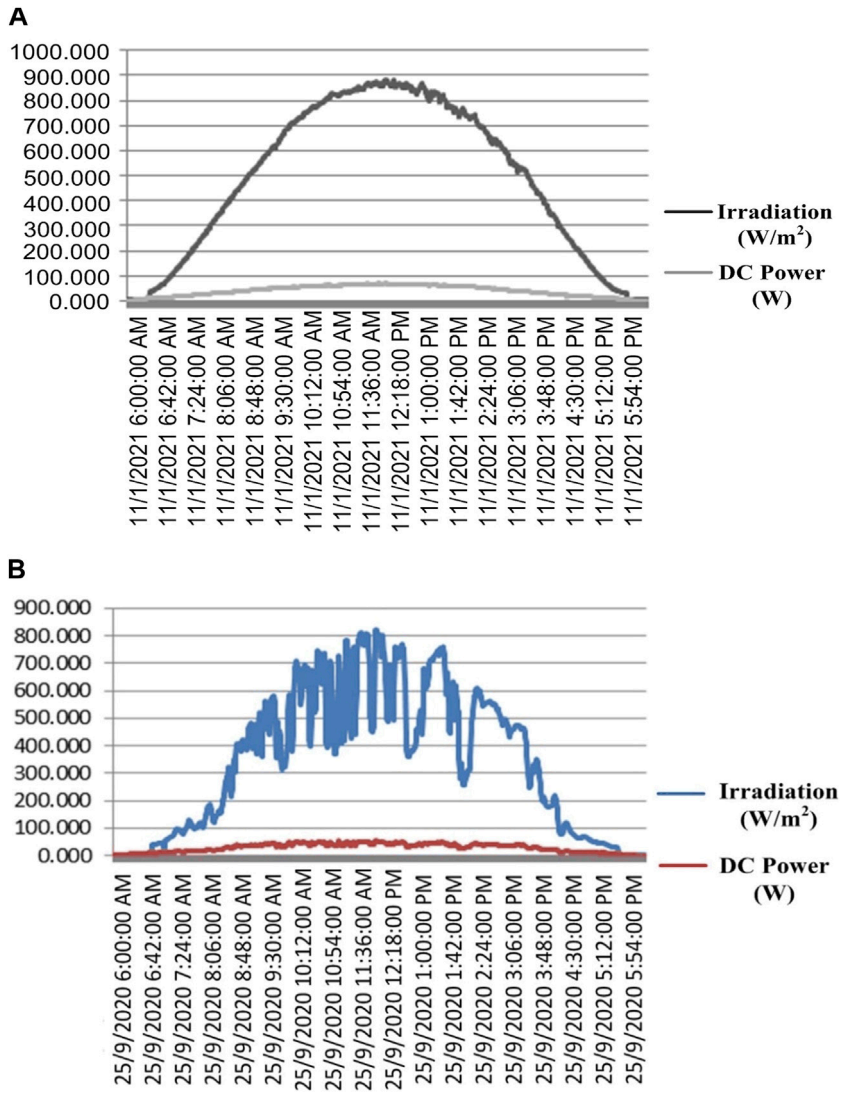

FIGURE 6
(A) Normal irradiation variations on a day, **(B)** Severe irradiation variations on a day.

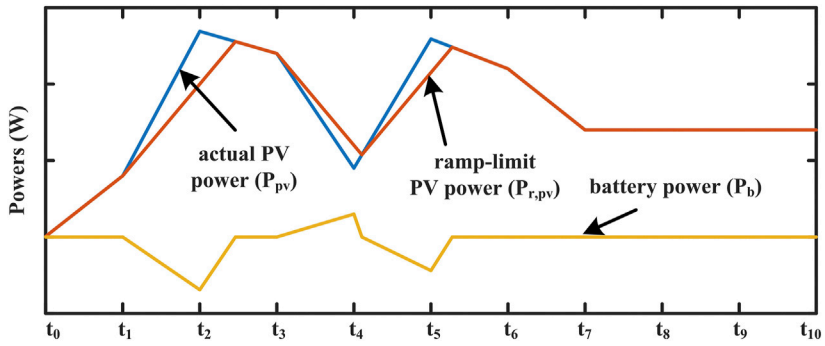

FIGURE 7
BESS characteristics using RRC.

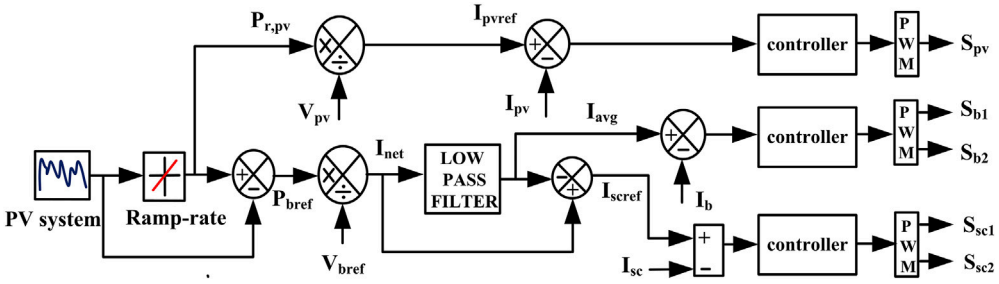

FIGURE 8
Control diagram for PV system with HESS.

array. Three nonlinear loads in each phase are simulated using an uncontrolled bridge rectifier with an R-L load. To minimize current and voltage fluctuations, interfacing inductors (L_f) and ripple filters (R_f, C_f) are utilized to connect to the PCC.

Solar PV array power production fluctuates with changes in the time of day, temperature, and insolation. To mitigate these variations, HESS are integrated into solar PV-grid-connected MG systems (Zahedmanesh et al., 2020; Patel et al., 2023). The HESS, connected to the DC link of a VSC through a bidirectional converter, proves highly effective. Figure 4 illustrates a power flow chart for a solar PV-HESS grid system. Excess power from the solar PV is directed to the grid after meeting the load requirements, and any surplus is used to charge the battery during off-peak load hours. During peak load times, both the PV and HESS contribute power to the grid. If the PV supply falls short of meeting the load demand, the HESS provides additional power during peak load times. Conversely, during off-peak load periods, the grid supplies power to the load. Furthermore, if the BESS reaches its maximum discharge limit, the grid must supply the load demand even during peak load hours.

2.3 Control scheme

2.3.1 PV power variations and ramp-rate control

Various system operators have distinct requirements regarding the connection of Renewable Energy Source (RES) power stations to the grid. Reference (Brahmendra Kumar et al., 2018) emphasizes the need for smoothing RES fluctuations and implementing ramp-rate limits for grid connection of the power plant. The RRC is employed to ensure the smooth solar output depicted in Figure 5.

There have been recorded normal and severe variations of up to 70% and 90%/min, shown in Figure 6A, B. Therefore, in order to smoothen the PV output power, compliance with these regulations includes the combination of PV generators with ESS technologies to add or subtract power to or from the PV supply. Figure 7 depicts abrupt decreases from full power to zero, which are obviously the maximum possible fluctuations. Power and energy storage capacity have simply been presented from a few rather direct and intuitive calculations regarding PV output profiles. An analytical theoretical model has been proposed and validated for this fluctuation scenario by comparing the related battery requirements with those obtained from detailed simulations using real power data.

The RRC sets the ramp-rate value, which increases the reliability of the grid and reduces power fluctuations (Gundumalla and Eswararao, 2018). The BESS power (P_b) is measured by the difference between the PV power (P_{pv}) and the ramp-limit power ($P_{r,pv}$). Figure 7 depicts the characteristics of BESS using RRC. The BESS is charged when the P_{pv} surpasses the ramp capacity. In addition, when the PV power falls below the power of the ramp, the BESS is discharged.

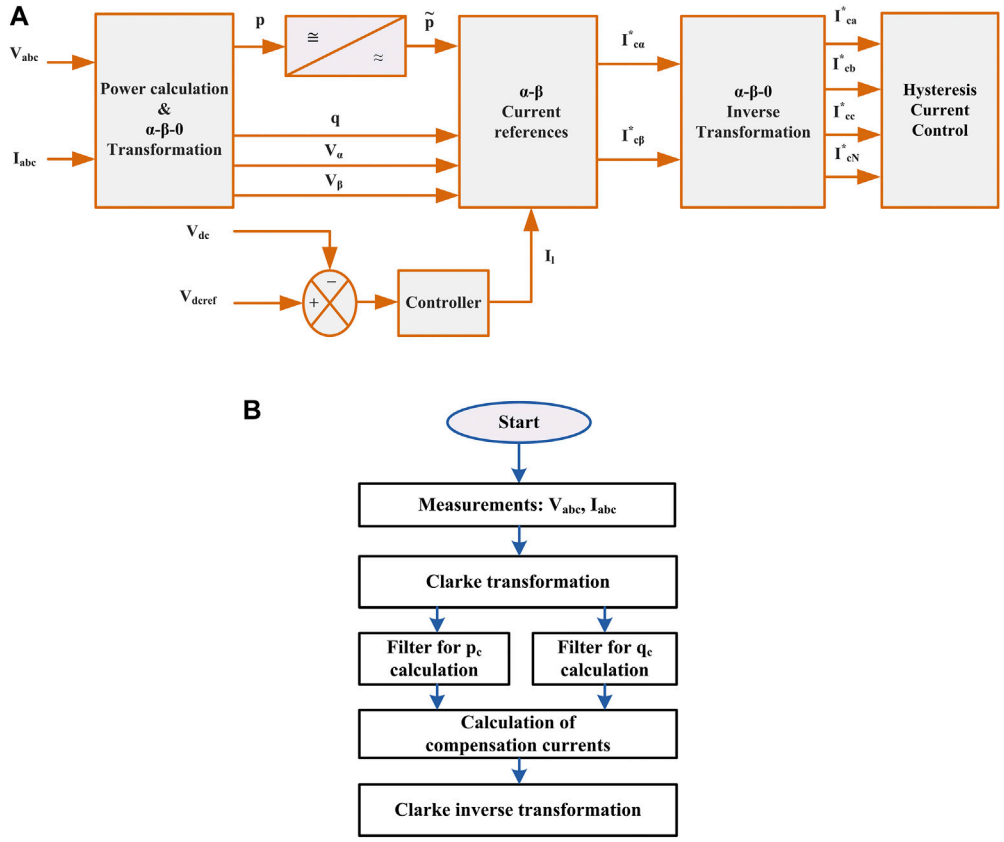

FIGURE 9
p-q method: **(A)** block diagram, **(B)** flow chart.

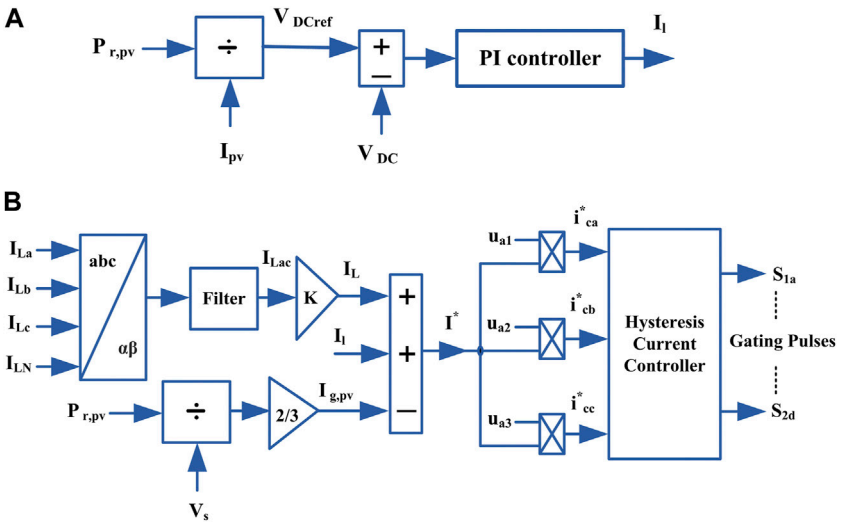

FIGURE 10
(A) Control diagram of loss current component **(B)** Control diagram for shunt APF.

2.3.2 Control structure of PV and HESS

Figure 8 illustrates the reference currents for the PV, battery, and SC. The PV reference current generation through the RRC. The PI current controller compares the PV reference current (I_{pvref}) with the IBC's actual current (I_{pv}), which is then passed to the PI controller to generate the signals. The reference current

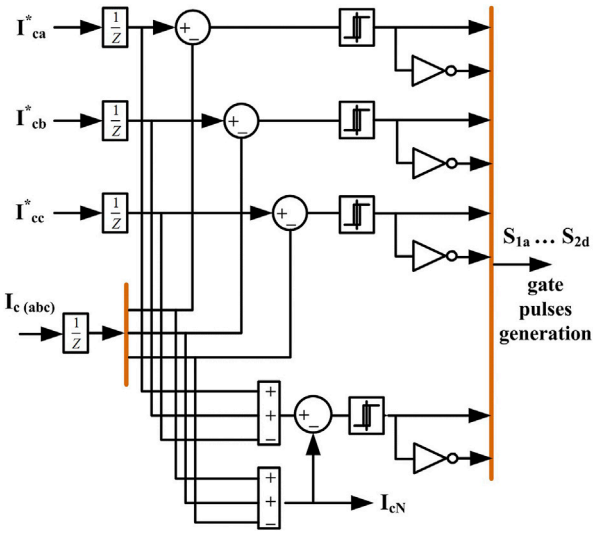

FIGURE 11
Hysteresis controller.

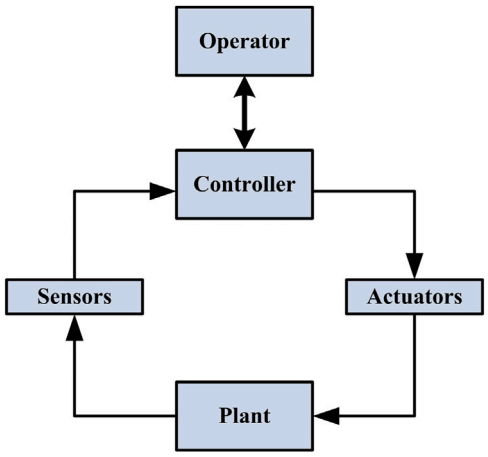

FIGURE 12
Control system block diagram.

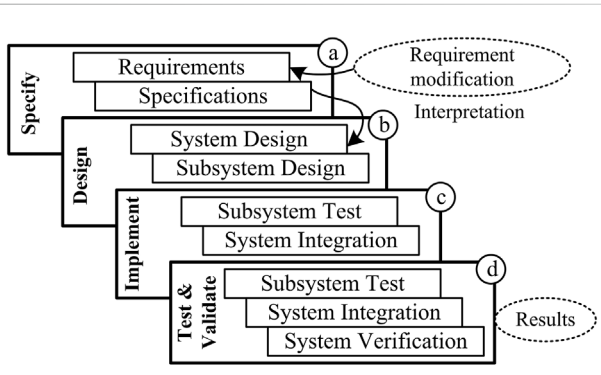

FIGURE 13
HIL design process.

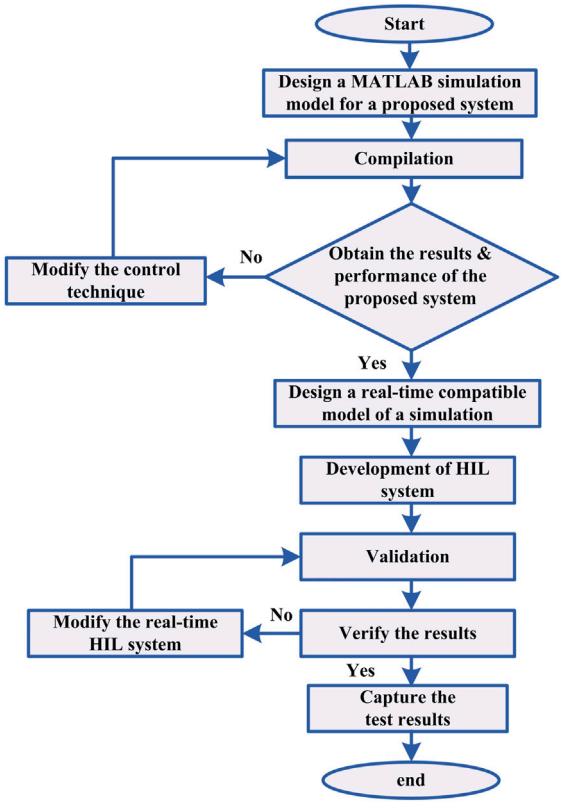

FIGURE 14
Flow chart of the proposed system operation using the HIL test-bench.

generation and LPF are used in the battery converter control. The low-pass filter (LPF) generates the battery net current (I_{net}), which is divided into the average value (I_{avg}) of net current for the battery and the transient component of current (I_{trs}) for the SC. The I_{avg} is calculated using the given Eq. 1 (Rauf and Khadkikar, 2015),

$$I_{avg}(t) = \left(\frac{1}{1 + s\tau_c}\right) i_{net}(t) \tag{1}$$

The modulating signal for the PV and battery converter are taken from the following Eqs 2, 3,

$$\delta_{pv} = K_{p,pv} i_{pv,e}(t) + \frac{K_{i,pv}}{T_{pv}} \int_{t-T_{pv}}^{t_0} i_{pv}(t)dt \tag{2}$$

$$\delta_b = K_{p,b} i_{b,e}(t) + \frac{K_{i,b}}{T_b} \int_{t-T_b}^{t_0} i_b(t)dt \tag{3}$$

As shown in Figure 8, the supercapacitor control loop consists of current control and reference current generation ($I_{sc,ref}$), and The reference current generation block extracts transient current component of I_{trs}. The SC reference current (I_{scref} or I_{trs}) is generated by the difference between (I_{net}) and (I_{avg}), as given below (Rauf and Khadkikar, 2015),

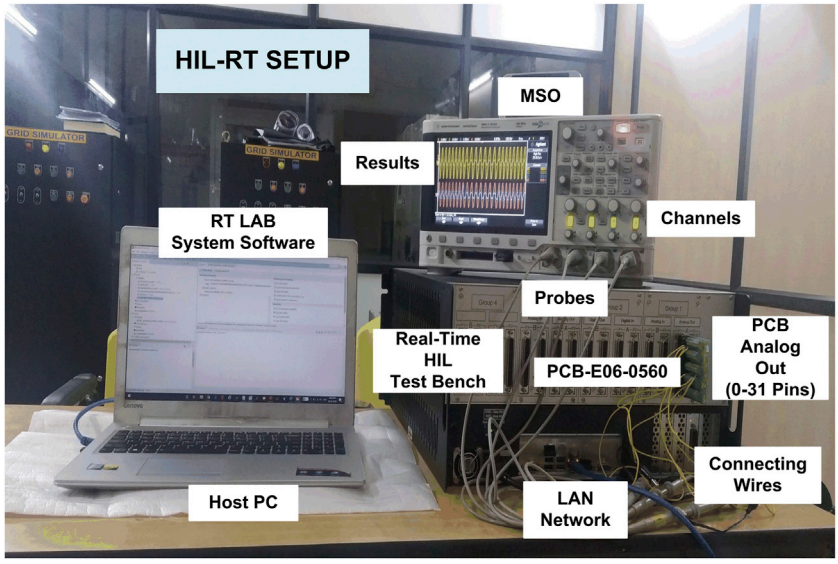

FIGURE 15
HIL experimental set-up.

$$I_{trs}(t) = \left(1 - \frac{1}{1 + s\tau_c}\right) i_{net}(t) \tag{4}$$

The control block uses the reference current derived in (4) and other input variables to determine the supercapacitor pack's operating mode. The current control loop uses the SC's reference current ($I_{sc,ref}$) to generate switching pulses. The following Eq. 5 can be used to derive the SC converter's modulating signal (δ_{sc}):

$$\delta_{sc} = K_{p,sc} i_{sc,e}(t) + \frac{K_{i,sc}}{T_{sc}} \int_{t-T_{sc}}^{t_0} i_{sc}(t)dt \tag{5}$$

Where K_p, K_i, t_o, $I_{b,e\ or\ sc,e}$, $T_{b\ or\ sc}$ are proportional and integral time constants, arbitrary time constant, battery or SC error current, and SC block average time window.

Accurate state of charge (SoC) calculations is crucial for battery-powered systems as they significantly impact battery performance. Precise SoC estimations not only safeguard the battery by preventing overcharging, but also extend its lifespan while enhancing overall system accuracy and energy efficiency (Saxena et al., 2017). The SoC is typically determined using the count-coulomb method, and the following Eq. 6 describes the SoC for the battery.

$$SoC_b = SoC_{bin} + \frac{1}{3600 C_{Nb}} \int i_b dt \tag{6}$$

Where SoC_{bin}, C_{Nb} and I_b represent the initial SoC, nominal capacitance, and current of the battery, respectively.

2.3.3 p-q theory-based control strategy

The instantaneous p-q theory is mainly based on instantaneous power measurements in the time domain. It primarily applies to a 3-phase 3-wire system or a 3-phase 4-wire system. It is evaluated on a time-domain basis. Therefore, it is suitable not only for stable conditions but also for transient conditions (Abdullah et al., 2016). In an instantaneous theory of real and reactive power, the p-q theory is primarily used in the design of controllers for active power filters, and power conditions based on power electronic devices (Barva and Arkdev, 2023). The p-q principle first transforms the voltages and currents linearly. Then it determines the instantaneous power in those coordinates from the abc-coordinate system to the 0αβ-coordinate system. Figure 9 displays the block diagram and flow chart of the p-q theory. The p-q theory is effective for designing active filter controllers as it converts voltage and current from abc to αβ0 coordinates, enabling the determination of instantaneous power.

The reference current is measured using the p-q methodology. By using the Clark transformation, the source voltages and load currents will be converted from abc coordinates to 0αβ coordinates in Eqs 7, 8 (Belaidi et al., 2013; Wategaonkar et al., 2018), respectively.

$$\begin{bmatrix} V_0 \\ V_\alpha \\ V_\beta \end{bmatrix} = \sqrt{\frac{2}{3}} \begin{pmatrix} 1/\sqrt{2} & 1/\sqrt{2} & 1/\sqrt{2} \\ 1 & -1/2 & 1/2 \\ 0 & \sqrt{3}/2 & -\sqrt{3}/2 \end{pmatrix} \begin{bmatrix} V_{sa} \\ V_{sb} \\ V_{sc} \end{bmatrix} \tag{7}$$

$$\begin{bmatrix} I_0 \\ I_\alpha \\ I_\beta \end{bmatrix} = \sqrt{\frac{2}{3}} \begin{pmatrix} 1/\sqrt{2} & 1/\sqrt{2} & 1/\sqrt{2} \\ 1 & -1/2 & 1/2 \\ 0 & \sqrt{3}/2 & -\sqrt{3}/2 \end{pmatrix} \begin{bmatrix} I_{La} \\ I_{Lb} \\ I_{Lc} \end{bmatrix} \tag{8}$$

The matrix format can be used to represent instantaneous active/real and reactive/imaginary powers in the following Eq. 9.

$$\begin{bmatrix} p \\ q \end{bmatrix} = \begin{pmatrix} V_\alpha & V_\beta \\ V_\beta & -V_\alpha \end{pmatrix} \begin{bmatrix} I_\alpha \\ I_\beta \end{bmatrix} \tag{9}$$

The active (p) and reactive (q) instantaneous powers, which includes AC and DC values referring to the fundamental and harmonic currents, are given by Eqs 10, 11 (Wategaonkar et al., 2018),

$$p = \bar{p} + \tilde{p} \tag{10}$$

$$q = \bar{q} + \tilde{q} \tag{11}$$

TABLE 1 System parameters.

PV parameters	Values
Irradiance	1,000 (W/m^2)
Cell temperature (T)	25^0 C
Series connected modules	12
Parallel connected modules	12
Open circuit voltage (V_{oc})	64.2 V
Short circuit current (I_{sc})	5.96 A
MPP Voltage (V_{mp})	58.3 V
MPP Current (I_{mp})	5.48 A
Battery Pack Specifications	Values
Type	Li-ion
Capacity	12 Ah
Terminal voltage (V_b)	48 V
No. of batteries in series	16
SC Pack Specifications	Values
Rated Capacitance	58 F
Terminal voltage (V_{sc})	16 V
Converter parameters	Values
PV system	$L_1 = L_2 = 10$ mH, $C_{pv} = 220$ uF
Battery device	$L_b = 10$ mH, $C_b = 220$ uF
SC device	$L_{sc} = 10$ mH, $C_{sc} = 220$ uF
Grid System Parameters	Values
Phase-Phase Voltage ($V_{ph\text{-}ph}$)	415 V
Type of system	3-Phase, 4-wire
Frequency (f)	50 Hz
Source Resistance (R_S)	0.04 Ω
Source Inductance (L_S)	0.2 mH
Load Resistance/phase (R_L)	5 Ω
Load Inductance/phase (L_L)	10 mH
Shunt APF Interfacing Inductor (L_f)	1 mH
Ripple filter Resistance (R_f)	10 Ω
Ripple filter Capacitance (C_f)	10 μF
DC link capacitance (C_{DC})	7.1 mF
DC link voltage (V_{DC})	700 V

Where $\bar{p}$ and $\bar{q}$ of DC are obtained from the load current positive-sequence components and the $\tilde{p}$ and $\tilde{q}$ of AC values are obtained from the load current harmonics components. The real and imaginary powers divided into average and oscillating power helps calculate compensating power for compensation current. The inverse of the matrix is calculated using Eq. 7 as follows (Wategaonkar et al., 2018),

$$\begin{bmatrix} I_\alpha \\ I_\beta \end{bmatrix} = \frac{1}{V_\alpha^2 + V_\beta^2} \begin{pmatrix} V_\alpha & V_\beta \\ V_\beta & -V_\alpha \end{pmatrix} \begin{bmatrix} \tilde{p} \\ \tilde{q} \end{bmatrix} \tag{12}$$

The compensation currents obtained in Eqs 13, 14 in abc coordinates using Eqs 8, 12 are as follows (Wategaonkar et al., 2018),

$$\begin{bmatrix} I_{ca}^* \\ I_{cb}^* \\ I_{cc}^* \end{bmatrix} = \sqrt{\frac{2}{3}} \begin{pmatrix} 1/\sqrt{2} & 1 & 0 \\ 1/\sqrt{2} & -1/2 & \sqrt{3}/2 \\ 1/\sqrt{2} & -1/2 & \sqrt{3}/2 \end{pmatrix} \begin{bmatrix} I_\alpha \\ I_\beta \end{bmatrix} \tag{13}$$

$$I_{cN} = I_{ca} + I_{cb} + I_{cc} \tag{14}$$

I_{CN} is a combination of three 3-phase compensation currents. The voltage control loop provides a basic proportional-integral (PI) function. The PI control is aimed at maintaining the V_{DC} at the reference voltage (V_{DCref}) level and providing the magnitude of the reference current signals (I_l). The active power in this loop is kept balanced between the grid, load, and DC bus of the VSI. If there is a power imbalance in the network, a voltage deviation of the reference voltage is present at the DC bus. The voltage control loop appropriately adjusts the grid active current amplitude and retrieves the V_{DC} according to the V_{DCref} level. To keep the DC voltage from changing and to keep it at a constant value with a fixed reference value, an extra flow of energy to and from the capacitor is needed. The surplus real power is denoted as P_l and is incorporated to compensate for real power (p), which is subsequently forwarded to the current reference calculation block along with compensating reactive power (q).

2.3.4 Control structure of a shunt compensation

The control method for SAPF is depicted in Figure 10A, B, where the shunt APF reference is required grid current which must be sinusoidal and UPF. The active fundamental component is extracted by the shunt compensator in order to compensate load current. The shunt compensator operates by extracting the active component of the load current.

The active current injected into the grid (I*) is calculated as Eq. 15,

$$I^* = I_L + I_l - I_{g,pv} \tag{15}$$

Where I_L is the load active current component, I_l is the loss current component due to switching, conduction, filter, and inductor losses, and $I_{g,pv}$ is the grid current corresponds to the ramp-limited PV power. The Eqs 16, 17 represent the equivalent grid current for load active power.

$$I_L = K \times I_{Lac} \tag{16}$$

$$K = \frac{V_L^*}{V_s} \tag{17}$$

Where V^*_L, V_s are the reference load voltage and PCC voltage magnitudes.

The $I_{g,pv}$ is taken from the Eq. 18 below,

$$I_{g,pv} = \frac{2}{3} \frac{P_{r,pv}}{V_s} \tag{18}$$

The DC-link voltage (V_{DC}) and capacitance (C_{DC}) are calculated based on the following Eqs 19, 20,

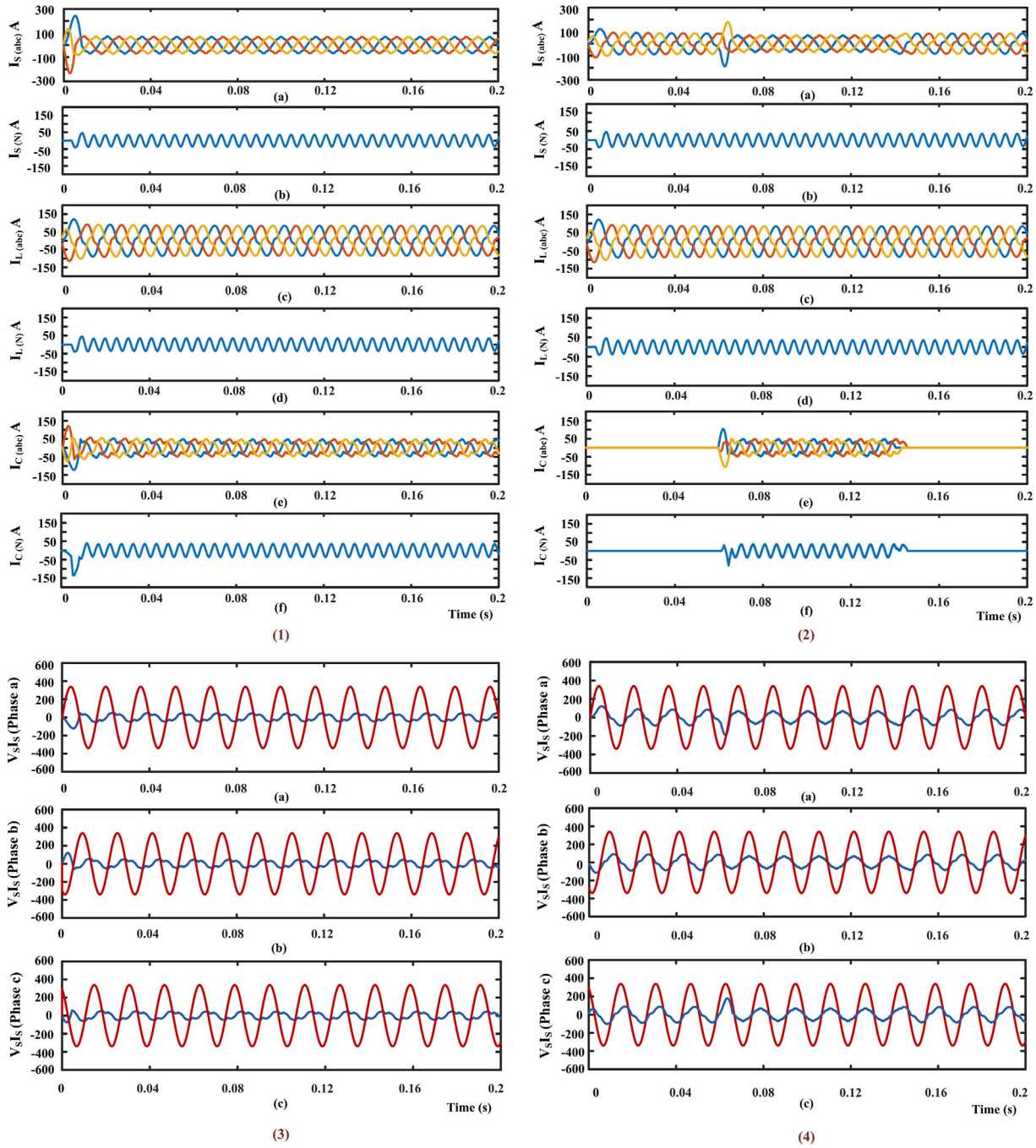

FIGURE 16
Simulation results.

$$V_{DC} = \frac{2\sqrt{2}V_{LL}}{\sqrt{3}m} \tag{19}$$

$$C_{DC} = \frac{3kaV_{ph}I_{sh}t}{0.5 \times \left(V_{DCref}^2 - V_{DC}^2\right)} \tag{20}$$

Where "m" is the modulation index, "k" is a dynamic energy change factor, denote '*a*' as the overloading factor, 'V_{ph}' as the per-phase voltage, 't' as the minimum time required to achieve steady state following a disturbance, and 'I_{sh}' as the shunt-compensator current per phase. The size of the C_{DC} is determined by the power demand and the V_{DC}.

The shunt compensator inductor rating relies on ripple current, switching frequency (f_{sw}), and V_{DC}. The equation of the interfacing inductor (L_f) is given in Eq. 21,

$$L_f = \frac{\sqrt{3}V_{DC}}{12af_{sw}I_{L,r}} \tag{21}$$

Where $I_{L,r}$ is ripple current of the inductor (5%–20% of $I_{sh,rms}$). The instantaneous reference currents in Figure 11 are derived by multiplying the magnitude reference of the SAPF with the unit templates of the PCC voltage. The current control references in Figures 9, 10 are generated in

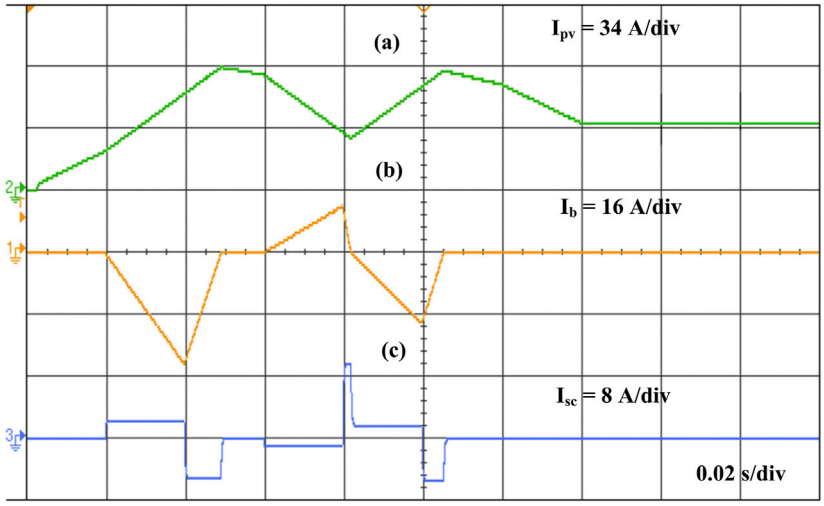

FIGURE 17
(a) Variable PV current (I_{pv}), (b) Battery current (I_b), (c) SC current (I_{sc}).

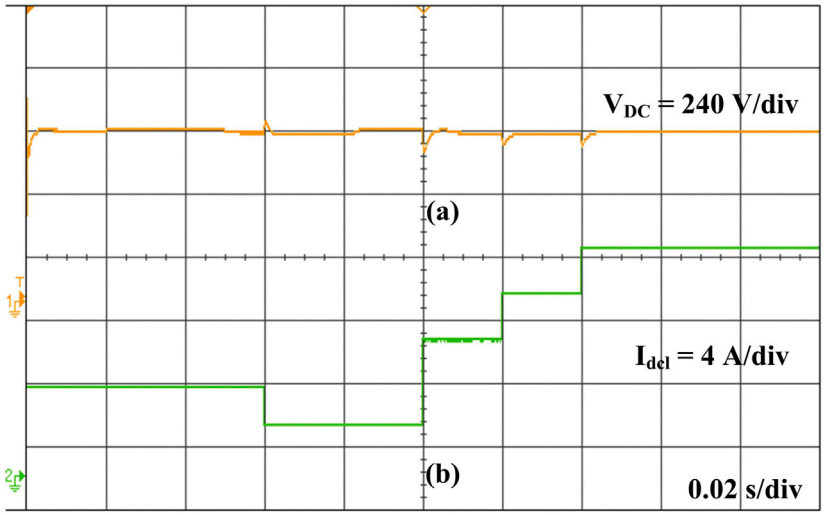

FIGURE 18
(a) DC bus voltage (V_{DC}), (b) Load current (I_{dcl}).

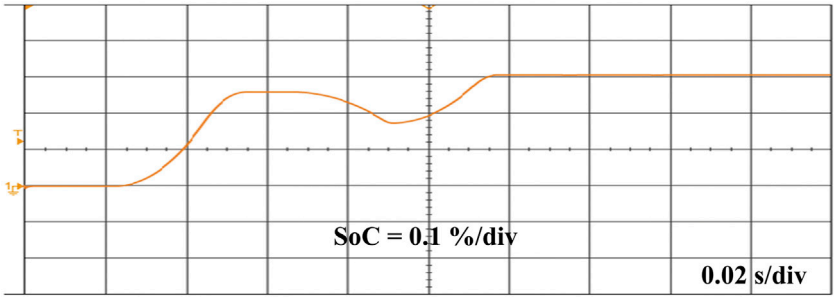

FIGURE 19
SoC of the battery.

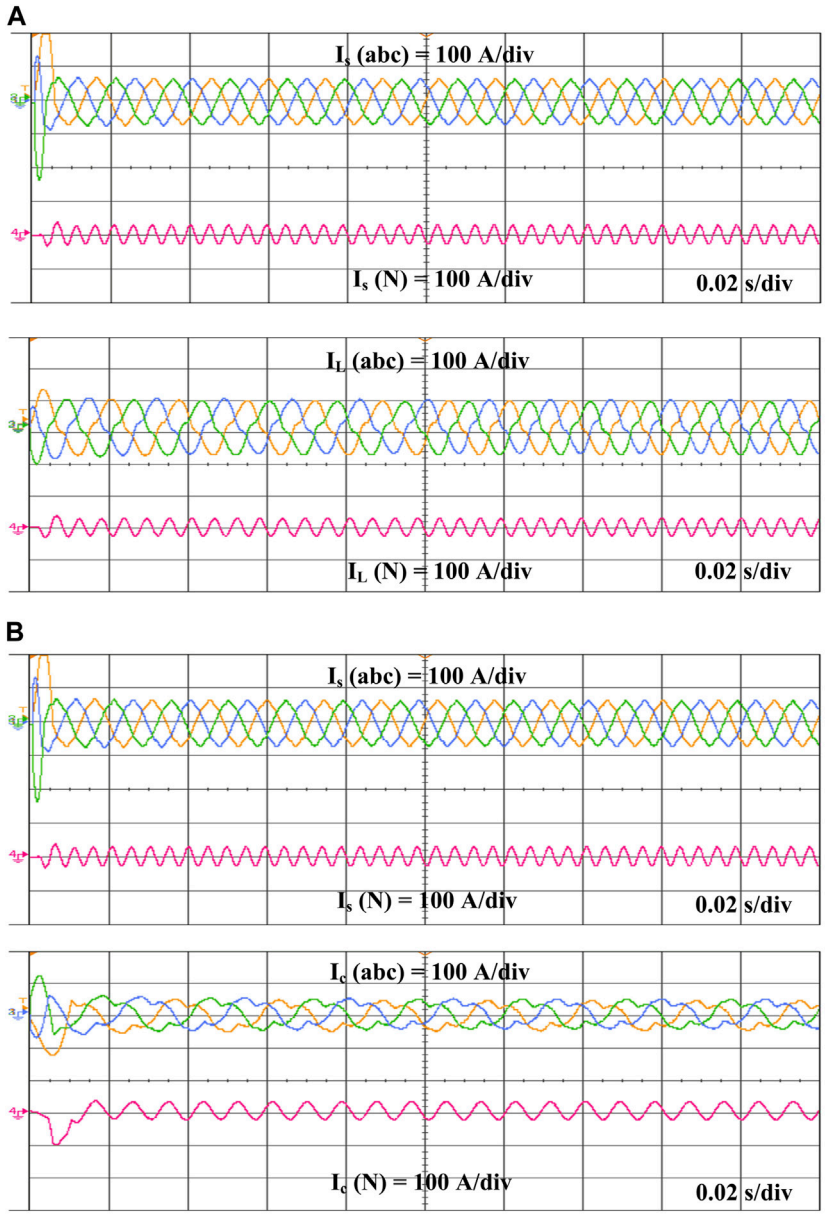

FIGURE 20
(A) Source $I_S(abc)$, load $I_L(abc)$ currents, and **(B)** Source $I_S(abc)$ and compensation $I_c(abc)$ currents.

the proposed model using the p-q theory computational block and the hysteresis current controller block. This method is stable, fast, accurate, and limits peak current. To regulate the shunt compensator, the error between (i^*_{ca}, i^*_{cb}, i^*_{cc}) and (i_{ca}, i_{cb}, i_{cc}) is passed to the controller, which produces gate pulses. The generated gate pulses from the hysteresis controller are fed to the inverter.

3 Results and discussion

3.1 HIL implementation

HIL systems are widely employed in engineering applications for conducting real-time simulation tests prior to pre-prototyping. Engineers utilise RT simulations for power electronics and motor drives as a phase in the design process, either to simulate the entire system in RT, or to connect a portion of the system to the rest of the system in what is generally referred to as a "HIL" application.

3.2 Control of HIL system

For a power electronics control system, the plant (power source, converter, and load) is typically made up of a controller and the power circuit (Figure 12). In closed-loop systems, sensors and actuators play a vital role by transmitting feedback signals from the plant to the controller and by regulating the signals transferred

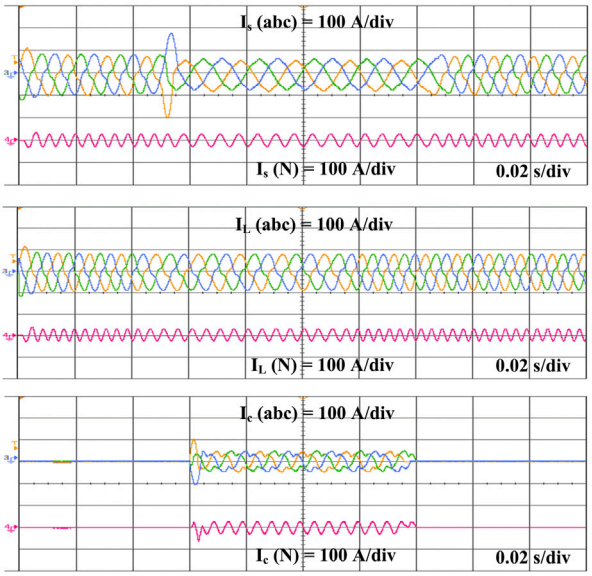

FIGURE 21
Source $I_S(abc)$, load $I_L(abc)$, and compensation $I_C(abc)$ currents using a p-q based controller.

from the controller to the power switches (such as the firing pulse unit and gate drives).

3.3 Design process of HIL system setup

The design process for most engineering projects, including power electronics, consists of four steps: requirements and specifications, design, execution, and validation.

First, text-based documentation communicates and manages design information. Text-based documentation is hard to understand and prone to interpretation errors (Figure 13A).

In a typical project, design needs may vary due to addition or modification (Figure 13B). This requirement change would require new development and verification, and the following iterative loop is inadequate and often affects development and testing times.

Developing code manually from specification and requirements documents is time-consuming and prone to implementation problems (Figure 13C). The system changes are tracked to assure their implementation.

Finally, in this design process, obtaining a system result during initial stages is challenging (Figure 13D). Design and requirements problems are identified late in the design cycle, causing delays in the process, and adversely affecting the project.

The laboratory is equipped with OPAL-RT stacks on the HIL test bench, and its flow chart and experimental setup are shown in Figures 14, 15. Stacks can swiftly construct prototypes and hardware synchronization quickly. In the RT-LAB environment, the plant and controller are configured within OPAL-RT system to operate at physical clock time. The rapid Nano-to-microsecond sampling rate of OPAL-RT constitutes a real-time dynamic system. The OP5700 HIL test bench, RT-LAB system software, MSOX3014A, PCBE06-0560 control board, probes, and connecting wires are used to validate the simulated results. The user's PC manages the RT-LAB Digital Simulation (RTDS) commands. The model is modified, built, loaded, and executed using the RT-LAB application.

3.4 System parameters

The PV, battery, and SC parameters are presented in Table 1. The system comprises a three-phase AC source voltage rated at

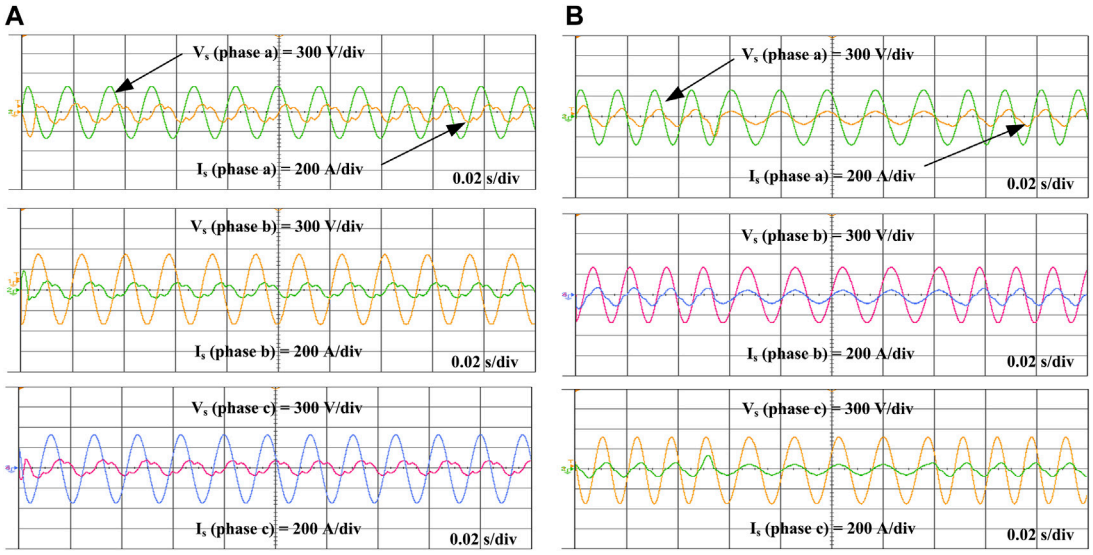

FIGURE 22
(A) Source voltage ($V_S(abc)$) and current ($I_S(abc)$) waveforms with non-linear load, **(B)** Source voltage ($V_S(abc)$) and current ($I_S(abc)$ waveforms after compensation.

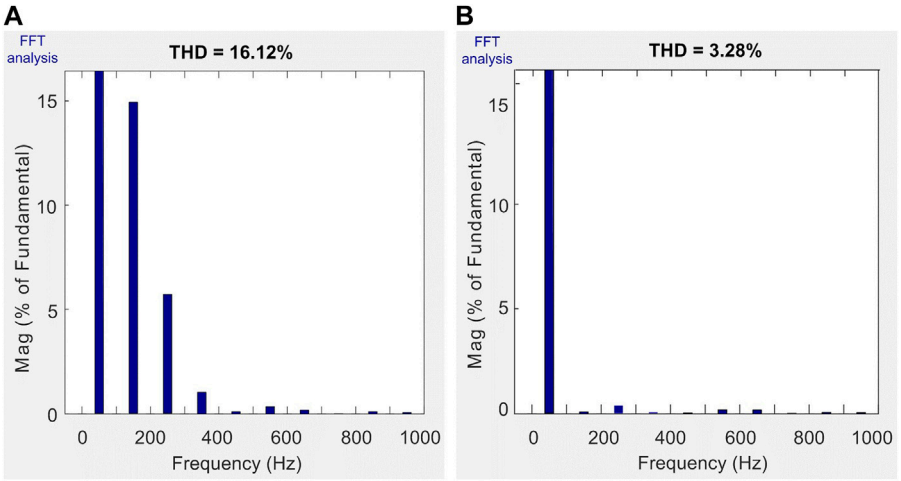

FIGURE 23
(A) I_L (phase-a) harmonics, **(B)** I_g (phase-a) harmonics.

415 V with a frequency of 50 Hz, along with non-linear load resistance and inductance parameters of 5 Ω and 10 mH. The minimum required V_{DC} is 677.7 V for a line voltage of 415 V. The V_{DC} is set at approx. 700 V.

3.5 Simulation results

The SAPF performance is verified using MATLAB-based Simulink and simulation results are depicted in Figure 16. Three-phase 415 V and 50 Hz are considered. The SAPF is linked to the load via three-phase circuit breaker (CB) that is initially open, and the results are presented in Figure 16.1. The SAPF connects to a non-linear load and uses a diode rectifier to test its performance. The nonlinear voltage and current results are presented in Figure 16.3. SAPF performance is analysed in nonlinear and unbalanced conditions through THD performance.

3.6 HIL experimental set-up results

The RRC is presented in this system to control the PV power fluctuations, and the battery power is obtained based on the difference between P_{pv} and P_r. The variable PV current and battery current profiles are presented in Figures 17A, B. The BESS in a steady state gives/takes the fraction of deficit/surplus power, and the SC absorbs the transient change in PV and load power. Whenever the battery experiences an abrupt change, the battery current undergoes a significant increase or decrease. If the battery responds to these sudden changes, it will create stress on the battery. Hence, the lifetime of the battery will be reduced. As shown in Figure 17C, the SC eliminates transients from the battery and reduce stress on the battery. The load current required for the variable DC load is shown in Figure 18B. The V_{DC} is shown in Figure 18A. The DC grid voltage remains constant during sudden variations in load. The battery state of charge (SoC) is illustrated in Figure 19.

A 3-phase CB is connected to the p-q theory-based controller between the source and the VSI. The shunt APF with a PV array system when a controller is not present, and the CB is disconnected from the source is shown in Figure 20A, B. When the controller is removed from the device, the source current continues to follow the sinusoidal wave pattern. The availability of the neutral wire has led to a reduction in the amplitude of current flowing through the device.

Due to the non-linear nature of the load, harmonics occur between 0.06 and 0.14 s when the CB is closed, and the controller is connected to the device. The compensated current (I_c) produced by the p-q theory-based controller is shown in Figure 21. It injects current into sources that are similar in amplitude but opposite in phase to the reverse harmonics in the p-q theory-based system. It produces compensated currents that nullify the harmonics generated by the current source by comparing the source and load currents. The source current (I_{sabc}) is sinusoidal in Figure 21 for the time interval of 0.06–0.14 s. The AC source (I_s), compensation (I_c), and load (I_L) currents are depicted in Figure 21. The generated I_c balances the difference measured between the I_L and I_s associated with the PV system through a C_{DC}. The source voltage (V_s) and current (I_s) waveforms without a controller are not sinusoidal due to non-linear load harmonics presented in the system, as shown in Figure 22A. Figure 22B displays the source voltage (V_s) and current (I_s) waveforms, which are sinusoidal in nature during the interval from 0.06 to 0.14 s. The harmonic spectra for grid THD with SAPF is 3.28%, as depicted in Figure 23, indicating an enhancement in the performance and power quality of the system. Table 2 compares the THD analysis between the proposed method and existing approaches. The table displays different control strategies outlined in referenced papers, highlighting that the conventional methods utilizing solar PV, APF, and Grid control exhibit higher THD values compared to the proposed approach. In contrast, the proposed method integrates PV and HESS with RRC strategy, along with compensation techniques using APF, resulting in superior outcomes.

TABLE 2 A comparison study of THD between the proposed and existing methods.

Ref. No.	Existing methods	THD (%)	Advantages	Limitations
Panigrahi and Subudhi (2017)	Kalman filter (KF) based H_{∞} control scheme	4.1	The system acts as a self-regulator of V_{DC} without the need for a PI controller. Merely utilizing source current sensors is adequate to establish the reference current, reducing the overall cost of SAPF implementation	There is a higher variation in V_{DC} and settling time is more
Alfaris and Bhattacharya (2019)	Versatile convertible static transmission controller (CSTC)	3.3	Utilized in parallel building block converters to regulate power flow and enhance power quality and regulates stable V_{DC}	In real-world scenarios, two challenges could arise: the cost implications of an expanded power electronic system and increased control complexity resulting from integrating a PV source into a Back-to-Back VSCs system
Parchure et al. (2017)	UAPF + PV + Grid	3.9	Quasi-steady-state power flow serves as a reference for identifying solar customers who should be managed by the utility to provide reactive power support	The settling time is longer, and there is a failure to generate smooth and continuous PV power in real applications
Zahedmanesh et al. (2020)	An Adaptable Correlated Control + PV + Grid	4.4	Optimize active and reactive power independently, enabling the minimization of energy costs	Fail to generate smooth and continuous PV power in real-world applications
Saxena et al. (2017)	PV + MPPT + VSC + Grid	4.28	capability to generate maximum power under varying insolation and enhances the system's efficiency	Settling time is longer, and fail to generate smooth and continuous PV power in real-world applications
Rahmani et al. (2015)	PV + MPPT + APF + Grid	5	Suppress grid-end current harmonics and distortions, even when faced with unbalanced nonlinear load conditions	Fail to generate smooth and continuous PV power in real-world applications
Golla et al. (2023)	PV + BSS + UAPF	3.63	Suppress grid-end current harmonics and distortions, even when faced with unbalanced nonlinear load conditions	Sudden changes in battery currents have an impact on the battery system
Sharma et al. (2022)	PV + ESS + ESOGI-FLL-WIF Control Algorithm + Grid	3.6	It compensates for neutral current and controls RPC under unbalanced load conditions	Fail to generate smooth and continuous PV power and Sudden changes in battery currents have an impact on the battery system
Hoon et al. (2018)	SAPF + self-tuning filter (STF)+Grid	3.47	Accurately computing the fundamental components	The computational burden is higher, leading to time delays due to reliance on numerical filters, and is ineffective under non-ideal source voltage conditions
Barva and Arkdev (2023)	PV + APF + Grid	4.3	Operates efficiently in both balanced and unbalanced supply and load scenarios	Computational burden is higher and fail to generate smooth and continuous PV power
Proposed method	PV + HESS + RRC + APF + Grid	3.28	• Capable of generating smooth and continuous power • Able to remove battery current transients • Eliminates source current harmonics • Regulates stable V_{DC} • Enhances overall system performance	Necessary to consider the transition between modes

4 Conclusion

This paper introduces a RRC approach for enhancing the power quality of a PV system integrated with HESS. This method effectively mitigates harmonics and compensates for non-linear reactive power, offering simultaneous control over harmonic currents and RPC. HIL tests demonstrate the filtering of current and voltage waveforms. With the integration of a shunt APF, the grid THD is reduced to 3.28%, showcasing the robust filtering capabilities for harmonic currents and optimal compensation for reactive power. This improvement in power quality aligns with the IEEE-519 standard criterion. The output of the PV system fluctuates depending on the irradiance levels. When the PV power output is low, the battery steps in to provide power, ensuring a steady supply. By doing so, it smooths out fluctuations in PV power and maintains a constant voltage across the DC-link capacitor, resulting in more stable power delivery to the system. However, sudden changes in battery power can put stress on the battery. To address this issue, a SC is employed to eliminate transients from the battery, ensuring smoother operation. This combination of distributed generation with enhanced power quality offers a promising approach for future distribution systems.

5 Future scope

The inherent unpredictability of RESs poses significant technical hurdles in both grid and island-mode operations. Moreover,

designing suitable management strategies for ensuring the reliable and uninterrupted operation of the system demands careful attention to the transition between these modes. Therefore, future research will focus on implementing various control techniques and algorithms to enhance power quality in grid-integrated MGs equipped with HESSs. Additionally, the fluctuating output of PV power can be mitigated using advanced smoothing control techniques, which hold promise for large-scale power applications aiming to maintain stability and enhance overall system power quality. Furthermore, the effective implementation of advanced techniques for controlling HESS brings several benefits to renewable energy producers and system operators.

Data availability statement

The original contributions presented in the study are included in the article/supplementary material, further inquiries can be directed to the corresponding author.

Author contributions

GK: Conceptualization, Data curation, Formal Analysis, Methodology, Resources, Software, Validation, Writing–original draft, Writing–review and editing. KP: Investigation, Project administration, Supervision, Validation, Visualization, Writing–review and editing. ED: Funding acquisition, Investigation, Project administration, Supervision, Validation, Visualization, Writing–review and editing.

Funding

The author(s) declare that financial support was received for the research, authorship, and/or publication of this article. This work was supported by the Department of Science and Technology (DST), Government of India (GOI), with project grant SR/FST/ETI-420/2016(C) under the FIST scheme. It was also supported by the European Union Next-Generation EU (National Recovery and Resilience Plan (NRRP), Mission 4 Component 2 Investment 1.3) under the Network 4 Energy Sustainable Transition (NEST) Extended Partnership (Italian Ministry of University and Research Decree No. 1561 of 11/10/2022) under Project PE00000021.

Conflict of interest

The authors declare that the research was conducted in the absence of any commercial or financial relationships that could be construed as a potential conflict of interest.

Publisher's note

All claims expressed in this article are solely those of the authors and do not necessarily represent those of their affiliated organizations, or those of the publisher, the editors and the reviewers. Any product that may be evaluated in this article, or claim that may be made by its manufacturer, is not guaranteed or endorsed by the publisher.

References

Abdullah, A., Biswal, G. R., Roy, A. K., Ijaz, M., Parveen, S., Murtaza, S., et al. (2016). "Molecular diagnosis and phylogenetic analysis of human papillomavirus type-16 from suspected patients in Pakistan," in 2016 IEEE 1st International Conference on Intelligent Control and Energy Systems (ICPEICES), Delhi, India, July 4-6, 2016, 1–6.

Alfaris, F. E., and Bhattacharya, S. (2019). Control and real-time validation for convertible static transmission controller enabled dual active power filters and PV integration. *IEEE Trans. Ind. Appl.* 55 (4), 4309–4320. doi:10.1109/tia.2019.2910782

Barva, A. V., and Arkdev, (2023). "Analysis of SAPF based on p-q and SRF theory for different supply and load conditions," in 2023 International Conference on Power, Instrumentation, Energy and Control (PIECON), Aligarh, India, 10-12 February 2023, 1–6.

Belaidi, R., Hatti, M., Haddouche, A., and Larafi, M. M. (2013). "Shunt active power filter connected to a photovoltaic array for compensating harmonics and reactive power simultaneously," in 4th International Conference on Power Engineering, Energy and Electrical Drives, Istanbul, Turkey, 13-17 May 2013, 1482–1486.

Benchouia, M. T., Ghadbane, I., Golea, A., Srairi, K., and Benbouzid, M. E. H. (2015). Implementation of adaptive fuzzy logic and PI controllers to regulate the DC bus voltage of shunt active power filter. *Appl. Soft Comput.* 28, 125–131. doi:10.1016/j.asoc.2014.10.043

Beniwal, N., Hussain, I., and Singh, B. (2018). Control and operation of a solar PV-battery-grid-tied system in fixed and variable power mode. *IET Generation, Transm. Distribution* 12 (11), 2633–2641. doi:10.1049/iet-gtd.2017.1095

Brahmendra Kumar, G. V., Kumar, G. A., Eswararao, S., and Gehlot, D. (2018). "Modelling and control of BESS for solar integration for PV ramp rate control," in 2018 International Conference on Computation of Power, Energy, Information and Communication (ICCPEIC), Chennai, India, 28-29 March 2018, 368–374.

Brahmendra Kumar, G. V., and Palanisamy, K. (2019). A review on microgrids with distributed energy resources. *2019 Innovations Power Adv. Comput. Technol. (i-PACT)* 2019, 1–6. doi:10.1109/i-pact44901.2019.8960189

Dashtdar, M., Flah, A., Hosseinimoghadam, S. M., and El-Fergany, A. A. (2022). Frequency control of the islanded microgrid including energy storage using soft computing. *Sci. Rep.* 12, 20409–20418. doi:10.1038/s41598-022-24758-6

Devassy, S., and Singh, B. (2018). Design and performance analysis of three-phase solar PV integrated UPQC. *IEEE Trans. Ind. Appl.* 54 (1), 73–81. doi:10.1109/tia.2017.2754983

Devassy, S., and Singh, B. (2019). Implementation of solar photovoltaic system with universal active filtering capability. *IEEE Trans. Ind. Appl.* 55 (4), 3926–3934. doi:10.1109/tia.2019.2906297

Echalih, S., Abouloifa, A., Lachkar, I., Aroudi, A. E., Hekss, Z., Giri, F., et al. (2022). A cascaded controller for a grid-tied photovoltaic system with three-phase half-bridge interleaved buck shunt active power filter: hybrid control strategy and fuzzy logic approach. *IEEE J. Emerg. Sel. Top. Circuits Syst.* 12 (1), 320–330. doi:10.1109/jetcas.2022.3152535

Fabricio, E. L. L., Júnior, S. C. S., Jacobina, C. B., and Corrêa, M. B. (2018). Analysis of main topologies of shunt active power filters applied to four-wire systems. *IEEE Trans. Power Electron* 33, 2100–2112. doi:10.1109/tpel.2017.2698439

Golla, M., Thangavel, S., Simon, S. P., and Padhy, N. P. (2023). An enhancement of power quality with efficient active power transfer capability in a PV–BSS-fed UAPF for microgrid realization. *IEEE Syst. J.* 17 (1), 1614–1625. doi:10.1109/jsyst.2022.3179182

Gundumalla, V. B. K., and Eswararao, S. (2018). "Ramp rate control strategy for an islanded DC microgrid with hybrid energy storage system," in 2018 4th International Conference on Electrical Energy Systems (ICEES), Chennai, India, 7-9 February 2018, 82–87.

Hoon, Y., Radzi, M. A. M., Hassan, M. K., and Mailah, N. F. (2018). Operation of three-level inverter-based shunt active power filter under non-ideal grid voltage conditions with dual fundamental component extraction. *IEEE Trans. Power Electron* 33 (9), 7558–7570. doi:10.1109/tpel.2017.2766268

Jasim, A. M., Jasim, B. H., Flah, A., Bolshev, V., and Mihet-Popa, L. (2023). A new optimized demand management system for smart grid-based residential buildings adopting renewable and storage energies. *Energy Rep.* 9, 4018–4035. doi:10.1016/j.egyr.2023.03.038

Khan, I., Vijay., A. S., and Doolla, S. (2022). Nonlinear load harmonic mitigation strategies in microgrids: state of the art. *IEEE Syst. J.* 16 (3), 4243–4255. doi:10.1109/jsyst.2021.3130612

Kumar, G., Sarojini, R., Palanisamy, K., Padmanaban, S., and Holm-Nielsen, J. (2019). Large scale renewable energy integration: issues and solutions. *Energies* 12 (10), 1996–2017. doi:10.3390/en12101996

Kumar, G. V. B., and Palanisamy, K. (2019). "Interleaved boost converter for renewable energy application with energy storage system," in 2019 IEEE 1st International Conference on Energy, Systems and Information Processing (ICESIP), Chennai, India, 4-6 July 2019, 1–50.

Kumar, G. V. B., and Palanisamy, K. (2020). A review of energy storage participation for ancillary services in a microgrid environment. *Inventions* 5 (4), 63–36. doi:10.3390/inventions5040063

Kumar, G. V. B., and Palanisamy, K. (2023). Ramp-rate control for mitigation of solar PV fluctuations with hybrid energy storage system. *Distributed Generation Altern. Energy J.* 38 (03), 817–840. doi:10.13052/dgaej2156-3306.3835

Kumar, G. V. B., Palanisamy, K., Padmanaban, S., Holm-Nielsen, J. B., and Blaabjerg, F. (2020). Effective management system for solar PV using real-time data with hybrid energy storage system. *Appl. Sci.* 10 (3), 1–15. doi:10.3390/app10031108

Kumar, G. V. B., Palanisamy, K., and Tuglie, E. D. (2021). "Energy management of PV-Grid-Integrated microgrid with hybrid energy storage system," in 2021 International Conference on Environment and Electrical Engineering and 2021 IEEE Industrial and Commercial Power Systems Europe (EEEIC/ I&CPS Europe), Bari, Italy, 7-10 September 2021, 1–6.

Kumar, R., and Bansal, H. O. (2019). Hardware in the loop implementation of wavelet-based strategy in shunt active power filter to mitigate power quality issues. *Electr. Power Syst. Res.* 169, 92–104. doi:10.1016/j.epsr.2019.01.001

Kuznetsov, P., Kotelnikov, D., Yuferev, L., Panchenko, V., Bolshev, V., Jasiński, M., et al. (2022). Method for the automated inspection of the surfaces of photovoltaic modules. *Sustainability* 14 (19), 11930. doi:10.3390/su141911930

Liang, W., Liu, Y., and Shen, Y. (2023). Active power control integrated with reactive power compensation of battery energy stored quasi-Z source inverter PV power system operating in VSG mode. *IEEE J. Emerg. Sel. Top. Power Electron.* 11 (1), 339–350. doi:10.1109/jestpe.2021.3137397

Panigrahi, R., and Subudhi, B. (2017). Performance enhancement of shunt active power filter using a kalman filter-based h_{α} control strategy. *IEEE Trans. Power Electron.* 32 (4), 2622–2630. doi:10.1109/tpel.2016.2572142

Parchure, A., Tyler, S. J., Peskin, M. A., Rahimi, K., Broadwater, R. P., and Dilekm, M. (2017). Investigating PV generation induced voltage volatility for customers sharing a distribution service transformer. *IEEE Trans. Ind. Appl.* 53 (1), 71–79. doi:10.1109/tia.2016.2610949

Patel, N., Bansal, R. C., Adam, A. A., Elnady, A., and Hamid, A. K. (2023). Multimode control for power quality improvement in an electronically coupled distributed generation unit under grid connected and autonomous modes. *IEEE Trans. Power Deliv.* 38 (4), 2274–2289. doi:10.1109/tpwrd.2023.3237835

Pradeep Reddy, G., Kumar, Y. V. P., Kalyan Chakravarthi, M., and Flah, A. (2022). Refined network topology for improved reliability and enhanced dijkstra algorithm for optimal path selection during link failures in cluster microgrids. *Sustainability* 14 (16), 10367. doi:10.3390/su141610367

Rahmani, B., Li, W., and Liu, G. (2015). An advanced universal power quality conditioning system and MPPT method for grid integration of photovoltaic systems. *Electr. Power Energy Syst.* 69, 76–84. doi:10.1016/j.ijepes.2014.12.031

Rauf, A. M., and Khadkikar, V. (2015). Integrated photovoltaic and dynamic voltage restorer system configuration. *IEEE Trans. Sustain Energy* 6 (2), 400–410. doi:10.1109/tste.2014.2381291

Ray, P., Ray, P. K., and Dash, S. K. (2022). Power quality enhancement and power flow analysis of a PV integrated UPQC system in a distribution network. *IEEE Trans. Ind. Appl.* 58 (1), 201–211. doi:10.1109/tia.2021.3131404

Saxena, N., Singh, B., and Vyas, A. L. (2017). Single-phase solar PV system with battery and exchange of power in grid-connected and standalone modes. *IET Renew. Power Gen.* 11 (2), 325–333. doi:10.1049/iet-rpg.2016.0143

Sharma, R., Kewat, S., and Singh, B. (2022). Power quality improvement in SyRG-PV-BES-based standalone microgrid using ESOGI-FLL-WIF control algorithm. *IEEE Trans. Industry Appl.* 58 (1), 686–696. doi:10.1109/tia.2021.3128371

Tareen, W. U. K., and Mekhielf, S. (2018). Three-phase transformer less shunt active power filter with reduced switch count for harmonic compensation in grid-connected applications. *IEEE Trans. Power Electron* 33 (6), 4868–4881. doi:10.1109/tpel.2017.2728602

Wang, C., Yang, T., Hussaini, H., Huang, Z., and Bozhko, S. (2022). Power quality improvement using an active power sharing scheme in more electric aircraft. *IEEE Trans. Ind. Electron* 69 (4), 3588–3598. doi:10.1109/tie.2021.3076401

Wategaonkar, S. S., Patil, S. S., and Jadhav, P. R. (2018). "Mitigation of current harmonics using shunt active power filter," in 2018 3rd International Conference for Convergence in Technology (I2CT), Pune, India, 6-8 April 2018, 1–5.

Zahedmanesh, A., Muttaqi, K. M., and Sutanto, D. (2020). An adaptable correlated control for maintaining voltage quality in low-voltage distribution grids containing PVs and PEVs. *IEEE Trans. Industrial Inf.* 18 (9), 5804–5814. doi:10.1109/tii.2021.3131820

Frontiers in
Energy Research

Advances and innovation in sustainable, reliable and affordable energy

Explores sustainable and environmental developments in energy. It focuses on technological advances supporting Sustainable Development Goal 7: access to affordable, reliable, sustainable and modern energy for all.

Discover the latest Research Topics

See more →

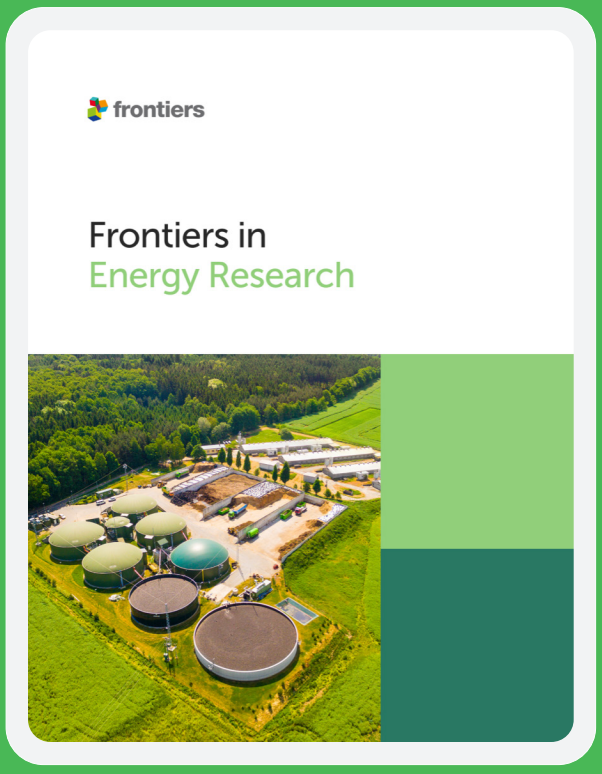

Frontiers

Avenue du Tribunal-Fédéral 34
1005 Lausanne, Switzerland
frontiersin.org

Contact us

+41 (0)21 510 17 00
frontiersin.org/about/contact